ELECTROMAGNETIC FIELDS IN MECHATRONICS, ELECTRICAL AND ELECTRONIC ENGINEERING

Studies in Applied Electromagnetics and Mechanics

Volume 27

Previously published in this series:

Vol. 26. G. Dobmann (Ed.), Electromagnetic Nondestructive Evaluation (VII)
Vol. 25. L. Udpa and N. Bowler (Eds.), Electromagnetic Nondestructive Evaluation (IX)
Vol. 24. T. Sollier, D. Prémel and D. Lesselier (Eds.), Electromagnetic Nondestructive Evaluation (VIII)
Vol. 23. F. Kojima, T. Takagi, S.S. Udpa and J. Pávó (Eds.), Electromagnetic Nondestructive Evaluation (VI)
Vol. 22. A. Krawczyk and S. Wiak (Eds.), Electromagnetic Fields in Electrical Engineering
Vol. 21. J. Pávó, G. Vértesy, T. Takagi and S.S. Udpa (Eds.), Electromagnetic Nondestructive Evaluation (V)
Vol. 20. Z. Haznadar and Ž. Štih, Electromagnetic Fields, Waves and Numerical Methods
Vol. 19. J.S. Yang and G.A. Maugin (Eds.), Mechanics of Electromagnetic Materials and Structures
Vol. 18. P. Di Barba and A. Savini (Eds.), Non-Linear Electromagnetic Systems
Vol. 17. S.S. Udpa, T. Takagi, J. Pávó and R. Albanese (Eds.), Electromagnetic Nondestructive Evaluation (IV)
Vol. 16. H. Tsuboi and I. Vajda (Eds.), Applied Electromagnetics and Computational Technology II
Vol. 15. D. Lesselier and A. Razek (Eds.), Electromagnetic Nondestructive Evaluation (III)
Vol. 14. R. Albanese, G. Rubinacci, T. Takagi and S.S. Udpa (Eds.), Electromagnetic Nondestructive Evaluation (II)
Vol. 13. V. Kose and J. Sievert (Eds.), Non-Linear Electromagnetic Systems
Vol. 12. T. Takagi, J.R. Bowler and Y. Yoshida (Eds.), Electromagnetic Nondestructive Evaluation
Vol. 11. H. Tsuboi and I. Sebestyen (Eds.), Applied Electromagnetics and Computational Technology
Vol. 10. A.J. Moses and A. Basak (Eds.), Nonlinear Electromagnetic Systems
Vol. 9. T. Honma (Ed.), Advanced Computational Electromagnetics
Vol. 8. R. Collins, W.D. Dover, J.R. Bowler and K. Miya (Eds.), Nondestructive Testing of Materials

Volumes 1–6 were published by Elsevier Science under the series title “Elsevier Studies in Applied Electromagnetics in Materials”.

ISSN 1383-7281

Electromagnetic Fields in Mechatronics, Electrical and Electronic Engineering

Proceedings of ISEF'05

Edited by

Andrzej Krawczyk

Central Institute for Labour Protection, Department of Bioelectromagnetics, Warsaw, Poland

Sławomir Wiak

Technical University of Lodz, Institute of Mechatronics and Information Systems, Lodz, Poland

and

Xose M. Lopez-Fernandez

University of Vigo, Department of Electrical Engineering, Vigo, Spain

IOS Press

Amsterdam • Berlin • Oxford • Tokyo • Washington, DC

ISBN 1-58603-627-0
Library of Congress Control Number: 2006928635

Publisher
IOS Press
Nieuwe Hemweg 6B
1013 BG Amsterdam
Netherlands
fax: +31 20 687 0019
e-mail: order@iospress.nl

Distributor in the UK and Ireland
Gazelle Books Services Ltd.
White Cross Mills
Hightown
Lancaster LA1 4XS
United Kingdom
fax: +44 1524 63232
e-mail: sales@gazellebooks.co.uk

Distributor in the USA and Canada
IOS Press, Inc.
4502 Rachael Manor Drive
Fairfax, VA 22032
USA
fax: +1 703 323 3668
e-mail: iosbooks@iospress.com

PRINTED IN THE NETHERLANDS

Electromagnetic Fields in Mechatronics, Electrical and Electronic Engineering
A. Krawczyk et al. (Eds.)
IOS Press, 2006

Preface

This book contains the papers presented at the International Symposium on Electromagnetic Fields in Mechatronics, Electrical and Electronic Engineering ISEF'05 which was held in Baiona, Spain on September 15–17, 2005. ISEF conferences have been organized since 1985 as a common initiative of Polish and European researchers who deal with electromagnetic fields applied to electrical engineering. Until now the conferences have been held every two years, either in Poland or in one of European academic centres renowned for electromagnetic research. The Royal Village of Baiona is well-known in the world for its beauty and historical background and meaning, as it was the place where Columbus landed after his travels to the New World. The venue of the conference is very close to Vigo, which is one of the most important cities in Spanish Galicia. The University of Vigo was the logistic centre of the conference.

It is the tradition of the ISEF meetings that they try to tackle quite a vast area of computational and applied electromagnetics. Moreover, the ISEF symposia aim at joining theory and practice, thus the majority of papers are deeply rooted in engineering problems, being simultaneously of high theoretical level. Continuing this tradition, we hope to touch the heart of the matter in electromagnetism.

After the selection process 211 papers were accepted for presentation at the Symposium and almost all of them were presented at the conference both orally and in the poster sessions. The papers have been divided into the following groups:

- *Computational Electromagnetics*
- *Electromagnetic Engineering*
- *Coupled Field and Special Applications*
- *Micro- and Special Devices*
- *Bioelectromagnetics and Electromagnetic Hazards*
- *Magnetic Material Modelling*

The papers which were presented at the symposium had been reviewed and assessed by the sessions' chairmen and the Editorial Board assembled for the post-conference issue of ISEF'05. All the papers accepted for further publication were divided into two parts: those of more computational and those of more applicable nature. The latter ones are published here while the first, which contains less papers (26), went to COMPEL journal.[1]

The papers selected for this volume have been grouped in three chapters which cover the topics:

- *Fundamental Problems*
- *Computational Electromagnetics*
- *Applied Electromagnetism*

[1] COMPEL: The International Journal for Computation and Mathematics in Electrical and Electronic Engineering, vol. 25, No. 3/2006.

They introduce some necessary order while reading the book and somehow represent the main directions which are penetrated by researchers dealing with contemporary electromagnetics. Looking at the content of the book one may also notice that more and more researchers are engaging in investigation of electromagnetic applications, especially these connected with mechatronics, information technologies, medicine, biology and material sciences. This is readily seen when looking at a number of papers which belong to each part of the book. Computational techniques which were under development during the last three decades and are still being developed serve as good tools for discovering new electromagnetic phenomena. This means that computational electromagnetics belongs to an application area rather than to research area. Anyway, a lot of researchers are still working on this subject.

The first chapter is devoted to fundamental problems which appear in electromagnetics. The subject has been intensively developed from the very beginning of the history of electromagnetism. Some problems are still the subject of scientific discussions and are still unsolved; other problems are discussed as the background for building numerical models. There is a group of papers dealing with the analysis of material properties (magnetic, dielectric or even biological), and thus the papers have more physical than computational considerations. Such an analysis is somehow out of the scope of international conferences, like COMPUMAG, AEM or CEFC, which rather focus their attention on computational aspects. Also, there are some papers in the chapter which show analytical solutions of the electromagnetic field problems. The analytical approach is nowadays mostly not of interest for researchers, especially those of the younger generation, but this attitude seems not to be supported by the reality of electromagnetism. The analysis of electromagnetic field sometimes requires deeper insight into the structure of mathematical model and this can be done just by means of analytical approach.

The second chapter is devoted to problems widely discussed at all conferences, namely how to improve the efficiency, accuracy and ability of numerical models. Older participants of the conference and readers of the book will remember that a few decades ago the majority of papers concentrated on the problems of how to build FEM solver or how to regard nonlinearity or dynamics in computer modelling. Also, there were strong discussions about the advantages and disadvantages of such numerical methods, such as FEM, FDM, BEM, and during the conferences followers of each particular method tended to form separate groups. Nowadays, these problems are mostly behind us and the interest of researchers is focused on some specific contributions to the existing solvers.

The last chapter, the richest in papers, is a good mirror of what the ISEF conference is. As has already been mentioned, most papers deal with some applications of electromagnetic field and the stress in these papers is put on the phenomena or devices or both, and computational technique is there just as a tool to understand the phenomena, to design a device or to know what hazards can occur. It seems to be very difficult, even impossible, to find some common idea which joins the papers in some groups because, in fact, each paper deals with its own particular problem. Prospective readers are recommended to look at this chapter very carefully and find the paper of their personal interest.

At the end of these remarks let us, the Editors of the book, be allowed to express our thanks to our colleagues who have contributed to the book by peer-reviewing the

papers at the conference as well as in the publishing process. We also convey our thanks to IOS Press (Publisher) for their effective collaboration in shaping this editorial enterprise. As ISEF conferences are organised biannually we do hope to keep our strong links with IOS Press in the future.

Xose M. Lopez-Fernandez
Chairman of the
Organising Committee

Andrzej Krawczyk
Scientific Secretary

Sławomir Wiak
Chairman of the ISEF
Symposium

This page intentionally left blank

Contents

This page intentionally left blank

Chapter A

Fundamental Problems

This page intentionally left blank

Electromagnetic Fields in Mechatronics, Electrical and Electronic Engineering
A. Krawczyk et al. (Eds.)
IOS Press, 2006

Chapter A

A.0 Introductory remarks

The first chapter is devoted to foundations of electromagnetism in its engineering issue. Therefore, while the discussed problems do not touch the electromagnetic phenomena in micro-scale or in very high or very low temperatures, they are fundamental enough to be dealt with in this Chapter. According to the logic of this book the fundamental problems cover:

- optimal design and system analysis,
- analytical solutions and their properties,
- electromagnetism in materials,
- teaching of electromagnetics.

The problems of optimal design and the system analysis constitute a very modern approach to electromagnetic engineering. These problems create the core of electromagnetism in engineering and technology. Therefore, a relatively large number of papers is devoted to such problems. The papers in this subgroup touch on the following subjects:

- co-evolutionary augmented lagrangian method (CEALM) applied to constrained optimization problem on the example of superconducting magnetic energy storage (SMES) optimization benchmark problem,
- criteria concerning extension of duality rule of E. Colin Cherry to the case of time varying networks,
- influence of thickness of electromagnetic screen is analyzed varying it for different plane shape ferromagnetic and conductive materials (Fe, Al and Cu),
- software tool dedicated to design of electromechanical devices based on a serial implementation of analytical (datasheet specification) and numerical procedure (sensitivity analysis),
- data structure optimization by implementing business rules in object-oriented model applied to a multi-physics numerical simulation software,
- calculation mode of mathematical model parameters starting from catalogue data presenting simplified mathematical model,
- microwave imaging technique for reconstructing the shape of two-dimensional perfectly conducting scatters by means of particle swarm optimization algorithm,
- Particle Swarm Optimisation used to find optimal geometry and excitation yielding best radial stiffness of levitated disc while maintaining strong and uniform axial support.

In spite of extensive development of numerical (computer) modelling, analytical solutions are still an attractive tool for looking at electromagnetic phenomena. Especially, they give possibilities to analyze influences of various factors on the final electromagnetic field solution. Also, analytical solutions are not to be overpriced in the teaching process. The short reviewing of the papers in this group shows that the papers deal with:

- system consisting of infinite long metal cylinder and two infinite long conductors perpendicular to its axis, which conduct AC current regarding displacement current,
- analytic approach to deal with vector diffusion problems into hysteretic materials,

- semi-analytical method of calculation of SAR (Specific Absorption Rate) coefficient with investigation of its distribution in model of human body,
- comprehensive procedure to determine radiation of a mobile phone in the presence of a human head by means of variational principle method and supplied boundary conditions using R-functions,
- software tool dedicated to design of electromechanical devices based on serial implementation of analytical and numerical procedure.

The third group gathers papers which deal with very important and difficult problems. Indeed, the real problem that researchers have to face is how to find electromagnetic parameters in matter with all the complexities it has. The papers in this subgroup address the problems of:

- effects of the kinetics of polarization switching in ferroelectrics, taking into account the spatial-temporal fluctuations of the polarization field, given by the Langevin and Fokker-Planck equations,
- new dynamical hysteresis model based on the second derivative of the measured reversal curves,
- relation of power losses caused by higher order harmonics with temporary shape of the wall which is connected with temporary value of fundamental harmonics.

And then the problems of teaching. Actually, we have one paper devoted to them but it is strongly believed that in many papers, placed here, the problem of education is somehow involved. Teachers all over the world discuss whether electromagnetism with related subjects should be considered in an inductive or deductive way. In other words, do we teach our students starting from very general laws, like Hamilton's theorem, and then go on to each particular equation and law or do we teach students starting from very simple models and then go on to more complicated equations like Maxwell's?

Electromagnetic Fields in Mechatronics, Electrical and Electronic Engineering 5
A. Krawczyk et al. (Eds.)
IOS Press, 2006

CO-EVOLUTIONARY APPROACH APPLIED TO THE CONSTRAINED OPTIMIZATION PROBLEM OF ELECTROMAGNETIC DEVICES

Kwang-Ok An, Chang-Hwan Im, and Hyun-Kyo Jung

ENG420-040, School of Electrical Engineering, Seoul National University, Shillim-dong, Kwanak-gu, Seoul 151-742, Korea, anko04@elecmech.snu.ac.kr, ichism@elecmech.snu.ac.kr, hkjung@snu.ac.kr

Abstract *– In this paper, co-evolutionary augmented lagrangian method (CEALM) is applied to the constrained optimization problem of electromagnetic devices. To verify the performance of the CEALM, it is applied to the superconducting magnetic energy storage (SMES) optimization benchmark problem. As a result, accurate global solution can be found with less computational efforts. However, the conventional CEALM has a problem that the convergence speed decreases as the solution approaches near a global optimum. In this paper, to solve the problem, an improved scheme for CEALM is proposed. The effectiveness of the improved CEALM will be proven by the comparison with the conventional one.*

Introduction

To solve highly constrained optimization problems, various approaches have been introduced. Unfortunately, most of conventional gradient-based deterministic methods failed to find an exact solution for complex constrained cases, due to some difficulties: First, constrained optimization problems may not satisfy some conditions (differentiability or convexity). Moreover, a computational cost abruptly increases as constraints of the problem become more complex. On the other hand, evolutionary algorithms have some advantages over the deterministic algorithms: the gradient information and initial guess are not required and the chance of finding global optimum is relatively high [1-4]. Nevertheless, the existing evolutionary algorithms have not been fully developed yet.

To solve constrained optimization algorithm, the existing evolutionary algorithms, proposed during the last few years, are usually grouped as follows [5]: 1) methods based on preserving feasibility of solutions, 2) methods based on penalty functions, 3) methods based on the superiority of feasible solutions over in feasible solutions, and 4) other hybrid methods [6]. To solve constrained optimization problems, a well-formulated co-evolutionary approach, named as the co-evolutionary augmented lagrangian method (CEALM), is proposed by M. J. Tahk, et al [1]. This method was firstly devised to solve minmax problems arising in robust control design and usually used for optimal evasion problems. Since it turns a constrained optimization problem into an unconstrained minmax problem using the augmented lagrangian method, it has a terrific merit that various types of constraints are handled in a very systematic manner.

In this paper, the CEALM is applied to the constrained electromagnetic devices optimization problem. Using the superconducting magnetic energy storage (SMES) optimization benchmark problem (TEAM workshop problem 22 [7]), it is demonstrated that accurate solution can be obtained very effectively. However, it has some disadvantage that the convergence speed decreases as the solution approaches near a global optimum. As a result, computational cost grows unnecessarily. In constrained electromagnetic optimization problems such as the SMES problem, because analysis time of electromagnetic devices occupies most of computational time, just to reduce the number of function calls can improve the whole computational efficiency. In this paper, therefore, to reduce the number of function calls, an improved procedure is proposed. At each generation, the standard deviation of solutions is calculated. Then, the type of evolutionary algorithm is changed when the standard deviation is reduced below a predetermined criterion. From this process, the number of function calls and

computational time can be considerably reduced. Finally, the effectiveness of the improved technique will be verified by the comparison with the conventional one.

CEALM for Electromagnetic Device Optimization

Co-evolutionary Augmented Lagrangian Method (CEALM)

As stated previously, the CEALM turns a constrained optimization problem into an unconstrained minmax problem using the augmented lagrangian formulation. The co-evolutionary algorithm consists of two population groups with opposite objective functions: the parameter vector $\boldsymbol{x}$, and the lagrangian multiplier $\boldsymbol{\lambda}$. The parameter vector group has a strategy minimizing the augmented lagrangian, whereas the lagrangian multiplier group has that maximizing it. Each group has its own evolutionary process and evolves to generate the best individual who guarantees the best payoff for the group itself. In this paper, evolution strategy is applied for this purpose. Fig. 1 shows the flowchart of the co-evolutionary algorithm for constrained optimization.

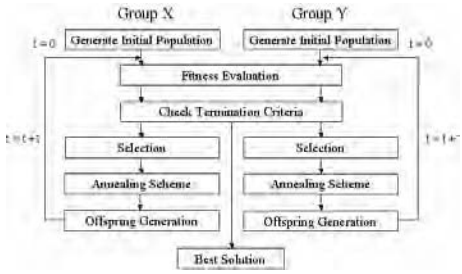

Fig. 1 Flowchart of co-evolutionary algorithm

The general constrained optimization problem is to find x which satisfying:

$$\min_{x} f(x), \quad x \in S \subset R^n \tag{1}$$

$$s.t. \quad g_i(x) \le 0, \; i = 1, \cdots, m \;, \quad h_j(x) = 0, \; j = 1, \cdots, l \tag{2}$$

where, objective function $f(x)$ is defined on the search space S. Usually, the search space is defined as a n-dimensional rectangle. Whereas, the feasible region, belonged to S, is defined by a set of additional constraints such as (2): the inequality constraints $g_i(x)$, and equality constraints $h_i(x)$. For this primal problem, the augmented lagrangian dual problem is expressed as

$$\max_{\lambda} L_A(\lambda) = \max_{\lambda} \min_{x} L_A(x, \lambda), \; \lambda \in R^k \;, \; k = m + l \tag{3}$$

$$s.t. \;\; \lambda_i \ge 0, i = 1, \cdots, m \tag{4}$$

where, the augmented Lagrangian is defined as

$$L_A(x, \lambda) = f(x) + \sum_{i=1}^{m} g_i(x, \lambda_i) + \sum_{i=1}^{l} \{\lambda_{m+i} h_i(x) + \rho \, h_i^2(x)\}. \tag{5}$$

As we can easily seen from (5), in the fitness evaluation processes, no further calculation of objective function and constraint functions is required for the multiplier group. It can reduce the computational cost considerably compared to the conventional '*single*' evolutionary method with augmented lagrangian method.

Numerical Model (SMES Optimization Benchmark)

The numerical model is SMES as depicted in Fig. 2. The SMES shall be optimized with respect to the following objectives: 1) the storage energy in the device should be 180 (MJ), 2) the magnetic field must not violate a certain physical condition which guarantee superconductivity, and 3) the stray field (measured at a distance of 10 meters from the device) should be as small as possible. To satisfy these conditions, the objective function of the problem is defined as

$$\min f(x) = \frac{B_{stray}^2}{B_{norm}^2} + \frac{|\, Energy - E_{ref}\,|}{E_{ref}} \tag{6}$$

$$B_{stray}^2 = \frac{\sum_{i=1}^{21} |\, B_{stray_i}\,|^2}{21} \tag{7}$$

where, E_{ref} = 180 (MJ) and B_{norm} = 3.0e-3 (T). In this model, only the inequality constraints exist. They are concerned with total current density of coil 1, 2. The constraints are given as

$$g_i(x) = J_i + 6.4\,|\,B_{\max,i}\,| - 56 \le 0,\ \ i = 1,2\ \ . \tag{8}$$

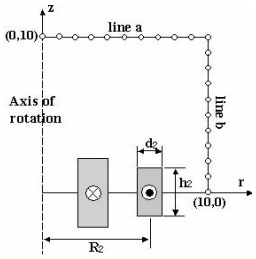

Fig. 2 The Structure of SMES Model

As seen from Fig.2, the SMES model has an axis-symmetric structure with three design variables – R_2, $h_2/2$, d_2. To calculate the objective function, axis-symmetric finite element method (FEM) is used. Each geometrical constraint and exact result of design variables is given in Table I.

TABLE I
THE GEOMETRICAL CONSTRAINTS AND EXACT RESULTS OF DESIGN VARIABLES

	R_2	$h_2/2$	d_2
Min.	2.6	0.204	0.1
Max.	3.4	1.1	0.4
Results	3.08	0.239	0.394

Simulation Results

As the type of evolutionary algorithm, (μ+λ) evolution strategy (ES) is selected. The (μ+λ) ES is that first parent individual reproduce, and later the best feasible individuals (from both parents and offspring) are selected for the next population. From such selection or mutation processes, more solutions can have an opportunity of survival than (1+1) ES. Hence, it reduces the risk of being trapped by a local solution, as well as avoiding premature freezing, i.e. this method can obtain more accurate results than (1+1) ES. In case of the co-evolutionary algorithm, the population ratio μ /λ is not a critical parameter since noticeable performance

degradation is not observed for any value of μ/λ between 0.1 and 0.3 [1]. Therefore, in this paper, (8+40) ES is used. The optimization is terminated when the populations converge the one point. Fig. 3 shows population distribution with respect to generation.

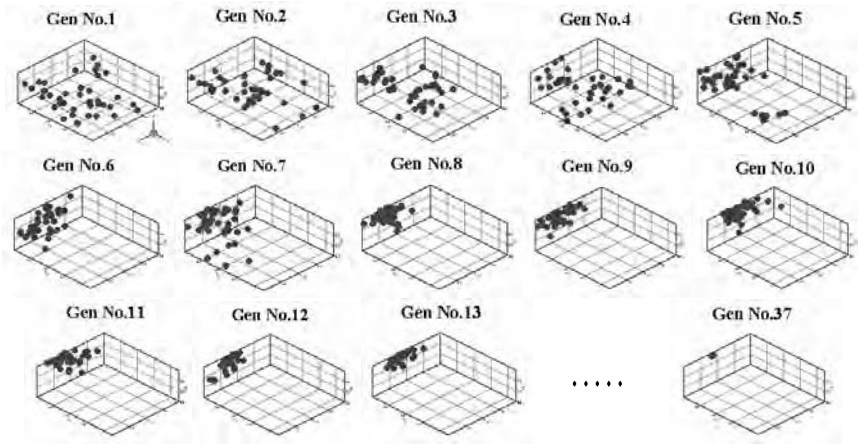

Fig. 3 The result of typical co-evolutionary algorithm with respect to generation

From the results, it can be concluded that the CEALM can be successfully applied to the electromagnetic optimization. However, it is also detected that the population is stationary from about 13th generation, i.e. the convergence speed decreases as the solution approaches near a global optimum. Due to this property, the unnecessary computational cost increases, although the populations are already gathered near the global optimum. Until the solutions perfectly converge to one point, total number of function calls and the computational time are measured as shown in Table II.

TABLE II
THE TOTAL NUMBER OF FUNCTION CALLS AND COMPUTATIONAL TIME IN TYPICAL CEALM

Total # of function calls	Computational time
1517	25341.9 [s]

Improvement of CEALM Process

From the results of conventional method, it is known that the computational cost increases needlessly. In the optimization of electromagnetic devices, the time for calculating objective function value is dominant compared to the other processes. Hence, just to reduce the number of function calls can improve the whole computational efficiency. In this paper, to improve the convergence rate, a modified procedure is proposed.

Basically, to apply the proposed procedure, the standard deviation of solutions should be calculated. If offspring of a generation are $x_1, x_2, \ldots, x_N$, the standard deviation is defined as follows:

$$s = \sqrt{\frac{1}{N}\sum_{i=1}^{N} x_i^2 - \bar{x}^2} \tag{9}$$

where, N represents the number of offspring and $\bar{x}$ is the average value of the offspring.

To begin with, $(\mu+\lambda)$ ES is used as the case of the conventional method. Then, the type of evolutionary algorithm is changed, when the standard deviation is reduced below a predetermined criterion. The criterion is

defined as (standard variation of initial generation) * α , where $\alpha = 0.2$ is used in this paper. When the standard deviation for a generation is reduced below the criterion, we can consider the situation as stationary state that the solutions are gathered near the global optimum and the risk of being trapped by the local optimum is little. Then, simple and fast optimization strategy, which uses only one population in evolution, is enough to solve the 'easy' optimization problem. Among various optimization schemes such as (1+1) ES, simulates annealing, etc., (1+1) ES is selected, because the already programmed (μ+λ) ES code can be used without any modification. The best solution and the standard deviation of previous generation are used for the initial parent and the initial variation width of (1+1) ES, respectively. The iteration for (1+1) ES is terminated, when the change of solution is not detected any more. The results for the SMES benchmark problem are shown in Fig. 4.
At 12th generation, the standard deviation of populations was decreased below the predetermined criterion. From 13th generation, (1+1) ES is applied. Only 24 additional function calls were required to obtain the exact optimum solution. Table III shows the total number of function calls and computational time for the improved technique.

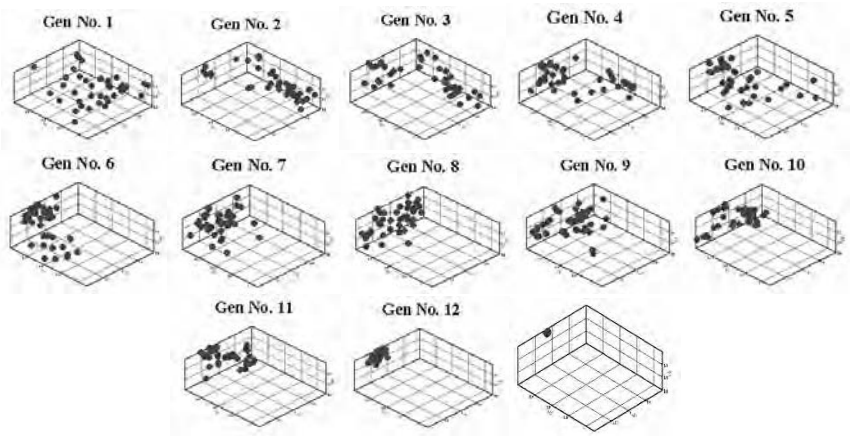

Fig. 4 The result of improved co-evolutionary algorithm with respect to generation

TABLE III
THE TOTAL NUMBER OF FUNCTION CALLS AND COMPUTATIONAL TIME IN IMPROVED CEALM

Total # of function calls	Computational time
515	8617.8 [s]

By the comparison of previous results, it can be seen that the improved technique yielded about 1/3 reduction of both total number of function calls and computational time. Therefore, it can be concluded that the optimization of electromagnetic devices can be performed more effectively, using the improved CEALM.

Conclusion

In this paper, the CEALM was applied to the constrained electromagnetic optimization problem. Using the SMES optimization benchmark problem, it was known that accurate solution can be obtained very effectively. However, the convergence speed decreases as the solution approaches near a global optimum. In this paper, therefore, to improve the convergence speed, a modified procedure was proposed, i.e. the type of evolutionary algorithm is changed with respect to the standard deviation of generation. From the results, it was verified that the constrained electromagnetic device optimization could be performed accurately and effectively, using the improved technique.

Appendix – Augmented Lagrangian Method

This section summarizes the key ideas of the augmented lagrangian methods [8]. Consider a constrained optimization problem

$$\min_x f(x), \quad x \in R^n \tag{10}$$

subject to

$$\begin{aligned} & g_i(x) \le 0, \ i=1,\cdots,m \ , \quad h_i(x)=0, \ j=1,\cdots,l. \\ & L_i \le x_i \le U_i \quad i=1,\cdots n \end{aligned} \tag{11}$$

Let S be the search space. For this primal problem, we have the lagrangian dual problem

$$\max_{\mu,\lambda} \theta(\mu,\lambda) \tag{12}$$

subject to

$$\mu_i \ge 0, \quad i=1,\cdots,m \tag{13}$$

where

$$\theta(\mu,\lambda) = \min_x \{ f(x) + \mu^T g(x) + \lambda^T h(x) \} \tag{14}$$

Here, μ is an $m\times1$ multiplier, and λ is an $l\times1$ multiplier for the inequality and equality constraints, respectively. If the primal problem is convex over S (f and g are convex and h is affine over S), the strong duality theorem states that

$$\begin{aligned} & \min\{ f(x); g(x) \le 0, h(x)=0, x \in S \} \\ & = \max\{ \theta(\mu,\lambda); \mu > 0 \} \end{aligned} \tag{15}$$

In fact, the solution x^* of the primal problem along with (μ^*,λ^*) of the dual problem satisfies the Kuhn Tucker condition, and corresponds to the saddle point of the Lagrangian function defined by

$$L(x,\mu,\lambda) = f(x) + \mu^T g(x) + \lambda^T h(x) \tag{16}$$

That is

$$L(x^*,\mu,\lambda) \le L(x^*,\mu^*,\lambda^*) \le L(x,\mu^*,\lambda^*) \tag{17}$$

for any $x \in S$ and $\mu \ge 0$. Note that the right side of (17) implies that x* is the unconstrained minimum of $L(x,\mu^*,\lambda^*)$. If (μ^*,λ^*) is known, then x^* can be searched in S without considering the constraints.

References

[1] Min-Jea Tahk, et al., "Coevolutionary Augmented Lagrangian Methods for Constrained Optimization," IEEE Trans. evolutionary computation, vol. 4, pp. 114-124, July, 2000

[2] Han-Lim Choi, et al., "Co-evolutionary Optimization of Three-dimensional Target Evasive Manever against a Proportionally Cuided Missile," IEEE Trans. evolutionary computation, vol. 2, pp. 1406-1413, 2001.

[3] Michalewicz, Z., et al., "Evolutionary Operators for Continuous Convex Parameter Spaces," 3rd Annual Conference on Evolutionary Programming, pp. 84-97, 1994

[4] Michalewicz, Z., et al., "Evolutionary Optimization of Constrained Problems," 3rd Annual Conference on Evolutionary Programming, pp. 98-108, 1994

[5] Jong-Hwan Kim, et al., "Evolutionary Programming Techniques for Constrained Optimization Problems," IEEE Trans. evolutionary computation, vol. 2, pp. 129-140, July, 1997

[6] Z. Michalewicz, et al., "Evolutionary Algorithms for Constrained Parameter Optimization Problems," Evol. Comput., vol. 4, pp. 1-32, 1996

[7] http://www-igte.tu-graz.ac.at/team/team3dis

Electromagnetic Fields in Mechatronics, Electrical and Electronic Engineering
A. Krawczyk et al. (Eds.)
IOS Press, 2006

ASSESSMENT OF INFLUENCE OF MAXWELL DISPLACEMENT CURRENTS ON ELECTROMAGNETIC FIELD'S DISTRIBUTION

Stanisław Apanasewicz, Stanisław Pawłowski

Technical University of Rzeszow,
35-959 Rzeszów, W. Pola 2, Poland,
sapanas@prz.rzeszow.pl, spawlo@prz.rzeszow.pl

Abstract ***- System consisting of infinite long metal cylinder and two infinite long conductors perpendicular to its axis, which conduct sinusoidally alternating (both in relation to time and spatial coordinate) exciting current is considered in the paper. Aim of the present work is estimate of influence of displacement currents on electrodynamics field's distribution in close zone.***

1. Aim of work

In case of calculation of eddy currents in metals, influence of displacement currents is very often omitted in dielectric area and close zone if frequencies are low. Authors of this paper noticed that it was not always possible. As evidence we present an example of system, where above mentioned simplification leads to essential errors.
We consider system consisting of infinite long metal cylinder and two infinite long conductors perpendicular to its axis, which conduct sinusoidally alternating (both in relation to time and spatial coordinate) exciting current. Studied system is presented on the Fig 1.

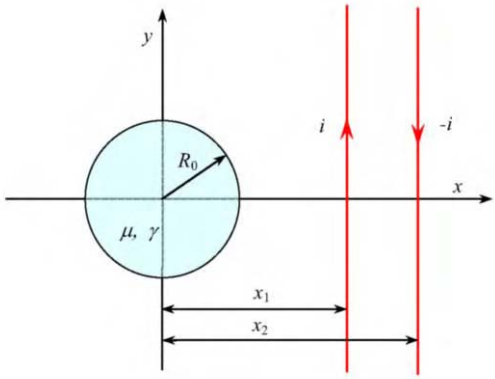

Fig. 1. Analysed system

We assume that:

a) For of exciting current is following:

$$i(y,t) = i_0 e^{j\omega t} \cos \lambda y \tag{1}$$

b) Cylinder's radius is enough large in comparison with depth of field's penetration that impedance boundary conditions may be applied.

One of solutions concerns the case, where ideal conductance of cylinder can be assumed. Consideration of more general case (for example more precise field structure inside a cylinder) is connected with incomparable more laborious mathematical calculations, though they have analytic form also and do not provide any essential matters refer to the main aim: convictions of persons calculating rotary currents that Maxwell's displacement currents should not be omitted inconsiderately.

2. Description of Electromagnetic Field

As a illustrating example we consider electromagnetic field in the system presented on Fig.1. As a basis of analyse we assume Helmholtz's equation, which must be fulfilled by vectors (complex amplitudes) of magnetic field strength $\boldsymbol{H}$ and electric field strength $\boldsymbol{E}$ in the air:

$$\Delta \boldsymbol{E} + k^2 \boldsymbol{E} = 0\,, \qquad \Delta \boldsymbol{H} + k^2 \boldsymbol{H} = 0\,, \qquad k = \frac{\omega}{c} \tag{2}$$

They result of Maxwell's equations:

$$rot\boldsymbol{H} = j\omega\varepsilon_0 \boldsymbol{E}\,, \qquad rot\boldsymbol{E} = -j\omega\mu_0 \boldsymbol{H} \tag{3}$$

We accept searched solutions of equations (2) and (3) in the following form:

$$\boldsymbol{E} = \boldsymbol{E}_0 + \boldsymbol{E}_i\,, \qquad \boldsymbol{H} = \boldsymbol{H}_0 + \boldsymbol{H}_i \tag{4}$$

where $\boldsymbol{H}_0$ and $\boldsymbol{E}_0$ – exciting field connected with flow of current (1) in the conductors in direction of y axis, and $\boldsymbol{H}_i$, $\boldsymbol{E}_i$ – field induced by eddy currents arisen in the metal cylinder.

2.1 Description of excited field

Electromagnetic field, excited by current flowing in conductors, can be calculated with use of generalized Biot-Savart's formulas, which take into account Maxwell's displacement currents. Omitting detailed mathematical operations, we present final formulas. Vector potential in Cartesian system $\boldsymbol{A}_{*0}$ has only one component in direction of y axis:

$$\boldsymbol{A}_{0*} = (0, A_{0*}, 0), \qquad A_{*0} = \frac{i_0 \mu_0}{2\pi} F(\rho_1, \rho_2) \cos \lambda y \tag{5}$$

where: $\rho_i^{\,2} = z^2 - (x - x_i)^2\,, \quad F(\rho_1, \rho_2) = F_0(\rho_1) - F_0(\rho_2)$

We use asterisk for designation of Cartesian components A_{1*} , A_{2*} A_{3*} as opposed to cylindrical components A_1, A_2, A_3 (radial, circumferential and axial, adequately). For the individual conductor:

$$F(\rho)=\begin{cases}\ln\rho, & \text{for } \lambda=0, \text{ or } \lambda=k=\dfrac{\omega}{c}\\ \mathrm{K}_0\left(\rho\sqrt{\lambda^2-k^2}\right), & \text{for } \lambda>k\\ -\dfrac{\pi}{2}j\mathrm{H}_0^{(2)}\left(\rho\sqrt{k^2-\lambda^2}\right), & \text{for } \lambda<k\end{cases} \tag{6}$$

Components of magnetic fields we calculate with use of formula $\boldsymbol{H}_* = \dfrac{1}{\mu_0} rot\boldsymbol{A}_*$:

$$H_{1*}=-\frac{i_0}{2\pi}F_z\cos\lambda y\,, \quad H_{2*}=0\,, \quad H_{3*}=\frac{i_0}{2\pi}F_x\cos\lambda y\,, \tag{7}$$

and electric field with use of formula (3):

$$E_{1*}=\frac{i_0}{2\pi}jpWF_x\sin\lambda y\,, \quad E_{2*}=-\frac{i_0\mu_0\omega}{2\pi}j\left(1-p^2\right)WF\cos\lambda y\,, \quad E_{3*}=\frac{i_0}{2\pi}jpWF_z\sin\lambda y \tag{8}$$

In formulas (7), (8):

$$W=\sqrt{\frac{\mu_0}{\varepsilon_0}}\,, \quad \lambda=pk\,, \quad p=\frac{\lambda c}{\omega}\,, \quad F_z=\frac{dF}{d\rho}\cdot\frac{z}{\rho}\,, \quad F_x=\frac{dF}{d\rho}\cdot\frac{x-x_i}{\rho} \tag{9}$$

Complex component of Poynting's vector in direction of axis is:

$$\Pi_{2*}=\frac{1}{2}\left[E_{1*}\overline{H}_{3*}-E_{3*}\overline{H}_{1*}\right] \tag{10}$$

Result of formulas (8) is $\Pi_{2*} = 0$, if $\lambda = 0$. It means that energy is not transported in direction of current's flow, what is unconformable with experiment.

2.2 Description of induced field

Applying method of variables' separation and taking into account the parity of current (1) in relation to y axis, we are able to present the solution of equation (2) for electric field and magnetic field (cylindrical components) in the following form:

$$E_{1i}=\int_0^\infty\left[\sum_{n=1}^\infty U_n(r,\tau)\sin n\theta\right]\cos\tau z d\tau\,, \quad E_{2i}=\int_0^\infty\left[\sum_{n=0}^\infty W_n(r,\tau)\cos n\theta\right]\cos\tau z d\tau\,,$$
$$E_{3i}=\int_0^\infty\left[\sum_{n=1}^\infty Q_n(r,\tau)\sin n\theta\right]\sin\tau z d\tau \tag{11}$$

$$H_{1i}=\int_0^{\infty}\left[\sum_{n=0}^{\infty}S_n^1(r,\tau)\cos n\theta\right]\sin\tau z\,d\tau\,,\quad H_{2i}=\int_0^{\infty}\left[\sum_{n=1}^{\infty}S_n^2(r,\tau)\sin n\theta\right]\sin\tau z\,d\tau\,,$$
$$H_{3i}=\int_0^{\infty}\left[\sum_{n=0}^{\infty}S_n^3(r,\tau)\cos n\theta\right]\cos\tau z\,d\tau \tag{12}$$

In formulas (11):

$$U_n=C_nK_{n-1}(\delta r)+C_n^*K_{n+1}(\delta r),\qquad W_n=C_nK_{n-1}(\delta r)-C_n^*K_{n+1}(\delta r),\qquad Q_n=\left(C_n+C_n^*\right)\frac{\delta}{\tau}K_n(\delta r)$$
$$\text{for}\quad n\neq 0,\ \text{and:}\quad W_0=C_0K_1(\delta r),\qquad \delta^2=\tau^2-k^2 \tag{13}$$

Next, taking into account equations (3), we will obtain relations between factors U_n, W_n, Q_n and S_n^1, S_n^2, S_n^3

$$S_n^1=\frac{j}{\omega\mu_0}\left(C_nR_n+C_n^*R_n\right),\quad R_n=\frac{\delta n}{\tau}\cdot\frac{1}{r}K_n(\delta r)+\tau K_{n-1}(\delta r),\quad R_n^*=\frac{\delta n}{\tau}\cdot\frac{1}{r}K_n(\delta r)-\tau K_{n+1}(\delta r)$$
$$S_n^1=-\frac{j}{\omega\mu_0}\left(C_nG_n+G_n^*R_n\right),\quad G_n=-\frac{\delta^2 n}{\tau^2 r}K_n(\delta r)+\frac{k^2}{\tau^2}K_{n-1}(\delta r),\quad G_n^*=\frac{\delta^2 n}{\tau^2 r}K_n(\delta r)+\frac{k^2}{\tau}K_{n+1}(\delta r),$$
$$S_n^3=-\frac{j\delta}{\omega\mu_0}\left(C_n-C_n^*\right)K_n(\delta r),\quad \text{for}\quad n\neq 0,\ \text{and:}\ S_0^1=\frac{j\tau C_0}{\omega\mu_0}K_1(\delta r)\,,\ S_0^3=-\frac{j\delta C_0}{\omega\mu_0}K_0(\delta r) \tag{14}$$

Obtained form of solutions is correct also for $\lambda = 0$: then $\delta = \tau$. As it is seen, full description of electromagnetic field is expressed as a dependence on two sequences of factors: C_n and C_n^*. Their calculation can be performed on the basis of boundary conditions on the surface of cylinder for $r = R$. We have for the ideally conducting cylinder ($\gamma=\infty$):

$$E_{2i}(R,\theta,z)+E_{2*}(R,\theta,z)\cos\theta-E_{1*}(R,\theta,z)\sin\theta=0$$
$$E_{3i}(R,\theta,z)+E_{3*}(R,\theta,z)=0 \tag{15}$$

If depth of field penetration is small in comparison with its radius R, we use boundary conditions of impedance type (Leontovitch's conditions)

$$E_{2i}+E_{2*}\cos\theta-E_{1*}\sin\theta=-\frac{\alpha}{\gamma}\left(H_{3i}+H_{3*}\right)$$
$$E_{3i}+E_{2*}=\frac{\alpha}{\gamma}\left(H_{2i}+H_{2*}\cos\theta-H_{1*}\sin\theta\right) \tag{16}$$

Factors C_n and C_n*, obtained on such bases, have very complex form and for the sake of limited amount of place we do not present them.

3. Examples of Numerical Calculation

Algorithm described above was the basis for a computing programs written in Fortran 77 and adopted to widely available personal computers. Some results of calculations are presented below on the graphs (Fig. 2, 3). Parameters of exemplary model are: $R_0 = 0.1$m, $x_1 = 0.2$m, $x_2 = 0.3$m, $i_0 = 1$A, $f =$ 50Hz.

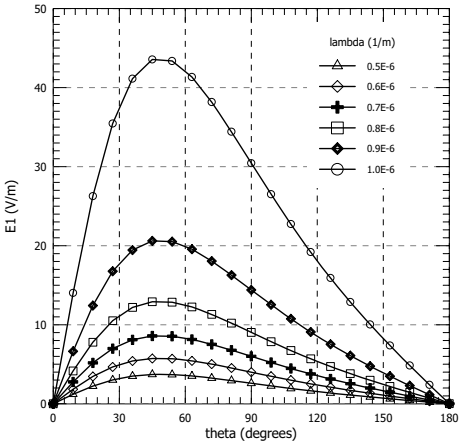

Fig.2 Distribution of the radial component of electric field intensity on the cylinder surface, for $z = 0$, and different parameters λ (see eq. (1)).

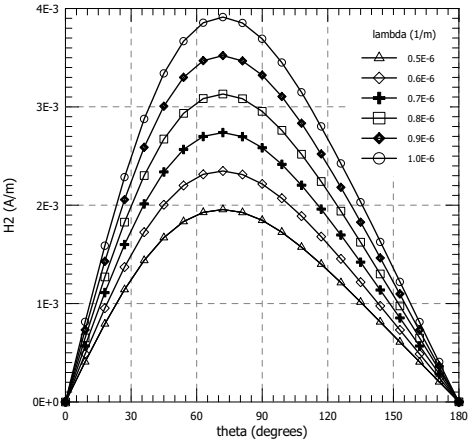

Fig.3 Distribution of the circuital component of magnetic field intensity on the cylinder surface, for $z = 0$, and different parameters λ (see eq. (1)).

4. Conclusions

By omitting Maxwell's displacement currents, we omit exciting electric field perpendicular to the conductors. It means that transportation of electromagnetic energy in direction of current flow (formula (10)) is omitted, what is physically incorrect. In the close zone, influence of Maxwell's displacement currents on magnetic field distribution is significantly smaller then influence on electric field.

Electromagnetic Fields in Mechatronics, Electrical and Electronic Engineering
A. Krawczyk et al. (Eds.)
IOS Press, 2006

DUAL ELECTRIC AND MAGNETIC NETWORKS: EXTENSION TO TIME-VARYING AND HYSTERETICAL CONDITIONS

°A. Giovanni Beccuti, *Sonia Leva, *Adriano P. Morando

°Institut fur Automatik, ETH Zürich, Physikstrasse 3, Zürich, Switzerland
e-mail: beccuti@control.ee.ethz.ch
*Dipartimento di Elettrotecnica, Politecnico di Milano, Piazza Leonardo da Vinci 32, Milano, Italy
e-mail:sonia.leva@polimi.it, adriano.morando@polimi.it

Abstract *– **Having defined the applicative limits of the duality rule of E. Colin Cherry, the criteria concerning the extension to the case of time varying networks is analyzed. A topological criterion emerges that, while confirming the efficacy already seen for the analysis of transformers, is suited for being adapted in a unified interpretation involving rotating machinery**.*

Introduction

The analysis originally performed by Colin Cherry [1] on magnetically coupled electrical circuits emphasizes the duality relation correlating magnetic networks associated to magnetoelectric systems in quasi stationary conditions and the corresponding electric circuits. This analysis translates into an extremely efficacious "duality topological rule" whose application (Fig. 1) allows the formal transition, by means of a direct topological inspection, from the original magnetic circuit constructed on the basis of the magnetic field map to the related electrical network. The applicability of such an analysis, of great conceptual utility, is subordinated to the following preliminary requirements:

a) The magnetic graphs must be planar;
b) The windings must all feature the same number of turns;
c) There must be no more than three windings [2][1];
d) The characteristic relations pertaining to the single flux tubes, although not necessarily linear, must nonetheless exhibit no hysteresis nor time varying features.

Retaining conditions (a) and (c), requirement (b) assumes a purely formal nature. Indeed, as is frequently done in applications, it can be conveniently circumvented simply by taking the number of turns to be a priori different and subsequently introducing an appropriate set of ideal transformers taking this into account. This procedure may be subsumed by the related correspondences depicted in Table I, wherein p=d/dt is the Heaviside operator [3][2].

---

[1] Technicallly the duality method can be employed also for a higher number of windings by neglecting multiply linked leakage fluxes.

[2] Consider a simply connected magnetic graph. Assuming that all windings have the same number of turns, mesh analysis yields:

$[m] = N \cdot [i] = [\vartheta] \cdot [\varphi]$

wherein $[\vartheta]$ is the equivalent reluctance matrix with respect to the averagely linked cyclic fluxes. If these fluxes vary in time, the following fems are induced in the windings linked with them:

$[v] = Np[\varphi]$

By solving with respect to the currents, one then obtains:

$$[i] = \frac{1}{N^2 p}[\vartheta][v] = \left[\frac{1}{Lp}\right] \cdot [v]$$

Such a system, representative of the relation between the currents circulating in the different windings and the fems therein induced, can be interpreted as the *independent nodal equations* of an electrical network where [v] are the *independent poten-*

Table I. Duality transformation for topologically deducing the electric circuit from the magnetic one

	Magnetic Circuit	Electric Circuit
Circuit elements	MMF: m=Ni	Current source: i
	pψ	v
	Reluctance: ϑ	Operational susceptance: $\frac{1}{Lp} = \frac{\vartheta}{N^2 p}$
Topology	Meshes	Nodes
	Nodes	Meshes

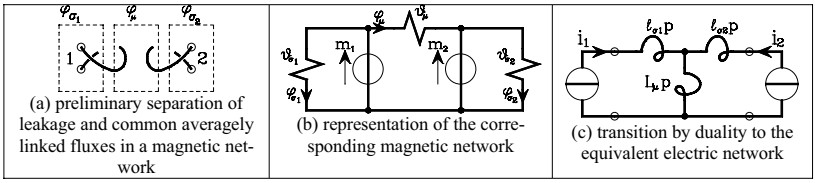

(a) preliminary separation of leakage and common averagely linked fluxes in a magnetic network

(b) representation of the corresponding magnetic network

(c) transition by duality to the equivalent electric network

Fig.1. An applicative example of Cherry's rule: the case of the mutual inductor with n=2

Dual electric and magnetic networks: the role of the characteristic relation

Concerning the characteristic relations, it may be preliminarly observed how the eventually present non linearities do not limit in any way the applicability of the method as they affect only the typology and not the topology of the circuit [4, 5]. The magnetizing reluctances ϑ_μ may be viewed as monotonous functions of the related excitation currents i_μ, and the leakage reluctances ϑ_σ remain linear. The case in which hysteretical phenomena are present however is quite different, as then it is the very topology of the graphs that is modified. This can also be established with the traditional "intuitive" approach [6] provided that one observes that the energetic equivalence of the electric network representative of the circuit is obtained connecting appropriate energetically equivalent conductances in parallel to the magnetizing reactances. It has furthermore been proven [2,7] how, with the assumption that one is operating in an "equivalent sinusoidal steady state", the duality rule can still be applied even in the presence of hysteresis. Indeed, what is required is to substitute the real hysteresis cycle with an ellipse of equal area. In this way the losses due to hysteresis remain the same and the characteristic relation can be formalized in an equivalent phasorial expression $\overline{B} = \overline{\mu} \cdot \overline{H}$. The magnetizing reluctance in this case takes on a complex series formulation $\overline{\vartheta}_\mu = \vartheta_r + j\vartheta_i$, to which, by duality, a complex parallel inductance whose real component G is representative of hysteretical losses may be associated. To the authors' best knowledge the topological aspects related to the case for which the characteristic relation is expressed by the functional F(b,h)=0, typically pertaining to hereditary phenomena, have not been investigated as yet.

Time varying conditions, for which the characteristic relation, in the absence of hereditary phenomena, become of the type[3] f(b,h,t)=0 are not usually considered. Assuming that one were to employ Cherry's rule uniquely for the case of transformers, one hypothesizes that the magnetic network be necessarily

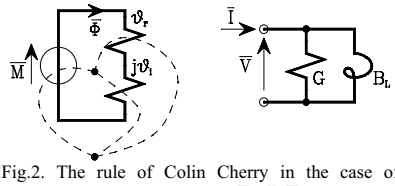

Fig.2. The rule of Colin Cherry in the case of complex characteristic relation $\overline{B} = \overline{\mu} \cdot \overline{H}$.

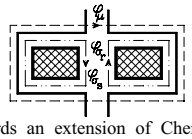

Fig.3. Towards an extension of Cherry's rule for rotating machinery.

tials and [1/Lp] are the *self and mutual operational susceptances* relative to the various *independent nodes*. From the comparison between the first system involving the meshes and the second involving the nodes one can deduce that the process by which fluxes arise in a magnetic circuit because of the fmms is dual to that through which fems emerge due to the current circulating in the windings. One can conclude that the circuits relative to the two phenomena can be deduced one from the other through duality by employing the rules shown in Table I.

time-invariant so that one can deduce through duality the electric correspondent starting from the magnetic configuration. The extension to the time varying case, when it is considered, has an educational purpose. This is the case of the simple (Fig.3) [6] or double cage asynchronous machine. In any case the analysis is carried out with reference to the operation of the machine in three phase sinusoidal direct sequence steady state. In this way the statoric and rotoric fields at the air gap are in relative rest and therefore allow the application of Cherry's rule.
On the other hand, were one to consider, as is the case in the unified theory of rotating machines, the presence of dynamics for which the stator and rotor fields are not in relative rest, then one proceeds directly by operating uniquely on the electric network [8]. In such a case, having observed that (Fig.4):

$$v(t) = pL(t)\cdot i(t) = L(t)pi(t) + i(t)\dot{\xi}\frac{d}{d\xi}L(\xi) = e_i(t) + e_m(t) \tag{1}$$

$\xi(t)$ being the Lagrangian coordinate of the system, the time varying magneto-electric system can be directly represented with an electric network (Fig. 4) deduced from its time invariant configuration having added onto this the controlled voltage source representing the motional contribution. This is the case for example of the mutual time varying inductor (Fig.5):

$$[v] = [R]\cdot[i] + p[L(\vartheta)]\cdot[i] = [R]\cdot[i] + [L(\vartheta)]p[i] + \Omega[dL/d\vartheta]\cdot[i] \tag{2}$$

The correspondence with the original magnetic network interpreting the map of the magnetic field on the other hand is not taken into account. It is therefore of interest to investigate the sense of such a correspondence even in the case in which time-varying features are present. Such an investigation is im-

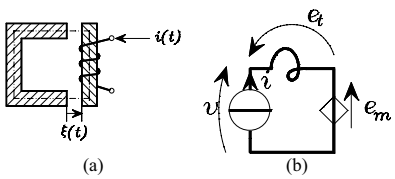

Fig.4. Time-varying magnetoelectric system with one mesh and corresponding electric network.

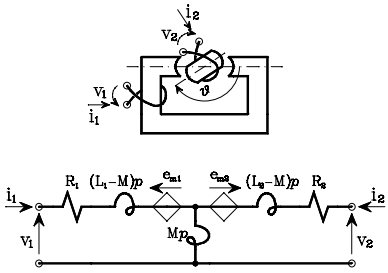

Fig.5. The time varying case for n=2

posed by two relevant necessities. The first is related to the fact that if this were not done then this theory, conceived for transformers, would not be extendable to rotating machinery and would therefore result in only being partially complete. The second corresponds instead to a specific requirement of methodological unity and consistency. In this sense it is part of a research line of activity developed by the authors and having as objective the re-interpretation and advancement of magnetic circuit theory from the point of view of hysteretical phenomena [7], from the systems theory aspect by considering state models and their related order [9], and, in the case of the present paper, from the viewpoint of the relative motion between the various field sources.
Bearing this in mind, after having recalled the methodological foundations of time-invariant magnetic circuit theory, the further step to the time-varying case will be made and, from here, as an extension to Cherry's classic rule, the duality correspondence with the related electric circuit will be made.

The notion of magnetic circuit: the role of time-variance

Having formulated, on the basis of the vortices and sources field equations, the notion of electric network:

[3] In this paper F indicates a functional and f a function.

$$\begin{cases} \nabla \times \mathbf{e} = 0 \\ \nabla \bullet \mathbf{j} = 0 \\ \mathbf{j} = \sigma \cdot (\mathbf{e} + \mathbf{e}^*) \end{cases} \Rightarrow \begin{cases} \int_A^B \mathbf{e} \bullet \mathbf{t}\, ds = v_A - v_B \overset{\Delta}{=} v \\ \int_{\Gamma_{AB}} \mathbf{e}^* \bullet \mathbf{t}\, ds \overset{\Delta}{=} e \\ \int_\Sigma \mathbf{j} \bullet \mathbf{n}\, dS \overset{\Delta}{=} i \end{cases} \Rightarrow \begin{cases} \sum_{meshes} v = 0 \\ \sum_{cuts} i = 0 \\ v + e = Ri \end{cases} \tag{3}$$

the subsequent concept of magnetic circuit is deduced in terms of formal correspondence, having observed that the magnetic field represented by it is expressed by vortices and sources equations and by ensuing circuit relations expressible in the following way:

$$\begin{cases} \nabla \times \mathbf{h} = \mathbf{j} \\ \nabla \bullet \mathbf{b} = 0 \\ \mathbf{b} = \mu \cdot \mathbf{h} \end{cases} \Rightarrow \begin{cases} \int_A^B \mathbf{h} \bullet \mathbf{t}\, ds = u_A - u_B \overset{\Delta}{=} u \\ \int_{\Gamma_{AB}} \mathbf{j} \bullet \mathbf{n}\, ds \overset{\Delta}{=} m \\ \int_\Sigma \mathbf{b} \bullet \mathbf{n}\, dS \overset{\Delta}{=} \varphi \end{cases} \Rightarrow \begin{cases} \sum_{meshes} u = 0 \\ \sum_{cuts} \varphi = 0 \\ m + u = \vartheta \varphi \end{cases} \tag{4}$$

The correspondence between the two types of phenomena, solely of formal nature, is naturally such provided that the different boundary conditions, implicit in the transition conductor-air for the electric case and in the transition ferromagnetic material-air, be neglected. Another important aspect is then the difference in the two energetic processes. Conductive, and therefore dissipative, in the first case, displacive and therefore conservative in the second. The deduction of the magnetic current is then immediate, as shown for example in Fig.6. Taking into account –for a higher degree of generality- the leakage flux φ_σ that, linked with the solenoid that generates it, does not reach the other column and closes itself in air (Fig.6a), from the map thus drawn one can trace the circuit in Fig.6b.
In the case of a time varying circuit the air gaps will be regarded as a given function of time. The deduction of the circuit equations then requires the formulation of the field equations (3) for the two observers S, stationary with respect to the solenoid carrying current density j, and S', moving with speed **u** with respect to S. Taking into account, respectively, the hypotheses of quasi stationary steady state operation and of negligibility of the velocity **u** if compared to the speed of light from the relations $\frac{\partial}{\partial t}\mathbf{d} \cong 0$ and $\mathbf{u}/c \cong 0$ the field equations for the two observers S and S' are of the same type:

$$S \begin{cases} \nabla \times \mathbf{e} = -\frac{\partial}{\partial t}\mathbf{b} \\ \nabla \times \mathbf{h} = \mathbf{j} \\ \nabla \bullet \mathbf{b} = 0 \\ \nabla \bullet \mathbf{d} = \rho \\ \nabla \bullet \mathbf{j} + \frac{\partial}{\partial t}\rho = 0 \end{cases} \Leftrightarrow S' \begin{cases} \nabla \times \mathbf{e}' = -\frac{\partial}{\partial t}\mathbf{b}' \\ \nabla \times \mathbf{h}' = \mathbf{j}' \\ \nabla \bullet \mathbf{b}' = 0 \\ \nabla \bullet \mathbf{d}' = \rho' \\ \nabla \bullet \mathbf{j}' + \frac{\partial}{\partial t}\rho' = 0 \end{cases} \tag{5}$$

and correlate the fields as seen from S and S' in the following form:

$$\begin{cases} \mathbf{j}' = \mathbf{j} - \rho \mathbf{u} & \rho = \rho' \\ \mathbf{e}' = \mathbf{e} + \mathbf{u} \times \mathbf{b} & \mathbf{h}' = \mathbf{h} - \mathbf{u} \times \mathbf{d} \\ \mathbf{d}' = \mathbf{d} & \mathbf{b}' = \mathbf{b} \end{cases} \tag{6}$$

The theory of magnetic circuits as seen from the observer S then yields:

$$\begin{cases} \oint_\Gamma h \bullet t\, ds = \int_{\Gamma_{fe}} h \bullet t\, ds + \int_{\Gamma_{\xi(t)}} h \bullet t\, ds = \{\vartheta_\mu + \vartheta_\xi(t)\} \cdot \varphi(t) = \int j \bullet n\, dS = Ni(t) \\ \oint b \bullet n\, dS = \sum \varphi(t) = 0 \end{cases} \tag{7}$$

Analogous relations can be obtained for S' having observed that:

$$\int \mathbf{h}' \bullet \mathbf{t}\, ds = \int \{\mathbf{h} - \mathbf{u} \times \mathbf{d}\} \bullet \mathbf{t}\, ds \cong \int \mathbf{h} \bullet \mathbf{t}\, ds \tag{8}$$

The following then holds:

$$\begin{cases} \oint_{\Gamma} \mathrm{h}' \bullet \mathrm{t}\, ds = \int_{\Gamma_{fe}} \mathrm{h}' \bullet \mathrm{t}\, ds + \int_{\Gamma_{\xi(t)}} \mathrm{h}' \bullet \mathrm{t}\, ds = \{\vartheta_{\mu} + \vartheta_{\xi}(t)\} \cdot \varphi'(t) = \int \mathrm{j}' \bullet \mathrm{n}\, dS \\ \oint \mathrm{b}' \bullet \mathrm{n}\, dS = \sum \varphi'(t) = 0 \end{cases} \tag{9}$$

Observing that:

$$\begin{cases} \varphi' = \int \mathbf{b}' \bullet \mathbf{n}\, dS = \int \mathbf{b} \bullet \mathbf{n}\, dS = \varphi \\ \mathrm{m}' = \int \mathbf{j}' \bullet \mathbf{n}\, \mathrm{dS} = \int (\mathbf{j} - \rho \mathbf{u}) \bullet \mathbf{n}\, \mathrm{dS} = \mathrm{m} \end{cases} \tag{10}$$

one can deduce the full invariance of magnetic circuit theory with regard to the two observers S and S'.

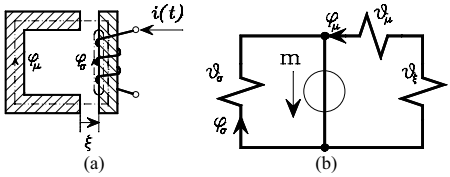

Fig.6. Deduction of the magnetic network in the time invariant case.

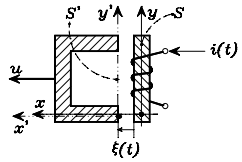

Fig.7. The manetic network in the time varying case. Two stationary and moving reference frames are employed.

Dual electric and magnetic networks: the presence of time-variance

Concerning duality, one must also consider at the circuit level and on the basis of a rule obtained by topological means the motional contribution. With reference to the network in Fig.6b, neglecting for simplicity the leakage flux, one has:

$$\mathrm{Ni}(t) = \vartheta(t) \cdot \varphi(t) = \{\vartheta_{\mu} + \vartheta(\xi)\} \cdot \varphi(t) \tag{11}$$

from which, in terms of the characteristic relation:

$$\mathrm{i}(t) = \left\{\frac{\vartheta_{\mu} + \vartheta(\xi)}{\mathrm{N}}\right\} \varphi(t) = \left\{\frac{\vartheta_{\mu} + \vartheta(\xi)}{\mathrm{N}^2}\right\} \psi(t) = \left\{\frac{1}{\mathrm{N}^2 \mathrm{p}} (\vartheta_{\mu} + \vartheta(\xi))\right\} \mathrm{v}(t) = \left\{\frac{1}{\mathrm{L}(t)\mathrm{p}}\right\} \mathrm{v}(t) \tag{12}$$

The correspondence between mesh reluctances and operational susceptances can also be found in this case, bearing in mind that to the original time varying reluctance – representable as the sum of two reluctances - a time varying operational susceptance sum of two operational susceptances is associated. By expressing (2) in the form:

$$\mathrm{v}(t) = \mathrm{pL}(t) \cdot \mathrm{i}(t) = \left\{\mathrm{L}(t)\mathrm{p} + \dot{\xi} \frac{\mathrm{d}}{\mathrm{d}\xi} \mathrm{L}(\xi)\right\} \cdot \mathrm{i}(t) \tag{13}$$

(12) becomes:

$$\mathrm{i}(t) = \left\{\frac{1}{\mathrm{L}_{\mu}\mathrm{p}} + \frac{1}{\mathrm{L}(\xi)\mathrm{p} + \mathrm{u} \dfrac{\mathrm{dL}(\xi)}{\mathrm{d}\xi}}\right\} \mathrm{v}(t) \tag{14}$$

which recalls the network in Fig.8. The extension of duality to the time varying case therefore implies, regarding the time varying reluctances, the substitution of the transform inductance

Lp with the more general series connection (Lp+pL) of the tranformer and motional inductances.

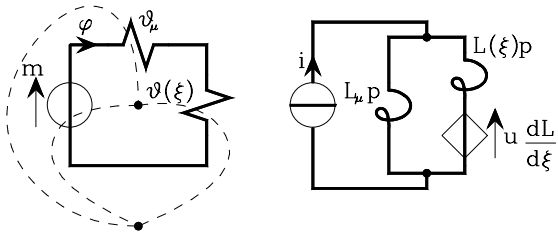

Fig.8. An example of magnetoelectric duality in the time varying case.

Table II. Duality transformation in presence of time variance

	Magnetic Circuit		Electric Circuit	
Circuit elements and Typology	MMF: m=Ni		Current source: i	
	pψ		v	
	Reluctance	ϑ	Inductance	$\frac{1}{Lp}=\frac{\vartheta}{N^2p}$
		Hysteresis $\overline{\vartheta}_\mu=\vartheta_r+j\vartheta_i$		$\overline{Y}=\frac{\vartheta_i}{\omega N^2}-j\frac{\vartheta_r}{\omega N^2}=G-jB_L$
		Time variance $\vartheta(t)=\vartheta_\mu+\vartheta(\xi)$		$\frac{1}{L_\mu p}+\frac{1}{L(\xi)p+u\frac{dL(\xi)}{d\xi}}$
Topology	Meshes		Nodes	
	Nodes		Meshes	

Conclusions

The duality rule of Colin Cherry, conceived for the transformer case, can be extended to time varying systems by furthermore considering the relevant connection of the additional motional contribution. There is thus conceptual unity of the topological magnetolelectric correspondence regarding the cases of static and rotating machinery. The result relates to the formal invariance of the Maxwell equations when changing from a stationary to a moving reference frame.

References

[1] E. Colin Cherry, *The duality of interlinked electric and magnetic circuits and the formation of transformer equivalent circuits*, Proc. Phys. Soc. of London (B), 1949, Vol. 62, p. 101;
[2] S. Leva, A.P. Morando, *Topological transition from magnetic networks to the electric equivalent ones when iron losses are presemt*, Proc. 43rd IEEE Midwest Symposium on Circuit and Systems (MWSCAS), Lansing-USA, 2000, n.pp.4
[3] Slow Transient Task Force of the IEEE Working Group on Modeling and Analysis of Systems Transient Using Digital Programs, *Modeling and Analysis Guidelines for Slow Transient – Part III: The Study of Ferroresonance*, IEEE Transactions on Power Delivery, Vol.15, No. 1, January 2000, pp.255-265
[4] C. Cherry, *Some general theorems for non-linear systems possessing reactance*, Phil. Mag. Ser. 7, Vol. 42, p. 1161, october 1951,
[5] G. R. Slemon, *Equivalent Circuits for transformers and machines including non linear effects*, Monograph N° 68, IEE Supply Section, 1953, p. 129;
[6] G. S. Brosan, J.T. Hayden, *Advanced Electrical power and Machines*, Sir Isaac Pitman, London, 1966;
[7] L. Cristaldi, S. Leva, A. P. Morando, *Electric Circuit Representation Of A Magnetic Circuit With Hysteresis*, in "Computer Engineering in Applied Electromagnetism", Springer, pp.261-266 - ISBN 1-4020-3168-8
[8] G.J. Retter, *Matrix and space-phasor theory of electrical machines*; Akadémiai Kiadò - Budapest, 1987
[9] A.G. Beccuti, S. Leva, A. P. Morando, *On The Use Of The Current And Flux State Variables In The Dynamic Analysis Of Magnetoelectric Networks*, in "Computer Engineering in Applied Electromagnetism", Springer, pp.119-124 - ISBN 1-4020-3168-8

Electromagnetic Fields in Mechatronics, Electrical and Electronic Engineering
A. Krawczyk et al. (Eds.)
IOS Press, 2006

OPTIMAL SHIELDING THICKNESS OF LOW FREQUENCY MAGNETIC FIELDS

H.Beltran, V.Fuster, A.Quijano

Instituto de Tecnologia Eléctrica.
Avda. Juan de la Cierva, 24 – Parc Tecnològic Paterna 46980 Paterna (Valencia). Spain
Phone: +34961366670 Fax: +34961366680
E-mail: Hector.Beltran@itenergia.com, Vicente.Fuster@itenergia.com, Alfredo.Quijano@itenergia.com

Abstract ***The reduction of the magnetic field emitted by industrial sources, such as MV/LV substations, has been faced by means of computation and experimentation. The proper selection of parameters and dimensions of the magnetic screens is critical for their efficiency. In this paper, the influence of the thickness is analyzed varying it for different plane shape ferromagnetic and conductive materials (Fe, Al and Cu). A typical three phase conductor distribution has been used as magnetic source. The results of the measurements validate those of the simulations. The graphics presented show the limitation phenomenon appearing in the efficiency of the different materials which demonstrates that shielding effectiveness is not lineally improved by an increment in screen thickness. For each of the materials there is one optimal value for the thickness which is shown and analyzed in this paper.***

Introduction

With the development of telecommunications and the increase experienced in the number of electrical devices and installations, society has become concerned around possible dangers related to magnetic fields. The frequency and intensity of the emissions are multiple and vary largely as a function of the electrical infrastructure considered. This new scenario has forced governments and international organizations to get involved with the problems and regulate the situation. Specific responses to it, coming from the European Union, are the recommendation from 1999 and the recently approved Directive 2004/40/CE [1], which establishes limits for the exposure of both professionals and the general public to electromagnetic fields, values which vary with the range of frequency.

From now on, new installations will have to be kept under limits and old ones will have to be controlled to check they agree with the legislation. Therefore, the design will have to consider these limits as a new requirement. For those applications or infrastructures where field emission can not be kept under the limits, magnetic shielding will have to be performed to reduce the field levels in the zones where people could have access or even work. Traditionally, ferromagnetic materials have been considered to be the best solution for magnetic screening. This is due to their high permeability. However, several studies performed lately on this topic have probed that shielding by means of conductive sheets, such as aluminium ones, has some advantages with respect to ferromagnetic foils [2]-[5]. This behaviour is described in this paper as a result of the research carried on.

The research has focused on the magnetic field created in the MV/LV substations as a part of a project developed with the utility Union Fenosa. The goal of the project was to establish certain rules of design for substations in order to reduce, as much as possible, the field emissions generated by these

installations. Apart from improving the substation designs, screening solutions are provided to decrease the magnetic fields emitted. The results of the project were included in the final report [6].

The aim of this paper is to present the results obtained in the screening effect study, performed with different thicknesses of different kind of materials, conductive (Al and Cu) and ferromagnetic (Fe). The study has been developed using a three phase conductor distribution line, which represents the low voltage output line coming out of the substation, observable at the right bottom of figure 1. The results can anyway be extended for the magnetic field created by all the electrical components existing in a substation. Only the geometry of the field will have to be known in order to adapt the results for each magnetic source. A good application model is shown in reference [7].

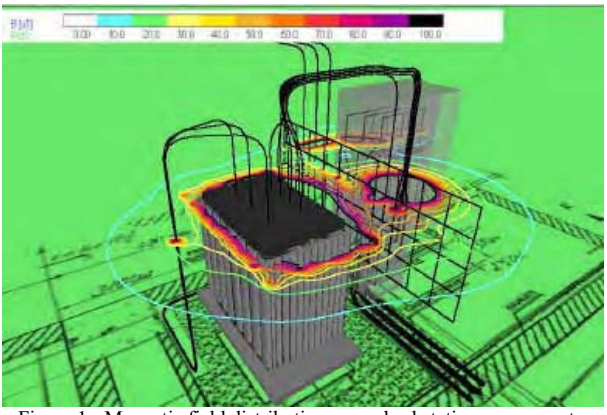

Figure 1 - Magnetic field distribution around substation components.

Experimental Procedure And Simulations

For the experimental study a three-phase conductor distribution was used. The material employed for the 6m long conductors with a 240mm^2 section was copper. The three conductors were 285mm apart and the level of current forced to flow through them was established at 500A. A three-phase current generator was used to feed the system. With this set-up, a series of measurements were carried out in the laboratory. The values of magnetic field around the conductors were compared later on with the values obtained by means of the simulations.

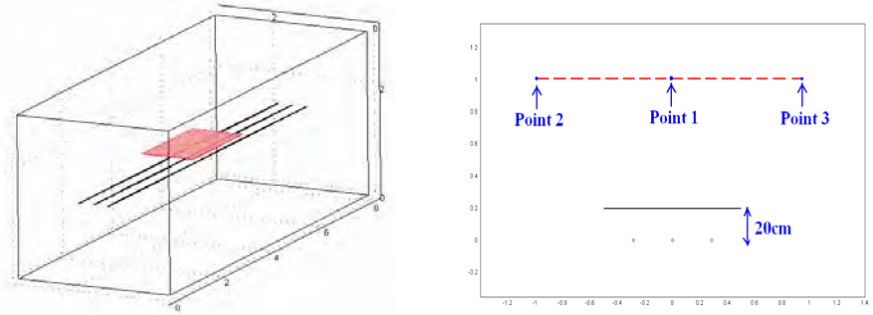

Figure 2 - Conductors distribution with upper screening.

The simulation was done using a 3D model [6], as shown in Figure 1, and simplified into a 2D model which represented a section of the distribution. This 2D model was used to analyze the influence of the parameters variation easing the calculations and improving the precision of the simulator, which worked applying the finite elements method (FEM). Comparing the results of both procedures, simulation and measurements, it could be assured the 2D computer model properly represented the real situation.

	Conductivity (S/m)	Relative Permeability
Aluminium	3.774e7	1
Copper	5.998e7	1
Iron	1.12e7	4000

The main characteristics of the materials employed are showed in the previous table. The cases analyzed during the initial trials and for the whole study were the following:

- Without any kind of shielding.
- With an iron screen.
- With an aluminium screen.
- With a copper screen.

Upper Screening

The upper screening used in the experimental measurements corresponds to the points depicted in figure 2. But now, instead of the initial 3 points, a total number of 11 points have been registered. Those points are placed over the dashed line from figure 2 and separated every 20cm. That results in a total distance of 2m long, going from 1m towards the left to 1m to the right of the conductor's distribution centre and 1m above it, where the magnetic field level has been registered in a discrete way. This gives out as a result the values summarized in Figure 3 corresponding to the screening behaviour of iron, aluminium and copper (left to right).

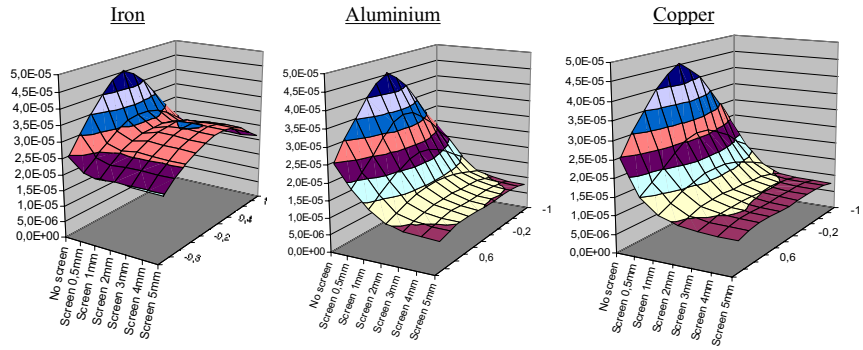

Figure 3 - Magnetic field lines obtained with iron, aluminium and copper plates.

These graphics represent the existing magnetic field (in Tesla) with different plate thicknesses of the three materials tested. The thicknesses used for each of the plates were: 0.5, 1, 2, 3, 4 and 5mm. All the plates simulated have been placed 20cm above the conductors. Thus, the points depicted are 80cm above the screen as it can be appreciated in Figure 2. In order to clarify the results, a 2D representation can be obtained, (see Figure 4), by taking the central line of the 3 previous images which correspond with the magnetic field at a point just 1m above the conductors, centered in the same vertical, and with variations of field regarding the different plates interposed between its location and the conductors distribution.

From the different graphics it can be concluded that aluminium or copper have better response than iron in these conditions of magnetic field. It can be easily observed too, that the screening effect is limited and does not present a linear response over a certain value of thickness. This limitation point that bends the surface is dependent on the material and can be observed in the same manner in the following graphic:

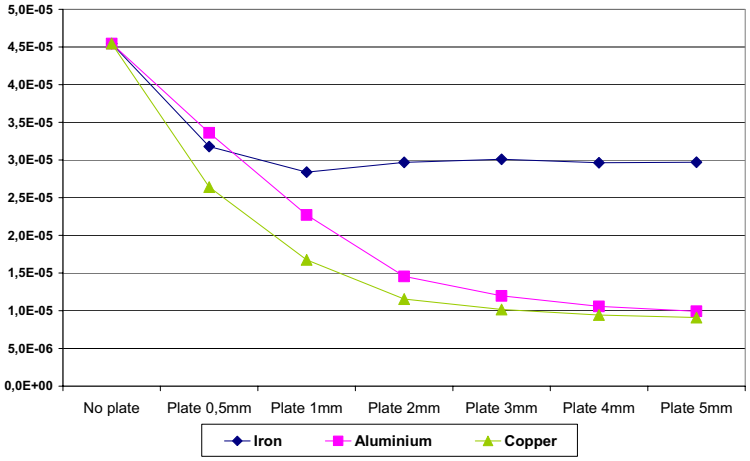

Figure 4 - Magnetic field (in Tesla) for different thicknesses in superior screening.

In this representation, apart from the limitation point, a better performance of the metallic materials is observed. That is because in the position where the screen has been placed, magnetic flux density lines are perpendicular to the plates' surfaces. That explains the good shielding behaviour observed for conductive materials (aluminium, copper). They reduce the field better than iron due to the induction of Eddy currents as an effect of the flux lines crossing their surfaces [8].

Lateral Screening

In the case of lateral screening, the same distribution of the conductors was maintained but the plates were placed on the side of the distribution as it can be appreciated on figure 5. This second study was carried out in order to validate the thicknesses influence on the screening effect resulting from the study on upper screening.

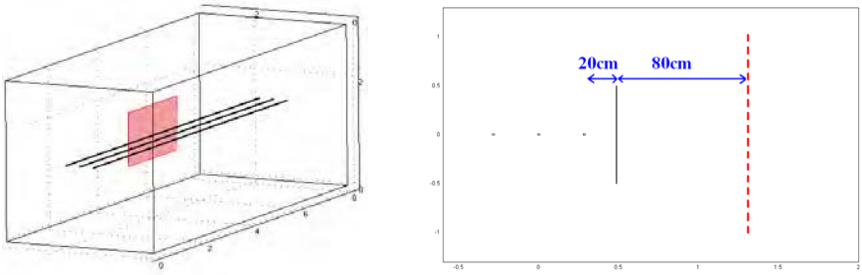

Figure 5 – 3D and 2D scheme for lateral screening.

On Figure 5 it can be observed that plates were now 20cm to the right of the lateral conductor. Once again, 11 points situated every 20cm were controlled. Those points were distributed regularly throughout the dashed line depicted and 1m towards the right of the same conductor, that is, 80cm away from the plate.

As for the upper screening case, three 3D graphics summarize the results obtained at the simulations. The thicknesses considered are exactly the same as in the previous case, that is: 0.5, 1, 2, 3, 4, and 5mm thick.

The following graphics correspond to the magnetic field values existing along the dashed line of Figure 5 for the iron, aluminium and copper screens.

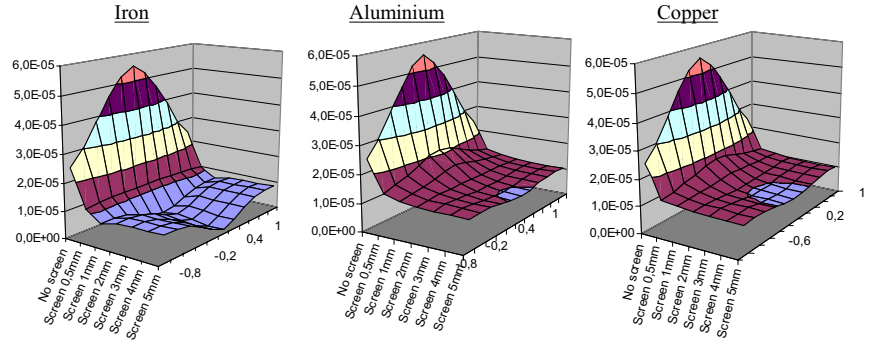

Figure 6 - Lateral screening with iron, aluminium and copper.

Unlike in previous results, iron shows now the best behaviour out of the three materials. This is due to the fact that in this second position for the screen the magnetic flux lines are not perpendicular to the surface of the plate. In this case they are mostly parallel to the surfaces and then, it is principally the permeability of the material which disturbs the path of the flux lines and not the effect of Eddy currents. Then, the magnetic field flux lines modification is higher in the presence of iron. This effect can be clearly appreciated in the 2D graphic of figure 7, representing, as in Figure 4, the central line of the three 3D graphics showed before (Values of field in the middle point in the series of 11 points). Nevertheless, it can be observed in this case that the difference in behaviour among materials is lower.

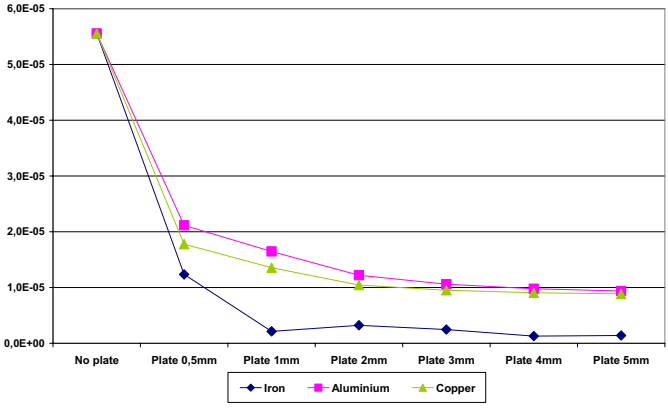

Figure 7 - Magnetic field (in Tesla) for different thicknesses in lateral screening.

According to the results, which confirm that the permeability of the material is the most important characteristic in the lateral screening whilst in the superior screening it was the Eddy currents which had the most important influence, it is proven that the orientation of the shield referred to the source is fundamental to shielding effectiveness [9].

Conclusions

The influence of material thickness on the screening efficiency has been studied by means of measurements and simulations. Many characteristics of the screening theory have been confirmed. Different materials behave in different ways facing the same magnetic field as a function of the position of the screen in relation to the magnetic flux lines. Apart from that, it has been shown that at thicker screens, the higher the field reduction obtained. However, this relation is not linear and has a clear limitation value characteristic for each of the materials. For iron, increasing thickness beyond 1.5mm will bring no great improvement. On the other hand, the limiting efficiency point for both copper and aluminium is situated around 2mm. These values are to be taken as a reference for the future developments of screening applications, along with other previous studies on the subject [10].

Acknowledgements

This work is part of a project supported by Unión FENOSA in cooperation with the Instituto de Tecnología Eléctrica. We would like to thank the company for their support and the confidence they deposited in our group.

References

[1] Directive 2004/40/EC of the European Parliament and of the Council of 29 April 2004 on the minimum health and safety requirements regarding the exposure of workers to the risks arising from physical agents (electromagnetic fields) (18th individual Directive within the meaning of Article 16 (1) of Directive 89/391/EEC) European Parliament ; Council of the European Union

[2] O.Bottauscio, M.Chiampi, D. Chiarabaglio, F. Fiorillo, L. Rocchino, and M. Zucca, “Role of magnetic materials in power frequency shielding: numerical analysis and experiments”. Proc.Inst.Elect.Eng., vol.148,pp. 104-110, Mar.2001.

[3] A.Canova, A.Manzin, and M,Tartaglia, “Evaluation of different analytical and semi-analytical methods for the design of ELF magnetic field shields,”. IEEE Trans.Indust.Applicat.,vol. 38, pp. 788-796, May/June 2002.

[4] T.Barbarics, A.Kost, D.Lederer, P.Kis, “Electromagnetic Field Calculation for Magnetic Shielding with Ferromagnetic Material”, IEEE Transaction on magnetics, July 2000.

[5] B.A.Clairmont, R.J.Lordan, “3D Modeling of Thin Conductive Sheets for Magnetic Field Shielding: Calculations and measurements” IEEE Transaction on Power Delivery, Vol.14, No.4, October 1999.

[6] “Estudio y diseño de sistemas de apantallamiento para centros de transformación frente a los campos electromagnéticos”. Internal document published by UNION FENOSA in collaboration with the Instituto de Tecnologia Electrica. January 2005.

[7] H.Beltran, V.Fuster, M.García, “Magnetic field reduction screening system for a magnetic field source used in industrial applications” 9th Spanish-Portuguese Congress on electrical engineering (9 CHLIE) June 2005.

[8] O.Bottauscio, M.Chiampi, A.Manzin, “Numerical Analysis of Magnetic Shielding Efficiency of Multilayered Screens”, IEEE Transactions on Magnetics, Vol.40, No.2, March 2004

[9] R.Olsen, “Some Observations about Shielding Extremely Low-Frequency Magnetic Fields by Finite Width Shields”, IEEE Transaction on electromagnetics compatibility, Vol.38, No.3, August 1996.

[10] H.Beltran, V.Fuster, C.García, V.Ferrer, I.Piqueras “Optimal screen width for field reduction applications of low frequency magnetic fields in three-phase conductors” 9th Spanish-Portuguese Congress on electrical engineering (9 CHLIE) June 2005.

Electromagnetic Fields in Mechatronics, Electrical and Electronic Engineering
A. Krawczyk et al. (Eds.)
IOS Press, 2006

ANALYTIC METHOD FOR DEALING WITH ROTATING MAGNETIC FIELD

[1]M. Bologna, [2]B. Tellini, [3]D. Pelliccia

[1]Departamento de Física/Universidad de Tarapacá, Velásquez 1775, Casilla 7-D, Arica, Chile,
mbologna@uta.cl
[2]Dipartimento di Sistemi Elettrici e Automazione/Università di Pisa, via Diotisalvi 2, I-56122, Pisa, Italy,
bernardo.tellini@dsea.unipi.it
[3]G.S.D. s.r.l., via Marmiceto 8, I-56014, Pisa, I-56122, Pisa, Italy,
d.pelliccia@gsd.it

***Abstract** – In this paper an analytic approach to deal with vector diffusion problems into hysteretic materials is presented. A first procedure attempts to find a solution to the nonlinear problem approximating the differential magnetic permeability tensor by a set of polynomials; the second method reduces the tensor nonlinear terms to equivalent optimized linear coefficients. Scalar hysteresis cycles are reported to better show how the methods work and a hypothetic anisotropy is chosen to carry out preliminary results and discussions for vector problems.*

Introduction

The treatment of magnetic hysteresis is a central matter for many industrial applications, such as magnetic cores for inductors and transformers, rotating electrical machines, magnetic shields, etc. Important models appeared in the literature during the years, even if many studies are still in progress due to the complexity of the problem [1-5]. For many practical applications the possibility of handling analytic formulations remains a useful tool for understanding the main quantities and parameters determining the phenomenon and is generally appreciated by the industry [6]. In a previous paper, the authors presented a new analytic approach for dealing with magnetic field diffusion problems into hysteretic materials [7]. The basic idea was to consider the nonlinear $B(H)$ characteristic as a perturbation of a linear $B(H)$ relation. Results obtained for one-dimensional problems showed a very good agreement with data obtained from more complex numerical models. Following the same approach, we present here the analytic formulation for treating vector nonlinear diffusion problems. The case of a rotating magnetic field into an indefinite magnetic conducting half-space is treated.

Analytic formulation

Slightly changing the more traditional way to treat nonlinear magnetic field diffusion problems, i.e. basing the technique on the perturbation of the exact field solution [6], we search for a solution to the investigated problem expanding the differential magnetic permeability tensor elements into a set of polynomials. More in detail, the perturbation procedure is applied to the nonlinear terms rather than to the field solution. We follow this way on the assumption that the nonlinear elements are perturbation

of linear coefficients and that the main contribute to the whole behaviour of the diffusing magnetic field is due to the first term of the expansion; in other words we assume that the relation ***B*(*H*)** can be written as: $B_i(\boldsymbol{H}) = \mu_{ik} H_k + \eta_i(\boldsymbol{H})$ where μ_{ik} is a constant tensor and $\eta_i(\boldsymbol{H})$ is a small vector quantity, i.e. the i th component is small compared to $\mu_{ik} H_k$. We stress the fact that being $\eta_i(\boldsymbol{H})$ small does not imply the field ***H*** to be small too. For sake of clarity, we shall start from the description of a one-dimensional problem and then we shall extend the method to vector cases. Let us consider the nonlinear diffusion equation:

$$\sigma \frac{\partial B}{\partial t} = \sigma \frac{\partial B}{\partial H} \frac{\partial H}{\partial t} = \nabla^2 H \tag{1}$$

and define the differential magnetic permeability:

$$\mu(H) = \frac{\partial B}{\partial H} \tag{2}$$

with $-H_s \le H \le H_s$. Under the hypothesis that along the ascending and descending branch the permeability is a limited function, we can develop it using a complete set of functions; a convenient choice is the Legendre polynomial set $P_n(H/H_s)$ with the following orthogonal property [8]:

$$\int_{-a}^{a} P_n\left(\frac{x}{a}\right) P_m\left(\frac{x}{a}\right) dx = \frac{2a}{2n+1} \delta_{nm} . \tag{3}$$

"Projecting" $\mu(H)$ on this base of functions the *n*th series expansion coefficient and the differential magnetic permeability are obtained;

$$\mu_n = \frac{2n+1}{2H_s} \int_{-H_s}^{H_s} \mu(H) P_n\left(\frac{H}{H_s}\right) dH , \tag{4}$$

$$\mu(H) = \sum_{n=0}^{\infty} \mu_n P\left(\frac{H}{H_s}\right) . \tag{5}$$

It is clear that (1) can be decomposed for each μ_n into a corresponding linear equation assuming for the magnetic field the expression: $H(z,t) = \sum_{n=0}^{\infty} H_n(z,t)$ where, for sake of completeness, we made explicit the argument of the field. In general we can decompose (1) in a series of linear equations that can be analytically solved [7]. We stress the fact that the procedure is the same for any type of *B*(*H*) relation; differences are contained only in the resulting parameters μ_n. The initial and boundary conditions are set by the first equation of the series that corresponds to the linear term or, in other words, to the ordinary diffusion problem with constant permeability coefficient. Here we report only the first two equations:

$$\nabla^2 H_0 - \sigma \mu_0 \frac{\partial H_0}{\partial t} = 0 , \tag{6}$$

where, by definition

$$\mu_0 = \frac{1}{2H_s} \int_{-H_s}^{H_s} \mu(H) P_0\left(\frac{H}{H_s}\right) dH = \frac{1}{2H_s} \int_{-H_s}^{H_s} \mu(H) dH \tag{7}$$

that is the average permeability of the cycle and that gives, as assumed, the main contribute to the whole behaviour of the diffusing field. Without any further algebraic steps, the second equation is:

$$\nabla^2 H_1 - \sigma\mu_0 \frac{\partial H_1}{\partial t} = \sigma\mu_1 P_1'\left(\frac{H_0}{H_s}\right)\frac{\partial H_0}{\partial t}\,. \tag{8}$$

To make clearer to the reader how a nonlinear branch is approximated by its polynomial expansion series, the ascending branch of a soft magnetic ferrite and the equivalent approximation truncated at the second and fourth order are reported in Fig. 1. Dashed line is referred to the measured ascending branch, while solid lines represent the equivalent approximation.

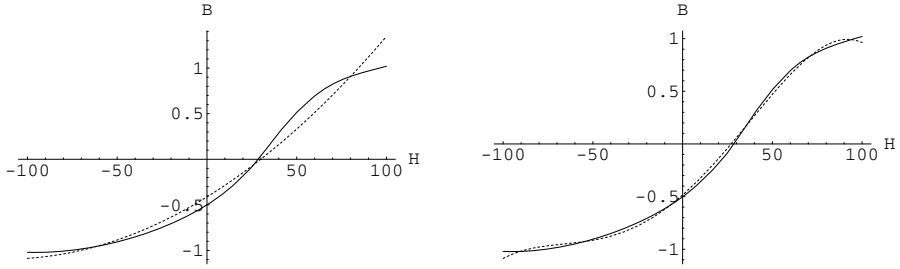

Fig. 1. Soft magnetic ferrite ascending branch (solid line) and its equivalent approximation (dashed line) truncated at the second order (left plot) and truncated at the fourth order (right plot).

In Table I a comparison between analytic calculation and data obtained by a Preisach model for a non oriented grains magnetic iron, cut at 90 degrees respect to the rolling direction is reported [7, 9].

Table I. Comparison between Preisach model and analytic calculation.

Material	f	H_M (A/m)	Preisach	analytic	diff %
C1e90 Iron	50 Hz	150	2.4 W/m^2	2.3 W/m^2	4

In principle this technique can be applied to a more general relation and, in particular, it can be extended, formally, to the vector $\boldsymbol{B}(\boldsymbol{H})$ relation. Recalling the definition of the differential magnetic permeability tensor the generic element can be expressed by:

$$\mu_{ik}(\boldsymbol{H}) = \frac{\partial B_i}{\partial H_k} \tag{9}$$

and the diffusion equation, in a completely general way, by:

$$\sigma\mu_{ik}(\boldsymbol{H})\frac{\partial H_k}{\partial t} = \nabla^2 H_i\,, \tag{10}$$

where the repeated index k is understood summed. Again considering the nonlinear terms as a small perturbation of linear coefficients we can develop the tensor $\mu_{ik}(\boldsymbol{H})$ in a power series of $\boldsymbol{H}$ components utilizing a complete set of functions $e_j(H_k)$ with $j = 1, 2, \ldots r$ and $k = 1, 2, 3$:

$$\mu_{ik}(\boldsymbol{H}) = \sum_{j,m,n=0}^{\infty} \mu_{ik}^{jmn} e_j(H_1) e_m(H_2) e_n(H_3)\,. \tag{11}$$

Assuming that the field $\boldsymbol{H}$ varies in a finite range of values along each axis we can choose as basis vectors $e_n(H_k) = P_n(H_k / H_{sk})$ where $-H_{sk} \le H_k \le H_{sk}$. As for the one-dimensional case, the coefficients μ_{ik}^{jnm} can be obtained projecting the permeability tensor elements on the basis vectors:

$$\mu_{ik}^{jnm} = \frac{(2j+1)(2n+1)(2m+1)}{8H_{s1}H_{s2}H_{s3}} \int \mu_{ik}(\boldsymbol{H}) P_j\left(\frac{H_1}{H_{s1}}\right) P_n\left(\frac{H_2}{H_{s2}}\right) P_m\left(\frac{H_3}{H_{s3}}\right) d\boldsymbol{H} \,. \tag{12}$$

Another possible approach to the problem is defined by a linear optimization procedure of the differential magnetic permeability tensor. Disregarding the exact magnetic behaviour, we can suppose that each element of the new tensor is obtained by adding to the average value of the corresponding nonlinear term a constant quantity representing the average distance between the nonlinear term itself and its average value. Since we are interested in estimating the power losses entering the medium and not to the field behaviour in its whole, we can take as evaluation of this distance for each nonlinear term $\mu_{ik}(\boldsymbol{H})$ the variance with respect to the corresponding average value evaluated at the interface of the investigation domain. Thus:

$$\mu_{ik}(\boldsymbol{H}) = \overline{\mu}_{ik} + \Delta\mu_{ik} \,, \tag{13}$$

where $\overline{\mu}_{ik}$ represents the average value of the nonlinear relation during a cycle, while $\Delta\mu_{ik}$ is defined as:

$$\Delta\mu_{ik} = \sqrt{\frac{1}{V_H}\int[\mu_{ik}(\boldsymbol{H})]^2 d\boldsymbol{H} - \overline{\mu}_{ik}{}^2} \,, \quad V_H \equiv \int d\boldsymbol{H} \,; \tag{14}$$

the vector nonlinear diffusion equation is now reduced to a constant coefficient diffusion equation that can be solved. For sake of clarity, the scalar hysteresis cycle and its average magnetic permeability are reported together to the equivalent linear cycle in Fig. 2.

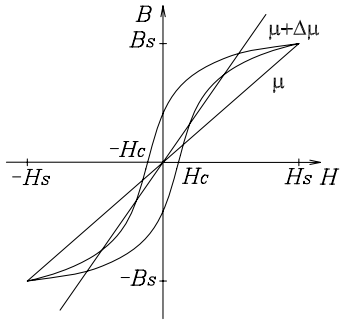

Fig. 2. Hysteresis cycle at the interface, average magnetic permeability and equivalent linear cycle.

A comparison between experimental data and calculations, obtained for a linear polarized magnetic field diffusing into a FeSi lamination, is reported in Table II [11].

Table II. Comparison between measurement and analytic calculation.

Material	f	H_M (A/m)	Measured	Linear Opt.	diff %
Fe-Si	1600 Hz	322	115 mJ/kg	117 mJ/kg	1.7

Discussions and results

It is known that if a uniform rotating magnetic field diffuse into an isotropic material also the magnetization is circularly polarized and between the two fields a lag angle is observed. Because of the isotropy the elements of the differential magnetic permeability tensor are not dependent on the

field direction, but they depend on its absolute value; the terms of the tensor vary penetrating into the medium but are constant if we refer at the interface or at any plane orthogonal to the diffusion direction. As a consequence the application of the proposed formulations reduces to a trivial task; of course once the tensor is known. For our treatment it is more interesting the case of anisotropic materials; indeed the terms of the tensor are not more constant, but they vary during the rotation of the magnetic field direction. It is to stress that an accurate experimental characterization of the magnetic permeability tensor, i.e. the $\boldsymbol{B}(\boldsymbol{H})$ relation, is a serious task and no many data are available in the literature. Thus, following the approach of Mayergoyz [4], i.e. assuming that a vector formulation can be derived from the knowledge of scalar formulations, and adopting a parallelogram-based hysteresis model [10], we identified a magnetic permeability tensor on the basis of a hypothetic anisotropy. More in detail, we assumed to choose a fixed saturation field and to vary the corresponding magnetization saturation value following a law of the type, $B_{S-\phi} = B_{S-x} + k\cos(2\phi)$, where k is an arbitrary constant.

Then, by the use of the Fourier expansion technique and truncating at the second order, we defined the magnetic permeability tensor. The resulting anisotropy is shown by the loci of magnetic field and induction field reported in Fig. 3 and 4, and it is expressed by the next equations:

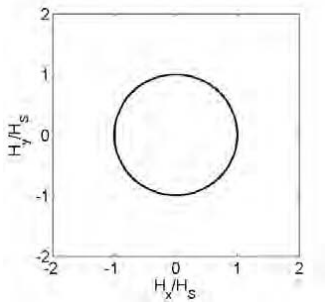

Fig. 3. Circular magnetic field – normalized locus of H_x vs. H_y.

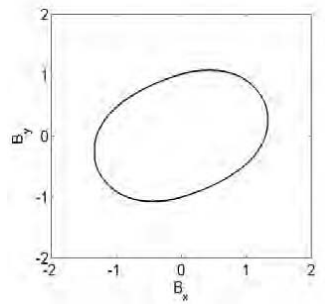

Fig. 4. Hypothetic anisotropy - locus B_x vs. B_y.

$$B_x = \cos(\omega t)(a + b\cos(2\omega t) + c\sin(2\omega t)) + \sin(\omega t)(d + e\cos(2\omega t) + f\sin(2\omega t)), \quad (15)$$

$$B_y = \sin(\omega t)(a + b\cos(2\omega t) + c\sin(2\omega t)) - \cos(\omega t)(d + e\cos(2\omega t) + f\sin(2\omega t)). \quad (16)$$

where *a, b, c, d, e* and *f* are constants related to the chosen anisotropy. The expression of the differential magnetic permeability tensor elements are:

$$\mu_{xx} = a + 3bH_x^2 + (2f - b)H_y^2 + (4c + 2e)H_xH_y \qquad \mu_{xy} = d + (2c + e)H_x^2 - 3eH_y^2 + (4f - 2b)H_xH_y$$

$$\mu_{yx} = -d + (2c + e)H_y^2 - 3eH_x^2 - (4f - 2b)H_xH_y \qquad \mu_{yy} = a - 3bH_y^2 + (b - 2f)H_x^2 + (4c + 2e)H_xH_y. \quad (17)$$

By means of (12) the resulting $\bar{\mu}_{xx}$ component at the zero order is:

$$\mu_{xx}^{00} = \frac{1}{4H_s^2}\int \mu_{xx}(\boldsymbol{H}) P_0\left(\frac{H_x}{H_s}\right) P_0\left(\frac{H_x}{H_s}\right) dH_x dH_y = a + \frac{2}{3}(b + f)H_s^2 \equiv \bar{\mu}_{xx}, \quad (18)$$

where H_s is the extreme value for the magnetic field in both the directions (see Fig. 3). In analogy with (7) for the one-dimensional case, the truncation at the zero order of the expansion is simply the average value of the considered element. For sake of conciseness, we do not report all the tensor elements, but we write the difference between the terms on the main diagonal

$$\overline{\mu}_{xx} - \overline{\mu}_{yy} = -\frac{4}{3}(b+f)H_s^2 \tag{19}$$

and the sum of the elements out of the main diagonal:

$$\overline{\mu}_{xy} + \overline{\mu}_{yx} = \frac{4}{3}(c-e)H_s^2\,; \tag{20}$$

it is to stress how for isotropic materials the quantities expressed by (19) and (20) vanish. In this way we can write the first equation for the field $\boldsymbol{H}$ that is simply the equivalent linear problem with permeability $\overline{\mu}_{ik}$:

$$\nabla^2 H_i^{(0)} - \sigma\overline{\mu}_{ik}\frac{\partial}{\partial t}H_i^{(0)} = 0\,. \tag{21}$$

For the next order, combining (10) and (11) for the two-dimensional case, we find:

$$\nabla^2 H_i^{(1)} - \sigma\overline{\mu}_{ik}\frac{\partial}{\partial t}H_i^{(1)} = \sigma\mu_{ik}^{10}P_1\left(\frac{H_x^{(0)}}{H_s}\right)\frac{\partial H_i^{(0)}}{\partial t} + \sigma\mu_{ik}^{01}P_1\left(\frac{H_y^{(0)}}{H_s}\right)\frac{\partial H_i^{(0)}}{\partial t}\,; \tag{22}$$

the factors $P_0\left(H_i^{(0)}/H_s\right)$ have been omitted being their value one. Equations (21) and (22) are, in general, analytically solvable and, as for the one-dimensional case, the information about the $\boldsymbol{B}(\boldsymbol{H})$ relation is contained in the quantities μ_{ik}^{jn}. The further orders of the expansion keep the same structure of (22) so that in principle the problem is reduced to an infinite set of solvable equations. Once the magnetic field is calculated the other significant quantities such as induction field and electric field via $\nabla\times\boldsymbol{H} = \sigma\,\boldsymbol{E}$ can be found; using the Poynting vector the power losses per unit area can be estimated:

$$P = \oint_S \boldsymbol{E}\times\boldsymbol{H}\cdot d\boldsymbol{S} \tag{23}$$

where S is the unit area of the investigate domain. The linear optimization method defines an equivalent material with a constant coefficient tensor. It is to say that these elements are, in general, different from the corresponding terms evaluated by the use of the Legendre expansion truncated at the 0th order, as a result of the different way of calculation. Measurements and definition of comparisons between experimental data and our calculations aimed at better defining and showing the capabilities of the proposed approach are, currently, in progress.

Conclusions

We presented an approach to deal with scalar and vector hysteresis problems. Two procedures have been presented: the first procedure has been developed on the basis of a technique used in MHD nonlinear problems, i.e. the expansion of the differential magnetic permeability tensor elements into Legendre polynomials while a linear optimisation procedure has been used for the second method. Results and comparison for one-dimensional problems have been reported while the case of circular rotating magnetic field diffusing into a hypothetic anisotropic material has been treated as a vector problem.

References

[1] E. C. Stoner, F. R. S and E. P. Wohlfahrt, “A Mechanism of Magnetic Hysteresis in Heterogeneous Alloys,” Phil. Trans. Roy. Soc., vol. 240A, 1948, pp. 599-642.

[2] R. M. Del Vecchio, “Two Dimensional Hysteresis Model,” IEEE Trans. Magn., vol. MAG20, no. 5, 1984.

[3] D. C. Jiles, and D. L. Atherton, “Theory of Ferromagnetic Hysteresis,” J. Magn. Magn. Mater., vol. 61, 1986, pp. 48-60.

[4] I. D. Mayergoyz, Mathematical Models of Hysteresis, Springer-Verlag, New York, USA 1991.

[5] E. Cardelli, E. Della Torre, E. Pinzaglia, “Confocal Vector Hysteresis Model,” Compumag 2005, Shenyang China, 26-30 June.

[6] I. D. Mayergoyz, Nonlinear Diffusion of Electromagnetic Fields, New York: Academic, 1998.

[7] B. Tellini, M. Bologna, D. Pelliccia, A New Analytic Approach for Dealing With Hysteretic Materials, IEEE Trans. Magn., vol. 41, no. 1, 2005, pp. 2-7,.

[8] M. Bologna and L. Nocera, Self oscillations of a forced inhomogeneous hydromagnetic cavity, Astron. Astrophys., Vol. 336, pp. 735 1998.

[9] E. Cardelli, E. Della Torre, B. Tellini, “Direct and Inverse Preisach Modelling in Soft Materials,” IEEE Trans. Magn., vol. 36, no. 4, pp. 1716-1718, 2000.

[10] E. Cardelli, B. Tellini, “Analysis of rotating magnetic field hysteresis through a parallelogram model,” Compumag 2005, Shenyang China, 26-30 June.

[11] V. Basso, G.Berttotti, O. Bottauscio, F. Fiorillo, and M. Pasquale, “Power losses in magnetic laminations with hysteresis: finite element modeling and experimental validation,” J. Appl. Phys., vol. 81, no. 8, pp. 5606-5608, 1997.

Electromagnetic Fields in Mechatronics, Electrical and Electronic Engineering
A. Krawczyk et al. (Eds.)
IOS Press, 2006

THE INFLUENCE OF THE ELECTROMAGNETIC WAVE PARAMETERS ON SAR COEFFICIENT

Katarzyna Ciosk[1)], Andrzej Krawczyk[2)], Roman Kubacki[3)]

[1)] Kielce University of Technology, Kielce, Poland, kciosk@tu.kielce.pl
[2)] Central Institute for Labour Protection, Department of Bioelectromagnetics, Warsaw, Poland, ankra@ciop.pl
[3)] Military Institute of Hygiene and Epidemiology, Warsaw, Poland, kubacki@wihe.waw.pl

***Abstract** – The paper presents semi-anlytical method of the calculation of SAR (Specific Absorption Rate) coefficient and such approach enables investigating of the internal structure of the coefficient. It is possible to trace the influence of electromagnetic parameters, such as frequency and polarisation on the value of SAR. The biological model is an isotropic lossy dielectric spheroid. The excitation is a uniform plane wave. The correctness of this approach has been verified by an experiment made on spheroidal phantom.*

Introduction

The SAR (Specific Absorption Rate) plays and will play more and more in the future key-role in the evaluation of possible electromagnetic hazard coming from industrial and wireless communication sources. That is why, the calculation of the SAR becomes a target for many computational centers [1], [2]. The distribution of SAR can be achieved by computational technique or by experiment made on phantom. Both are very approximate solutions as they introduce very strict assumptions. This paper presents semi-analytical solution of the problem and such approach enables investigating of the internal structure of the coefficient. We consider the biological model as a prolate spheroid. The spheroid is an isotropic lossy dielectric. The external medium is assumed to be free space. Time-harmonic fields with the time-dependence $e^{j\omega t}$ as a uniform plane wave with the magnetic field vector polarized along long axis of spheroid (polarisation H) or the electric field vector polarized along the long axis of spheroid (polarisation E) are suppressed. The SAR is the coefficient which determines the thermal effect on the biological tissue subjected to the electromagnetic field and is expressed by:

$$\mathrm{SAR} = \frac{\gamma E^2}{\rho} \tag{1}$$

where γ is conductivity, ρ is the mass density and E is the electric field strength

Method of Solution

The method of calculations at polarisation H was described in [3]. Here we present method at polarisation E. The model as a prolate spheroid. with major axis l, minor axis a and the interfocal distance d is shown in Fig.1. The primary electric field is given by

$$\mathbf{E}_0 = \hat{\mathbf{z}} E_{0z} \tag{2}$$

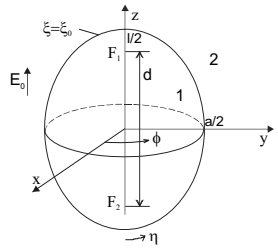

Fig. 1. Schematic diagram of spheroidal model

In order to describe the electromagnetic fields for spheroidal body, the prolate spheroidal coordinates ξ, η, ϕ are introduced, [4]. In view of the rotational symmetry of the configuration the magnetic field strength has one component (2) and has been selected as the unknown field.

$$\mathrm{H} = \hat{\varphi}\,\mathrm{H}_{\varphi}\left(\eta\,,\xi\right) \tag{3}$$

The electromagnetic field is described by the Maxwell's equations, which reduce to Helmholtz's equation in terms of spheroidal coordinates given by

$$\frac{\partial}{\partial\xi}\left(\left(\xi^2-1\right)\frac{\partial}{\partial\xi}\mathrm{H}_{i\varphi}+\frac{\partial}{\partial\eta}\left(\left(1-\eta^2\right)\frac{\partial}{\partial\eta}\right)\mathrm{H}_{i\varphi}\right)+\left(\mathrm{c}_i^2\left(\xi^2-\eta^2\right)+\frac{1}{\xi^2-1}-\frac{1}{1-\eta^2}\right)\mathrm{H}_{i\varphi}=0 \tag{4}$$

where: $\mathrm{c}_i=\mathrm{k}_i\dfrac{\mathrm{d}}{2}$, $\mathrm{i}=1,2$, $\mathrm{k}^2=\omega\mu_0\left(\varpi\varepsilon-\mathrm{j}\gamma\right)$

In region 2 outside the spheroid the magnetic field can be expressed in terms of associated Legendre functions of the first and second kind [4]

$$\mathrm{H}_{2\phi}\left(\eta,\xi\right)=\mathrm{E}_{0z}\,\mathrm{j}\omega\mu\frac{\mathrm{d}}{2}\left[\frac{1}{2}\sqrt{\xi^2-1}\,\mathrm{P}_1^1\left(\eta\right)+\sum_{n=1}^{\infty}\mathrm{B}_n\,\mathrm{Q}_n^1\left(\xi\right)\mathrm{P}_n^1\left(\eta\right)\right] \tag{5}$$

The electric field strength **E** has two components and they outside the spheroid are given by

$$\mathrm{E}_{2\eta}\left(\eta,\xi\right)=\frac{\mathrm{E}_{0z}}{\sqrt{\xi^2-\eta^2}}\left[\xi\,\mathrm{P}_1^1\left(\eta\right)+\sum_{n=1}^{\infty}\mathrm{B}_n\,\mathrm{U}_{1n}\left(\xi\right)\mathrm{P}_n^1\left(\eta\right)\right] \tag{6}$$

$$\mathrm{E}_{2\xi}\left(\eta,\xi\right)=-\frac{\mathrm{E}_{0z}}{\sqrt{\xi^2-\eta^2}}\left[\frac{1}{2}\sqrt{\xi^2-1}\;\mathrm{V}_{11}\left(\eta\right)+\sum_{n=1}^{\infty}\mathrm{B}_n\,\mathrm{Q}_n^1\left(\xi\right)\mathrm{V}_{1n}\left(\eta\right)\right] \tag{7}$$

where:

$$\mathrm{U}_{mn}\left(\xi\right)=\frac{\mathrm{d}}{\mathrm{d}\xi}\left[\sqrt{\xi^2-1}\;\mathrm{Q}_n^m\left(\xi\right)\right] \tag{8}$$

$$\mathrm{V}_{mn}\left(\eta\right)=\frac{\mathrm{d}}{\mathrm{d}\eta}\left[\sqrt{1-\eta^2}\;\mathrm{P}_n^m\left(\eta\right)\right] \tag{9}$$

In region 1 inside spheroid the magnetic field is considered in the expression

$$H_{1\phi}(\eta,\xi) \approx H_{2\phi}(\eta,\xi_0) e^{-jk_1 \int_{\xi_0}^{\xi} d\xi' h_\xi(\eta,\xi')} \quad ; \quad h_\xi(\eta,\xi) = \frac{d}{2}\sqrt{\frac{\xi^2-\eta^2}{\xi^2-1}} \tag{10}$$

For electric field yields

$$E_{1\eta}(\eta,\xi) \approx \frac{2}{j\omega\varepsilon_z d}\left[\frac{\xi}{\sqrt{(\xi^2-\eta^2)(\xi^2-1)}} - ic_1\right] H_{1\phi}(\eta,\xi) \tag{11}$$

where: $\varepsilon_z = \varepsilon - j\,\gamma/\omega$. The unknown coefficients B in equation (5) are determined by boundary condition and can be obtain from equations:

$$\begin{aligned} &B_{2m-1}\left[\frac{\varepsilon_z}{\varepsilon_0} U_{1(2m-1)}(\xi_0) - \frac{\xi_0}{\sqrt{\xi_0^2-1}} Q^1_{2m-1}(\xi_0)\right] + jc_1 \sum_{n=1}^{\infty} B_{2n-1}\, Q^1_{2n-1}(\xi_0)\Pi_{(2m-1)(2n-1)}(\xi_0) = \\ &= -\xi_0 \frac{2\varepsilon_z - \varepsilon_0}{\varepsilon_0}\delta_{(2m-1)1} - \frac{jc_1}{2}\sqrt{\xi_0^2-1}\;\Pi_{(2m-1)1}(\xi_0) \end{aligned} \tag{12}$$

$$\Pi_{mn}(\xi) = \frac{2m+1}{2m(m+1)} \int_{-1}^{1} d\eta \sqrt{\xi^2-\eta^2}\; P_m^1(\eta) P_n^1(\eta) \tag{13}$$

The whole-body SAR are calculated by integrating (1) in whole body of spheroid.

Calculation Results

To demonstrate the influence of the electromagnetic wave parameters such frequency and polarisation on SAR the computations was made. The spheroidal body dimensions were taken to be l = 41mm, a = 30m (see Fig. 1) and mass m = 20g. The calculations were carried out for frequency range from 800 MHz to 1800 MHz and two cases of polarisation. Fig.2 shows the distributions of the SAR. The value of SAR grows with frequency and is grater at polarisation E than that of polarisation H for all frequency range.

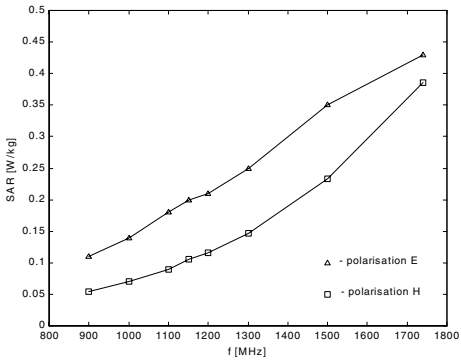

Fig. 2. The SAR distributions

Comparison the Calculated and Measured Results

In order to verify the method of calculation of SAR, the calculations were compared with measurements. They were carried out for the spheroidal object filled up the phantom, corresponding to biological tissues in accordance with European standard CENELEC for phantoms subjected to the GSM-frequency electromagnetic radiation. The incident field was a uniform plane wave . The procedure based on the measurement of the total energy absorbed . The difference between input and output energy determines the energy lost in the object, [5]. The object was placed in a waveguide. The frequency was GSM frequency and two kinds of polarisation were taken into consideration.. The results of measurements and calculation for polarisation H are shown in Table 1 and for polarisation E in Table 2. Small discrepancies between two curves illustrate a relatively good accuracy that can be reached by means of the analytical method.

Tab. 1. The values of SAR at polarisation H

f [MHz]	SAR [W/kg]		δ [%]
	measured	calculated	
900	0,06	0,054	-10%
1740	0,4	0,386	-3,5%

Tab. 2. The values of SAR at polarisation E

f [MHz]	SAR [W/kg]		δ [%]
	measured	calculated	
900	0,12	0.11	-8%
1740	0,41	0,43	5%

Conclusions

Semi-analytical method used here to calculate the coefficient SAR in biological tissues is easy in use and gives a good enough accuracy. The correctness of this approach has been verified by an experiment made on spheroidal phantom. It requires a short calculation time and a small PC memory and it makes this method competitive in some cases with the FTDT and other numerical methods. It is possible to trace the influence of electromagnetic parameters, such as frequency and polarisation on the value of SAR. Needless to add that such a knowledge is indispensable while evaluating the electromagnetic hazard. The method is complementary to all, better and worse developed, numerical approaches and its main feature is to make fast calculations with many configurations of the EM field and the object.

References

[1] C.H.Durney, D.A Christensen: Basic Introduction to Bioelectromagnetics, , CRC Press 2000

[2] C. Furse, S. Hagness, U. Jakobus (eds): ACES Journal, Special Issue on Computational Bioelectromagnetics, vol. 16, no.1, 2001

[3] K. Ciosk, A. Krawczyk, R. Kubacki : The comparison of phantom model and simulation results in SAR analysis , in: Computer Engineering in Applied Electromagnetism (ed. S. Wiak, A. Krawczyk, M. Trlep), Springer,2005 C. Flammer: Spheroidal Wave Functions.Stanford, CA: Stanford Univ. Press, 1957

[4] C. Flammer: Spheroidal Wave Functions.Stanford, CA: Stanford Univ. Press, 1957

[5] R. Kubacki, J. Sobiech, K. Wardak: The measurements of coefficient SAR in biological objects. in Electromagnetic compalibility in biology and medicine, INB ZTUREK, Warszawa, 2003 (in Polish)

Electromagnetic Fields in Mechatronics, Electrical and Electronic Engineering
A. Krawczyk et al. (Eds.)
IOS Press, 2006

SENSITIVITY STUDY WITH FRACTIONAL FACTORIAL DESIGN AND ITS INTEGRATION IN A CAD PACKAGE FOR ELECTROMECHANICAL SYSTEM

E. de Cecco, Z. Makni, C. Marchand, M. Besbes

Laboratoire de Génie Electrique de Paris / SPEE labs,
CNRS UMR 8507, Supelec, Université Paris VI, Université Paris XI
Plateau de Moulon, F 91192 Gif sur Yvette
E-mail : dececco@lgep.supelec.fr

***Abstract** – The aim of this paper is to describe a software tool dedicated to the design of electromechanical devices. It is based on a serial implementation of an analytical and a numerical procedure. The first one, from datasheet specification give a raisonnable preliminary structure. The second one uses a finite element calculation, associated to a sensitivity analysis and optimization method. For the sensitivity analysis, useful fractional factorial designs are performed to identify the most influential factors and to determine an initial configuration for the optimization procedure.*

I. Introduction

This paper presents a development of a new approach of a software tool dedicated to design electromechanical devices, by taking into account datasheet specifications. This tool is organized in two complementary procedures [1]. The first one is based on an analytical model with simplifying assumptions [2]. The second one is a numerical analysis which is based on finite element calculation [3]. It deals with local quantities and gives much more accurate results. As shown on figure 1, each step of the design progression (analytical and numerical) is associated with optimization procedures. The results obtained with the analytical model give a reasonable structure, which is used as an initial design to start the study with the numerical one. To reduce computation time, a sensitivity study is performed by using factorial fractional designs. This allows the choice of influential parameters to be used in optimization process.

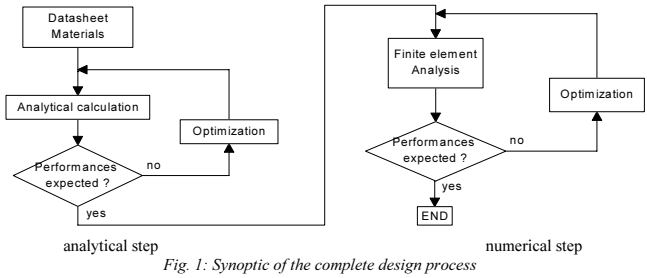

Fig. 1: Synoptic of the complete design process

II. Numerical Analysis

The numerical analysis is based on a magnetic vector potential formulation, which consists in solving the differential equation:

$$\nabla\times\left(\nu\nabla\times\vec{A}\right)=\vec{J}_0-\sigma\frac{\partial\vec{A}}{\partial t}+\nabla\times\left(\nu\,\vec{B}_r\right) \tag{1}$$

Where $\vec{A}$ is the magnetic potential vector, $\vec{B}_r$ the remanent induction of magnets, σ the conductivity of material and $\vec{J}_0$ the density current and ν the reluctivity. The electrical circuit (converter) is composed by a voltage source U, a resistor R, an inductor L (witch can represents the flux leakage) and a non linear element γ(I) (semiconductor switches). Solving (2), we obtain the current in each phase.

$$U=RI+\gamma(I)I+L\frac{\partial I}{\partial t}+\frac{\partial\phi}{\partial t} \tag{2}$$

$$\text{with}\quad \phi=\oint\vec{A}d\vec{l}\quad and\quad I=\iint\vec{J}_0.d\vec{S}$$

This system, composed by (1) and (2) is descretised and resolved in the time domain by application of Euler time scheme. So, a symmetrical matrix is obtained by multiplying the second row by the -Δt/λ factor. Finally, we have to solve the following coupled system [2]:

$$\begin{bmatrix}[S]+[T]/\Delta t & -[D]\\ -[D]^T & -\Delta t/\lambda\,[R+\gamma]+[L]/\Delta t\end{bmatrix}\cdot\begin{bmatrix}[A]\\ [I]\end{bmatrix}=\begin{bmatrix}[F]\\ [U]\end{bmatrix} \tag{3}$$

Moreover, the non linearities of materials are taken into account, and the non linear system (3) is solved by applying a Newton-Raphson method .

III. Sensitivity Analysis And Optimization

The approach, using finite element method associated to optimization techniques, to satisfy an objective function, is gready on computational time, particularly when the number of parameters is important with a wide interval of variation, or/and when stochastic methods are used. To reduce computation time for optimisation, the main idea consists in guiding the designer in order to choose the most influent parameters to be taken into account.

So, a "Sensitivity Analysis" module, which has been developed and integrated in the software tool, is used before the optimization step, as shown on figure 2.

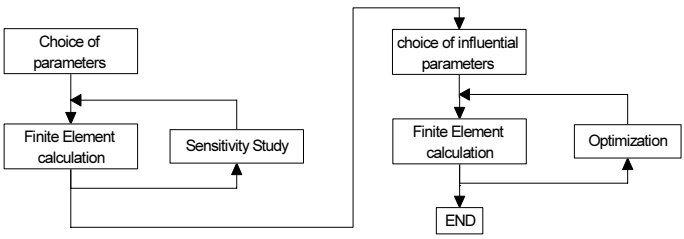

fig. 2: Sensitivity study and optimization process for numerical analysis

III.1. Sensitivity study step

This study consists in evaluating the influence of several parameters on objective function. The developed method is based on two-level factorial design [4] (FD), where each factor has two levels,

respectively 1 and 2, corresponding to their minimum and maximum values. FDs allow to determine every factors effects and every interactions effects [4]. The term interaction is used when the influence of a factor depends on the level of one or several other(s) factor(s). An interaction between *n* factors is named interaction of order *n*. Effects mesure the influence of the factors and interactions on objective function. In the following, the name *action* is used to designate a factor or an interaction. The notation A-B refer to the interaction between factors A and B.

For a lot of parameters, the number of experiments (finite element calculations) becomes prohibitive. For example, 10 factors with 2 levels need $2^{10} = 1024$ experiments. In order to evaluate the influence of the parameter set, fractional factorial designs (FFD) can be used with a limited number of experiments [4]. FFDs result from FD with less experiments. Therefore, all effects can not be evaluate, but only some of them. So, the difficulty is how to choose the experiments to keep and then to draw the conclusion from this partial results. The fact of having less experiments than FDs creats “alias”. An *alias* is a superimposing of the effects of two actions.

We use the Taguchi method which gives help to the problem about FFDs mentioned above. Two assumptions are considered:

- all interactions of order greater than two are neglected,
- all interactions of order two are neglected, except some of them perfectly indentified by user.

This method gives several FFDs which some of them are accompanied by an “interaction triangle”. This one gives informations about alias. For example, $L_8(2^7)$ (an eight experiments Taguchi standard tab issus from a seven-factors two-levels FD) is shown in tab 1 with its interaction triangle shown in tab 2.

N° column / N° experiment	1	2	3	4	5	6	7
1	1	1	1	1	1	1	1
2	1	1	1	2	2	2	2
3	1	2	2	1	1	2	2
4	1	2	2	2	2	1	1
5	2	1	2	1	2	1	2
6	2	1	2	2	1	2	1
7	2	2	1	1	2	2	1
8	2	2	1	2	1	1	2

tab 1 : Taguchi tab $L_8(2^7)$

N° column / N° column	2	3	4	5	6	7
1	3	2	5	4	7	6
2		1	6	7	4	5
3			7	6	5	4
4				1	2	3
5					3	2
6						1

tab 2 : Interaction triangle for $L_8(2^7)$

In table 1, In each column a factor can be placed. The numbers 1 and 2 correspond to the two levels: high and low corresponding to their intervals of variation.

The table 2 gives the column number which represents the interaction between two others columns. For example, let *f* be an application depending on factors A, B and C. If A is placed in column 1 and B in column 2, their interaction will be present in column 3 (see tab 2, column 2 and row 1, in bold zone). So, if one place C is this column 3, an alias is crested. This is a problem only if AB is not negligible.

So, it is necessary to determine *a priori* the negligible interactions. Therefore, there are two difficulties for using Taguchi method: choosing an adapted standard tab for a given application and placing all factors without creating alias.

These two steps has been automated in the module "Sensitivity Analysis". So, the user has only to input the factors to study and the non negligible interactions.

The results of the FFD allows the identification of the most influential parameters, which will be considered for the optimization step. Moreover, among the performed experiments, the best value of the objective function gives the initial value of the parameters.

III.2. Optimization step

This step is based on on the use of optimization procedures as determinist and stochastic.

The simplex method converges very slowly if the number of parameters is important and if the initial point is far from the solution. The use of this algorithm is possible for two reasons. On one hand, the number of studied factors is limited thanks to the use of the FFD. On the second hand, the initial point is close to the solution thanks to accurate preliminary sizing and the FFD. Indeed, from this last is extracted the nearest experiment to the optimum among those carried out.

IV. Application

The studied structure is a three phases surface mounted permanent magnet synchronous machine. The analytical analysis gives a solution shown on figure 3, used as initial design for numerical model.

For this application, the torque is optimised. The objective function is given by the following expression:

$$f = \sum_{i=1}^{N} \left(\frac{C_i - C_{imp}}{C_{imp}} \right)^2$$

where C_{imp} is the imposed torque, C_i the calculated torque and N the number of points during rotation. C_{imp} is equal to 3,2N as specified in datasheet. N is equal to 60.

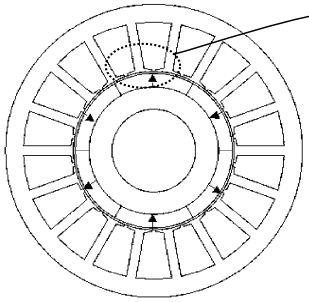

fig. 3 : Initial design of the machine

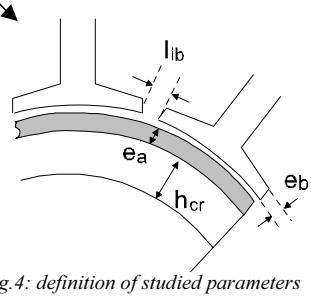

fig.4: definition of studied parameters

We choose for this study five parameters: l_{ib}, e_a, e_b, h_{cr}, defined on figure 3, and b_i the ratio between pole length and magnet length. Thirty-two experiments would be necessary with a two-levels factorial design. We suppose that only l_{ib} - e_b and l_{ib} - e_a interactions cannot be neglected. So, only eight experiments are necessary with a fractional factorial design, as shown on table 3.

These experiences allow calculating the effects of the five chosen factors, as shown on figure 5. We can see that the h_{cr} factor has quasi no effect on objective function, and e_b has the most important influence. l_{ib}, e_a and b_i factors have approximatively the same effect.

N°	l_{ib}	e_b	b_i	e_a	h_{cr}	Objective function
1	1	1	1	1	1	2.09
2	1	1	2	2	2	13.9
3	1	2	1	1	2	15.6
4	1	2	2	2	1	19.0
5	2	1	1	2	1	1.19
6	2	1	2	1	2	6.20
7	2	2	1	2	2	7.37
8	2	2	2	1	1	2.84

Tab 3 : The used fractional factorial design and the objective function

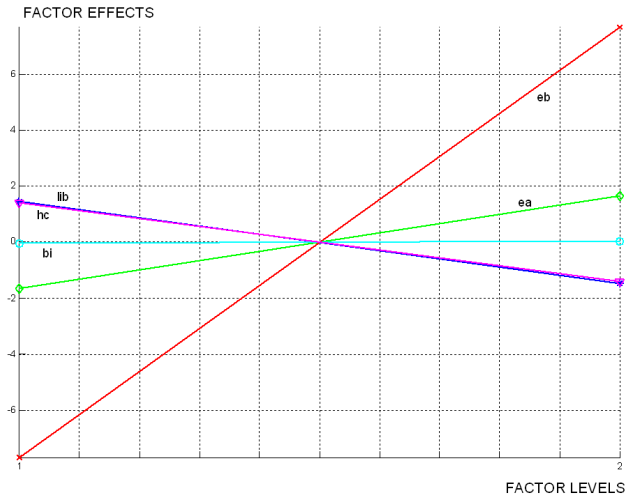

fig.5 : Effects of chosen factors in sensitivity study vs factor levels.

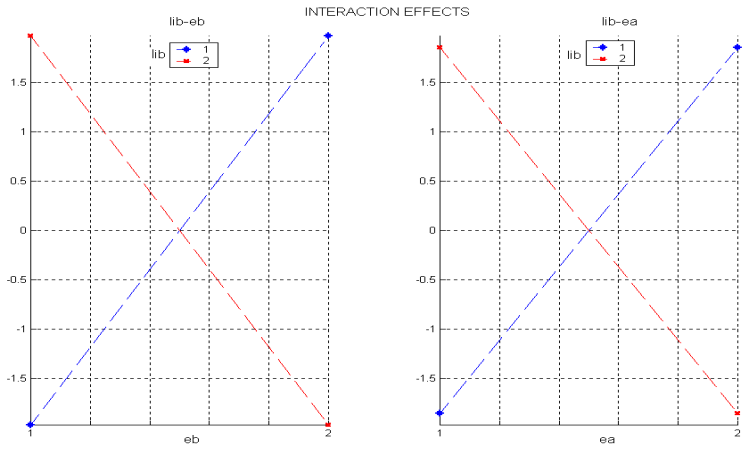

fig. 6 : Interaction effects of chosen factors in sensitivity study vs factor levels

For each interaction effect, l_{ib} - e_b and l_{ib} - e_a, there are four points because both factors have two levels. Figure 6 shows that interactions are of the same order than factor effects. Moreover, interaction effects have quasi the same values.

For the optimisation step, l_{ib} and e_b factors are chosen due to their important influence on objective function and also their interaction effects. Furthermore, the fifth experiment is the best solution, because it minimizes the objective function. The corresponding parameter levels are given at this line and are used as initial point to perform optimisation.

For the geometries issue from the analytical analysis, the fifth experiement of FFD and the simplex method optimisation, torque has been simulated. On figure 6, the torque versus rotor position is plotted.

The mean torque value of initial design is 5.1N. The fifth experiment of FFD is near optimum, with a mean torque equal to 4.2N. From optimisation process, the obtained result is corresponding to a torque with a mean value of 3.6N, and with minimal ripple.

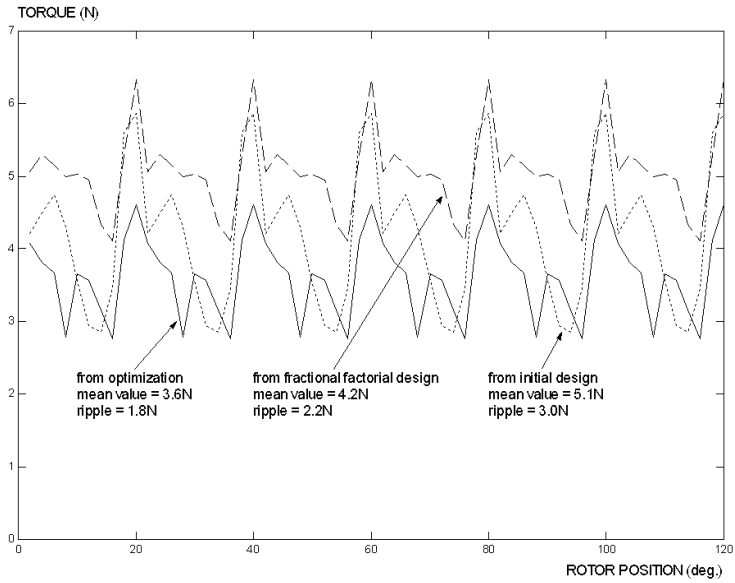

fig.7 : Torque obtained for analytical study, fractional factorial design (experiment n°5) and optimization.

V. Conclusion

In this paper, an optimization methodology using a software tool, based on finite element method, coupled with fractional factorial design (FFD) and an optimization process is described. The FFD analysis gives the most influential parameters which are chosen as optimisation variables. Among the performed experiments with the FFD, the best value of objective function gives the initial values of parameters and varaibles. Thus, a fast simplex method optimization is performed.

A complete description of fractional factorial designs procedure has been described.

References

[1] Z. Makni, E. de Cecco, M. Besbes, C.Marchand, F. Wurtz, "Analytical and Numerical Analysis Based Design of a Permanent Magnet Synchronous Machine", VIII-th International Workshop on Optimisation and inverse Problems in Electromagnetism, Grenoble, FRANCE, 6-8 September 2004.

[2] F.Wurtz, "A Methodology and a tool for the computer aided design with constraints of electrical devices", IEEE, Trans. on mag., vol 32, n°3, may 1996.

[3] E. de Cecco, C. Marchand, M. Besbes, "Software tool for conception and optimisation of permanent magnet synchronous machine", International Journal of Applied Electromagnetics and Mechanics, 2004, pp 643-646.

[4] G.E.P. Box, W.G. Hunter & J.S. Hunter; "Statistics for experimenters", Wiley-Interscience, 1978.

Electromagnetic Fields in Mechatronics, Electrical and Electronic Engineering
A. Krawczyk et al. (Eds.)
IOS Press, 2006

EXAMINATION OF ELECTROMAGNETIC FIELD CAUSED BY CELLULAR PHONE

Lívia Fejérvári Führer, Tamás Barbarics

Budapest University of Technology and Economics Egri József u. 18., H-1521, Budapest,
Hungary flivia@evt.bme.hu, barbarics@evt.bme.hu

***Abstract** – Our goal is to describe a comprehensive procedure to determine the radiation of a mobile phone take into consideration the influence of the presence of a human head hard by. In the course of our calculations we have been concerned chiefly with the physical effect, namely the influence of the head on radiation characteristic and efficiency. We applied variational principle method and supplied boundary conditions with using R-functions.*

Motivations

It is well-known for a long time, that several electromagnetic radiations make interactions with living organism and these interactions could not be investigated successfully even today. Especially the research of the radiation caused by cellular phones became of the greatest importance owing to the vast spreading of mobile gadgets. Since the 1950s generations of cellular phone systems have got in current use and became eliminated on and on. Today there are almost 1.5 billion subscribers in the world. None of the recent scientific results have led to the conclusion that the radio-frequency field originating from the phones would have any kind of damaging sanitary consequences. But considering the huge number of phone-users even less disadvantageous biological effects can be the cause of significant side-effects. Our goal is to describe a comprehensive procedure to determine the radiation of a mobile phone take into consideration the influence of the presence of a human head hard by. First we shortly summarize the general information related to radiation caused by cell phones special regard to GSM 900 system. Then we describe the attributes of the chosen model and the applied numerical computation method. At last we appraise numerical result and give conclusions.

Radiation Properties

During investigation connecting to biological effects caused by mobiles, first we have to know the nowadays usual cellular phone systems, the working gadgets and antennas. Second generation of cellular phone systems (GSM, DECT, TETRA,.UMTS) developed in the framework of international collaboration are applied world-wide scale. Through these digital data can already be sent too. Parameters considered of the each other completing GSM 900 and DCS 1800 systems, general in Europe, can be summarized as following. Transmitting frequency bands are 890-915 MHz or 1710-1785 MHz, TDMA/FDMA multiplexing with 8 time hole pro RF carrier and cells can be formed with 35 km (GSM) or 10 km (DCS) maximal radius.

Radiophones are low-capacity transceivers in radio frequency, they beam by antennas belonging to the gadgets. Output power can be controlled in compliance of current wavetravelling conditions by adaptive power regularity controlled by the basis station. Therefore the average power of handies is much lower than the peak-power, near to 20-25% of the nominal, about 20 mW. So gadgets consume less and minimize interferences. Basic requirement to antennas of mobile gadgets is easy to manage, for this purpose direction of development, beside keeping radiation characteristics, head to miniaturization. Using of monopole antenna with quarter wavelength and its reduced-quality version became possible by introduction of digital cell phones. Significant proportion of mobiles has been still equipped with this. But nowadays integrated planar antennas (BIFA, PIFA), placed inside in the handy, are used more and more, they are suitable for advantageous radiation qualities beside of easy handling.

Composition

The modelling of the human organism is an exceptionally difficult task, the attitude of biological materials in an electromagnetic field has not been mapped completely so far. Computations attaining the required accuracy are complicated because of their inhomogeneous and nonlinear nature, while the consideration of active and passive human thermoregulation makes the determination of the local field components even more complex. The simplest delineations neglect the inhomogeneity inside the organs and the tissues, in which way several layer-models emerge. During investigating the interaction of electromagnetic field and biological tissue it is indispensable to know macroscopic quality and structure of material. Biological materials can be considered non-magnetic tissues, namely relative magnetic permeability is approximately 1 and independent of frequency. Contrary to this electric permittivity and conductivity shows intensive dispersion and dependence of temperature.. Because of the low emitted power the radiation of a mobile phone only makes observable interaction with its immediate surroundings. It follows that in modelling the person using the cell phone it is enough to take the head and the hand holding the phone into consideration. Other parts of the body find place so far, that the power reaching them can be ignored, but they can exert an influence on the working radiation characteristic of the phone.

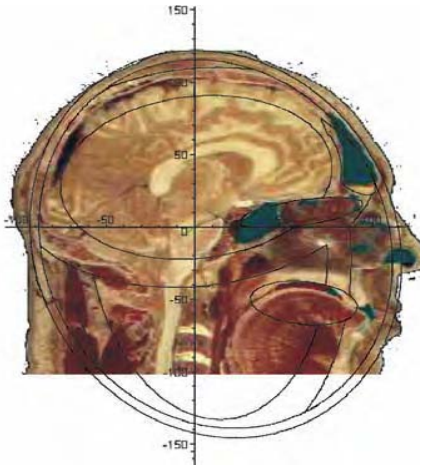

Figure 1. : Approximating surfaces in symmetry planar

Applied model

Our model was created on the basis of photo series taken of cross-sections (Visible Human Project - http://www.meddean.luc.edu/lumen/MedEd/GrossAnatomy/vhp/Visible.htm). In compliance with the chosen numerical method we tried to approximate the certain organs by the possibly best boundary surfaces. To create boundaries we fit second-ranged surfaces, mostly ellipsoids, to 4650 measured points, considering sagital symmetry (Figure 1). We only examined relatively large-sized and contiguous organs, so our model includes the following tissues: skin, fat, bone (brain-skull, cheek-skull), muscle (facial muscle, tongue), brain and cavities (frontal sinus, nasal cavity, facial cavity, eyes). Since in both examined frequency band respectively permittivity variation is less than 1% and conductivity variation in all the tissues is less than 5%, we can consider them independent of frequency and simulate without dispersion. Used dielectric parameters are in Table 1.

Table1.: Parameters of human tissues

Tissue	ε		σ (S/m)		ρ (kg/m^3)
	915 MHz	1800 MHz	915 MHz	1800 MHz	
Air (inside)	1		0		1.3
Eye (lens)	46.53	45.35	0.8009	1.1473	1053
Fat	5.46	5.35	0.0516	0.0784	916
Muscle	54.97	53.55	0.9515	1.3410	1046
Brain (grey)	52.61	50.08	0.9529	1.3913	1038
Bone	12.43	11.78	0.1463	0.2752	1990
Skin	41.28	38.87	0.8750	1.1847	1125

We modelled the cell phone with monopole antenna with quarter wavelength functioning in a GSM 900 system; it is situated in vertical position near the ear. We ignored the influence of the gadget on radiation. In our computations the emitted power was substituted by 20 mW based on the average power. GSM system applies pulse-modulation on 217 Hz (less than 1 MHz), so the SAR induced by electromagnetic wave can be approximated with the character of the carrier. Thus we have simulated the output signal of the antenna with sine curve in the middle of the transmitting frequency band, namely on 902.5 MHz. Only far field component of radiation has been regarded because experiments supported that *SAR* (Specific Absorption Rate) and absorbed power induced by far field component is significantly higher.

Calculation Method

Basic equations of electromagnetic fields can be summarized in Maxwell equations, or partial differential and integral equations deduced from them. Maxwell equations provide the relationships between the field quantities and the source elements. Using these, any kind of electromagnetic problem can be solved. The equations given in general form can be simplified in special cases, making it considerably easier to apply them. Introducing electric vector potential ($\boldsymbol{D} = \text{“}\mu\boldsymbol{F}$) and applying the Lorentz gauge, we can deduce the following partial differential equation from Maxwell equations.

$$\nabla \times \left(\frac{1}{\varepsilon_i} \nabla \times F \right) - \nabla \cdot \left(\frac{1}{\varepsilon_i} \nabla \cdot F \right) - \omega^2 \mu_i \left(1 + \frac{\sigma_i}{j\omega\varepsilon_i} \right) F = G \qquad (1)$$

Boundary conditions valid to electric flux density are satisfied by the help ***R***-functions. ***R***-functions have been elaborated by the Russian mathematician V. L. Rvachev. When applying them to the description of boundary surfaces we have to find a geometrical function that follows the simple requirement to produce positive value inside, negative value outside and zero along the boundary surface of the realm. Boundary surfaces with a complex geometrical description can always be constructed with several subregions, using ***R***-conjunction, ***R***-disjunction and ***R***-negation applying. Important advantage of the method is that normalized ***R***-functions can be generated easily, which gradient defines normal-vector of the surface.

$$n = -\nabla w^n \tag{2}$$

Duly Ritz-method vector potential can be approximated by a variety of functions. We have chosen Tschebisev polynomials multiplied with normalized R-function describing boundary surface.

$$F_i = \sum_{k=1}^{n_x} w^n a_{ik} f_{ik} = w^n f_i^T a_i \qquad i=x,y,z \tag{3}$$

The solution can be obtained by minimizing the following functional. The partial derivatives of the functional give the first variation as per ***a*** coefficients, that produces zero by extreme value.

$$W = \int_\Omega \left(\nabla \times F^*\right) \cdot \left(\frac{1}{\varepsilon_i} \nabla \times F\right) + \left(\nabla \cdot F^*\right) \cdot \left(\frac{1}{\varepsilon_i} \nabla \cdot F\right) - \omega^2 \mu_i \left(1 + \frac{\sigma_i}{j\omega\varepsilon_i}\right) F^* F d\Omega = \min \tag{4}$$

Finally we get a linear equation system, which can be solved easily by using MATLAB.

Computation Results

Calculations have been executed with the model reviewed, changing distance between the head and the antenna, inclination angle and transmitting frequency. All results are compared with one basic composition, in which vertical antenna is placed 2.5 cm away from the head and radiating in the middle of the transmitting frequency band of GSM 900 system, namely 902.5 MHz (Figure 2.).

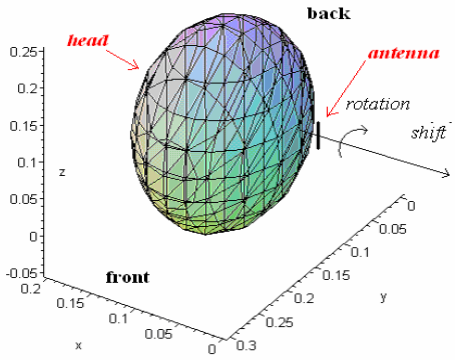

Figure 2: Basic composition

Changing radiation efficiency can be followed in Table 2, basic case is extracted.

Table 2.: Radiation efficiency depending of antenna position, inclination angle and frequency

Distance	***2.5 cm***	3 cm	3.5 cm	5 cm	10 cm	30 cm
η_{rad} (%)	***48.13 %***	55.31 %	60.5 %	67.05 %	69.57 %	77.91 %
Inclination angle	***0 ° (vertical)***	15°	30°	45°	60°	75°
η_{rad} (%)	***48.13 %***	49.45 %	51.17 %	53.69 %	54.56 %	55.1 %
Frequency	890 MHz	***902.5 MHz***	915 MHz	1710 MHz	1747.5 MHz	1785 MHz
η_{rad} (%)	49 %	***48.13 %***	47.45 %	42.47 %	42.71 %	41.29 %

From the results it can be determined that radiation efficiency is growing with distance, but 22.09% of the power is absorbed even if 30 cm distance. In case of monopole antenna greater part of radiation is absorbed in vertical position than in horizontal position. Using higher transmitting frequency absorption of biological tissues is growing, but in DCS 1800 system lower radiation power is necessary, so total effects are less intensive. Because of using higher and higher frequencies is general tendency, third generation of cellular phone systems, whose connection performance exceeds GSM by about 4 dB, have to be mentioned also. Beside its lower operating power we should also consider multimedia applications, since using them mobile gadgets can be accessible to users for a longer time. Besides absorption rate have to be reduced for the sake of protecting health, for mobile-designers it is important to describe changing of radiation characteristic, by managing cellular systems. Modified characteristic have been illustrated in case of basic composition in Figure 3.

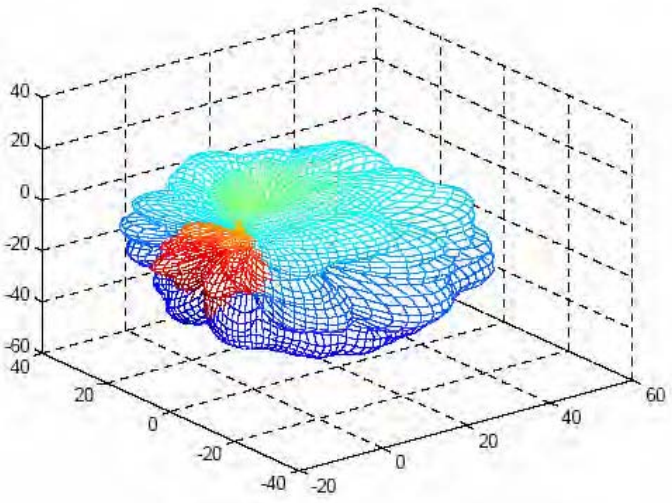

Figure 3: Radiation characteristic

Open air characteristic of a monopole is an ideal toroid, which distortion is obtrusive. We signed with red color the directions slitting the head, transmission can be with even more than 20 dB worse here. Obviously phone systems are ready to manage this loss. But we have to notice that in case of crowd or in closed shielded places (like elevator or garage) radiation power can be much higher to achieve adequate transmission. And at that time big part of radiation is absorbed in human organs.

Conclusion

This field of researches is extraordinary ramifying, the presented questions cover only a little part of it. There are many problems we have not engaged in, but we are planning to, like biological effects. Or it can be possibly to search for hot points. It can be interesting to reveal the influence of special appurtenances also, like a headset or mobile shield, or simulating radiation absorbed in children head. In the foregoing we summarized necessary information to investigate radiation emitted by cell phones, while supporting the theory with numerical computations. Computations are only demonstrations, since resulted values exactly because of applied simplifications. But it completely serves the theoretical conditions expounded in the foregoing and it characterize well the evolved electromagnetic field. In the course of our following studies we would like to state precisely our computations, by approximating boundaries of tissues with higher degree surfaces, and taking into consideration other organs and the hand too. We are going to execute calculations with the radiation of other kind of antennas (integrated planar antennas).

References

[1] A. Iványi, Magnetic Field Computation with R-functions, Budapest: Akadémiai Kiadó, 1998, pp 1-53

[2] G. Mátay and L. Zombory, Biological effects of RF radiation and medical applications, Budapest: Műegyetemi Kiadó, 2000, pp 136-145

[3] Á. Dárdai, Mobile telecommunication systems, Budapest: Cédrus Kiadó, 1994

[4] Our life and the cell phone, Budapest: Scientific Association of Infocommunication, 2001 [5] Gy. Thuróczy and J. Bakos, Electromagnetic field and our environment, Budapest, BME-OMIKK, 2002

Electromagnetic Fields in Mechatronics, Electrical and Electronic Engineering
A. Krawczyk et al. (Eds.)
IOS Press, 2006

IMPLEMENTING BUSINESS RULES IN OBJECT-ORIENTED TECHNOLOGY: APPLICATION IN MULTI-PHYSICS NUMERICAL SIMULATION

HUYNH Quoc Hung[(1)], Yves MARECHAL[(2)], Jean-Louis COULOMB[(3)]

Laboratoire d'Electrotechnique de Grenoble - UMR 5529 INPG/UJF - CNRS
ENSIEG - BP 46 - 38402 Saint-Martin-d'Hères Cedex - FRANCE
[(1)]Hung.Huynh-Quoc@leg.ensieg.inpg.fr, [(2)]Yves.Marechal@leg.ensieg.inpg.fr, [(3)]Jean-Louis.Coulomb@leg.ensieg.inpg.fr

***Abstract* - The evolution in the field of modeling software, especially in numerical simulation, leads to the complication of its organization. Thus, the needs of data structure optimization are also growing progressively. This paper describes an approach to what may be called implementing business rules in an object-oriented model applied to a multi-physics numerical simulation software. Thanks to this proposition, the complexity of data model manipulations may be reduced.**

I. Introduction

Multi-physics applications can be looked at as a linkage of varied analyses performed iteratively. In reality, the multiplicity of physics obviously increases the complexity of data model. In order to obtain a satisfactory performance, the data model of the software needs to be well-organized and extensible. The aim of this paper is to suggest a combination of logical and oriented-object programming language to execute the rules implemented on data model. This provides the possibility of managing data structure complexity in a multi-physics simulation software.

II. Database Structure Of The Physics Description

Our approach was originated in the need of data model organization in our multi-physics solver structure [1]. The solver contains two parts: the description of physics and the description of resolution. Considering the first part, it involves a sophisticated database structure composed by many entities serving to describe the physics.

The figure 1 shows a simplified global structure which contains the most important objects (s*tudy, discipline, region, domainType, material and property*) of our model. A study related to a discipline contains one or more regions, each of them relates to a domain type and has a material, which, at last, includes one or more properties. In fact, this model is common to all physics and should be extended, by inheritance mainly, to describe one or more physical disciplines.

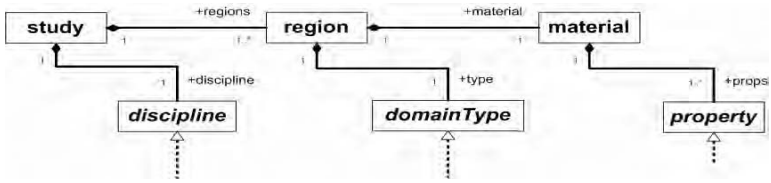

Figure 1 - Simplified global structure of the physics description

Let us consider the example of the magneto-static case. The entities related to this physics will be introduced as subclasses. An advantage of this type of classification is that the subclasses can inherit all properties of their abstract classes. The figure 2 presents the data model with inherited objects in our example.

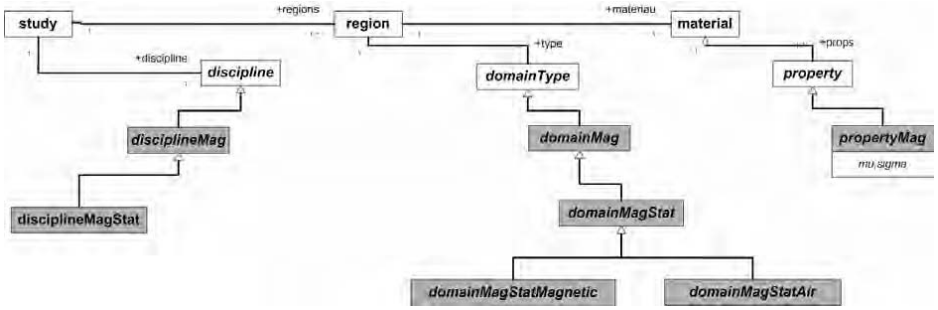

Figure 2 – Data model with added classes in magneto static case

III. Constraints Integrated In Database Structure

As a next step, consider now two physics: the magneto-static and the thermal with its new entities (shaded objects in the figure 3).

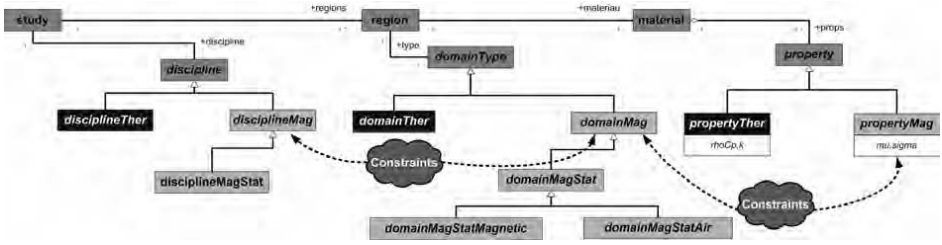

Figure 3 - Data structure in the two-physics case with constraints implementation

While the software development leads to an unavoidable increase of the structure complexity, the global organization of the data model is not modified. In fact, the number of realizations of these abstract structures may be important. For example, there are about 5000 terminal classes in Flux [10].

On the other hand, such an application needs a consistency checker to ensure that any command or object construction is valid [4]. For example, a magnetic region needs material with at least one magnetic property. This is not expressed by the data model that allows a mix of thermal regions with magnetic properties for instance. Thus, some constraints will be imposed over the data model. Let us consider for instance the magnetic aspects.

In order to implement these rules, the chosen language is naturally an international standard: Object Constraint Language (OCL [5]) which has been developed to enhance the Unified Modeling Language (UML) with constraints.

Two examples of rules, associated to the figure 3 diagram in the magneto-static case, implemented in OCL will be presented. These rules ensure the validation of a choice when being in the magneto-static study.

(1) The discipline of *study* must be of type *disciplineMagStat* and all regions must be of type *domainMagStat*:

```
context study def:
    let caseDomain(d:OclType,t:OclType):
        Boolean = (d=disciplineMagStat and t=domainMagStat)
    let validAllType(d:discipline,t:domainType):
        Boolean = caseDomain(d.type,t.type)
                or t.type.supertypes->exists(type:OclType|caseDomain(d.type,type))

context study inv typeOfDomain:self.regions->forAll(r:region|validAllType(self.discipline,r.type))
```

(2) The *region* must be of type *domainMagStat* and among the properties of the region's material; at least one is of type *propertyMag*.

```
context region def:
    let caseProp(t:OclType,p:OclType):
        Boolean = (t=domainMag and p=propertyMag)
    let validProp(t:domainType,p:property):
        Boolean = caseProp(t.type,p.type)

context region inv propertyOfMaterial: self.material.props->exists(p:property|validProp(self.type.type,p.type))
```

However, OCL is not a programming language so we need to use either coding or a logical programming language like PROLOG [6],[7],[8],[9]. Indeed, to reduce the simulation software designer task, the consistency management should not require any hand coding. Moreover, PROLOG offers the possibility of inversibility. These are the main reasons explaining our translation of the rules formalism into a PROLOG clause.

First of all, two requirements on the implementation of the rules in the model will be presented:

(1) The rules management must be as simple as possible and independent of the code. This aspect concerns the maintenance point of view.

(2) The rules have to be not only evaluatable but also invertible. This will allow not only the validation of the rules for any input entered by the end-user but also the proposition of valid choices to the end-user if required.

These two requirements also explain the reasons why we have chosen to couple Prolog, a logical and declarative programming language, to the object-oriented language. In order to translate OCL expressions into PROLOG predicates, we have defined for each OCL syntactic element an equivalent Prolog predicate. If we turn back to the two examples of the previous section regarding the magneto-static case, they are now expressed in PROLOG.

(1)

```
caseDomain(disciplineMagStat,domainMagStat).

validAllType(Discipline,Domain):-
        isTypeOf(Discipline,DisciplineType),
        isKindOf(Domain,DomainType),
        caseDomaine(DisciplineType,DomainType).

inv(typeOfDomain,'study',Study):-
        getField(Study,'discipline',Discipline),
        getField(Study,'regions',Regions),
        forall(Regions,R,(getField(R,'type',DomainType),
        validAllType(Discipline,DomainType))).
```

(2)

```
caseProp('domainMag','propertyMag').

validExistProp(Domain,Prop):-
        isKindOf(Domain,DomainType),
        isKindOf(Prop,PropType),
        caseProp(DomainType,PropType).

inv(propertyOfMaterial,'region',Region):-
        getField(Region,'type',Type),
        getField(Region,'material',Material),
        getField(Material,'props',Props),
        exist(Props,P,(validExistProp(Type,P))).
```

From this point, we just need to add some lines of rules for each new physic. For example, in the case of thermal physics, just some rules lines should be added:

```
caseDomain('disciplineTher','domainTher').

caseProp('domainTher','propertyTher').
```

Otherwise, PROLOG, with its capacity of invertible queries, gives us the possibility of not only validation (initial aim of OCL rules) but also proposition and explanation for input data:

-- Data input by users will be checked for the validation. For instance, in our magneto-static case, the discipline and the domain type of a given study are verified by applying the rules to assure their compatibility.

-- When a field is not filled in, the potential field values will be proposed to complete the object creation. For example, if we haven't chosen a domain type for a region, two potential domain types will be proposed. In our magneto-static case, they are *domainMagStatMagnetic* and *domainMagStatAir*.

-- We have added a predicate 'why' in order that the errors would be explained. We consider two examples:

(1) If the discipline of a study is not given, the error will be notified by a message:

```
why(typeOfDomain,'study',Study,Why):-
        getField(Study,'discipline',null),
        Why=['Field discipline of study is not filled','\n'].
```

(2) If the discipline of a study is not given, the error will be notified by a message:

```
why(typeOfDomain,'study',Study,Why):-
        getField(Study,'discipline',Discipline),
        Discipline\== null,
        Why=['Study discipline and domain type are not compatible','\n'].
```

Considering a simple example described in the tables below, we have three regions with their domain type and material. In the second table, we have three studies with their regions and their discipline defined by user. We will try to verify these studies and let the engine proposes potential values for incomplete or incorrect fields.

region	domainType	material
air	*domainMagStatAir*	*vacuum*
circuit	*domainMagStatMagnetic*	*steel*
core	*domainTher*	*steel*

study	regions	discipline
Study MagStat	*air,circuit*	*Discipline MagnetoStatic*
Study Ther	*core*	*X*
Study Ther_1	*core*	*Discipline MagnetoStatic*

-- Verifying the validation of Study MagStat

*?-**check('study','Study MagStat',Obj).***

➔Study MagStat is valid.

➔Obj=study('Study MagStat',[regions=[region(air),region(circuit)], discipline=disciplineMagStat('Discipline MagnetoStatic')])

-- Verifying the validation of Study Ther

*?-**check('study','Study Ther',Obj).***

➔Field discipline of study is not filled.

➔Obj=study('Study Ther',[regions=[region(core)], discipline=null])

-- Proposing the incomplete field 'discipline' of Study Ther

*?-**propose('study','Study Ther',study('Study Ther', [regions=[region(core)], discipline=Discipline])).***

➔Discipline= disciplineTher('Discipline Thermic')

-- Verifying the validation of Study MagStat_1

*?-**check('study','Study Ther_1',Obj).***

➔Study discipline and domain type are not compatible.

➔Obj=study('Study Ther',[regions=[region(core)],discipline=disciplineMagStat('Discipline MagnetoStatic')])

-- Proposing the incorrect field 'discipline' of Study MagStat_1

*?-**propose('study','Study Ther_1',study('Study Ther_1',[regions=[region(core)], discipline=Discipline])).***

➔Discipline= disciplineTher('Discipline Thermic')

Once completely constituted, the rules need to be implemented in the software. Figure 4 presents the process of database treatment with rules implementation. The entry data through data input user interface is stored temporarily before the checker verifies data validation. The validation checker is described with more details in the figure 5.

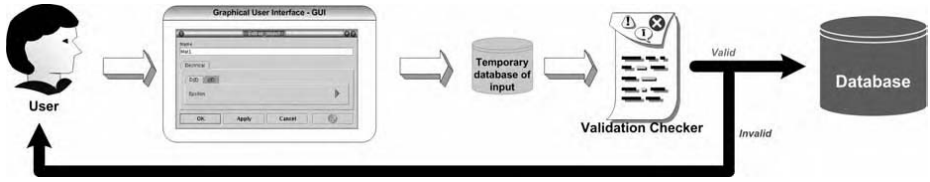

Figure 4 - The database treatment process with the implementation of rules

Thanks to a *database of OCL operators written in PROLOG*, a rules interpreter establishes the communication between *Graphical User Interface (GUI)* and the *business rules in OCL*. Inside the rules interpreter, a *parser* helps us to transform PROLOG rules into OCL business rules. These rules will be applied over the data model.

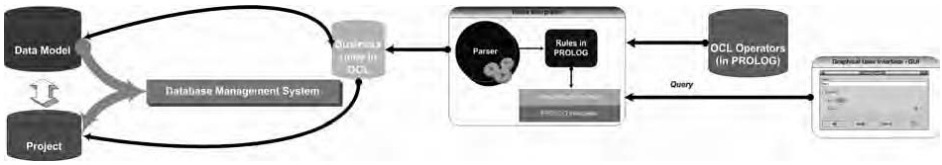

Figure 5 - Rules integration in database structure – Validation checker description

We have implemented the rules created to support the description of our simulation software FLUX. The constraints integrated will verify the validation of objects construction. It is believed that this approach will give a possibility to manage the structures which contain complex entity relationships.

IV. Conclusions

We have proposed a solution for managing the complexity of the data model in a multi physics solver by implementing a set of rules into the data model of a physics descriptor in our multi-physics solver. We have translated the unambiguous syntactic belonging to the standard object-oriented UML and OCL into Prolog, a logical programming language. Hence, the proof-mechanism is reusable for any model described with this standard.

The goal of this proposition is to permit developers to efficiently manage, modify and execute the software data model. The use of Prolog allows us to satisfy the requirements on the rules implementation in our model: the simplicity and the code independence. As a result, the time spent to describe a physical problem is reduced. Besides, the rules permit to establish a well-organized data structure, which naturally simplifies the work of a physicist who wants to add a new discipline in the global structure without modification.

This approach can be developed by reaching to a dynamic business rules implementation with adaptive object-models, as proposed in [2],[3].

References

[1] H.T.Luong, Y.Maréchal, *"Modélisation numérique multi physique et multi méthode: une description formelle pour construire un environnement de simulation général"*, MajecSTIC 2003, Marseille, Octobre 29-31, 2003.

[2] J.W.Yoder, R.Johnson, *"Metadata and Adaptive Object-Models"*, ECOOP'2000 Workshop Reader – Lecture Notes in ComputerScience, vol. no. 1964 – Springer Verlag 2000.

[3] J.W.Yoder, R. Johnson. *"Implementing Business Rules with Adaptive Object-Models"* - Business Rules Approach. Prentice Hall. 2002.

[4] O.Defour, Y.Maréchal, *"Static and dynamic consistency checking for numerical simulation: a mixed logic and object oriented programming approach"*, Saratoga Springs, New York USA, 14th Conference on the Computation of Electromagnetic Fields – COMPUMAG, July 13-17, 2003.

[5] OMG documents – *"Unified Modeling Language, v1.5 – Object Constraint Language Specification"*, March 2003,
http://www.omg.org.

[6] M.A.Covington, *"Some coding guidelines for Prolog"*, Artificial Intelligence Center, The University of Georgia, December 2, 2002.

[7] J.R.Fisher, *"Prolog tutorial"*, Pomona, California, 1999-2004,
http://www.csupomona.edu/~jrfisher/www/prolog_tutorial/.

[8] M.Banbara, N.Tamura, *"Prolog Cafe Documentation version 0.6"*, February 12, 2003,
http://kaminari.istc.kobe-u.ac.jp/PrologCafe/PrologCafe061/doc/.

[9] J.Wielemaker, *"SWI-Prolog 5.4.1 Reference Manual",* Dept. of Social Science Informatics (SWI) Roeterstraat, 2004,
http://www.swi-prolog.org/.

[10] Flux documentation – *"Notice d'utilisation générale de Flux 3D, version 8.1"* – CEDRAT, Juillet 2003.

Electromagnetic Fields in Mechatronics, Electrical and Electronic Engineering
A. Krawczyk et al. (Eds.)
IOS Press, 2006

NUMERICAL ANALYSIS OF FOKKER-PLANCK EQUATION IN FERROELECTRICS WITH REGARD TO POLARIZATION FLUCTUATIONS

J.Kaupužs[§], J.Rimshans[§] and N.Smyth[§§]

[§] Institute of Mathematics and Computer Science, University of Latvia, 29 Raiņa Boulevard, Riga LV1459, Latvia, rimshans@mii.lu.lv
[§§] School of Mathematics, University of Edinburgh, James Clerk Maxwell Building, The King's Buildings, Mayfield Road, Edinburgh EH9 3JZ, U.K., N.Smyth@ed.ac.uk

Abstract – ***The effects of the kinetics of polarization switching in ferroelectrics, taking into account the spatio-temporal fluctuations of the polarization field, given by the Langevin and Fokker-Planck equations, are studied. A Fokker-Planck equation is derived, which describes the polarization reversal in terms of Fourier amplitudes. A monotone and stable exponential-type finite volume difference scheme is elaborated to solve this equation numerically in a spatially homogeneous case, where the equation is one-dimensional. The temporal behaviour of the polarization probability distribution is calculated in presence of a sinusoidal field and white noise. The resulting hysteresis of the mean polarization is discussed for different noise intensities.***

Introduction

The stochastic description of collective phenomena like phase transitions is a key destination in solid-state physics. The problems of this kind are nontrivial and usually are solved by means of the perturbation theory [1-3]. Here we study the kinetics of polarization switching in ferroelectrics, taking into account the spatio-temporal fluctuations of the polarization field, given by the Langevin and Fokker-PLanck equations [4-5]. The problem has been studied earlier [6-7] by means of the Feynman diagram technique. The resulting thermal noise controlled relaxation has also been studied in [8-9] by using symplectic integration. Now we derive the Fokker-Planck equation in the Fourier representation and solve it numerically in the simplest spatially homogeneous case, where only the zero-vector mode is retained.

Basic Equations

We consider a ferroelectric with the Landau-Ginzburg Hamiltonian:

$$H = \int\left(\frac{\alpha}{2} P^2(\mathbf{x}) + \frac{\beta}{4} P^4(\mathbf{x}) + \frac{c}{2} \left(\nabla P(\mathbf{x})\right)^2 - \lambda(\mathbf{x},t) P(\mathbf{x},t) \right) d\mathbf{x} \ , \qquad (1)$$

where $P(\mathbf{x},t)$ is the local polarization and $\lambda(\mathbf{x},t)$ is the time-dependent external field. Only those configurations of the polarization are allowed which fall below the cut-off $k < \Lambda$ in the Fourier space, with $\Lambda = \pi / a$, where a is the lattice constant. It is most appropriate to approximate Hamiltonian (1) by a sum over discrete cells, where the size of one cell can be even larger than the lattice constant,

with subsequent Fourier transformation of the polarization. Each of N cell is a small domain with almost constant polarization. Thus, the Hamiltonian of a system with volume V reads

$$H = \Delta V \sum_{\mathbf{x}} \left(\frac{\alpha}{2} P^2(\mathbf{x}) + \frac{\beta}{4} P^4(\mathbf{x}) + \frac{c}{2} (\nabla P(\mathbf{x}))^2 - \lambda(\mathbf{x},t) P(\mathbf{x},t) \right) , \tag{2}$$

where $\Delta V = V/N$ is the volume of one cell, and the coordinates of their centres are given by the set of discrete d-dimensional vectors $\mathbf{x} \in \mathrm{R}^d$.

The stochastic dynamics of the system is described by the Langevin equation:

$$\dot{P}(\mathbf{x},t) = -\gamma \frac{\partial H}{\partial P} + \xi(\mathbf{x},t) , \tag{3}$$

with the white noise:

$$\left\langle \xi(\mathbf{x},t) \xi(\mathbf{x}',t') \right\rangle = 2\gamma\theta \delta_{\mathbf{x},\mathbf{x}'} \delta(t-t') . \tag{4}$$

In the case of the Gaussian white noise, the probability distribution function

$$f(P(\mathbf{x}_1), P(\mathbf{x}_2), \ldots, P(\mathbf{x}_N), t)$$

is given by the Fokker-Planck equation [5]

$$\frac{1}{\gamma} \frac{\partial f}{\partial t} = \sum_{\mathbf{x}} \frac{\partial}{\partial P(\mathbf{x})} \left(\frac{\partial H}{\partial P(\mathbf{x})} f + \theta \frac{\partial f}{\partial P(\mathbf{x})} \right) . \tag{5}$$

In the equilibrium we have a vanishing flux which corresponds to the Boltzmann's distribution $f \propto \exp(-H/\theta)$ with $\theta = k_B T$.

Assuming periodic boundary conditions, we consider the Fourier transformation

$$\begin{aligned} P(\mathbf{x}) &= N^{-1/2} \sum_{\mathbf{k}} P_{\mathbf{k}} e^{i\mathbf{k}\mathbf{x}} , \\ P_{\mathbf{k}} &= N^{-1/2} \sum_{\mathbf{x}} P(\mathbf{x}) e^{-i\mathbf{k}\mathbf{x}} . \end{aligned} \tag{6}$$

The Fourier amplitudes are complex numbers $P_{\mathbf{k}} = P'_{\mathbf{k}} + iP''_{\mathbf{k}}$. Since $P(\mathbf{x})$ is real, $P'_{-\mathbf{k}} = P'_{\mathbf{k}}$ and $P''_{-\mathbf{k}} = -P''_{\mathbf{k}}$ hold. It is supposed that the total number of modes N is an odd number. It means that there is the mode with $\mathbf{k} = \mathbf{0}$ and the modes with $\pm\mathbf{k}_1, \pm\mathbf{k}_2, \ldots, \pm\mathbf{k}_m$, where $m = (N-1)/2$ is the number of independent nonzero modes. According to this Fourier transformation, the Fokker--Planck equation for the probability distribution function

$$f = f(P_{\mathbf{0}}, P'_{\mathbf{k}_1}, P'_{\mathbf{k}_2}, \ldots, P'_{\mathbf{k}_m}, P''_{\mathbf{k}_1}, P''_{\mathbf{k}_2}, \ldots, P''_{\mathbf{k}_m}, t)$$

reads

$$\frac{1}{\gamma} \frac{\partial f}{\partial t} = \sum_{\mathbf{k} \in \Omega} \frac{\partial}{\partial P'_{\mathbf{k}}} \left\{ \frac{1}{2} \left(1 + \delta_{\mathbf{k},\mathbf{0}} \right) \cdot \left[\frac{\partial H}{\partial P'_{\mathbf{k}}} f + \theta \frac{\partial f}{\partial P'_{\mathbf{k}}} \right] \right\} + \sum_{\mathbf{k} \in \bar{\Omega}} \frac{\partial}{\partial P''_{\mathbf{k}}} \left\{ \frac{1}{2} \left[\frac{\partial H}{\partial P''_{\mathbf{k}}} f + \theta \frac{\partial f}{\partial P''_{\mathbf{k}}} \right] \right\} , \tag{7}$$

where $P'_{\mathbf{0}} \equiv P_{\mathbf{0}}$, $\overline{\Omega}$ is the set of m independent nonzero wave vectors, and Ω includes also $\mathbf{k} = \mathbf{0}$. Here the Fourier-transformed Hamiltonian is given by

$$H = \Delta V \cdot \left(\frac{1}{2} \sum_{\mathbf{k}} \left(\alpha + d\mathbf{k}^2 \right) \cdot |P_{\mathbf{k}}|^2 + \frac{\beta}{4} N^{-1} \sum_{\mathbf{k}_1+\mathbf{k}_2+\mathbf{k}_3+\mathbf{k}_4=\mathbf{0}} P_{\mathbf{k}_1} P_{\mathbf{k}_2} P_{\mathbf{k}_3} P_{\mathbf{k}_4} - \sum_{\mathbf{k}} \lambda_{-\mathbf{k}}(t) P_{\mathbf{k}} \right). \tag{8}$$

Some of the variables in Eq.(8) are dependent according to $P'_{-\mathbf{k}} = P'_{\mathbf{k}}$ and $P''_{-\mathbf{k}} = -P''_{\mathbf{k}}$, and $\lambda_{\mathbf{k}}(t) = \lambda'_{\mathbf{k}}(t) + i\lambda''_{\mathbf{k}}(t)$ is the Fourier transform of $\lambda(\mathbf{x}, t)$. The Fokker--Planck equation (7) can be written explicitly as

$$\begin{aligned} \frac{1}{\gamma} \frac{\partial f}{\partial t} = & \sum_{\mathbf{k} \in \Omega} \frac{\partial}{\partial P'_{\mathbf{k}}} \left\{ \Delta V \cdot f \cdot \left[\left(\alpha + d\mathbf{k}^2 \right) P'_{\mathbf{k}} + \beta S'_{\mathbf{k}} - \lambda'_{\mathbf{k}}(t) \right] + \frac{\theta}{2} \left(1 + \delta_{\mathbf{k},\mathbf{0}} \right) \frac{\partial f}{\partial P'_{\mathbf{k}}} \right\} \\ & + \sum_{\mathbf{k} \in \overline{\Omega}} \frac{\partial}{\partial P''_{\mathbf{k}}} \left\{ \Delta V \cdot f \cdot \left[\left(\alpha + d\mathbf{k}^2 \right) P''_{\mathbf{k}} + \beta S''_{\mathbf{k}} - \lambda''_{\mathbf{k}}(t) \right] + \frac{\theta}{2} \frac{\partial f}{\partial P''_{\mathbf{k}}} \right\} \end{aligned}, \tag{9}$$

where

$$S'_{\mathbf{k}} = N^{-1} \sum_{\mathbf{k}_1+\mathbf{k}_2+\mathbf{k}_3+\mathbf{k}_4=\mathbf{k}} \left\{ P'_{\mathbf{k}_1} P'_{\mathbf{k}_2} P'_{\mathbf{k}_3} - 3P'_{\mathbf{k}_1} P''_{\mathbf{k}_2} P''_{\mathbf{k}_3} \right\}, \tag{10}$$

$$S''_{\mathbf{k}} = N^{-1} \sum_{\mathbf{k}_1+\mathbf{k}_2+\mathbf{k}_3+\mathbf{k}_4=\mathbf{k}} \left\{ -P''_{\mathbf{k}_1} P''_{\mathbf{k}_2} P''_{\mathbf{k}_3} + 3P''_{\mathbf{k}_1} P'_{\mathbf{k}_2} P'_{\mathbf{k}_3} \right\}. \tag{11}$$

The simplest case is spatially homogeneous polarization when only the $\mathbf{k} = \mathbf{0}$ mode is retained in (9) with spatially homogeneous external field $\lambda(\mathbf{x}, t) = \lambda_{\mathbf{0}}(t) = \sin(\omega t)$. In this case we have a one-dimensional Fokker-Planck equation [5,10]:

$$\frac{1}{\gamma} \frac{\partial f}{\partial t} = \frac{\partial}{\partial P_0} \left\{ Vf \left[\alpha P_0 + \beta P_0^3 - A \sin(\omega t) \right] + \theta \frac{\partial f}{\partial P_0} \right\}. \tag{12}$$

For simplicity we have omitted the vector notation for the subscript index of the amplitude P_0.

Method of Solution

In order to solve (12), a monotone, exponential difference scheme is developed by using a special exponential-type substitution for the distribution function $f(P_0, t)$:

$$f(P_0, t) = w(P_0, t) \exp\left(- \int_{(P_0)_0}^{P_0} \frac{V}{\theta} \left(\beta (P)^3 + \alpha P - A \sin(\omega t) \right) dP \right),$$

where $w(P_0, t)$ - is a normalization function and $(P_0)_0$ - is a real number. As it was shown in [11], both these quantities should not affect the final coefficients of a difference scheme. By using the method for elaboration of exponential, monotone, finite volume difference schemes proposed in [11,12], the difference scheme for equation (12) is constructed. It reads:

$$\left(\Lambda(\eta)f^{l+1}\right)_i = \frac{1}{h_i^*}A_i f_{i-1}^{l+1} + \frac{1}{h_i^*}B_i f_{i+1}^{l+1} - Q_i f_i^{l+1} = -\frac{f_i^l}{\tau_{l+1}}, \tag{13}$$

where

$$A_i = \theta\eta_{i-1/2}\frac{1}{h_i\left(\exp\left(\eta_{i-1/2}\right)-1\right)}, \tag{14}$$

$$B_i = \theta\eta_{i+1/2}\frac{\exp\left(\eta_{i+1/2}\right)}{h_{i+1}\left(\exp\left(\eta_{i+1/2}\right)-1\right)}, \tag{15}$$

$$Q_i = \frac{1}{h_i^*}\left(A_{i+1} + B_{i-1}\right) + \frac{1}{\tau_{l+1}}, \tag{16}$$

$$\eta_{i+1/2} = \frac{V}{\theta}\left(\beta\left(P_0\right)_{i+1/2}^3 + \alpha\left(P_0\right)_{i+1/2} - A\sin\left(\omega t\right)\right)h_{i+1}, \tag{17}$$

$$h_{i+1} = \left(P_0\right)_{i+1} - \left(P_0\right)_i, \quad h_i^* = \frac{1}{2}\left(h_{i+1} + h_i\right), \quad 0 < i < M,\ l = 0,1,2\ldots,$$

and i, l are space and time indices, respectively.

Elaborated difference scheme (13)-(17) has a first order truncation error in time and a second order truncation error in space $O(\tau + h^2)$ for $|\eta| \to 0$. In the limit $|\eta| \to \infty$, so that transport is advection dominated, when $\theta \to 0$, the difference scheme (13)-(17) has first order truncation errors $O(\tau + h)$ in time and space.

In order to prove stability features of the scheme (13)-(17), we will consider the case $|\eta| \to \infty$, or advective dominated transport. The case of $|\eta| \to 0$ can be reduced to central difference scheme for a diffusion equation. The absolute stability features of this scheme are well known [13]. For the limit case, when $h \to 0$, the difference scheme (13)-(17) can be written with $O(\tau + h)$ precision as:

$$\frac{V}{h}\left(\beta\left(P_0\right)_i^3 + \alpha\left(P_0\right)_i - A\sin\left(\omega t\right)\right)\left(f_i^{l+1} - f_{i-1}^{l+1}\right) = \frac{f_i^{l+1} - f_i^l}{\tau}, \quad \eta \to -\infty, \quad 0 < i < M, \tag{18}$$

and

$$\frac{V}{h}\left(\beta\left(P_0\right)_i^3 + \alpha\left(P_0\right)_i - A\sin\left(\omega t\right)\right)\left(f_{i+1}^{l+1} - f_i^{l+1}\right) = \frac{f_i^{l+1} - f_i^l}{\tau}, \quad \eta \to \infty, \quad 0 < i < M. \tag{19}$$

By using von Neumann method for difference equations (18)-(19) it can be shown that the elaborated difference scheme (13)-(17) is unconditionally stable.

Results and Discussion

Equation (13) has been solved numerically within $P_0 \in$ [-2; 2] for the parameter values $\gamma = \beta = V = 1$, $\alpha = -1$, $A = 0.309$, $\omega = 10^{-3}$ at three different values of the noise

intensity: $\theta = 0.01$, $\theta = 0.05$, and $\theta = 0.1$. The zero flux boundary conditions and the initial condition:

$$f(P_0,0) = \frac{1}{2}\frac{1}{\sqrt{2\pi}\sigma}\left(\exp\left(-\frac{(P_0 - P_+)^2}{2\sigma^2}\right) + \exp\left(-\frac{(P_0 - P_-)^2}{2\sigma^2}\right)\right), \tag{20}$$

have been used with $\sigma = 0.3$, $P_+ = 1$ and $P_- = -1$. The calculated mean polarization $\overline{P}_0$ which depends on the external field $\lambda_0(t)$, forms a hysteresis loop, as shown in Fig.1 (top), as it is observed in ferroelectrics.

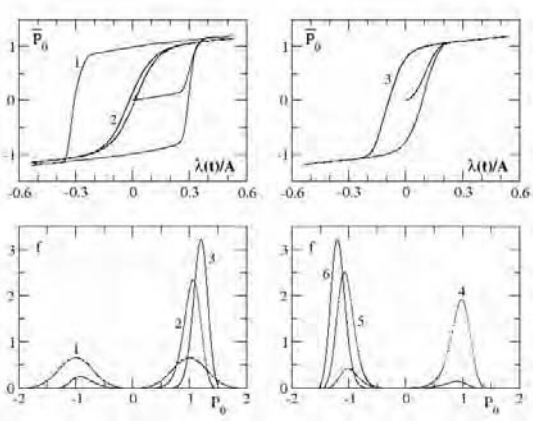

Fig.1 Hysteresis of the mean polarization depending to the external field (top) and the probability distribution over the polarization values at different time moments (bottom). The hysteresis loops 1, 2 (left), and 3 (right) correspond to the noise intensities θ=0.01, θ=0.1, and θ=0.05, respectively. The curves 1 to 6 in the lower pictures show the probability distribution for θ=0.05 at the time moments t=0.0002, 266.68, 1600.4, 3200, 3466.7, and 4667. The corresponding values of the external field are $6.18 \cdot 10^{-8}$, 0.08143, 0.30886, -0.01804, -0.0987, and -0.30868.

In the left top picture we compare the hysteresis at a relatively small noise intensity $\theta = 0.01$ with that at larger noise intensity $\theta = 0.1$. In the first case the hysteresis is much more distinct. Physically, the reason of the hysteresis is the potential barrier which has to be overcome to change the polarization from positive values to negative ones and vice versa. The larger is the noise intensity the larger is the probability to overcome the potential barrier in a given time interval $[t; t+dt]$ to switch from one (local) minimum of the Hamiltonian $H = V\left(\frac{\alpha}{2}P_0^2 + \frac{\beta}{4}P_0^4 - \lambda_0(t)P_0\right)$ to another (global) minimum. Therefore, at very small θ (curve 1) an almost jump-like switching occurs near time moments when the potential barrier vanishes. Since the jump almost surely occurs towards the deepest H minimum, the cyclical variation of the external field leads to the hysteresis. Larger noise (curve 2) reduces the area of the hysteresis loop, since the system can easily switch between both minima of the Hamiltonian irrespective to the previous history or direction of the variation of the external field. The hysteresis loop at an intermediate noise intensity $\theta = 0.05$ (curve 3) is shown in the upper right picture. The polarization reversal can be seen in more detail from the temporal variation of the probability distribution function $f(P_0,t)$. We have illustrated it in Fig.1 (bottom) for the case $\theta = 0.05$. Curve 1 shows the probability distribution after a short time when the external field still is very small and the distribution consists of two almost symmetrical maxima which correspond to the

minima of the Hamiltonian. Further on, the external field grows with time and the minimum at $P_0 > 0$ becomes dominating, i.e., the maximum of the probability distribution at $P_0 > 0$ becomes larger (curve 2). At later time moments, when the external field $A\sin(\omega t)$ approaches its maximum, the probability density maximum at $P_0 < 0$ disappears (curve 3). Then the external field decreases from positive to negative values and the corresponding polarization reversal takes place (curves 4,5,6). It manifests itself in the decrease of the maximum of $f(P_0, t)$ located at $P_0 > 0$, which is accompanied by the increase of the other maximum at $P_0 < 0$. After that the reversal occurs in the opposite direction, and so on. Due to the potential barrier, the maximum at $P_0 > 0$ still is higher than that at $P_0 < 0$ at a time moment when the decreasing external field vanishes. It remains true also when the external field becomes slightly negative (curve 4). Obviously, the scenario is opposite for the increasing external field. It is the reason for the hysteresis of the mean polarization.

Conclusions

In the present work a Fokker-Planck equation in the space of Fourier amplitudes has been derived, which describes the polarization reversal in ferroelectrics. In the simplest case, when only the zero Fourier mode is retained, the Fokker-Planck equation is one-dimensional. This equation has been solved numerically by the proposed monotone, exponential difference scheme, which has been developed by using a special exponential-type substitution. The probability distribution as well as the mean value of the polarization have been calculated depending on time in presence of a sinusoidal external field and white noise of different intensities. The mean polarization vs external field makes a hysteresis, observed in real ferroelectrics. The area of the hysteresis loop becomes smaller at larger noise intensities.

The second author would like to acknowledge the support of the European Commission's Research Infrastructure activity of the Structuring the European Research Area programme, contract number RII3-CT-2003-506079 (HPC-Europa).

References

[1] Shang-Keng Ma, Modern Theory of Critical Phenomena, W.A. Benjamin, Inc., New York, 1976.
[2] J. Zinn-Justin, Quantum Field Theory and Critical Phenomena, Clarendon Press, Oxford, 1996.
[3] J. Kaupužs, Ann. Phys. (Leipzig), Vol. 10, pp 299-331, 2001.
[4] G. Parisi, N. Sourlas, Phys. Rev. Lett., Vol. 43, pp 744-745, 1979.
[5] H.Haken, Synergetics, Berlin/Heidelberg/New York, Springer-Verlag, 1978.
[6] J. Kaupužs, Phys. Stat. Sol., Vol. 195, pp 325-339, 1996.
[7] J. Kaupužs, E. Klotins, Ferroelectrics, Vol. 296, pp 239-248, 2003.
[8] E. Klotins, Fokker-Planck equation for coupled anharmonic oscillators: symplectic integration and application to mean-field model of cooperative behaviour, cond-mat/0501339, 2005.
[9] E. Klotins, Relaxation dynamics of metastable systems: application to polar medium, PHYSICA A Vol. 340, pp 196-200, 2004.
[10] J.Kaupužs, J.Rimshans, Polarization kinetics in ferroelectrics with regard to fluctuations, cond-mat/0405124, 2004.
[11] B.S. Polsky, J.S. Rimshans, Half-implicit difference scheme for numerical simulation of transient processes in semiconductor devices, Solid State Electronics, Vol. 29, pp 321–324, 1986.
[12]J. Kaupužs, J. Rimshans, Numerical solution of semiconductor Fokker--Planck kinetic equations, In: Proc. of the European Congress ECCOMAS 2000, Barcelona, Spain, pp 1 - 18, 2000.
[13]C.A.J. Fletcher, Computational Techniques for Fluid Dynamics 1.Springer Series in Computational Physics, Springer-Verlag, 2st edition, New York, 1991.

Electromagnetic Fields in Mechatronics, Electrical and Electronic Engineering
A. Krawczyk et al. (Eds.)
IOS Press, 2006

THE PARAMETERS OF THE SYNCHRONOUS MACHINE

Gloria Ciumbulea[*], Xose Fernandez Lopez[**], Rafael Vives Fos[***], Neculai Galan[*]

[*]Universitatea "Politehnica" Bucuresti, Splaiul Independentei 313, Bucarest, Romania,
e-mail:ciumbulea@yahoo.com;galannicolae@yahoo.com,
[**]Universidad de Vigo, Lagoas – Marcosende 9, Vigo, Spain, e-mail: xmlopez@uvigo.es,
[***]Universidad Politecnica de Valencia, Camino de Vera 14, Valencia, Spain, e-mail: rvives@grea.upv.es

Abstract ***The paper shows the calculation mode of mathematical model parameters starting from catalogue data and presents the simplified mathematical model where are introduced the catalogue data as well as calculated parameters. This model is valuable for slow process. These parameters of the mathematical model can be determinated as well by experimental tests being structured in way to permit the determination of all the parameters. The stator resistance winding, the field winding one, the synchronous reactances longitudinal and quadrature unsaturated have been determinated by classic methods; for the determination of the other parameters one has employed the static methods (fixed rotor) – for the direct-axis d, the system is a quadripole permitting by a supplying of a terminal couple two kinds of tests by short-circuiting or by no load operation of the two other terminals.***

1. The Correlation Of The Mathematical Model With The Catalogue Data

In order to carry out the mathematical model parameters, one presents the equivalent diagrams in the axes d and q of the synchronous machine (Fig. 1). The resistances and reactances of these equivalent diagrams have significances well known.

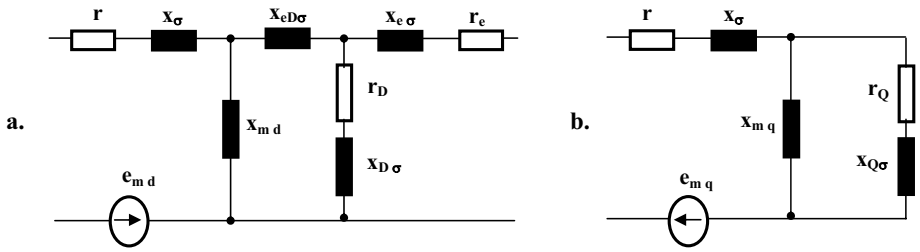

Fig. 1 Equivalent diagrams of the synchronous machine: a) axis d; b) axis q

As known, the catalogue data of the synchronous machine are: T'_{d0}, T''_{d0}, T''_{q0}, T'_d, T''_d, T''_q, x_d, x_q, x_{md}, x_{mq}, x'_d, x''_d, x''_q ,J.

These catalogue data permit to determinate the resistances and the reactances in the equivalent diagrams in order of this determination one has to write the expressions of the magnitudes of the reactances and the time constants:

$$x_d^{'} = x_\sigma + \left(\frac{1}{x_{md}} + \frac{1}{x_{e\sigma}}\right)^{-1} \quad ; \quad x_d^{''} = x_\sigma + \left(\frac{1}{x_{md}} + \frac{1}{x_{e\sigma}} + \frac{1}{x_{D\sigma}}\right)^{-1} ; x_q^{''} = x_\sigma + \left(\frac{1}{x_{mq}} + \frac{1}{x_{Q\sigma}}\right)^{-1} \tag{1}$$

$$\tau_{d0}^{'} = \omega_1 T_{do}^{'} = \frac{x_e}{r_e} \quad ; \quad \tau_{d0}^{''} = \omega_1 T_{do}^{''} = \frac{1}{r_D}\left[x_{D\sigma} + \left(\frac{1}{x_{md}} + \frac{1}{x_{e\sigma}}\right)^{-1}\right];$$

$$\tau_d^{'} = \omega_1 T_d^{'} = \frac{1}{r_e}\left[x_{e\sigma} + \left(\frac{1}{x_{md}} + \frac{1}{x_\sigma}\right)^{-1}\right]; \quad \tau_d^{''} = \omega_1 T_d^{''} = \frac{1}{r_D}\left[x_{D\sigma} + \left(\frac{1}{x_{md}} + \frac{1}{x_{e\sigma}} + \frac{1}{x_\sigma}\right)^{-1}\right]; \tag{1}$$

$$\tau_q^{''} = \omega_1 T_q^{''} = \frac{1}{r_Q}\left[x_{Q\sigma} + \left(\frac{1}{x_{mq}} + \frac{1}{x_\sigma}\right)^{-1}\right]$$

On the basis of these expressions one calculates the electrical parameters of the equivalent diagrams in the axes d and q:

$$x_{md} = x_d - x_\sigma \; ; \quad x_{D\sigma} = \left(\frac{1}{x_d^{''} - x_\sigma} - \frac{1}{x_d^{'} - x_\sigma}\right)^{-1} \; ; \quad x_{e\sigma} = \left(\frac{1}{x_d^{'} - x_\sigma} - \frac{1}{x_d - x_\sigma}\right)^{-1} ;$$

$$x_{mq} = x_q - x_\sigma \; ; \quad x_{Q\sigma} = \left(\frac{1}{x_q^{''} - x_\sigma} - \frac{1}{x_q - x_\sigma}\right)^{-1} \; ; \quad r_e = \frac{1}{\tau_d^{'}}\left[x_{e\sigma} + \left(\frac{1}{x_{md}} + \frac{1}{x_\sigma}\right)^{-1}\right]; \tag{2}$$

$$r_D = \frac{1}{\tau_d^{'}}\left[x_{D\sigma} + \left(\frac{1}{x_{md}} + \frac{1}{x_{e\sigma}} + \frac{1}{x_\sigma}\right)^{-1}\right]; \quad r_Q = \frac{1}{\tau_q^{''}}\left[x_{Q\sigma} + \left(\frac{1}{x_{mq}} + \frac{1}{x_\sigma}\right)^{-1}\right];$$

$$x_{eD\sigma} = \tau_{do}^{'} r_e - x_{e\sigma} - x_{md}.$$

One remarks the time constant $\tau_d^{''}$ has not be employed, that means there are more equations than are unknown; the time constant $\tau_d^{''}$ being used for verifications.

Knowing these parameters one can write the conventional synchronous machine complete mathematical model permitting an analysis of all the state magnitudes. This model has the disadvantage of being to complicate, often the physical interpretation of the results becomes difficult. One has to remark the simplified mathematical model gives results sufficiently exacts for slow process to the technical interest applications. One has to make some remarks concerning the simplified mathematical model whose electrical parameters are partially represented by the catalogue data and partially resulted by the calculation on the catalogue data basis using the relationships (2).

2. The Synchronous Machine Simplified Mathematical Model

Taking into account the slow variations of the electromechanical model one can neglect derivates in regard with the magnetical fluxes time surrounding stator windings that means in these circuits one neglects the transformation electromove force ($e_t = -d\varphi/dt$) in regard with the electromove force ($e_m = \nu\varphi$). One can as well neglect transformation electromove force in damping circuits. By neglecting also the stator windings resistances one obtains:

$$\begin{aligned} &\nu_d = \varphi_q; \quad \varphi_q = x_q i_q; \quad -\nu_q = \varphi_d; \quad \varphi_d = x_d i_d + x_{md} i_e; \\ &-\nu_e = r_e i_e + \frac{d\varphi_e}{d\tau}; \quad \varphi_e = x_{md} i_d + x_e i_e; \\ &H\frac{d^2\delta}{dt^2} = m_M - m_G, \quad m_G = p_G = \nu_d i_d + \nu_q i_q; \quad \nu = 1; \quad H = \frac{\omega_1^2 J}{pM_B} \end{aligned} \tag{3}$$

where: ν is rotation speed per unit, H is the inertia moment per unit, M_B is the basis torque to which are referred all the torques of the move equation, δ is the electrical angle between the axis and the rotation synchronous axis.

On the basis of the hypothesis established, one has taken into account only two inertia: the electrical inertia (of the field winding) and the mechanical one (of the rotor), this fact leading to important simplifications, resulting only two differential equations to be solved.

In the case of the generator connected to the u_0 voltage bars and to the f frequency both being constant, by transport lines characterized by a phase equivalent reactance x_L the system (3) becomes:

$$\begin{aligned} &u_0 = \nu - jx_L i = je'_q - j(x'_d + x_L)i_d + (x_q + x_L)i_q; \\ &\nu = \nu_d + j\nu_q; \quad -\frac{x_{md}}{r_e}\nu_e = x_{md} i_e - \tau'_{d0}\frac{de'_q}{d\tau}; \quad -\nu_e = r_e i_e + \frac{d\varphi_e}{d\tau}; \quad \varphi_e = x_{md} i_d + x_e i_e; \end{aligned} \tag{4}$$

The equations system (4) characterizes the synchronous machine simplified mathematical, model including the catalogue data parameters as well as the catalogue data relationships (2) calculated parameters.

To the first equation in the system (4) corresponds the phasorial diagram in figure 2 on this basis one calculates the current I_d:

$$i_d = \frac{e'_q - u_0\cos\delta}{x'_d + x_L} \tag{5}$$

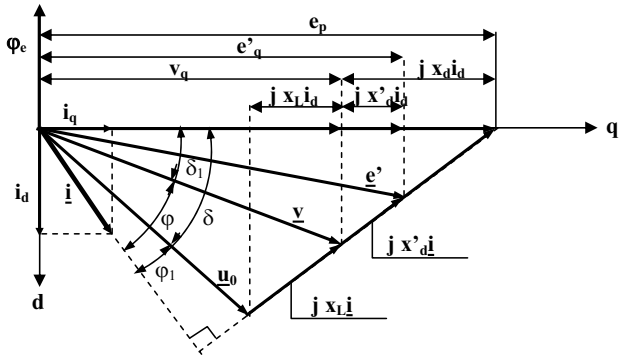

Fig.2. The phasorial diagram of the stator equation

For transient states in electrical circuits one considers the angle δ varies in restrained limits. Introducing the relationships (5) in the second equation of the system (4) and applying the Laplace transformate one will obtain:

$$e'_q(p) = \frac{k}{1+pk\tau'_{d0}}\left(\frac{x_{md}}{r_e}\mathrm{v_e} + \frac{x_d x'_d}{x'_d + x_L}u_0\cos\delta\right);\quad k = \frac{x'_d + x_L}{x_d + x_L};\quad e'_{q0} = \mathrm{v}_q + x'_d i_d \tag{6}$$

For the electromove force initial magnitude e'$_{q0}$ one employs the magnitudes v_d and I_d corresponding to the stationary state.
In per unit, the electromagnetic torque m_G is numerically equal to the electromagnetic power p_G:

$$p_G = \mathrm{v}_d i_d + \mathrm{v_q} i_q = m_G;\quad \mathrm{v_d} = u_0\sin\delta - x_L i_q = x_q i_q;\quad \mathrm{v_q} = u_0\cos\delta + x_L i_d = e'_q i_d \tag{7}$$

The electromagnetic torque expression is:

$$m_G = \frac{e'_q u_0}{x'_d + x_L}\sin\delta - \frac{u_0^2}{2}\left(\frac{1}{x'_d + x_L} - \frac{1}{x_q + x_L}\right)\sin 2\delta = m'_m\sin\delta - m''_m\sin 2\delta \tag{8}$$

The expression (8) is similar to that of steady state, except the magnitudes of transient state will appear. Because x'$_d$ < x_q the anisotropic torque m"$_m$ gets opposite sign in regard with the steady state case. The dynamic state, for an approximately constant maintaining of the voltage magnitude e'$_q$ the dynamic stability limit corresponds to angles δ bigger than those of 90^0, the more bigger than the difference between x'$_d$ and x_d is bigger. The angle δ_m for which one obtains the torque will be:

$$\delta_m = arc\cos\frac{1-\sqrt{1+32\alpha^2}}{8\alpha};\quad \alpha = \frac{m''_m}{m'_m} \tag{9}$$

Having these elements envisaged the simplified mathematical model can be used in order to simulate slow process in operating of a synchronous generator.

3. Experimental Methods For Parameters Determination

Equivalent scheme on axis d has 2 access gates and only one on axis q; consequently there are 2 supplying possibilities for axis d and one for axis q. The organization mode of the experimental tests is made function of equivalent scheme. R, X_{do}, X_{qo} are defined experimentally for equivalent scheme of fig.1.These magnitudes refer to the stator basic impedance: $Z_b = U_b/I_b$. The method consists in supplying of the access terminals of axis d with an alternating single phase voltage and a rotor positioning so that the longitudinal axis coincides with magnetic field axis produced by the stator winding (Fig.3.a). Then the rotor is positioned to 90 electrical degrees versus previous position and parameters determinations on transverse axis q are made (Fig.3b).

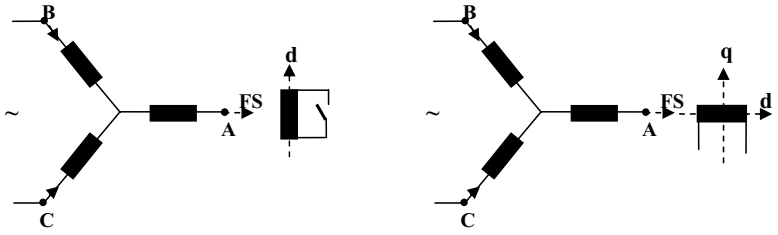

Fig. 3. a) The scheme for axis d; b) The scheme for axis q

Experimental determinations for the longitudinal axis are made with the field circuit both open and closed. Resistance and basic impedance of operating winding R_e, Z_{eb} are determined, too. I_{eb}-

operating winding basic current is defined from symmetrical short circuit characteristic. The tests are made at low voltage, unsaturated magnetic field and the established relationships operate with unsaturated synchronous reactances.

Saturated synchronous reactances are introduced in the diagram which is made on the basis of experimental dates and used for various calculations. It considers that the influence of saturation against leakage reactances can be neglected.

For the direct-axis the experimental determinations are effected both in closed and open field circuits. As it results from the scheme of figure 3.a, the angle between the winding AX magnetic axis and the direct axis d is $\theta = 90^0$ and the currents and the stator voltages are:

$$\underline{I}_A = 0; \quad \underline{I}_B = -\underline{I}_C = \underline{I}; \quad \underline{U} = \underline{U}_B - \underline{U}_C; \quad \underline{U}_A = 0 \tag{10}$$

In this case, on the basis of spatial phasors theory, one calculates the electrical magnitudes in the direct axis d:

$$\begin{aligned} \underline{I}_d &= \frac{2}{3}\left[\underline{I}_A \cos\theta + \underline{I}_B \cos\left(\theta - \frac{2\pi}{3}\right) + \underline{I}_C \cos\left(\theta - \frac{4\pi}{3}\right)\right] = \frac{2}{\sqrt{3}}\underline{I} \\ \underline{U}_d &= \frac{2}{3}\left[\underline{U}_A \cos\theta + \underline{U}_B \cos\left(\theta - \frac{2\pi}{3}\right) + \underline{U}_C \cos\left(\theta - \frac{4\pi}{3}\right)\right] = \frac{1}{\sqrt{3}}\underline{U} \end{aligned} \tag{11}$$

The magnitudes in the axis q correspond for $\theta = 0$ (Fig. 3.b) being:

$$\begin{aligned} \underline{I}_q &= \frac{2}{3}\left[\underline{I}_A \sin\theta + \underline{I}_B \sin\left(\theta - \frac{2\pi}{3}\right) + \underline{I}_C \sin\left(\theta - \frac{4\pi}{3}\right)\right] = 0 \\ \underline{U}_q &= \frac{2}{3}\left[\underline{U}_A \sin\theta + \underline{U}_B \sin\left(\theta - \frac{2\pi}{3}\right) + \underline{U}_C \sin\left(\theta - \frac{4\pi}{3}\right)\right] = 0 \end{aligned} \tag{12}$$

From the relationships (11) is results that by measuring the magnitudes U, I, P, one determinates the equivalent scheme parameters in axis d. In this case one can effect two experimental determinations the first determination with open field winding ($I_e = 0$) determining Z'_M; the second one with short-circuited field winding ($U_e = 0$) determining Z''_M. One determinates experimentally the excitation winding resistance R_e and from the three-phased symmetrical short circuit characteristic, one obtains of basis current of the field current I_{eb} respectively the basis impedance Z_{eb}. By the last data one can calculate the magnitude reported of the field winding resistance $r_e = R_e / Z_{eb}$. By particularizing the equivalent scheme in figure 1.a, for the two cases one will obtain:

$$\begin{aligned} jx_{eD\sigma} + \underline{z}_{\sigma D} &= \frac{1}{\dfrac{1}{\underline{z}'_M - \underline{z}_\sigma} - \dfrac{1}{jx_{md0}}} = z'; \quad i_e = 0; \quad \nu = 0; \\ jx_{eD\sigma} + \frac{\underline{z}_{\sigma D}\underline{z}_{\sigma e}}{\underline{z}_{\sigma D} + \underline{z}_{\sigma e}} &= \frac{1}{\dfrac{1}{\underline{z}''_M - \underline{z}_\sigma} - \dfrac{1}{jx_{md0}}} = z''; \quad u_e = 0; \quad \nu = 0 \end{aligned} \tag{13}$$

where notations have been done: $\underline{z}_\sigma = r + jx_\sigma; x_{eD\sigma} = x_{eD} - x_d; \underline{z}_{\sigma D} = r_D + jx_{\sigma D}; \underline{z}_{\sigma e} = r_e + jx_{\sigma e}$

The magnitudes z' and z" being known, the calculations being effected, one will obtain the following unknown parameters:

$$r_D = \mathrm{Re}\{\underline{z}'\}$$
$$x_{\sigma D} = \frac{br_D \pm \sqrt{\left(a^2+b^2\right)\left[r_D^2 - a\left(r_e + r_D\right)\right]}}{a}; \quad x_{\sigma e} = \frac{2x_{\sigma D}r_D - ax_{\sigma D} - b\left(r_e + r_D\right)}{a}; \tag{14}$$
$$x_{eD\sigma} = \mathrm{Im}\left\{\underline{z}_M'\right\} - x_{\sigma D}; \quad \underline{z}' - \underline{z}'' = a + jb$$

For the reactances $x_{\sigma D}$ and $x_{\sigma e}$ it results two solutions, the positive solutions being correct.

For the quadrature axis q only an experimental test is possible (there are only two access terminals). From the relationships (12) it results by measuring U, I, P, one determines the complex impedance Z''_{Mq}. From the equivalent electrical scheme in figure 1.b it will result

$$\underline{z}_{\sigma Q} = \frac{jx_{mq0}\left(\underline{z}''_{Mq} - \underline{z}_\sigma\right)}{x_{mq0} + \underline{z}''_{Mq} - \underline{z}_\sigma} = r_{\sigma Q} + jx_{\sigma Q} \tag{15}$$

The relationships (14) and (15) permit to determinate the parameters in the two axes. Because the tests are made at low voltages, it results the magnetic circuit is unsaturated reactances x_{d0} and x_{q0}. One has to remark in the equivalent scheme in figure 1 for the longitudinal reactance as well as for the quadrature one, their values saturated are to be introduced, $x_{md} = k_{sd}\, x_{md0}$, $x_{mq} = k_{sq}\, x_{mq0}$ (k_{sd} and k_{sq} being their saturation factors in the two axes).

Following the previous procedure one has experimentally determined the equivalent electrical scheme parameters for a synchronous machine with reference data: P_n = 3kW, n_n = 1500 rot/min, U_n = 220V/380V and one has obtained the values: r = 0,0519; x_σ = 0,0967; x_{md} = 0,427; r_D = 0,0947; $x_{\sigma D}$ = 0,0161; r_e = 0,113; $x_{\sigma e}$ = 0.255; x_{mq} = 0,187; r_Q = 0,106; $x_{\sigma Q}$ = 0.87.

4. Conclusions

1. It establishes relationships between catalogue dates and the parameters of the equivalent scheme both for longitudinal and transverse axis. These relationships are useful for synchronous machine designing.
2. One has done analysis of the simplified mathematical model permitting the study of slow process taking place in the synchronous machine operating.
3. The experimental determination methods were so organized that on their basis all parameters of the equivalent schemes on axes d and q can be determined. The stator winding resistance, the field winding one, the synchronous reactances, longitudinal and quadrature unsaturated have been determined by classical methods, in order to determine the other parameters one has employed static methods (fixed rotor) for the longitudinal axis system is a quadripole permitting by the supplying of a terminals couple two kinds of experimentations by short-circuiting or by no load operating of the two other terminals.
4. On the basis of the experimental results the catalogue dates can calculated and check., this being a validation method of designing.
5. If the parameters are expressed in basis X_d and X_d, respectively and not in basis X_{ad} and X_{aq} then the electrical equivalent diagrams on axes d and q can be organized simpler. This way the leakage reactance X_q disappears from schemes, the calculation relationships of synchronous machine parameters become simpler and additional experimental tests in order to determine the leakage reactance X_σ are not necessary.

References

[1]. Yhao, Z.; Yheng, J.; Gao, J.; Xu, L., "A dynamic on line parameter identification and full scale system experimental verification for large synchronous machines", IEEE Trans. EC, vol.10, nr. 3, 1995, pp. 392 – 398.

[2]. Câmpeanu, A. "Introducere în dinamica maşinilor electrice de curent alternativ", Editura Academiei Române, Bucureşti, 1998.

[3]. Krause, P. C., "Analysis of Electric Machinery", New York, McGraw Hill, 1992.

[4]. N.Galan, D. Emanoil, M. Mihalache, A. Craciunescu, I. Bestea, I. Dumitrache, C. Mucichescu, S. Dumitriu. "Modelul matematic simplificat al masinii sincrone trifazate", EEA Electrotehnica, 37, no. 7, 1989, pp 279-284.

[5]. N. Galan, M. Mihalache, „Identificarea experimentala a schemei electrice echivalente pentru masina sincrona conventionala", EEA Electrotehnica, 32, no. 2, 1984, pp 54-58.

Electromagnetic Fields in Mechatronics, Electrical and Electronic Engineering
A. Krawczyk et al. (Eds.)
IOS Press, 2006

ANALYSIS OF FREQUENCY DEPENDENCE OF MULTICONDUCTOR RESISTANCES

G. Martínez[1], M. Sancho[1], D. Méndez[1] and C. Díaz[2]

[1] Depto. Física Aplicada III, Fac. de Física, Universidad Complutense, 28040-Madrid, Spain
[2] Centro Español de Metrología, C/ Alfar 2, 28760-Tres Cantos, Spain

***Abstract** – An essential step in the development of quantum Hall devices for ac metrological standards is the frequency characterisation of multiconductor resistances [1]. The needed resistance values would require the use of rather long wires; a proposed solution consists in folding the wire into multiconductor geometries. In this work we present an accurate modeling of a quadrifilar resistance in the range 0−10 kHz, using a transmission-line approach. Capacitances were obtained with a version of the Boundary Element Method optimised to treat very different length scales; inductances, eddy currents and skin effects are computed through analytical formulae paying special attention to the singularities occurring in the problem.*

The Quadrifilar Resistor

The resistor for a metrological standard must fulfill the conditions of voltage and current connections proximity and compactness. One of the most commonly used systems is the quadrifilar resistor enclosed in a shielding cylindrical box [2]. The full characterization of such resistance would require the solution of Maxwell's equations in a complex 3D geometry. A common approach is to treat the resistor as a uniform transmission line. This implies to neglect longitudinal field components and to establish a model of the system in terms of a circuit made of distributed electrical parameters. The approximation is reasonable since the transverse dimensions of the resistor are much smaller than its length. Using this approach, the main sources of variation with frequency are the capacitances between wires and with the shell and the corresponding inductances. Skin and eddy current effects are also analyzed, neglecting small contributions arising from interacting elements.

The goal of our study is the characterization of the quadrifilar resistor Rq 1131, used as a resistance standard at the Centro Español de Metrología, Tres Cantos, Spain.

Geometrical and electrical characteristics

The geometry and excitation of the resistor are schematically shown in Figure 1. The resistor was made of Evanohm and surrounded by a cylindrical aluminium shell. The Evanohm is a low-thermal-e.m.f. alloy that minimizes errors due to Peltier effect. The wire is folded into four smaller conductors occupying the edges of a square prism. The current enters through one of the ends, flows in opposite sense through each pair of contiguous wires and gets out through the other end. The medium filling the space is assumed to be air, thus ignoring shunt conductance influence.

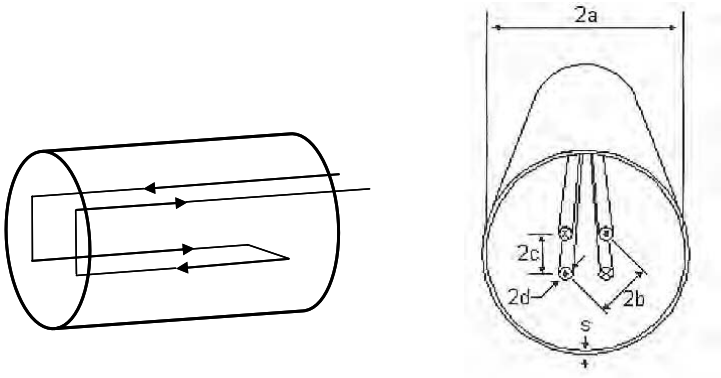

Fig. 1 Geometrical and electrical parameters of the studied resistor: a = 47.5 mm; b= 7.07 mm; c = 5 mm; d = 16 μm; s = 3 mm; length of wires h = 51 cm; length of shield h_s = 55 cm. Wire dc resistance R_{dc}=12906.403555 Ω, aluminium resistivity $\rho_a = 2.655\times10^{-8}\ \Omega\,\mathrm{m}$; Evanhom and aluminium magnetic susceptibility $\mu = \mu_0 = 4\pi\times10^{-7}$ H/m; terminal capacitance $C_t = 4.07\times10^{-14}$ F.

Capacitance Coefficients

The capacitance parameters are defined as functions of the potential coefficients. For a system of *N* conductors, the potential of the *i*-th conductor is given by

$$\varphi_i = \sum_{i=1}^{N} p_{ij} Q_j \tag{1}$$

The matrix of potential coefficients p_{ij} is symmetric and, due to the relative position of the four conductors, only three of them, p_{11}, p_{12} and p_{13}, are independent. To obtain these coefficients, the charge distribution on the conductors has been computed for a set of fixed potential values.

Given the different scales of the diameter of wires and their length, a BEM solution has proved to be the most efficient [3]. The conducting surfaces are divided into small subareas that have the form of cylindrical sectors or circular sectors so that they reproduce exactly the boundaries of the system. Under the assumption that the charge density is constant on each subarea, the problem is reduced to solve an algebraic system of equations. For the geometry represented in Fig. 1, the contours were divided (typically) into 5800 subareas. The coefficients of the algebraic system A_{kl} represent the electrostatic potential that a unit charge density on the subarea S_l creates at the centre of subarea S_k and are expressed as,

$$A_{kl} = \frac{1}{4\pi\varepsilon_0} \int_{S_l} \frac{ds'}{\left|\mathbf{r}_k - \mathbf{r}_l'\right|} \tag{2}$$

They can be integrated analytically to one of the surface variables for both types of subareas. To integrate numerically to the second variable, an adaptive technique with adjustable accuracy has been used. It was necessary to perform a Taylor series development of the integrand in the case of close subareas in order to assure nine digits stability in the resulting value.

Once the p_{ij} are computed, the capacitance coefficients can be obtained from the relations:

Capacitance between one wire and the shield $$C_0 = \frac{4h}{p_{11} + 2p_{12} + p_{13}} \tag{3-a}$$

Capacitance between a pair of adjacent wires $$C_1 = \frac{p_{12}}{\left(p_{11} + p_{13}\right)^2 - 4{p_{12}}^2} \tag{3-b}$$

Capacitance between diagonally opposite wires $$C_2 = \frac{h p_{13}\left(p_{11} + p_{13}\right) - 2{p_{12}}^2}{\left(p_{11} - p_{13}\right)\left\{\left(p_{11} + p_{13}\right)^2 - 4{p_{12}}^2\right\}} \tag{3-c}$$

Equivalent capacitance $$C_q = \frac{5C_1 + 3C_2 - C_0 + 6C_t}{6} \tag{3-d}$$

The numerical values obtained for the studied resistor are given below.

Self- And Mutual Inductance Coefficients

These coefficients can be obtained from the interaction energy between currents flowing along the wires [4]. For the mutual inductance we have,

$$M_{ij} = \frac{\mu}{4\pi I_i I_j} \int_{C_i} dv_i \int_{C_j} \frac{\mathbf{J}(\mathbf{r}_i) \cdot \mathbf{J}(\mathbf{r}_j')}{\left|\mathbf{r}_i - \mathbf{r}_j'\right|} dv_j' \tag{4}$$

here $\left|\mathbf{r}_i - \mathbf{r}_j'\right|$ means the distance between the volume elements dv_i and dv_j'. The self inductance is obtained from Eq. (4) making $i = j$. The computation of M_{ij} can be performed by using a numerical integration routine extended to both wires; however, it is more precise to calculate its value through a series development. For the dimensions specified in Fig. 1, the expression is given by

$$\begin{aligned} M_{ij} = \frac{\mu}{2\pi} h \Bigg[& \ln 2 - \ln\sigma - 1 + \sigma\left(1 + \frac{1}{4}\kappa^2 + \frac{5}{192}\kappa^4 + \frac{7}{512}\kappa^6 + \cdots\right) - \frac{\sigma^2}{4}\left(1 + \kappa^2\right) \\ & + \frac{\sigma^4}{96}\left(3 + 12\kappa^2 + 5\kappa^4\right) - \frac{\sigma^6}{192}\left(2 + 18\kappa^2 + 30\kappa^4 + 7\kappa^6\right) + \cdots \Bigg], \end{aligned} \tag{5}$$

being $r = d/2$ the radius of the wires, and $\sigma = s/h$, $\kappa = r/s$ non-dimensional quantities less than unity, assuring thus the quick convergence of the series. The computation of the self-inductance includes a singularity but can also be evaluated through a series development:

$$L = \frac{\mu h}{4\pi}\left(-\frac{3}{2} + 2\ln\frac{2}{\chi} + \frac{256}{45\pi}\chi - \frac{1}{2}\chi^2 + \frac{5}{48}\chi^4 - \frac{7}{96}\chi^6 + \frac{21}{256}\chi^8 + \cdots\right), \tag{6}$$

where $\chi = r/h$. We have taken in eqs. (5) and (6) a number of terms sufficient to assure nine digits of precision.

The above series developments were obtained by means of symbolic programming with *Mathematica* [5]. They can be extended to any desired order.

The effects of capacitance and inductance on the relative variation of the quadrifilar resistance $R_{ac}/R_{dc} = 1 + \alpha,$ are given by a coefficient $\alpha = \alpha_0 \omega^2$, such that

$$\alpha_0 = \left[\frac{1}{R_{dc}^{\,2}} \left(4L - 8M_1 + 4M_2\right)^2 + \frac{R_{dc}^{\,2}}{11520} \left\{ 240 C_0^{\,2} - 15\left(C_0 + 8C_1 + 8C_2\right)^2 - \left(C_0 + 16C_1\right)^2 \right\} \right] \tag{7}$$

being M_1 the mutual inductance between a pair of adjacent wires and M_2 the mutual inductance between a pair of diagonal opposite wires. This mechanism has a quadratic dependence on the angular frequency $\omega = 2\pi f$ of the applied current.

Eddy Currents And Skin Effects

The main influence of eddy-current losses comes from the induced currents in the cylindrical shield, the effect of the adjacent wires being negligible. They can be modeled using the classical treatment [2], through the relative variation of resistance β given by:

$$\beta = \frac{8\mu_0 m \omega h}{\pi R_{dc}} \left(\frac{1}{4 + m^2} \right) \left(\frac{b}{a} \right)^4 ; \quad m = \frac{\omega \mu_0 \mu_a a s}{2\rho_a} \tag{8}$$

that shows a rather complex variation with ω.

Skin effects are due to the current distribution in the wires and can also be analytically computed as a solution of the corresponding Helmholtz equation. The relative variation can be expressed using a coefficient δ that approximately depends on the wire parameters and the frequency of operation in the form:

$$\delta = \frac{\omega^2}{12} \left(\frac{\mu}{4\pi r_{dc}} \right)^2 - \frac{\omega^4}{180} \left(\frac{\mu}{4\pi r_{dc}} \right)^4 , \tag{9}$$

where r_{dc} is the dc resistance per unit length of he wire.

Main Results

Using the methods described in the previous section, the representative parameters of the resistor have been obtained. All computations were done using double precision; in the algorithm for calculating potential coefficients, a test with quadruple precision was also performed. The values obtained taking the geometrical and electrical data given in Fig. 1 as input are listed in Table 1.

Table 1 Capacitance and inductance coefficients of the resistor

C_0 (F)	8.95511564×10^{-12}
C_1 (F)	4.87006792×10^{-13}
C_2 (F)	3.07295360×10^{-13}
C_q (F)	$-8.92332598\times10^{-13}$
L (H)	1.12260036×10^{-6}
M_1 (H)	3.71737424×10^{-7}
M_2 (H)	3.37205542×10^{-7}

The above described contributions were added to give the total variation of the resistance with the frequency of the ac signal:

$$R_{ac} = R(1+\Delta);\quad \Delta = \alpha + \beta + \delta \tag{10}$$

At a given frequency, for example 10 kHz, the magnitudes of these three contributions are: $\alpha = 8.82183570\times10^{-7}$, $\beta = 1.84123214\times10^{-11}$, $\delta = 8.37376011\times10^{-14}$, which clearly illustrates the predominance of coefficient α. Figure 2 shows the global variation of the resistance with frequency in the range 0 − 10 kHz.

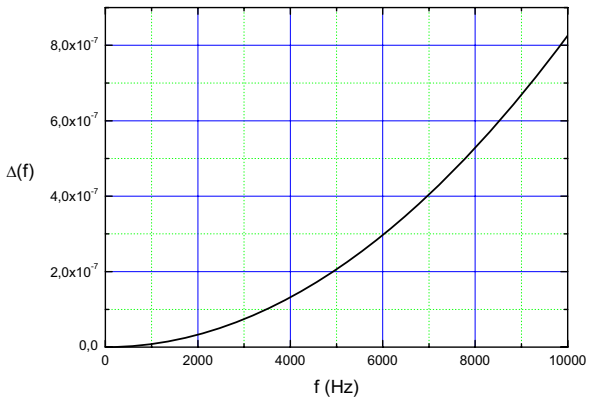

Fig. 2 Relative variation of the resistance as a function of the signal frequency

Using the actual resistor design, if a variation of resistance less than a few parts in 10^7 is sought, a frequency of about 6 kHz should not be exceeded. More stable designs could be obtained using a different geometry. The method shown here could be easily adapted to simulate other prototypes.

Conclusions

We have investigated the physical factors that contribute to the variation of a quadrifilar resistance with the frequency. The results show that the most influent factors are capacitance and inductances. The total variation has been characterised from 0 to 10 kHz with an accuracy that improves the existing analytical approximations. New series developments for self- and mutual inductance have been derived. The resistance for the frequency interval studied does not differ from the dc resistance by more than one part in 10^6. The developed methods constitute a useful tool for designing resistance standards and optimizing possible geometries in order to minimize the deviation from unity of ac/dc resistance ratio.

This work has been supported by research contract 5281779 CEM. We also acknowledge the valuable suggestions of G. Álvarez-Galindo and A. Muñoz.

References

[1] J. Bohácek, Frequency performance of 12906 Ω and 6453 Ω reference resistors for ac quantum Hall effect, Metrologia, Vol. 39, pp 231-237, 2002

[2] D.L.H. Gibbings, A design for resistors of calculable ac/dc resistance ratio, Proc. IEE, Vol. 110, pp 335-347, 1963

[3] G. Martínez and M. Sancho, Application of the Integral equation Method to the analysis of Electrostatic Potentials and Electron Trajectories, Adv. Electronics Electron Physics, Vol. 81, pp 1-41, 1991

[4] D. Jackson, Classical Electrodynamics, New York: Wiley and Sons, 3rd edition, 1998, pp 215-218

[5] http://www.wolfram.com/products/mathematica/introduction.html

Electromagnetic Fields in Mechatronics, Electrical and Electronic Engineering
A. Krawczyk et al. (Eds.)
IOS Press, 2006

COMPUTATIONAL ELECTROMAGNETICS IN AN ELECTROMAGNETIC LABORATORY

Paulo G. Pereirinha[1,2] , Carlos F. R. Lemos Antunes[1]
E-mail: ppereiri@mail.isec.pt, lemos.antunes@deec.uc.pt

[1] Lab. CAD/CAE, DEEC, Pólo II
Univ. of Coimbra, 3030-290 Coimbra – Portugal

[2]Instituto Superior de Engenharia de Coimbra, ISEC –IPC
Rua Pedro Nunes, 3030-199 Coimbra – Portugal

Abstract *– In this paper it is presented some of the authors experience in teaching computational electromagnetics to students of university level in an electromagnetic laboratory . It is described the practical case of an E core electromagnet used to give "hands on experience" on finite element modelling of electromagnetic devices.*

1-Introduction

During the last two decades, under the supervision of Prof. Carlos Lemos Antunes, people at the CAD/CAE Lab. from the Electrical and Computer Engineering Department (DEEC) of the University of Coimbra, Portugal, have been involved with the development of finite element software packages for electromagnetic and thermal analysis, like CADdyMAG and CADdyTERM. These softwares have been used in academic and industrial research in many areas going from the electric field analysis in high voltage insulators [1] and lines [2], thermal and electromagnetic analysis of actuators [3], transformers and induction motors [4], eddy current losses [5-6], and Finite Element Method methodology [7], just to mention a few, but also as a tool for teaching and introduction to electromagnetic analysis and design.
In modern applied electromagnetism courses it is important to give the students a good understanding of the physical behaviour of the electric and magnetic fields acting in the devices, as well as the heat transfer phenomena, and provide them with some knowledge on the modern design and analysis techniques of electromagnetic devices like the Finite Element Method (FEM). The students should gain experience in designing real electromagnetic devices with trial and error approaches of different design alternatives of the same device.
These ideas have been successfully tested in electromagnetic laboratory classes of undergraduate students of university level, namely with the small electromagnet presented further on.

2 - Test Device

During several years a great number of electromagnetic and electrostatic devices were designed and analysed, under the authors supervision, using the traditional method of the electric and magnetic circuits analogy and the finite element method. Some of those devices have been built by students and can be used in electromagnetic laboratory. The example presented in this paper is a small electromagnet with adjustable air gap using DC excitation, shown in Fig. 1. Both the core and the armature are made of magnetic steel laminations with the magnetization curve presented in Fig. 2 (points with circles were assumed by the authors as the data provided by the manufacturers was only for $B \leq 1.8$ T).

As can be seen in Fig. 1 some lead was glued to the armature in order to increase its weight to 1 kg. The geometry of the magnetic steel laminations is shown in Fig.3. The core and armature depth l is 38 mm. In Fig. 4 it is shown the electromagnet in attracted position and the experimental setup used for DC supply. The coil has N=1798 turns of 0.6 mm diameter copper wire and its wound around a 2.5 mm thickness plastic housing that is inserted in the core central column.

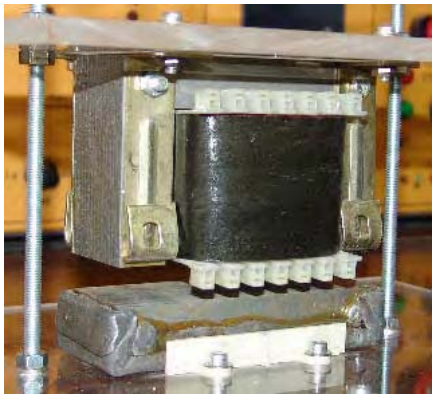

Fig.1 Variable air gap E core electromagnet.

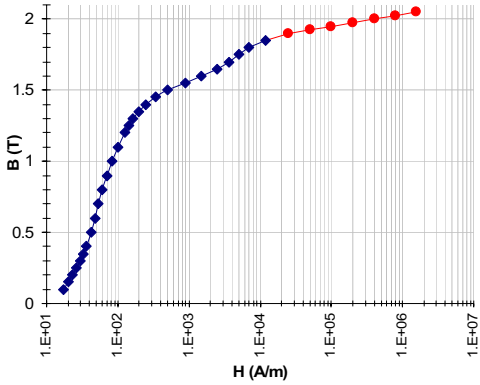

Fig.2 Magnetization curve of the magnetic steel used in the electromagnet.

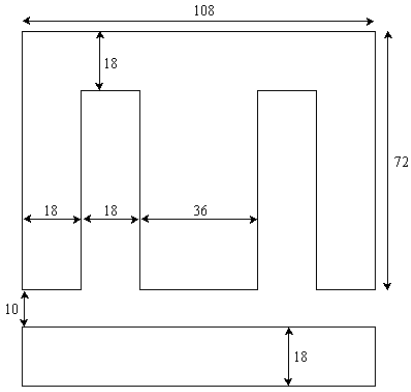

Fig.3 Dimensions of the magnetic steel laminations (depth l = 38 mm).

Fig.4 Electromagnet in attracted position and experimental setup for DC supply.

3. Calculation Of The Current Required To Attract The Armature

The objective of the students was the calculation of the current needed to attract the armature at a 10 mm distance, that is for a 10 mm air gap. They should be able to calculate this current using the analytical and numerical finite element approach and compare it with the experimental measured value.

3.1 -Analytical calculation using classical magnetic circuit analysis

According to this analogy [8-9], the reluctance R of the magnetic circuit is given by

$$R = \nu_{iron}\frac{l_{iron}}{S_{iron}} + \nu_0\frac{l_{airgap}}{S_{airgap}} \tag{1}$$

where ν_{iron} is the reluctivity of the magnetic laminations (it was considered an average value of 100 m/H for B smaller than 1.2 T), S_{iron} the area of the cross section of the central column of the core laminations stack (38×36 mm^2 =1368×10^{-6} m^2), l_{iron} is the mean length of the ferromagnetic circuit (in this case 0.234 m, considering the magnetic parallel of the lateral columns) and l_{airgap} is the total length of the air gap equal to 2×10 mm. S_{airgap} was made equal to S_{iron}, so flux fringing effects were neglected. For the presented magnetic circuit with the 10 mm air gap, $R = R_{iron} + R_{air\ gap}$ $1.711\times10^4 + 1.163\times10^7 = 1.165\times10^7$ A-t/Wb. From these values, it can clearly be seen the much bigger contribution of the air gap to the total reluctance. The magnetic force F is given by

$$F = \frac{B^2}{\mu_0}S_{iron} \tag{2}$$

where B is the magnetic induction. As for a 1 kg armature the force must be bigger than 9.8 N, it results that $B \geq 0.09488$ T and $\phi \geq 1.298\times10^{-4}$ Wb, as $\phi = B\times S_{iron}$. Since the magnetomotive force F is

$$\mathsf{F} = Ni = \mathsf{R}\,\phi \tag{3}$$

where i is the current in the coil, we have $F = R\phi \approx 1.512284\times10^3$ A-t and finally $i \approx 0.8411$ A. The inductance of the device L is equal to 0.2775 H and was calculated from its definition relatively to the flux coupled with the coil, ψ

$$L = \frac{\psi}{i} \approx \frac{N\phi}{i} \tag{4}$$

The voltage supply V is calculated by Ohm's Law, multiplying the current i by the coil resistance R. This later can be very easily calculated by

$$R = \rho\frac{l_{coil}}{S_{wire}} \tag{5}$$

where ρ is the copper wire resistivity, l_{coil} is the total length of the wire in the coil and S_{wire} the wire cross section (0.2827 mm^2). The total coil length l_{coil} is given by multiplying N by the turn length average l_{av}

$$l_{av} = 2(a_1 + a_2) + \pi b_1 \tag{6}$$

where a_1, a_2 and b_1 are the dimensions shown in Fig. 5: 41 mm, 43 mm and 13 mm, respectively (plastic housing and coil external insulation subtracted). For the present device, l_{av}=208.84 mm, l_{coil}=375.4956 m and R= 22.70 Ω. The supply voltage has then to be bigger than 19.1 V.

3.2 - Finite element calculation

For the finite element calculation of the DC current needed to attract the armature, a 2D magnetostatic model of the device has to be solved using CADdyMAG. In this case, due to symmetry, only one half of the device has to be modelled, as can be seen in Fig. 6. Air, plastic and copper have reluctivity equal to ν_0 and the core and armature laminations have the BH curve in Fig. 2. The Dirichlet boundary conditions are A=0 Wb/m (cf. Fig. 6) and the current density J to input the same F is

$$J = \frac{Ni}{S_{coil}} \tag{7}$$

where S_{coil} = 15.5×49=759.5 mm^2 is the area of the copper rectangle shown in Fig. 6.
The magnetic force vector **F** can be estimated calculating the line integral of the Maxwell Stress Tensor **T** [10]. For a 2D problem in the *xy* plane **F** and **T** are given by

$$\mathbf{F} = \frac{1}{\mu}\oint \mathbf{T}\cdot d\mathbf{S}\,; \quad \mathbf{T} = \begin{bmatrix} \left(B_x^2 - \frac{1}{2}|\mathbf{B}|^2\right) & B_x B_y \\ B_y B_x & \left(B_y^2 - \frac{1}{2}|\mathbf{B}|^2\right) \end{bmatrix} \tag{8}$$

where B_x and B_y are the x and y components of the **B** vector, $\mathbf{B} = \nabla \times \mathbf{A}$. One important point is that the line integral has to be calculated only over air finite elements and at least at two finite element layers from the iron; otherwise, there will be important errors (due to the large imprecision in the tangential components of **B** in the elements bordering the boundaries between materials of different ν). The mesh has to be very refined in this area in order to increase the precision, as in Fig 7.

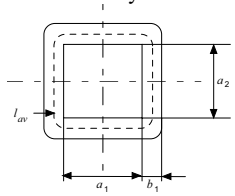

Fig. 5. Coil dimensions (top view).

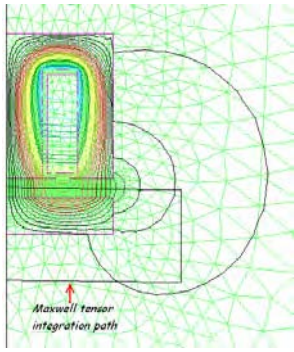

Fig.7. FE mesh and magnetic flux lines in the electromagnet for 10 mm air gap (i=0.8173 A).

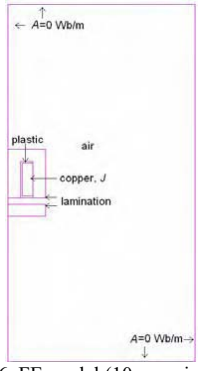

Fig. 6. FE model (10 mm air gap).

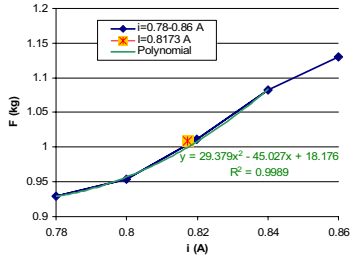

Fig.8. FE calculation of the current to attract the armature at 10 mm air gap.

The inductance of the device can be calculated from the flux coupled with the winding ψ or from the energy stored in the magnetic field, W, that lead to the same result only in the linear behavior zone of the laminations magnetization curve

$$L = \frac{\psi}{i} = \frac{l\int_S A \cdot J \, dS}{i^2}; \quad L = \frac{2W}{i^2} \tag{9}$$

The problem was solved for five different values of i around the 0.8411 A value given by the analytical approximation: from 0.78 A to 0.86 A. For these values of i the force was calculated using (8). It was verified that the results could be very well fitted by a 2nd order polynomial equation, as can be seen in Fig. 8, and the current needed to attract the armature at 10 mm, was calculated to be equal to 0.8173 A. Solved the FE problem with this current (Fig. 7), the error in the force was 0.95%. From now on the presented units of the force will be kg (1 kg = 9.81 N) as it is easier to see the differences relatively to the armature's weight (1 kg).

4 – Experimental Results And Comparison With Analytical And FE Results

The device was experimentally tested in Electromagnetics Laboratory. The minimum measured values (cf. Fig. 4) of i needed to attract the armature are shown in Fig. 9 for each one of the represented air gaps (to keep the armature attracted, i=5 mA). The forces calculated by the FEM using the Maxwell Stress Tensor for those currents are represented in Fig. 10 by the curve "F_MaxwellT_iexp". As can be seen, there is a certain difference to the 1 kg value (the average difference in the force is 10.5%), specially for 0.5 mm air gap. At this point, a recall can be made to the students to the unavoidable accuracy problems and measurement errors. As can be seen, the minimum attraction current can be very well fitted by a linear function (Fig. 9). Using the corrected values of the current calculated by this linear fitting, better, and specially more regular, results can be obtained (curve "F_MaxwellT_iLinInterp", Fig. 10), now with an average difference of 9.31 %.

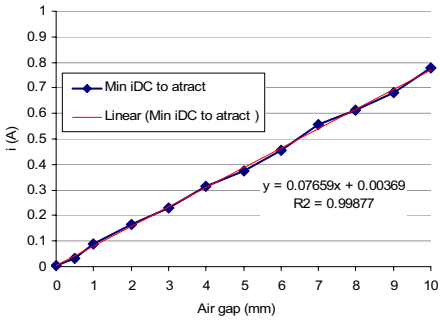

Fig. 9. Measured DC currents to attract the armature and linear fitting.

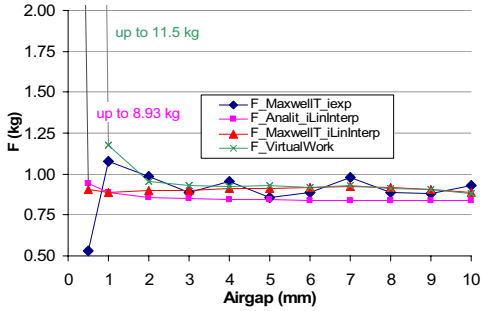

Fig.10. Forces calculated by the different methodologies.

"F_VirtualWork" represents the force calculated by the two step Virtual Work Principle, by the quotient between the difference of coenergies for two meshes with the armature nearby the intended point (with i for this point) and the displacement of the armature, between these two positions [3]. For the air gaps bigger than 1 mm, the virtual work presents slightly better results. "F_Analit_iLinInterp", represents the force calculated by the analytical approach.

Again for air gaps bigger than 1 mm, the discrepancies between the FE calculated forces and the armature weight are mainly due to two factors: errors in the current measurement (it were used several multimeters as ammeters and one oscilloscope: this one presented slightly bigger values of the current than the ammeters – leading to bigger forces – but the ammeters values were chosen due to the approximate concordance among them); the second one is that in a 2D FE software, the end effect (3rd

dimension) is not considered.
For attracted position ("0" mm), the 8.93 kg presented by "F_Analit_iLinInterp" is due to the fact that it was calculated considering the interpolated current i=3.69 mA for 0 mm. However, in attracted position the air gap is not exactly "0 mm" due to insulation and imperfect contact. With the same i=3.69 mA but with a microscopic 29 μm air gap, the force would be 1 kg. For "F_VirtualWork" the problem is similar, as the coenergy for the attracted position was calculated for 0 mm air gap.
The attraction force for i=0.78 A (value needed to attract with 10 mm air gap) is presented in Fig. 11.
The average of the measured resistance $R_{meas}=V/i$ was 22.36 Ω, quite near the calculated 22.7 Ω.
Finally, the students can change the setup and supply the electromagnet with AC current through a autotransformer. First, they will verify that the armature vibrates a lot but is not attracted, even, for example, with only 1 mm air gap and 240 V rms. This is due to the fact that the force vanishes each time that the alternating flux is zero. To avoid this behavior, the AC electromagnets must have copper loops surrounding part of the core poles, called shading coils, which is not the case. Nevertheless, as in AC the electromagnet is very nearly a pure inductance, the inductance can be calculated from the measured values by $V \approx 2\pi f L i$. In Fig. 12, it is presented the experimental inductance values "L_exp_AC" together with the values calculated analytically and by FE using the W and the ψ. It can be clearly seen that the FE results are much better than the analytical ones, especially when the air gap is important or when saturation is attained.

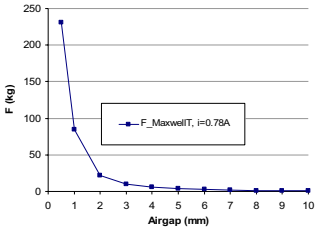

Fig. 11. Forces calculated by Maxwell Stress Tensor for constant i=0.78 A.

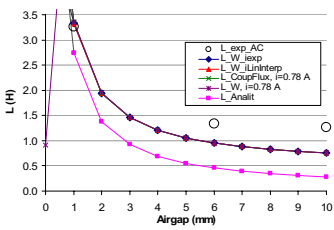

Fig.12. Inductances calculated by different approaches: experimental, FE and analytical.

5 - Conclusions

This simple "home made" device allows the students to have a good insight of the finite element method utilization in the design and analysis of electromagnetic devices as well as to recall some cares and critical spirit needed regarding the measured values and the experimental setup.

Acknowledgments
The authors wish to thank the former ISEC students C. Monteiro, C. Carvalho and F. Graça for building the test device presented.

References

[1] C.L. Antunes, A.P. Coimbra, "Computer aided insulator design", Proc. of Melecon 1989, Mediterranean Electrotechnical Conference, pp 454-457, Lisbon, Portugal, April 11-13, 1989.

[2] J.A. Pinto, A.P. Coimbra, P.G. Pereirinha, C.L Antunes, "Evaluation of the high voltage transmission line inductance and capacitance using the finite element approach", COMPEL - The International Journal for Computation and Mathematics in Electrical and Electronic Engineering, vol. 17, pp 313-317, 1998.

[3] P.G. Pereirinha, C.L. Antunes, "Force Calculation on a E Core Actuator using the Virtual Work Principle and Derived from Non Linear Finite Element Potential Solutions", Proc. of the ICEM, Vol. III, pp 46−50, Vigo, Spain, September 10−12, 1996.

[4] J.A. Pinto, C.L. Antunes, A.P. Coimbra, "Transient heating and cooling analysis in an electromagnetic device", IEEE Trans. Magn., vol. 30 (nº5, Sept. 1994), pp 3339-3342, 1994.

[5] P.G. Pereirinha, J. Gyselinck, C.L. Antunes "Study of the Local Eddy Current Loss Density near the Edges in Steel Laminations of Finite Width", Proc. of COMPUMAG 2003, 14th Conference on the Computation of Electromagnetic Fields, Saratoga Springs, vol. IV, pp.194-195, New York, USA, July 13-17, 2003.

[6] P.G. Pereirinha, C.L. Antunes, "Chart and Expressions for Eddy Current Losses Calculation in Steel Lamination derived from Finite Element Numerical Results in 2D", Computer Engineering in Applied Electromagnetism, Springer 2005, ISEF Monograph, 2005, pp. 197-203.

[7] P. G. Pereirinha, C.L. Antunes, "Equivalent thermal conductivity of insulating materials for high voltage bars in slots of electrical machines", Proc. of the ICEM'2004, 16th International Conference On Electrical Machines, in CD-ROM, Cracow, Poland, September 5-8, 2004.

[8] H. C. Roters, Electromagnetic Devices, New York: John Wiley & Sons, 1941.

[9] S. Nasar, Schaum's Outline of Theory and Problems of Electric Machines and Electromechanics, New York: McGraw-Hill, 2nd ed., 1997.

[10] D. A. Lowther, P. P. Silvester, Computer-Aided Design in Magnetics, New York: Springer-Verlag New York Inc., 1986. pp.46-47, 194-195.

Electromagnetic Fields in Mechatronics, Electrical and Electronic Engineering
A. Krawczyk et al. (Eds.)
IOS Press, 2006

MICROWAVE IMAGING OF TWO-DIMENSIONAL CONDUCTING SCATTERERS USING PARTICLE SWARM OPTIMIZATION

Ioannis T. Rekanos and Maria A. Kanaki

Department of Informatics and Communications, Technological and Educational Institute of Serres, Terma Magnesias, GR-62124, Serres, Greece

Abstract* – *In this paper, a microwave imaging technique for reconstructing the shape of two-dimensional perfectly conducting scatterers by means of the particle swarm optimization algorithm is proposed. The reconstruction is based on scattered field simulated measurements derived by transverse magnetic illuminations. Two different implementations of the particle swarm optimization algorithm, namely the synchronous and the asynchronous one, are considered. Furthermore, the robustness of the algorithm with respect to different initial particle populations is investigated. Finally, the performance of the technique in the case of noisy scattered field data is examined.

Introduction

Microwave imaging is related to the reconstruction of the electromagnetic properties of unknown scatterers and it is of significant interest due to its numerous applications, such as biomedical imaging, nondestructive testing, and geophysical exploration. This inverse scattering problem is nonlinear and ill-posed and it is usually solved by means of iterative optimization algorithms and regularization schemes [1]. A particular problem of this kind is the estimation of the location as well as the shape of perfectly conducting scatterers [2], [3]. Previously, deterministic techniques [2] have been utilized to cope with the reconstruction of 2D conducting scatterers, while stochastic algorithms like the differential evolution algorithm [3] have been proposed.

Recently, the particle swarm optimization (PSO) algorithm [4] has attracted the interest of the electromagnetics community as a promising technique for the solution of optimization and design electromagnetic problems [5-6]. Actually, the PSO algorithm has already been applied to the solution of inverse scattering problems related to the reconstruction of dielectric scatterers [7-8].

In this paper, the PSO is applied to the reconstruction of the shape of perfectly conducting scatterers. The objective of the PSO is to minimize a cost function that describes the discrepancy between the measured and estimated scattered field data. In particular, the estimation of the scattered field data is based on the integral formulation of the direct scattering problem, while the contour of the scatterer is described by a parametric model utilizing cubic B-splines [9].

Description of the Problem

Our goal is to reconstruct the contour of the 2D perfectly conducting scatterer, given a set of monochromatic transverse magnetic (TM) scattered field measurements. Concerning the direct scattering problem, if C is the contour of the scatterer, then the scattered field at any position r, on the surface or outside the scatterer domain, is given by the closed line integral

$$E(r) = -\frac{\omega\mu_0}{4}\oint_C J(r')H_0^{(2)}(k_0|r-r'|)dr' \quad (1)$$

where $J(r')$ is the equivalent surface current density. Since the total field on the surface vanishes, $J(r')$ is derived by the solution of the integral equation

$$E^i(r) = \frac{\omega\mu_0}{4}\oint_C J(r')H_0^{(2)}(k_0|r-r'|)dr',\ r \in C \quad (2)$$

where $E^i(r)$ is the known TM incident field. Given the incident field, in order to compute the scattered field, we solve (2) with respect to $J(r')$ and then we substitute the solution into (1). The equivalent surface current density can be computed by applying the method of moments [10] to the integral (2).

Cubic B-Spline Representation of the Scatterer

The contour of the scatterer is described by a parametric model utilizing closed cubic B-splines [9] with N control parameters $p_0, p_1, ..., p_{N-1}$. According to this approach, the contour is assumed smooth, since its second derivative is continuous, while its third derivative is piecewise continuous. In particular, the contour is written as

$$C(\theta) = R\left(\frac{N}{2\pi}\theta\right),\quad \theta \in [0, 2\pi] \quad (3)$$

where the curve $R(\tau)$, $(0 \le \tau \le N)$ is composed of N curve segments $r_n(t)$, i.e.,

$$R(\tau) = \sum_{n=0}^{N-1} r_n(\tau - n)\,. \quad (4)$$

Each curve segment $r_n(t)$ is a linear combination of four cubic polynomials defined in the normalized domain $t \in [0,1]$, i.e.,

$$r_n(t) = p_{n-1}Q_0(t) + p_nQ_1(t) + p_{n+1}Q_2(t) + p_{n+1}Q_3(t),\ \ n = 0,1,...,N-1 \quad (5)$$

where $p_{-1} = p_{N-1}$, $p_0 = p_N$, $p_1 = p_{N+1}$, while the cubic polynomials are given by

$$Q_0(t) = \frac{1}{6}(1-t)^3,\quad Q_1(t) = \frac{1}{2}t^3 - t^2 + \frac{2}{3},\quad Q_2(t) = -\frac{1}{2}t^3 + \frac{1}{2}t^2 + \frac{1}{2}t + \frac{1}{6},\quad Q_3(t) = \frac{1}{6}t^3\,.$$

Therefore, the contour C is described by the N-dimensional vector, $\mathbf{p} = [p_0, p_1, ..., p_{N-1}]$, of the control parameters associated with the B-spline representation of C.

A significant advantage of the cubic B-spline representation of the scatterer contour is that the cubic polynomials are nonnegative. Thus, the reasonable constraint $C(\theta) \ge 0$ can be simply imposed by requiring all control parameters p_n to be positive. Actually, this approach of imposing the constraint $C(\theta) \ge 0$ is based on the property

$$\min_{0 \le n \le N-1} p_n \le R(\tau) \le \max_{0 \le n \le N-1} p_n,\quad 0 \le \tau \le N\,. \quad (6)$$

Inverse Scattering

Let us assume that the scatterer is illuminated by a number of incident fields and that for each incidence the scattered field is measured at a set of measurement positions around the scatterer domain. The objective is to estimate the scatterer contour from the total set of measurements. To cope with this inverse scattering problem, we define a cost function representing the discrepancy between measured and estimated scattered field. In this study, the shape of the scatterer is reconstructed by minimizing the cost function

$$F(C)=\left[\sum_{i=1}^{I}\sum_{m=1}^{M}\left(E_{im}^{d}-E_{im}^{e}(C)\right)^{2}\right]\Big/\left[\sum_{i=1}^{I}\sum_{m=1}^{M}\left(E_{im}^{d}\right)^{2}\right] \tag{7}$$

where I is the total number of incidences, M is the number of measurements per incidence, E^d denotes the measured scattered field and E^e is the estimated one. Actually, since the contour is a function of $\mathbf{p}=[p_0, p_1, ..., p_{N-1}]$, (7) is minimized with respect to $\mathbf{p}$.

Particle Swarm Optimization Algorithm

In this study, the minimization of the cost function (7) is carried out by the PSO algorithm. Initially, a randomly generated set of K candidate solutions $\{\mathbf{p}_k : k=1,2,...,K\}$ compose the swarm, where each solution is a position in the N-dimensional solution space. Moreover, each particle $\mathbf{p}_k$ has its own velocity $\mathbf{v}_k$, which is also initially randomly selected. The particles of the swarm are allowed to travel in the solution space searching for better solution positions in terms of their performance with respect to the cost function. A particular position of a particle is considered better that another if the corresponding value of the cost function is lower. Each particle remembers its best position $\mathbf{f}_k$ ever visited, while the best position $\mathbf{g}$ among all particles, namely the global best, is communicated to all particles.

After the initialization step of the PSO, the algorithm enters an iterative process where all particles update their velocities and positions. In particular, during each iteration of the PSO, the velocities and the positions are updated according to the scheme

$$v_{kn}^{new}=A\cdot v_{kn}^{old}+B_1\cdot r_1\cdot(f_{kn}-p_{kn}^{old})+B_2\cdot r_2\cdot(g_n-p_{kn}^{old}) \tag{8}$$

$$p_{kn}^{new}=p_{kn}^{old}+v_{kn}^{new} \tag{9}$$

where $1\le k\le K$ and $1\le n\le N$. In (8), A is the inertia, B_1 the cognitive, and B_2 the social parameter, while r_1 and r_2 are random numbers uniformly distributed between 0 and 1. The inertia parameter A describes the tendency of the particle to travel along the same direction it has been traveling [11]. A large inertia value allows wide range search in the solution space, while a small one facilitates local exploration. It is generally accepted that a large inertia is suitable for the beginning of the PSO algorithm, while its value should slowly decrease as the iterations of the algorithm proceed. The cognitive parameter B_1 controls the attraction of a particle toward the best position it has ever visited, while the social parameter B_2 tunes the attraction of the particles toward the global best position [11]. According to the updating scheme described by (8) and (9) it is possible for all particles in the swarm to profit from their individual as well as the swarm community discoveries about the solution space. Finally, if the new position of a particle is better than its best position ever visited, then its current position is considered as the individual best one.

It has to be mentioned that the positions updating scheme (9) may result in candidate solutions that are not feasible. For example (9) may give negative values for the control parameters of the cubic B-spline representation. In such a case, the particle position is corrected by placing it back into the admissible solution space. This can be done by applying the "reflecting wall" boundary condition [5].

There are two basic approaches in the way the global best position $\mathbf{g}$ is communicated to all particles, namely the synchronous and the asynchronous mode. According to the synchronous mode, the global best is found and communicated after the updating procedure has been carried out for all particles and their performance with respect to the cost function has been evaluated. In the asynchronous mode the global best position is evaluated and communicated whenever a particle has reached a better position compared to the current global best. In general, the asynchronous mode may speedup the convergence of the PSO, since it is more elitist. However, the synchronous mode may allow the search of wider regions of the solution space.

Numerical Results

As a first application example of microwave imaging by means of the PSO algorithm, we have considered the reconstruction of the contour of a single 2D perfectly conducting scatterer. The scatterer, whose original contour is shown in Fig. 1, is illuminated by 7 TM plane wave incidences, uniformly distributed. The maximum radius of this particular scatterer is approximately 1.5λ, where λ is the wavelength of the monochromatic incidences. For each incidence, the scattered field is measured at 32 positions, uniformly placed around the scatterer at a distance from the scatterer center equal to 10λ. These measurements were simulated by means of the method of moments. For the reconstruction of the scatterer shape, the contour has been represented by $N = 10$ control parameters of the cubic B-spline model.

The population size, K, of the particle swarm was selected equal to 40. The initial values of the components of the particles that correspond to the control parameters were chosen randomly (uniformly distributed in the range $[0, 2]$). The initial values of the components of the particle velocities were also chosen randomly (uniformly distributed in the range $[-1, 1]$). Then, 200 iterations of the PSO algorithm have been completed, following the synchronous mode implementation. For all iterations, the cognitive and the social parameter were kept constant ($B_1 = B_2 = 0.5$) [11], whereas the inertia parameter was initially $A = 0.9$ and dropped linearly to 0.7 after 200 iterations. The value of the cost function after the completion of the optimization process was lower than 5.8×10^{-3}. The reconstruction result is shown in Fig. 1, where the original shape of the scatterer and the finally reconstructed one are illustrated. In addition, Fig. 1 depicts the best contour estimate, which was included in the randomly generated initial swarm.

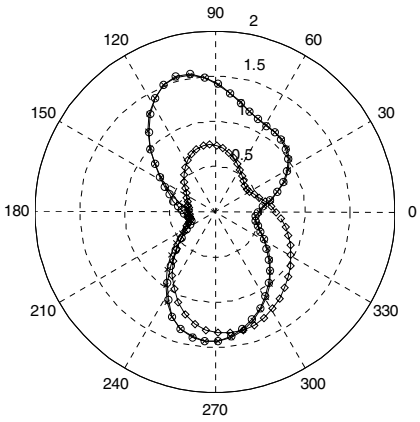

Fig.1. Shape reconstruction result. Original contour (circles), best estimate included in the initial swarm (diamonds), best estimate after 200 iterations (crosses).

To quantify the accuracy of the shape reconstruction, we define the reconstruction error given by

$$E(C) = \left[\frac{\sum_{l=1}^{L} \left[C^d(\theta_l) - C^e(\theta_l) \right]^2}{L} \right]^{1/2} \tag{10}$$

where $C^d(\theta)$ and $C^e(\theta)$ stand for the original and the estimated contour (radius function) of the scatterer. In (10), L is the total number of distinct points along the contours, where the original and

the estimated radius are evaluated. Actually, the corresponding angular coordinates of the distinct point are $\theta_l = (2\pi / L)l$ with $l = 1,2,...,L$. In the application examples, L was selected equal to 60. The reconstruction error after 200 iterations was lower than 2.9×10^{-2}. The cost function and the reconstruction error versus number of iterations are illustrated in Fig. 2.

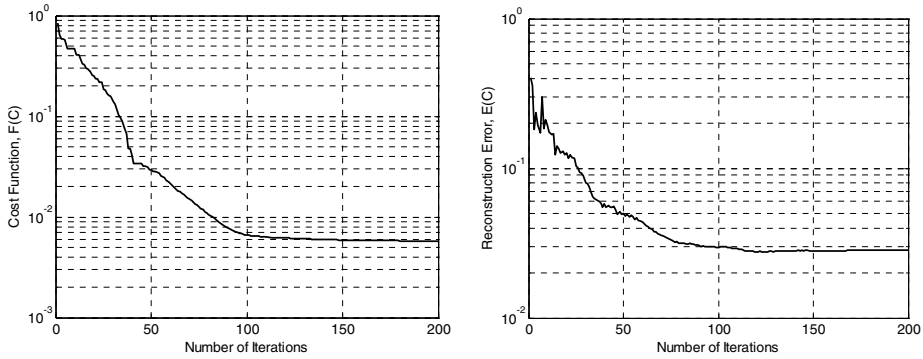

(a) (b)

Fig.2. Results related to the reconstruction of the scatterer shown in Fig. 2. Cost function (a) and reconstruction error (b) versus number of iterations of the PSO algorithm.

In the second application example of the PSO algorithm, we compare the synchronous and the asynchronous mode of implementation. We consider 30 different realizations of perfectly conducting scatterers. Each scatterer has been reconstructed by applying both the synchronous and the asynchronous mode of the PSO. All the parameters related to the second application were set as in the first application described above. Along the 30 realizations examined, the minimum, the maximum, and the mean values of the cost function and the reconstruction error, after 200 iterations of the PSO algorithm (for the case of the synchronous and asynchronous mode) are shown in Table I. It is clear that the asynchronous implementation of the PSO outperforms the synchronous one. However, it should be noted that a parallel implementation of the asynchronous mode is not advantageous. From Table I we can also conclude that the PSO is efficient in reconstructing the scatterer contour for various particle swarm initializations.

TABLE I
Cost Function and Reconstruction Error after 200 Iterations of the PSO Algorithm.
Minimum, Maximum, and the Mean Values along 30 Realizations
for the Synchronous and the Asynchronous Mode of the PSO Algorithm.

PSO Mode	Cost Function, $F(C)$			Reconstruction Error, $E(C)$		
	Min	Max	Mean	Min	Max	Mean
Synchronous	3.7×10^{-8}	2.0×10^{-2}	9.1×10^{-4}	3.8×10^{-5}	5.3×10^{-2}	4.2×10^{-3}
Asynchronous	2.1×10^{-8}	1.7×10^{-2}	8.5×10^{-4}	2.8×10^{-5}	4.8×10^{-2}	3.8×10^{-3}

Finally, the robustness of the PSO in the presence of noisy scattered field measurements has been examined. In particular, a circular perfectly conducting scatterer, with radius equal to λ, has been considered and reconstructed following the same measurement and PSO setup as in the first application. The measurements have been corrupted by additive white Gaussian noise, while the performance of the algorithm for different signal-to-noise ratio (SNR) levels has been tested. The SNR level in dB is given by

$$\mathrm{SNR} = 10\log_{10}\frac{\sum_{i=1}^{I}\sum_{m=1}^{M}\left|E_{im}^{d(noiseless)}\right|^2}{2IM\sigma^2}\ (dB) \tag{11}$$

where σ^2 is the variance of the Gaussian noise. In Table II, the cost function and the reconstruction error after 200 iterations of the asynchronous PSO algorithm are shown, for different SNR levels. From Table II, we can conclude that the PSO results in accurate reconstruction ($E(C) < 5.0\times10^{-3}$) even for SNR level equal to 15dB.

TABLE II
Cost Function and Reconstruction Error after 200 Iterations of the Asynchronous PSO Algorithm. Results for Various SNR Levels of the Measurements.

SNR (dB)	∞	25	20	15	10	5
$F(C)$	4.27×10^{-7}	1.08×10^{-4}	9.03×10^{-3}	2.69×10^{-2}	9.35×10^{-2}	2.45×10^{-1}
$E(C)$	1.05×10^{-4}	8.42×10^{-3}	2.45×10^{-3}	3.53×10^{-3}	7.83×10^{-3}	1.51×10^{-2}

Conclusions

A microwave imaging technique based on the PSO algorithm has been proposed for the reconstruction of the shape of 2D perfectly conducting scatterers. Numerical results show that the PSO is an efficient and very promising algorithm for microwave imaging applications. Both the synchronous and the asynchronous modes of the PSO have been examined. The asynchronous mode seems to give more accurate results (for the same number of iterations) compared to the synchronous one. Furthermore, the PSO algorithm is robust in the presence of noisy scattered field measurements.

Acknowledgement

This work has been supported by the Greek Ministry of Education under the "Archimedes" Project of the Technological and Educational Institute of Serres.

References

[1] I.T. Rekanos and T.D. Tsiboukis, A Finite Element based Technique for Microwave Imaging of Two-Dimensional Objects, IEEE Trans. Instument. Measurement, Vol. 49, pp. 234-239, 2000.
[2] I.T. Rekanos and T.D. Tsiboukis, An Inverse Scattering Technique for Microwave Imaging of Binary Objects, IEEE Trans. Microwave Theory Techn., Vol. 50, pp. 1439-1441, 2002.
[3] A. Qing, "Electromagnetic Inverse Scattering of Multiple Two-Dimensional Perfectly Conducting Objects by the Differential Evolution Strategy, IEEE Trans. Antennas Propagat., Vol. 51, pp. 1251-1262, 2003.
[4] J. Kennedy and R.C. Eberhart, Swarm Intelligence, San Francisco CA: Morgan Kaufmann, 2001.
[5] J. Robinson and Y. Rahmat-Samii, Particle Swarm Optimization in Electromagnetics, IEEE Trans. Antennas Propagat., Vol. 52, pp. 397-407, 2004.
[6] D.W. Boeringer and D.H. Werner, Particle Swarm Optimization Versus Genetic Algorithms for Phased Array Synthesis, IEEE Trans. Antennas Propagat., Vol. 52, pp. 771-779, 2004.
[7] S. Caorsi, M. Donelli, A. Lommi, and A. Massa, Location and Imaging of Two-Dimensional Scatterers by Using a Particle Swarm Algorithm, J. Electromagn. Waves Applicat., Vol. 18, pp. 481-494, 2004.
[8] M. Donelli and A. Massa, Computational Approach Based on a Particle Swarm Optimizer for Microwave Imaging of Two-Dimensional Dielectric Scatterers, IEEE Trans. Microwave Theory Techn., Vol. 53, pp. 1761-1776, 2005.
[9] E.L. Miller, M. Kilmer, and C. Rappaport, A New Shape-Based Method for Object Localization and Characterization from Scattered Field Data, IEEE Trans. Geosci. Remote Sens., Vol. 38, pp. 1682-1696, 2000.
[10] R.F. Harrington, Field Computation by Moment Methods, Piscataway NJ: IEEE Press, 1993.
[11] K.E. Parsopoulos and M.N. Vrahatis, Recent Approaches to Global Optimization Problems through Particle Swarm Optimization, Natural Computing, Vol. 1, pp. 235-306, 2002.

Electromagnetic Fields in Mechatronics, Electrical and Electronic Engineering
A. Krawczyk et al. (Eds.)
IOS Press, 2006

NEW DYNAMICAL HYSTERESIS MODEL

Adam Schiffer, Amalia Ivanyi

Department of Information Technology, University of Pécs, Rókus u. 2., H-7624 Pécs, Hungary
E-mail: adam@morpheus.pte.hu

Abstract*: *In this paper a new dynamical hysteresis model is introduced that based on the second derivates of the measured reversal curves. The advantages of the model are its easy identification, past memory representation and numerical simplicity. The accommodation property of the model can be ensued from the construction philosophy of the model. The feasibility of the extrapolation is defined by the boundary conditions. The convenience of this model is its efficiency in reduction of the calculation time. The parameters can be determined from the measured data points. Reported results prove the accuracy of the model.

Introducion

However, there exist several approaches of the hysteresis it is not easy to select the most suitable model for an engineering application. Three main types of scalar hysteresis models exist in the literature. The Preisach approach is an attractive one because of its wiping-out property, it has stable minor loops, but for the identification many experimental data is needed (discretised first order reversal curves or symmetric minor loops) [1]. For proper accuracy many measured points are needed and the prehistory of the material must be stored in broken line [6]. On the other hand some other models like analytical ones are simple, resulted in differential equations and can be calculated quickly. However but sometimes they have sticklers with the accurate identification. Third type of the hysteresis models are constructed on domain behavior [2-4] [7].

The hysteresis model presented below is introduced by a modification vector field $\boldsymbol{\psi}$, that can be derived from ascending and descending measurement loops. Introducing this modification vector field the next $B(i+\Delta t)$ point on the hysteresis can easily be calculated from the actual value of the magnetic field $H(i)$ and from the required differential permeability $\hat{\boldsymbol{\mu}}_{diff}(H_i, B_i)$ as the past local memory representation of the model. The hysteresis characteristic can be determined as

$$B = \mathcal{H}\left\{H, \frac{\partial B}{\partial H}, \boldsymbol{\psi}_m(H_m, B_m)\right\} \tag{1}$$

where $\frac{\partial B}{\partial H} = \mu_{diff}$ is local differential permeability and $\boldsymbol{\psi}_m(H_m, B_m)$ can be calculated from the measured ascending and descending reversal loops and m represents the actual measured point. H is the magnetic field strength and B is the magnetic induction. Without accommodation an inner $\rho(H_x, B_x)$ point in the hysteresis loop can be achieved only from the direction that is defined by $\mu_{diff,x} = \left.\frac{\partial B}{\partial H}\right|_{H=H_x, B=B_x}$. This represents the memory of the hysteresis in this model.

Identification of the Model

Denote $\hat{\boldsymbol{\mu}}_{diff}(H_i,B_i): S \to \mathbb{R}^2$ $S \subset \mathbb{R}^2$, $S=\{(H_i,B_i), i=1..Z\}$ where Z is the number of measured points and $\rho(H_i,B_i)$ represents the measured data. From the measured points of the first-order reversal curves the local differential permeability vectors $\hat{\boldsymbol{\mu}}_{diff}(H_{xx},\cdot)$ can be calculated along $H_{xx}=const$ lines as

$$\hat{\boldsymbol{\mu}}_{diff}(H_i,B_i)=(\Delta B_i,\Delta H_i), \tag{2}$$

where H is the magnetic field intensity and B is the magnetic flux density while $\Delta f_i = f_i - f_{i-1}$ specifies the segment of validity. If $\hat{\boldsymbol{\mu}}_{diff}(H_i,B_i)$ and $\hat{\boldsymbol{\mu}}_{diff}(H_{i+1},B_{i+1})$ values are known the modification vector $\boldsymbol{\psi}$ can be defined and calculated from the measured points

$$\boldsymbol{\psi_m}(H_i,B_i)=\left(2\Delta H_{i+1}-\Delta H_i, 2\Delta B_{i+1}-\Delta B_i\right). \tag{3}$$

If the measured $\rho(H_i,B_i)$ are equidistant in H then the $\boldsymbol{H}\in\mathbb{R}, H_k=H_{\min}+k(H_{\max}-H_{\min})/K$, $k\in[1,K], k\in\mathbb{Z}^+$ vector is defined where K is the number of the equidistant points in $\boldsymbol{H}$. The limiting points are specified as $H_0=-H_{sat}, H_K=H_{sat}$. Let introduce in matrix form the measured of the flux density

$$\mathbf{B}\in\mathbb{R}^2, B_{k,n}=B_i:\exists\rho(H_i,B_i), H_i\in\boldsymbol{H}, k\in[1,K]\subset\mathbb{Z}^+, n\in[1,N]\subset\mathbb{Z}^+ \tag{4}$$

where N is the number of the first order reversal curves. Applying this nomination the $k.$ rows in $\mathbf{B}$ means the $k.$ assignment in $\boldsymbol{H}$ and the $n.$ column means the $n.$ ascending or descending curve. The $\boldsymbol{\psi}^{\bullet}_m$ must also be stored in the same sequence as above. From the negative reversal curves $\boldsymbol{H}^-, \mathbf{B}^-, \boldsymbol{\psi}^-_m$, from the positive loops $\boldsymbol{H}^+, \mathbf{B}^+, \boldsymbol{\psi}^+_m$ can be defined. To the simulation of the hysteresis loop at H_j, B_j point any $H^{\bullet}_k\in\boldsymbol{H}, B^{\bullet}_{k,n}\in\mathbf{B}$ measured points can be found as $\left|H^{\bullet}_k-H^{\bullet}_j\right|=\min_k, \left|B^{\bullet}_{k,n}-B^{\bullet}_j\right|=\min_n$, and then $\boldsymbol{\psi}^{\bullet}_m(H_k,B_{k,n})$ can be determined for (k,n) pairs with $\bullet\in[+,-]$. So

$$\boldsymbol{\psi}^{\bullet}:\mathbb{R}^2\to\mathbb{R}^2, \boldsymbol{\psi}^{\bullet}(H_j,B_j)=\boldsymbol{\psi}^{\bullet}_{\boldsymbol{m}}(H_k,B_k):\left|H^{\bullet}_k-H^{\bullet}_j\right|=\min_k, \left|B^{\bullet}_k-B^{\bullet}_j\right|=\min_n. \tag{5}$$

The direction of the change in H can be determined as $\bullet=sign(\Delta H_j)$. In the other hand $\boldsymbol{\psi}^{\bullet}(H_j,B_j)$ can be interpolated if $H_j\notin\boldsymbol{H}^{\bullet}$.

If $\boldsymbol{H}^{\bullet}$ contains equidistant elements, $\Delta H_{i+1}-\Delta H_i=0$, then from the measured values $\boldsymbol{\psi}^{\bullet}_{\boldsymbol{m}}(H_i,B_i)=(\Delta H_{i+1}, 2\Delta B_{i+1}-\Delta B_i)$ where $\Delta H_{i+1}=\Delta H_z: z\in[2,Z]\subset\mathbb{Z}^+$ so $\boldsymbol{\psi}^{\bullet}_{\boldsymbol{m}}(H_i,B_i)[1]=const$. Calculating the required B_i value

$$\Delta B_{i+1}=(\boldsymbol{\psi}^{\bullet}(H_i,B_i)[2]+\Delta B_i)/2 \tag{6}$$

so

$$B_{i+1}=(\boldsymbol{\psi}^{\bullet}(H_i,B_i)[2]+\Delta B_i)/2+B_i. \tag{7}$$

On definition $\boldsymbol{\psi}^{\bullet}(H_i,B_i)[2]$ means the second scalar component of the modification field vector $\boldsymbol{\psi}^{\bullet}(H_i,B_i)$, that is equal with the change of the vector in B. The prehistory of the material is represented by the local $\hat{\boldsymbol{\mu}}_{diff}(H_i,B_i)$ vector. It is supposed that without accommodation a $\rho(H_k,B_k)$ inner point can be achieved from a $\rho(H_j,B_j)$ point only with one curve that can be represented by $\hat{\boldsymbol{\mu}}^{\bullet}_{diff}(H_k,B_k)$. Using this model and get a $\rho(H_k,B_k)$ inner point the next point

$\rho(H_{k+1}, B_{k+1})$ will definitely be different if two differential permeability vectors $\hat{\boldsymbol{\mu}}^{\bullet}_{diff}(H_k, B_k)$ are applied during the simulation as memory representation. Three different simulated results can be seen in Fig. 9. that shows different behavior of the hysteresis applying three local differential permeability vectors as memory representations. In other hand the algorithm is recursive, changing any past $\rho(H_{k-z}, B_{k-z})$ points different $\rho(H_{k+1}, B_{k+1})$ points would be resulted. Fig. 1. shows the vector representation of the hysteresis model. The modification field vector $\boldsymbol{\psi}^{\bullet}(H_i, B_i)$ is calculated from $\hat{\boldsymbol{\mu}}_{diff}(H_i, B_i)$ and $\hat{\boldsymbol{\mu}}_{diff}(H_{i+1}, B_{i+1})$ vectors. The measured grid points for the identification can be seen in Fig. 2. The negative modification vector field is showed by Fig. 3.

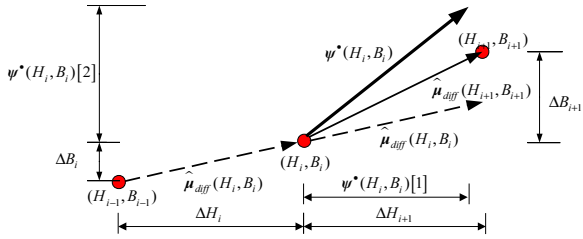

Fig. 1: Representation of the model

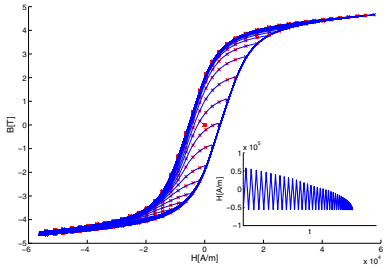

Fig. 2: Measured discrete descending curves and the calculated points for identification

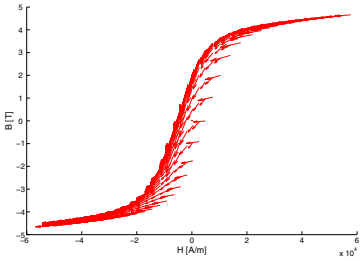

Fig. 3: The modification field $\boldsymbol{\psi}^{-}_{m}$ vectors derived from the ascending loops

Application of the Model

Generally if $\boldsymbol{H}^{\bullet}$ is equidistant $H_j \in \boldsymbol{H}^{\bullet}$, any B_j magnetic flux density can be calculated from B_{j-1}, and from the local measured $\hat{\boldsymbol{\mu}}^{\bullet}_{diff}(H_{j-1}, B_{j-1})$ and determined from $\boldsymbol{\psi}^{\bullet}(H_{j-1}, B_{j-1})$:

$$B_j = (\boldsymbol{\psi}^{\bullet}(H_{j-1}, B_{j-1})[2] + \Delta B_{j-1})/2 + B_{j-1}. \quad (8)$$

Simulating a hysteresis loop if $H_j \notin \boldsymbol{H}^{\bullet}$ and ΔH_j is different from the measured ΔH_i data then $\boldsymbol{\psi}^{\bullet}(H_{j-1}, B_{j-1})[2]$ must be scaled with a scalar as $\eta \cdot \boldsymbol{\psi}^{\bullet}(H_{j-1}, B_{j-1})[2]$, i.e.

$$B_j = (\eta \cdot \boldsymbol{\psi}^{\bullet}(H_{j-1}, B_{j-1})[2] + \Delta B_{j-1})/2 + B_{j-1}. \quad (9)$$

The scalar η is calculated from the simulated $\Delta H_j, H_{j-1}, B_{j-1}$ and from the measured

$\boldsymbol{\psi}^{\bullet}(H_{j-1},B_{j-1})[1]$ values:

$$\eta=\frac{\Delta H_j}{\boldsymbol{\psi}^{\bullet}(H_{j-1},B_{j-1})[1]} \tag{10}$$

where $\boldsymbol{\psi}^{\bullet}(H_{j-1},B_{j-1})[1]$ can be calculated from the measured data according to equation (5).

Boundary Conditions

For the exact simulation the boundary conditions must be specified. If $H_j \notin \boldsymbol{H}^{\bullet}$ and $H_j < -H_{\max}$ or $H_j > H_{\max}$ the hysteresis loop is in saturation condition,

$$\left.\frac{\partial^2 B}{\partial H^2}\right|H=H_{\pm\max}=0 \text{ and } \left.\frac{\partial B}{\partial H}\right|H=H_{\pm\max}=const. \tag{11}$$

If in the model $\boldsymbol{\psi}^{\bullet}(H_j,\cdot):|H_j|>H_{\max}$ then from equation (9) $B_j=B_{j-1}$. When the magnetic field excitation $\boldsymbol{H}$ has local maxima or minima then $\bullet=\operatorname{sign}(\Delta H_j)$ is changing. The reversal loops are measured from the local maxima. Because at the first point of the reversal loops $\Delta B_i=\Delta H_i=0$ it means that $\boldsymbol{\psi}^{\bullet}(H_i,B_i)=(H_i,0)$ defines the reversible permeability in that points. This cannot be expressed as a function from the field intensity because of it depends on the domain confiuration that comes from the past field history. The most important thing is this reversible permeability vector cannot be calculated as the opposite of the differential permeability reached the reversal point. As well as in saturation case in the demagnetized state there is no difference between the direction of the reversible permeability in the ascending and the differential permeability in the descending loops [5]. Fig. 4. shows the vector field B components $\boldsymbol{\psi}^{+}(\boldsymbol{H}^{+},\mathbf{B}^{+})[2]$ without boundary values. The boundary conditions are specified above and can be seen in Fig. 5.

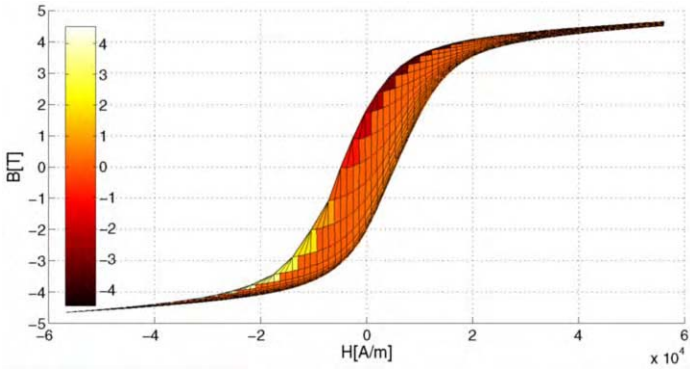

Fig. 4: $\boldsymbol{\psi}^{+}(\boldsymbol{H}^{+},\mathbf{B}^{+})[2]$ vector field without boundary conditions

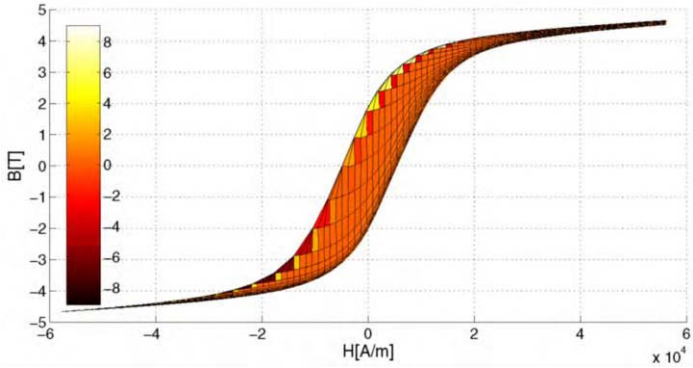

Fig. 5: Boundary conditions of $\boldsymbol{\psi}^{+}(\boldsymbol{H}^{+},\mathbf{B}^{+})[2]$ vector field

Validation of the Model

The investigated material is structural steel (C19). The amplitude of excitation current is: $I_p = 0.4$ A and the frequency is f=1 Hz. Number of turns of the excitation and the measuring coils are identical, N=70. The average magnetic length of the ferromagnetic ring is 173 mm. The area of ferromagnetic material's cross-section is A=20 mm^2. The measured data and the points on the descending curves, calculated by the new model are shown in Fig. 2.

Properties of the Model

After the $\boldsymbol{\psi}_m^{\bullet}$ modification vector fields are derived from the ascending and descending curves the simulation results show the accuracy of the model. Fig. 6. shows the simulated and measured points. If the boundary conditions are defined well the accommodation property of the hysteresis curve can be ensued from the construction philosophy that can be seen in Fig. 7. The identification was calculated by 40 reversal curves. Fig. 8. shows the simulation with 11 reversal curves that is ensured by a measurement.

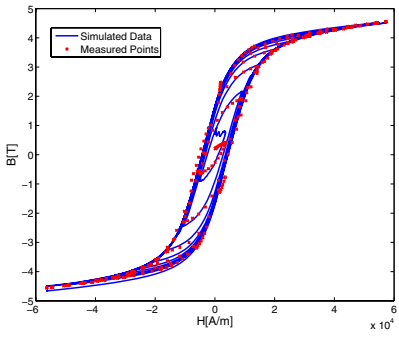

Fig. 6: Simulation result and measurement data of concentrical loops

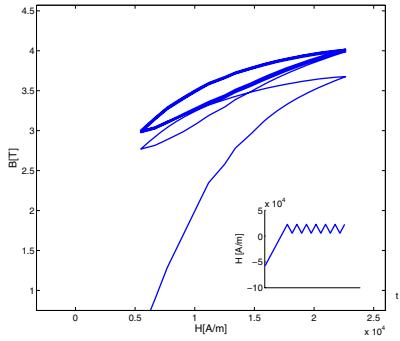

Fig. 7: Accommodation property

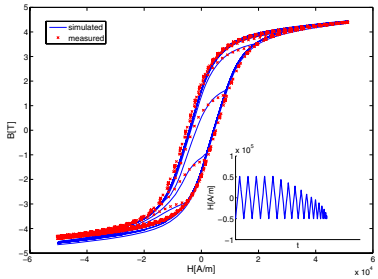

Fig. 8: Simulation result and measurement data of 11 reversal curves

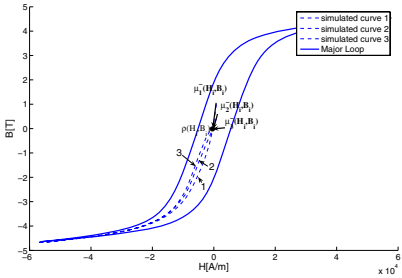

Fig. 9: Simulation result of descending curves with three different vectors $\hat{\boldsymbol{\mu}}_{diff}(H_i, B_i)$ as memory representations

Conclusion

In the presented model the differential permeability $\hat{\boldsymbol{\mu}}_{diff}$ and the vector fields $\boldsymbol{\psi}^{\bullet}$ can be obtained from the positive and negative reversal loops. In spite of its simplicity the model can be prove the accommodation property (Fig.4.). Because of in the practice it is not realistic to measure a large set of reversal curves an interpolation technique is recommended for determination of modification field $\boldsymbol{\psi}^{\bullet}(H_j, B_j): H_j \notin \boldsymbol{H}^{\bullet}$. From $\left\{\boldsymbol{H}^{\bullet}, \mathbf{B}^{\bullet}, \boldsymbol{\psi}^{\bullet}, H_i, B_{i-1}, \Delta H_i, \Delta B_{i-1}\right\}$ the next B_i can be determined. Defining the boundary conditions, the extrapolation is possible when $H_j \notin \boldsymbol{H}^{\bullet}, \left|H_j\right| > H_{\max}$. In the model the relations between the field intensity H and the flux density B are simulated, however several cases the relations are defined between the field intensity H and the magnetization M. The identification steps and the algorithm is similar, because of the magnetic induction is equal with $B = \mu_0(H + M) = \mu_0 H + \mu_0 M$, where μ_0 is the permeability of the vacuum. The relation between $M(H)$ and the $B(H)$ curve the vector field $\boldsymbol{\psi}^{\bullet}$ is proportional to the relation because of the relation $\dfrac{\partial B}{\partial H} = \mu_0\left(1 + \dfrac{\partial M}{\partial H}\right)$.

References

[1] F. Ossart, O. Hubert, R. Billardon, *A new internal variables scalar hysteresis model respecting the wiping-out property*, Journal of Magnetism and Magnetic Materials 254-255 (2003) 170-172
[2] I.D. Mayergoyz, *Mathematical Models for Hysteresis*, New York, Springer-Verlag, 1991.
[3] E. Della Torre, *Magnetic Hysteresis*, New York, IEEE Press, 1999.
[4] A. Iványi, *Hysteresis Models in Electromagnetic Computation,* Budapest, Akadémia Kiadó, 1997.
[5] Giorgio Bertotti*, Hysteresis in Magnetism, San Diego*, Academic Press, 1998
[6] Zsolt Szabo, *Hysteresis Models from Elementary Operators and Integral Equations*, PhD degree, Budapest, 2002
[7] Edward Della Torre, *Problems in physical modeling of magnetic materials*, Physica B 343 (2004) 1-9

Electromagnetic Fields in Mechatronics, Electrical and Electronic Engineering
A. Krawczyk et al. (Eds.)
IOS Press, 2006

STABILITY ANALYSIS OF A LEVITATED MICRO-MOTOR

Stephen Wilkinson, Rafal Wrobel, Philip Mellor, Derrick Holliday

Department of Electrical and Electronic Engineering, Merchant Venturers Building, Woodland Road,
Bristol BS8 1UB, UK
Stephen.Wilkinson@bristol.ac.uk

Abstract *– **Finite element modelling is used to investigate and optimise the radial stiffness of a levitated disc thereby improving its radial stability. The disc is to be used as a bearing for high-speed micro-machines such as micro-motors and micro-turbine generators. Particle Swarm Optimisation is used to find the optimal geometry and excitation which yield the best radial stiffness while maintaining strong and uniform axial support.***

Introduction

Micro Electro-Mechanical Systems (MEMS) emerged from efforts to integrate miniaturised sensors and actuators into a single package using batch fabrication techniques derived from the micro-electronics industry. In particular, researchers have devised micro-scale equivalents of conventional machinery, such as micro-motors and micro-turbines (referred to as micro-machines [1]). However, scaling laws imply that the ratio of surface-area to volume increases as dimensions shrink, so that contact forces (such as stiction) dominate inertial forces. This has obvious detrimental effects on the performance of micro-machines which use hub bearings to provide radial and axial support for the rotor. The dominating friction forces not only cause loss of power but also mechanical wear which reduces the lifetime of the device. Non-contact bearings are therefore essential in micro-machines such as micro-turbines [2], micro-motors and micro-gyroscopes [3], which must achieve very high peripheral speeds. In this paper, the optimisation of the stiffness and load capacity of an electromagnetically borne micro-motor is presented.

Electromagnetic Bearing

The function of the bearing is to restrain axial and radial movement of the rotor whilst allowing unrestricted rotation. Important characteristics for bearings include load capacity, stiffness, static and dynamic stability, power required to operate, losses and dynamic response [4]. Among the possible methods of levitation, electrostatic and magnetostatic techniques are inherently unstable in at least one degree of freedom without feedback control, according to Earnshaw's theorem [5]. Work by Williams et al. [3] has shown that a rotor can be stably levitated by induction without feedback by careful selection of the micro-motor geometry. The micro-motor consists of a conducting metallic rotor supported vertically and constrained laterally by electromagnetic forces generated by time varying currents in two concentric stator coils (see Fig. 1). However initial investigations [3] have shown that the angular speed of the rotor is limited by radial vibration modes resulting from weak radial stiffness at low speeds. Use of electrostatic forces between the stator and rotor has been proposed as a means of improving the radial stiffness [3], but such forces act predominantly in a direction normal to the rotor (except where fringing occurs) and are inherently unstable. Instead, the radial stability at high angular speeds can be improved by optimising the radial stiffness against geometrical and electrical parameters.

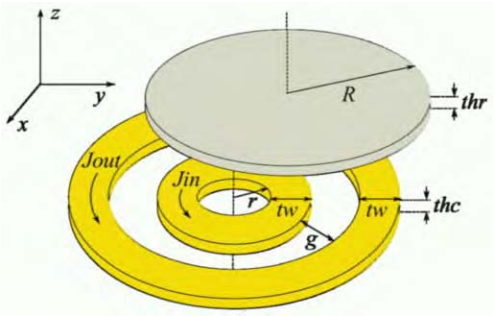

Fig. 1 Micro-motor geometry

Geometrical parameters		
Rotor radius	*R*	250 μm
Coil inner radius	*r*	185 μm *
Coil gap	*g*	10 μm *
Track width	*tw*	67 μm *
Rotor thickness	*thr*	15 μm
Coil thickness	*thc*	20 μm

Electrical parameters		
Current density	J_{in}, J_{out}	*See text*
Frequency	*F*	15 MHz
Phase	ϕ_{in}, ϕ_{out}	0°, 90° *

(*) optimised values

Tab. 1 Geometrical and electrical parameters

Modelling and Optimisation

Modelling and Calculation

The topology and dimensions of the motor are illustrated in Fig. 1. The rotor is made from a highly conducting material such as aluminium (μ_r=1, σ=37 S.m^{-1}) or copper (μ_r=1, σ=58 S.m^{-1}). The thicknesses of the coils and disc are limited by fabrication constraints to approximately 20 μm. This in turn determines the optimal frequency of excitation: if the frequency is too low, insufficient current is induced in the rotor; if the frequency is too high, the skin depth decreases and the rotor appears to have increased electrical resistance, incurring greater power losses. Previous investigations [6] have shown 15 MHz to be optimal.

If the current density is kept constant for different coil geometries, coils of larger volume produce a relatively greater force and dissipate more power. Conversely, if the total current is kept constant, coils of smaller volume produce a relatively greater force but also dissipate more power, as verified by numerical simulations. To achieve a balanced comparison of different rotor geometries, the current density is adjusted so that the same power is dissipated for all coils – the datum configuration was arbitrarily chosen to have a track width of tw_0=40 μm with a sinusoidal current density of 2mA/μm^2. To maintain the same power loss in a coil of track width *tw*, the current density must be modified according to:

$$J_{in} = J_{out} = J_0 \sqrt{\frac{1}{1+(tw - tw_0)/tw_0}} \qquad (1)$$

where $J_0 = 2\ \mathrm{mA/\mu m^2}$ and $tw_0 = 40\ \mu\mathrm{m}$

The large surface-area per unit volume of micro-devices improves the heat dissipation and affords the use of such high current densities. The quasi-static approximation holds because the wavelength of the excitation is much larger than the physical dimensions of the device.

The electromagnetic forces on the conducting rotor are calculated by the three-dimensional finite element method (FEM) using the Maxwell stress tensor. The coils, rotor and air are modelled respectively as reduced scalar potential, vector potential and total potential regions. The radial stiffness is approximated by differentiating the radial force with respect to rotor displacement. In this case, the coil is moved relative to the rotor in order to keep a constant mesh, so the force is differentiated with respect to the negative of the displacement.

Objective Function Formulation

Improving the radial stiffness without sacrificing the axial load capacity is a multi-criteria optimisation task which consists of building a suitable objective function as a linear combination of the design objectives. The task can be complicated if the design objectives are contradictory and depend on the same design parameters

(namely the coil geometrical and electrical properties). When conflicting objectives are optimised simultaneously, there may be several compromise solutions, corresponding to different weightings of the objectives. Initially equal weights are attributed to each criterion.

The quality of the radial and axial support can be measured by several criteria, illustrated in the force-displacement characteristics shown in Fig. 2.

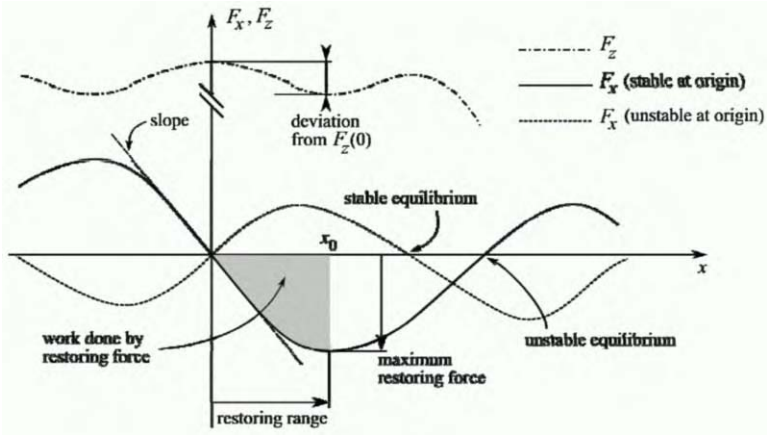

Fig. 2 Radial and axial force-displacement characteristics

From symmetry considerations, it is intuitive that the rotor is at radial equilibrium when centred above the coils (x=0). The slope of the radial force-displacement characteristic at the origin determines the stability of this equilibrium, while the magnitude of the slope gives the radial stiffness. Therefore the optimisation of the radial stiffness can be expressed by the following objective function:

$$\lambda_1 = \begin{cases} 0 & \text{if} \quad dF_x/dx\big|_{x=0} > 0 \\ dF_x/dx\big|_{x=0} & \text{if} \quad dF_x/dx\big|_{x=0} < 0 \end{cases} \qquad \text{to be minimised} \qquad (2)$$

where F_x is the radial force

Unstable solutions are filtered out by limiting the objective function to zero if the slope is positive.

The ability of the radial support to overcome large disturbances can be measured by the magnitude of the restoring force and the work done by the radial force over the restoring range. Therefore, the following objectives should also be considered for optimisation:

$$\lambda_2 = \min_x \left(F_x\right) \qquad \text{to be minimised} \qquad (3)$$

$$\lambda_3 = \int_{x=0}^{x=x_0} F_x dx \,,\; x_0 : F_x\left(x_0\right) = \min_x \left(F_x\right) \qquad \text{to be minimised} \qquad (4)$$

To optimise the radial support while maintaining the best possible axial load capacity, the axial force F_z when the rotor is centred (x=0) should be maximised:

$$\mu_1 = F_z\left(0\right) \qquad \text{to be maximised} \qquad (5)$$

Ideally, the vertical position of the rotor should remain constant over the allowed range of radial displacements, so the deviation of the axial force from its value at radial equilibrium ($F_z(0)$) should be minimised:

$$\mu_2 = \sqrt{\frac{1}{x_0}\int_{x=0}^{x=x_0}\left(F_z(x)-F_z(0)\right)^2 dx}\ ,\ x_0 : F_x(x_0) = \min_x(F_x) \qquad \text{to be minimised} \tag{6}$$

The radial and axial qualities expressed in equations (2)-(6) are to be optimised against a combination of geometrical and electrical design parameters. The geometrical parameters include the inner coil radius (*r*), the coil track width (*tw*) and the coil gap (*g*). The electrical parameters are the magnitudes of the excitation current densities (*Jout*, *Jin*), the excitation frequency (*f*) and the phase difference ($\phi = \phi_{in} - \phi_{out}$) between the coil currents. The excitation current density and frequency are fixed as explained in the previous section, so only the remaining design parameters form the control variable vector **v**:

$$\mathbf{v} = [r, g, tw, \phi] \tag{7}$$

Since unstable force-displacement characteristics are filtered out, the objectives in equations (2), (3) and (4) are all negative and bounded by zero, so the radial objective function can be formulated as:

$$\Lambda(\mathbf{v}) = \min_{\mathbf{v}}\left(\hat{\lambda}_1(\mathbf{v})\,\hat{\lambda}_2(\mathbf{v})\,\hat{\lambda}_3(\mathbf{v})\right) \tag{8}$$

where normalisation, denoted by the ^ symbol, ensures that each term within the objective function has the same weight, as previously mentioned.

Similarly, the objectives in equations (5) and (6) are both positive and are bounded by zero, so the axial objective function can be formulated as:

$$\mathrm{M}(\mathbf{v}) = \max_{\mathbf{v}}\left(\hat{\mu}_1(\mathbf{v})/\left(1+\hat{\mu}_2(\mathbf{v})\right)\right) \tag{9}$$

Fabrication and geometric limitations are taken into account by constraining the gap (*g*) and inner radius (*r*) to be greater than 10 μm and 50 μm respectively.

Particle Swarm Optimisation

Particle Swarm Optimisation (PSO) is a robust stochastic algorithm that imitates the individual and social behaviour of swarming species seeking the optimum location in a search space [7]. Each coordinate of the search space corresponds to a design parameter and the fitness of a point in space is given by the objective function evaluated with the corresponding design parameters. The first iteration (or generation) of individuals (or particles) is initialised with random positions and random velocities in the search space. At each generation the new velocity of each particle is calculated based on its own "personal best" and on the swarm's "global best", and integrated to yield the new position, enabling the swarm to converge towards the "global optimum".

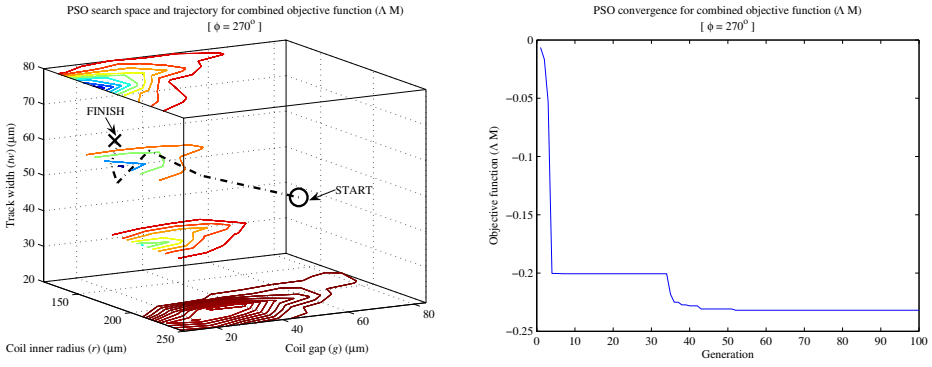

Fig. 3 Particle Swarm Optimisation of the combined radial and axial objective functions

The PSO algorithm was chosen for its simplicity of implementation, and was applied to the optimisation of equations (8) and (9), first separately and then as a combined product, subject to the constraints mentioned previously. The PSO implementation used 10 particles, with "acceleration constants" of 1.49, and an "inertial weight" factor decreasing linearly from 0.9 to 0.4 over 100 generations [7]. The axial and radial forces required for evaluation of the objective functions at each iteration were calculated by running the FEM software [8] in parallel on ten computers.

To graphically confirm that the PSO algorithm has correctly converged to the optimum, the trajectory to the optimum was plotted against contour lines delineating the search space, as illustrated in Fig. 3 a) for the particular phase difference $\phi = 270°$ for the combined product of equations (8) and (9). The search space was outlined by evaluating the objective function at discrete points and interpolating between these points, requiring over 20,000 FEM simulations in total. As shown in Fig 3. b), PSO converges in 60 iterations, each requiring seven simulations (one for each coil displacements) per particle, a total of 4,200 FEM simulations.

Results and Discussion

Tab.2 summarises the results for the optimisation of the radial objective (8), the axial objective (9) and the combined product of the two objective functions. The results show that the best compromise between strong axial support and uniform axial support is obtained when the coils are fed with in-phase currents, while the optimal radial stiffness and strongest radial restoring force require the outer coil current to lead the inner coil current by 90°. The optimal geometry is summarised in Tab. 1.

	r	*g*	*tw*	ϕ	Objective function
Radial	189.0 µm	10.0 µm	65.8 µm	270°	-0.85
Axial	108.9 µm	52.1 µm	80.0 µm	0°	0.56
Radial and axial	185.0 µm	10.0 µm	66.8 µm	270°	-0.24

Tab. 2 Summary of optimisation results

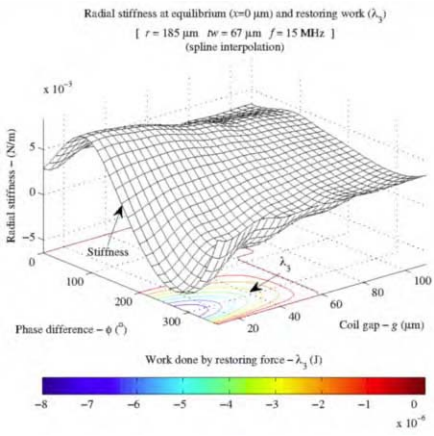

Fig. 4 Verification of radial optimum

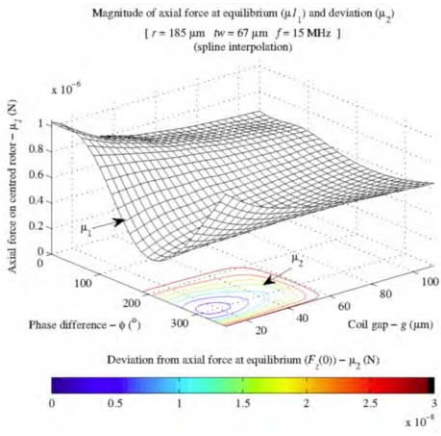

Fig. 5 Verification of axial optimum

The data collected to outline the search space was used to further verify the PSO results by plotting the design objectives against two of the design parameters, as illustrated in Figs. 4 and 5. The surface plot in Fig. 4 shows that the optimal radial stiffness of $5x10^{-3}$ N/m is indeed obtained for $\phi = 270°$ and that the lateral support becomes more compliant as the gap between the coils increases. The surface plot also confirms that the radial stiffness can by dynamically adjusted by changing the phase difference between the coil currents and that the equilibrium x=0 can also become unstable. The contour plot in Fig. 4 also shows that the restoring force does most work when $\phi = 270°$ and the coil gap is small. Fig. 5 indicates that axial support strength and uniformity are mutually exclusive objectives: the axial support is most uniform near $\phi = 270°$ and g=15 μm, where the average axial force is almost at its weakest. However the deviation of the axial force over the range of stable lateral displacements is below 10% of the force at equilibrium.

Conclusion

PSO can be successfully used to find the geometric and electric parameters that yield the optimal radial support of the induction levitated disc. PSO can also save computation time: whereas tens of thousands of FEM simulations were needed to investigate the entire search space, PSO found the optimum configuration with just over four thousand FEM simulations.

The optimal configuration found in this investigation yields $5.0x10^{-3}$ $N.m^{-1}$ radial stiffness, an order of magnitude better than that reported in [3]. The results show that the radial stiffness is significantly improved by supplying the outer coil with current leading the inner coil current by 90°. Controlling the phase difference between the coil currents could be used to dynamically improve the response of the bearing under different loading conditions or to compensate for manufacturing imperfections.

Acknowledgment

The authors acknowledge Chris Riley of Vector Fields Ltd. for providing a multi-user license for the Opera software.

References

[1] I. Fujimasa, Micromachines: a new era in mechanical engineering, Oxford : Oxford University Press, 1996

[2] A. H. Epstein, S. D. Senturia *et. al.*, Power MEMS and Micro-engines, Proc. International Conference on Solid-State Sensors and Actuators, pp. 753-756, 1997

[3] C. B. Williams, C. Shearwood, P. H. Mellor, and R. B. Yates, Modelling and testing of a frictionless levitated micromotor, Sensors and Actuators A, 61, pp. 469-473, 1997

[4] F. M. Stanfield, Hydrostatic bearings for machine tools and similar applications, Machinery Publishing, 1970

[5] M. D. Simon, L. O. Heflinger, A. K. Geim, Diamagnetically stabilized magnet levitation, American Journal of Physics, Vol. 12, pp. 702-713, 2001

[6] S. G. Wilkinson, P. H. Mellor, D. Holliday, Design of a Magnetic Bearing for High Speed Micro Rotating Machines, PREP2004 Postgraduate Research Conference, Hertfordshire, 2004

[7] Y. Rahmat-Samii, Genetic Algorithm and Particle Swarm Optimisation in Engineering Electromagnetics, 17th International Conference on Applied Electromagnetics and Communications, Dubrovnik, Croatia, 2003

[8] Opera, Vector Fields Limited, www.vectorfields.com

Electromagnetic Fields in Mechatronics, Electrical and Electronic Engineering
A. Krawczyk et al. (Eds.)
IOS Press, 2006

THE FREQUENCY ANALYSIS OF THE FERROMAGNETIC POWER LOSSES USING CLASSICAL AND DOMAIN MODELS

Grzegorz Zwoliński, Zbigniew Gmyrek

Institute of Mechatronics and Information Systems, Technical University of Lodz,
90-924 Lodz, ul. Stefanowskiego 18/22, Poland, phone: (+ 4842) 6312571
e-mail: zwolinsk@p.lodz.pl, gmyrek@p.lodz.pl

Abstract* - The calculation of the power losses in a ferromagnetic is often executed with the utilisation of analytic dependence. This dependence was marked on the basis of the Maxwell equations. So, it accepts the ferromagnetic material as devoid of the magnetic domains. The domains behaviour in external magnetic field is imitated with help of the magnetic permeability. However, when in a real ferromagnetic two field harmonics coexists (the fundamental harmonic which establish the magnetic work conditions and the higher order harmonic with small amplitude), the computed power loss values can be unreal. The authors of this paper show the dependence of the power losses (the power losses caused by higher order harmonic) in relation with the temporary shape of the wall (the temporary shape is connected with the temporary value of the fundamental harmonic field integrated over a cross section).

Introduction

The problem of the power loss calculation and distribution of the magnetic field quantities in ferromagnetic has been well known for many years. There are many methods enabling the calculation of the ferromagnetic power losses. The analytical methods [3,4,5] use dependence of the power losses from the values of the flux density, the frequency and the material parameters. The accuracy of these formulas has been confirmed for many kinds of electrotechnical steel sheets. To solve this kind of problem many different models were built, but results of power losses obtained from them can differ from values obtained during the measurements. In such conditions the numerical models are very useful [6]. Among them, the Dynamic Preisach Model deserves special attention [2]. The authors of this paper are especially interested in the power loss calculation executed for the small flux density values (up to some dozen mT) and frequencies up to some kHz.

The Numerical Models And The Power Losses

The classical ferromagnetic model bases on the Maxwell equations. On this basis the numerical model which uses the Poyting's vector to calculate the power losses, inside the ferromagnetic material. The numerical simulation was carried out at considerably simplified assumptions:

- isotropic and non-linear character of the environment,
- the excitation is of an electromagnetic polarised flat wave character,
- the simulation was limited to a single steel sheet.

The ferromagnetic model is described by Maxwell equations (see eq.1)

$$\text{curl}\, H = J \;; \qquad \text{curl}\, E = -\frac{\partial B}{\partial t} \tag{1}$$

A value of magnetic permeability μ_D based on measurements, was used to take into account the occurrence of hysteresis phenomenon [6]. The numerical model were presented in difference form of equation (2) with DuFort-Frankel scheme (3).

$$\nabla^2 H = \frac{\partial H}{\partial t}\mu_D(t)\gamma \tag{2}$$

$$\frac{1}{2\Delta t}\left[u_j^{n+1} - u_j^{n-1}\right] = \frac{\lambda}{(\Delta x)^2}\left[u_{j+1}^{n} - \left(u_j^{n+1} + u_j^{n-1}\right) + u_{j-1}^{n}\right] \tag{3}$$

The main problem was the power loss value – the power losses caused by the flow of the eddy currents in a conductor of γ conductivity with respect to the hysteresis phenomenon. The temporary value of these losses p_t and mean value P were estimated with the formula (4).

$$p_t = \int_S \frac{j_t^2}{\gamma} dS = b\sum_{i=1}^{n} j_{i,t}^2 \Delta z_i \;; \qquad P = \frac{1}{2\pi}\int_{t=t_0}^{t_0+T} p_t \, dt \tag{4}$$

The value of the Joule losses P was calculated using the average value of power loss p_t and next compared with the results taken from 2D model. The 2D model is based on the Pry and Bean model with moving domain wall. The magnetic domain has been applied into account in model proposed by Pry and Bean a few years ago. Every such area consists two of elementary areas magnetised to saturation B_s. External magnetic field penetrates all area of magnetic domain and causes the shift of the Bloch wall. Assumption of this method is that eddy currents are mainly induced by the shift of Bloch wall. Induced eddy currents change the field distribution near wall what causes the deformation of the wall shape. Thus for investigated model the electromagnetic equations to be satisfied are:
In each domain

$$\text{curl}\; J = 0; \quad \text{div}\; J = 0 \tag{5}$$

In each domain wall

$$\text{curl}\; J = -\gamma\frac{dB}{dt}; \quad \text{div}\; J = 0 \tag{6}$$

The boundary conditions are:
- the component of electric current normal to the sheet plane vanishes at the surface,
- the component of electric current normal to each domain wall is continuous through the wall,
- the difference in the tangential component of the electric current across any domain wall is

$$\frac{\partial J_y}{\partial x} = -\frac{\partial B}{\partial x}\frac{\partial x}{\partial t}\gamma \tag{7}$$

Accepting, that in the domain area the field strength vector has only Z component is possible to write the following equation (8)

$$\frac{\partial^2 H_z}{\partial x^2}+\frac{\partial^2 H_z}{\partial y^2}=0 \tag{8}$$

This equation was represented in final difference form with help of the DuFort-Frankel scheme (9)

$$H_{i,j}^{k+1}=-H_{i,j}^{k-1}+\alpha\left(H_{i+1,j}^{k}+H_{i-1,j}^{k}\right)+\beta\left(H_{i,j+1}^{k}+H_{i,j-1}^{k}\right) \tag{9}$$

where:
$\alpha=\Delta y^2/(\Delta x^2+\Delta y^2)$,
$\beta=\Delta x^2/(\Delta x^2+\Delta y^2)$,
Δx^2 – the square of the distance between the mash nodes along the X axis,
Δy^2 – the square of the distance between the mash nodes along the Y axis,
$H_{i,j}^{k+1}$ – the field strength (the Z component), determined for the specified node of the 2D mesh.

Using described above 2D mathematical model, the ferromagnetic power losses P was calculated (see Figs. 1 -2). In Fig.1 the power loss results are presented, calculated for the different sheets.
The EP 600 50A sheet is practically isotropic and the EP 470 50A and the ET 122 30 sheets are anisotropic. In Fig.2 the same problem was analysed with respect to the domain width. The symbol aa visible in this figure, describes the half of the domain width – see Fig.3. The simulations were carried out for the ferromagnetic width d=0.3 mm. The domain widths were chosen from very small value – 0.005 mm to the value, which exists in a real material – 0.5 mm. The results comparison were carried out for the 2D model, in refer to the results obtained from calculations for domain with aa=0.005 mm. The results obtained for the parameter aa=0.005mm was accepted as results for the classic model (the skipping existence of the magnetic domains).

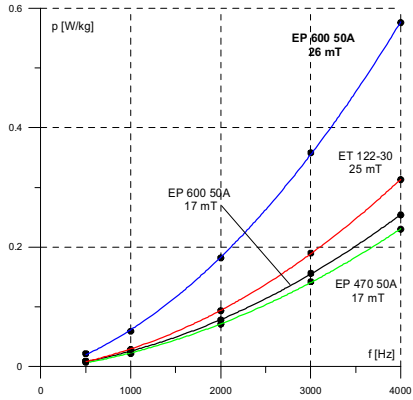

Fig.1 The specific power losses vs. frequency.

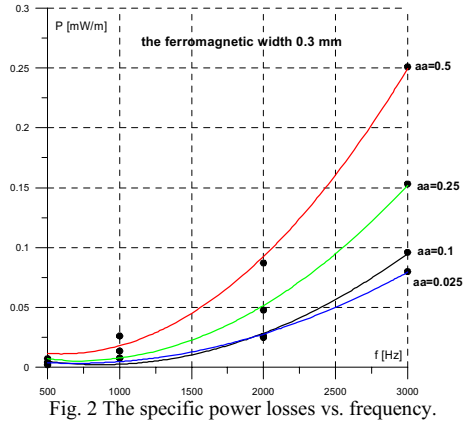

Fig. 2 The specific power losses vs. frequency.
aa – the half of the domain width

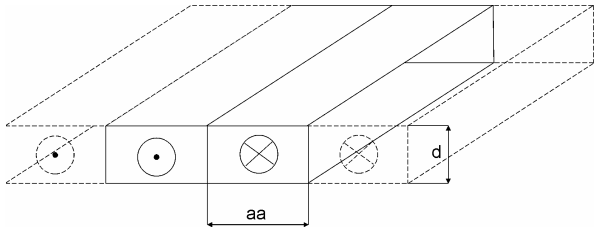

Fig. 3 The domain view. The symbol indication used during the calculation process.

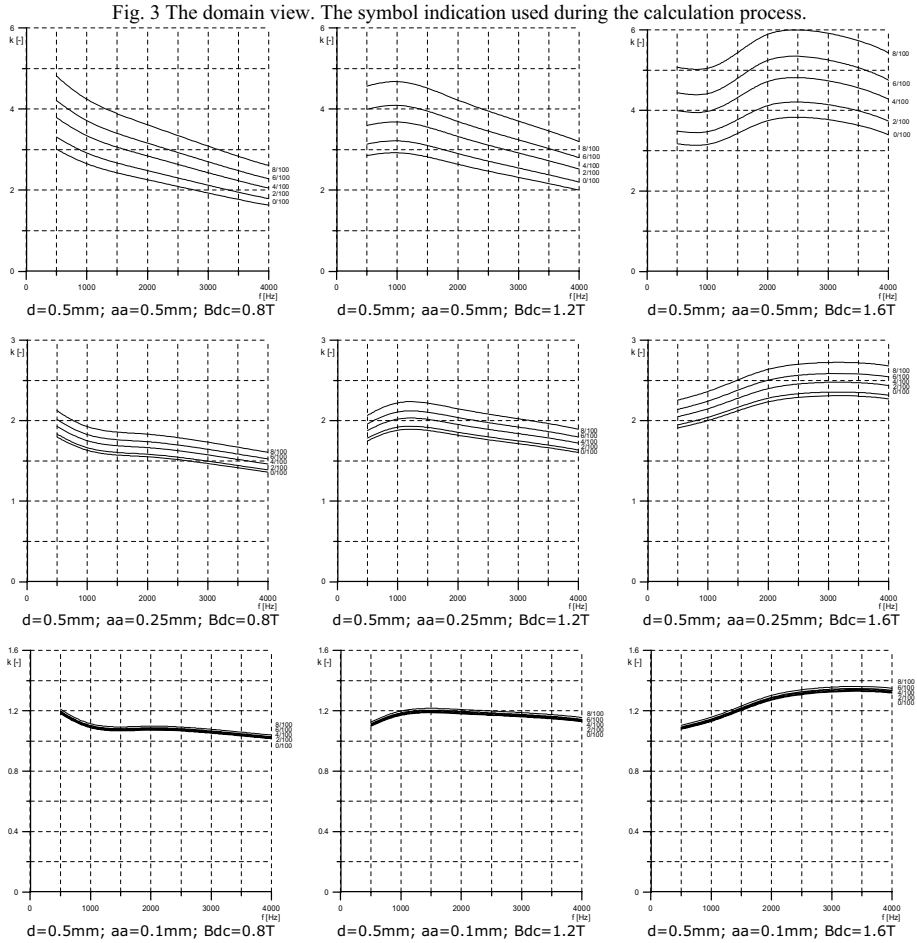

Fig.4 The factor of the power loss increase vs. the B_{DC} bias and domain width.

The coefficient of the power loss increase presented in Fig.4, was computed as relation of the power loss in case of the skew wall to the power loss calculated from the classic model. As classic model authors uses the 2D model with introduced value aa=0.005 mm , accepting into this way the absence

of the magnetic domains in studied material. In introduced figures is visible that for the small relation aa/d (in this case for aa=0.1 mm), the influence of the initial shape of the wall onto the coefficient value is small. It is completely different for the case of the wide domain (in this case aa=0.5 mm). It is clear visible the influence of the skewed wall. This skew can represent the temporary position of the Bloch wall, caused by fundamental field harmonic. So, is possible to apply passed investigation results to the analysis of the power loss in case of coexistence two harmonics of the magnetic field.

The differences between the values of the coefficients result from the field strength distribution inside the magnetic domain. In studied model, authors skipped the power losses generated by changing external magnetic field. The power losses are mainly generated by moving Bloch wall. In applied model is possible to regard the currents induced by external changing field.

Then we have to add a new element in equation (8). The different field distributions generate the different power loss value. To compare the power loss values obtained for different domain width, we have to express them as specific loss in the volume.

The sample field strength distributions calculated for the specified temporary moment are presented in Fig. 5-6. Presented results concern magnetic domains with size from 0.005 mm to 0.5 mm. Introduced examples of calculations show unambiguously, that with the width domain change, the area in which the eddy currents flow is completely different. With the growth of the domain width, the influence of the induced eddy currents onto itself is completely different. Therefore, the flow of currents across domain is possible (the flowing currents do not cancel each other). This is perfectly visible on the field strength distribution - see Fig. 5-6.

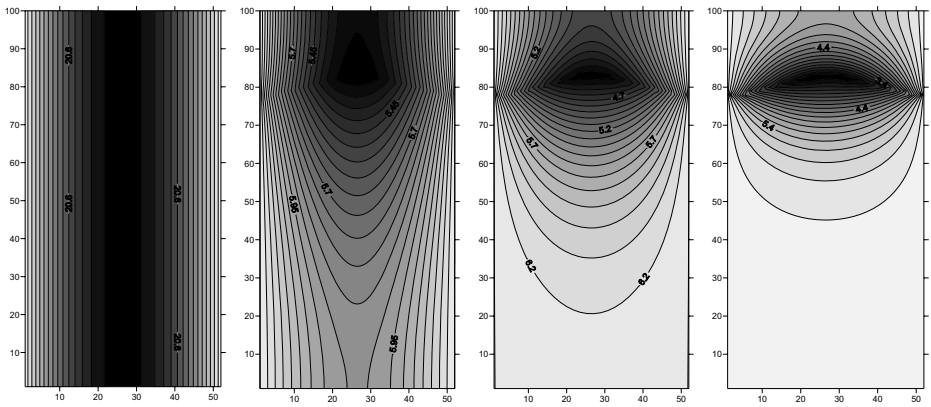

aa = 0.005 mm aa = 0.1 mm aa = 0.25 mm aa = 0.5 mm

Fig.5 The temporary fields strength distribution. The field frequency – 500 Hz, the ferromagnetic width – 0.5 mm. Model bra-ket 6/100.

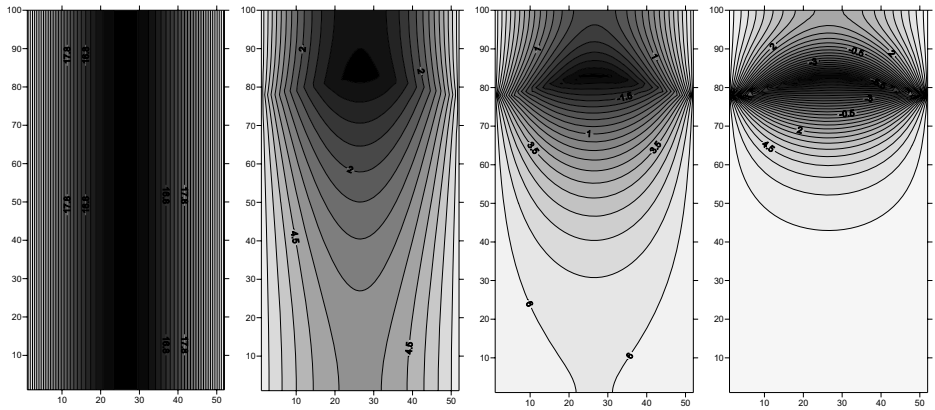

aa = 0.005 mm aa = 0.1 mm aa = 0.25 mm aa = 0.5 mm

Fig.6 The temporary fields strength distribution. The field frequency – 4000 Hz, the ferromagnetic width – 0.5 mm. Model bra-ket 6/100.

Conclusions

Presented results of the power loss calculation have to be completed with the excess power loss value. The models used during the calculation process, make possible the calculation of the so called classical power losses. Presented results show the essential differences in the power loss values with respect to the skew of the Bloch wall. It can be the cause of the mistakes during the "classical" calculations, where we skip the domain structure of the ferromagnetic. The results obtained from the numerical models are useful to rapid power loss calculations, in deformed flux conditions also (in this case it is possible use the results with help of the special procedure).

References

[1] R. H. Pry, P. Bean, Calculation of the energy loss in magnetic sheet materials using a domain model, Journal of Applied Physics, march 1958.
[2] J. Gyselinck, L. Dupre, L. Vandevelde, J. Melkebeek, Calculation of iron losses in electrical machines using the Preisach model, Proceedings of 3rd International Workshop on Electric and Magnetic Fields, Liege Belgium, 1996,
[3] A. Krawczyk, S. Wiak, J. Turowski, Electromagnetic fields in electrical engineering, London, James&James, 1994.
[4] P. Hammond, J. K. Sykulski , Engineering electromagnetism (Physical Process and Computation), Oxford Science Publications, 1994.
[5] K. Zakrzewski, Method of calculation of unit power losses and unit reactive power in magnetic laminations in a wide range change of induction and frequency, Proceedings of ISEF'99, Pavia, pp.208-211, 1999.
[6] Z. Gmyrek, G. Zwoliński, modeling of ferromagnetic using classical and domain model, Proc. of ISEF'2003, September 2003, Maribor Slovenia, pp.353-358.

This page intentionally left blank

Chapter B

Computational Electromagnetics

This page intentionally left blank

Electromagnetic Fields in Mechatronics, Electrical and Electronic Engineering
A. Krawczyk et al. (Eds.)
IOS Press, 2006

Chapter B

B.0 Introductory remarks

The problems of how to improve the efficiency, accuracy and ability of numerical models are the essence of the chapter. As it has already been mentioned, the problems are relatively new as at the very beginning of computer modelling the effort of researchers was focused on building computer programs and discussion on what numerical method is better. The followers of each particular method, FEM, FDM, BEM and mixed, quarrelled with passion trying to prove the advantages of their favourite method. Nowadays, these problems are mostly out of interest for the majority of researchers but their activities are focused on improving efficiency, accuracy and ability of the software (sometimes it is impossible, as software has a mainly commercial nature and is not open for any intervention). The papers gathered in the chapter also show some specific contributions to the existing solvers.
The papers in the Chapter can be grouped as follows:

- new approaches and software,
- modelling of electrical devices and systems,
- modelling of magnetic structures,
- computational electromagnetics in physical and biological media.

The papers that show new approaches and software may also be treated as those of fundamental nature (Chapter A) and their presence in Chapter B has been dictated by the need to emphasize their computational aspect. They are particularly involved in the following problems:

- coupling between Finite Element and Element-Free Galerkin methods which appear to be advantageous when part of the analysis domain is subject to deformations - Lagrangian multipliers are used to treat the interface between the two regions,
- effective methods for computing electromagnetic field sensitivity in time domain versus conductivity perturbations in finite elements,
- problem of fixed and moving parts of a linear actuator which are discretised by Finite Integration Technique (FIT) at two independent Cartesian grids,
- new approach to designing simulation software that on one hand minimizes both development and maintenance costs, and on the other helps the designer to deal with the growing complexity of the simulation process,
- new 3D finite element scheme for non-destructive eddy-current testing (ECT) problems concerning perturbation technique applied to magnetodynamic $h-\phi$ formulation.

The next group of papers, also very important and deeply rooted in the ISEF tradition, concentrates on the following subjects:

- numerical simulation of electromagnetic devices with motion by finite element method which requires some method to couple the fixed and moving parts,
- improvement of accuracy/speed in induction motor optimization based on reduction of the number of variables involved by first finding similarities between different geometrical shapes in magnetic circuit,

- performance analysis of an axial flux PM motor based on finite element analysis (FEA),
- comparison of numerical results obtained by using different couplings of electromagnetic field formulations in different conducting or non-conducting, magnetic or non-magnetic regions for transverse flux induction heating analysis,
- two-dimensional (2D) multi-slice finite element (FE) modelling of squirrel-cage induction motors having one or more broken bars,
- 3-D finite element analysis of static characteristics of thrust and torque actuator system oscillating with both linear and rotational motion,
- new, control-oriented, nonlinear modelling methodology for a series of DC motors,
- algorithm for coupled field-circuit simulation of transients in a three-phase, three-limb power transformer,
- optimization procedure using Response Surface Methodology (RSM) to determine design parameters for reducing torque ripple,
- operating strategy for variable reluctance motor based on sequential excitation of phase windings aiming at achieving acceptable system performance with simple architecture and minimal hardware.

The third group is devoted to modelling of magnetic structures and covers the following problems:

- approach enabling to deal with different models for anisotropy in grain-oriented steel sheets with nonlinearity, anisotropy and hysteresis,
- material representation and theoretical method to derive macroscopic matter-field equations from microscopic scale including extra-losses and dynamic hysteresis occurring within soft magnetic materials,
- model of polar magnetization in small motor with permanent magnet rotor.

At the end we have the subgroup of papers which evokes new activity in computational electromagnetics, namely electromagnetic field analysis in various media, either biological or physical. The papers deal with:

- effect of presence of human head in proximity of a mobile source which is investigated by innovative numerical procedure, called Robin Boundary Condition,
- nested evolutionary algorithm to automatically designed rectangular unequally spaced grounding grids; the algorithm consists of internal genetic algorithm to find maximum touch voltage generated by grounding grid and external genetic algorithm to find the two optimized values of compression ratio,
- finite element method analysis of grounding grid and how this method is utilized to assess the influence of additional substance on the following grounding system parameters: ground potential rise, earth surface potential, touch voltage, step voltage, and grounding resistance,
- ELCID (Electromagnetic Core Imperfection Detector) test used for testing of inter-lamination insulation in stator cores of large electrical generators and motors,
- 2D computationally-efficient scheme, which combines the finite element method (FEM) with a Padé approximation procedure,
- higher-order (2,N) (second-order temporal and Nth-order spatial) FDTD scheme with perfectly matched layer (PML) absorbing boundary condition (ABC) for long-distance

and/or time-prolonged electromagnetic (EM) wave propagation in Debye and Lorentz media of arbitrary number of poles,

- Mode Stirred Chamber excited by wires analyzed by using Transmission Line Modelling (TLM) method.

Electromagnetic Fields in Mechatronics, Electrical and Electronic Engineering
A. Krawczyk et al. (Eds.)
IOS Press, 2006

THE MODELLING OF A ROTATING AXIAL FLUX PERMANENT MAGNET MOTOR WITH REMESHING

Gordon Aird[(1)], Simon Taylor[(1)], Alex Michaelides[(1)], Asmo Tenhunen[(2)]

[(1)] Vector Fields Ltd, 24 Bankside, Kidlington, Oxford, U.K. info@vectorfields.co.uk
[(2)] KONE Corporation, R&D, Hyvinkää, Finland

Abstract
The numerical simulation of electromagnetic devices with motion by the finite-element method requires some method to couple the fixed and moving parts. Improvements in automatic meshing techniques have enabled a gap remeshing method to be included in the finite-element analysis package OPERA-3d/CARMEN to achieve this coupling. This method allows devices, such as motors, with complex air gap geometries to be modelled and has some advantages over other techniques which can be employed. The gap remeshing approach is demonstrated for an axial flux permanent magnet motor where the open circuit back e.m.f. characteristics of the motor are presented.

Introduction

The numerical simulation of 3d eddy currents induced by motion is an important aspect in the design of electromagnetic devices. For many years the OPERA-3d/CARMEN analysis package [1] has proved to be a useful tool for the study of rotating machines. CARMEN is a finite-element time domain analysis package which uses a reduced edge vector A, V formulation. The formulation and use of the reduced / total vector implementation is described in [2-3].

An important feature of any motional analysis is the method by which the moving parts are coupled together. Until now CARMEN has relied on a lock-step method. The elements on a slip surface are defined to have a constant subtended angle and the mesh is rotated at each time step by this angle. The continuity of the mesh on the slip surface is maintained at the expense of having to work with a discrete time step and consequently a constant speed governed by the mesh density at the slip surface.

Other methods for examining motional problems exist. For example, boundary-element/finite-element methods have the advantage that only the active sections require to be modelled. This removes the need to maintain a volume mesh between these parts and they are therefore free to move with respect to each other. The method can suffer from the computational effort required to store and solve the fully populated matrix formed by this type of analysis. Another approach, Lagrange Multipliers [4], allows the finite-element mesh to be discontinuous on slip surfaces within the model. This method has recently been extended to include an overlapping finite-element scheme which increases the flexibility of the method by removing the need to specify a fixed slip surface [5].

The gap remeshing approach of this paper introduces an interface layer of elements between the moving sections of the model. The gap layer of elements is remeshed whenever the positions are

updated and this ensures that the finite-element mesh remains continuous and valid for all configurations.

Gap Remeshing

When the model is constructed it is divided into a number of sections of which there are two types; component parts and gap regions. The component parts represent the structure of the model and are free to move as the analysis progresses. The gap regions provide a buffer between the component parts and as the component parts move the continuity of the finite-element mesh is maintained by rebuilding the set of elements within the gap regions. The connectivity of the mesh within the component parts remains unaltered throughout the entire analysis.

The remeshing step is performed in two stages. Gap regions must have no internal structure and are therefore defined by a set of bounding faces. The first stage is to rebuild the surface mesh on faces that have become invalid by the movement of the component parts. These faces can be identified because they either lie on the boundaries of the finite-element model or specify the interface between two adjacent gap regions. Once a valid set of surface meshes has been constructed, a mesh of tetrahedral elements is generated using a Delaunay technique with a conforming step to match the volume mesh to the bounding surface meshes. The key aspect of the technique is that the volume meshing algorithm generates a conforming mesh. This means that the non gap region sections of the mesh remain unaffected. Figure 1 shows a simple model with one gap region allowing the free rotation of the inner section of the model.

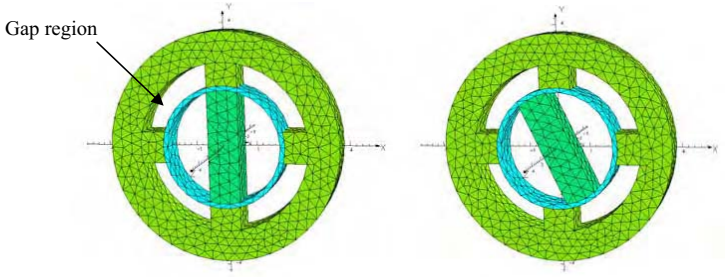

Figure 1. Model geometry showing the use of a gap region to buffer the rotating inner part from the static outer section. Left, initial configuration. Right, configuration after several time-steps.

There are several advantages to this approach. The gap remeshing technique allows the component parts to move to any position enabling the motion to be accurately controlled as a function of time. A significant improvement over the discrete movement inherent in the lock-step method; the moving parts do not need to rotate at a constant speed.

With a new mesh, with a different connectivity, in the gap regions, sections of the finite-element matrix need to be reformed after every update. The matrix, however, retains it sparse characteristic which allows the use of efficient algorithms to solve the system of equations. Furthermore, the number of elements in the gap regions of the model tends to be small compared to the number of elements in the complete mesh. This allows the reuse of large section of the mesh during the analysis and helps to limit the amount of storage space required. To save a configuration only the gap region meshes need to be saved along with a transformation to give the orientation of the component parts.

Another advantage is the ability to represent a wide variety of gap region geometries. At present, however, CARMEN is limited to the study of radial machines with gap regions similar to the shape shown in figure 1 or to axial machines as illustrated in the figure 2, shown later.

A problem with this approach, however, is the reliability of the volume meshing algorithms. If the gap region cannot be remeshed the analysis must stop. This problem can be exaggerated by the types of gap region geometries that are found in rotating the machines. Generally, these regions tend to be thin in relation to their overall size. One approach to overcome this, is to specify a fine mesh around the gap region so that the region can be meshed with near regular tetrahedral. In addition, the geometry of the gap region can be analysed to identify axial gap structures that can be expanded before being remeshed and then returned to their original dimensions. This has the advantage of allowing these very thin gap regions to be remeshed reliably. Gap expansion is possible for axial gap region geometries but not for radial gap regions.

Through the study of some devices it has been observed that the time required to perform the remeshing is relatively small compared to total run time of the analysis. It should be noted that the remeshing time can vary significantly from one model to another depending on the complexity of the gap region. Apart from the overall size of the gap region, the remeshing time depends heavily on the thickness of the gap region relative to the size of the elements. If the meshing algorithm is required to form distorted elements to fill the region then it is generally more difficult for it to capture all the surface facets present on the bounding surface meshes of the region.

Application : 14-Pole Axial Flux Permanent Magnet Motor

Initial tests of the gap remeshing method have started on a 14 pole, 3-phase, permanent magnet synchronous axial flux motor as shown in figure 2. The device being studied has a diameter of 420mm with a height of 114mm. The rotor consists of 14 poles and the stator has 84 slots. The rotor and stator sections have a relative permeability of 1000. The magnets have been defined to have an coercivity of -700000 Am^{-1}. One set of the three windings in the stator section is shown. The gap region has a thickness of 3 mm.

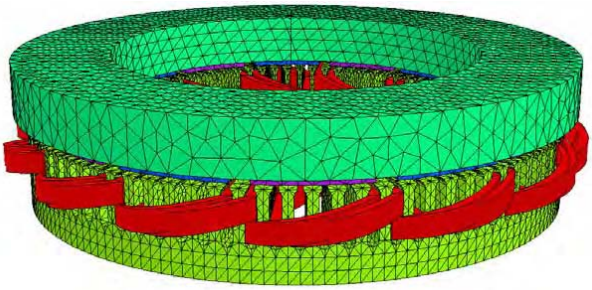

Figure 2. 14 pole, 3-phase, permanent magnet synchronous axial flux motor. 1 set of 3 windings shown.

The first step in motor analysis is to evaluate the open circuit back e.m.f. waveform of the stator windings. The motor of figure 2 was analysed at a speed of $2\pi/7/0.02$ $rads^{-1}$. With 14 poles the rotor has 7 fold rotational symmetry, the rotation speed corresponds to the rotor moving 1/7th of a revolution in 0.02 seconds. The open circuit voltage induced in the windings was measured as a

function of time, graph 1. The voltage was logged at 0.0005 second intervals. The fundamental pole rotation frequency of 50Hz and the higher order harmonics created by the slots can be identified.

The model consists of around 500000 elements of which approximately 30000 are present in the gap region. The above analysis was performed in 494 minutes on a standard desktop computer of which 63 minutes were spent performing all the remeshing steps. For this model the remeshing operation accounts for 12.7% of the total run time.

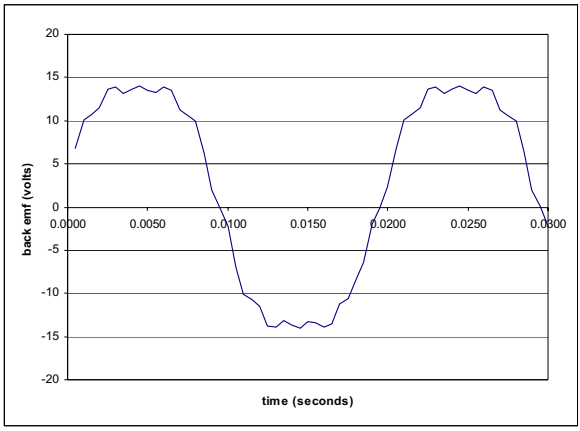

Graph 1. Open circuit back e.m.f. in windings of 14-pole axial flux motor of figure 2.

Conclusion

A new gap remeshing algorithm in the OPERA-3d/CARMEN analysis package has been presented. The method has been successfully applied to several rotating devices and results for an axial flux permanent magnetic motor have been presented. With help form the KONE Corporation trials are still in progress and some developments are still ongoing.

With future developments it is hoped that the gap remeshing scheme can be extended to exploit periodicity in models and to study eccentric rotations. It is also planned to develop this method to study problems involving linear motion.

References

[1] C.R.I. Emson, C.P. Riley, D.A. Walsh, K. Ueda, T. Kumano, Modelling eddy currents induced by rotating systems, IEEE Trans. Mag., Vol. 34(5), 1998

[2] J. Simkin, S.C. Taylor, E. Xu, Calculation of magnetic vector potential jump on edges in reduced-total formulations, IEE Proc.-Sci. Meas, Technol., Vol. 151(6), pp 419-422, 2004

[3] E. X. Xu, J. Simkin, Total and reduced magnetic vector potentials and electric scalar potential for eddy current calculation, IEEE Trans. Mag., Vol. 40(2), pp 938-940, 2004

[4] H. C. Lai, D. Rodger, P. J. Leonard, Coupling meshes in 3D problems involving movements, IEEE Trans. Mag., Vol. 28(2), pp 1732-1734, 1995

[5] H. C. Lai, D. Rodger, P. C. Coles. A 3-D overlapping finite-element scheme for modeling movement. IEEE Trans. Mag., Vol. 40(2), 2004

Electromagnetic Fields in Mechatronics, Electrical and Electronic Engineering
A. Krawczyk et al. (Eds.)
IOS Press, 2006

ON THE USE OF UNSUPERVISED NEURAL NETWORKS TO ASSIST THE DIMENSIONALITY REDUCTION IN AN INDUCTION MOTOR REDESIGN

Pablo Arboleya, Guzmán Díaz, Tania Gil

University of Oviedo, Campus de Viesques, s/n, 33204 Spain, arboleyapablo@uniovi.es

Amalia Barrera

ABB Automation Products, 08192 Sant Quirze del Valles (Spain), amalia.barrera@es.abb.com

Abstract*– *In this paper a contribution to the improvement of accuracy/speed in induction motor optimization is presented. It is based on the reduction of the number of variables involved by first finding similarities between different geometrical shapes in the magnetic circuit. Therefore, a prior filtering of the „shapes" to be computed is performed, allowing the use of accurate optimization algorithms with a reduced number of specimens to be tested. This allows the use of more accurate optimization procedures that conventionally have been limited in their scope due to the time required to simulate every single motor (for instance, finite element analysis).

Introduction

Redesign of induction motors so that better efficiency is achieved is a continuous practice in motor manufacturing. Actually, around 60% of the industrial energy consumption is due to these devices, and therefore maximization of their efficiency is nowadays regarded as a goal. Motors have improved in efficiency by an average of 3 percent over the last decade

While USA and Canada have introduced the EPAct as a way to specifically compel improvements in motors ranging from 0.75 to 150 kW, the EU is working with CEMEP (European Committee of Manufacturers of Electrical Machines and Power Electronics) to expand the use of high efficiency motors. In this latter case, the European Commission and EU motor manufacturers have agreed on the EU/CEMEP motor efficiency classification scheme, based of three bands of efficiency, for standard TEV, 2 and 4 pole, squirrel cage induction motors in the power range of 1.1 to 90kW.

The redesign of the induction motor searching for an optimal has been approached by a number of authors, accepting that the problem is a multivariable and multiconstraint one. The problem in fact is faced as a general nonlinear programming problem, in which a vector $\underline{\mathbf{x}} = (x_1, x_2, ..., x_n)$ composed of n motor geometric variables must be found, so that an objective function (for instance efficiency) is minimized (or maximized), and some constraints are complied with. The constraints sometimes must be equalled (for instance the starting torque to rated torque ratio be equal to 1.6) or, giving a greater freedom degree, not exceeded (for instance the stack length be less than 200 mm for given frame size and power rating, or the efficiency be not less than 89.8%). All around this mess, the model adds further complexity to the task, since a balance must be accomplished between closed-form design methods (with low accuracy, but fast search capability) or numerical design (higher accuracy with reduced computation speed).

In order to account the nonlinear multi-objective optimization task, several methods have been proposed in the literature. For instance, in [1] three ways two face the problem are proposed. Liuzzi *et al.* and other authors (such as [2]) claim that the problem must be simultaneously solved for several objective functions (namely, for instance, efficiency, starting torque,…). Hooke-Jeeves search routine has been used as a deterministic option for

design optimization in several works [1, 3, 4]. It has the desirable quality of avoiding first order derivatives (note that this is a pursued advantage due to that an explicit mathematical depiction of the objective and constraints functions is not accessible). But as an important drawback, the final solution may stop trapped in the neighbourhood of a local optimum, without the ability to find new optima. A possible solution to this problem is approached in [5], where the search is done by first introducing random starting points and afterwards performing a deterministic search within the neighbourhood. A variant and enhancement of this methodology is presented in [6], where niching genetic algorithms are used. The proposal in this latter work is to find regions of global optima with the aid of evolutionary strategies, and then switch to a conventional deterministic search, using a modified Hooke-Jeeves algorithm, to search for local optima. Niching algorithms are also presented in [7] as a means of finding multiple optimal profiles instead of deriving an only optimal solution. This way, the designer's preferences can be met since a number of possible choices are allowed. Kim *et al.* argue that multiobjective functions optimization can lead to a trapped solution into a local minimum [8]. With the aid of a proposed change in the production of offsprings by reproduction, the authors claim to get around the local minimum using this technique. More about evolutionary algorithms can be found in [9]. Idir *et al.* base their search algorithm in an iterative minimization of the difference (error) between objective function and the maximum limit of the objective function, within a feasible range of values [10]. This is performed employing quadratic penalty functions, which add more weight on the error function when constrains are violated.

Above, a short literature review has been presented, with the aim of providing an insight on optimization procedures. It is obvious that all the references at least have as a common denominator a recognition of the multivariable feature. Two additional papers about optimization are detailed here. The first one is the paper by Nurdin *et al.* [11]. An interesting proposal about a motor design philosophy is presented in their work. Along with a comprehensive analysis of variables involved in motor performance, they introduce a useful viewpoint about some key concepts during design stages, based on the definition of primary variables, equality constraints, and iterative analysis. It is remarkable their investigation on the division of the information into "numerical" and "fuzzy" information. Their work has been further followed and analyzed by some other authors [12-16]. As a result a reduction in the final problem dimension is obtained but, as a drawback, considering significant simplifications about the motor calculation. Nonetheless, the idea presented in [11] about motor "synthesis" prior to optimization is of valuable help to assist in the motor design process, since it reduces the computational burden an accelerates the convergence speed during optimization. A second paper of interest for the purposes of the present work is presented by Fei *et al.* in [17]. In his paper Fei focuses on the visualization in planes of a relatively reduced number of input and output variables, so that prompt relations can be obtained.

In this paper, also a correlation method is searched. It is the aim of the work to provide a fast visualization method based on artificial neural networks, so that optimization methods can be improved. The idea is to provide a means to correlate design variables (inputs and outputs) so that a reduction in the number of variables involved in the design can be obtained. Thus, the relations obtained allows to drastically reduce the number of computations needed to optimize, and therefore allows to attain better accuracy by using iterative numerical models to account non-linear magnetic phenomena instead of closed-form models.

Theoretical Background

Data classification

In this paper Self Organizing Maps (SOM) are used to obtain relationships among the large number of variables involved in the motor design. The following explains the reasons why SOM can be advantageously applied in order to simplify the analysis of the variable relations.

As an unsupervised learning artificial neural network, SOM presents classification and interpolation-like properties. SOM maps the input data space in $\mathbf{R}^n$ onto a discrete two-dimensional lattice of neurons in a topologically ordered fashion [18, 19]. For each neuron, a codebook vector $\underline{\mathbf{m}}_i$ is associated. Each input vector is compared with the codebook vectors, and the input is mapped to the location of the best matching unit c. A usual way of doing the comparison is minimizing the Euclidean distance as follows:

$$c = \arg\min_i \left\{ d\left(\underline{\mathbf{x}}, \underline{\mathbf{m}}_i\right) \right\} \tag{1}$$

Where $\underline{\mathbf{x}}$ is the input vector.

In the learning process the codebook vectors are restructured according to the input vectors $\underline{\mathbf{x}}$ as follows:

$$\underline{\mathbf{m}}_i(t+1) = \underline{\mathbf{m}}_i(t) + h_{ci}(t)\left[\underline{\mathbf{x}}_i(t) - \underline{\mathbf{m}}_i(t)\right] \tag{2}$$

In this expression h_{ci} is the neighbourhood function and t is the learning time step. During the learning process, the learning rate and the neighbourhood radius are reduced. The learning process leads to a smoothing effect on the codebook vectors in the neighbourhood.
This defines the SOM mapping which has the following properties:
1. The SOM mapping performs a dimensionality reduction as it takes an n-dimensional point $\underline{\mathbf{x}}$ from the input space and maps it onto a low-dimensional (usually 2D) visualization space.
2. It provides a good approximation of the joint pdf (probability density function) of the input data in the sense that its nodes are distributed in the same manner as the input examples, allocating more nodes in regions with a high density of input vectors.
3. It gives a topology-preserving mapping, since input vectors that are close in the input space, are mapped into close points of the visualization space.

Network training, data projection and analysis

Let us assume a motor with input variables a_1 and b_1 (geometrical dimensions) and an arbitrary output variable c_1 (for instance, efficiency or slot permeance). The goal is to modify these variables so that a feasible and optimum motor can be obtained.
Let the sets A and B be two arbitrary sets of input data including all of the possible values of the input variables (within a finite space), and C an arbitrary set of output data, being the elements of such sets $\{a_i\} \in A$, $\{b_i\} \in B$, and $\{c_i\} \in C$, where subscript i is the order of the motor after an iterative process.
Let us define the subset A_V, so that:

$$A_v \subset A \,/\, \forall \{a_i\} \in A_v, \{a_i\} \neq a_1 \tag{3}$$

Where a_1, as stated before, is the value of the input variable represented by the set A for the first motor (the initial motor to be optimized). Similar subsets B_v and C_v can be defined comprising the values of the input variables of set B that are not equal to the value of the first motor, and the corresponding values of the output variables of set C.
If the training procedure of the neural network follows the condition *ceteris paribus* (i.e., an input variable changes when no other input variable changes), advantages can be achieved, as it is going to be shown.
SOM projection results in different planes for every involved variable. For a given motor of order i, a pair of 2D coordinates (x_i, y_i) is obtained, so that a suprayective application is found for every point in the 2D planes. That is, the coordinates (x_i, y_i) for the element $\{a_i\}$ in the projection plane corresponding to set A, and the (x_i, y_i) coordinates for the element $\{b_i\}$ in the projection plane corresponding to set B are exactly the same. The same conclusion is applied to the output set C.
Due to the *ceteris paribus* training procedure, a condition is obtained so that:

$$\forall \{a_i\} \in A_v \Rightarrow \{b_i\} \in \overline{B}_v \tag{4}$$

Once more, it must be remarked that the element $\{a_i\}$ and the element $\{b_i\}$ are projected on their respective planes with the same 2D coordinate (x_i, y_i), and a 3D plot of every projection plane can be obtained.
So, if gradient is computed for the elements of sets A, B, and C, new sets G_A, G_B, and G_C are obtained respectively. I.e., if elements of set A are plotted as a 2D function $F(x,y)$, the gradient can be computed as

$$\nabla \overline{F}(x,y) = \frac{\partial F}{\partial x}\bar{\mathrm{i}} + \frac{\partial F}{\partial y}\bar{\mathrm{j}} \tag{5}$$

Now let $\{g_{ai}\}$ be the modulus of the gradient, $\left|\nabla \overline{F}(x,y)\right|$, for an element of set G_A. If

$$\forall\{g_{ai}\} \in G_A / \{g_{ai}\} \neq 0, \{a_i\} \neq 0 \tag{6}$$

then a correlation is demonstrated between elements $\{a_i\}$ and $\{c_i\}$. That is, a correlation is found between the variable corresponding to set A and the output values. This procedure allows to clearly trace the borders of significant clusters.

Results Analysis Using The Unsupervised Neural Network

The procedure can be observed in Fig. 1. Values of the slot width nearest the air gap, b_{s11}, and of the slot height , h_{s1}, (say elements of set A and B, for instance) are represented in two projection planes, in a 2D coordinate system. As output plane, the slot permeance is presented in the third map. A motor is defined by a unique pair of values x and y in the planes. Values ranging from 3.2 through 7.2, with a first value (initial motor) of 5.13 are represented for the slot width. The line labelled as 5.13 (in fact 5.1316) represents the set of motors in which the value of the variable has been kept to the value of the first motor, while the rest of variables can be changed (*ceteris paribus*). The $\nabla\overline{F}(x,y)$ vectors, are represented for a number of motors. Sudden variations are thus indicated when large values of the vector moduli are represented, corresponding to well defined clusters.

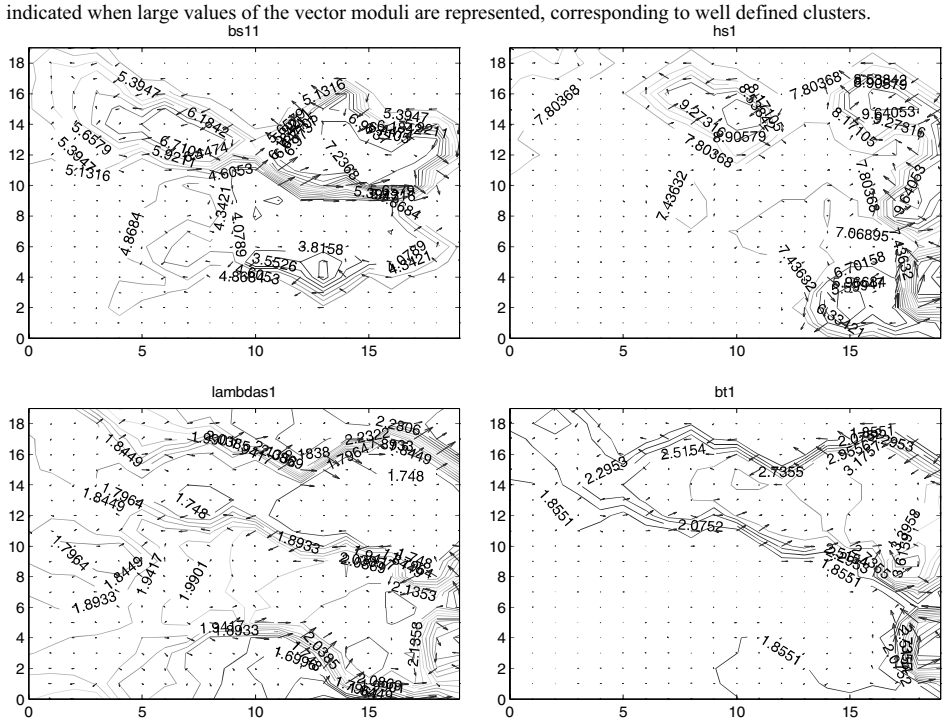

Fig. 1. Projection of the stator slot width, height, permeance, and the teeth maximum flux density.

These projections have been obtained by training the network with 250 motors. Although for simplicity only two input and an output maps are presented, a plane or map was obtained for each of more than 300 variables (inputs and outputs) involved in the motor performance computation.

Once the cluster is obtained, by comparison of maps, it is also obtained an inverse relation between these two variables. This inverse relation is readily obtained from the fact that the slot permeance can be calculated as:

$$\lambda_{s1} = k_{s1} F_1 \left[\frac{h_{so1}}{b_{so1}} + \frac{h_{sc1} - h_{so1}}{\frac{b_{s11} + b_{so1}}{2}} \right] + \frac{(3k_{s1} + 1)}{4} \left[\frac{(h_{s1} - h_{sc1})}{3\left(\frac{b_{s11} + b_{s12}}{2}\right)} \sqrt{\frac{b_{s12}}{b_{s11}}} \right] \tag{7}$$

Where k_{s1} is a coil pitch correction factor and F_1 a factor accounting the saturation mainly in the teeth tips. Rest of the variables are geometrical dimensions. This complete expression of the slot permeance shows the inverse influence of the slot width on the slot permeance (neglecting the last squared root term due to the skewing of slots).

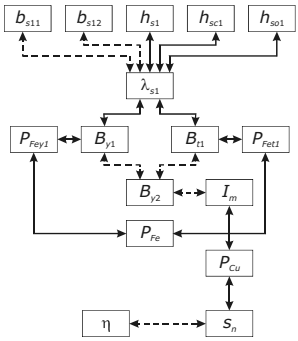

Fig. 2. Sort of strongest relations between geometric dimensions, magnetic variables and motor performance variables, as obtained from the proposed method.

More correlations obtained for a computed problem according to the proposed methodology are represented in Fig. 2. In this Figure direct (solid lines) and inverse (dashed lines) relations are presented. Most noticeable relations are represented according to the data processed following the above discussed methodology of data classification and cluster identification. Sixteen variables have been processed using sixteen projection planes. Input variables: slot widths (b_{s11} and b_{s12}), and heights (h_{s1}, h_{sc1} and h_{so1}); output variables: slot permeance (λ_{s1}), flux densities in yoke and teeth (B_{y1}, B_{y2}, and B_{t1}), core and copper losses, rated slip (s_n), and efficiency (η). It must be pointed that these sixteen variables are a reduced number of the variables used in the calculation of the motor performance. Although the numerical integration method involves more than 300 variables, for the sake of clarity just these sixteen has been represented. Observe that some relations are obvious, while some others remain more obscure. Lines represent the strongest relations found. However, syllogism rules must be applied in order to obtain relations between two variables not directly connected. That is, if there exist a direct relation between the stator slot total height (h_{s1}) and the slot permeance (λ_{s1}), and an inverse relation between the permeance and the flux density in the stator teeth (B_{t1}), then an inverse relation between h_{s1} and B_{t1} is obtained.

Moreover, when direct or inverse relationships are accepted following this procedure, a convenient reduction in the dimensionality of the problem can be conducted, observing that an effect (output value) can be caused by a number of causes (values of input variables). It is to be remarked that this is possible if (i) the abovementioned *ceteris paribus* neural network training rule is conducted, and (ii) if the SOM suprayective projection for every plane is carried in the way discussed in this paper.

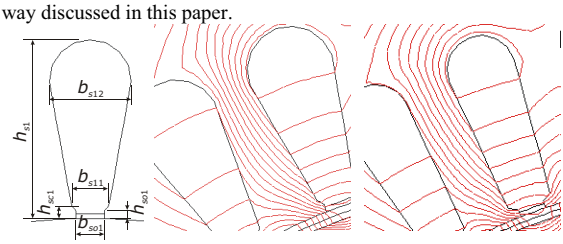

Fig. 3. Comparison of two similar slots, with data obtained form finite element simulations.

A reduction in the dimensionality is obtained if, for instance, the slot of Fig. 3 is reduced using this method to a cipher, representing all the embedded geometric information that gives as a result the slot permeance. Although both slots are quite different in their dimensions, their permeance is the same. A previous assessment of the slot cipher would avoid to simulate the two cases, thus implying a reduction of the computational time.

Conclusions

A method to reduce the number of motors to be simulated during optimization processes has been presented in this paper . The reduction implies a consequent reduction of computation time, what in turn allows to introduce more accurate simulation methods (numerical iterative methods that account for nonlinear magnetic calculations). Based on SOM classification and analysis a ceteris paribus training procedure of the neural network , a methodology for detecting correlations prior to clusters definitions has been developed . Strong and weak correlations are found by this method , therefore allowing to define similarities between, for instance, different slot shapes. As a conclusion, computation time required for an optimization batch is reduced after this prior filtering.

References

[1] G. Liuzzi, S. Lucidi, F. Parasiliti and M. Villani, Multiobjective optimization techniques for the design of induction motors, IEEE Transactions on Magnetics, Vol. 39, pp 1261-1264, 2003.
[2] W. Jazdzynski, Multicriterial optimization of squirrel-cage induction-motor design, IEE Proceedings-b Electric Power Applications, Vol. 136, pp 299-307, 1989.
[3] Ramarath.R and B.G. Desai, Optimization of polyphase induction motor design - nonlinear programming approach, IEEE Transactions on Power Apparatus and Systems, Vol. PA90, pp 570-&, 1971.
[4] J. Faiz and M. Sharifian, Optimal design of three phase induction motors and their comparison with a typical industrial motor, Computers & Electrical Engineering, Vol. 27, pp 133-144, 2001.
[5] A. Daidone, F. Parasiliti, M. Villani and S. Lucidi, A new method for the design optimization of three-phase induction motors, IEEE Transactions on Magnetics, Vol. 34, pp 2932-2935, 1998.
[6] D.W. Zhou, C.B. Rajanathan, A.T. Sapeluk and C.S. Ozveren, Finite-element-aided design optimization of a shaded-pole induction motor for maximum starting torque, IEEE Transactions on Magnetics, Vol. 36, pp 3551-3554, 2000.
[7] D.H. Cho, H.K. Jung and C.G. Lee, Induction motor design for electric vehicle using a niching genetic algorithm, IEEE Transactions on Industry Applications, Vol. 37, pp 994-999, 2001.
[8] M.K. Kim, C.G. Lee and H.K. Jung, Multiobjective optimal design of three-phase induction motor using improved evolution strategy, IEEE Transactions on Magnetics, Vol. 34, pp 2980-2983, 1998.
[9] J.P. Wieczorek, O. Gol and Z. Michalewicz, An evolutionary algorithm for the optimal design of induction motors, IEEE Transactions on Magnetics, Vol. 34, pp 3882-3887, 1998.
[10] K. Idir, L.C. Chang and H.P. Dai, Error-based global optimization approach for electric motor design, IEEE Transactions on Magnetics, Vol. 34, pp 2861-2864, 1998.
[11] M. Nurdin, M. Poloujadoff and A. Faure, Synthesis of squirrel cage motors - a key to optimization, IEEE Transactions on Energy Conversion, Vol. 6, pp 327-335, 1991.
[12] S. Lie and C. Dipietro, Copper die-cast rotor efficiency improvement and economic-consideration, IEEE Transactions on Energy Conversion, Vol. 10, pp 419-424, 1995.
[13] J.T. Park, C.G. Lee, M.K. Kim and H.K. Jung, Application of fuzzy decision to optimization of induction motor design, IEEE Transactions on Magnetics, Vol. 33, pp 1939-1942, 1997.
[14] M.K. Kim, C.G. Lee and H.K. Jung, Multiobjective optimal design of three-phase induction motor using improved evolution strategy, IEEE Transactions on Magnetics, Vol. 34, pp 2980-2983, 1998.
[15] C.G. Lee, D.H. Cho and H.K. Jung, Niching genetic algorithm with restricted competition selection for multimodal function optimization, IEEE Transactions on Magnetics, Vol. 35, pp 1722-1725, 1999.
[16] D.H. Cho, H.K. Jung and C.G. Lee, Induction motor design for electric vehicle using a niching genetic algorithm, IEEE Transactions on Industry Applications, Vol. 37, pp 994-999, 2001.
[17] R. Fei, E.F. Fuchs and H. Huang, Comparison of 2 optimization techniques as applied to 3-phase induction-motor design, IEEE Transactions on Energy Conversion, Vol. 4, pp 651-660, 1989.
[18] T. Kohonen, Self Organizing Maps, Springer-Verlag GmbH & Company KG, Berlin, Germany 1995.
[19] T. Kohonen, E. Oja, O. Simula, A. Visa, and J. Kangas, Engineering Applications of the Self Organizing Map, Proceedings of the IEEE, Vol. 84, pp1358-1384, 1996.

Electromagnetic Fields in Mechatronics, Electrical and Electronic Engineering
A. Krawczyk et al. (Eds.)
IOS Press, 2006

EVALUATION OF THE ELECTROMAGNETIC COUPLING MECHANISMS IN THE BRUSHLESS DOUBLY-FED INDUCTION MACHINE

F. Blázquez, C. Veganzones, D. Ramírez

E.T.S. de Ingenieros Industriales. Universidad Politécnica de Madrid
José Gutiérrez Abascal, 2. 28006 Madrid (Spain). E-mail: fblazquez@etsii.upm.es

Abstract. *– The great development of Large Variable Speed Wind Turbine Generators has caused a new interest in the Brushless Doubly-Fed Induction Machines (B.D.F.I.M) because they could be a feasible alternative to Wound Rotor Induction Machines (W.R.I.M). The B.D.F.I.M. has two different stator windings and a rotor cage that make it more robust than the W.R.I.M. The operation of the B.D.F.I.M. is possible due to the two stator magnetic fields couple each other through the rotor cage which has a special configuration. This paper studies these coupling mechanisms comparing simulation results, obtained with a Finite Element (FE) Model, and experimental result, obtained with a Prototype of B.D.F.I.M.*

Introduction

The Brushless Doubly-fed Induction Machine (B.D.F.I.M.) concept has been developed since the second half of the XXeth century. Nowadays, the interest in B.D.F.I.M has grown because it is a possible alternative to the Wound Rotor Induction Machine (W.R.I.M.) in Large Variable-Speed Wind Turbine Generators.

Basic configuration and operation principle of B.D.F.I.M are presented now.

Basic Configuration

The B.D.F.I.M. has two isolated stator windings, called power winding and control winding. Each one has a different pole-pair number, and they are connected to sources with different amplitude and frequency. The power winding has p_p pole-pair and it is directly connected to the electric network; the control winding has p_c pole-pair and it is connected to a variable frequency electronic converter.

The rotor electrical circuit is composed of short-circuited bars making closed loops which are grouped among each other making up some nests. The number of nests (N) depends on the number of pole-pair in the stator windings ($N = p_p+p_c$). Fig. 1 shows a diagram of a B.D.F.I.M:

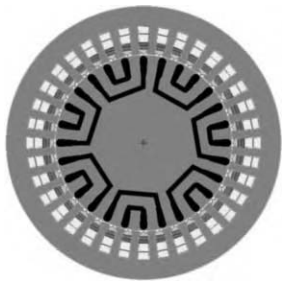

Fig. 1. B.D.F.I.M. diagram

Operation principle

For each frequency value of the currents in the control winding, there is a rotor speed at which the fields created by both stator windings, $\vec{H}_c$ and $\vec{H}_p$, rotate at the same speed with respect to the electrical conductors fixed in the rotor. That speed is according to the next expression:

$$\Omega_r = 2\pi \cdot \frac{f_p + f_c}{p_p + p_c} \tag{1}$$

where f_p and f_c are the frequencies of the power and control windings, respectively [1].

In the rotation speed conditions given by (1), $\vec{H}_p$ and $\vec{H}_c$ induce currents with the same frequency in the rotor conductors. These induced currents create a magnetic field spatial distribution in the air gap, which has components of p_p and p_c pole-pair. The magnetic field components generated by the rotor currents couples with the stator fields $\vec{H}_p$ and $\vec{H}_c$ [2]. Fig. 2 shows a simple scheme of these magnetic couplings:

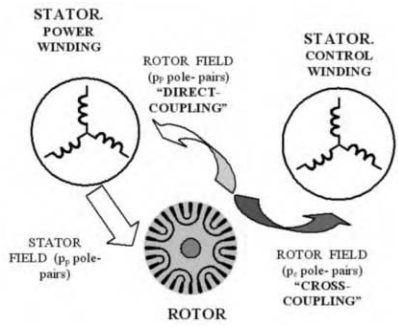

Fig. 2. Magnetic coupling mechanism

This paper means to show, with a FE model and a real prototype, the magnetic coupling mechanism that has just been described. First, the characteristics of the final prototype have been defined by means of a FE model. Second, it is presented the prototype. Third, it is shown the tests that allow evaluating the rotor field component that guarantees the cross-coupling mechanism. Finally, the results obtained with the prototype and the FE model are presented and compared.

Finite Element Model

From the structure of a conventional machine with 36 slots in the stator and 28 slots in the rotor, and taking into account the low speed that the wind turbines need, the following parameters have been chosen: 5 pole-pair (p_p) for the power stator winding, 2 pole-pair (p_c) for the control stator winding and 5+2=7 nests (N) for rotor winding. The choice of the number of pole-pair is the result of a theoretical study presented in [3].

Following the recommendations made by several authors [4], [5], a double layer configuration has been chosen for power and control stator windings. Each winding is distributed in all the stator slots, occupying them partially. The number of turns of both windings has been chosen calculating the induction level that they produce in the magnetic circuit. Each winding must produce the half of the total induction level.

A similar structure to the one present in [4], without any short-circuit ring, has been used for the rotor. Each nest is formed by two concentric loops. In the FE model (2D) all loops have been represented like zero value voltage sources, including the end of the loop in the total impedance value.

Prototype Description

The same parameters determined by the FE model have been repeated in the prototype. Fig. 3 shows a photograph of the stator, as well as a detailed diagram of the windings disposition in the slots.

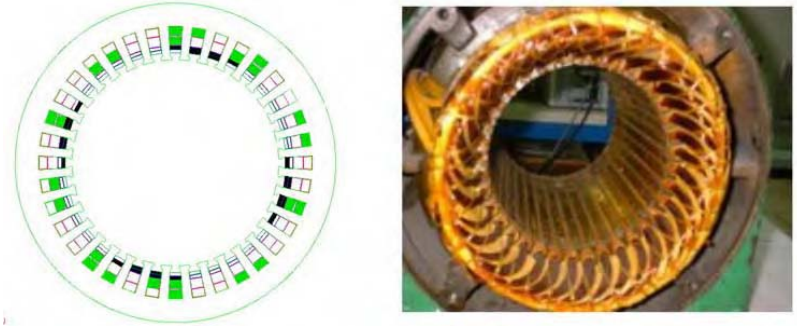

a) Power and control winding distribution. Phase U b) Prototype

Fig. 3. Stator Configuration

Related to the rotor, the 14 loops are made of copper strap mechanized with the same shape as the slot. All of them are electrically isolated from the rotor core with several insulating paper layers. Fig. 4 shows a photograph of the rotor and a diagram of its electric circuit.

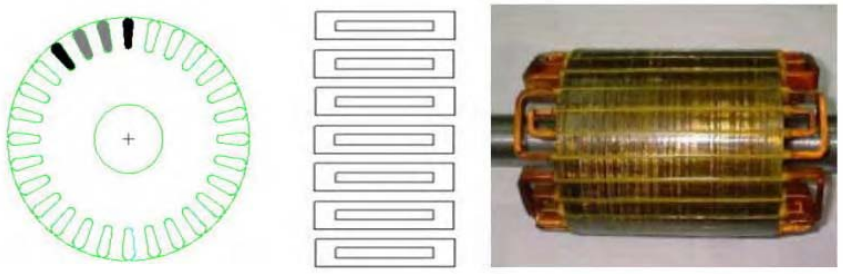

a) Nest distribution b) Rotor loops scheme c) Prototype

Fig. 4. Rotor Configuration

Results

In both cases, with the FE model and the prototype, the main goal to be achieved through the tests is evaluating the rotor field component that allows the cross-coupling between the stator windings and guarantees the B.D.F.I.M. operation. The tests have been carried out connecting the power winding to a constant amplitude 50 Hz source, with the rotor running at constant speed. In the experiments with the prototype the speed is fixed by a direct current motor.

The voltage (e.m.f.) induced in the control winding is registered and its amplitude and frequency are measured at open circuit. The frequency depends on two variables: the pole-pair number in the rotor field component that establishes the cross-coupling, theoretically p_c (fig. 2), and the speed, according to the following expression:

$$f_c = \Omega_r \cdot \frac{p_p + p_c}{2\pi} - f_p = \frac{n_r}{60} \cdot (p_p + p_c) - f_p \qquad (2)$$

In order to clearly identify the pole-pair number in the rotor field components, the tests are repeated at different speeds with the prototype and the FE model. Besides, the analysis of the cross-coupling component, with p_c pole-pair, at those speeds allows evaluating the prototype behavior.

As an example, the result of the tests at 522.5 and 364.5 rpm are presented.

FE model results

If the power winding is supplied with a voltage level of 174 V and 50Hz, with the control winding at open circuit, appears a field distribution showed in fig. 5:

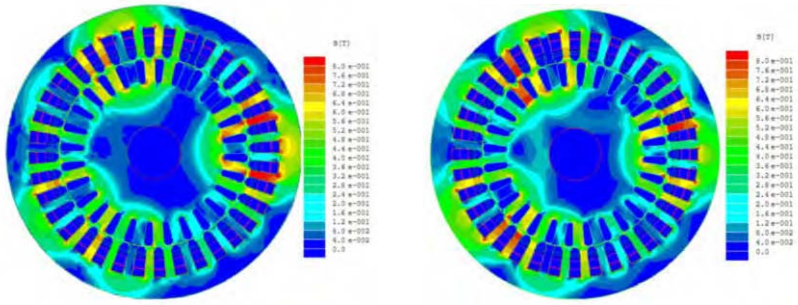

a) n = 364.5 rpm b) n = 522.5 rpm

Fig. 5. Field distribution

The inducted voltages in the control winding and their spectra are presented in fig.6.

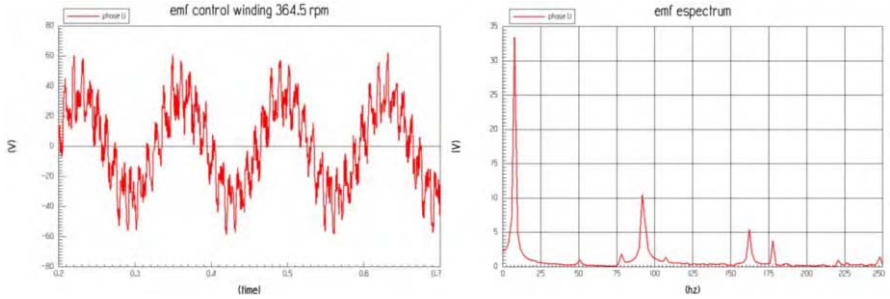

a) 364.5 rpm

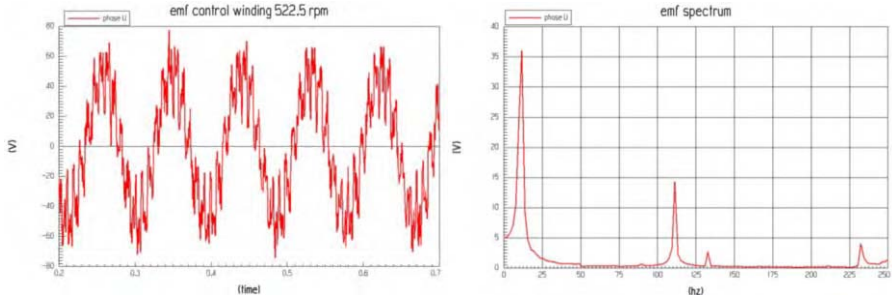

b) 522.5 rpm

Fig. 6. Simulation Results of the induced voltage in the control winding.

Prototype results

With the same simulation conditions, several tests have been done in the prototype. Fig. 7 shows the registers of the inducted voltages in the control winding and their spectra. In these figures, positions X1 and X2 have been used to identify the main frequencies for each spectrum.

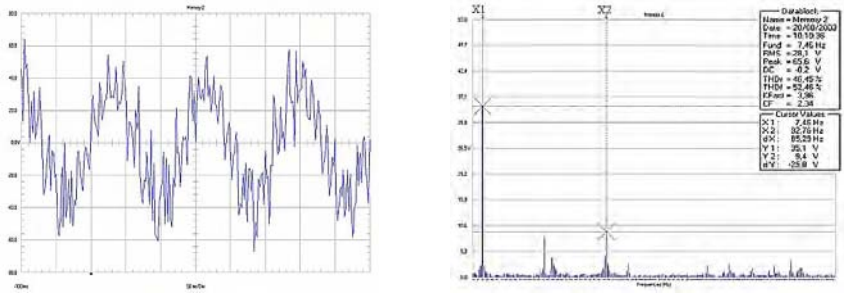

a) 364.5 rpm

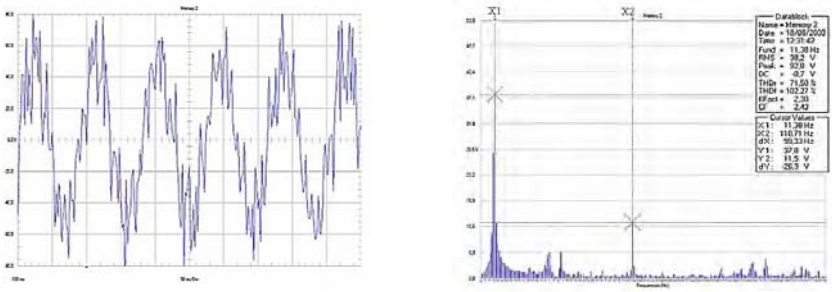

b) 522.5 rpm

Fig. 7. Register and spectrum of induced voltage in the control winding

Analysis

First, the cross-coupling component of the rotor field is evaluated by the comparison between the theoretical frequency and the main frequencies of the spectra, in FE model and prototype, for each speed. Table 1 shows the frequencies in all cases: column 2 presents the theoretical values according to eq. (2), column 3 presents the values obtained with the FE model and column 5 presents the values obtained with the prototype.

Table 1. Main frequency vs theoretical frequency.

n (r.p.m.)	f_c (Hz) (theoretical)	f_c (Hz) (FE model)	error (%)	f_c (Hz) (prototype)	error (%)
364.5	7.47	7.8	4.4	7.46	0.13
522.5	10.95	11.7	6.8	11.38	3.9

It is observed, in columns 4 and 6, that the errors between the theoretical values and the values in the FE model and the prototype are smaller than 7 per cent. Therefore, the special rotor which has been implemented in the FE model and the prototype, justifies the cross-coupling mechanism that appears in the B.D.F.I.M.

In the spectra presented in fig. 6 and fig. 7, other components appear in addition to the component induced by the cross-coupling component of the rotor field. Table 2 presents the 2 main components of the induced voltage (e.m.f.) in the control winding. Columns 2 and 3 present the principal component (cross-coupling component) in the FE model and the prototype. Column 4 and 5 presents the second component in amplitude.

Table 2. Main components of the inducted voltage spectra.

n (r.p.m.)		Main component		Second component	
		Amplitude (V)	Frequency (Hz)	Amplitude (V)	Frequency (Hz)
364.5	Prototype	35.1	7.46	9.4	92.76
	FE Model	33.4	7.8	10.4	91.7
522.5	Prototype	37.8	11.38	11.5	110.71
	FE Model	36.05	11.7	14.3	111.3

It is observed a good correlation in the values of amplitude and frequency between the FE model and the prototype.

Column 5 shows that the frequency of the second component depends on the speed (n_r) and therefore it can only be induced by a rotor field spatial component. Analyzing these frequency values, a component of 12 pole-pairs has been identified in the rotor field. Other rotor field components, that are not present in the bibliography, appear in the B.D.F.I.M. The detailed identification of all these rotor field components is shown in [6].

Conclusions

It has been demonstrated by means of a FE model and a prototype that the rotor configuration, with concentric copper loops isolated from the rotor core, is suitable for the B.D.F.I.M. operation because causes the cross-coupling mechanism.

In the analysis, rotor field components different of cross-coupling component have been detected. As a consequence, it is necessary to develop a new formulation that, based on the algorithms that determine the magnetic coupling between the windings, finds the relationship between the pole-pair number in the stator and rotor windings, and justifies the appearance of all the rotor magnetic field experimental components.

Due to these components are not useful for the B.D.F.I.M. performance they might be reduced in future B.D.F.I.M. designs. Considering the goods results obtained in the cross-coupling evaluation, the FE models can be important tools for the optimization of the B.D.F.I.M. desing.

References

[1] Willianson S., Ferreira A.C., Wallace A.K., “Generalized theory of brushless double fed machine. Part 1 Analysis”, IEE Proc Electric. Power Appl. Vol 144, n2, pg 111-122, Mach 1997.

[2] Wiedenbrug, E; Boger, M.S.; Wallace, A.K.; Patterson, D.: “Electromagnetic mechanism of synchronous operation of the brushless doubly-fed machine”, Industry Applications Conference, 1995. Conference Record of the 1995 IEEE, Volume:1, 1995. Pages: 774-780.

[3] F. Blázquez; C. Veganzones; D. Ramírez; J. R. Arribas; M. Lafoz; "Brushless Doubly-fed Asynchronous Generator for Variable Speed Wind Generation Systems". International Conference on Electrical Machines. ICEM'02. Brujas, Ag. 2002.

[4] Willianson S., Ferreira A.C., Wallace A.K., "Generalized theory of brushless double fed machine. Part 1 Analysis", IEE Proc Electric. Power Appl. Vol 144, n2, pg 111-122, Mach 1997

[5] Chris S. Brune, René Spée, Alan K. Wallace. "Experimental Evaluation of a Variable-Speed, Doubly-Fed Wind-Power Generation System" IEEE Transactions on Industry Applications. Vol. 30, Nº 3, May/June 1994.

[6] F. Blázquez: "Desarrollo de un nuevo generador asíncrono de doble bobinado en el estator para grandes aerogeneradores de velocidad variable", Tesis Doctoral, Universidad Politécnica de Madrid. April 2004

Electromagnetic Fields in Mechatronics, Electrical and Electronic Engineering
A. Krawczyk et al. (Eds.)
IOS Press, 2006

TRIGONOMETRIC APPROXIMATIONS FOR THE COMPUTATION OF THE RADIATION PATTERN OF A MOBILE ANTENNA IN PRESENCE OF HUMAN HEAD

Giuseppe Borzì [(1)]
Cinzia Giuffrida [(2)]

[(1)] Dipartimento di Ingegneria Civile
Università di Messina, Contrada di Dio, Messina I-98166 E-mail: gborzi@ieee.org
[(2)] Dipartimento di Ingegneria Elettrica Elettronica e dei Sistemi
Università di Catania, Viale Andrea Doria 6, Catania I-95125,
Italy. E-mail cgiuffrida@diees.unict.it

Abstract *– In this paper, the effect of the presence of human head in proximity of a mobile source is discussed, in terms of radiation pattern. An innovative numerical procedure, called Robin Boundary Condition*
Iteration (RBCI) [1], is used for the solution of electromagnetic radiation problems in open boundary domains. From spherical near field values, the radiation field is then decomposed in a finite series of spherical harmonics, by resorting to Wacker Method [2]. The decomposition coefficients are used to compute the transmitted power and to efficiently store the far field profile.

Introduction

The study of interaction of electromagnetic waves with objects is a complex task for computational electromagnetism, dealing with an unbounded domain with radiation boundary conditions imposed at infinity. To front this problem, several numerical methods have been devised [3], the most representative of which are the hybrid finite-element/boundary integral (FE-BI) methods [4], the absorbing boundary condition (ABC) methods [5] , and the artificial absorber (AA) methods [6].
In all these methods, a fictitious boundary is introduced to truncate the unbounded domain to a bounded one, where the finite-element method is applied. The methods differ in the way in which the unknown boundary condition on the fictitious boundary is treated.
In the FE-BI methods, the condition on the truncation boundary is generally a Neumann one and is specified by means of an integral equation on the boundary itself, which requires the radiation condition to be satisfied. This method does not introduce any approximation besides that due to the discretization, but the resulting linear algebraic system is no longer symmetric or sparse. Moreover, at high frequencies, there is the problem of interior resonance, which can produce an almost singular system.
In the ABC methods, the condition on the truncation boundary is an approximated local one derived from the asymptotic expansion of the radiated solution or numerically. From a physical point of view, ABC uses an homogeneous boundary condition, which tries to absorb the scattered waves, minimizing the reflection toward the scatterer. The locality of the condition preserves the sparsity of the FE matrix and limits the complexity of the building procedure; some kinds of ABC lose the symmetry of the FE matrix , whereas others maintain symmetry . The main drawbacks of ABC are the introduction of a truncation error in the solution, whose size is not known a priori, and the necessity to discretize a large

domain outside the scatterer because the absorbing boundary must be placed in the radiation zone to be effective. In the AA methods, the reflectionless truncation boundary is a metal-backed dielectric, whose geometrical and constitutive characteristics are chosen in such a way as to minimize the reflection coefficient in the case of plane wave incidence. Although good results can be achieved using anisotropic dielectrics [the so-called perfectly matched layer (PML)], AA suffers from many of the same drawbacks as ABC.
Inthis paper, the finite-element solution of the electromagnetic problem is performed by resorting to Robin Boundary Condition Iteration Method [1] in which the condition on the truncation boundary for the interior problem is an appropriate nonhomogeneous Robin (mixed) condition, that is specified by means of an integral equation—the integration being performed on a closed surface different from the truncation boundary.
The computed field is decomposed in a finite series of vector spherical harmonics using the technique described in [2] that is an adaptation of the Wacker's method for antenna measurements to numerically computed electromagnetic fields. The portrayal of the radiated field by means of the coefficients of the vector spherical wave decomposition allows a compact and accurate description of the radiation properties. In fact, from these coefficients it is possible to compute the radiation pattern of the antenna with arbitrary angular resolution and also to compute the radiated power. Also, they contain information about the phase of the scattered field. Their storage does not requires large amount of memory, because only those up to a limited order (generally up to order 6) are significant.

Formulation

The radiation problem is set up in terms of electric field, satisfying the vector Helmholtz equation, inside a bounded domain. On the fictitious boundary, enclosing the scatter, the termination condition is expressed, assuming a nonhomogeneous Robin boundary condition:

$$\hat{n}\times\nabla\times\vec{E}+jk_0\hat{n}\times(\hat{n}\times\vec{E})=\vec{U} \qquad (1)$$

where $\hat{n}$, is the outward normal to the truncating boundary, k_0 is the free-space wavenumber and $\vec{U}$ is an unknown vector that is initially guessed as:

$$\vec{U}_0=\vec{U_{inc}}=\hat{n}\times\nabla\times\vec{E}+jk_0\hat{n}\times(\hat{n}\times\vec{E_{inc}}). \qquad (2)$$

Then the closed differential problem is solved and using the dyadic Green's integral $\vec{U}$ is recomputed. The procedure is repeated until convergence takes place. It has been shown that this iterative procedure converges to the correct solution in less than ten steps if the fictitious boundary is placed at $\lambda/10$ or more from the scatterer.
From the computed near field on a spherical surface S_R of radius R enclosing the radiating system (antenna and human head), the coefficients of the vector spherical harmonics are obtained as:

$$\zeta_{slm}=\frac{1}{f_{sl}(kR)}\oint_{S_R}\vec{E}(\vec{r})\cdot\left[\vec{X}_{slm}(K,h)\right]dS \qquad (3)$$

where f_{sl} and $\vec{X}_{slm}$ describe the radial and angular dependency of the harmonic of order *slm*, respectively. The surface integral in (2) is computed by decomposing the field and the vector spherical harmonics as a superposition of elementary trigonometric functions by means of an FFT, and then by analytically computing the resulting integrand function, that is in turn composed by elementary trigonometric functions.

Numerical Results

In the following the influence between a mobile antenna and an human head is evaluated in terms of modification of the antenna radiation pattern.
For the model of the cellular telephone antenna, at the frequencies of 900 and 1800 MHz, an hertzian dipole antenna has been used.
For the head, two kinds of models have been taken into account ; a first one consisting of four meaningful tissues, muscle (ε_r=53.5, C=1.38 S/m), bone (ε_r=7.3, C=0.1 S/m), cerebro-spinal fluid (CSF) (ε_r=62.5, C=1.67 S/m) and brain (ε_r=43.4, C=0.57 S/m) [7] and a second homogeneous head model suitably characterized. It is worth noticing that the dielectric permittivity and conductivity of human tissues are not known with great accuracy because they depend on different subjective properties.
In a second set of simulations, where an homogeneous head model has been adopted, the dielectric permittivity and conductivity has been computed as a weighted mean of the above values, using as the weights the volumes of the tissues. The obtained values are very close to the electrical property of the muscle. By comparing the results with the two model, it can be determined if an homogeneous model gives accurate results, thus allowing easier and less time consuming analysis.
For each model the antenna was placed on the left side of the head, close to the ear and oriented along the direction of the $\hat{z}$ axis. The face, i.e. the frontal part of the head, points toward the positive $\hat{x}$ axis.

Fig.1 Radiation pattern of a dipole antenna in the presence of a human head at 900 (left) and 1800 (right) Mhz – Non uniform (4-tissues) model.

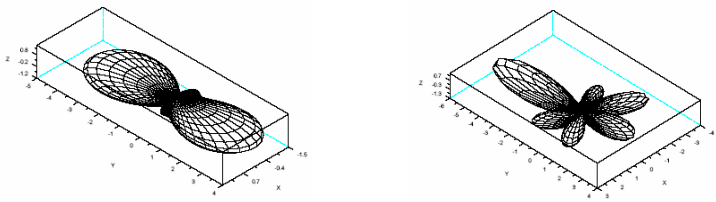

Fig.2 Radiation pattern of a dipole antenna in the presence of a human head at 900 (left) and 1800 (right) Mhz – Uniform (1-tissue) model.

The figures above show the three-dimensional radiation patterns at 900 MHz and 1800 MHz for the non-homogeneous and homogeneous models, with a 5 degrees resolution. It is clear that to estimate the effect of the human head an homogeneous model is satisfactory. In order to give a more detailed picture of the differences between the non-uniform model and uniform model, in Fig. 3 the radiation patterns on the horizontal plane are reported along with the (constant) radiation pattern of the dipole antenna.

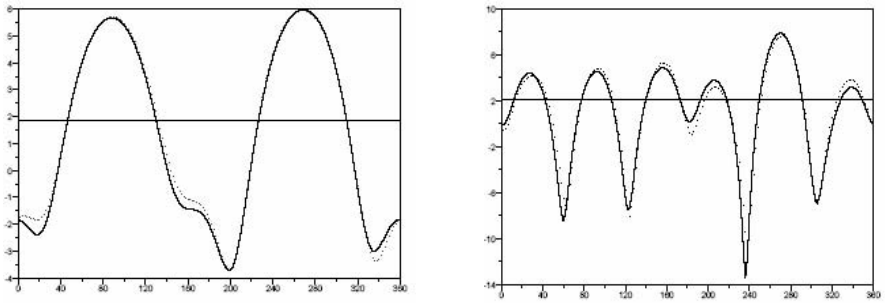

Fig.3 Radiation pattern of a dipole antenna on the horizontal plane in the presence of a human head at 900 (left) and 1800 (right) Mhz – full line: non-uniform (4-tissues) model; dotted line: .uniform (1-tissue) model; horizontal line: dipole antenna in free space

Conclusions

The effect of the human head on the radiation pattern of a cellular phone like antenna has been determined by means of the finite element technique known as the RBCI method and the spherical wave decomposition technique. The analysis shows that an homogeneos model gives almost the same results of a non-homogeneous one.
Since the former model is much simpler and less time consuming with respect to the latter, its use appears more appropriate in similar contexts, while the homogeneous model still remains necessary in other kinds of problems, for example for SAR analysis.

References

[1] S. Alfonzetti and G. Borzì, "Finite-Element Solution to Electromagnetic Scattering Problems by Means of the Robin Boundary Condition Iteration Method"- *IEEE Transaction On Antennas And Propagat.*, Vol. 50, No. 2, February 2002, pp.132-140.
[2] G.Borzì, "Trigonometric Approximations for the Computation of Radar Cross Sections"- *IEEE Transaction On Antennas And Propagat.*, Vol. 52, No. 6, June 2004, pp.1596-1602.
[3] J.M. Jin, "The Finite Element Method in Electromagnetics"- 2nd EditionJohn Wiley & Sons, Inc.
[4] J. M.. Jin and L. Volakis, " A finite element- boundary integral formulation for scattering by three-dimensional cavity- backed apertures- "*IEEE Trans. Antennas Propagat.*, Vol. 39, pp. 97-104, Jan. 1991
[5] R. Mittra, O. M. Ramahi, A. Khebir, R. Gordon, and A. Kouki, " A review of absorbing biundary conditions for two and three- dimensional electromagnetic scattering problems "- *IEEE Trans. Antennas Propagat.*,vol.39, pp.350-353, Marc.1991.
[6] J.P. Berenger, "A perfectly matched layer for the absorption of electromagnetic waves"- *J. Comp. Phis.*, Vol.114, pp.185-200, 1994.
[7] P. Bernardi, M. Cavagnaro, and S. Pisa, "Evaluation of the SAR Distribution in the Human Head for Cellular Phones Used in a Partially Closed Environment"-*IEEE Trans. Elec. Comp.*, Vol. 38, pp. 357-366, Aug. 1996.

Electromagnetic Fields in Mechatronics, Electrical and Electronic Engineering
A. Krawczyk et al. (Eds.)
IOS Press, 2006

COUPLED FE-MESHLESS METHODS FOR ELECTROMAGNETIC LOW-FREQUENCY PROBLEMS

V. Cutrupi, A. Formisano, R. Martone

Dip. Ingegneria dell'Informazione/Seconda Università di Napoli, Real Casa dell'Annunziata, Via Roma 29, Aversa(CE), I-81031, Italy, vincenzo.cutrupi@unina2.it

***Abstract:** A numerical approach to the resolution of a class of electromagnetic problems, based on the coupling between Finite Element and Element-Free Galerkin methods, is discussed. Such coupling reveals advantageous when part of the analysis domain is subject to deformations. To take the best advantages from both formulations, the analysis domain is subdivided in two regions, each treated with the most suitable method. Lagrangian multipliers are used to treat the interface between the two regions. A simple application is presented with the aim of highlighting features and performance of the approach.*

Introduction

The Finite Element Method (FEM) is a widely used method in different scientific areas, thanks to its effectiveness in terms of accuracy and efficiency [1]; further advantages of this method are the flexibility and the robustness, so that nowadays this is the reference tool to numerically solve a huge number of scientific and technical problems in different application areas. Unfortunately, as typical in all tessellation-based approaches, FEM requires a suitable meshing of the domain of interest, and the quality of the results strongly depends on the "quality" of the mesh. This reveals particularly critical in the treatment of problems involving geometric deformations of the analysis domain, such as mechanical or coupled problems [2], and shape optimization applications [3]. In these cases multiple re-meshing of the domain may reveal mandatory, impacting on the final computer burden.
A different class of numerical approaches, allowing to avoid this difficulty, was introduced some years ago in the field of structural mechanics, under the name of Meshless Methods (MM) [4]. The main benefit of this class of methods is that no reticulation of the domain is required, but just a distributed set of nodes is called for, to obtain the discrete model of the problem. MM present also a number of drawbacks, some of them being intrinsic to the method, e.g. the treatment of the boundary conditions, that requires a Lagrange Multipliers approach, while others show up when adopting MM to solve other class of problems than structural mechanic ones, e.g. the high degree of smoothness of the functions used to represent the unknown quantities, that in some cases may lead to unphysical results (just think of the normal component of electric field across a surface separating different materials).
The most diffuse MM are the Element-Free-Galerkin Method (EFGM) [4], the Reproducing Kernel Particle Method [5], and the Radial Bases Weighted Method [6].
Recently, the interest of the scientific community in the possibility of applying MM for electromagnetic problems has been steadily increasing [7], and limits and advantages of such methods are becoming evident. As discussed above, the natural framework for MM to show their capabilities is in the treatment of moving domain. However, in most cases, just a small part of the complete domain is supposed to change. Therefore, to pursue the best effectiveness, other methodologies could be applied in the "fixed" part (e.g. FEM, where they give their usual high performance), while MM could be used in the "changing" part of the domain (where the mesh-free approach does its best).
In literature, several techniques to couple different numerical methods have been presented, examples being FEM coupled with Boundary Element Method [1], or FEM coupled with Element Free Galerkin Method [8]. On the basis of such strategy, in this paper a suitable combination of FEM and MM, in particular EFGM, will be considered.

Of course, when coupling different methods, suitable congruency relationships must be enforced at the separation interfaces among the various subdomains, together with the boundary conditions at the external boundaries, assigned by the problem itself. To enforce the required conditions in coupling FEM and MM, it's possible to use two different approaches; the first one requires a transition region between the two subdomains, where a transition function is chosen to combine the trial functions of the two numerical methods [9]; the second technique, used in this work, is based on the use of the Lagrange multipliers, similarly to what done to apply the boundary conditions.
In order to show an example of FEM-MM coupling, the discussed formulation is applied to a classical electrostatic test problem in 1D simplified geometry.

Mathematical Model

As discussed in the previous section, MM were first proposed in the fluid dynamics area, and their original formulation inherited some of the characteristics peculiar to those applications. Nevertheless, the application of MM in different sectors, although requiring some "translational" effort, may reveal particularly fruitful in the treatment of moving geometries. In order to show the advantages of coupling MM and FEM for the treatment of electromagnetic problems, for the sake of exposition, the discussion will be focused on the classical electrostatic problem in linear isotropic media:

$$-\nabla\cdot\varepsilon(\mathbf{x})\nabla\varphi(\mathbf{x})=\rho(\mathbf{x}) \qquad \forall\mathbf{x}\in\Omega \tag{1}$$

where **x** is the coordinate vector of a point in the open domain Ω, eventually subject to deformations, φ is the scalar potential, ε is dielectric permeability, and ρ is the electric charge density. Suitable boundary conditions must of course be added on $\partial\Omega$, together with continuity conditions on possible interfaces among different media.
A generalization of (1) can be obtained by means of an integral formulation and of the application of Green's formulae:

$$\int_{\Omega}(\nabla\psi\cdot\varepsilon\nabla\varphi)\mathrm{d}\Omega-\int_{\partial\Omega}\psi\,\varepsilon\frac{\partial\varphi}{\partial\mathrm{n}}\mathrm{d}\Gamma=\int_{\Omega}\psi\,\rho\,\mathrm{d}\Omega \qquad \forall\,\psi\in\Psi \tag{2}$$

where Ψ is a test functions set with suitable properties. If assuming that only a part of Ω, say Ω^{MM}, is interested by deformations, it is profitable to numerically solve (1), or its integral counterpart (2), by adopting MM in the moving part of the domain, and FEM in the complementary, fixed part of Ω, say Ω^{FEM} (See Fig. 1).
In each subdomain, the unknown function $\varphi(\mathbf{x})$ will be approximated by using a different expansion, in terms of specific basis functions:

$$\varphi^{FEM}(\mathbf{x})=\sum_{i=1}^{\mathrm{N}^{FEM}}\Phi_i^{FEM}(\mathbf{x})\varphi_i^{FEM} \qquad \forall\mathbf{x}\in\Omega^{FEM}, \tag{3}$$

$$\varphi^{MM}(\mathbf{x})=\sum_{j=1}^{\mathrm{N}^{MM}}\Phi_j^{MM}(\mathbf{x})\varphi_j^{MM} \qquad \forall\mathbf{x}\in\Omega^{MM} \tag{4}$$

where N^{FEM} is the number of nodes in the FEM mesh used to discretize the subdomain Ω_{FEM}, while N^{MM} is the number of nodes in the subdomain Ω^{MM}; Φ_i^{FEM} and Φ_j^{MM} are the shape functions for the FEM and MM respectively, the latter ones obtained by means of the MLS (Moving Least Square) approximation method.

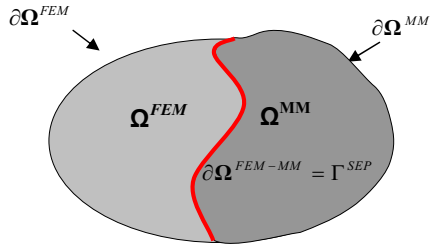

Fig. 1: Geometrical configuration of domain problem Ω

The way to obtain the basis functions Φ_j^{MM} used for the expansion (3) through Moving Least Squares algorithm is a standard technique for MM using Element Free Galerkin (EFG) approach. Details can be found in [10].
If substituting the approximations (3) and (4) into (2), and assuming $\Psi=\{\Phi_i^{FEM}, \Phi_j^{MM}\}$ $i=1,..,N^{FEM}$, $j=1,..,N^{MM}$, the original problem can be solved in weak form using the Galerkin approach. From the mathematical view point, this reduces to solving the following set of equations:

$$\sum_{i=1}^{N^{FEM}}\left[\int_\Omega \nabla\Phi_{i'}\cdot\varepsilon\varphi_i^{FEM}\nabla\Phi_i^{FEM}\mathrm{d}\Omega\right]-\int_\Omega\Phi_{i'}\rho\mathrm{d}\Omega=0 \qquad \forall\Phi_{i'}\in\Psi \quad in\ \Omega^{FEM} \tag{5a}$$

$$\sum_{j=1}^{N^{MM}}\left[\int_\Omega \nabla\Phi_{j'}\cdot\varepsilon\varphi_j^{MM}\nabla\Phi_j^{MM}\mathrm{d}\Omega\right]-\int_\Omega\Phi_{j'}\rho\mathrm{d}\Omega=0 \qquad \forall\Phi_{j'}\in\Psi \quad in\ \Omega^{MM} \tag{5b}$$

The cross terms in (5a) and (5b) are cancelled, either thanks to the compactness of the support of FEM basis functions, or by defining MM basis functions in such a way that they vanish outside of Ω^{MM}. Boundary conditions could be simply enforced on $\partial\Omega^{FEM}$ using standard techniques thanks to the delta-Kronecker property verified by Φ^{FEM}, while they must be enforced using the Lagrange Multipliers on $\partial\Omega^{MM}$. Anyway, in this work, boundary conditions have been enforced on both boundary sections using Lagrange multipliers to get similar discrete systems for both subdomains. The final discrete formulation will be composed of two systems, one for each domain:

$$\mathbf{K}^{FEM}\boldsymbol{\varphi}^{FEM}=\mathbf{f}^{FEM} \tag{6a}$$

$$\mathbf{K}^{MM}\boldsymbol{\varphi}^{MM}=\mathbf{f}^{MM} \tag{6b}$$

In order to get coherent solutions in the two subdomains Ω^{FEM} and Ω^{MM}, suitable continuity conditions must be enforced on the separation surface Γ^{SEP}. As told above, in this work the Lagrangian Multipliers technique is adopted to enforce $\varphi^{MM}=\varphi^{FEM}$ at each node on Γ^{SEP}, with the further hypothesis that for each FEM mesh node a MM node is available on the other side. This is not a necessary condition, but slightly simplifies the problem formulation. In this way a single algebraic equation system is obtained, representing the discrete formulation of problem (1), with related boundary conditions.

$$\begin{bmatrix} \mathbf{K}^{FEM} & \mathbf{0} & \mathbf{H}^{\partial\Omega^{FEM}} & \mathbf{0} & \underline{\underline{\mathbf{G}}}^{FEM} \\ \mathbf{0} & \mathbf{K}^{MM} & \mathbf{0} & \mathbf{H}^{\partial\Omega^{MM}} & \underline{\underline{\mathbf{G}}}^{MM} \\ \mathbf{H}^{\partial\Omega^{FEM}} & \mathbf{0} & \mathbf{0} & \mathbf{0} & \mathbf{0} \\ \mathbf{0} & \mathbf{H}^{\partial\Omega^{MM}} & \mathbf{0} & \mathbf{0} & \mathbf{0} \\ \left(\underline{\underline{\mathbf{G}}}^{FEM}\right)^T & \left(\underline{\underline{\mathbf{G}}}^{MM}\right)^T & \mathbf{0} & \mathbf{0} & \mathbf{0} \end{bmatrix} \begin{Bmatrix} \boldsymbol{\varphi}^{FEM} \\ \boldsymbol{\varphi}^{MM} \\ \boldsymbol{\lambda}^{\partial\Omega^{FEM}} \\ \boldsymbol{\lambda}^{\partial\Omega^{MM}} \\ \boldsymbol{\lambda}^{\Gamma^{sep}} \end{Bmatrix} = \begin{Bmatrix} \mathbf{f}^{FEM} \\ \mathbf{f}^{MM} \\ \mathbf{q}^{\partial\Omega^{FEM}} \\ \mathbf{q}^{\partial\Omega^{MM}} \\ \mathbf{0} \end{Bmatrix} \tag{7}$$

where **H**'s are the matrix used to enforce the boundary conditions, $\mathbf{G}^{FEM}$ and $\mathbf{G}^{MM}$ are the matrices used to enforce the interface conditions (one matrix for each subdomain), the terms **λ** represent the unknown Lagrange Multipliers used to enforce the various conditions, and finally $\mathbf{q}^{\partial\Omega FEM}$ and $\mathbf{q}^{\partial\Omega MM}$ are the vectors containing the boundary conditions.

Application Example

The exposed approach represents an efficient technique to exploit the best suited formulation in each subdomain, and it is quite generally applicable to a large number of problems in mathematical physics. As anticipated, the main interest in this work is to highlight the advantages of FEM-MM coupling for the resolution of shape-deforming electromagnetic problems, and in this perspective the exposition has been limited to electrostatic problems. In this section, a very simple example of application is discussed, keeping the complexity of geometry and material properties to a minimum, yet keeping the basic features in order to show the properties of the coupled approach.

The example considered here is a simple 1D problem [2], consisting in the determination of the electrostatic potential between two parallel conducting plates, connected to the terminals of a DC voltage source. The capacitor is filled with two different dielectric materials, separated by a mobile septum (see fig.2 for a schematic view of the device). The septum position x_a varies with time (but no force balance equation is considered here), so that a very simple moving geometry problem appears. This 1D test problem allows to compare the numerical result with analytical solution [2]. The mathematical model for the direct problem includes the Laplace equation for the electric potential $\varphi(x)$, valid in each subdomain, the usual continuity constraints at $x=x_a$, and finally a suitable set of boundary conditions; in this particular example, Dirichlet boundary conditions $\varphi(0)=0$ and $\varphi(h) = 100$ are assumed, where h = 1m . The left part of the capacitor is analyzed by means of FEM, $\Omega^{FEM}=[0,x_a)$, while the right part is analyzed by means of MM, $\Omega^{MM}=(x_a, h]$. The separation surface in this case reduces to just one point ($\Gamma^{SEP}=x_a$) Note that at the interface between the two media, if using expansion (4) with standard basis functions, MM would provide continuous electric field components.

It is therefore necessary to modify (4) in order to get the correct discontinuities on the electric field normal component. From the mathematical point of view, this amounts to introducing a "jump function" χ_a in (4) [4], able to take into account the "jump" in the derivatives of φ showing up at $x = x_a$:

$$\varphi^{MM}(\mathbf{x}) = \sum_{j=1}^{N^{MM}} \Phi_j^{MM}(\mathrm{x})\varphi_j^{MM} + b\chi(\mathrm{x}, x_a) \qquad \forall \mathrm{x} \in \Omega^{MM} \tag{8}$$

where b is the amplitude of the jump (in this case, the ratio between ε_1 and ε_2), x_a is the position of the discontinuity point, while **χ** is the jump function that generates the discontinuous derivative. Examples of useful jump functions are cubic splines, and ramp functions. In this work a triangular jump function has been used. The solution of the problem is performed with the coupled FEM-MM approach using $N^{FEM} = 7$ evenly spaced nodes in the domain Ω^{FEM} and $N^{MM} = 5$ nodes in the domain Ω^{MM}. The relative dielectric constants for the two media are $\varepsilon_1 = 1$, and $\varepsilon_2 = 2$ respectively.

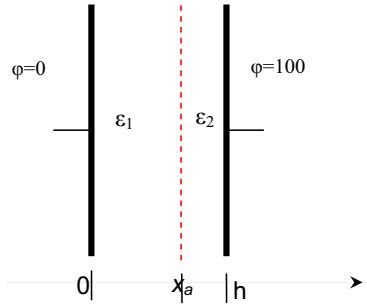

Fig. 2: Geometry of the 1-D test problem

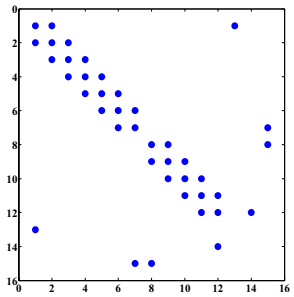

Fig. 3: Sparsity Pattern of the global system matrix

The sparsity pattern of the global system matrix is reported in Fig. 3 (a dot indicates a non-vanishing entry). From fig. 3, the structure of the system can be easily compared to (7). Note that the amplitude of the discontinuity in the electric field normal component is known in advance, so the contribution of jump function does not appear in the system matrix, but rather in the known term.

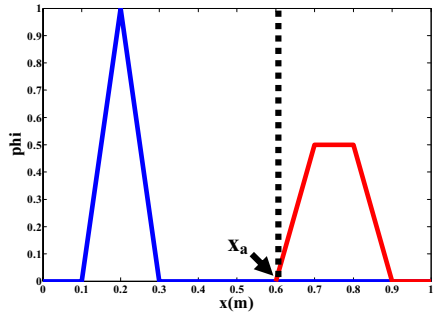

Fig. 4: Plot of the shape functions

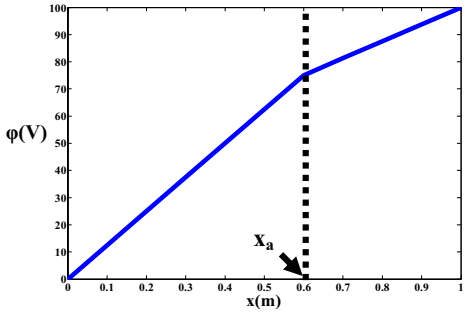

Fig. 5: Plot of the scalar potential φ

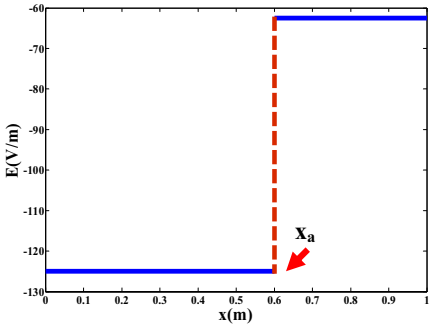

Fig. 6: Plot of the electric field E

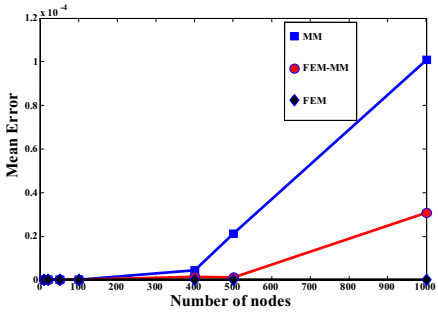

Fig. 7: Plot of the mean error, for FEM only solutions (♦), MM only solutions (■), and FEM-MM solutions (●).

In fig.4 it is reported an example of linear profile of the shape functions for both methods, in particular the classical *triangular shape function* for the Φ^{FEM} of the FEM subomain, and a *trapezoidal shape function* for the Φ^{MM} for the meshless subdomain.
In fig. 5 it is reported the profile of the scalar potential φ, while in fig.6 it is reproduced the profile of the electric field normal component E (other components vanish in this elementary geometry), showing the expected discontinuous behaviour. Finally, in fig.7 it is reported the profile of the mean error function defined as:

$$MEAN\ \ ERROR = \frac{1}{N}\sum_{i=1}^{N}\frac{\varphi_{exact}(i)-\varphi_{num}(i)}{\varphi_{exact}(i)} \tag{9}$$

for various number of nodes N, in order to assess the convergence properties. Three cases are considered: the solution obtained using FEM only, that one obtained using MM only, and that one obtained using coupled method. In the latter case, the ratio between N^{FEM} and N^{MM} is kept fixed. The mean error increases when increasing the number of nodes N due to the enforcement of boundary conditions by means of the Lagrange Multipliers Method. It's important to observe that the node to the interface is considered in each subdomain with the aim to assemble the two discrete systems.
The convergence of the combinations of the MM and the FEM is dominated by the FEM discretizations; in particular the convergence for the coupled method can even be slower than the convergence for the FEM in this particular case.

Conclusions

Meshless methods represent an interesting approach for the analysis of physical problems on moving domains, typical of structural mechanics applications, but show some drawbacks with respect to finite elements for the study of fixed domains. A possible approach, combining the advantages of both methods, has been discussed in the paper and demonstrated for the resolution of electromagnetic problems. The combined approach takes advantage from the most appropriate method by subdividing the domain into a fixed part, where finite elements are used to discretize the governing equations, and a moving part, where a meshless method can be applied. The approach has been discussed with reference to a simple electrostatic problem, but its range of applicability is much wider. A very simple example has been presented to highlight the properties of the system matrices obtained after coupling the two partial ones.
Possible applications of the combined approach are in the analysis of coupled mechanical-electromagnetic problems, and in shape optimization problems.

Acknowledgment

This work was supported by the Euratom Communities under the contract of Association between EURATOM/ENEA. The views and opinions expressed herein do not necessarily reflect those of the European Commission.

References

[1] A. Bossavit, Computational Electromagnetism, San Diego: Academic Press, 1998.

[2] A. Formisano, R. Martone, F. Villone, "Unified Approach to Electromagnetic shape-inverse and mechanically coupled problems via a Lagrangian technique", *IEEE Transaction on Magnetics*, Vol. 34, N. 2, 1998.

[3] N. H. Kim, K. K. Choi, M. E. Botkin, "Numerical Method for Shape Optimization Using Meshfree Method", *Structural Multidisc. Optim.*, Vol. 24, pp. 418-429, 2003.

[4] T. Belytschko, Y. Krongauz, D. Organ, M. Fleming and P. Krysl, "Meshless method : an overview and recent developments", *Comput.Meth.Appl.Mech.Engeng.*, Vol. 139, pp. 3-47, 1996.

[5] W. K. Liu, Y. Chen, S. Jun, Y. F. Zhang, "Reproducing Kernel Particle Methods", *International Journal for Numerical Methods in Engineering*, Vol. 20, pp. 1081-1106, 1995.

[6] J. R. Xiao, M. A. McCharty, "A local Heaviside weighted meshless method for two dimensional solids using radial basis functions", *Computational Mechanics*, Vol.31, pp. 301-315, 2003.

[7] Yong Zhang, K. R. Shao, D. X. Xie, J. D. Lavers, "Meshless Method Based on Orthogonal Basis for Computational Electromagnetics", *IEEE Transaction on Magnetics*, Vol. 41, N. 5, 2005.

[8] S. L. Ho, S. Yang, H. C. Wong, E. W. C. Lo, G. Ni, "Refinement Computations of Electromagnetic Fields using FE and Meshless Methods", *IEEE Trans. on Magnetics,* vol. 41, n° 5, pp. 1456-1459, 2005.

[9] D. Hegen, "Element-free Galerkin methods in a combination with finite element approaches", *Comput. Methods Appl. Mech. Engrg.*, 135, pp. 143-166, 1996.

[10] V. Cutrupi, A. Formisano, R. Martone, "Advantages of Meshless Methods in Shape Optimization", *Proceedings of the 15th Conference on the Computation of Electromagnetic Fields* (CMAG 2005), pp. III-116 Shenyang, China, 2005.

Electromagnetic Fields in Mechatronics, Electrical and Electronic Engineering
A. Krawczyk et al. (Eds.)
IOS Press, 2006

PERFORMANCE EVALUATION OF AN AXIAL FLUX PM MOTOR BASED ON FINITE ELEMENT ANALYSIS

Goga CVETKOVSKI **Lidija PETKOVSKA**

Sts. Cyril & Methodius University, Faculty of Electrical Engineering, P.O. Box 574, 1000 Skopje, Macedonia
Tel. + 389 2 3099 143, Fax: + 389 2 3064 262, e-mail: gogacvet@etf.ukim.edu.mk

***Abstract** – In this paper a performance analysis of an axial flux PM motor based on finite element analysis (FEA) is presented. The quasi-3D method which is adopted for this analysis is consisted of a 2D FEM calculation of the magnetic field in the three dimensional radial domain of the disc motor. The magnetic field distribution is calculated at different armature current and different rotor displacements for all five segments of the motor. Using the results from the FEA the electromagnetic and electromechanical characteristics are going to be presented and a performance evaluation of the motor will be carried out.*

Introduction

The determination of the motor parameters for the performance evaluation is a procedure that needs to be done as accurately as possible especially if the motor is in a developing stage. Therefore it is necessary to calculate the motor parameters with methods that will give the most adequate results. The Finite Element Method (FEM) is such a method that gives very accurate results when compared to the measured ones.

In order to have sufficient data for the calculation of the motor parameters there is a need of computing the magnetic vector potential in the whole three-dimensional domain of the motor. Due to the complex form of the analysed motor a quasi-3D magnetic field calculation is performed. The quasi-3D method consists of a 2D FEM calculation of the magnetic field in the three dimensional radial domain of the disc motor. The 2D FEM analysis is very suitable for this type of geometry and has a lot of advantages over the 3D calculation, such as lower memory storage and reduced time computation. The results of the numerical computer calculations of the magnetic vector potential in the post-processing stage are used to determine the parameters of the motor. The accurately calculated values of the motor parameters can be used for further motor analysis or as an input data for static and dynamic motor analysis.

PM Disc Motor Description

The modelled motor is a brushless three phase synchronous permanent magnet disc motor, with rated torque 54 Nm and speed 750 rpm@50 Hz, fed by a pulse width modulated (PWM) inverter and rechargeable batteries or fuel cell. The PMDM is a double sided axial field motor with two laminated stators having 36 slots and a centred rotor with 8 skewed neodymium-iron-boron permanent magnets with B_r=1.17 T and H_c=-883 kA/m. The real side view test rig of the prototype permanent magnet disc motor is given in Fig. 1.

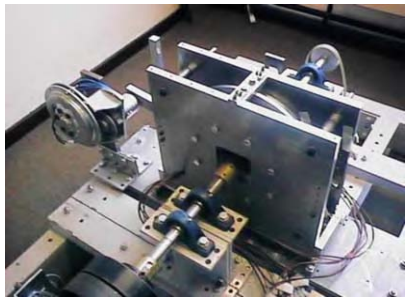

Fig. 1. Permanent magnet disc motor test rig

PM Disc Motor FEM Modelling

In order to be able to get the necessary data for the PM disc motor, a calculation of the magnetic field has to be performed. The 2D analysis is very suitable for this type of geometry and has a lot of advantages over the 3D calculation, such as lower memory storage and reduced time computation. The quasi-3D method [1] which is adopted for this analysis consists of a 2D FEM calculation of the magnetic field in a three dimensional radial domain of the axial field motor. For this purpose, a notional radial cut through the two stators and one rotor of the disc motor is performed and then opened out into linear form, as shown in Fig.2. By using this linear quasi three-dimensional model of the disc motor, which is divided into five segments, it is possible to model the skewing of the magnets and also to simulate the vertical displacement and rotation of the rotor. Due to the symmetry of the machine the calculation of the motor is performed only for one quarter of the permanent magnet disc motor or for one pair of permanent magnets.

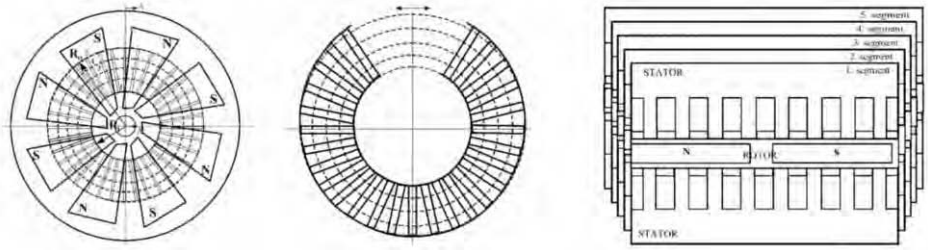

a) motor b) radial cut c) segments

Fig.2. Radial division of the motor into 5 segments

Finite Element Analysis

After the proper modelling of the PMDM and the adequate mesh size refinement, especially in the air gap a magnetic field calculation is performed for each segment separately, for different current loads and different rotor displacements. As an example the magnetic field distribution of the motor at no load and one rotor position for the 1st, 3rd and 5th segment, as specific ones, is presented in Fig 3a, Fig.3b and Fig. 3c, respectively. On the other hand the magnetic field distribution of the motor at rated current load at the same rotor position, for the 1st, 3rd and 5th segment, is presented in Fig 4a, Fig.4b and Fig. 4c, respectively.

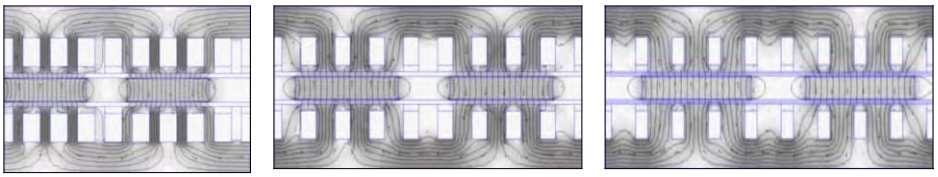

a) 1st segment b) 3rd segment c) 5th segment

Fig. 3. Magnetic field distribution at no load

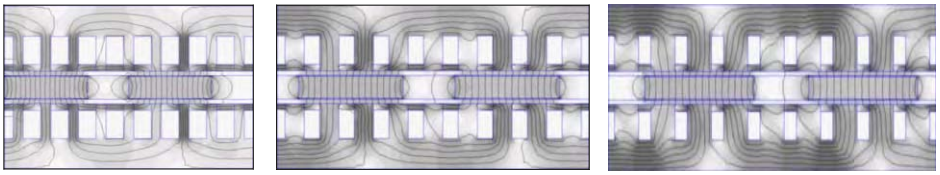

a) 1st segment b) 3rd segment c) 5th segment

Fig. 4. Magnetic field distribution at rated current load

PM Disc Motor Parameter Determination

The calculated data from the FEM magnetic field analysis in the postprocessor mode could also be used to estimate certain magnetic and electric parameters [2] necessary for further investigation and performance evaluation of the permanent magnet disc motor. Due to the complexity of the analysed motor model, such as specific geometry and proper modelling for the FEM calculation, certain modifications of the standard equations for parameters calculation using FEM data are made.

Air Gap Flux Density Calculation

An interesting and very important parameter that can be used for further motor analysis is the average value of the air gap flux density and its distribution under different current load conditions. The air gap flux density is calculated by using the results of the FEM magnetic field calculation, applying them in equation (1) and solving it numerically by the same programme:

$$\mathbf{B} = \text{curl } \mathbf{A} \tag{1}$$

The distribution of the air gap flux density is calculated and presented for no load and for rated load for the 1st, 3rd and 5th segment in Fig. 5 and Fig. 6, respectively.

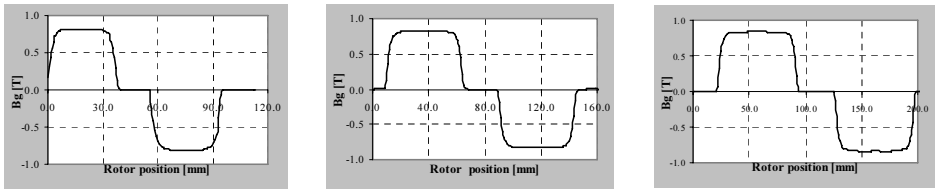

a) 1st segment b) 3rd segment c) 5th segment

Fig. 5. Air gap flux density distribution at no load

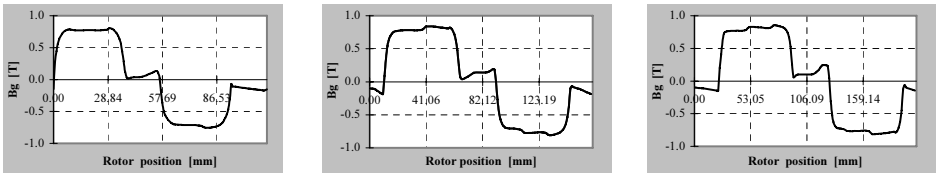

a) 1st segment b) 3rd segment c) 5th segment

Fig. 6. Air gap flux density distribution at rated current load

Air Gap Flux Linkage

The numerical calculation of fluxes is based on the field theory, applied on a bounded and closed systems. If the calculations are performed per pair of excited poles, it is:

$$\Phi_g = \int_{\Sigma} \mathrm{rot}\mathbf{A} \cdot d\mathrm{S} = \oint_{C} \mathbf{A} \cdot \mathrm{d}r = \int_{\Sigma} \mathbf{B} \cdot \mathrm{d}S \tag{2}$$

In this paper the air gap flux linkage for different rotor displacements at various current loads is calculated, and its distribution in relation to the current load and rotor displacement is presented in Fig. 7.

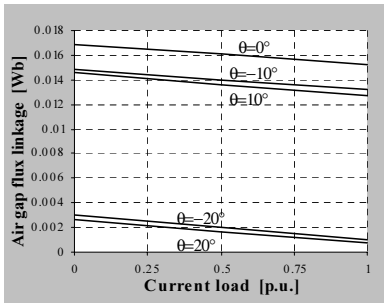

Fig. 7. Air gap flux linkage for different current loads at various rotor displacements

Inductance and Reactance Calculation

The direct and quadrate axis synchronous inductance and reactance are very important in steady state performance of a synchronous machine. Based on the FEM data the value of the direct axis inductance and reactance using the modified equation, due to the specific motor geometry, is calculated by the following equations:

$$L_d = \frac{N \cdot (R_o - R_i) \cdot \Delta A_d \cdot p}{I \cdot m / 2} \qquad X_d = \omega \cdot L_d \tag{3}$$

where: R_i-inside radius of the stator, R_o-outside radius of the stator and W-number of turns per phase.

The quadrate axis synchronous inductance could be calculated in the same manner, as it was the direct axis inductance. Based on the FEM data the value of the direct axis inductance and reactance using the modified equation, due to the specific motor geometry, is calculated by the following equations:

$$L_q = \frac{N \cdot (R_o - R_i) \cdot \Delta A_q \cdot p}{I \cdot m / 2} \qquad X_q = \omega \cdot L_q \tag{4}$$

The values of the direct and quadrate axis inductance and reactance calculated by using FEM data and the measured ones are presented in Table 1.

TABLE 1. Direct and Quadrate Axis Inductance and Reactance

Parameter	FEM calculated	Measured
L_d [mH]	16.33	16.14
X_d [Ω]	5.13	5.07
L_q [mH]	14.26	14.59
X_q [Ω]	4.48	4.58

Electromagnetic Torque Calculation

The torque represents significant information about the motor that needs to be known as accurately as possible, often as a function of the rotor position, as well. There are several methods for calculating the torque using Finite Element Method (FEM) data, but for this research the *Maxwell stress method* has been adopted [3]. This method has been selected, since with it the torque can be calculated very easy by using the data from the quasi three-dimensional calculation of the magnetic vector potential. The necessary data for the determination of the torque by the Maxwell stress method is provided by calculating the magnetic vector potential for different current loads and for different rotor displacements. The *Maxwell stress method (MSM)* is based on the Faraday-Maxwell's theory on electromagnetic forces interacting on a closed surface, in this case that is the air-gap between the rotor and the two stators, where the net force is produced on the rotor. The force produced on the rotor for each segment and different rotor displacement, in the postprocessor stage, is calculated by the Maxwell stress method (MSM) described with the following equation:

$$dF = \frac{1}{2} \cdot \left[H(B \cdot n) + B(H \cdot n) - (H \cdot B)n \right] \tag{5}$$

The calculated force for each segment and different rotor displacements is than implemented in (6) in order to calculate the total electromagnetic torque produced by the motor for different rotor displacements.

$$T_{emMSM} = \sum_{x=1}^{5} \left(F_x \cdot R_x \cdot p \cdot N_{st} \cdot (R_o - R_i) \right) \tag{6}$$

The calculated values of the total electromagnetic torque in relation to the different load angles for the analysed PM disc motor are presented in Fig. 8. Based on the assumption that the characteristic of the electromagnetic torque in relation to the load angle is sinusoidaly distributed, the load angle can be calculated as:

$$\sin \delta = T_{em} / T_{em\,\max} \tag{7}$$

where: T_{em} - rated value of the electromagnetic torque and $T_{em\ max}$ - maximum value of the electromagnetic torque. The calculated value of the load using FEM data and the measured one at rated electromagnetic torque T_{em}=60.515 Nm are presented in Table 2.

TABLE 2. Load angle

Parameter	FEM calculated	Measured
δ [°]	21.38	22.22

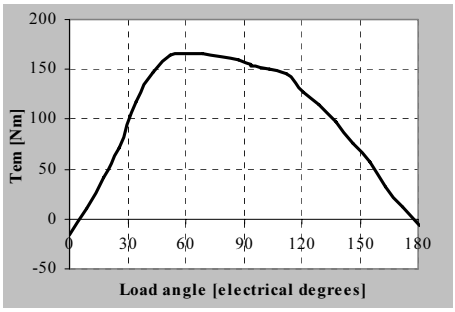

Figure 8. Electromagnetic torque for SMC strip slot closure topology

Performance Evaluation of PM Disc Motor

The Finite Element Analysis enables to evaluate the magnetic field properties in the whole investigated domain of the motor. From the air gap flux density distribution presented in Fig. 6 the influence of the armature reaction on the main PM excitation field is quite evident in comparison with the distribution presented in Fig. 5. Using a particular FEM calculation the reactance along the d, q axes are determined. By using them, the phasor diagram of the PMDM of the motor at rated load conditions could be constructed and valuable data could be determined from it about the performance of the motor. From the presented data it was justified that the presented methodology for calculation performance characteristics of the PMDM is quite accurate and correct. Consequently, it can be recommended for similar calculations of any type of synchronous motor.

Conclusion

A parameter and performance evaluation procedure for PMDM using FEM data is presented and performed. Due to the specific geometry of the motor a proper modelling of the motor and an adequate mesh size refinement, especially in the air gap, has been performed and presented. The proposed methodology by implementing different methods for calculation of steady-state characteristics under different operating conditions, enabled the authors to carry out a deepened performance analysis of the PM disc motor, and an evaluation of its behaviour at various loads.

References

[1] G. Cvetkovski, L. Petkovska, M. Cundev, S. Gair, Quasi 3D FEM in Function of an Optimisation Analysis of a PM Disk Motor, Proceedings of the 14th IEEE International Conference on Electrical Machines-ICEM '2000, Helsinki, Finland, Vol. 4/4, p.p. 1871-1875, 2000.

[2] G. Cvetkovski, L. Petkovska, M. Cundev, PM Disc Motor Parameter Estimation Using FEM Data, Proc. of the 6th Int. Symposium on Electric and Magnetic Fields-EMF2003, Aachen, Germany, pp. 191-194, 2003.

[3] G. Cvetkovski, L. Petkovska, M. Cundev, Torque Evaluation of Direct Drive PM Disc Motor for Electric Vehicle, Proc. of the 7th Int. Conf. ELECTRIMACS2002 on CD, Montreal, Quebec, Canada, pp. 1-6, 2002.

Electromagnetic Fields in Mechatronics, Electrical and Electronic Engineering
A. Krawczyk et al. (Eds.)
IOS Press, 2006

A NESTED EVOLUTIONARY ALGORITHM TO SIMULTANEOUSLY OPTIMIZE THE COMPRESSION RATIOS IN DESIGNING RECTANGULAR GROUNDING GRIDS

Giuseppe Delvecchio, Francesca Lerario, Ferrante Neri, Diego Sylos Labini

Dipartimento di Elettrotecnica ed Elettronica, Politecnico di Bari, Italy,
g.delvecchio@area-tecnica.uniba.it francesca.lerario@email.it neri@deemail.poliba.it d.sylos@deemail.poliba.it

***Abstract** – A nested evolutionary algorithm to automatically design rectangular unequally spaced grounding grids is proposed. The arrangement of the conductors of the grid along the two sides of the rectangular grid is done according to an exponential regularity by means of two adequate values called compression ratios. The algorithm proposed optimizes both these values. It consists of an internal genetic algorithm to find the maximum touch voltage generated by a grounding grid and an external genetic algorithm to find the two optimized values of compression ratio. The external genetic algorithm studies the dependence of the maximum touch voltage generated by each grounding grid on both the compression ratios by means of a two-variable objective function. An exhaustive comparison with the other methods given in literature is made and the results prove that the algorithm proposed competes, in terms of safety and calculation times, with the other methods.*

Introduction

The problem of the grounding grid design has been intensively discussed over the years and several approaches have been proposed. In the latest years, in particular, the unequally spaced structures have been turned out to be more efficient, in terms of low values of touch voltages, than the equally spaced ones [1]. Although some automatic methods and formulas have been proposed in [1-8], the problem of how to arrange the conductors has not yet been solved by general formulas and rules. An arrangement according to an exponential regularity has been proposed in [9-14] and the problem of the grounding grid design has been formalized as the choice of two adequate parameters defined as "conductor compression ratios" (or simply compression ratios). This problem has been solved, in literature, according to considerations based on experience (i.e. by empirical formulas) [10], or assuming that a grounding grid can be represented by only one compression ratio obtained by means of graphical considerations (see [9], [14]) or simple iterative methods [13]. In this paper the Authors prove that the choice of the two optimal compression ratios in the design of rectangular grounding grids is not trivial and that an empirical approach is not, in general, reliable. The Authors, therefore, propose here a Nested Evolutionary Algorithm (NEA) to simultaneously determine both the compression ratios which guarantee the minimum value of touch voltage.

Correspondence Between A Rectangular Grounding Grid And Two Compression Ratios

Let us consider a meshed rectangular grounding grid having N_x conductors running perpendicular to a side (x axis) and N_y conductors running perpendicular to the other side (y axis). Let us indicate with L_x and L_y the length of the sides arranged along the x and y axes, respectively, and with N_x and N_y the number of conductors perpendicular to the x and y axes, respectively.
Let us briefly refer to the conductors arranged according to any of the two directions, and so let us indicate with N_c and L_c the number of conductors and their length, respectively; as a consequence, the

arrangement of these conductors according to the exponential regularity from the centre of the grounding grid is given by [9-10]:

$$D_n = D_{max}\ C^n \tag{1}$$

where: D_n is the distance of the n^{th} conductor from the $(n\text{-}1)^{th}$ conductor, n=1, 2, …, N_c/2 if N_c is even; n=1, 2, …, (N_c-1)/2 if N_c is odd; C is the compression ratio related to the axis under examination. It defines the arrangement of the conductors along this axis and varies in the interval]0, 1[.

As can be seen from (1), the distances D_n are the terms of a geometrical progression having C as the ratio between two generic contiguous terms and $D_1 = D_{max} \cdot C$ as a first term; the distance of the first conductor from the centreline of the grid is equal to D_1 if N_c is odd, and to $D_1/2$ if N_c is even.

As to D_{max}, it can be obtained in the following way. We can impose:

if the number of conductors N_c is even: $$\sum_{n=1}^{N_c/2} D_n = D_{\max} C \frac{1-C^{N_c/2}}{1-C} = \frac{L_c}{2} + C\frac{D_{\max}}{2} \tag{2}$$

or if the number of conductors N_c is odd: $$\sum_{n=1}^{(N_c-1)/2} D_n = D_{\max} C \frac{1-C^{(N_c-1)/2}}{1-C} = \frac{L_c}{2} \tag{3}$$

From (2) and (3) it is possible to get D_{max} for N_c even and N_c odd, respectively:

$$D_{\max} = \frac{L_c(1-C)}{C(1+C-2C^{N_c/2})} \qquad D_{\max} = \frac{L_c(1-C)}{2C(1-C^{(N_c-1)/2})} \tag{4}$$

From what said above, it is clear that to each value of C corresponds an arrangement of conductors for each axis, and the problem concerning the design of rectangular grounding grids consists therefore in determining two compression ratios C_x and C_y along the two axes x and y, respectively. So, once the number of conductors of the rectangular grid perpendicular to the x and y axes, their length, cross-section and burying depth are fixed, to each couple of compression ratios corresponds a rectangular grid that we will indicate with $G(C_x, C_y)$ where G stands for grid [9-10].

Formulation of the Min-Max Problem

The problem concerning the design of grounding grids consists in finding the couple (C_x, C_y) of compression ratios which ensures minimal values of touch voltages. More formally the problem consists of the following:

$$\text{Minimize } U_{Tmax}(C_x, C_y) \quad \text{in }]0, 1[\times]0, 1[\tag{5}$$

where U_{Tmax} (C_x, C_y) is the maximum value of touch voltage generated by the rectangular grid $G(C_x, C_y)$. In other words, for a fixed number of conductors, we have to find, among all the possible configurations of grounding grids $G(C_x, C_y)$, the one which guarantees the best performances in terms of safety.

This Min-Max problem has been solved by our Nested Evolutionary Algorithm (NEA). Briefly, NEA consists of two nested genetic algorithms: the Internal Genetic Algorithm (IGA), and the External Genetic Algorithm (EGA).

Description of the Algorithm

For each grid $G(C_x, C_y)$ the touch voltages in the soil surface points are calculated by the Maxwell's subareas method [15] and, consequently, an Internal Genetic Algorithm (IGA) finds the maximum touch voltage $U_{Tmax}(C_x, C_y)$. Fig. 1 shows an example of trend of touch voltages obtained through a computationally expensive calculation of the $U_T(P)$ made on a big number of the soil surface points by means of the Maxwell's subarea method.

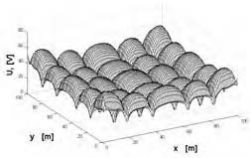

Fig.1 Trend of the touch voltages generated by an unequally spaced grounding grid $G(C_x, C_y)$

The Internal Genetic Algorithm is a steady-state algorithm [16], which works only on a population of N^{IGA} points P of the soil surface. These points are initially sampled pseudo-randomly. Each point $P(x, y)$ is an individual having x and y as chromosomes. Since the touch voltage is a continuous function in each point P of the soil surface, a real encoding has been chosen. In consideration of the rectangular shape of the grounding grid and therefore of the rectangular shape of the decision space the arithmetic crossover technique has been chosen [17]. The naïve elitist selection [16] has been performed and the probability of random mutation [17] has been set on 0.1. The algorithm is stopped when at least one of the two following conditions occurs: 1) the difference between the maximum touch voltage and the average value among all the touch voltages $U_{T\,k}$ (P) calculated in the generic k^{th} iteration is smaller than a pre-arranged value of accuracy ε^{IGA}; 2) the number of iterations $N_{iter}{}^{IGA}$ reaches a pre-arranged value $N_{iter\text{-}max}{}^{IGA}$.

The External Genetic Algorithm is a steady-state algorithm [16], which uses the values of the maximum touch voltage $U_{Tmax}(C_x, C_y)$ generated by the various grounding grids $G(C_x, C_y)$ and calculated by the Internal Genetic Algorithm. $U_{Tmax}(C_x, C_y)$ is considered as a fitness function to find the two optimal compression ratios $C_x{}^{opt}$ and $C_y{}^{opt}$, that is, to find the configuration $G(C_x{}^{opt}, C_y{}^{opt})$ of the grid which generates the minimum value of the maximum touch voltage.

Each individual of the population is a grounding grid $G(C_x, C_y)$ and the population is made up of N^{EGA} grids. Each grid (individual) has a genotype composed by two compression ratios that are two real numbers, each belonging to the interval]0, 1[. The arithmetic crossover technique and the random mutation with a probability set on 0.2 have been chosen and the tournament selection of the individuals has been performed [17]. The stop criterion follows the same logic as that chosen for the IGA.

Fig.2 shows a graphical representation of the algorithm proposed.

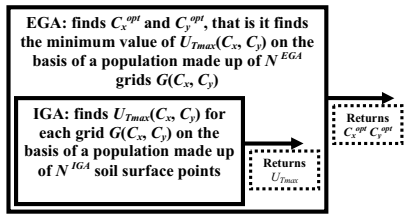

Fig.2 Graphical representation of the NEA

Numerical Results

The Nested Evolutionary Algorithm (NEA) has been implemented in three different cases and it has been compared with some practical problems found in literature. Table I and II show the algorithmic parameters for both the internal (IGA) and the external (EGA) Genetic Algorithm.

Table I IGA algorithmic parameters to find $U_{T\,max}$

Population Size	N^{IGA}	200
Mutation Probability	$p_{mut}{}^{IGA}$	0.1
Crossover Probability	$p_{cr}{}^{IGA}$	1
Maximum No. of Iterations	$N_{iter\text{-}max}{}^{IGA}$	250
Accuracy	ε^{IGA}	0.01

Table II EGA algorithmic parameters to find $C_x{}^{opt}$ and $C_y{}^{opt}$

Population Size	N^{EGA}	50
Mutation Probability	$p_{mut}{}^{EGA}$	0.2
Crossover Probability	$p_{cr}{}^{EGA}$	0.8
Maximum No. of Iterations	$N_{iter\text{-}max}{}^{EGA}$	250
Accuracy	ε^{EGA}	0.0001

First case: comparison between NEA and a method based on empirical formulas

A criterion for designing unequally spaced grounding grids has been proposed in [1]. Table III gives the parameters of the problem. The empirical method proposed in [1] determines the proper number of conductors to be used (in this case $N_x = 21$ and $N_y = 14$) and arranges these conductors by means of empirical formulas.

For the same problem, using the same conductors $N_x = 21$ and $N_y = 14$, our NEA has been applied and the results have been compared with the ones obtained by the method proposed in [1] (see Table IV). The arrangement of the conductors is expressed in terms of distance in meters between each couple of subsequent conductors (for the method proposed in [1]) and in terms of compression ratios (for our NEA). As the results show, the solution given by NEA outperformed the one obtained by the method proposed in [1] since it generates a lower value of U_{Tmax} using the same amount of conductors.

Table III Parameters of the first case

Fault Current	I_F	5280 A
Resistivity	ρ	500 Ωm
Area under study	A_s	107 m x 72 m
Cross-Section of the conductors	S_c	85 mm^2

Table IV Comparison between NEA and a method based on empirical formulas

Method	Arrangement of the conductors	U_{Tmax} [V]
[1]	[1.1, 2.4, 3.4, 4.4, 5.3, 6.1, 6.7, 7.4, 7.9,8.4] [1.6, 3.5, 5.1, 6.3, 7.2, 8.0, 8.6]	966.6517
NEA	$C_x^{opt} = 0.8750$ $C_y^{opt} = 0.8875$	943.0464

A Discussion about Grounding Grid Designing Methods

The problem concerning the design of grounding grids has been discussed over the latest years and several methods have been therefore proposed in literature. These methods can be distinguished in two groups (see Table V):

1) methods based on the optimization of an objective function without geometrical assumptions [5-8];
2) methods based on the compression ratios [9-14].

The main difference between these two approaches is that the decision space is discrete for the methods of group 1) while it is continuous for the methods based on the compression ratios. Obviously this difference is extremely significant as concerns the implementation of the optimization methods. Group 2) takes into account an infinite set of configurations of grounding grids but it assumes that the conductors are arranged according to an exponential regularity and symmetrically with respect to the centrelines. These assumptions allow the description of a grounding grid by only two real parameters; consequently they reduce the computational complexity but they obviously lose the generality of the search. The methods of group 1) do not make, in general, any assumption about the arrangement of the conductors but they discretize the decision space considering a big number of possible configurations of grounding grids.

Table V shows an analysis of both the features of several methods belonging to group 1) and those of the methods based on the compression ratios. In this Table the assumptions and the cardinalities of the decision spaces have been highlighted.

Table V Comparison between methods based on the compression ratio and other methods

Method	Objective	Assumptions	Decision Space
[6]	Cost	Symmetry	$2^{\frac{Lx}{2}+\frac{Ly}{2}+2}$
[7]	Touch voltage	None	$(Lx+1)^{Nx}(Ly+1)^{Ny}$
[8]	Touch voltage	None	$\frac{(Nx+Lx)!}{Nx!Lx!}\cdot\frac{(Ny+Ly)!}{Ny!Ly!}$
Compression Ratios	Touch voltage	Exponential regularity and Symmetry	Continuous

Second case: comparison between NEA and other designing optimization methods

A numerical comparison among the methods proposed in Table V has been carried out for the set of parameters shown in Table VI. The numerical results of this comparison are shown in Table VII.

Table VI Parameters of the second case

Fault Current	I_F	5000 A
Resistivity	ρ	100 Ωm
Area under study	A_s	80 m × 60 m
Cross section	S_c	69 mm^2
Burying depth	h_d	0.5 m
Conductors perpendicular to the x axis	N_x	7
Conductors perpendicular to the y axis	N_y	5

Table VII Comparison between NEA and other designing optimization methods

Method	Arrangement of the Conductors	U_{Tmax} [V]	Decision Space	Calculation Time
[6]	[0,6,22,40,58,74,80][0,10,30,50,60]	818.2894	4.7224x10^{21}	6h 41min
[7]	[0,7,22,40,58,73,80][0,10,30,50,60]	801.5457	1.9322x10^{22}	8h 12min
[8]	[0,7,22,40,58,73,80][0,10,30,50,60]	801.5457	4.8265x10^{16}	3h 28min
NEA	C_x^{opt} = 0.5833 C_y^{opt}= 0.5333	810.1916	Continuous]0, 1[×]0, 1[	36 min

The arrangement of the conductors is expressed, for [6], [7] and [8], in terms of distances of each conductor from the reference axes, the origin of these reference axes being in the lower left corner of the grounding grid. As concerns NEA, the arrangement of the conductors is obviously expressed in terms of compression ratios.

As to the values of U_{Tmax}, the results in Table VII show that NEA leads to slightly better results than [6]; moreover, as shown in Table VII, NEA leads to slightly worse results than [7] [8] since our method considers the exponential regularity while [7] and [8] don't make this assumption. On the other hand, the NEA calculation times needed for the design are much lower than those obtained from the other methods.

Third case: comparison between NEA and other methods based on compression ratios

NEA has been compared also with other methods which make use of the compression ratios to design the grounding grids. In [10] the optimal compression ratio is obtained by an algorithm based on empirical formulas. In [9] it has been assumed that, for a rectangular grounding grid, the optimization can be performed on only one value of compression ratio by assuming $C_x = C_y$ and so an analytical study of the dependence of the maximum touch voltage on this compression ratio has been carried out. The parameters related to this third case are given in Table VIII. The optimization results are given in Table IX.

Table VIII Parameters of the third case

Fault Current	I_F	1000 A
Resistivity	ρ	100 Ωm
Area under study	A_s	100 m x 60 m
Cross section	S_c	85 mm^2
Burying depth	h_d	0.5 m
Conductors perpendicular to the x axis	N_x	11
Conductors perpendicular to the y axis	N_y	7

Table IX Comparison between NEA and other designing methods based on the compression ratio

Method	Optimal Compression Ratios (C_x^{opt}, C_y^{opt})	U_{Tmax}	
		[V]	%GPR
[9]	(0.6, 0.6)	105.4768	17.60
[10]	(0.72, 0.74)	110.8938	18.36
NEA	(0.6938, 0.6625)	91.5869	15.28

The last two columns of Table IX give the values of U_{Tmax} for each couple of compression ratios; these values are expressed in absolute value as well as in percentage of GPR, where GPR stands for Ground Potential Rise [18]. The results show that the design carried out by NEA as minimization of the two-variable function $U_{Tmax}(C_x, C_y)$, leads to significantly lower values of touch voltages. Consequently, using the same amount of conductors, the method proposed leads to a significantly better design in terms of electrical safety.

Conclusions

In this paper a Nested Evolutionary Algorithm to design rectangular grounding grids has been proposed. This method, unlike the methods given in literature, studies the dependence of the maximum touch voltage on both the compression ratios, simultaneously. A two-variable objective function has been formalized and its minimization has been performed in a proper decision space. NEA offers a numerical approach for the problems concerning the design of grounding grids without making use of any empirical formula but analyzing, by means of two nested genetic algorithms, the behaviour of the touch voltages on the soil surface. The numerical results show that NEA leads to better results than other methods based on compression ratio or on empirical formulas. As expected, the methods which do not make geometrical assumptions, such as the exponential regularity, can lead to slightly better results than NEA, since they in practice consider more possible configurations of grounding grids. On the contrary, these methods are not competitive at all with NEA in terms of calculation times.

Finally, it is also important to notice that the application of NEA, for the three cases shown in Tables IV, VII and IX, leads to three couples of compression ratios which are quite different among them. This result has to be considered as a further confirmation that the values of the optimal compression ratios could vary significantly with each problem under study and therefore they cannot be efficiently established a priori, according to consideration based on experience.

References

[1] L. Huang, X. Chen,. H. Yan, Study of unequally Spaced Grounding Grids, IEEE Transactions on Power Delivery ,Vol. 10, No 2, pp 716-722, 1995.
[2] B. Phitakwong, N. Kraisnachinda, S. Bayjongijt, C. Choompo-Inwai, M. Kando, New Techniques the Computer-Aided Design for Substation Grounding, Proceedings of the IEEE Power Engineering Society Winter Meeting, Vol. 3, pp 2011-2015.
[3] S. S. El-Dessouky, M. A. El Aziz, A Khamis, An Accurate Design of Substation Grounding System Aid Expert System Methodology, Conference Record of the IEEE International Symposium on Electrical Insulation, Vol. 2, pp 411-414, 1998.
[4] D. J. Pieterse, J. A. Deacon, Substation Grounding Grid Design with the aid of a Computer Program, 12th International Conference on Electricity Distribution, Vol. 2, pp 2.24.1-2.24-4, 1993.
[5] M. C. Costa, M.L.P., Filho, Y. Marechal, J. L. Coulomb, J. R. Cardoso, Optimization of Grounding Grids by Response Surface and genetic Algorithms, IEEE Transactions on Magnetics, Vol. 39 No 3, pp 1301-1304, 2003.
[6] A. F. Otero, J. Cidras, C. Garrido, Genetic Algorithm Based Method for Grounding Grids Design, Proceedings of the IEEE International Conference on Evolutionary Computation, World Congress of Computational Intelligence, pp 120-123, 1998.
[7] F. Neri, A New Evolutionary Method for Designing Grounding grids by Touch Voltage Control, Proceedings of the IEEE International Symposium on Industrial Electronics, Vol. 2, pp 1501-1505, 2004.
[8] F. Neri, A. Kononova, G. Delvecchio, M. Sylos Labini, A. Uglanov, A Hierarchical Evolutionary Algorithm with Noisy Fitness in Structural Optimization Problems, in F. Rothlauf et al. eds., Applications of Evolutionary Computation, Lecture Notes in Computer Science, Vol. 3449, pp 610-616, Springer, 2005.
[9] L. Hyong-Soo, K. Jung-Hoon, F. P. Dawalibi, J. Ma, Efficient ground grids design in layered soils, IEEE Transactions on Power Delivery, Vol.13, No 3, pp 745-751, 1998.
[10] W. Sun, J. He, Y. Gao, R. Zeng, W. Wu, Q. Su, Optimal Design Analysis of Grounding Grids for Substations built in non-uniform soil, Proceedings of Powercon International Conference on Power System Technology, Vol.3, pp 1455-1460, 2000.
[11] Y. Gao, R. Zeng, X. Liang, J. He, W. Sun, Q. Su, Safety Analysis of Grounding Grid for Substations with Different Structure, Proceedings of the IEEE International Conference on Power System Technology, Vol. 3, pp 1487-1492, 2000.
[12] J. He, R. Zeng, Y. Gao, Y. Tu, W. Sun, J. Zou, Z. Guan, Seasonal Influences on Safety of Substation Grounding System, IEEE Transactions on Power Delivery, Vol. 18, No 3, pp 788-795, 2003.
[13] M. Sylos Labini, M. Castellitti, G. Delvecchio, F. Neri, A New Method for Designing Meshed Square Grounding Grids by Genetic Algorithms and Optimal Compression Ratio, Proceedings of VIII-th International Workshop on Optimisation and Inverse Problems in Electrical Engineering, pp 57-58, 2004.
[14] J. He, Y. Gao, R. Zeng, W. Sun, J. Zou, Z. Guan, Optimal Design of Grounding Systems Considering the Influence of Seasonal Frozen Soil Layer, IEEE Transactions on Power Delivery, Vol. 20 No 1, pp 107-115, 2005.
[15] M. Sylos Labini, A. Covitti, G. Delvecchio, C. Marzano, A Study for Optimizing the Number of Subareas in the Maxwell's Method, IEEE Transactions on Magnetics, Vol. 39, No 3, pp 1159-1162, 2003.
[16] L. J. Eshelman, The CHC adaptative search algorithm: How to have safe search when engaging in non traditional genetic recombination, in FOGA-1 pp 265-283, 1991.
[17] Z. Michalewicz, Genetic Algorithms + Data Structures = Evolution Programs, 3rd edition, Springer-Verlag, 1996.
[18] ANSI/IEEE Standard 367-1996– Recommended practice for determining the electric power station ground potential and induced voltage from a power fault.

Electromagnetic Fields in Mechatronics, Electrical and Electronic Engineering
A. Krawczyk et al. (Eds.)
IOS Press, 2006

COUPLINGS OF ELECTROMAGNETIC FIELD FORMULATIONS IN FINITE ELEMENT ANALYSIS OF TRANSVERSE FLUX INDUCTION HEATING SYSTEMS

V. Fireteanu, T. Tudorache

POLITEHNICA University of Bucharest, EPM_NM Laboratory, 313 Splaiul Independenței, Bucharest, Romania,
e-mail: VirgiliuFIRETEANU@electro.masuri.pub.ro, tudorach@amotion.pub.ro

***Abstract** – Based on the comparison of the numerical results obtained by using different couplings of the electromagnetic field formulations in different conducting or non-conducting, magnetic or non-magnetic regions, this paper establishes which is the most convenient model of electromagnetic field computation in transverse flux induction heating analysis.*

Introduction

One of the most effective technologies in continuous induction heating of metallic sheets is the Transverse Flux Induction Heating (TFIH) that can be distinguished by a high electric efficiency at relatively low frequency operation [1]. A TFIH system, Fig.1, consists mainly of one or several pairs of coils, magnetic cores and a moving metallic sheet passing through the middle of the inductor air gap. The magnetic field produced by the coils, normally oriented in the symmetry plane of the air gap, determines eddy currents and consequently, the sheet heating. Such a system represents the physical support for the study of different couplings of electromagnetic field formulations in this paper.

The coils of a transverse flux inductor, of stranded conductor type, where the current - source of the electromagnetic field is known, are non-magnetic and non-conducting regions (1) and the magnetic cores are no-source, magnetic and non-conducting regions (2).

The sheet to be heated is a no-source, conducting, magnetic or non-magnetic region (3).

The air surrounding the inductor and the sheet, which has the properties of vacuum is a no-source, non-conducting and non-magnetic region (4).

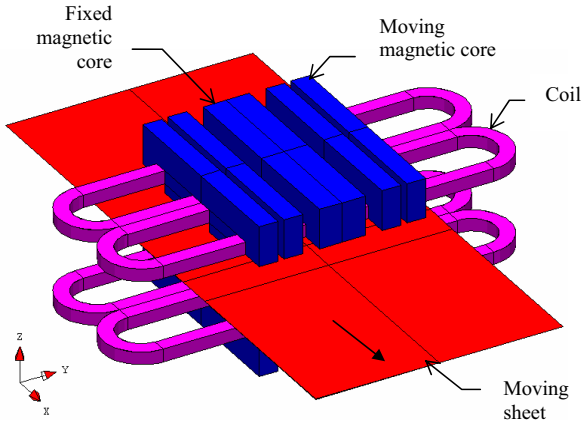

Fig. 1. Geometry of a TFIH system

Couplings of Electromagnetic Field Formulations

The field models are couplings between different formulations of the electromagnetic field in regions with different physical properties [2-3]. The following three models are studied:

(a) **T**Φ-Φ-Φ_{red} model, which is the coupling of **T**Φ formulation, in electric vector potential **T** and magnetic scalar potential Φ in the eddy current and no-source region (3), of Φ formulation in the magnetic, non-conducting and no-source region (2) and of Φ_{red} formulation, in reduced magnetic scalar potential in the non-conducting, non-magnetic and source region (1) and in the non-conducting, non-magnetic and no-source region (4).

- The **T**Φ formulation is characterized by the following equations expressed in potentials:

$$\text{rot}\,[(1/\sigma)\,\text{rot}\mathbf{T}\,] - \text{grad}\,[(1/\sigma_p)\,\text{div}\mathbf{T}] + j\omega\mu(\mathbf{T} - \text{grad}\,\Phi) = 0 \quad (1)$$

$$\text{div}\,[\mu(\mathbf{T} - \text{grad}\,\Phi)] = 0 \quad , \quad (2)$$

where -grad $[(1/\sigma_p)\cdot \text{div}\mathbf{T}]$ is a penalty term by which the Coulomb's gauge div**T** = 0 is imposed, μ, σ are the magnetic permeability and the electric conductivity of the region and ω is the field pulsation.

- The Φ formulation is characterized by the equation:

$$\text{div}\,[\mu(-\text{grad}\,\Phi)] = 0 \quad (3)$$

- In case of Φ_{red} formulation the magnetic field source, $\mathbf{H_0}$, generated by the coils regions, where the current density J_{ex} is given, is computed using the Biot – Savart formula. The equation associated with this formulation is:

$$\text{div}\,[\mu_0(-\text{grad}\,\Phi_{red} + \mathbf{H_0})] = 0, \quad (4)$$

where μ_0 represents the magnetic permeability of the vacuum.

(b) **A**V-**A-A** model, which is the coupling of **A**V formulation, in magnetic vector potential **A** and electric scalar potential V in the eddy current and no-source region (3) and of **A** formulation in the other three regions (1), (2) and (4).

- The **A**V formulation is characterized by the following equations expressed in potentials:

$$\text{rot}\,[(1/\mu)\,\text{rot}\mathbf{A}] - \text{grad}\,[(1/\mu_p)\,\text{div}\mathbf{A}] + \sigma(j\omega\mathbf{A} + \text{grad}V) = 0 \quad (5)$$

$$\text{div}\,[\sigma(j\omega\mathbf{A} + \text{grad}V)] = 0 \quad , \quad (6)$$

where - grad $[(1/\sigma_p)\,\text{div}\,\mathbf{A}]$ represents the penalty term by which the Coulomb's gauge div**A** = 0 is imposed.

- The **A** formulation is characterized by the equation:

$$\text{rot}\,[(1/\mu)\,\text{rot}\mathbf{A}] - \text{grad}\,[(1/\mu_p)\,\text{div}\mathbf{A}] = \mathbf{J_{ex}} \quad (7)$$

(c) **A**V-Φ-Φ_{red} model, which is the coupling of **A**V formulation, in magnetic vector potential **A** and electric scalar potential V in the eddy current and no-source region (3), of Φ formulation, in the magnetic, non-conducting and no-source region (2) and of Φ_{red} formulation in reduced magnetic scalar potential, in the non-conducting, non-magnetic and source region (1) and in the non-conducting, non-magnetic and no-source region (4). The equations in potentials of this model are

(5), (6), (3) and (4).

The boundary conditions, Fig. 2, associated to the **T**Φ-Φ-Φ_{red} model, are as follows:

- $\partial\Phi/\partial n = 0$, $\partial\Phi_{red}/\partial n = 0$ and $\mathbf{T}\cdot\mathbf{n} = 0$, on boundaries where $\mathbf{B}\cdot\mathbf{n} = 0$,
- Φ = constant, Φ_{red} = constant and $\mathbf{T} \times \mathbf{n} = 0$, on boundaries where $\mathbf{H} \times \mathbf{n} = 0$,

The boundary conditions associated to the **A**V-**A**-**A** model, are the following:

- $\mathbf{A} \times \mathbf{n} = 0$ and V = constant, on boundaries where $\mathbf{B}\cdot\mathbf{n} = 0$,
- $\mathbf{A}\cdot\mathbf{n} = 0$ and $\partial V/\partial n = 0$, on boundaries where $\mathbf{H} \times \mathbf{n} = 0$.

The boundary at infinity of the electromagnetic field open boundary problems is modeled in the FLUX3D software by a particular region named infinite box, which represent an inverse transformation of the real unbounded region in parallelepiped layers.

Numerical Results with the Three Field Models

The numerical applications consider the following data:

- inductor with two pairs of coils, pole pitch length 465 mm, magnetic core height 235 mm,
- non-magnetic steel sheet, thickness 1 mm, electrical conductivity σ =1e-6 S/m,
- linear magnetic cores with relative magnetic permeability $\mu_r = 1000$,
- current flowing through each coil 14,000 A,
- frequency supply 1000 Hz.

Two values of the sheet width *2b* are considered, 1000 mm, case (1), and 1500 mm, case (2). For each case the number of finite elements and the number of nodes is the same for all three models of electromagnetic field computation.

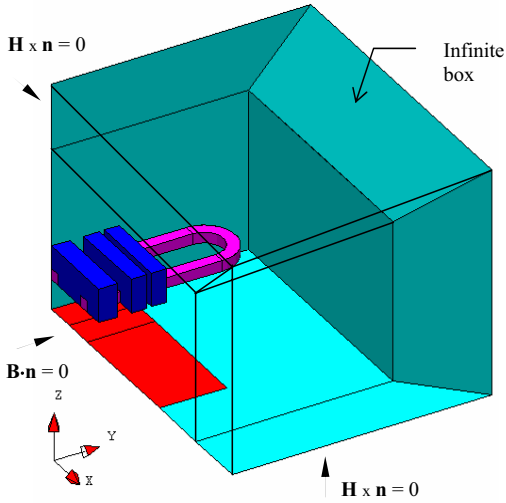

Fig. 2. Computation domain and boundary conditions

The main interest of electromagnetic field computation in TFIH systems is represented by the induced current and power densities in the sheet. The color shaded plots in Fig. 3 emphasize a strong non-uniformity of the induced power density distribution that entails a certain transversal non-uniformity of sheet heating.

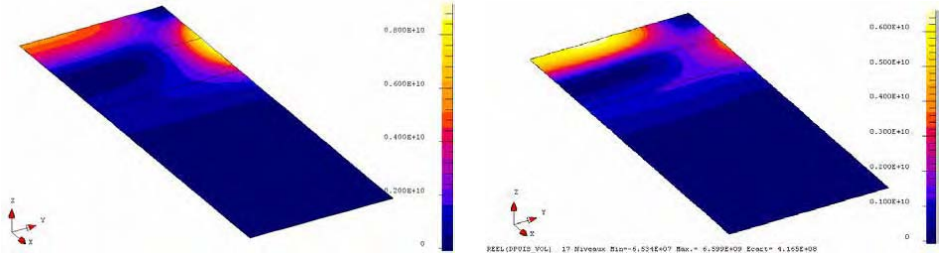

a) b)

Fig. 3. Chart of the induced power density
a) case (1); b) case (2)

The transversal non-uniformity of the sheet heating is very well reflected by the transversal profile *P(y/b)* of the induced power density integrated along the sheet and on the sheet thickness [4]. The transversal profiles in Fig. 4 show that the three electromagnetic field models offer very close results, both in case (1) and in case (2). The relative differences with respect to the average between the results obtained using the three electromagnetic field models, Fig. 5, increase toward the sheet edges and are larger in case (1) than in case (2). The numerical results of **A**V-**A**-**A** model are under the average of the results of the three models and the results of **T**Φ-Φ-Φ_{red} and **A**V-Φ-Φ_{red} models are over the average. Consequently, the differences between the results related to the transversal profile of induced power density obtained with the three models of electromagnetic field computation being so small, the choice of one or of the other must be established by other results or characteristics of the numerical simulations that are further discussed.

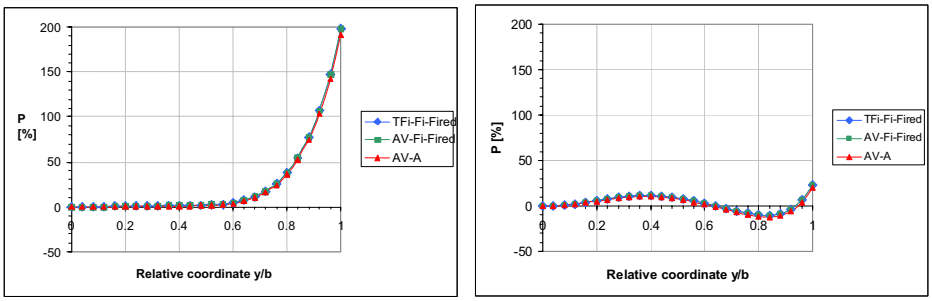

a) b)

Fig. 4. Transversal profile of induced power density
a) case (1); b) case(2)

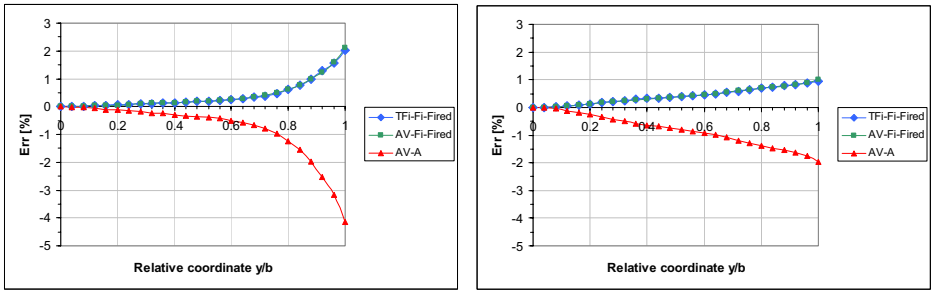

a) b)

Fig. 5. Relative differences of induced power density profiles with respect to the average of three profiles
a) case (1); b) case (2)

Based on the results in Tables 1 and 2, related to the power P_2 induced in the sheet, power losses P_m in the magnetic cores, maximum value J_{2max} of the induced current density, minimum and maximum of the transversal profile function *P(y/b)*, memory requirements and computation time, the following remarks can be formulated:

- Globally, the differences between the results of the three models are small;
- The results obtained using the **T**Φ-Φ-Φ_{red} model and **A**V-Φ-Φ_{red} model are practically identical;
- Concerning the quantities P_2, P_m, J_{2max}, Max_profile, Min_profile, the results of **A**V-**A**-**A** model are slightly smaller than the results obtained using the other two models;

- The **T**Φ-Φ-Φ_{red} model is the most economical as number of equations and CPU time; compared to the **A**V-**A**-**A** model this model needs 5.78 less CPU time in case (1) and 6.74 less CPU time in case (2). In comparison with the **A**V-Φ-Φ_{red} model, the **T**Φ-Φ-Φ_{red} model needs 3.7 less CPU time in case (1) and 5.58 less CPU time in case (2);
- The **A**V-**A** model is the most expensive regarding the number of equations and CPU time; indeed, the use of magnetic vector potential **A** in the non-conductive regions entails six unknowns per node compared to two unknowns per node in case of Φ or Φ_{red} formulations.

Table 1. Results, memory requirements and computation time on a Pentium IV, 3GHz - case (1)

Elmg. field model	P_2 [kW]	P_m [kW]	J_{2max} [A/mm^2]	Max_profile [%]	Min_profile [%]	No. eq.	CPU time [s]
TΦ-Φ-Φ_{red}	311.00	12.25	136.0	197.78	0	64535	116
AV-**A**-**A**	297.68	11.82	132.7	191.63	- 0.01	179137	671
AV-Φ-Φ_{red}	311.00	12.25	135.9	197.90	0	75216	429

Table 2. Results, memory requirements and computation time on a Pentium IV, 3GHz - case (2)

Elmg. field model	P_2 [kW]	P_m [kW]	J_{2max} [A/mm^2]	Max_profile [%]	Min_profile [%]	No. eq.	CPU time [s]
TΦ-Φ-Φ_{red}	432.87	10.37	115.5	23.07	- 10.36	80496	169
AV-**A**-**A**	413.35	10.06	112.7	20.17	- 12.55	212817	1139
AV-Φ-Φ_{red}	432.87	10.37	115.2	23.14	- 10.36	97825	943

Consequently, it is very clear that the **T**Φ-Φ-Φ_{red} model is the most convenient between the three models.

Influence of the Computation Domain Meshing on Results

The optimal design of electromagnetic devices based on finite element analysis needs typically to solve an important number of applications piloted by an optimization algorithm in order to find the best solution [4]. The minimization of computation time in such researches supposes field models able to fulfil two contradictory criteria: accurate results and short CPU time. The trade-off between these criteria imposes to use the most economical field model (a) and finite element discretization (b) of the computation domain. This section explains the meaning of (b) attribute by using the **T**Φ-Φ-Φ_{red} model of TFIH analysis, case (1).

The results in Table 3 emphasize the influence on numerical results of mesh refining in the sheet region. The quantities J_{2max} and B_{2max} are the maximum values of induced current density and magnetic flux density in this region.

From *Mesh1* application to *Mesh5* in Table 3, the mesh of the sheet region is more and more refined and consequently the number of equations and the computation time are more and more important. The smallest mesh point applied to the points defining the sheet region decreases from a size equal to the *skin depth* of the sheet material for *Mesh1* application, to five times smaller than the *skin depth* for *Mesh5* application.

Table 3. Influence of mesh size on the numerical results

Application	P_2 [kW]	J_{2max} [A/mm^2]	B_{max} [T]	Max_profile [%]	Min_profile [%]	No. eq.	CPU time [s]
Mesh1	432.95	115.9	0.1489	20.55	-10.43	39245	76
Mesh2	432.70	116.5	0.1533	22.75	-10.41	51007	100
Mesh3	432.87	115.5	0.1462	23.07	-10.37	80496	169
Mesh4	432.59	115.2	0.1439	23.00	-10.42	230395	544
Mesh5	432.64	115.2	0.1480	23.03	-10.40	340364	841

Since the comparisons between the numerical results of the five applications in the first five columns of Table 3 are not so relevant for the influence of mesh refinement, the sum of square differences between the successive transversal profiles *P(y/b)* was considered. Thus, the step 1 of mesh refinement in Fig. 6 represents the comparison between the *Mesh2* and *Mesh1* applications, the step 2 the comparison between the *Mesh3* and *Mesh2* applications etc. The graph shows that the step 1 of mesh refinement has a very strong impact on the result accuracy in comparison with the following steps. Taking into account this finding on the one hand, and the increase of the computation time and memory requirements on the other hand, we can state that the best mesh configuration is that of *Mesh2* application.

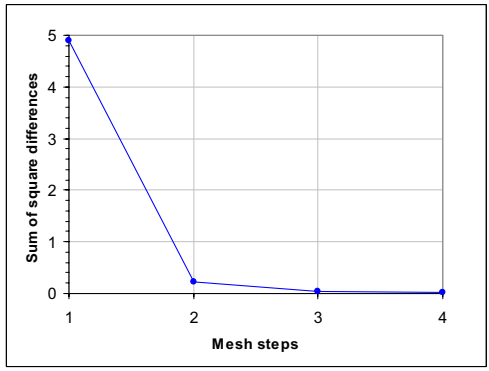

Fig. 6. Sum of square differences between successive transversal profiles for different mesh refinement steps

Conclusions

Extrapolating the result of TFIH finite element analysis with three models of electromagnetic field we can conclude that the **T**Φ-Φ-Φ_{red} model is the best for eddy current magneto-harmonic problems. There are no relevant differences between the global or local numerical results obtained with **T**Φ-Φ-Φ_{red}, **A**V-**A**-**A** or **A**V-Φ-Φ_{red} models, but the computation time and memory requirements are drastically increased when the last two models are used.

The study of the influence of the mesh refinement on the numerical results shows that a good numerical model needs the research of the optimal mesh that corresponds to the compromise between the accuracy of the simulation results on the one hand and the computation time and memory requirements on the other hand.

References

[1] A. Ruhnke, A. Muhlbauer, A. Nikanoriv, V. Demidovitch: "Numerical and Experimental Investigation of Transverse-Flux Induction Heating", Proc. of IHS'98 Seminar, Padova, pp. 109-115, 1998.

[2] V. Fireteanu, B. Paya, J. Nuns, T. Tudorache: "Numerical Evaluation of Eddy Currents in Thin conducting Regions modeled as Surface Regions", Proc. of the Evian TEAM Workshop and Applications Forum, Vol. I, pp. 12-13, 2001.

[3] V. Fireteanu, T. Tudorache: "Formulations magnétodynamiques FLUX3D, appliquées à la modélisation d'un inducteur a flux transverse", Revue FLUX-MAGAZIN, Grenoble, 1998.

[4] V. Fireteanu, E. Vladu, M. Popa, B. Paya, Y. Neau, T. Tudorache: "Optimization of Transverse Flux Inductors with Respect to Transversal Profile of Sheet Heating and Inductor Electric Efficiency", VIII-th International Workshop on Optimization and Inverse Problems in Electromagnetism, Grenoble, 2004.

Electromagnetic Fields in Mechatronics, Electrical and Electronic Engineering
A. Krawczyk et al. (Eds.)
IOS Press, 2006

TIME DOMAIN SENSITIVITY ANALYSIS OF ELECTROMAGNETIC QUANTITIES UTILISING FEM FOR THE IDENTIFICATION OF MATERIAL CONDUCTIVITY DISTRIBUTIONS

Konstanty M. Gawrylczyk, Mateusz Kugler

Szczecin University of Technology, Chair of Theoretical Electrotechnics and Computer Science
Sikorskiego 37, PL-70-310 Szczecin, Poland
kmg@ps.pl, mkugler@ps.pl

Abstract *– This paper presents effective methods for computing electromagnetic field sensitivity in the time domain versus conductivity perturbations in finite elements. The resultant gradient information may be used for solving inverse problems such as the identification of material conductivity distributions. The algorithms described are based on known methods from established circuit theory - incremental circuit and adjoint circuit, these have been expanded to apply in electromagnetic field theory.*

Introduction

The usual purpose of sensitivity evaluation methods is the design of electromagnetic devices, however it may also be used for the determination of materials parameters through inverse iteration. Electrical parameters may be tested using the eddy-current method. In this work, we consider the application of impulses generated by non-harmonic excitations. Material testing with this technique depends on the excitation of an alternating field around the sample, the positioning of the sample and the processing applied to the output signal from the measurement sensors (coils). The data gathered is employed as the basis for obtaining the inverse problem solution. By establishing the material parameters distribution, a numerical simulation can then be back-fitted to the measurement results. To carry out this inverse job, a large number of electromagnetic field distribution measurements are necessary. This problem suits the impulse method very well. The excitation coil may be driven with relatively long impulses; this makes it possible to identify surface shape as well as being able to penetrate into the conducting material. The inverse job is solved by iteration so, for faster convergence, the gradient information derived from sensitivity analysis is necessary.

In this work only two-dimensional cases in linear, isotropic media were considered. Two effective methods for sensitivity analysis of a magnetic vector potential in the time domain are described.

Finite Element Method in the Simulation of Pulsed Eddy Current Testing

In describing the magnetic field with the vector magnetic potential $\boldsymbol{A}$, the transient field of eddy-currents may be discretized using the generalized time stepping scheme *theta* described in [1,2]. Dividing the time range $(0, T)$ into n time steps of length $\Delta t = T / n$, the two level scheme can be shown as follows:

$$\left[\Theta[\boldsymbol{K}]+\frac{1}{\Delta t}[\boldsymbol{M}]\right]\{\boldsymbol{A}_i\}=\left\{\left(\frac{1}{\Delta t}[\boldsymbol{M}]-(1-\Theta)[\boldsymbol{K}]\right)\{\boldsymbol{A}_{i-1}\}+(1-\Theta)\{\boldsymbol{R}_{i-1}\}+\Theta\{\boldsymbol{R}_i\}\right\}, \tag{1}$$

where [K] and [M] are the stiffness and mass matrices of finite elements containing the material parameters and geometric properties of the simulated sample, $\{\boldsymbol{A}_i\}$ is the vector of the desired node values and $\{\boldsymbol{R}_i\}$ is the discretized excitation for time steps $i \cdot \Delta t$, with $i = 1,...,n$, and the parameter Θ determines the time stepping scheme [1]. The numerical formulation used for the calculation of the induced voltage (emf) in the measurement coil by means of magnetic vector potential $\boldsymbol{A}$ given in [3] has been adopted.

Sensitivity Analysis in the Time Domain through the Finite Element Method

The sensor sensitivity versus conductivity $\gamma^{(e)}$ in single finite element e is defined for the time step $i \cdot \Delta t$ as:

$$\bar{\boldsymbol{S}}_{i,(e)}=\frac{1}{\Omega_c}\frac{\partial}{\partial\gamma^{(e)}}\int_{\Omega_c}\boldsymbol{A}_i\,\mathrm{d}\Omega\,, \tag{2}$$

where: Ω_c is the cross-section of the measurement coil. For the purposes of the sensitivity calculation in the time domain, two equivalent techniques might be applied, i.e. the incremental system method and Tellegen's method of adjoint system.

The Incremental System Method

This method calls for the differentation of equation (1) versus the electric conductivity in element e $\gamma^{(e)}$ [4]. The stiffness matrix [$\boldsymbol{K}$] and the excitation vector $\{\boldsymbol{R}_i\}$ do not depend on conductivity, so for the nodal sensitivities,

$$\frac{\partial}{\partial\gamma^{(e)}}\left\{\boldsymbol{S}_{i,(e)}\right\}=\frac{\partial}{\partial\gamma^{(e)}}\{\boldsymbol{A}_i\}\,, \tag{3}$$

the following sensitivity equation may be obtained:

$$\left[\Theta[\boldsymbol{K}]+\frac{1}{\Delta t}[\boldsymbol{M}]\right]\left\{\boldsymbol{S}_{i,(e)}\right\}=\left(\frac{1}{\Delta t}[\boldsymbol{M}]-(1-\Theta)[\boldsymbol{K}]\right)\left\{\boldsymbol{S}_{i-1,(e)}\right\}+\frac{1}{\Delta t}\frac{\partial[\boldsymbol{M}]}{\partial\gamma^{(e)}}\left(\{\boldsymbol{A}_{i-1}\}-\{\boldsymbol{A}_i\}\right). \tag{4}$$

This equation is solved step-by-step with zero initial condition $\{\boldsymbol{S}_{0,(e)}\} = \{\boldsymbol{0}\}$. In this manner the vectors of nodal sensitivities for all time steps are obtained. The sensor sensitivity is derived by integrating nodal values over the cross-section of the coil.

The Adjoint System Method

This method is based on the Tellegen theorem which is well known in circuit theory [5,6]. The application of this method in field theory for the frequency domain was shown in [7]. It has been extended by the authors of the this paper for application in the time domain [8,9].

Neglecting displacement currents, the following sensitivity equation was obtained:

$$\int_0^T \iint_{\Omega} \left(\Delta \boldsymbol{H} \mu^+ \frac{\partial \boldsymbol{H}^+}{\partial t} - \boldsymbol{H}^+ \mu \frac{\partial}{\partial t} \Delta \boldsymbol{H} + \boldsymbol{E}^+ \gamma \Delta \boldsymbol{E} - \Delta \boldsymbol{E} \gamma^+ \boldsymbol{E}^+ + \boldsymbol{E}^+ \Delta \gamma \boldsymbol{E} - \Delta \boldsymbol{E} \boldsymbol{J}_S^+ + \Delta \boldsymbol{H} \boldsymbol{L}_S^+ \right) \mathrm{d}\Omega \, \mathrm{d}t = \\ = \int_0^T \oint_{\Gamma(\Omega)} \left(\Delta \boldsymbol{E} \times \boldsymbol{H}^+ - \boldsymbol{E}^+ \times \Delta \boldsymbol{H} \right) \boldsymbol{n} \mathrm{d}\Gamma \, \mathrm{d}t, \tag{5}$$

where $\boldsymbol{E}$ is the electric intensity vector, $\boldsymbol{H}$ is the magnetic intensity vector, $\boldsymbol{J}_S$ is the excitation current density, μ is the magnetic permeability and γ is the electric conductivity. The symbol ($^+$) means the value referred to in the adjoint system, the remaining parameters belong to the original system. Both systems are analyzed for the same area Ω with the boundary Γ. The original system is analyzed at time t and the adjoint system at time $\tau = T - t$, where T is the time of the sensitivity evaluation. In the sensitivity equation (5) one can find the component $\boldsymbol{L}^+_S$ which can be interpreted as a magnetic current density vector and is equal to zero for all physical models.

The sensitivity equation (5) determines how to construct the adjoint model. Assuming the same material parameters for both models $\mu = \mu^+$ and $\gamma = \gamma^+$ simplifies this equation. The boundary integral in (5) may be eliminated assuming appropriate boundary conditions in the adjoint model. The excitation in the adjoint model can be chosen so that the sensitivity for the desired area, e.g. the coil, can be calculated directly. While assuming excitation only with an electric current and calculating versus electric conductivity, the sensitivity equation simplifies to:

$$\int_0^T \iint_{\Omega_C} \boldsymbol{J}_S^+ \Delta \boldsymbol{E} \, \mathrm{d}\Omega_C \, \mathrm{d}t = \int_0^T \iint_{\Omega} \boldsymbol{E}^+ \Delta \gamma \boldsymbol{E} \, \mathrm{d}\Omega \, \mathrm{d}t \, . \tag{6}$$

Comparison of the Methods

Numerical calculation with both methods involves the analysis of the original model followed by analysis either of an incremental model or an adjoint model. Both models employ the same stiffness and mass matrices. While using the constant time step Δt, the matrices remain unchanged during the calculation. If the model of the measurement coil consists of m finite elements, the sensor sensitivity with the adjoint model can be calculated immediately, and, with the help of the incremental circuit, as much as m calculations are necessary (there is no need for any additional factorization of the matrices).

Inverse Problem

Sensitivity analysis can be applied to both shape recognition and the identification of material parameters such as conductivity distributions. When the simulated field distribution (time function) agrees with experimental measurement, it is assumed that the conductivity distribution is correct. As the discrete goal function $\boldsymbol{F}$ for optimization of the quadratic error is assumed:

$$\boldsymbol{F} = \frac{1}{2} \sum_{p=1}^{q} \sum_{i=1}^{n} \left(\boldsymbol{A}_i^p - \underline{\boldsymbol{A}}_i^p \right)^2 \tag{7}$$

where: $\boldsymbol{A}_i^p$ is the magnetic vector potential for the time step $i = 1,...,n$, and for the position p of the coil $p = 1,...,q$, and $\underline{\boldsymbol{A}}_i^p$ is the referenced value from experimental measurement.

For optimization, the Gauss-Newton algorithm with truncated singular value decomposition of

the sensitivity matrix was used [10]. The process starts with initial configuration, for example, with a conductivity distribution without cracks. In successive iterations, the sensitivity is calculated and then the conductivity corrections $\Delta\gamma$ in finite elements. The iterations are repeated until the error $\boldsymbol{F}$ is minimized.

Numerical Example

Let us consider the following example for sensitivity evaluation. Three coils have been placed inside a long conducting pipe, (Fig.1). The coil in the middle is used for measurement, other two are excited differentially. Excitation is in the form of a half sinusoidal wave (Fig.2).

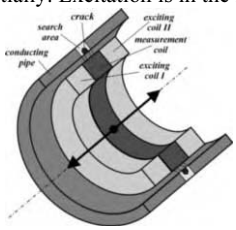

Fig. 1. Three coils inside the pipe

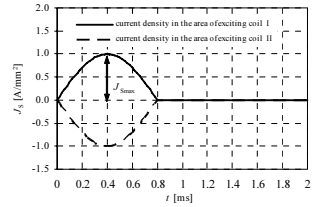

Fig. 2. Excitation shape

The model exhibits cylindrical symmetry and can be analyzed using a 2D formulation. The zero Dirichlet condition was assumed along the axis of symmetry and the zero Neumann-conditions on the remaining boundaries. The area was divided into 2304 finite elements with 1201 nodes (Fig.4).

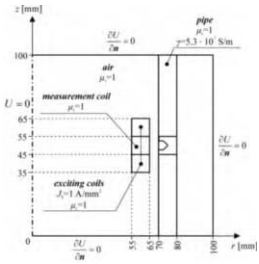

Fig. 3. Simulated model

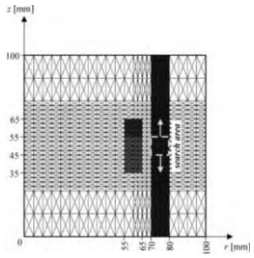

Fig. 4. Finite element mesh

The analysis in the time domain was carried out with a backward Euler scheme, with a constant time step of $\Delta t = 20$ μs.

Sensitivity Analysis

The sensor sensitivity (2) will be evaluated using a modified vector potential $U = A_\varphi r$ versus conductivity in the search area (Fig.4) consisting of 320 elements with 100 time steps, i.e. $320 \cdot 100 = 32\,000$ sensitivity values were calculated.

The distribution of the modified potential U in the original model for three values of t is shown in Fig.5. The penetration of the magnetic field into the pipe wall can be observed. Fig.5 shows that the time step Δt was chosen correctly for the transient analysis.

For the adjoint model build and analysis, the excitation was assumed to be in the form of a Dirac impulse driven into the finite elements of the measurement coil [9]. The field distribution for the adjoint model is shown in Fig.6.

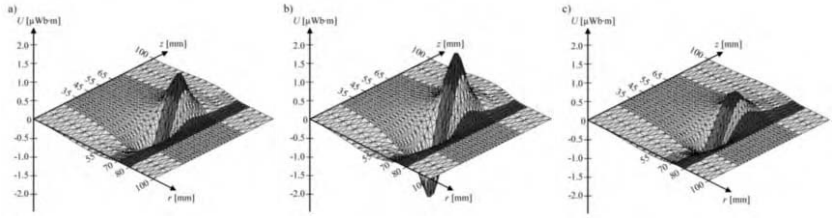

Fig. 5. Modified vector potential U distribution for: a) t = 200 μs, b) t = 400 μs, c) t = 1000 μs obtained with FEM on original model

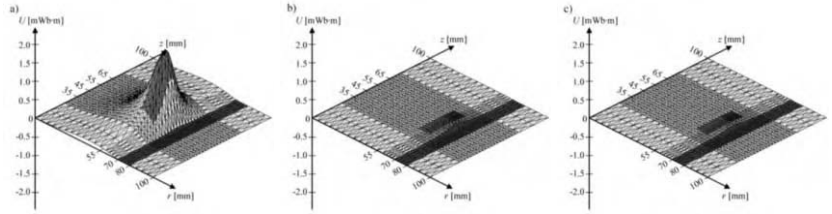

Fig. 6. Modified vector potential U distribution for: a) t = 200 μs, b) t = 400 μs, c) t = 1000 μs obtained with FEM on adjoint model

On the basis of the above field distributions for the original and adjoint models, the values of sensor sensitivity versus conductivity were calculated (Fig.7).

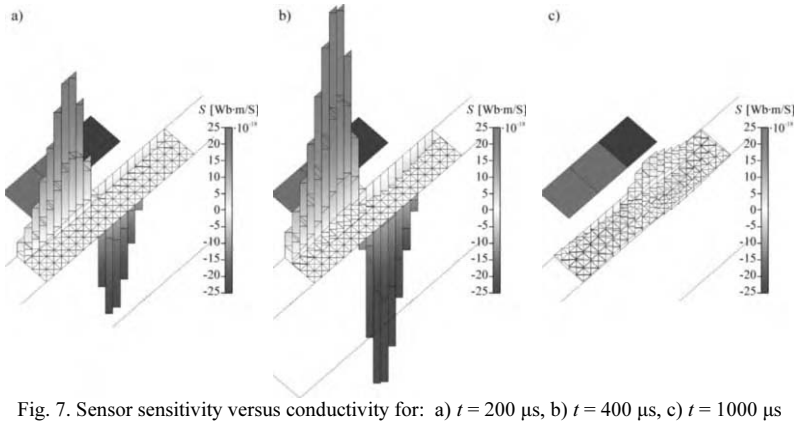

Fig. 7. Sensor sensitivity versus conductivity for: a) t = 200 μs, b) t = 400 μs, c) t = 1000 μs

Inverse Job

This example shows the exploitation of sensitivity knowledge to identify the conductivity distribution inside the pipe wall. The eddy-current probe, consisting of three coils, moves inside the pipe with increments of 2.5 mm. In each position, the probe is excited and the voltage impulse in the measurement coil registered. For the purposes of simulation, this is equivalent to 17 locations for the probe (q = 17). The measurement was simulated with the help of FEM adding random 1% relative error. The search area consisted of 64 elements with a conductivity of $\gamma = 2 \cdot 10^7$ S/m (Fig. 8a). This means that, in every iteration step, there were $17 \cdot 64 \cdot 100 = 108\,800$ sensitivity values calculated providing gradient information for iterative Gauss-Newton with TSVD algorithm. The conductivity distribution, as well as crack shape, was correctly identified after 8 iterations.

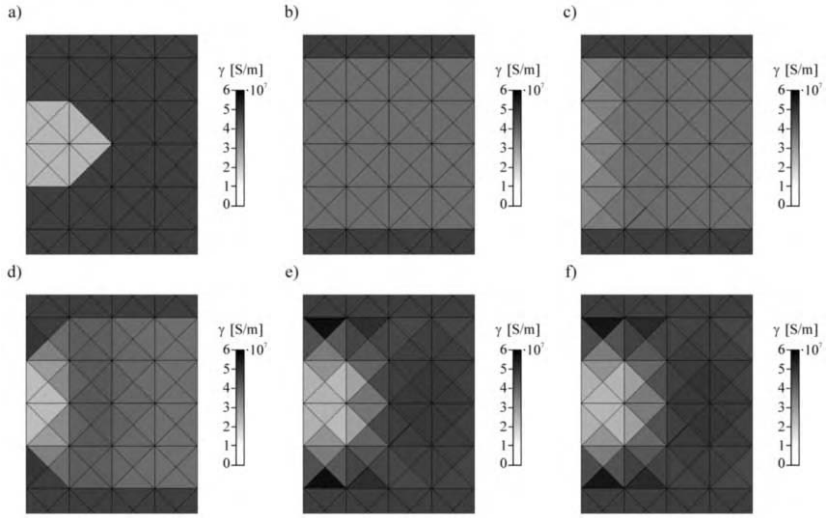

Fig. 8. Identification process: a) assumed distribution of conductivity, b) initial distribution of conductivity, c) recognition of conductivity after 2 iteration, d) after 4 iteration, e) after 6 iteration, f) after 8 iteration

Conclusions

The convergence of numerical identification algorithm described in the paper depends strongly on exact measurement of magnetic flux density (it's time function). The authors have simulated the measurement using finite element model with additional noise. While using real measurement data the results of identification would be worse.

A very good choice is the solution of over-determined equation systems for the case of excess of measurement data. For identification of real cracks the application of data filtering and TSVD regularization of Gauss-Newton algorithm is necessary.

To analyze the wide class of real cracks the three-dimensional analysis should be applied. For 3D-formulation a new form of sensitivity equations has to be obtained. It will be aim of future work. The three dimensional algorithm will consume much more computation time, so it must be optimized carefully.

References

[1] O.C. Zienkiewicz, K. Morgan, Finite Elements and Approximation Method, New York: Jonh Willey & Sons, 1983, pp. 283-289.
[2] K.J. Binns, P.J. Lawrenson, C.W. Trowbridge, The Analytical and Numerical Solution of Electric and Magnetic Fields, New York: John Willey & Sons, 1995, pp. 320-323.
[3] X.W. Dai, R. Ludwig, R. Palanisamy, Finite Element Prediction of Pulsed Eddy Current Response in 2-D and Axisymmetric Geometries, Review of Progress in Quantitative Nondestructive Evaluation. Vol. 10A, 1991, pp. 325-331.
[4] K.M. Gawrylczyk, M. Kugler, Sensitivity Analysis of Electromagnetic Quantities in Time Domain by Means of FEM, Serbian Journal of Electrical Engineering, Vol. 1, No. 2, June 2004, pp. 167-174.
[5] B.D.H. Tellegen, A General Network Theorem, with Applications, Philips Research Reports, Vol. 7, 1952, pp. 259-269.
[6] P. Penfield, R. Spence, S. Duinker, Tellegen's Theorem and Electrical Networks, Massachusetts: M.I.T. Press, 1970.
[7] D.N. Dyck, D.A. Lowther, E.M. Freeman, A Method of Computing the Sensitivity of Electromagnetic Quantities to Changes in Materials and Sources, IEEE Transactions on Magnetics, Vol. 30, No. 5, September 1994, pp. 3415-3418.
[8] K.M. Gawrylczyk, Sensitivity Analysis of Electromagnetic Quantities in Time Domain, 10th International Symposium on Electromagnetic Fields in Electrical Engineering, Cracow, Poland, September 20-22, 2001, pp. 347-350.
[9] K.M. Gawrylczyk, M. Kugler, Identification of cracks with sensitivity analysis in time domain basing on Tellegen method (in polish), IX ZKwE, Poznań-Kiekrz, 19-21 April 2004, pp. 123-126.
[10] K.M. Gawrylczyk, M. Kugler, P. Putek, A Gauss-Newton algorithm with TSVD for crack shape recognition in conducting materials, Post-Conference Monograph, Computer Application in Electrical Engineering, Poznan University of Technology 2005, (accepted for printing)

Electromagnetic Fields in Mechatronics, Electrical and Electronic Engineering
A. Krawczyk et al. (Eds.)
IOS Press, 2006

MULTI-SLICE FINITE ELEMENT MODELLING OF INDUCTION MOTORS CONSIDERING BROKEN BARS AND INTER-BAR CURRENTS

J. Gyselinck[1], J. Sprooten[1], L. Vandevelde[2] and X.M. L´opez-Fern´andez[3]

[1]Department of Electrical Engineering, Universit´e Libre de Bruxelles, Brussels, Belgium
phone: +32 2 650 26 69 – fax: +32 2 650 26 53 – e-mail: Johan.Gyselinck@ulb.ac.be
[2]Department of Electrical Energy, Systems and Automation, Ghent University, Belgium
[3]Department of Electrical Engineering, University of Vigo, Spain

***Abstract** – This paper deals with the finite element (FE) modelling of squirrel-cage induction motors having one or more broken bars. A two-dimensional (2D) multi-slice FE model allows to consider the position of the bar breakage (at one of the endrings rather than in the middle), the skew of the rotor bars and the interbar (IB) currents. The latter are effected by resistances distributed in the electrical circuit that connects the different slices of the cage. The multi-slice model is applied to a 3kW induction motor. An order-ofmagnitude estimate of the IB resistance follows from a short-circuit test (with healthy rotor). Next the effect of a broken bar and of the IB currents on the stator current spectrum is studied.*

Introduction

The existence of inter-bar (IB) currents in cast cage rotors of small induction motors is due to the absence of perfect insulation between the cage and the core [1]. These parasitic currents, which flow from bar to bar through the iron rotor core, are limited by the high but finite bar-core contact resistance rather than by the resistivity of the steel laminations. The accurate measurement of the IB resistance is by no means trivial. Some measuring methods and results of extensive experimental work are discussed in [1, 2]. Nominally identical rotors can have significantly different IB resistances, even when manufactured at the same plant, using the same equipment, and on the same day. Therefore, order-of-magnitude estimation of "the" bar-to-bar resistance may be thought to be sufficient [1]. Enhanced per-phase equivalent circuits of (healthy) induction motors show that IB currents are strongly promoted by rotor skew and may have a significant effect on their starting performance [2]. At load their influence is usually much less pronounced. Skew and IB currents can be taken into account more precisely when using a multi-slice FE-model. In such a model, the IB currents are easily effected by inserting lumped resistances in the electrical circuit of the cage [3, 4].

When one or more rotor bars are broken, the IB currents are locally promoted, attenuating the magnetic disturbance due to the broken bars and thus rendering their detection more difficult [5, 6, 7, 8]. Indeed, depending on the finite IB resistance, current continues to flow into the broken bar from its healthy side, through the laminations and toward the adjacent bars. A simple analytical expression for the axial current distribution in the broken bar(s) can be derived [5, 6]. This paper is concerned with a detailed multi-slice FE analysis of this effect. After a brief discussion of the multi-slice FE model, its application to a 3kW induction is detailed. Particular attention is paid to the frequency spectrum of the stator phase currents in the presence of skew and a broken rotor bar.

Multi-Slice FE Model With IB Currents

A multi-slice FE model of a machine of total axial length l_z (along the z-axis) consists of n_{sl} unskewed slices of axial length $l_z^{(i)}$ ($1 \leq I \geq n_{sl}$), in which the rotor position, denoted by $\theta_{rot}^{(i)}$, is shifted with respect to the average rotor position θ_{rot}. An approximation with three slices is shown in Fig. 1.

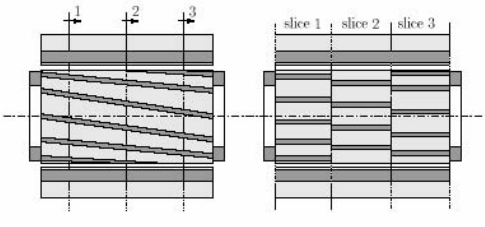

Fig. 1. Multi-slice model: approximation of skew by means of three slices of equal length

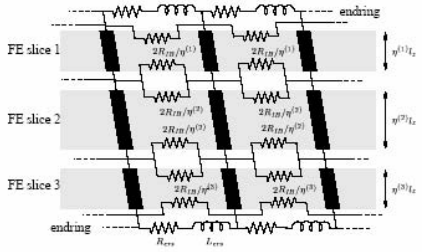

Fig. 2. Electrical circuit of rotor cage with three FE slices and distributed IB resistance

In each slice a 2D magnetic field is assumed and the same FE discretisation is commonly adopted in stator and rotor [3, 4, 9]. The layer of finite elements connecting stator and rotor mesh, the so-called moving band, is rotor position dependent and thus varies from slice to slice. Denoting the length and the rotor position of the i-th slice by $l_z^{(i)}$ and $\theta_{rot}^{(i)}$ respectively, the discretisation of the skew can be defined by means of the dimensionless coefficients $\eta^{(i)}$ and $\gamma^{(i)}$:

$$l_z^{(i)} = \eta^{(i)} l_z \quad \text{and} \quad \theta_{rot}^{(i)} = \theta_{rot} + \gamma^{(i)} \frac{\theta_{sk}}{2}, \tag{1}$$

where θsk is the skew angle, and with $\Sigma \eta^{(i)} = 1$ and $-1 < \gamma^{(i)} < 1$. A uniform discretisation is commonly used [3]:

$$\eta^{(i)} = \frac{1}{n_{sl}} \quad \text{and} \quad \gamma^{(i)} = \frac{2i - n_{sl} - 1}{n_{sl}}. \tag{2}$$

Alternatively, a classical 1D Gauss integration scheme can be adopted [9]. Herein the position $\eta^{(i)}$ and the weight $\gamma^{(i)}$ of the n_{sl} evaluation points in the reference interval [-1,1] are such that the numerical integration is exact for all polynomials of degree $\leq 2n_{sl}$ -1. The Gauss scheme allows significant savings as for a given accuracy less slices are required.

In a single-slice FE model, the stator windings are each modelled as a so-called stranded conductor whereas the rotor bars are each modelled as a so-called massive conductor (thus ignoring and allowing for skin effect respectively) [10]. The series connection of the corresponding conductors in the n_{sl} slices of a multi-slice model, their connection to the endrings, and the voltage supply of the stator windings are effected through electrical circuit equations. The endwindings and endrings are taken into account by means of lumped resistances and inductances. One thus obtains a large system of differential equations in terms of the nodal vector potential values and bar voltages of each slice, and a number of loop currents [10, 3, 4].

The electrical circuit of the rotor cage is easily extended with a view to the approximate inclusion of the IB currents. The latter are indeed allowed for by $2n_{sl}$ resistances $2R_{IB}=\eta^{(i)}$ distributed over the n_{sl} slices and between each pair of adjacent bars, as is shown in Fig. 2. Directly connected in parallel,

these $2n_{sl}$ resistances amount to the IB resistance R_{IB} . Note that each segment of the upper and the lower endring is shunted by a resistance $R_{IB}/\eta^{(1)} = R_{IB}/\eta^{n_{sl}}$. The generic FE and electrical circuit equations remain valid, but the number of independent current loops in the cage circuit now depends on both the number of rotor bars and the number of slices.

Application To A 3kw Induction Motor

We consider a 4-pole 220V 50 Hz 3kW induction motor. The commercial version of the rotor has 32 closed and skewed slots (θ_{sk} = 12.4°). Three other rotors having open and/or unskewed slots have been constructed for research purposes. Using a single-slice and a multi-slice FE model, the stator current waveforms at noload and at full load, and with either of the four different rotors can be calculated with a satisfactory precision [9]. The effect of the IB currents on the short-circuit and load operation has been studied in [4]; this study was limited to the (healthy) rotors with open slots.

Which is also the case in this paper. It has been observed that the IB currents have minor effect (e.g. on torque output and losses), whereas the skew effectively reduces slotting harmonics and results in a decrease and increase of copper and iron losses respectively.

In this paper we focus on the combined effects of the IB currents and a broken rotor bar.

A FE discretisation having 6000 first order triangular elements per slice is used. The stator and the rotor iron are separated by three layers of elements, the middle one being the moving band. A typical flux pattern at load is shown in Fig. 3.

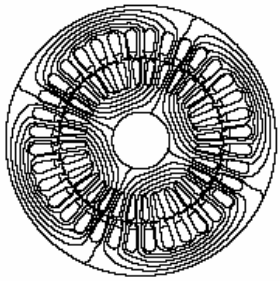

Fig. 3. Cross-section of 3kW induction motor – flux pattern at full load

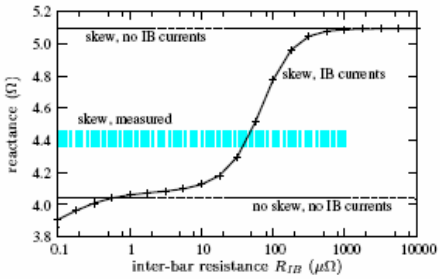

Fig. 4. Locked-rotor motor reactance (with skew) as a function of IB resistance

IB resistance estimation from locked rotor test

From the contact resistance value of 0.04 Ωmm2 found in [2] and the dimensions of the 3kW motor at hand (core length 127mm and rotor bar periphery 31 mm), a rough order-of-magnitude estimation follows: R_{IB} = 10 $\mu\Omega$. By way of comparison, the endring segment resistance and inductance values (see Fig. 2) are R_{ers} = 0.87 $\mu\Omega$ and L_{ers} = 4.8 nH respectively; the rotor bars have a DC resistance of 107 $\mu\Omega$.

An estimate of the IB resistance may also be obtained through short-circuit measurements and calculations considering the rotors without and with skew (at reduced 50 Hz voltage supply) [4]. Measurements learn that the skew brings about an increase of the short-circuit motor reactance of 0.4Ω. Ignoring completely the IB currents, the increase can be estimated from the magnetising reactance and the skew factor of the fundamental 4-pole field [2], which produces a short-circuit reactance increase of 1Ω. This value agrees well with the increase predicted by means of the FE model if the IB currents are not taken into account(see Fig. 4). Assuming that the difference with these two values can be attributed to the IB currents, multi-slice FE simulations with different values of the IB

resistance R_{IB} are carried out. By comparison with the measured reactance, R_{IB} should be in the range from 10 $\mu\Omega$ to 100 $\mu\Omega$, as can be concluded from Fig. 4.

Load operation with healthy and faulty rotor

Time-stepping simulations at load under rated sinusoidal voltage supply are carried out. The stator phases are delta connected. For taking into account the skew a multi-slice model with 4 slices and Gauss distribution is used. The skewed cage is either healthy or has a broken bar (breakage in the first slice, i.e. near one of the endrings). The IB currents are either ignored ($RIB = \infty$) or considered (R_{IB} equal to 10 $\mu\Omega$ or 100 $\mu\Omega$). In order to reduce the computation time, magnetic saturation is ignored and a 10% slip (1350 rpm) is imposed. By simulating 25 fundamental time periods (with 150 steps per period) and by performing the Fourier analysis on the 20 last periods, i.e. [0.1s,0.5s], neat frequency spectra are obtained.

Fig. 5 shows the frequency spectrum of the stator phase currents for 3 cases without IB currents. The origin of the frequencies found can be explained by means of the rotating field theory [11]. Indeed, the airgap flux density can be written as a series of travelling waves:

$$B(\theta, t) = \sum_k \Re\{\bar{B}_k \exp[j(2\pi f_k t - \kappa_k \theta)]\} \tag{3}$$

where $\bar{B}_k$, f_k and K_k are the complex representation, the frequency and the spatial order respectively of the k-th induction component; θ is the angular coordinate in mechanical radians with respect to a stator reference frame, and $j = \sqrt{-1}$ is the imaginary unit.

Assuming an integral-slot stator winding with normal phase belt width (60°) and in series connected coil groups, the frequencies f_k and spatial orders K_k of the induction components that may occur in a three-phase induction motor having N_p pole pairs and N_r rotor bars, under sinusoidal voltage supply of frequency f_0, and at slip s are given in terms of the integer parameters η, l, ε_s, ε_d, and g:

$$f_k = \left(1 + 2\eta + (lN_r + \varepsilon_d)\frac{1-s}{N_p}\right) f_0 , \tag{4}$$

$$\kappa_k = (1 + 6g + 2\eta)N_p + lN_r + \varepsilon_s + \varepsilon_d \tag{5}$$

where g is related to the stator m.m.f. harmonics and slotting, l is related to the rotor m.m.f. harmonics and slotting, ε_s to the static rotor eccentricity if any, ε_d to the dynamic rotor eccentricity or one or more broken bars if any, and η to iron saturation [11]. An induction component (f_k, K_k) induces a sinusoidal voltage and current of frequency f_k in the stator windings only if the order K_k can be written as $K_k = (i+6m)N_p$, with m integer and i equal to 1, 3 or -1; if $f_k > 0$, these three values for i result in a direct, homopolar and inverse voltage and current component; if $f_k < 0$ this is inverse, homopolar and direct. (Note that the parameter g having coefficient $6N_p$ does not affect the fulfilment of this criterion.)

For the motor and operation under study ($N_p = 2$, $N_r = 32$, $f_0 = 50$Hz, $s = 0.1$, $\eta = 0$, $\varepsilon_s = 0$), the fundamental frequency $f_0 = 50$Hz ($l = 0$, $\varepsilon_d = 0$) is only slightly affected by skew and the broken bar, whereas the first rotor slotting and m.m.f. harmonics ($l = \pm 1$, $\varepsilon_d = 0$), at 670 Hz (inverse) and 770 Hz (direct), are significantly reduced thanks to the skew; the latter harmonic practically disappears.

The harmonics due to the broken bar correspond to values of ε_d that are multiples of 4. For instance, the lowest (direct) harmonic at $|1 - 2(1 - s)| * f_0 = (1 - 2s)f_0 = 40$ Hz is produced with $l = 0$ and $\varepsilon_d = -4$; $\varepsilon_d = 4$ gives the homopolar 140 Hz. $l = 0$ and $\varepsilon_d = \pm 8$ produces 230 Hz (inverse) and 130 Hz (homopolar). $l = 0$ and $\varepsilon_d = \pm 12$ produces 320 Hz (direct) and 220 Hz (inverse). This way all the other frequencies in Fig. 5 can be traced as well.

Fig. 6 evidences the attenuating effect of the IB currents on the magnetic disturbance due to a broken bar: the associated harmonics diminish as the IB resistance is decreased. The significant

reduction of the $(1 - 2s)f_0$ frequency is of particular interest as this may hamper broken-bar detection relying on the appearance of this harmonic [5, 12]. Note that a broken bar results in an additional $2sf_0$ torque harmonic, which may produce a speed variation, which in turn will create a harmonic $(1 + 2s)f_0$ in the stator winding currents [12]. One may expect the latter harmonic to be attenuated by the IB currents as well.

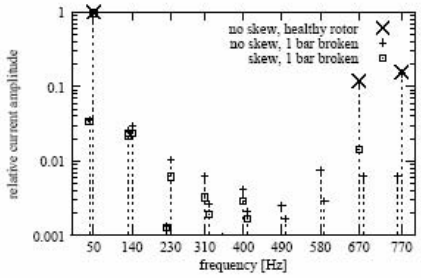

Fig. 5. Frequency spectrum of stator phase current at 10% slip in the absence of IB currents – influence of skew and a broken bar

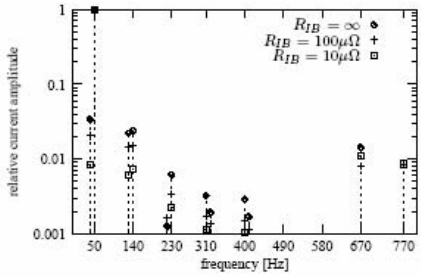

Fig. 6. Frequency spectrum of stator phase current at 10% slip with skew and 1 broken bar – influence of the IB resistance

The distribution of the current in the rotor bars when one bar (bar number 16) is broken is depicted in Fig. 7. Thanks to the finite IB resistance, current continues to flow into the broken bar from its healthy side. The current in the adjacent bars on either side increases, especially in slice 1, in which the bar breakage is situated. Note that in the current in bar 15 is greater than the one in bar 17. This symmetry is also reported in [7]. Note also the slight oscillation of the current profile further away from the broken bar. The simple analytical expression for the bar current profile given in [5, 6] does not feature this oscillation as the coupling of the rotor cage with the stator windings is not taken into account.

Conclusions

This paper has dealt with multi-slice FE modelling of squirrel-cage induction motors in the presence of IB currents and a broken bar. The multi-slice model has been applied to a 3kW induction motor for which different rotors were available. An order-of-magnitude estimate of the IB resistance was obtained by means of a short-circuit test with healthy rotor (unskewed and skewed version). Next the effect of a broken bar and of the IB currents on the stator current spectrum is studied. The origin of the harmonics has been explained and the attenuating effect of the IB currents on the magnetic disturbance due to a broken bar has been evidenced.

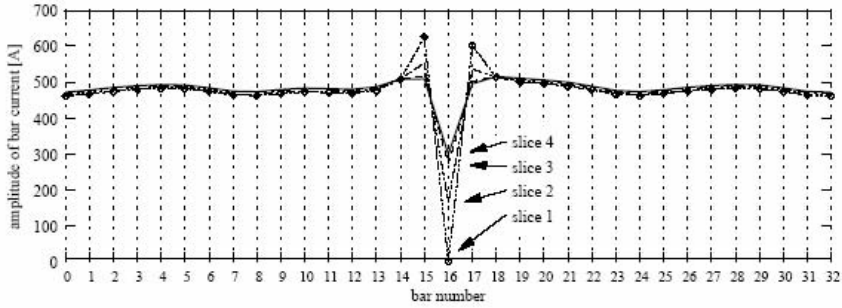

Fig. 7. Amplitude of the fundamental sf_0 component of the currents in the 32 bars and the 4 slices, with bar number 16 broken in slice 1 and $R_{IB} = 100\ \mu\Omega$

References

[1] S.Williamson, C. Poh and A. Smith, Estimation of the inter-bar resistance of a cast cage rotor, Proc. Electric Machines and Drives Conference (IEMDC), 1-4 June 2003, Vol. 2, pp. 1286–1291.
[2] D. Dorrell and T. Miller, Inter-bar currents in induction machines, IEEE Trans. Ind. Appl., Vol. 39, No. 3, pp. 677–684, May/June 2003.
[3] S.Ho, H. Li andW. Fu, Inclusion of interbar currents in a network-field coupled time-stepping finite-element model of skewed-rotor induction motors, IEEE Trans. Magn., Vol. 35, No. 5, pp. 4218–4225, Sept. 1999.
[4] J. Gyselinck and X.M. L´opez-Fern´andez, Inclusion of inter-bar currents in multi-slice FE modelling of induction motors - influence of inter-bar resistance and skew discretisation, Proc. ICEM2004, Cracow, Poland, 5-8 Sept. 2004, pp. 621-622, extended paper (790) on CD-ROM, accepted for COMPEL 2005.
[5] R. Walliser and C. Landy, Determination of interbar current effects in the detection of broken rotor bars in squirrel cage induction motors, IEEE Trans. Energy Conv., Vol. 9, No. 1, pp. 152–158, March 1994.
[6] G. M¨uller and C. Landy, A novel method to detect broken rotor bars in squirrel cage induction motors when interbar currents are present, IEEE Trans. Energy Conv., Vol. 18, No. 1, pp. 71–79, March 2003.
[7] X.M. L´opez-Fern´andez and P. Marius, Magnetodynamic performance in cage induction motors with a broken bar, Proc. ISEF2003, Maribor, Slovenia, 18-20 Sept. 2003, pp. 261–266.
[8] J. Sprooten and J.C. Maun, Induction machine fault detection and quantification by means of superposed analytical models, Proc. SPEEDAM, Capri, Italy, 16-18 June 2004, pp. 821–826.
[9] J. Gyselinck, L. Vandevelde and J. Melkebeek, Multi-slice FE modelling of electrical machines with skewed slots – the skew discretisation error, IEEE Trans. Magn., Vol. 37, No. 5, pp. 3233–3237, Sept. 2001.
[10] Lombard, P. and Meunier, G. (1992), ”A general method for electric and magnetic combined problems in 2D and magnetodynamic domain”, *IEEE Trans. Magn.*, Vol. 28, No. 2, pp. 1291–1294, March 1992.
[11] L. Vandevelde and J. Melkebeek, Numerical analysis of vibrations of squirrel-cage induction motors based on magnetic equivalent circuits and structural finite element models, Conference Record of the 2001 IEEE Industry Applications Conference / 36th IAS Annual Meeting, Chicago, Illinois, USA, September 30 - October 4, 2001, Vol. 4, pp. 2288–2295
[12] A. Bellini, F. Filippetti, G. Franceschini, C. Tassoni and G.B. Kliman, Quantitative evaluation of induction motor broken bars by means of electrical signature analysis, Conference Record of the IEEE Industry Applications Conference, 8-12 Oct. 2000, Vol. 1, pp. 484–491.

Electromagnetic Fields in Mechatronics, Electrical and Electronic Engineering
A. Krawczyk et al. (Eds.)
IOS Press, 2006

FEM ANALYSIS OF GROUNDING SYSTEM PARAMETERS CONSIDERING ADDITIONAL SUBSTANCE

Anton Habjanič, Mladen Trlep

University of Maribor, Faculty of Electrical Engineering and Computer Science
Smetanova ul. 17, 2000 Maribor, Slovenia
e-mail: anton.habjanic@uni-mb.si

***Abstract** – In this paper we examine the finite element method (FEM) analysis of grounding grid and how this method is utilized to assess the influence of an additional substance on the following grounding system parameters: ground potential rise, earth surface potential, touch voltage, step voltage, and grounding resistance. The innovation of this work is in the expansion of FIELD_GS program code in such a way that the local non-homogeneity, which has been caused by adding the electrolytic substance into the soil around the grounding grid, can be taken into account. Different soil structures and various volumes of soil layers impregnated with an additional substance have been analyzed.*

Introduction

A primary goal of embedding metallic structures (conductors) into earth is to provide a conducting path of electricity to earth and to create a grounding system, which ensures the safety of people or animals and prevents damage to all installations during normal or abnormal (fault) conditions. To provide safety and to assure correct operation of electrical devices, the grounding resistance of properly configurated grounding system must be low enough to assure sufficiently low voltage drops under all conditions. Sometimes, due to geo-electrical characteristics of the soil, the assurance of required low grounding resistance, without any additional interventions into soil surrounding the grounding system, is practically impossible. In such cases the use of additional grounding expedients like bentonite or Sanick gel can be of enormous help to improve the grounding resistance. Placing these low resistivity electrically conducting grounding substances into soil surrounding the grounding system, the resistivity of the soil in the immediate vicinity of the grounding system and the contact connection between the grounding system conductors and the surrounding soil are improved, consecutively the grounding resistance is decreased. Thus, not only building interventions but also building expenses can be considerably reduced.

Besides grounding expedients mentioned above, within the calculation region in the ground, a presence of an additional substance volume e.g. arbitrary type of soil, concrete, water, etc., with different resistivity than the immediate environment, can be possible. For the sake of calculation accuracy such local non-homogeneity has to be taken into account. Referring to this fact, we have expanded the program package FIELD_GS in the way that the actual non-homogeneity volume is replaced by the equivalent brick volume with sides parallel to the coordinate system axes (x, y, and z). To implement this innovation into the model, the equivalent brick dimensions and position of bricks corner (marked with ● in Fig. 1a) regarding the coordinate system origin, as well as the resistivities (or conductivities), have to be entered into the program code. By this means our program become capable to evaluate the effect of local non-homogeneity, where not only isotropic but also anisotropic properties of the material can be taken into account, on the grounding system performance.

As mentioned above, the aim of this paper is to study the influence of additional electrolytic substance on the grounding grid properties. The grounding grid presented in Fig. 1a is buried 0.8 m deep horizontally under the earth surface and it consists of five conductors in *x*-axis and five conductors in *y*-axis. The distance between conductors is 4 m (16 m by 16 m grounding grid). The grid is connected to a conductor carrying current of 1000 A from space above the earth surface. We supposed that by adding of additional substance, the resistivity of impregnated soil near the grounding grid is improved to the level of 50 Ωm. In order to verify such influence, an analysis of following grounding grid parameters: ground potential rise, earth surface potential, touch voltage, step voltage, and grounding resistance at different soil resistivities and different volumes of soil layers impregnated with an additional substance was carried out. For this purpose we have studied three different kinds of soil structure models: two single-layer (uniform) soil models with resistivities of 200 Ωm and 800 Ωm respectively (Fig. 1b), and two-layer soil model with first-layer resistivity (from earth surface to the depth of 4 m) of 200 Ωm and second-layer resistivity of 800 Ωm (Fig. 1c). The problem was solved numerically by using the program package FIELD_GS designed for 3D current field calculations of the grounding system by FEM.

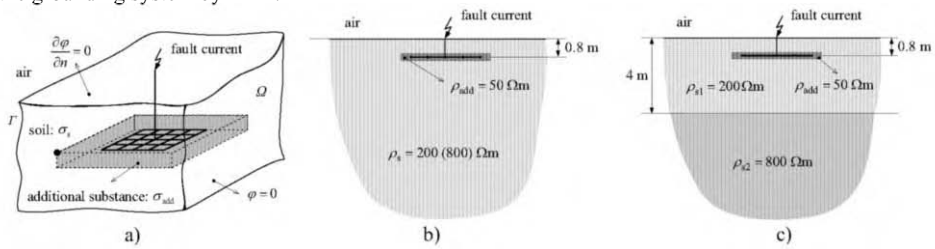

Fig. 1. Grounding grid and additional substance in soil: a) physical situation of the analyzed domain; b) scheme of a uniform soil model; c) scheme of a soil model with two horizontal layers.

Numerical Model

For the analysis of the grounding system the problem is described by the Laplace's equation:

$$\nabla\left(\left[\sigma\right]\nabla\varphi\right) = 0 \tag{1}$$

The current field in the space Ω is entirely described by (1), when the boundary conditions (2) on boundary Γ are known.

$$\varphi = 0 \;\; (r \to \infty), \;\; \frac{\partial\varphi}{\partial n} = 0 \;\; (\text{on the earth surface}) \tag{2}$$

By applying the Galerkin's formulation of FEM [1], the additional transformation of the "semi-infinite space" [2-3], the 3D finite elements for soil and local non-homogeneity discretization, and the 1D finite elements for the grounding system [4-5], the following equations are obtained.

- The equation of a twenty-node isoparametric 3D finite element (second-order hexahedron) in the transformed and non-transformed domain:

$$\iiint_{\Omega_{3D}} \nabla N_i \, \sigma \nabla\varphi \, \mathrm{d}\Omega = 0 \;\; , \;\; \varphi = \sum_{j=1}^{20} N_j \varphi_j \tag{3}$$

- The equation of a three-node 1D finite element (second-order line element) in the grounding system domain:

$$S_{1D} \iiint_{l_{1D}} \nabla N_i \, \sigma_{1D} \nabla\varphi \, \mathrm{d}l = 0 \;\; , \;\; \varphi = \sum_{j=1}^{3} N_j \varphi_j \tag{4}$$

Where N represents interpolation function, Ω_{3D} the volume of 3D finite element in the transformed and non-transformed domain. S_{1D}, l_{1D}, and σ_{1D} denote the cross-section, the length, and the conductivity of the grounding system element modelled by 1D finite elements respectively. The final form of the FEM equation is given by (5).

$$[A]\{\varphi\} = \{B\} \tag{5}$$

Results of Analysis

When a fault current is injected into the grounding system, its potential becomes different than zero. We shall refer to this potential as the ground potential rise (GPR). In Fig. 2 the influence of additional substance thicknesses, and of surface ratios S_{add}/S_{grid} between the surfaces of soil layers impregnated with an additional substance and surface of the grounding grid on the GPR for all of the three soil structure models is shown respectively.

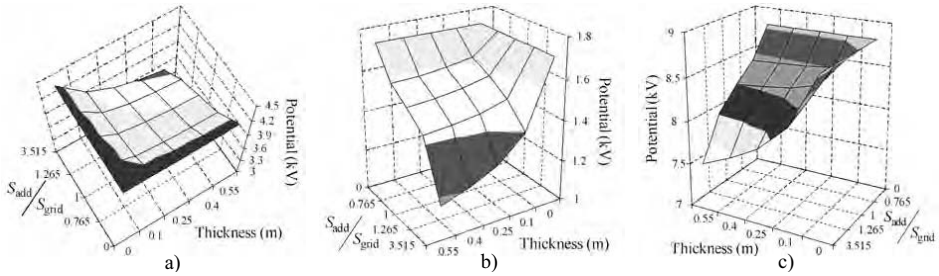

Fig. 2. 3D plot of the additional substance thickness and surface ratio influence on the ground potential rise in case of: a) uniform soil model 200 Ωm; b) uniform soil model 800 Ωm; and c) two-layer soil model 200/800 Ωm

It is not hard to see that most important design parameter of a grounding system is the GPR. Since the GPR depends, among other parameters, on the grounding resistances, an investigation of the GPR requires knowledge of the grounding resistances. Note that the electric currents are proportional to the GPR, thus a grounding resistance can be computed as the ratio of the GPR over the total earth current. In Fig. 3 the calculated results of grounding resistance R, obtained for different thicknesses and surfaces of soil layers impregnated with an additional substance, are shown respectively. In the following figures with index 0 all cases without the presence of additional substance are numerated. With index 1 all cases whit the surface of impregnated soil equal to the surface of grounding grid are numerated. Finally, with index 2 all cases with the surface of impregnated soil 30 m by 30 m are numerated. The thickness of impregnated soil of 0.25 m corresponds to the presence of additional substance of 0.2 m above and 0.05 m below the grid, and the thickness of impregnated soil of 0.55 m corresponds to the presence of additional substance of 0.4 m above and 0.15 m below the grid.

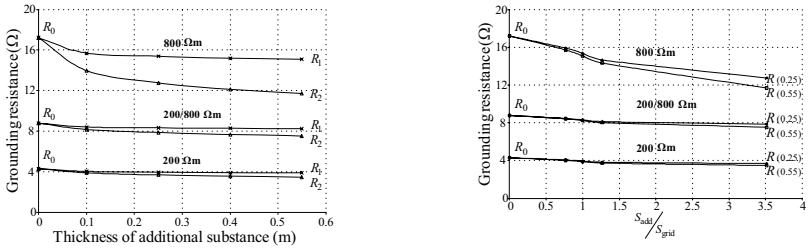

Fig. 3. The influence of: a) additional substance thickness; and b) surface ratio on grounding resistance.

The voltage to which the human body is subjected in case a person is touching a grounded structure, which has a potential that is different from that of the point of earth at which the person is standing, is called the touch voltage. The voltage, which is experienced between human beings feet in case a person is walking on the earth surface, is called the step voltage. Thus, what we need most in the analysis of grounding systems is the step and touch voltage profile in the area of interest, for which we previously need the distribution of the potential on the earth surface. For a grounding system to be safe, the maximum touch and step voltage should not exceed the maximum allowable values defined in the standards. In Fig. 4 the earth surface potential distributions, as well as touch voltage, and step voltage distributions along a diagonal of the grounding grid are shown respectively.

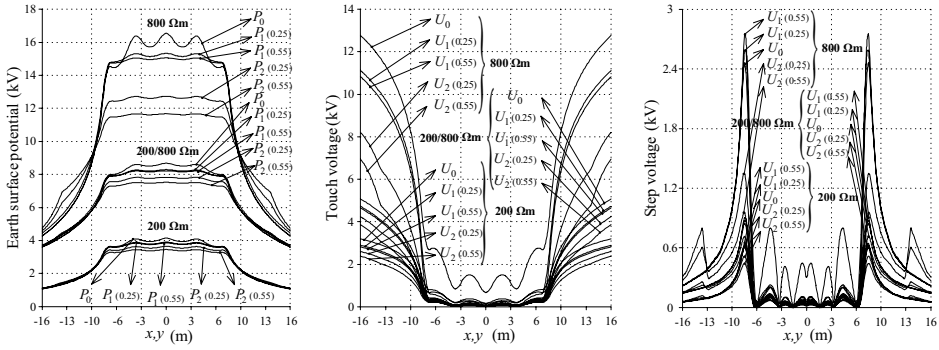

Fig. 4. Distribution of: a) earth surface potentials; b) touch voltages; c) step voltages along a diagonal of the grid for different volumes of soil layers impregnated with an additional substance in all three soil structure models.

Conclusion

The results of the analysis confirm the applicability of the grounding expedients in the immediate vicinity of the grounding grid, since an additional substance decreases the grounding resistance and the potential of grounding grid. Therefore, touch and step voltages are decreased as well. The decrease varies in a wide range, depending on soil structure characteristics and the volumes of soil layers impregnated with an additional substance. In this way much safer and effective protection against lightning or overvoltages in protection of people from injuries and buildings or devices from damage, as well as much more stable and safer operating conditions in electric power or communication systems, are also achieved. As mentioned above, the additional electrolytic substance can be applicable in technical manner for achieving small enough grounding resistances, as well as in economical manner for reduction of building expenses in construction of grounding systems.

References

[1] P. P. Silvester, R. L. Ferrari, *Finite Elements for Electrical Engineers*, Second edition, Cambridge, U.K., Cambridge University Press, 1991.

[2] A. Stochniol, "A general transformation for open boundary finite element method for electromagnetic problems", *IEEE Transactions on Magnetics*, vol. 28, no. 2, p.p. 1679-1681, March 1992.

[3] J. R. Cardoso, "FEM modeling of grounded systems with unbounded approach", *IEEE Transactions on Magnetics*, vol. 30, pp. 2893-2896, September 1994.

[4] V. C. Silva, N. M. Abe, A. Passaro, J. R. Cardoso, "A new line-element approach applied to 3D FEA of grounding systems", *7th International IGTE Symposium on Numerical Field Calculation in Electrical Engineering*, Proceedings, pp. 410-415, September 1996.

[5] M. Trlep, A. Hamler, B. Hribernik, "The analysis of complex grounding systems by FEM", *IEEE Transactions on Magnetics*, vol. 34, pp. 2521-2524, September 1998.

Electromagnetic Fields in Mechatronics, Electrical and Electronic Engineering
A. Krawczyk et al. (Eds.)
IOS Press, 2006

NEW ELECTROMAGNETIC ACTUATOR WITH MULTI-MOTION

Y. Hasegawa*, K. Hirata, H. Maeyoshi***, Y. Ishihara*** and T. Todaka*****

*Advanced Technologies Development Laboratory, Matsushita Electric Works, Ltd., 1048, Kadoma, Osaka 571-8686, Japan, hasegawa@ertc.mew.co.jp
** Department of Adaptive Machine Systems, Osaka University, Yamadaoka, 2-1, Suita-city, Osaka 565-0871, Japan, k-hirata@ams.osaka-u.ac.jp
***Department of Electric Engineering, Doshisha University, Kyotanabe, Kyoto 610-0321, Japan, yishihar@mail.doshisha.ac.jp

Abstract: ***In this paper, we propose an actuator system oscillating with both of linear and rotational motion at the same time. Static characteristics of the thrust and torque are computed using the 3-D finite element method (FEM). Furthermore, dynamic characteristics of amplitude and rotation angle are confirmed through the dynamic simulation and the measurement. Both results show good agreement.***

1. Introduction

In designing electromechanical devices, multi-dimensional movements have been usually accomplished by employing movement conversion gears in conjunction with traditional rotary motors. However, this movement conversion system has typically demonstrated unfavorable characteristics including significant vibration, noise, size constraints and limitations on operating speed. As a result, alternatives to the rotary and gears model to achieve multi-dimensional movements are a topic of great interest [1], [2], [3], [4].
This paper proposes a two-dimensional electromagnetic actuator system reciprocating along the linear and rotary directions. The operation of this actuator has been verified using the 3D-FEM [5] and a prototype model has been built and tested, demonstrating two-dimensional operation. The results of both dynamic simulation and measurement are in good agreement.

2. Basic Structure

Fig.1 shows the basic structure of the actuator, which mainly consists of mover, stator, and the resonance spring. The stator has three coils for linear and rotational motion. The mover has six ring-shaped magnets radially magnetized as shown in this figure, having four magnets at the top and bottom for linear motion and two magnets at the center for rotation. The stator has two couples of yokes; one is for linear motion, the other is for rotation. The magnetization of the magnet is 1.4 T. The gap length is 0.25 mm.

3. Operating Principle

3-1. Linear Motion

Fig.2 shows the operating principle of linear motion. When the coils are not excited, the magnetic flux by the magnet flows along the solid line, and the mover is balanced. After the coils are excited as shown in Fig.2 (a), the magnetic flux by the current flows along the dashed line. Then, the mover is forced to move by the attractive and repulsive forces shown in Fig.2 (b). This actuator can be reciprocated by changing the excitation direction.

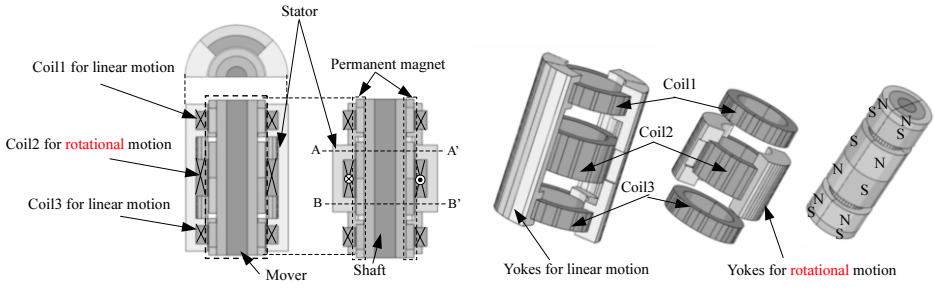

(a) cross-section of the actuator (b) mover and stator

Fig.1 Basic structure.

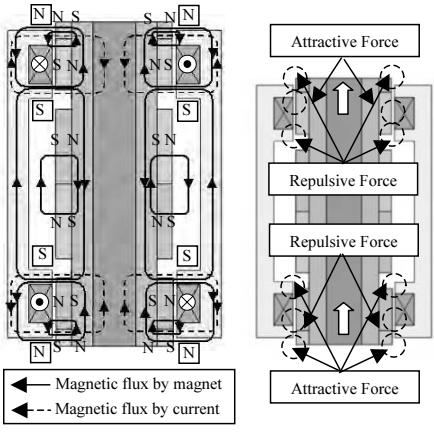

(a) flow of magnetic flux (b) generated force

Fig.2 Magnetic circuit for linear motion.

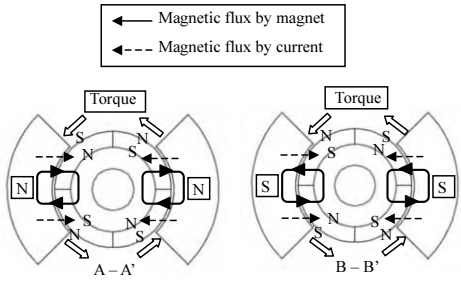

Fig.3 Magnetic circuit for rotation.

3-2. Rotation

Fig.3 shows the operating principle of rotation. Cross section of A-A' and B-B' is illustrated in Fig.1. When the coils are not excited, the magnetic flux by the magnet flows along the solid line, and the rotor is balanced. After the coils are excited as shown in this figure, the magnetic flux by the current flows along the dashed line. Then, the rotor is forced to rotate by the torque. This actuator can be rotationally reciprocated by changing the excitation direction.

4. Static Characteristics

4-1. Thrust Characteristics

Fig.4 shows the computed thrust characteristics employing the 3-D FEM as compared with measured ones when this actuator is operated by varying the mover position from –1.0 to 1.0 mm in steps of 0.2 mm. Both results show good agreement. It is found that this actuator has linear thrust characteristics between the stroke of -0.4 mm and 0.4 mm, and has the stable point at the stroke of 0.0 mm. The average thrust constant is 1.68 N/A.

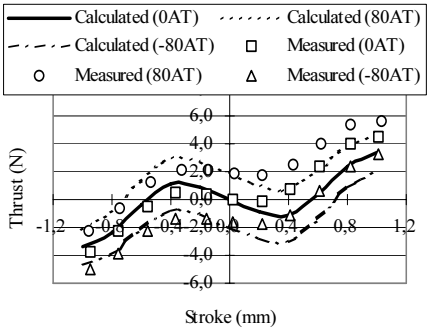

Fig.4 Comparison between measured and calculated thrust characteristics.

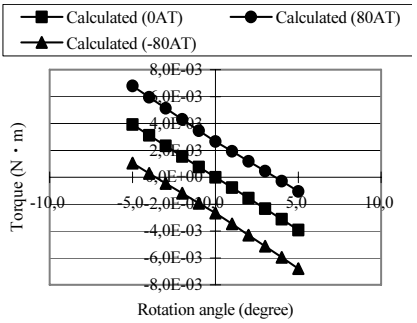

Fig.5 Torque characteristics.

Table 1 Analyzed conditions.

Applied voltage[V]			2.40
Rotar	Mass[g]		28.30
	Inertia[N・m・s^2]		3.44×10^{-7}
Coil	Number of turn[Turn]	Coil1	40
		Coil2	80
		Coil3	40
	Resistance[Ω]	Coil1	0.60
		Coil2	1.00
		Coil3	0.60
	L[μH]	Coil1	0.11
		Coil2	0.70
		Coil3	0.11

4-2. Torque Characteristics

Fig.5 shows the computed torque characteristics when this actuator is operated by varying the rotor position from –5.0 degree to 5.0 degree in steps of 1 degree. It is found that this actuator has linear torque characteristics between the rotation angle of –5.0 and 5.0 degree, and has the stable point at the rotation angle of 0.0 degree. The average torque constant is 2.78×10^{-3} N· m/A.

5. Dynamic Characteristic Analysis

The dynamic characteristics of the multi-motion are computed by coupling the motion equation and circuit equation employing Runge-Kutta Method [3].

$$E = V_0 - RI_0 - L\frac{dI_0}{dt} - \frac{d\Phi}{dt} = 0 \tag{1}$$

$$M\frac{d^2z}{dt^2} \pm F_s = F_z \tag{2}$$

$$I\frac{d^2\theta}{dt^2} \pm T_s = T_m \tag{3}$$

Where R is the resistance, L is the inductance of the coil, Φ is the magnetic flux by the magnet, M is the mass of the mover, F_s is the frictional force, F_z is the thrust obtained by 3-D FEM, I is the moment of the inertia, T_s is the friction and T_m is the torque obtained by 3-D FEM.

The analyzed conditions are shown in Table 1.

Figs.6 and 7 show the computed frequency characteristics of amplitude, rotation angle and average current for linear motion and rotation, respectively when the input voltage of 2.4 V is applied. It is found that this actuator has resonance frequencies of 210 Hz for linear motion and 265 Hz for rotation, and has the high quality factor. The average current almost keeps constant against the frequency change under the operation of rotation.

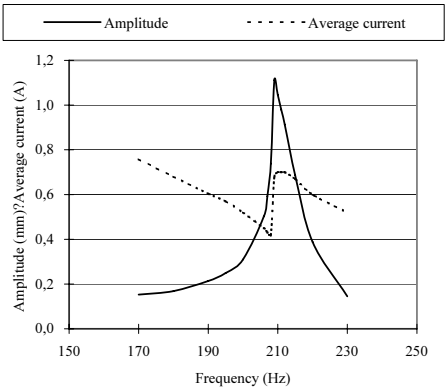

Fig.6 Computed frequency characteristics (linear motion).

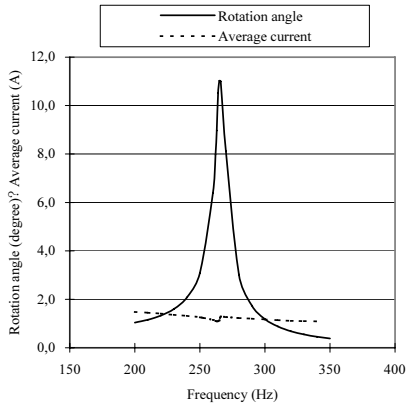

Fig.7 Computed frequency characteristics (rotation).

6.Measurement of Prototype

Figs.8 and 9 show the measured frequency characteristics of amplitude, rotation angle and average current for linear motion and rotation, respectively when the input voltage of 2.4 V is applied. It is found that this prototype has resonance frequencies of 220 Hz for linear motion and 260 Hz for rotation, and has the amplitude of 1.16 mm (peak to peak) and the rotation angle of 10.8 degree (peak to peak). The measured results are in good agreement with the calculated results mentioned above. The resonance spring is the common part for both rotation and linear motion. Next, the mutual influences between linear motion and rotation are investigated. Fig.10 shows the measured frequency characteristics of the amplitude and rotation angle when the operating frequency of linear motion is varied with the constant rotation frequency of 267 Hz. The influence of rotation on the amplitude is very small, but the rotation angle decreases when the operating frequency of linear motion

approaches resonance frequency. Fig.11 shows the measured frequency characteristics of the amplitude and rotation angle when the operating frequency of rotation is varied with the constant linear motion frequency of 221 Hz. The rotation angle of 3 degree increases because of rotation, but the amplitude of the linear motion is not influenced by the operating frequency. Fig.12 shows the computed and measured trajectory of the multi-motion (frequency of the linear motion is 221 Hz; frequency of the rotation is 267 Hz). Both results are in good agreement.

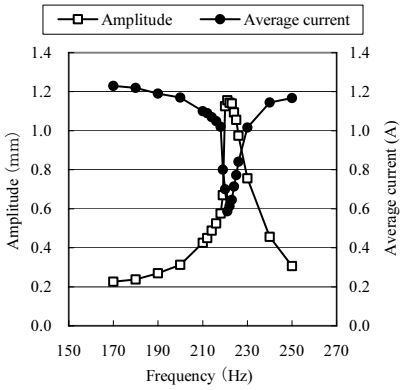

Fig.8 Measured frequency characteristics (linear motion).

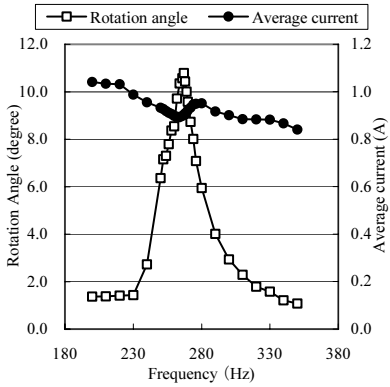

Fig.9 Measured frequency characteristics (rotation).

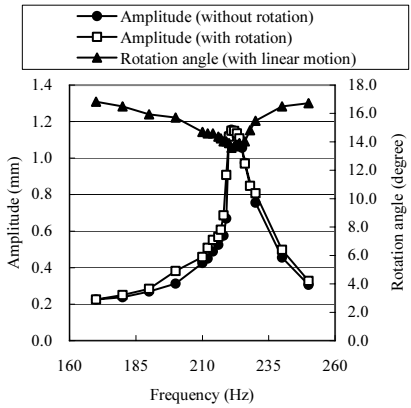

Fig.10 Mutual influences of linear motion frequency.

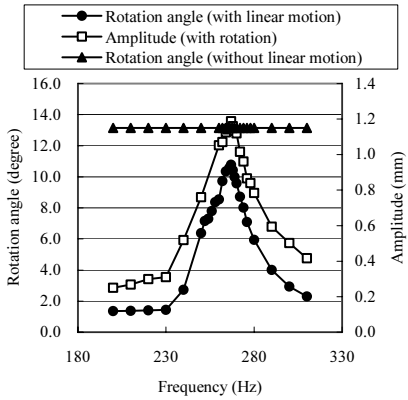

Fig.11 Mutual influences of rotation frequency.

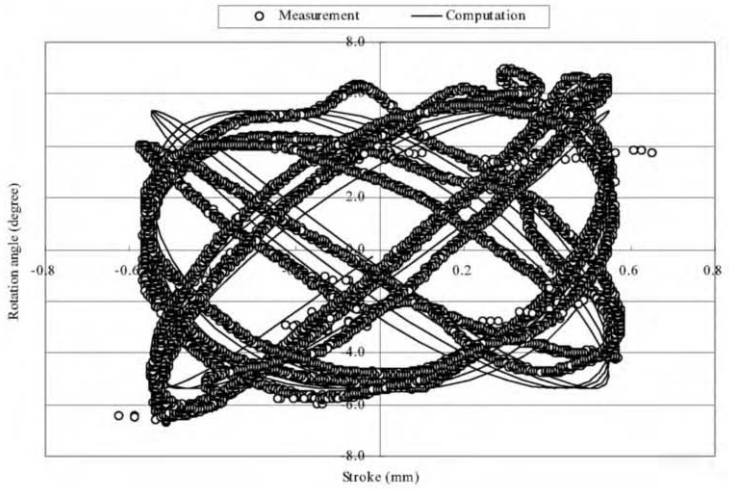

Fig.12 Trajectory of multi-motion.
(linear:221 Hz, rotation:267 Hz)

7. Conclusions

In this paper, we proposed an actuator system oscillating with both of linear and rotational motion at the same time. Static characteristics of the thrust and torque were computed using the 3-D finite element method (FEM). Furthermore, dynamic characteristics of amplitude and rotation angle were confirmed through the dynamic simulation and the measurement. Both results were in good agreement.

References

[1] K. Hirata and Y. Hasegawa: “An Application of Multi Dimensional Drive System (2) -An electromagnetic Actuator with Two-Degree-of-Freedom-”, Journal of the Japan Society of Applied Electromagnetics and Mechanics, Volume 12 Number 1, pp. 31-34 (2004).

[2] Y. Hasegawa and K. Hirata: “A Study on Electromagnetic Actuator with Two-Degree-of-Freedom”, IEEJ Trans. IA, Vol.125, No.5, pp.519-523, (2005).

[3] Y. Hasegawa, K. Hirata, Y. Mitsutake and T. Ota: “A Study on Actuator with Two-Degree-of-Freedom”, National Convention Record IEE Japan, No. 5076 (2003).

[4] T. Yano: “Actuators with Multi-Degree-of-Freedom”, Journal of the Robotics Society of Japan, Vol. 15, No. 3, pp. 330-333 (1997).

[5] Y. Kawase, T. Yamaguchi, H. Naito, M. Tanaka, Hasegawa and K. Hirata: “3D FEM coupled with the rotation and linear motion equations”, The Papers of Joint Technical Meeting on Static Apparatus and Rotating Machinery, IEE Japan, SA-04-24/RM-04-24 (2004).

Electromagnetic Fields in Mechatronics, Electrical and Electronic Engineering
A. Krawczyk et al. (Eds.)
IOS Press, 2006

SLIDING-SURFACE INTERFACE CONDITIONS AND FORCE CALCULATION FOR A LINEAR ACTUATOR DISCRETISED BY THE FINITE INTEGRATION TECHNIQUE

Mariana Ion, Herbert De Gersem, Thomas Weiland

Technische Universität Darmstadt, Institut für Theorie Elektromagnetischer Felder,
Schloßgartenstraße 8, D-64289 Darmstadt, Germany,
ion/degersem/thomas.weiland@temf.tu-darmstadt.de

***Abstract** – The fixed and the moving part of a linear actuator are discretised by the Finite Integration Technique (FIT) at two independent Cartesian grids. Both parts are coupled at a common surface (sliding surface) in the middle of the air gap. Two coupling techniques are compared: locked-step interpolation and linear interpolation. A comparison of the generated forces calculated with the Maxwell stress tensor and by a local analytical solution carried out by 2D Fast Fourier Transforms is presented.*

Introduction

Three dimensional models are important for many machine configurations when a 2D plane is not sufficient, e.g. for disk-type electrical machines. When it is necessary to calculate the model with a relative displacement between stator and rotor, it is convenable to use 2 separate meshes coupled through a common interface. In this way the two meshes can be moved relatively one from another in tangential direction at the contact surface. Examples are electrical machines and actuators. In this paper only actuators with linear motion are considered.

The fixed and the moving parts of a linear actuator are discretised at two independent, Cartesian grids by the Finite Integration Technique (FIT) [1]. Such approximation of 3D models coupling has been proposed in [2] and [3]. Fig. 1a) presents the model, where the fixed armature is considered to be the master part and the moving armature is the slave part of the model. The slave part can be displaced in x and z-direction, but not in the y-direction. This approach allows considering displacement without remeshing the models, which leads to a reduction of computation time especially in the pre- and post-processing phase, but necessitates the numerical coupling of the degrees of freedom at the interface between both model parts. The degrees of freedom (DOFs) at the slave side of the interface will be interpolated from the corresponding DOFs allocated at the master side of the interface.

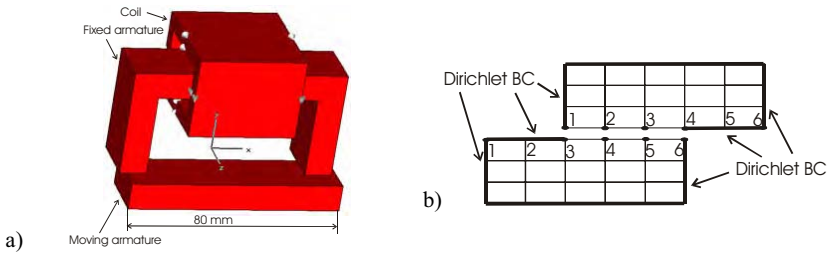

Fig.1 Linear actuator a) and test example with boundary conditions b)

In [4] three coupling techniques are compared for a rotating machine modelled in cylindrical coordinates: the locked-step approach, linear interpolation and trigonometric interpolation. The mesh at the interface is equidistant in both tangential directions. The locked-step interpolation is only exact for a rotation with a multiple of the mesh angle. The linear and trigonometric interpolations are more flexible and allow an arbitrary rotation angle.

Interface Coupling Techniques

A master mesh that contains the fixed armature and excitation coil and a slave mesh that contains the mobile armature are connected at a common plane situated in the middle of the air gap. A magnetoquasistatic formulation based on the magnetic vector potential $\vec{A}$ is used:

$$\nabla \times (\nu \nabla \times \vec{A}) = \vec{J}\,, \tag{1}$$

where $\vec{J}$ is the current density applied in the coil and ν is the reluctivity. The partial differential equation (1) is discretised at a dual-orthogonal grid pair $\{G, \tilde{G}\}$. The fields are represented by integrals over simplices. As quantities in the simulation, the vectors $\hat{a}$ and $\hat{\tilde{j}}$ which are integrals of $\vec{A}$ and $\vec{J}$ over edges of G and facets of $\tilde{G}$ respectively, are used. The coefficients ν are combined with metric information in a diagonal material matrix M_ν [1]. The discretisation of (1) by the FIT reads:

$$\underbrace{\tilde{C} M_\nu C}_{K} \hat{a} = \underbrace{\hat{\tilde{j}}}_{f}\,, \tag{2}$$

with C and $\tilde{C}$ the curl matrices at G and $\tilde{G}$ respectively. The magnetic flux is kept within the model, which corresponds to the application of Dirichlet boundary conditions (BCs) at the model boundaries. Due to the relative displacement, additional boundaries appear at which also Dirichlet BCs are applied (Fig. 1b).

For *locked-step interpolation* the grid is discretised equidistantly. At the sliding surface, the magnetic vector potential distribution at the slave side is brought into correspondence with the field distribution at the master side by:

$$\hat{a}_{slv,p} = k_{shift}^{[\Delta s / \Delta h + 0.5]} \hat{a}_{mst,p}\,. \tag{3}$$

Here, $\hat{a}_{slv,p}$ are the unknowns allocated at a set s_p of edges tangential to the slave side of the interface and $\hat{a}_{mst,p}$ are line-integrated magnetic vector potentials allocated at a set of edges tangential to the master side of the interface (Fig. 2). The set of edges s_p contains all edges at a certan position $q \in \{z, x\}$ perpendicular to the direction of motion $s \in \{x, z\}$. The interpolation is carried out for all sets independently. Δs represents the distance of the translation, Δh is the distance between two adjacent grid lines and the operator [] takes the integer part of a real number. The shift operator k_{shift}, for the displacement reported in Fig. 1b) (6 grid lines on the model in the coupling direction, $\Delta s = 2\Delta h$) with Dirichlet BCs, for the uncoupled nodes at the slave side, is the Toeplitz matrix:

$$k_{shift}^{[2+0.5]} = \begin{bmatrix} 0 & 0 & 1 & 0 & 0 & 0 \\ 0 & 0 & 0 & 1 & 0 & 0 \\ 0 & 0 & 0 & 0 & 1 & 0 \\ 0 & 0 & 0 & 0 & 0 & 1 \\ 0 & 0 & 0 & 0 & 0 & 0 \\ 0 & 0 & 0 & 0 & 0 & 0 \end{bmatrix}. \tag{4}$$

The locked-step interpolation has restricted possibilities of relative movement and imposes constraints to the mesh but does not require interpolation and therefore preserves the maximal accuracy attained by the FIT models.

In order to have more flexibility and in order to eliminate geometrical limitations to the mesh, the DOFs at the slave side of the interface are *interpolated* from the DOFs at the master side of the interface. Then, slave nodes can be situated between master nodes and a uniform grid meshing at the interface plane is not necessary.

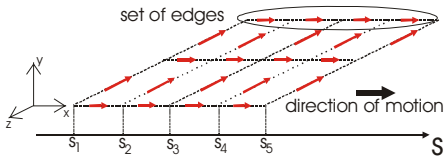

Fig.2 Set of edges

The *linear interpolation* between slave and master DOFs corresponds to:

$$\hat{a}_{slv,p} = k_\varepsilon k_{shift}^{[\Delta s/\Delta h]} \hat{a}_{mst,p}, \tag{5}$$

where $[\Delta s/\Delta h]$ represents the integer part of the displacement and $\varepsilon = \Delta s/\Delta h - [\Delta s/\Delta h]$ is the fractional part of the displacement between the standstill and the moving part, for the case of an equidistant mesh. In the case of a non-equidistant mesh, the $\{x_{1m}, x_{2m,}..., x_{nm}\}$ are the coordinates of the master grid lines in the *x*-direction and $\{x_{1s}, x_{2s,}..., x_{ns}\}$ are the coordinates of the slave grid lines in the *x*-direction. Then, the fractional displacement for the node i is defined as: $\varepsilon_i = (x_{js} - x_{im})/(x_{(i+1)m} - x_{im})$, where *j* is the node at the slave side situated between nodes i and $i+1$ at the master side. In this case, the interpolation operator k_ε, for the situation depicted in Fig. 3a), with Dirichlet BCs, reads:

$$k_{\varepsilon} = \begin{bmatrix} 1-\varepsilon_1 & \varepsilon_1 & 0 & \dots & 0 \\ 0 & 1-\varepsilon_2 & \varepsilon_2 & \dots & 0 \\ \dots & \dots & \dots & \dots & \dots \\ 0 & \dots & 0 & 1-\varepsilon_{n-1} & \varepsilon_{n-1} \\ 0 & \dots & 0 & 0 & 1-\varepsilon_n \end{bmatrix}. \tag{6}$$

The interpolation method connects each DOF at the slave grid to the neighbouring DOFs at the master side (Fig. 3a). For the *z*-direction, the interpolation procedure is similar.

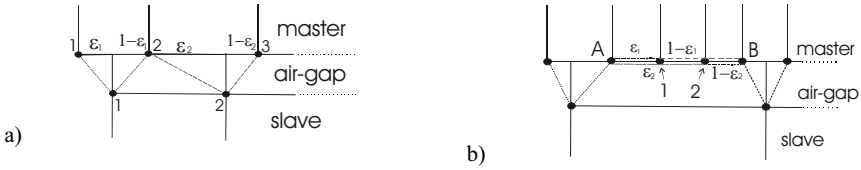

Fig.3 Linear interpolation for non-equidistant mesh a) and dangling nodes b)

In the case of a non-equidistant and highly non-uniform mesh, a staggered distribution of the master and slave grid lines as reflected by two-diagonal structure of (6) is not longer guaranteed. Then, the interpolation operator is unstructured but remains sparse. Moreover, in this general case, dangling nodes can occur: some of the nodes at the master side remain uncoupled with the slave nodes (Fig. 3b). Such DOFs will automatically experience natural BCs, which in this case are "magnetic BCs" and correspond to a boundary with an infinite permeability. This would cause large and unphysical magnetic fluxes at those boundary parts. To overcome this, the DOFs for those nodes are linearly interpolated from DOFs of neighbouring coupled nodes. In this way some nodes found at the master grid are transformed into slave nodes. The decoupled system of equation obtained by discretising both FIT models independently reads:

$$\underbrace{\begin{bmatrix} K_{mst} & 0 \\ 0 & K_{slv} \end{bmatrix}}_{K} \underbrace{\begin{bmatrix} \hat{a}_{mst} \\ \hat{a}_{slv} \end{bmatrix}}_{\hat{a}} - \underbrace{\begin{bmatrix} \hat{\hat{j}}_{mst} \\ \hat{\hat{j}}_{slv} \end{bmatrix}}_{\hat{\hat{j}}} = \underbrace{\begin{bmatrix} f_{mst} \\ f_{slv} \end{bmatrix}}_{f}, \tag{7}$$

where K_{mst} and K_{slv} are stiffness matrices, $\hat{a}_{mst}$ and $\hat{a}_{slv}$ are unknowns at the interface, f_{mst} and f_{slv} are the right hand side, $\hat{\hat{j}}_{mst}$ and $\hat{\hat{j}}_{slv}$ are surface currents at the sliding surface, which represents the influence of both models upon each other. The vector of line-integrated magnetic vector potentials $\hat{a}$ does not obey the sliding-surface interface conditions. The interpolation procedure described above is equivalent to a projection $\hat{a}_{proj} = P\hat{a}$ upon the vector satisfying the sliding-surface interface conditions. As explained in [5], the surface current $\hat{\hat{j}}_{surf}$ vanish under the projection by P^T, i.e., $P^T \hat{\hat{j}}_{surf} = 0$. The coupled system to be solved is:

$$P^H K P u = P^H f\,. \tag{8}$$

Force Calculation

On the FIT grid, the components B_x, B_y and B_z of the magnetic field density are allocated at facets of the grid (Fig. 4a). These have to be interpolated upon a common set of facets in order to use the classical *Maxwell* stress tensor approach:

$$T_{ij} = \frac{1}{4\pi}\left[B_i B_j - \frac{1}{2}\delta_{ij} B^2 \right]; \qquad F = \oint_S T_{ij} dS \ . \tag{9}$$

The classical Maxwell stress tensor approach requires all three components of B available in a number of integration points, for example in the points where B_y is defined. These points are located on the primary faces, which coincide with the integration plane.

The results of the simulations are the line-integrated magnetic vector potentials a. From a, the area integrated magnetic flux density vector b is obtained by $b = C\tilde{a}$. This vector is discomposed in the components b_x, b_y and b_z, from which B_x, B_y and B_z are obtained by dividing through the facet areas. The components B_x and B_z are brought at the same position as B_y by bilinear interpolation. In the case of an equidistant grid, the force can be calculated at the interface using 2D Fast Fourier Transforms. For calculating the force, the field is discomposed in its Fourier coefficients, the Maxwell stress tensor constructed and the interpolation is carried out analytically. In practice, the process consists of the identification of the coefficients $a_{\lambda,\xi}$ and $b_{\lambda,\xi}$ of a semi-analytical solution for the magnetic scalar potential calculated between two mesh planes situated in the air gap region (Fig. 4b):

$$\Psi(x,y,z) = \sum_{\lambda}\sum_{\xi} \mathrm{e}^{j\lambda x}\mathrm{e}^{j\xi z}\left(a_{\lambda,\xi}\cosh(\zeta y) + b_{\lambda,\xi}\sinh(\zeta y)\right), \tag{10}$$

where $\lambda = 2\pi(i-1)/Tx$, $= 2\ (k-1)/Tz$ and $\zeta = \sqrt{\lambda^2 + \xi^2}$. T_x and T_z are the model dimensions in the and z-direction and i and k are the harmonic orders. Equation:

$$\vec{B} = (B_x, B_y, B_z) = \left(-\mu_0 \frac{\partial \Psi}{\partial x}, -\mu_0 \frac{\partial \Psi}{\partial y}, -\mu_0 \frac{\partial \Psi}{\partial z} \right) \tag{11}$$

is evaluated at two distinct planes in the air-gap: $y = 0$ and $y =$ and are written as function of Fourier coefficients $d_y(i,k)$ (Fig. 4b):

$$B_y(i,k) = \sum_{\lambda}\sum_{\xi} d_y(i,k) e^{j\lambda x} e^{j\xi z} \ . \tag{12}$$

These Fourier coefficients $a_{\lambda,\xi}$ and $b_{\lambda,\xi}$ are identified from the Fourier coefficients $d_{y=0}$ for the magnetic flux densities B_y at the plane $y=0$ and from the Fourier coefficients $d_{y=\delta}$ for the plane $y=\delta$:

$$b_{\lambda.\xi} = -\frac{d_{y=0}}{\mu_0 \zeta}\ , \quad a_{\lambda,\xi} = -\frac{d_{y=\delta}}{\mu_0 \zeta \sinh(\zeta\delta)} - \frac{b_{\lambda,\xi}\cosh(\zeta\delta)}{\sinh(\zeta\delta)}\ . \tag{13}$$

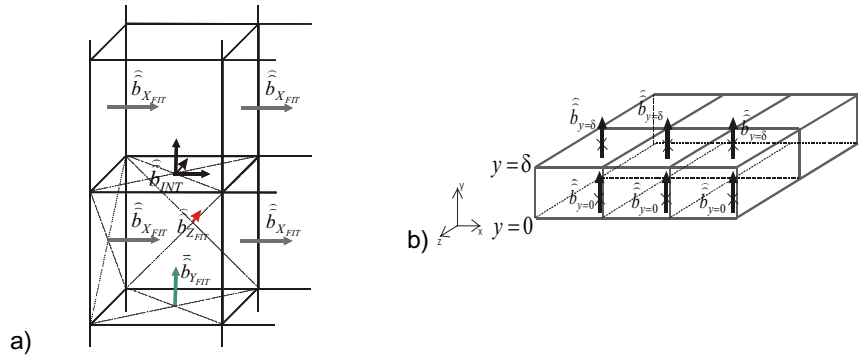

Fig.4 Magnetic flux density vector applied in FIT and interpolated a) and analytical model domain b)

The Maxwell stress tensor is then integrated analytically. The integration requires local values of the tangential and normal values of $\vec{B}$ [6]. In integral form, the equations are

$$F_t = \frac{1}{\mu_0}\int_0^{T_x}\int_0^{T_z} B_n^* B_t \, dx dz\ , \qquad F_n = \frac{1}{2\mu_0}\int_0^{T_x}\int_0^{T_z}\left(B_n B_n^* - B_t B_t^*\right) dx dz\ . \tag{14}$$

To apply Fast Fourier Transforms, a periodic field is necessary. Due to the fact that the model is not periodic, the magnetic field must be mirrored. In this way, the number of points is increased by four. The Maxwell stress tensor is integrated in the *x* and *z*-direction only at a quarter of the domain:

$$F_x = \sum_{\lambda}\sum_{\xi}\sum_{\lambda'}\sum_{\xi'} j\mu_0 \lambda a_{\lambda,\xi}\zeta' b^*_{\lambda',\xi'} \int_0^{Tx/2} e^{j(\lambda-\lambda')x} dx \int_0^{Tz/2} e^{j(\xi-\xi')z} dz\ , \tag{15a}$$

$$F_z = \sum_{\lambda}\sum_{\xi}\sum_{\lambda'}\sum_{\xi'} j\mu_0 \xi a_{\lambda,\xi}\zeta' b^*_{\lambda',\xi'} \int_0^{Tx/2} e^{j(\lambda-\lambda')x} dx \int_0^{Tz/2} e^{j(\xi-\xi')z} dz\ . \tag{15b}$$

In case of a periodic model, the sums can be simplified up to:

$$F_y = \frac{1}{4}\sum_{\lambda}\sum_{\xi}\frac{1}{2}\mu_0\left(\zeta^2 b_{\lambda,\xi} b^*_{-\lambda,-\xi} - \lambda^2 a_{\lambda,\xi} a^*_{-\lambda,-\xi} - \xi^2 a_{\lambda,\xi} a^*_{-\lambda,-\xi}\right) TxTz\ . \tag{15c}$$

The force calculation with Fast Fourier Transform must be carried out on an equidistant mesh. For a non-equidistant mesh of the model, the force can be interpolated on a virtual equidistant grid.

The magnetic flux for a displaced actuator is presented in Fig. 5a). A comparison was made between the generated forces calculated both by the Maxwell Stress Tensor and the Maxwell Stress Tensor approach with Fast Fourier Transform for a displacement of the mobile armature in the *x*-direction (Fig. 5b).

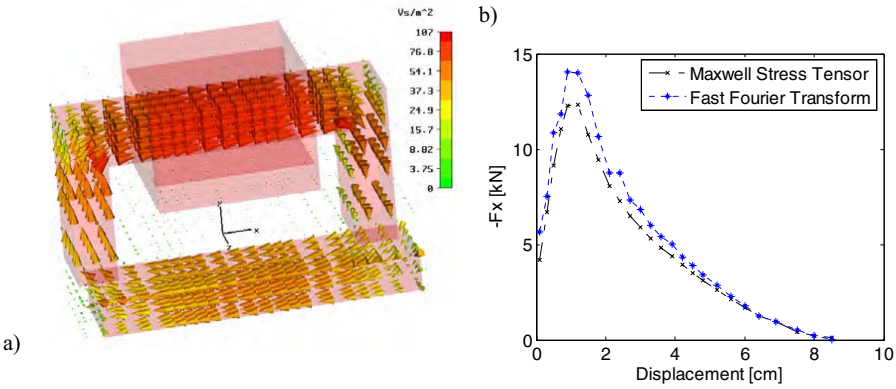

Fig.5 Magnetic field in a displaced actuator a) and force comparison b)

Conclusion

Two independent meshes are used for calculating electromagnetic devices with moving parts. Then, the mesh has to be generated just once, which speeds up the calculation process. The two meshes have a common interface, at which the degrees of freedom are coupled. Both the locked-step approach and a technique with linear interpolation are implemented. Coupling anomalies, such as dangling nodes on the master side require a special treatment.

Supplementary to the classical Maxwell stress tensor force formulation, an alternative Maxwell stress tensor approach is proposed. A semi-analytical solution of the magnetic scalar potential function is determined from the numerical results in a fraction of the air gap. The alternative procedure based on the discrete and therefore requires that the magnetic field is periodic. A non-periodical magnetic field is made periodical by mirroring. For the alternative integration of the Maxwell stress tensor approach, four imbricate sums substantially decrease the computational efficiency of the method (Eq. 15a,b).

References

[1] T. Weiland, A discretisation method for the solution of Maxwell's equations for six-component fields, AEÜ, vol. 31, pp 116-120, 1977

[2] H. C. Lai, D. Rodger and P. J. Leonard, Coupling meshes in 3D problems involving movements, IEEE Transactions on Magnetics, vol.28, no.2, March 1992.

[3] R. Perrin-Bit, J. L. Coulomb, A three dimensional finite element mesh connection for problems involving movement, IEEE Transactions on Magnetics, vol.31, no.3, May 1995.

[4] M. Ion, H. De Gersem, M. Wilke and T. Weiland, Sliding-surface interface conditions for 3D machine models discretised by the Finite Integration Technique, ICEM 2004, Cracow, Poland, September 5-8, 2004.

[5] H. De Gersem, M. Wilke, M. Clemens, T. Weiland, Efficient modelling techniques for complicated boundary conditions applied to structured grids, COMPEL, vol.23, pp. 904-912, October 2004.

[6] R. Mertens, U. Pahner, K. Hameyer and R. Belmans, Force calculation based on a local solution of Laplace's equation, IEEE Transactions on Magnetics, vol.33, no.2 1997.

Electromagnetic Fields in Mechatronics, Electrical and Electronic Engineering
A. Krawczyk et al. (Eds.)
IOS Press, 2006

A NEW CONTROL-ORIENTED MODELING METHODOLOGY FOR A SERIES DC MOTOR

Krzysztof J. Latawiec,[†] Czesław Marciak,[†] Gustavo H.C. Oliveira[‡]

[†] Dept. El. Engrg. and Automatic Control, Opole University of Technology, Opole, Poland; lata@po.opole.pl
[‡] *PPGEPS/CCET/PUCPR*, Curitiba, Brazil; gustavo.oliveira@pucpr.br

***Abstract** - This paper presents a new, control-oriented, nonlinear modeling methodology for a series DC motor. Orthonormal basis functions are effectively employed in a nonlinear, block-oriented systems approach to provide a computationally efficient strategy for adaptive identification of the motor under highly demanding, nonlinear time-varying operating conditions.*

1. Introduction

Modeling (and control) of nonlinear dynamical systems may present, in general, a real computational and numerical challenge. Seeking for computational simplicity usually demanded in adaptive control applications, we have turned our attention to modeling of the so-called nonlinear 'block-oriented' systems [8] and a number of new effective results have been obtained [4-7].

Nonlinear block-oriented systems basically involve Wiener, Hammerstein and feedback-nonlinear systems [8]. Simple structures of nonlinear Wiener and Hammerstein models make them attractive in control applications [3-8]. Therefore, Wiener and Hammerstein systems as well as more challenging feedback-nonlinear systems have been given a considerable research interest (see [3-8] and references therein). However, many elegant estimation methods are computationally involving and can hardly be used in the adaptive control environment, especially for 'fast' systems requiring frequent sampling. This also concerns the interesting techniques involving the inverse static nonlinearity [8], still suffering from the bilinearity problem. Recently, an attractive, adaptive least-squares, Wiener modeling method has been introduced [4,7], which employs the inverse static nonlinearity concept combined with orthonormal basis functions (OBF) in order to separate linear and nonlinear submodels to get rid of the bilinearity issue. On the other hand, it turns out that employing our new *inverse OBF* model concept [4-7] to a linear dynamic part of both Hammerstein and feedback-nonlinear models can, again, lead to submodel separation in the linear parameter estimation problem. We emphasize the capital role of *separation* of linear and nonlinear submodels in effective, bilinearity-free, OBF-based modeling of nonlinear block-oriented systems [4-7].

For illustration of our new, OBF-based, nonlinear modeling methodology we have chosen a challenging electromechanical system, which is a series DC motor. Problems in modeling and control of a series DC motor as a nonlinear system have been given a remarkable research interest [1,2,7]. Up-to-date results, which will be referred to as to a 'conventional' model of the motor [1,2], have all been based on the assumption that the load torque of the motor is constant and linearly dependent on the angular speed. The assumption has led to relatively simple modeling and control strategies for the motor. However, some applications, to mention "cruise control" for electric cars, may motivate a more sophisticated approach to the modeling task, in which the load torque is admitted to be time-varying and nonlinearly dependent on the angular speed. Such a challenging problem is tackled and effectively solved here via OBF-based, nonlinear block-oriented models. It is essential that incorporating the

time-varying and nonlinear effects into the conventional model of the motor would be extremely difficult, if feasible at all.

2. OBF-Based Modeling of Nonlinear Block-Oriented Systems

2.1. Wiener System

In a single-input single-output Wiener system, a linear dynamic part is cascaded with a nonlinear static element. The discrete-time output $y(t)$ can be expressed as $y(t)=f[G(q)u(t)+e_W(t)]$, where f is a nonlinear function, the transfer function $G(q)$ (in the shift operator q) models a linear part and $e_W(t)$ is the error/disturbance term. Under the standard assumptions [3,4], the output $\hat{y}(t)$ of the Wiener model, or the system output predictor, can be calculated as [4-7]

$$\hat{y}(t) = \hat{f}[\hat{G}(q)u(t)] \tag{1}$$

where the estimate of a transfer function of a linear part is given in terms of an OBF model $\hat{G}(q) = \sum_{i=1}^{M} c_i L_i(q)$, with $L_i(q)$ and c_i, $i=1,\ldots,M$, being orthonormal basis functions (or filters) and weighting parameters (to be estimated), respectively [4-7]. Advantages of using OBF, in particular simple Laguerre functions, have been widely documented both for linear and nonlinear systems [4-7].

Since a nonlinear static characteristic is assumed invertible we can rewrite equation (1) in form

$$\hat{f}^{-1}[\hat{y}(t)] = \hat{G}(q)u(t) \tag{2}$$

When using the output error-structured OBF model, unlike with ARX, the linear and nonlinear submodels are thus separated from each other, which contributes to essential computational savings.

The function $\hat{f}^{-1}[\hat{y}(t)]$ can be approximated with e.g. a polynomial expansion

$$\hat{f}^{-1}[\hat{y}(t)] = \hat{a}_1\hat{y}(t) + \hat{a}_2\hat{y}^2(t) + \ldots + \hat{a}_m\hat{y}^m(t) \tag{3}$$

It is worth mentioning that the approximation with e.g. cubic spline functions or radial basis neural networks may sometimes be more useful in case of specific forms of the inverse nonlinear function $\hat{f}^{-1}[\hat{y}(t)]$. Still, polynomial expansion approximation is often used in practice [4].

Without loss of generality, the leading coefficient can be put equal to unity. In fact, the gain of a linear contributor to the polynomial approximation can be estimated from a linear dynamic part of the Wiener model. Combining equations (2) and (3) while replacing, in the standard manner, parameter estimates with parameters themselves and the model output with the system output itself (wherever appropriate) we arrive at the linear regression function [4-7]

$$\hat{y}(t) = \sum_{i=1}^{M} c_i L_i(q^{-1})u(t) - \sum_{j=2}^{m} a_j y^j(t) \tag{4}$$

which can be presented in the familiar form $\hat{y}(t) = \boldsymbol{\varphi}^{\mathrm{T}}(t)\boldsymbol{\theta}$, with $\boldsymbol{\theta}^{\mathrm{T}} = [c_1\ c_2\ \ldots\ c_M\ a_2\ a_3\ \ldots a_m]$ and $\boldsymbol{\varphi}^{\mathrm{T}}(t) = [v_1(t)\ v_2(t)\ \ldots\ v_M(t)\ -y^2(t)\ -y^3(t)\ \ldots -y^m(t)]$, where $v_i(t)=L_i(q^{-1})u(t)$, $i=1,\ldots,M$, with q^{-1} being the backward shift operator. The unknown parameter vector $\boldsymbol{\theta}$ can now be easily estimated using e.g. *linear* regression tools.

Recall that in case of a similar, ARX-based Wiener modeling approach of Janczak [3], facing the bilinearity issue (that is *products* of parameters of *linear* and *nonlinear* parts unnecessarily appear in $\boldsymbol{\theta}$), a large number of parameters have to be estimated, of which only a part is finally utilized in the ARX-based model (1) of the Wiener system. In fact, the remaining parameters are 'needlessly'

estimated, thus increasing dimensions of the covariance matrix and so the variance error of a parameter estimator. In contrast, essentially lower number of parameters have to be estimated in the output error-related model of the OBF-structured Wiener system, and all these estimates are included in the model (1) [4-7]. Moreover, numerical conditioning of the OBF-based Wiener estimation problem is essentially better than that for the ARX-based one [4,7].

2.2. Hammerstein System

In the Hammerstein system, a nonlinear static part is cascaded with a linear dynamic element. The discrete-time output of the system can be given as $y(t)=G(q)[f(u(t))+e_H(t)]$, where $e_H(t)$ is the error/disturbance term. Assuming e.g. a polynomial approximation of the nonlinear part, the output $\hat{y}(t)$ of the Hammerstein model can be expressed as [4-7]

$$\hat{y}(t) = \hat{G}(q) \sum_{i=1}^{m} a_i u^i(t) \tag{5}$$

which can be rewritten in terms of the inverse OBF model [4-7]

$$\hat{G}^{-1}(q)\, \hat{y}(t) = \sum_{i=1}^{m} a_i u^i(t) \tag{6}$$

thus obtaining the *separation* of linear and nonlinear submodels.

Without loss of generality, the coefficient a_1 can, again, be put equal to unity. One can immediately bring equation (6) to the inverse OBF-related form $\hat{y}(t) = \boldsymbol{\varphi}^T(t)\boldsymbol{\theta}$, where $\boldsymbol{\theta}^T = [c_1 \ldots c_M\, \alpha_1 \ldots \alpha_m]$ and $\boldsymbol{\varphi}^T(t) = [-v_1 \ldots -v_M\, u(t\text{-}d)\; u^2(t\text{-}d) \ldots u^m(t\text{-}d)]$, with $v_i(t)=L_i(q^{-1})y(t)$, $i=1,\ldots,M$, and $\alpha_1 = r_0^{-1}$, $\alpha_i = r_0^{-1} a_i$, $i=2,\ldots,m$, where r_0 is the leading coefficient of $R(q)= \hat{G}^{-1}(q)$. Notice how the bilinearity involved in e.g. ARX-based Hammerstein modeling [8], or even OBF-based modeling [7], is avoided here thanks to the separation resulting from our *inverse* OBF approach. Again, this can offer essential computational savings and higher performance in terms of lower variance errors. The above inverse OBF-based method constitutes a new, effective analytical solution to the parameter estimation problem for the Hammerstein system.

2.3. Feedback-Nonlinear System

When the output from a linear dynamic block is fed (negatively) back through a nonlinear static element $f(.)$ we have $y(t)=G(q)[u(t)-f(y(t))+e_F(t)]$, where $e_F(t)$ is the error/disturbance term. Modeling and estimation of feedback-nonlinear systems is a real challenge. It is well known that without certain, sometimes unrealistic assumptions it is not possible to accurately reconstruct properties of the two blocks from input-output measurements only [8]. For example, an assumption on knowledge of a gain of the linear subsystem enables to estimate parameters of models of the two blocks. The problem is that such a knowledge is rather seldom available. Here we present a new, effective, inverse OBF-based solution to the problem of modeling and estimation of feedback-nonlinear systems.

The system model output is [4,7]

$$\hat{y}(t) = \hat{G}(q)\,[u(t) - f(\hat{y}(t))] \tag{7}$$

or, employing the inverse OBF approach and assuming e.g. the polynomial approximation

$$R(q)\hat{y}(t) = u(t) - \sum_{i=1}^{m} a_i\, y^i(t) \tag{8}$$

thus yielding, again, the *separation* of linear and nonlinear components of the model. However, the problem still remains how to discriminate between the gains of the two blocks (or between the parameters weighting $y(t)$ or $\hat{y}(t)$ at the two sides of equation (8)). One possible specific solution is to exclude a linear component from the polynomial approximation. Then we can arrive at the linear regression framework and, under the inverse OBF-based modeling approach, we have $\hat{y}(t) = \boldsymbol{\varphi}^T(t)\boldsymbol{\theta}$ where $\boldsymbol{\theta}^T = [c_1 \ ... \ c_M \ \alpha_0 \ \alpha_2 \ ... \ \alpha_m]$ and $\boldsymbol{\varphi}^T(t) = [-v_1 \ ... -v_M \ \ u(t\text{-}d) \ -y^2(t\text{-}d) \ ... \ -y^m(t\text{-}d)]$, with $\alpha_0 = r_0^{-1}$, $\alpha_i = r_0^{-1} a_i$, $i=2,\ldots,m$, and v_i's driven by $y(t)$. The exclusion of the linear component might be motivated by possible (indirect) presence of $y(t\text{-}d)$ in the inverse OBF-related part of the regressor (or direct presence when FIR is employed). However, such a solution was found in our simulations not to provide a sufficient estimation accuracy and the reason is the aforementioned inability to discriminate between the gains of the two blocks.

Another solution, which we advocate here, is to fix the linear gain parameter a_1 of the nonlinear block to some constant value. Then we can easily obtain

$$y(t) + \alpha_1 y(t-d) = \hat{y}(t) + r_0^{-1} e_F(t) \tag{9}$$

with $\hat{y}(t)$ as above. With properly fixed a_1 (or $\alpha_1 = r_0^{-1} a_1$), parameter estimation accuracy was found in simulations very high. However, the assessment of a correct α_1 may be an issue, at least in on-line identification experiments. Possible trial and error assessments may be burdensome. We suggest to off-line estimate α_1 using a standard minimization procedure based on e.g. the least squares criterion and then to fix α_1 to the obtained value, even in adaptive estimation schemes under time-varying parameters. The procedure for the assessment of a proper fix to α_1 can be essentially simplified, with still increased estimation accuracy for $\hat{\alpha}_1$, when an identification experiment with a low-range input signal is feasible, in which case only the linear mode of a plant is excited. In such a case the problem size can be reduced (all nonlinear components can be neglected).

3. Conventional Model of the Series DC Motor

Under simplifying assumptions, a nonlinear model of a series DC motor is usually presented in a state-space form [1,2]

$$\begin{aligned} \dot{x}_1 &= -\frac{D}{J} x_1 + \frac{K_m L_f}{J} x_2^2 - \frac{\tau_L}{J} \\ \dot{x}_2 &= -\frac{K_m L_f}{L} x_1 x_2 - \frac{R}{L} x_2 + \frac{1}{L} u \end{aligned} \tag{10}$$

where $x_1=\omega$, $x_2=I$, u and τ_L are the angular speed, motor current, input voltage and load torque, respectively, D is the viscous-friction coefficient, J is the mass moment of inertia, K_m is the torque/back EMF constant, $R = R_a+R_f$ and $L = L_a+L_f$ are the resistance and inductance of the equivalent circuit, with the subindices 'a' and 'f' related to the armature and field windings, respectively.

Assuming that the load torque is constant (and linearly dependent on x_1), effective, single-loop, speed control strategies have been proposed on a basis of the model (10) [1,2].

4. New Model Concepts for Nonlinear Adaptive Control

However, those classical modeling and control strategies may be inefficient when the load torque is time-varying and nonlinear vs. the speed. In such a case, the motor current can be used as a measurable disturbance in order to quickly detect possible changes in the load torque. Thus, a two-loop, cascade control strategy can be proposed according to Fig. 1. The main, speed controller C1

would then produce a reference signal for the auxiliary, current controller C2. The problem is to model the two nonlinear parts of the motor, that is M1 and M2.

It is well known that in a series DC motor there is an internal, nonlinear feedback from the angular speed to the input. Having rearranged a classical (simplified) block diagram of the motor, one can observe the feedback-nonlinear structure both in M1 and M2, in addition to the inherent (but known) nonlinearities as in (10) (of course, we have to be cautious when transforming block diagrams for nonlinear systems). The time-varying feedback nonlinearity is related to the load torque. Now, we propose the basic model structure for M1 as in Fig. 2. The part M11 of the model will be estimated as in Section 2.3, with the α_1 parameter fixed separately off-line (or scheduled depending on ω). The function $f(.)$ models a nonlinear behavior of the load torque vs. angular speed. In simulations we assume $f(\omega(t))=A*\text{atan}[\omega(t)]$, with A being either constant or slowly time varying.

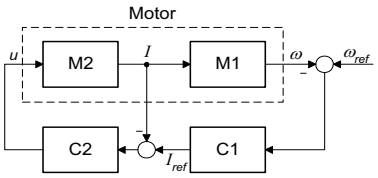

Fig.1. Cascade speed control of the motor.

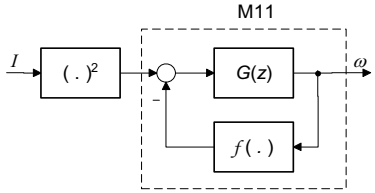

Fig. 2. Structure of model for M1.

The structure of a model for M2 is shown in Fig. 3. Since the known construction parameters R, L, L_f and K_m can be assumed constant, the estimation problem is reduced to the one for M1. Additionally, substituting the measurement $\omega(t)$ for the estimate $\hat{\omega}(t)$ brings the M2 model to the simple form: $I(t)=[-K_mL_fI(t)\omega(t)+u(t)/L]q^{-1}/[1+(-1+R/L)q^{-1}]$. Anyway, modeling (and control) of the auxiliary loop is no longer an issue.

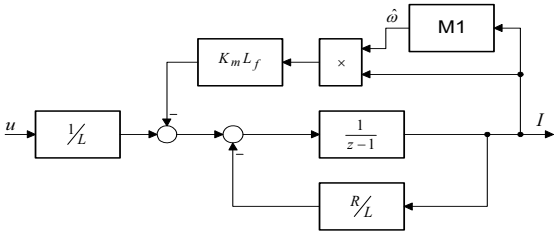

Fig. 3. Structure of model for M2.

5. Comparative Analysis of Nonlinear Block-Oriented Models

In a comparative analysis we use a simulated model of the motor, whose load torque is possibly time-varying and nonlinear with respect to the angular speed. In addition to the basic, Laguerre-based feedback-nonlinear (LFN) model, we examine alternative models for M11, that is the Laguerre-based Wiener (LW) and Laguerre-based Hammerstein (LH) models of Section 2 as well as the nonlinear Laguerre-based Volterra (LV) model of order 3 [4,7]. A classical adaptive least-squares (ALS) parameter estimation scheme is used, combining the recursive LS estimator with the exponential forgetting mechanism. The ALS loss function $\min\{V(\theta)=\sum_{t=1}^{N}\lambda^{N-t}e^2(t)\}$, where λ is the forgetting factor (set to 0.98), is used as the estimation performance index (V), with the number of input-output data taken as N=500. Results of the comparative analysis are presented in Table 1. As expected from

the physical relationship indicated above, it is the LFN model who has proved to provide the highest estimation accuracy, in terms of the minimum of the performance index. Observe that the LV model is the second best, but quite close comparable with Wiener and Hammerstein models. Fig. 4 presents the output ω of the simulated motor vs. the (discrete-time) model output $\hat{\omega}$ when M11 is feedback nonlinear-structured. The input voltage is multiple step-wise. The estimation accuracy can be considered excellent. Quite similar performance is obtained under the least mean squares (LMS) estimation method, with still lower computational burden [7].

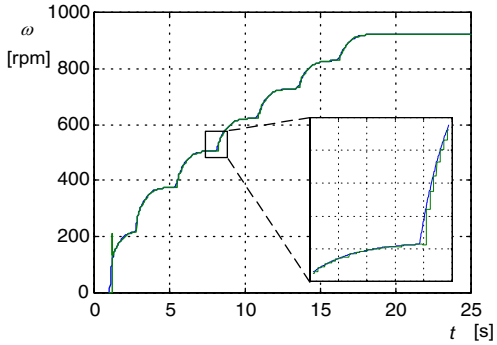

Table 1. Comparative analysis of estimation performance.

Model	LFN	LW	LH	LV
$V \times 10^{-4}$	**1.234**	64.1	60.6	37.2

Fig. 4. Outputs of the simulated motor and its model for the feedback-nonlinear submodel of M11.

6. Conclusions

A new methodology for control-oriented modeling and adaptive identification of a series DC motor has presented. The methodology has effectively employed new OBF-based modeling tools in the nonlinear block-oriented modeling environment. The OBF-based framework provides both numerical and computational effectiveness, in particular in terms of getting rid of the bilinearity issue plaguing the up-to-date modeling of nonlinear block-oriented systems. Parameters of a cascade model of the motor have been adaptively estimated under both time-varying and nonlinear load conditions of the motor. The feedback-nonlinear model has been recommended for the main part of the motor and its usefulness has been confirmed in a comparative simulation analysis.

References

[1] J.N. Chiasson, *Modeling and High Performance Control of Electric Machines*, John Wiley and Sons Inc., 2005.

[2] H.L. Choi, J.-T. Lim, Feedback linearization for a series DC motor using fuzzy adaptive diffeomorphism, Proc. the 7th World Multi-Conference on Systemics, Cybernetics and Informatics, Orlando, Florida, USA, vol. VII, pp. 167-172, 2003.

[3] A. Janczak, *Identification of Nonlinear Systems Using Neural Networks and Polynomial Models – a Block-oriented Approach*. Springer, Lecture Notes in Control and Information Sciences, vol. 310, 2005.

[4] K.J. Latawiec, *The Power of Inverse Systems in Modeling and Control of Linear and Nonlinear Systems*. Opole University of Technology Press, vol. 167, Opole, 2004.

[5] K.J. Latawiec, C. Marciak, R. Rojek, G.H.C Oliveira, Linear parameter estimation and predictive constrained control of Wiener/Hammerstein systems. Proc. 13th IFAC Symposium on System Identification (SYSID'2003), Rotterdam, The Netherlands, pp. 359-364, 2003.

[6] K.J. Latawiec, C. Marciak, R. Stanisławski, G.H.C. Oliveira, The mode separability principle in modeling of linear and nonlinear block-oriented systems. Proc. 10th IEEE MMAR Conference (MMAR'04), Miedzyzdroje, Poland, vol. 1, pp. 479-484, 2004.

[7] C. Marciak, Orthonormal basis functions in identification of nonlinear block-oriented systems with a series DC motor application (in Polish). Forthcoming Ph.D. thesis. Department of Electrical Engineering and Automatic Control, Opole University of Technology, Opole, 2005.

[8] R.K. Pearson, M. Pottman, Gray-box identification of block-oriented nonlinear models, Journal of Process Control, vol. 10, pp. 301-315, 2000.

Electromagnetic Fields in Mechatronics, Electrical and Electronic Engineering
A. Krawczyk et al. (Eds.)
IOS Press, 2006

INVESTIGATION OF ELCID TESTING USING FEM ANALYSIS AND TEST CORE MEASUREMENTS

Danilo Makuc, Maks Berlec, Konrad Lenasi

University of Ljubljana, Faculty of Electrical Engineering, Tržaška 25, Ljubljana, Slovenia
danilo.makuc@fe.uni-lj.si

Abstract *– **Since the interlamination short-circuits in stator cores can cause major damage to electrical machine a great emphasis is placed to detect such faults. One of the methods is ELCID (Electromagnetic Core Imperfection Detector) test [1], which is nowadays often used for testing of interlamination insulation in stator cores of large electrical generators and motors. To investigate this relatively young method a laboratory model of stator core was built, which enables measurements and analyses of intentional short-circuits in the core. Interlamination faults were also simulated and analysed using FEM. Both investigation results were compared and presented.***

Introduction

A traditional method for detection of interlamination faults is the *High Flux Ring Test*, often referred to as a *Thermal Loop Test*. The rotor is removed from the machine and the stator core is magnetically excited by a high voltage high current temporary winding. Magnetic flux produced in stator yoke should be near to that normally applied in service. Hot spots are detected by a variety of means including thermal cameras. Because of the required dismantling of the machine, high voltage excitation winding, high power source, that method is not very convenient.

The main advantages of the ELCID method are that the core is excited with just 4% of the rated flux and detection of damaged areas is sometimes possible even when the rotor of the machine is not removed. Positions and strength of the faults are determined with a measurement of leakage fluxes produced by the fault currents.

Investigation of the test method on a real working machine is difficult or almost impossible to perform, moreover the faults cannot be generated on purpose. To investigate the influence of the fault position and strength on measurements we performed several simulations of interlamination faults using FEM and compare them with measurements on a laboratory test core.

Laboratory Test Core

To verify the results obtained using FEM and to test different sensing coils we carry out measurements on a real model of stator core (Fig. 1, 2). All measurements were performed without a rotor in a stator bore. Since the model consists of separated sheets which are not welded together or fasten with building bars, the interlamination faults can be simulated using short-circuit turns.

In Fig. 3 an electrical scheme of the laboratory model is shown. It is similar to short-circuit of a transformer but in this case only a part of the core is short-circuited. Separated sheets and short-circuit turns enable also the investigation of the fluxes in the core, since every part of the core can be embraced with a test winding.

Fig. 1. Test core for investigation of interlamination short-circuits for different positions and strength.

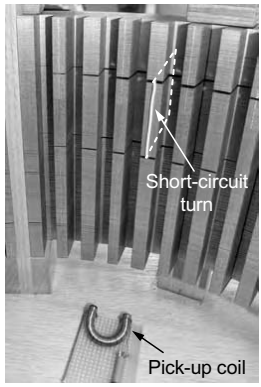

Fig. 2. Short-circuit turn at the top of the tooth and pick-up coil.

A length and position of the short-circuit turn can be arbitrary chosen, while the value of the fault current can be determined using an external resistor. Furthermore, the fault current can be simply measured and used as a reference value for results of a testing device. Introducing of artificial shorts at different places on the test core has been already presented in [2] where the core was intentionally irreversibly damaged. In such case the fault current could not be directly measured or changed.

Using a pick-up coil the induced voltage is measured. The positioning of the pick-up coil on stator teeth is shown in Fig. 4. If the short-circuit turn exists, the measured voltage should be proportional to the fault current in the turn [4].

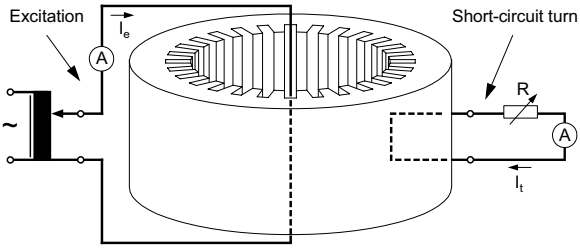

Fig. 3. Electrical scheme of the laboratory model.

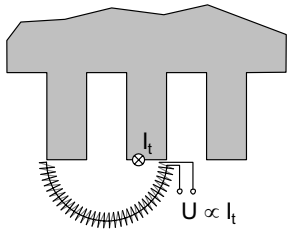

Fig. 4. Position of pick-up coil on stator teeth

FEM Model

Since the interlamination fault is a genuine 3D problem, a 3D FEM model would be adequate for simulation. In spite of that the investigation of ELCID core testing was performed using a 2D FEM model. The geometry of the model was simpler and the calculation of parametric analyses was not time consuming. Before the FEM model is introduced let us get familiar with the problem definition. Figure 5 shows the structure, which has to be calculated using FEM (figure does not include the excitation). Short-circuit turn does not embrace the whole cross-section of the core. Length of the core is l_c, while l_t is length of the short-circuit turn. The total magnetic flux in the core Φ can be written as

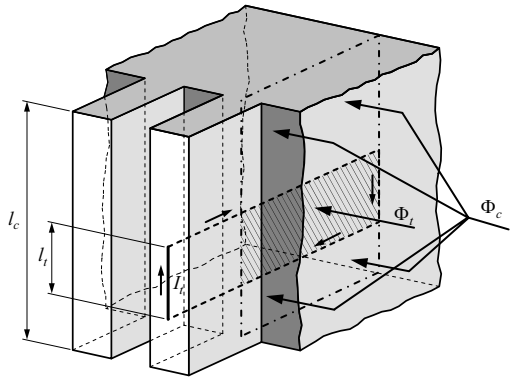

Fig. 5. Problem definition of interlamination short-circuit for FEM simulation.

the sum of a turn flux Φ_t and remaining core flux Φ_c. Since the excitation is sinusoidal, all mentioned magnetic quantities are complex.

Considering some negligible simplifications a magnetic circuit of such magnetic structure is shown in Fig. 6, where can be noticed a flux source Φ_f in a branch Φ_t, which represent a flux produced by a short-circuit current I_t. Having the magnetic circuit in mind a FEM model can be introduced. Figure 7 shows the geometry, material properties and boundary conditions of the model. The material properties were linear and eddy-current (AC) solver was used. Instead of the whole iron core only slots around the fault were included in the model. Since the fault (short-circuit turn) can have a variable but specific length, two parallel ferromagnetic branches were introduced also in the model geometry. The first branch (lower core) represents the core embraced with the short-circuit turn, while the second (upper core) represent a remaining stator core.

As can be seen the geometries of both branches are equal. Furthermore, the model does not

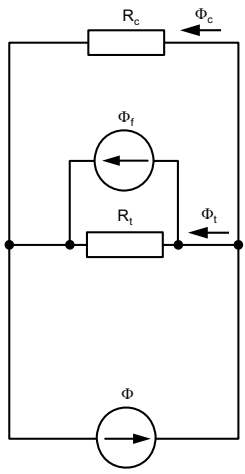

Fig. 6. Magnetic circuit of core model with interlamination short-circuit turn.

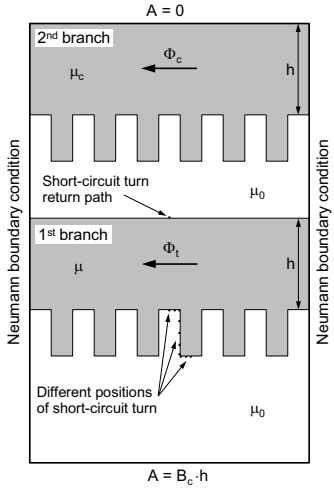

Fig. 7. FEM model with boundary conditions and material properties.

change if the length of the short-circuit turn changes. Different cross-sections of both magnetic branches are considered with applying appropriate permeability for the second branch. Permeability μ that defines the magnetic property of the real ferromagnetic core is assigned for the first branch, for the second branch a new fictitious permeability μ_c has to be calculated:

$$\mu_c = \left(\frac{l_c}{l_t} - 1 \right) \cdot \mu \tag{1}$$

where l_c is the length of the whole core and l_t is the length of the short-circuit turn. In such a way only permeability μ_c has to change when we analyse conditions at different fault lengths. Because the FEM model is two dimensional, different fault lengths can only be used to analyse the core fluxes and fault current values but not to find the influence of the length to induced voltage in the pick-up coil.

Excitation of the model was not a sinusoidal current source but a prescribed sinusoidal magnetic vector potential A at the lower boundary of the model (see Fig. 7). Considering relation B = curl A, the magnetic vector potential A for a specified magnetic flux density B_c is:

$$A = B_c \cdot h \tag{2}$$

where h is the height of the stator core (see Fig. 7). Using such boundary condition it was assured that the flux through the core is constant what is also the case in a real core.

Interlamination short-circuits were modelled as short-circuit turns at different positions and with different material properties. The FEM model consists of 10 conductors at different positions and one outer conductor as return path outside the core. If we would like to simulate a real interlamination fault the position of the short-circuit turn should be at the edge but in the ferromagnetic core. Since an insulated wire was used to make a short-circuit turn in the laboratory model, same position and properties were used also in FEM model.

Only one pair of conductors was included in every calculation. The pair consists of one conductor at specific position (1 to 10) and the outer conductor. Figure 8 shows the positions and numbers of conductors and the defined lines (1-2, 2-3, 3-4) along which the integrals $\int Hdl$ were calculated. Positions and labels of the defined lines were used also for positions of pick-up coil during the measurements on a test core.

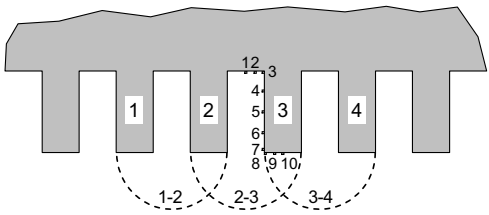

Fig. 8. Positions of the faults and defined lines between teeth.

Investigation Results

Fault Position

A fault position can be recognized by analysing the voltage induced in the pick-up coil, considering also results from the neighbouring teeth. Since the pick-up coil is actually a Rogowski coil [4] the measured voltage is proportional to derivative of the fault current. In conditions where the current is sinusoidal or almost sinusoidal and the frequency is constant we can simplify that and just say that the voltage is proportional to the current. Therefore, the results obtained from measurements

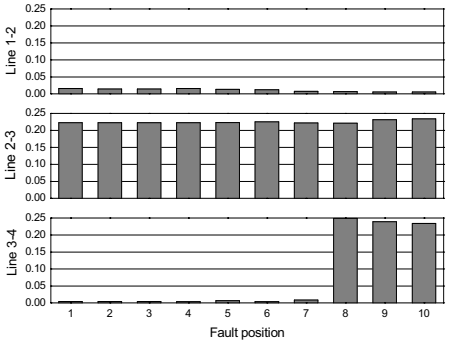

Fig. 9. Calculated $\int Hdl$ along defined lines at different fault positions using FEM.

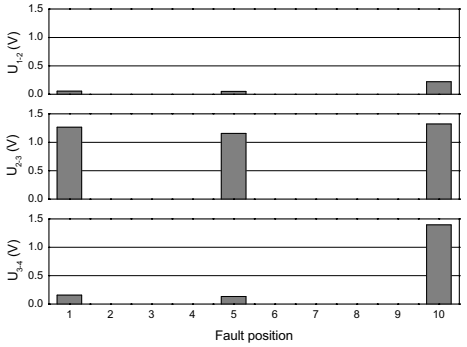

Fig. 10. Magnitudes of measured voltages using pick-up coil at different fault positions.

on the laboratory model are simply presented as voltages, while the results obtained using FEM are presented as integrals $\int Hdl$ along the defined lines between the stator teeth (Fig. 9, 10). We just compared the models therefore the absolute values were not so important.

In both measurements and calculations the induced voltage due to excitation flux was deducted from the obtained signal so we could analyse only a "clear" signal caused by the fault current. The influence of the fault length was not included in the investigation since the FEM model was only a 2D model, while the faults on the laboratory model were 40 mm long and much longer than the pick-up coil dimensions. Therefore, the end effect was neglected.

Figure 9 shows that we can only determine whether the fault is at the top of the tooth (positions 8-10) or in the slot (positions 1-7), while the exact position can not be specified. Authors [1], [3] describe that also the fault at the vertical edge of the slot can be determined (position 6 or 7 in the model, see Fig. 8), but unfortunately our calculated and measured results do not show that. On the laboratory model only three fault positions were examined (1, 5 and 10) and comparison of the measured results with the calculated values shows good agreement (Fig. 10).

Fault Strength

Using the FEM model the power losses of interlamination faults during the ELCID test can be simply calculated and investigated. The resistance of the short-circuit turn in the model represents a

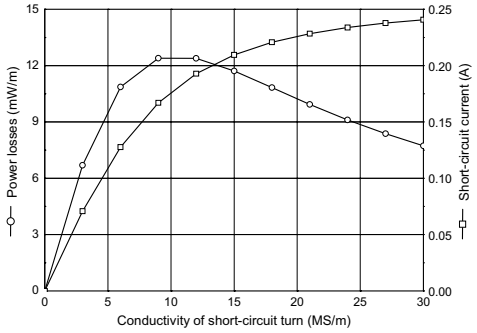

Fig. 11. Magnitudes of measured voltages using pick-up coil at different fault positions.

contact resistance together with resistance of lamination in a real stator core. The obtained results for different conductance of short-circuit turn were used just to show that the fault current, which can be recognized and evaluated by the ELCID test, can not be a measure for the fault strength (Fig. 11).

Conclusion

Laboratory test core and FEM model offer a lot of possibilities for investigation, evaluation and research in the field of diagnostics of laminated stator cores. Tests and calculations showed that the interlamination faults can be recognized using ELCID testing, but the fault strength can not be easily determined. There are possibilities to combine ELCID with additional methods, such as described in [5], to diminish the disadvantages of ELCID. Our goal is to develop a measuring device with the sensing coil which will automatically scan the whole circumference of the stator bore. The scan results would be used for generation of a "flux image" of the stator bore which could be an exchange for thermal image obtained from thermal camera at *Thermal Loop Test*.

References

[1] J. Sutton, EL Cid: an easier way to test stator cores, Electrical Review, Vol. 207, No. 1, pp 33-37, 1980.

[2] J. Stein, Generator core investigation and the importance of good lamination contact at the back of the core, Iris Rotating Machine Conference, Santa Monica, 2003, (paper obtained from 'http://www.irispower.com/techpapers').

[3] D. B. Paley, Current Low Power Core Testing Using EL CID, Adwel International Ltd., April 1999 (paper obtained from 'http://www.adwel.com/technical.html').

[4] D. A. Ward, J. La T. Exon, Using Rogowski coils for transient current measurement, Engineering science and education journal, June 1993, pp. 105-113, 1993.

[5] G. B. Kliman, S. B. Lee, M. R.Shah, R. M. Lusted and N. K. Nair, A New Method for Synchronous Generator Core Quality Evaluation, IEEE Transactions on Energy Conversion, Vol. 19, No. 3, pp. 576-582, 2004.

[6] Z. Posedel, Inspection of Stator Cores in Large Machines with a Low Yoke Induction Method - Measurement and Analysis of Interlamination Short-Circuits, IEEE Transactions on Energy Conversion, Vol. 16, No. 1, pp. 81-86, 2001.

Electromagnetic Fields in Mechatronics, Electrical and Electronic Engineering
A. Krawczyk et al. (Eds.)
IOS Press, 2006

A derivation of macroscopic Maxwell matter-field equations including dynamic magnetic hysteresis and extra-losses

O. Maloberti[1,2] , V. Mazauric[1], G. Meunier[2], A. Kedous-Lebouc[2], O. Geoffroy[3], Y. Rebière[1], P. Labie[2], Y. Maréchal[2]

[1] Schneider-Electric Corporate Research and Development: CRD/I2EA/DST 38TEC T3, 37 quai Paul-Louis Merlin, 38050 Grenoble cedex 9, France, olivier.maloberti@schneider-electric.com
[2] Laboratoire d'Electrotechnique de Grenoble: LEG-INPG/UJF-CNRS UMR 5529, BP 46, F-38402 Saint Martin d'Hères cedex, France, olivier.maloberti@leg.ensieg.inpg.fr
[3] Laboratoire Louis Néel: LLN-UJF/INPG-CNRS UPR 5051: 25 avenue des Martyrs 38042 Grenoble, France

Abstract –This paper proposes a material representation and a theoretical method to derive macroscopic matter-field equations from the microscopic scale. It includes extra-losses and dynamic hysteresis occurring within soft magnetic materials and its processing introduction in numerical simulation tools is investigated. It is based on microscopic physical phenomena (the motion of magnetic domain walls) and it is easily usable with the Finite Element Method (F.E.M.) since it saves calculation time and memory space, required by usual methods coupling classical Maxwell equations to hysteretic behavior laws.

I. INTRODUCTION

Microscopic magnetization reversal processes and related motion induced eddy currents are at the origin of dynamic hysteresis and extra-losses in soft magnetic materials (Fe, Ni, Co...) [1]. Actual short space variations are chaotic, abrupt, hard to predict and to calculate. Including these microscopic mechanisms in macroscopic formulations is the aim of this work. Nowadays, excess losses forecasts can only be done, for an entire device, thanks to post-processing calculations and „loss models" [2]. Dynamic hysteresis models [3-5] aren't often easily usable in numerical simulation tools because time and memory space consuming. Our goal is to propose a solution, based on physical considerations, compatible with the Finite Element Method, and complying with both accuracy and processing speed. Instead of coupling classical Maxwell equations to dynamic behavior models [6], we will search for Maxwell equations, including hysteretic matter-field interactions.

The part II is devoted to this research. In the part III, we discuss numerical implementations and recent results. In the conclusion and last part, we sum up, give the balance sheet and next developments planed.

II. DERIVATION OF MATTER-FIELD EQUATIONS

II.1 Microscopic magnetization reversal mechanisms

We may meet an infinite number of magnetic structures and magnetization dynamics. Nevertheless, most soft magnetic materials have got Weiss domains and Bloch walls [7]. Knowing that the main magnetization process is the Domain Walls Displacement (DWD) [8,9], and despite the fact that it is possible to study other mechanisms sometimes relevant for vectorial fields, or with higher frequencies; we first propose a DWD formulation, including losses due to this microscopic phenomenon. Thus we consider a magnetic structure, with domains and walls, submitted to a time varying magnetic field weak enough to keep walls plane and far from each other. If then the field is parallel to the favoured direction of domains, the main magnetization mechanism will probably be the motion of these walls, surrounded by microscopic eddy currents. To illustrate, we can see on Figure 1, that the representation of total eddy currents $\mathbf{j}$ is based on a superposition of classical macroscopic eddy currents $\mathbf{j_M}$ and microscopic ones $\mathbf{j_\mu}$ induced around each wall at position $\mathbf{x_w}$. The first is smooth whereas the

second is a Dirac like one Γ. Knowing the motion equations of statistically independent walls [8,9], the distribution of microscopic Joule losses reads

$$\sigma^{-1}\mathbf{j}_{\mu}^{2} = \sum_{w} \sigma\Lambda^{2}\left(\partial_{t}\mathbf{B}\right)^{2} N_{w}^{-1}\Gamma\left(\mathbf{x}-\mathbf{x}_{w}\right) \tag{1}$$

B is the macroscopic flux density (it comes from domains averaging procedures **B**= <**b**>). Λ^2 is a dynamic parameter, linked to the saturation magnetization $\mathbf{M}_s$, wall mobility m_w, surface S_w and volume density N_w. Since $(\partial_t\mathbf{B})$ is the relevant quantity, all complexity due to spatial dependencies of $\mathbf{j}_\mu$ will be lumped in Λ^2. It is a constant scalar for isotropic linear cases. From energy conservation, **h** being the total local magnetic field, the static classical macroscopic field $\mathbf{H}_M$, such that **curl**($\mathbf{H}_M$)=$\mathbf{j}_M$, is found damped by an anti-eddy field distribution

$$\mathbf{h} = \mathbf{H}_{M} + \sum_{w} \sigma\Lambda^{2}\left(\partial_{t}\mathbf{B}\right) N_{w}^{-1}\Gamma\left(\mathbf{x}-\mathbf{x}_{w}\right) \tag{2}$$

This distribution shown below on Figure 1 is the complementary of the current distribution displayed next to it.

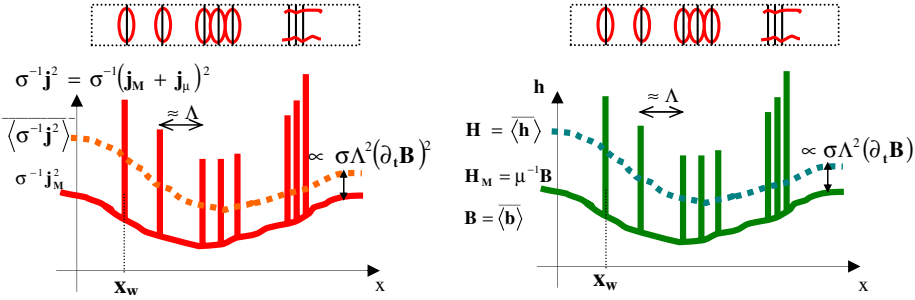

Figure 1: Actual (plain lines) and smoothed (dashed lines) squared eddy currents (on the left) and magnetic field (on the right) distributions. μ is the static permeability. < . > means to smooth and upper score to take the space average of the distribution as it will be developped in the following.

II.2 Smoothing procedure and power functional

We also know thanks to both thermodynamic [10] and power flux [11] considerations that Maxwell field equations result from variational principles used to minimize a certain amount of energy absorbed by the system considered. It is the main argument besides to justify that classical Maxwell equations might be true at the microscopic scale (the one corresponding to domains and walls). We plan to derive again these matter-field equations from the microscopic scale to the mesoscopic one (the one corresponding to the inside of a macroscopic device) as Russakoff did from the nanoscopic scale to the microscopic one [12]. So as to do that, we build a power functional Π inspired from [10,11], including both total Joule losses and total magnetization coupling powers (microscopic and macroscopic). Besides, this power functional can also be explained by considering both kinetic energy of free charges and potential energy of magnetic moments.

$$\Pi = \iiint_{\Omega}\left(\sigma^{-1}\mathbf{j}^{2} + \partial_{t}\left(\mathbf{bh}\right)\right)\mathbf{d}^{3}\mathbf{x} \tag{3}$$

Integrals are performed in the entire volume Ω of the system considered. **j**=**curl**(**h**), **h** and **b** are respectively the local current density, magnetic field and flux density at the microscopic scale. σ is the electrical conductivity. The microscopic part is developed thanks to previous work onto walls motion [8,9]. Actual magnetic field and Joule losses are quite disturbed with quick microscopic changes (Figure 1). We cannot use these distributions directly, we need continuous and smooth macroscopic quantities in order to use classical variational principles and integral transformations. Next part of the work is to apply well chosen smoothing and averaging procedures [12] (denoted by <.>) onto (2) and (3), in order to discard irrelevant short space variations. As a result, it can be expressed as a function of **B**, the macroscopic flux density and $\mathbf{H}_M$, the static macroscopic magnetic field

$$\Pi = \iiint \overline{\left\langle \sigma^{-1}\mathbf{j}^2 + \partial_t(\mathbf{b}\cdot\mathbf{h}) \right\rangle}\, \mathbf{d}^3\mathbf{x} = \iiint \left(\sigma^{-1}\left(\mathbf{curl}\left(\mathbf{H_M} + \sigma\Lambda^2\partial_t\mathbf{B}\right)\right)^2 + \partial_t\left(\mathbf{B}\left(\mathbf{H_M} + \sigma\Lambda^2\partial_t\mathbf{B}\right)\right)\right)\mathbf{d}^3\mathbf{x} \quad (4)$$

II.3 Variational principle, Euler-Lagrange equations

We will now satisfy a stationary condition for Π with respect to well chosen variables defined in the following. We can choose two different sets of variables depending on the Maxwell equations we want to focus on and solve. In the present paper, we assume the Maxwell-Ampere law and derive the Maxwell-Gauss and Maxwell-Faraday equations with the **T**-Φ formulation [13,14]. The static macroscopic magnetic field $\mathbf{H_M}$ can be expressed with the help of two regular functions called the reduced electric vector potential $\mathbf{T_M}$ and the reduced magnetic scalar potential Φ_M: $\mathbf{H_M}=\mathbf{T_M}-\mathbf{grad}(\Phi_M)$. These potentials will be our unknown variables but it is useful to introduce also two other total potentials **T** and Φ such that the total macroscopic magnetic field is $\mathbf{H}=\langle\mathbf{h}\rangle=\mathbf{H_M}+\sigma\Lambda^2\partial_t\mathbf{B}=\mathbf{T}-\mathbf{grad}(\Phi)$. From (2) and (4), we can choose to link the two sets of variables as follow (μ_d is the static differential permeability defined by $\mu_d=\mathbf{grad_{HM}}(\mathbf{B})^T$ or $\delta\mathbf{B}=\mu_d\delta\mathbf{H_M}$)

$$\mathbf{T} = \left(1 + \sigma\Lambda^2\mu_d\partial_t\,.\right)\mathbf{T_M} \quad (5)$$

$$\mathbf{grad}(\Phi) = \left(1 + \sigma\Lambda^2\mu_d\partial_t\,.\right)\mathbf{grad}(\Phi_M) \quad (6)$$

We admit that the system, constituted of both the material and the field, tends to minimize its power (4) [10]. If we consider a variation of Φ keeping **T** and $\sigma\Lambda^2\partial_t\mathbf{B}$ constant, the stationary condition on (4) with respect to the magnetic scalar potential Φ yields the divergence free condition for $\partial_t\mathbf{B}$ ($\mathrm{div}(\partial_t\mathbf{B})=0$), and the continuity of its normal component at each border.

$$\mathbf{div}(\partial_t\mathbf{B}) = 0 \quad (7)$$

Now we consider a variation of **T** keeping Φ and $\sigma\Lambda^2\partial_t\mathbf{B}$ constant and try to attain the stationary condition for (4) with respect to **T**. A variational principle gives a continuity condition on the tangential component of vector $\mathbf{E}=\sigma^{-1}\mathbf{curl}(\mathbf{H})=\sigma^{-1}\mathbf{curl}(\mathbf{H_M}+\sigma\Lambda^2\partial_t\mathbf{B})$ and Euler-Lagrange equations describing evolution of fields in space and time. It is equivalent to the following matter-field equation

$$\mathbf{curl}\left(\mathbf{E_M} + \mathbf{curl}\left(\Lambda^2\partial_t\mathbf{B}\right)\right) + \partial_t\mathbf{B} = 0 \quad (8)$$

$\mathbf{E_M}=\sigma^{-1}\mathbf{j_M}=\sigma^{-1}\mathbf{curl}(\mathbf{H_M})$ is the local static macroscopic electric field. Defining a modified total electric field **E** such that $\mathbf{E}=\mathbf{E_M}+\mathbf{curl}(\Lambda^2\partial_t\mathbf{B})$; equation (8) takes the form of the classical Maxwell-Faraday equation. The essence of these matter-field equations ((7) & (8)) is to include smoothed microscopic dynamic fields in macroscopic ones. It allows therefore the use of single valued (or quasi-static) behavior laws: $\partial_t\mathbf{B}=\mu_d\partial_t\mathbf{H_M}$ and $\mathbf{E_M}=\sigma^{-1}\mathbf{j_M}$; where μ_d is the static differential permeability and σ the electrical conductivity. Then (7) and (8) are solved to find (Φ_M, $\mathbf{T_M}$). Unfortunately the solution of previous system is not unic. One has to choose a gauge condition. The Coulomb gauge $\mathrm{div}(\mathbf{T_M})=0$ [14] seems appropriate here. Moreover, we have to ensure the continuity of the tangential component of $\mathbf{H}=\mathbf{H_M}+\sigma\Lambda^2\partial_t\mathbf{B}$ in order to enforce the Maxwell-Ampere law $\sigma\mathbf{E}=\mathbf{curl}(\mathbf{H})$ at each border of ∂Ω (**n** is a unit vector normal to the frontier considered). The entire system to solve becomes

$$\mathbf{div}\left(\mu_d\partial_t\left(\mathbf{T_M} - \mathbf{grad}(\Phi_M)\right)\right) = 0 \quad (9)$$

$$\begin{aligned}\mathbf{curl}\Big(\sigma^{-1}\mathbf{curl}\Big(\left(1 + \sigma\Lambda^2\mu_d\partial_t\,.\right)\left(\mathbf{T_M} - \mathbf{grad}\Phi_M\right)\Big)\Big) \\ - \mathbf{grad}\left(\sigma^{-1}\mathbf{div}\left(\mathbf{T_M}\right)\right) + \mu_d\partial_t\left(\mathbf{T_M} - \mathbf{grad}(\Phi_M)\right) = 0\end{aligned} \quad (10)$$

$$\left(1 + \sigma\Lambda^2\mu_d\partial_t\,.\right)\left(\mathbf{T_M} - \mathbf{grad}\left(\Phi_M\right)\right)\times\mathbf{n} \quad \mathbf{is} \quad \mathbf{continue} \quad (11)$$

This formulation includes the physics of domain walls and it saves memory space and time computation. It may be used for two dimensions problems with currents into plane, and for three dimensions problems.

III. NUMERICAL IMPLEMENTATION OF THE FORMULATION

Set of equations ((9), (10) & (11)) is compatible with Finite Element **T**-Φ [13,14] formulations. We will first implement this $\mathbf{T}_M$-Φ_M formulation and put it to the test onto simple geometries (Figure 2)

III.1. Implementation of a $\mathbf{T}_M$-Φ_M Finite Element formulation

Three dimensions formulations for transient and harmonic problems have been written and put to the test with the Finite Element Method (F.E.M.). The Galerkin and Newton-Raphson [15] methods for the projection of (7) and (8) on a shape functions space $\{\alpha_p,\gamma_p=\alpha_p\ [[1]]\}$ ([[1]] is the identity matrix) are an approximation of the formulation obtained by minimizing (4) and give the following residual and matrix equation in order to find $\mathbf{T}_M$ and Φ_M at each node p.

$$\mathbf{R}=\begin{pmatrix}\mathbf{R}_{1p}\\ \mathbf{R}_{2qj}\end{pmatrix}=\begin{pmatrix}\iiint\left(-\mathbf{grad}\alpha_p\partial_t\mathbf{B}\right)\mathbf{d}^3\mathbf{x}\\ \iiint\left(\mathbf{curl}\gamma_{qj}\sigma^{-1}\mathbf{curl}\left(\mathbf{H}_M+\sigma\Lambda^2\partial_t\mathbf{B}\right)+\mathbf{div}\gamma_{qj}\sigma^{-1}\mathbf{div}\left(\mathbf{T}_M\right)+\gamma_{qj}\partial_t\mathbf{B}\right)\mathbf{d}^3\mathbf{x}\end{pmatrix} \quad (12)$$

$$\begin{bmatrix}\mathbf{M}_{11} & \mathbf{M}_{12}\\ \mathbf{M}_{21} & \mathbf{M}_{22}\end{bmatrix}\cdot\begin{pmatrix}\mathbf{d}\Phi_{Mp}\\ \mathbf{dT}_{Mqj}\end{pmatrix}=-\mathbf{R} \quad (13)$$

$$\mathbf{M}_{11}(\mathbf{p},\mathbf{q})=\iiint\left(\mathbf{grad}\alpha_p\frac{\mu_d}{\mathbf{dt}}\mathbf{grad}\alpha_q\right)\mathbf{d}^3\mathbf{x}$$

$$\mathbf{M}_{12}(\mathbf{p},\mathbf{q},\mathbf{j})=\iiint\left(-\mathbf{grad}\alpha_p\frac{\mu_d}{\mathbf{dt}}\gamma_{qj}\right)\mathbf{d}^3\mathbf{x}$$

$$\mathbf{M}_{21}(\mathbf{q},\mathbf{j},\mathbf{p})=\iiint\left(-\gamma_{qj}\frac{\mu_d}{\mathbf{dt}}\mathbf{grad}\alpha_p\right)\mathbf{d}^3\mathbf{x}$$

$$\mathbf{M}_{22}(\mathbf{q},\mathbf{j},\mathbf{p},\mathbf{i})=\iiint\left(\mathbf{curl}\gamma_{qj}\sigma^{-1}\left(1+\frac{\sigma\Lambda^2\mu_d}{\mathbf{dt}}\right)\mathbf{curl}\gamma_{pi}+\mathbf{div}\gamma_{qj}\sigma^{-1}\mathbf{div}\gamma_{pi}+\gamma_{qj}\frac{\mu_d}{\mathbf{dt}}\gamma_{pi}\right)\mathbf{d}^3\mathbf{x}$$

III.2 Results, validation of the formulation

The formulation has been firstly applied onto test cases (one or two dimensions problems computed in three dimensions): an „infinite" iron sheet, cylinder or bar (Figure 2).

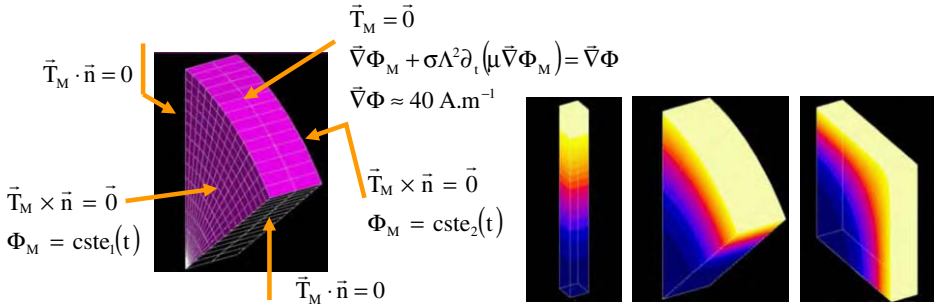

Figure 2: Geometry of some test cases studied, the limit constraints are given for the cylinder. They are similar for the bar and the metal sheet.

Linear harmonic: Using the Fourier theory, we solve complex equations corresponding to (13) with the Finite Element Method (F.E.M.) (we just replace 1/dt with j2πf) and plot the average flux density within the section as a function of the frequency f on Figure 3.

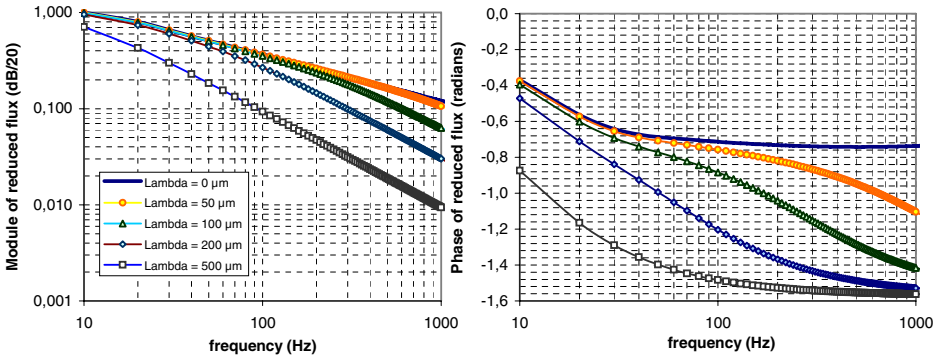

Figure 3: Module and phase of reduced mean flux within section of the cylinder.

Linear and non-linear transient: Some measurements with several induction (for μ and Λ) and frequency (for Λ) levels have been carried out in order to identify the characteristic transient variations of the properties μ(B) and Λ(B,f). We can fit the experimental data thanks to a surface which describes evolutions of walls population and mobility (Figure 4, left, standard deviation is for the moment around 50 μm). We then solve (13) with the Finite Element (F.E.M.) or Difference Method (F.D.M.), one step after one, onto the one dimensional problem corresponding to the Epstein experiment. We hope to be able to simulate with accuracy the flux density response expected to be triangular as it was firstly imposed during the experiment (Figure 4, right, the maximum relative error is for the moment around 8%). The dynamic hysteresis due to both classical macroscopic eddy currents and microscopic ones will be taken into account thanks to the formulation previously proposed. No static hysteresis has been introduced. It can be done through the $\mathbf{B}(\mathbf{H_M})$ or its inverse $\mathbf{H_M}(\mathbf{B})$ law.

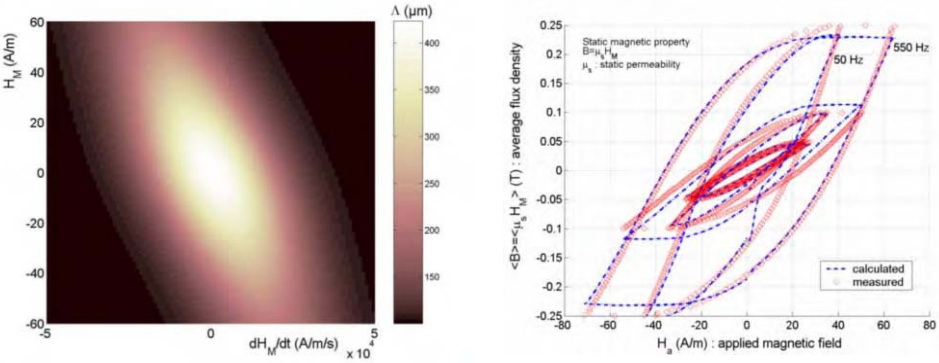

Figure 4: Comparisons between simulations and measurements carried out onto an Epstein frame (1-D problem) with the SiFe NO M40050a material (left) Identification of the homogenized dynamic magnetic property Λ as a function of field conditions (right) Transient cycles varying both μ and Λ.

III.3 Discussion

The low-pass filter plus dynamic hysreresis are correctly described and in accordance with observations onto macroscopic flux and power losses measured. Obviously, the representation is simplified and disregards possible irregularities, non-reproducibility in chaotic structures and static memory effects. It supposes that some similar average macroscopic arrangements are statistically reproduced for some identical field conditions (Figure 4,

left). These properties may however be independent of the macroscopic geometry and sources waveshape, which is quite interessant for simulation purposes. Unfortunately experimental identifications are limited in flux density and frequency levels because of non-linear processes. Predictions for a wide range won't be accurate without improving identification procedures and investigating varying parameters μ, with the flux density **B**, and Λ with both **B** and its first temporal derivative $\partial_t \mathbf{B}$ as it was initiated in the Figure 4.

IV. DISCUSSION, CONCLUSION AND FORTHCOMING

This representation helps us understand soft magnetic materials dynamics and make accurate its behavior description. As long as a linear approximation is valid, the method will introduce the dynamic hysteresis of such materials keeping linear the Maxwell equations. It avoids therefore Newton-Raphson loops. For non-linear problems, they seem to be still necessary with non-linear but single valued instead of hysteretic properties. Accuracy is preserved; calculation time and convergence should be improved. These formulations can be used to compute any large device supplied by transient signals or time harmonics within the quasi-static approximation. This contributes to the modeling of microscopic phenomena usable in macroscopic calculations taking accurate frequency power losses into account. Our goal is to provide general $\mathbf{T_M}$-Φ_M and $\mathbf{A_M}$-V_M formulations [14] compatible with the Finite Element Method, and use it for sensors and linear actuators. Further developments are currently under progress to widen its usefulness:

- Procedures onto more complex magnetic structures and magnetization mechanisms should be investigated to provide a more general three dimensions formulation.
- Magnetic behavior should be improved by acting on the static permeability μ and the dynamic parameter Λ.
- One more derivation from the mesoscopic scale to the macroscopic one will be necessary to deal with laminated cores and other complex inhomogenous architectures with anisotropy.

REFERENCES

[1] G. Bertotti, "General properties of Power losses in soft ferromagnetic materials", *IEEE Transactions on Magnetics*, vol. 24, n°1, pp.621-630, January 1988.
[2] T. Chevalier, A. Kedous-Lebouc, B. Cornut, C. Cester, "A new dynamic hysteresis model for electrical steel sheet ", *Physica B*, vol. 275, pp. 197-201, 2000.
[3] I.D. Mayergoyz, G. Friedman, "Generalized Preisach Model of Hysteresis", *IEEE Transactions on Magnetics,* vol. 24, n°1, pp. 212-217, January 1988.
[4] J. Szczyglowski, "Influence of eddy currents on magnetic hysteresis loops in soft magnetic materials", *Journal of Magnetism and Magnetic Materials*, vol. 223, pp. 97-102, 2001.
[5] G. Bertotti, V. Basso, M. Pasquale, "Application of the Preisach Model to the calculation of magnetization curves and power losses in ferromagnetic materials", *IEEE Trans. on Magn.*, may 1993.
[6] M.A. Raulet, B. Ducharne, J.P. Masson, G. Bayada, "The Magnetic Field Diffusion equation Including Dynamic Hysteresis", *IEEE. Trans. on Magn.*, vol.42, n°2, pp.872-875, March 2004.
[7] A. Hubert & R. Schafer, « Magnetic domains », Springer, 2000.
[8] H. Williams, W. Shockley, C. Kittel, "Studies of the propagation velocity of a ferromagnetic domain boundary", *Physical review*, vol.80, n°6, pp.1090-1094, 1950.
[9] R.H. Pry, C.P. Bean, "Calculation of the Energy Loss in Magnetic Sheet Materials Using a Domain Model", *Journal of Applied Physics*, vol.29, n°3, pp. 532-533, March 1958.
[10] V. Mazauric, "From Thermostatistics to Maxwell's Equations: A Variational Approach of Electromagnetism", *IEEE Transactions on Magnetics*, vol. 40, n°2, pp.945-948, March 2004.
[11] M.V.K. Chari, S.J. Salon, "Numerical methods in Electromagnetism", Academic Press, pp. 143-168, 2000.
[12] G. Russakoff, "A derivation of the macroscopic Maxwell equations", *American Journal of Physics*, vol.38, n°10, pp.1188-1995, October 1970.
[13] O. Biro, K. Preis, W. Renhart, G. Vrisk, F. Richter, "Computation of 3D current driven skin effect problems using a current vector potential", *IEEE Trans. on Magn.*, vol.29, n°2, pp.1325-1332, 1993.
[14] Y. Lefloch, "Développement de formulations 3D éléments finis pour la prise en compte de conducteurs massifs et bobinés avec un couplage circuit", PhD thesis INPG/EEATS, pp.17-37, 2002.
[15] F. Ossart, V. Ionita, "Convergence de la méthode du point fixe modifié pour le calcul du champ magnétique avec hystérésis", Eur.Phys.JAP, vol. 5, pp.63-69, 1999.

Electromagnetic Fields in Mechatronics, Electrical and Electronic Engineering
A. Krawczyk et al. (Eds.)
IOS Press, 2006

ADAPTIVE OBJECT MODELS ARCHITECTURE FOR SIMULATION SOFTWARE DESIGN

Yves Maréchal[1], Yves Souchard[1,2], Guy Jérome[2]
[1]Laboratoire d'Electrotechnique de Grenoble, ENSIEG BP 46.
38402 Saint Martin d'Heres, France. Yves.Marechal@leg.ensieg.inpg.fr
[2]Cedrat SA, 10 Chemin de Pré Carré, 38246 Meylan Cedex, France

Carlos Antonio França Sartori
Escola Politécnica da Universidade de São Paulo, Departamento de Engenharia Elétrica PEA/EPUSP
Av. Prof. Luciano Gualberto Trav. 3, 158. O5508-900. São Paulo, SP. Brazil. sartori@pucsp.br; cardoso@pea.usp.br

Abstract-*This paper presents a new approach for designing simulation software that minimizes both development and maintenance costs on the one hand, and on the other hand helps the designer to deal with the growing complexity of the simulation process. It is mainly based on meta modeling technique coupled to a reusable framework programmed at a meta level , sometimes called "adaptive object models" . A design tool is presented. The whole approach is used to model and build a new generation of simulation software.*

Introduction

Numerical simulation is now widely used in all companies that design electromagnetic devices. However, in the long run of technological improvements and reduction of costs, electrical devices tend to become more and more compact and complex. Multi-physics and multi methods analysis is often required for thorough sizing of the device. Thus, simulation software is becoming more and more complex, and their maintenance is a heavy task. Therefore, the designers of simulation software have recently moved to object oriented language, so as to increase the quality and minimize maintenance [1] [2].

In the computer science recent works, it can be noticed that a new information system landscape is emerging more model-centered than object-oriented. This seems to be a promising answer to the new challenge that software industry has to face in the next few years. Hence, following these works, it may be worthwhile to investigate the benefits for the numerical simulation community to move to this new approach of software design called "adaptive object models" [3] [4].

This paper presents our past few years work in that direction. In this paper, we will first introduce the concept of metamodeling and the simulation software developed on this technique. Last the main benefits of this approach will be summarized.

From Standard Object Oriented Programming To Metamodeling

Introducing The Metamodeling Concept

To introduce the metamodel concept, consider the following partial and simplified data model of some simulation software, described as a class diagram in the UML notation (figure 1). In a conventional object oriented programming approach, the developers would design and program

the previous classes (Region, Formulation, Material, Property, SimulationModel …) that the end-user will instantiate using a dedicated graphic user interface.

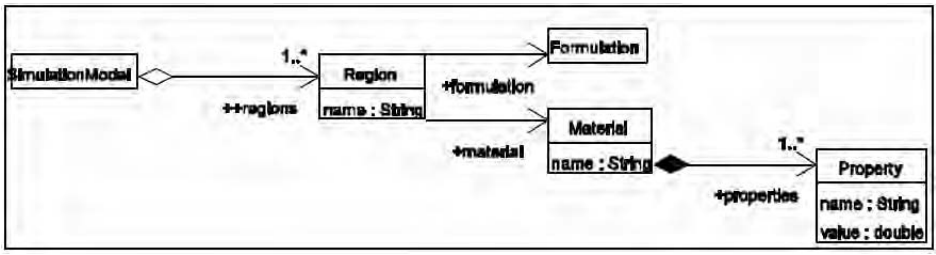

Fig. 1: Partial simplified class diagram of the data model of some simulation software

Considering the simulation of a transformer for instance, the end user will in fact create several instances of regions: core, primary winding, secondary winding, air, as well as materials and he will package them all into an unnamed Simulation Model.

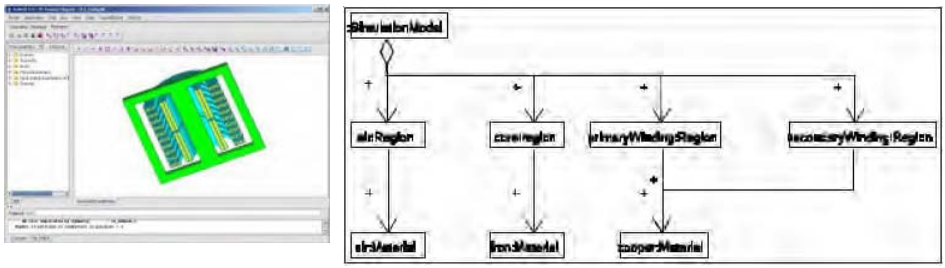

Fig. 2: Geometric model of a transformer and its object diagram

The mechanism that links an instance (Region('core')) to its model (class Region) can also be applied to the model itself: the class Region can be seen as an instance of a metaclass Entity, the field formulation of class Region can be expressed an instance of the metaclass Field. Thus, putting all these metaclass together leads to the following class diagram called the metamodel.

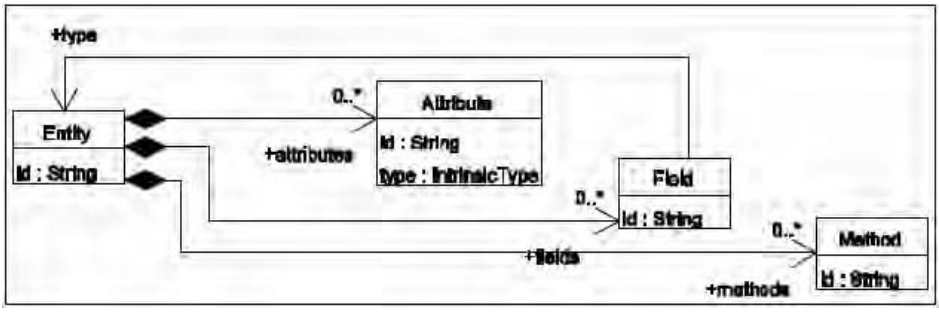

Fig. 3: A basic metamodel

The metamodel defines a language that allows describing a data model. Instances of metamodel are called metadata and does define a data model since it can be translated into object oriented concepts such as classes or interfaces.

This instantiation / abstraction process can indeed be carried out over and over. But in practice, only four levels are needed.

Four Layer Metadata Architectures

As defined in the UML standard, the classical framework for metamodeling is based on a four metalayers architecture [5]. These layers are conventionally described as follows:

- The information layer stores the data input of the end-user.
- The model layer is devoted to the designer of the simulation software. It defines the language of the information level.
- The metamodel layer is designed to produce models. A metamodel is an "abstract language" for describing different kinds of data.
- The meta-metamodel layer is comprised of the description of the structure and semantics of meta-metadata. In other words, it is the "abstract language" for defining different kinds of metadata.

Meta metamodel level	Hard wired meta (MetaModel , MetaClass, MetaField are coded here)
Metamodel level	MetaModel('meta model', [MetaClass('Entity', [MetaAttribute('id',String), MetaField('fields',List<Field>)]), MetaClass('Field',….)])
Model level	Entity('Region', [Field('name',String), Field('formulation',Formulation), Field('material',Material)])
Information level	Region('air',[ScalarFormuation, Air]), Region('core',[ScalarFormulation, Iron]),

Up to now, this presentation may be considered as a pure intellectual construction. But in fact, introducing metamodeling has brought many advantages in large software development.

From Metamodeling to Model Driven Architecture and Adaptive Object Model

Object oriented software programming consists in designing classes, with methods describing behaviors and fields for features. Traditionally, all developments are done at the model level. For instance, in class Region, the developer may need to implement a method that checks the material properties according to the chosen formulation.

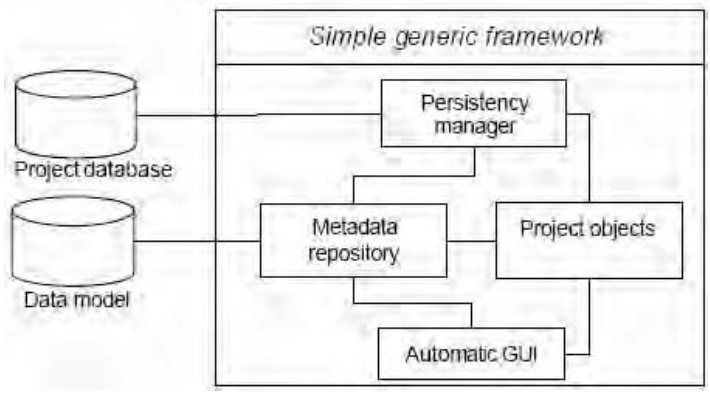

Fig. 4 a generic framework working at the metamodel level

However, object oriented programming techniques are applicable at any level of the abstraction scale. Thus, it is possible to add methods and features on the metamodel (and consequently on the meta metamodel as well). At the metamodel level, the developer may program methods for the classes Entity, Field … Hence it becomes possible to provide generic services for all instances of the metamodel, namely all classes of the model : generic persistency or automatic Graphic User interface (GUI) are at reach relying on both metadata for type information and project instances for content. Further more, it is even possible to provide a comple te generic framework of (meta) classes that is completely "parameterized" by the data model. Figure 4 shows the main components of such a generic framework.

In other words, it is no more required to program the classes of the model to provide a complete environment that meets the end user's requirements: the model is merely described as an instance of the metamodel. This is a radical change in the way of building new applications.

Scientific Researches And Industrial Applications

Several scientific communities or companies are involved in the development of metamodeling. The OMG group tries to provide a standard that will help the designers to implement large and complex software running on several platforms from the model description; The main key words in that field are 'Model Driven Architecture' (MDA) and 'Meta Object Facilities' (MOF). Up to now, the standard is still in development and only few companies are heavily relying on this technology [4].

Independently from the OMG, Yoder and al. proposed a so called "Adaptive Object-Model" approach that represents classes, attributes, relationships and behavior as metadata. The system is a model based on instances rather than classes. Consequently, the object model is fully adaptable; when the descriptive information is modified, the system immediately reflects those changes similar just like a kind of UML Virtual Machine would do [3].

On the whole, introducing such a generic framework and technology allows for a system to quickly adapt to new business needs by simply changing the meta database rather than changing the code. Conversely, the code programmed at the meta level is generally more complex.

Meta Modeling Of A Simulation Software

In the previous section, the basis of metamodeling and its main benefits were exposed. However, to reach full dynamicity of data model in complex simulation software, all behaviors of the desktop have to be parameterized using the description of this data model. Thus, the metamodel needs to be much more extensive compared to what was initially presented in figure 3. The MOF metamodel has not been retained since we found it not totally suited to the expected goal: it includes aspects that were useless whereas specific aspects such as localization of the applic ation according the country, end user competencies description, or logical organization of the application were lacking. Therefore, we decided to propose our own metamodel that grows according to our needs.

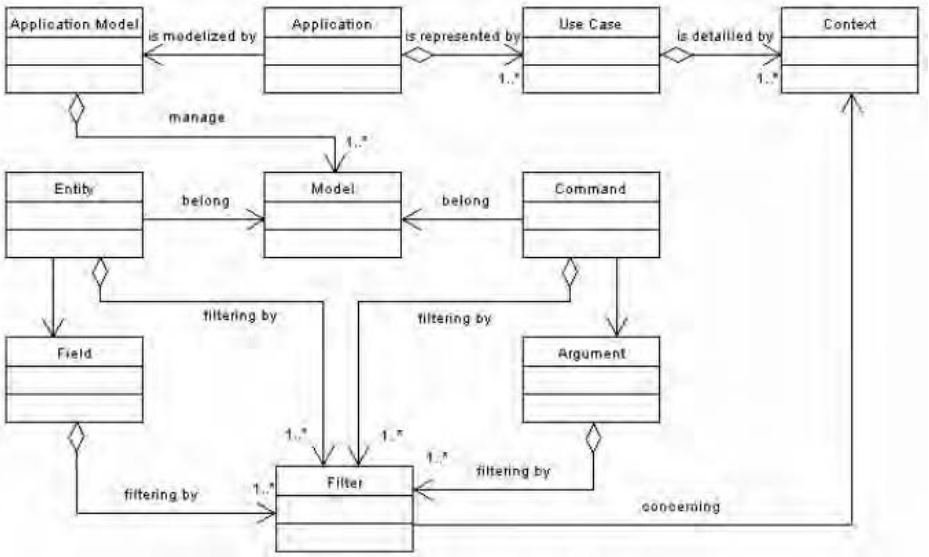

Fig. 5 Class diagram of the Application entity and related types (part of).

Metamodel For Static Description

Basically, the main requirements consist in modeling a kind of static class diagram, ornamented by some user interface information. We also need to describe the application behavior: the simulation process being potentially complex and extremely adjustable , it has been split into several “use cases” one for each aim of the simulation, a use case being itself divided into several steps called “contexts”.

Figure 5 is the UML simplified class diagram of an application, a part of our metamodel. An *Application* is made of a set of *Commands* and *Entities*, grouped into a *Model*. *Commands* and *Entities* are mainly composed of *Fields* and *Arguments* respectively, both being eventually set visible, disabled, or invisible to the end user thanks to the *Filter* notion. The software is made of a list of *Uses cases* (3D magnetostatics, 3D transient …). Use cases are split in *Contexts* (geometric modeler, physics, mesh …) that may be seen as modeling steps requested to achieve use case completion.

The Framework Description

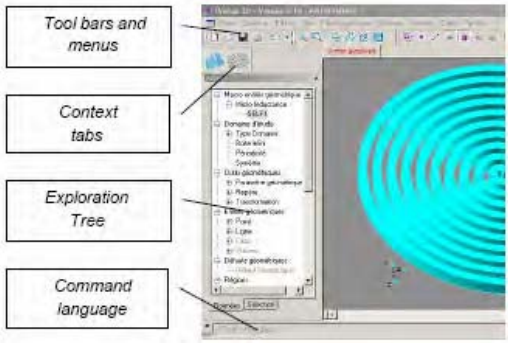

Fig. 6 Basic concepts of modern user interface.

Modern software must provide a powerful graphic interface including menus, toolbars, trees, 3D view … In our model driven approach, the user interface is parameterized by the data model: toolbars and menus can only display the commands or methods that are known from the data model. The tree view proposes an organized presentation of the database. The context tab allows reducing all commands and objects to those that are actually needed at any given step of the simulation: the preprocessor step will only show geometry and physics aspects, whereas post processor will provide its own reduce set of commands.

All these information are described using an appropriate part of the metamodel, as shown on the following figure.

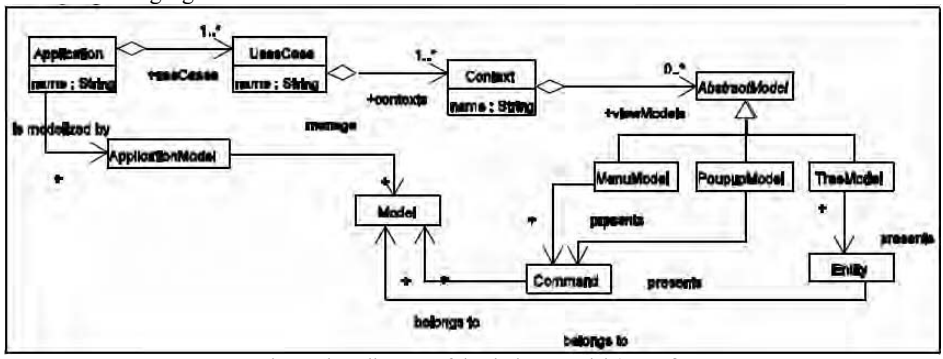

Fig. 7 Class diagram of the desktop model (part of).

The New Design Process of an Application

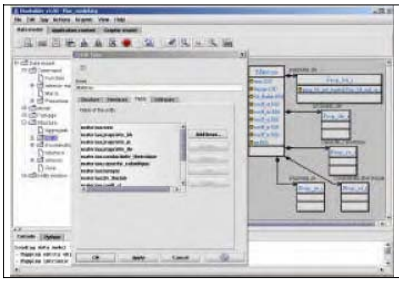

Fig. 8 Snap shot of the application builder.

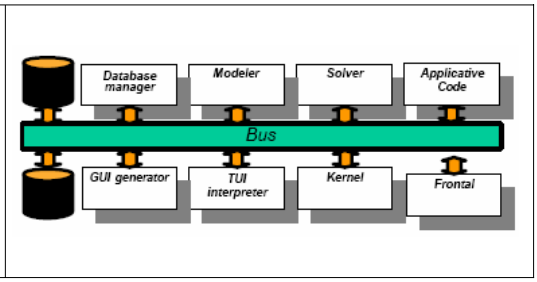

Fig. 9 The generic framework

Following that approach, we have built a dedicated tool to help the designer of an application to model it. Figure 8 shows a snap shot of this builder. We can notice the presence of the UML static class diagram on the background, a tree displaying all entity types, commands … already created and in the front, a dialog box to input a new type. Once the designer has completely described the contents of its application, it is stored in a database, called meta database.

This meta database is used to dynamically configure a reusable framework that takes in charge, at no additional cost, the user interface of all business concepts, the validity checking of user input, data persistence … The framework is made of a collection of modules (frontal, kernel …) plugged into a bus as shown on figure 9. Additional modules may also be plugged. For instance in the case of our finite element simulation software, we have plugged a solver, a geometric modeler, and some applicative code.

Main Benefits An Conclusions

Full simulation software [7] has been built using metamodeling technique and a generic framework. At the end, more than one thousand of "classes" together with hundreds of use cases and commands have been described for our simulation environment, This approach was first studied to manage the growing complexity of simulation software. It has been tested intensively on our own code, with success. Adopting such a strategy brings a large number of benefits:

- Changing the data model is much faster than with the standard Object Oriented Programming paradigm and can be done at nearly no cost
- Many services are built in once for all (graphic and textual user interface, desktop behavior…).
- Maintenance of the code is drastically reduced.

Of course, the programmer of numerical methods and formulations still has to produce the code of the algorithms he needs to implement.

References

[1] W. MAI, G HENNEBERGER, "Object-Oriented Design of Finite Element Calculations with Respect to Coupled Problems", IEEE Transactions on Magnetics, vol. 36, no. 4, July 2000.
[2] E. SILVA, R. MESQUITA, R. SALDANHA, P. PALMEIRA, "An object-oriented finite-element program for electromagnetic field computation", IEEE Transactions on Magnetics, vol. 30, no. 5, September 1994.
[3] JOSEPH W. YODER, REZA RAZAVI, "Adaptive Object-Models", OOPSLA 2000 conference, ACM.
[4] Model Driven Architecture, http://www.omg.org/mda
[5] Meta Object Facilities, V1.4, http://www.omg.org/technology/documents/formal/mof.htm
[6] ObjectDirect company, http://www.objetdirect.com/
[7] Flux, a finite element simulation environment for Electrical Engineering, http://www.cedrat.com/

Electromagnetic Fields in Mechatronics, Electrical and Electronic Engineering
A. Krawczyk et al. (Eds.)
IOS Press, 2006

THE 3D FIELD-CIRCUIT MODEL OF POWER TRANSFORMER SUPPLIED BY THREE-PHASE NON SYMETRIC VOTAGE SYSTEM

Lech Nowak, Krzysztof Kowalski

Poznań University of Technology, Institute of Industrial Electrical Engineering,
ul. Piotrowo 3a, PL-60695 Poznań, Poland
Lech.Nowak@put.poznan.pl, Krzysztof.Kowalski@put.poznan.pl

***Abstract** – In the paper an algorithm for coupled field-circuit simulation of transients in a three-phase, three-limb power transformer is presented. The transients state after the asymmetric supply voltage system has been analysed. The non-linearity and anisotropy of the transformer core have been take into consideration. The magnetic vector potential for three-dimensional magnetic field description has been applied. Also, the inverter fed transformer transients are considered.*

Introduction

Analysis of three-phase transformers are very often performed on the basis of the circuit model. However, such a model does not provide sufficient accuracy in the case of non-symmetrical or transient operations, especially in transformers with a non-linear magnetic core. During transients the non-periodic components of magnetic fluxes cause very strong saturation of some core parts (limbs, yokes) while other parts remain non-saturated. The reluctances of core parts may differ hundred times; their relations vary in time. This disrupts the symmetry of the magnetic field. Furthermore, in the case of a three limb transformer the magnetic field also penetrates the space surrounding the core due to the core saturation and to the non-periodic components of fluxes. Hence, the field, three-dimensional description is necessary. The transient magnetic field in transformer is usually voltage-excited, and this means that the currents in windings are not known in advance. Therefore, the equations of the electric circuits, and the equations describing connections of circuits must be included. Because of the nonlinearity and anisotropy, the magnetic vector potential (MVP) for 3D magnetic field description has been employed. Numerical implementation of the elaborated algorithm is based on the finite elements method. The nonlinear three-dimensional problem has been substituted with a sequence of two-dimensional tasks and the block relaxation method has been employed.

Iterative Field-Circuit Algorithm For 3D Magnetic Field Calculation

Magnetic field equations

The magnetic vector potential (MVP) approach is very convenient for 3D magnetic field modelling in non-homogenous, non-linear environment [2]. It is described by the equation:

$$\operatorname{curl} \nu \operatorname{curl} \vec{A} = \vec{J} \qquad (1)$$

where: $\vec{A}$ is MVP vector $\vec{J}$ is the current density vector, ν is the reluctivity.

The MVP components A_x, A_y, A_z, in eq. 1 are associated with one another even after imposing the Coulomb's gauge [1]. Therefore, as result of the application of the finite element method, one obtains the set of $3n_n$ equations of the form $\mathbf{SA} = \mathbf{F}$, where $\mathbf{S}$ is the stiffness matrix; $\mathbf{A}$ is the one-column matrix (vector) of nodal potentials; $\mathbf{F}$ is the vector of field sources. In the proposed algorithm matrices $\mathbf{S}$, $\mathbf{A}$, $\mathbf{F}$ are divided into n_b submatrices.
The obtained set of equations can be solved iteratively. The single basic iteration consist in a sequential solving of n_b „smaller" sets of equations [3]:

$$\mathbf{S}_{ii}\mathbf{A}_i^m = \mathbf{F}_i - \sum_{j=1, j\neq i}^{j=n_b} \mathbf{S}_{ij}\left(\omega\mathbf{A}_j^l + (1-\omega)\mathbf{A}_j^{l-1}\right) \qquad (2)$$

where m is the number of basic iteration, $l = m$ when $i > j$ or $l = m-1$ when $i < j$, $\omega \in \langle 1,2 \rangle$ is the over-relaxation factor.

In order to include nonlinearity of the ferromagnetic core an additional iterative procedure has been included. This procedure is superior in relation to the basic one used for the solution of the set of FEM equations [5].
Each of sets (2) contains $n_{nb} = n_n / n_b$ equations. The number n_{wb} is usually small enough to solve sets (2) by means of direct, non-iterative method. The Cholesky's method has been applied.
The first term in the right-hand side of equation (2) represents field sources corresponding to i-th block. Because the field is voltage-excited, at the beginning of each „non-linear" iteration, the sources are not known explicitly. The exact values of currents are computed on the basis of electric circuits equations [4,5]. The remaining terms in right side of equation (2) represent mutual connections between blocks. The elaborated procedure is very effective; for example it is up to four times faster than the ICCG algorithm.
In order to include nonlinearity of the ferromagnetic core an additional iterative procedure has been included. This procedure is superior in relation to the basic one used for the solution of the set of FEM equations [3].
Each of the sets (2) contains $n_{nb} = n_n / n_b$ equations. The number n_{nb} is usually small enough to solve sets (2) by means of direct, non-iterative method. The Cholesky's method has been applied.
The first term in the right-hand side of equation (2) represents field sources corresponding to i-th block. Because the field is voltage-excited, at each „non-linear" iteration, the sources are not known explicitly. The exact values of currents are computed on the basis of electric circuits equations [4,5]. The remaining terms in right side of equation (2) represent mutual connections between blocks. The elaborated procedure is very effective; it is even up to four times faster than the ICCG algorithm. Another advantage of the method is the smaller requirement for computer memory.

Circuit Equations

The transient magnetic field in nonlinear structures is produced under supply voltage constraint. Therefore, the Kirchhoff's equations of the transformer electric circuits must be included. In the example, it has been assumed that windings are connected in the non-zero star scheme. The system of line voltages: u_{12}, u_{23}, u_{31} has been forced. The voltages u_{12} and u_{23} have been assumed as independent variables. In this case, the phase voltages: u_1, u_2, u_3 and currents in the windings are not known in advance. In order to solve transient problem, the time-stepping algorithm has been employed The implicit, backward difference procedure, which is unconditionally stable, has been applied. After time-discretization, at the $n-th$ time step and $k-th$ non-linear iteration we have [5]:

$$(\Delta t)^{-1}\left(\boldsymbol{\Psi}_n^k - \boldsymbol{\Psi}_{n-1}\right) + \mathbf{R}\mathbf{i}_n^k = \mathbf{U}_n \qquad (3)$$

The structure of the transformer windings is described by the equation $\mathbf{i} = \mathbf{k}\mathbf{i}'$, where $\mathbf{k}$ is the incidence matrix and $\mathbf{i}'$ is independent loop currents matrix.
Currents $\mathbf{i}_n^k$ in k-th non-linear iteration are computed iteratively and simultaneously with the field [5].

Power Transformer Transients

A three-phase transformer of power $S_n = 160\,\text{kVA}$ and voltage $U_n = 20/0.525\,\text{kV}$ on no load operation has been investigated. The transient state after the application of the following voltage system:

$$u_{12} = k_1\sqrt{2}U_n \sin(100\pi t - \varphi),\ u_{21} = k_2\sqrt{2}U_n \sin\left(100\pi t + \frac{2}{3}\pi\right),\ u_{31} = k_3\sqrt{2}U_n \sin\left(100\pi t + \frac{4}{3}\pi\right) \qquad (4)$$

has been considered.
Figure 1 illustrates current waveforms for nominal (a) and non nominal operating conditions (b, c, d). The current peak values and form strongly depend on the voltage amplitude and asymmetry degree.

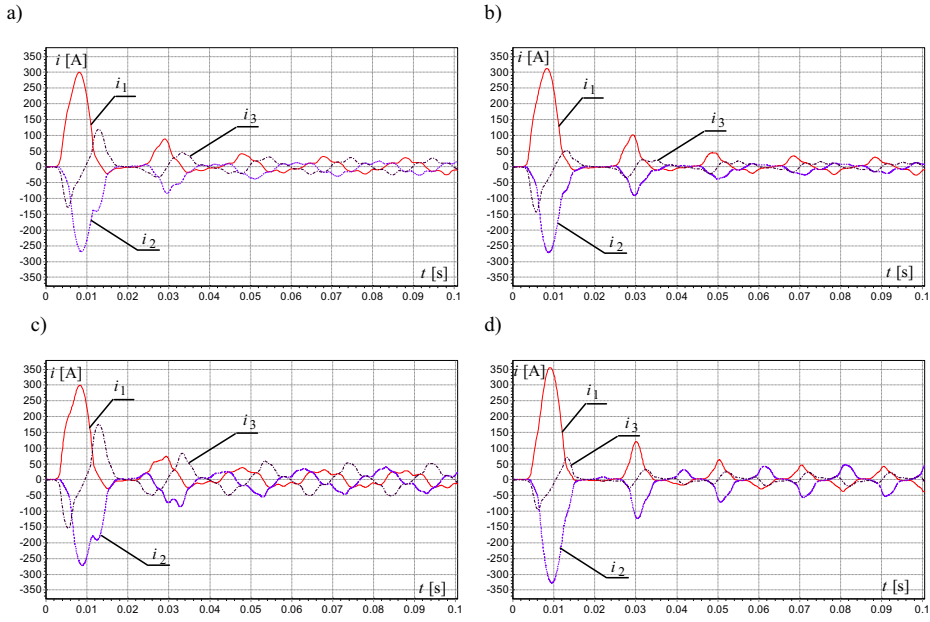

Fig.1 Current waveforms after the application of supply voltage
a) $k_1 = k_2 = k_3 = 1, \varphi = 0$, b) $k_1 = k_3 = 1, k_2 = 0.9, \varphi = 0$,
c) $k_1 = k_3 = 1, k_2 = 1.1, \varphi = 0$, d) $k_1 = 1.1, k_2 = k_3 = 1, \varphi = \pi/12$

The elaborated algorithm enables simulation of transformer transients supplied with the voltage inverter – Fig. 2 .

a) b)

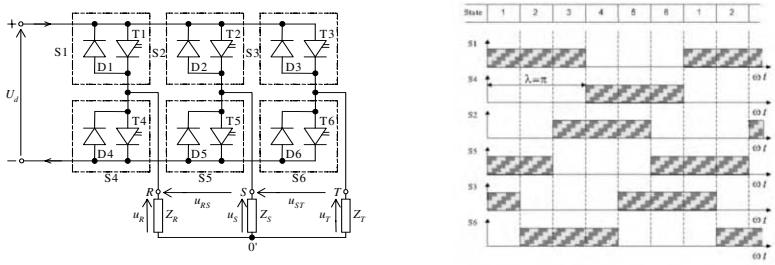

Fig. 2 Three-phase voltage inverter: a) circuit diagram, b) sequence of the switches states

Figure 3 illustrated the time variations of the no load currents for inverter supplied transformer.

a) b)

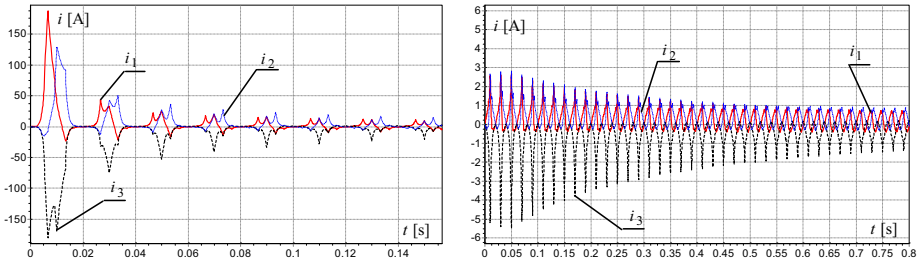

Fig.3 The time variation of the currents at the supply from voltage inverter: a) $U_d = U_n$, b) $U_d = 0.5U_n$

Conclusions

The elaborated algorithm and computer code can be an effective tool for transient analysis of three-phase power transformers. The computer program enables simulation of the transformer transients after the application of symmetric or non symmetric three phase voltage system. The analysis of voltage inverter fed transformer is also possible.

References

[1] N.A. Demerdash, T. Nehl, F.A. Fouad, O.A. Mohammed, Three dimensional finite element vector potential formulation of magnetic fields in electrical apparatus, IEEE Trans. on Power Apparatus and Systems, Vol.100, No.8, pp.4104-4122, 1981

[2] O. Biro, K. Preis, K.R. Richter, On the Use the Magnetic Vector Potential in the Nodal and Edge Finite Element Analysis of 3D Magnetostatic Problem, IEEE Transactions on Magnetics. Vol. 32, No. 3, pp.651-654, 1996

[3] L. Nowak, Iterative procedure for 3D modeling of electromagnetic actuators. IEEE Transactions on Magnetics, Vol.31, No.3, pp.1428-1431, 1995.

[4] L. Nowak, A. Demenko, W. Szeląg, Comparison of 3D and 2D field-circuit model of power transformer transients, COMPEL - The international Journal for Computation and mathematics in Electrical and Electronic Engineering Vol 23 No. 4, pp 1100-1109, 2004.

[5] L. Nowak, K. Kowalski, The 3D coupled field-circuit simulation of transients in non-linear systems. IEEE Transactions on Magnetics, Vol.32, No.3, pp.1078-1081, 1996

Electromagnetic Fields in Mechatronics, Electrical and Electronic Engineering
A. Krawczyk et al. (Eds.)
IOS Press, 2006

FAST FINITE ELEMENT COMPUTATION OF WAVE PROPAGATION PROBLEMS OVER A WIDE FREQUENCY RANGE USING PADÉ APPROXIMATION

Xavier Ojeda, Lionel Pichon

Laboratoire de Génie Electrique de Paris,
UMRS 8507 CNRS, Supélec, Université Paris-Sud, Université Pierre et Marie Curie
Plateau du Moulon, 91192 Gif-sur-Yvette, France

Abstract *- In electromagnetic wave propagation problems, it is usually necessary to compute the fields quantities over a broad frequency band. In this paper we present a 2D computationally-efficient scheme, which combines the finite element method (FEM) with a Padé approximation procedure. The approach is devoted to radiation problems in unbounded space. It allows to obtain an explicit expression of the solution over a large frequency band. The ability of the model is shown in the analysis of the coupling between an electromagnetic wave and a metallic enclosure.*

Introduction

To prevent damages or for electromagnetic shielding, electronic equipments are often located within a metallic enclosure. Apertures on the walls permit the coupling between the internal components and the external fields. These apertures may be intentional for various reasons as input and output connections, control panels, dials, ventilation and visual-access windows. They could also be unintentional, like cracks around doors or poor electrical joints at exterior surfaces. In an electromagnetic compatibility analysis, the shielding effectiveness of a metallic enclosure has to be characterized over a large frequency band. A rigorous analysis requires to solve a scattering problem. Numerical methods are commonly used to describe such electromagnetic scattering problems.

The main difficulty in solving the electromagnetic problem is that the frequency band generally includes several cavity resonance frequencies. With a frequency domain analysis (method of moments, finite elements) the unknowns are solution of a linear system whose matrix depends on frequency. If the field quantities have to be computed over a wide frequency band,the linear system has to be solved for each frequency of interest. This often leads to a huge computational cost. An alternative approach is to search for a power series expansion of the solution about a center frequency. The approach requires only one single matrix inversion. The radius of convergence is limited but it is possible to extend the interval using a corresponding Padé approximant. This technique is known as an asymptotic wave form analysis (AWE) and has been first combined with the method of moments [1][2]. Such an approach has been proposed in [3] for the finite element method in the 2D case. The ability of the method was demonstrated in the scattering of canonical obstacles having simple shapes.

In this work we present a 2D model combining the finite element method and a Padé approximation to study the coupling between an electromagnetic wave and a metallic enclosure. The efficiency of the approach is shown in the case of the scattering over a wide frequency range where sharp resonances occur. A comparison with a standard approach clearly underlines the advantages of the Padé approximation.

1. Finite Element Analysis

Let consider the 2D scattering of a plane wave by a perfectly conducting obstacle. In the TM (Transverse Magnetic) case the incident electric field has only one component along Oz denoted u^i . The

scattered field is searched with only one component u along Oz depending on x and y. In the plane Oxy, Γ is the boundary of the obstacle and Ω the outer region. The unknown u satisfies the Helmholtz equation :

$$\Delta u+k_0^2 u=0 \tag{1}$$

where $k_0=\frac{\omega}{c}$ is the wavenumber (ω is the angular frequency and c is the speed of light).

The scattered field satisfies the radiation condition at infinity :

$$\lim_{r\to+\infty}\sqrt{r}\left(\frac{\partial u}{\partial n}+ik_0 u\right)=0 \tag{2}$$

On Γ the following boundary condition holds :

$$u+u^i=0 \tag{3}$$

A computation by a finite element method is performed in a finite region which includes the obstacle and some of its surrounding medium. The computational domain is truncated by a fictitious outer boundary where the radiation condition is applied as an absorbing boundary condition:

$$\frac{\partial u}{\partial n}+ik_0 u=0 \tag{4}$$

A usual discretization of the domain Ω with first order triangular elements leads to a global matrix system of the form :

$$A(\omega)u=b(\omega) \tag{5}$$

where the matrix $A(\omega)$ can be written as in :

$$A(\omega)=A_0+\omega A_1+\omega^2 A_2\,, \tag{6}$$

with matrices A_0, A_1, A_2 depending on the geometry.

2. Fast Computational Scheme Using Padé Expansion

Consider an arbitrary ω_0 such that A_0 is non-singular, the Taylor series expansion of the matrix polynomial in (6), about ω_0 can be written as:

$$A(\omega)=\overline{A}_0+(\omega-\omega_0)\overline{A}_1+(\omega-\omega_0)^2\overline{A}_2 \tag{7}$$

where the matrices $\overline{A}_i, (i=0,1,2)$ can be obtained from (6) and (7).

The solution vector $v(\omega)$ has a power series representation about ω_0, given by

$$v(\omega)=\sum_{i=0}^{\infty} v_i(\omega-\omega_0)^i \tag{8}$$

The power series representation of the excitation vector $b(\omega)$ is written as:

$$b(\omega)=\sum_{i=0}^{\infty} b_i(\omega-\omega_0)^i \tag{9}$$

We can evaluate the coefficients of the power series of $v(\omega)$ by the following procedure:

$$(\overline{A}_0+(\omega-\omega_0)\overline{A}_1+(\omega-\omega_0)^2\overline{A}_2)(v_0+v_1(\omega-\omega_0)+\ldots)=b_0+b_1(\omega-\omega_0)+\ldots \tag{10}$$

If we equate both sides of (10) term by term, we obtain the following iterative expression:

$$v_i=\overline{A}_0^{-1}b_i-\sum_{j=1,\,j\le i}^{2}\overline{A}_0^{-1}\overline{A}_j v_{i-j}\quad,\ i=0,1,\ldots. \tag{11}$$

It is very important to note that only a single inverse $\overline{A}_0^{-1}$ is needed in the iteration procedure.

For each component $v^j(\omega)$ of $v(\omega)$ a Padé approximant is a rational function of the form $\frac{Q_N(\omega)}{P_M(\omega)}$, where P and Q are polynomials of degrees M and N respectively. The M+N+1 unknowns are obtained by identifying the coefficients of ω in the equation $v^j(\omega)=\frac{Q_N(\omega)}{P_M(\omega)}$. The resulting Padé approximation is valid over a frequency range larger than that given by (8). In the numerical computations we used the diagonal Padé approximation $(N=M)$ which is more accurate; in this case we have 2N+1 unknown coefficients.

3. Numerical Results

Computation of the scattered field in the cavity

The geometry of the studied enclosure is decribed on figure 1. All the results correspond to an exciting plane wave normally incident on the face containing the aperture with an electric field parallel to the z direction.

Fig. 1 : Studied enclosure

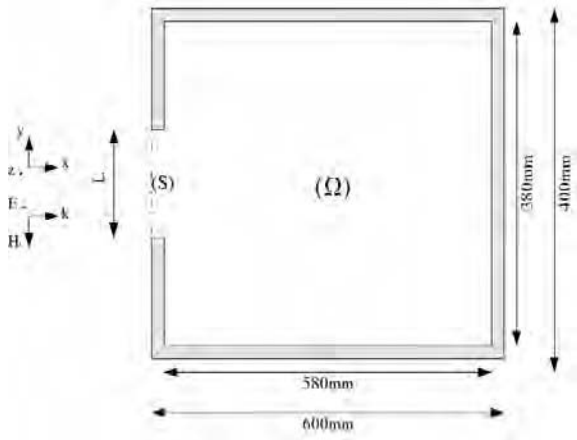

In this study, the dimension L will increase from 40mm to 160mm. Figure 3 shows the computed scattered field in the center of the cavity and in front of the aperture (160mm). It is calculated with a direct method (FEM method), a Taylor expansion (8^{nd} order) and a Padé approximation [4/4] for a center frequency at 830MHz .

The Padé approximant gives a good approximation of the scattered field in the range of 100MHz. So for the broadband study, the Padé approximation the frequency band is subdivided into 9 intervals of 100MHz. In each interval the Taylor series is obtained from a central frequency chosen in the middle of the interval. In order to increase the accuracy of the approximation, this frequency can be chosen near of a resonant peak. However, computations have shown that the approximation is very efficient when this frequency remains in a band of 20MHz around the peak.

The power transmitted through the aperture is computed into two ways. The first one results from the integration of the electric and magnetic energy over the domain Ω. The second one is obtained from the flux of the Poynting vector through the aperture. Figure 7 compares the power transmitted through the aperture (160 mm) calculated by a direct FEM method, by a Padé approximation with integration over Ω (Padé Ω), and by a Padé approximation with integration on S (Padé S).

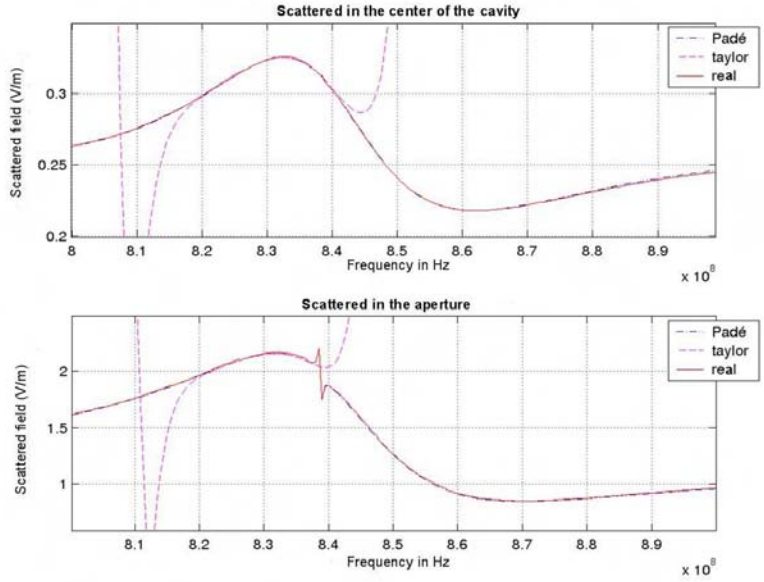

Fig. 2 : Computed scattered field

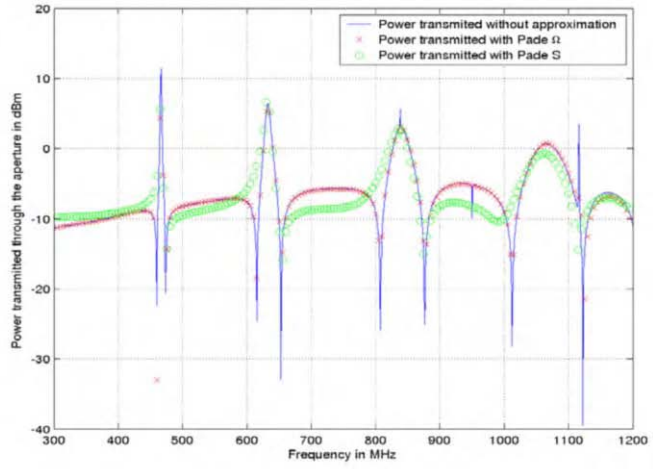

Fig 3 : Approximations of the power transmitted

A very good agreement is observed when calculation of the power transmitted by integration on Ω (Padé Ω). This can be explained since in this case all the nodal values of the computed solution u over Ω are used and the numerical errors do not influence the global value. On the contrary, in the line integral a few values of u are used; the numerical error has a significant influence on the result. Also, the computation time is

significantly reduced. For example the ratio between the direct computation and Padé S is about 15. The approximation of the power transmitted with integration on S is less efficient, but the time of computation is really short.

Application of the Padé approximant to shielding effectivness.

The presented model was studied for the analysis of shielding effectiveness for a thick metallic screen having multiple apertures. Figure 4 shows the different kinds of distribution of apertures on the frontal panel of the cavity. Figures 5,6 and 7 show the computed power transmitted for different distributions of apertures : 2, 4 and 8 apertures of 80 mm, 40mm and 20 mm respectively. Results clearly show how the shielding effect is increased in the case of multiple apertures. In each case results from Padé approximation are very similar to those obtained from a direct FEM method. In particular the resonance peaks are very well recovered. Each resonance peak is very narrow so in order to capture the behaviour of the solution a high number of frequency points is required. However, since the calculation time is very short for Padé approximation, a good deal can be found between computation time and physics representation.

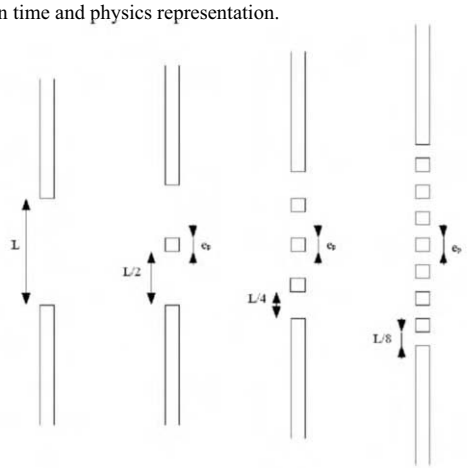

Fig 4 : Studied geometry

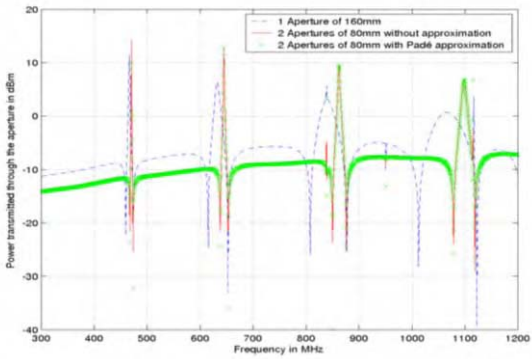

Fig 5 : Comparison between 1 aperture (160 mm) and 2 apertures (80 mm each).

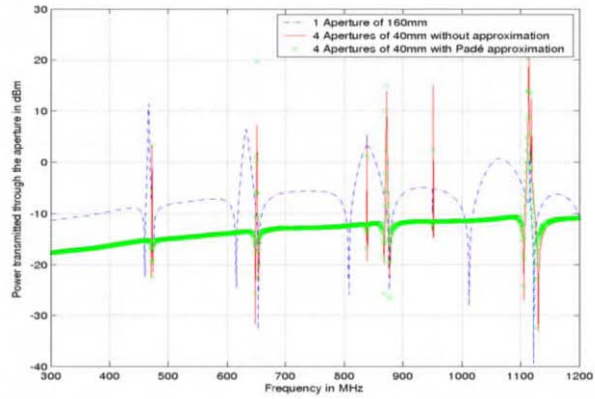

Fig 6 : Comparison between 1 (160 mm) and 4 apertures (40 mm each).

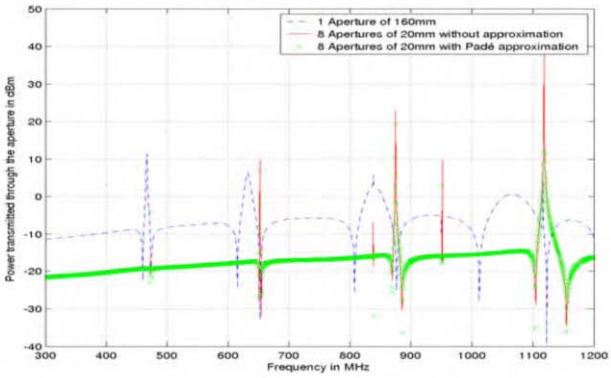

Fig 7 : Comparison between 1 (160 mm) and 8 apertures (20 mm each).

Conclusion

A 2D model combining the finite element method and a Padé approximation was presented for scattering analysis in the framework of radiated electromagnetic compatibility. The technique allows to significantly reduce the computational time in case of a wide frequency band analysis. The efficiency was demonstrated in the scattering of a plane wave by a metallic enclosure having apertures. In particular narrow resonance peaks are well recovered with a Padé approximation. Such an approach can improve the efficiency of the finite element method when used in optimization processes for example.

References

[1] C.J. Reddy, M.D. Deshpande, C.R. Cockrell, F.B. Beck, Fast RCS computation over a frequency band using method of moments in conjunction with asymptotic waveform evaluation, IEEE Transactions on Antennas and Propagation, Vol.46, pp 1229-1233, 1998.
[2] D. Jiao, X.Y. Zhu, J.M. Jin Fast and accurate frequency sweep calculations using asymptotic waveform evaluation and the combined field integral equations, Radio Science, Vol.34, pp 1055-1063, 1999.
[3] M. Kuzuoglu, R. Mittra, Finite element solution of electromagnetic problems over a wide frequency range via the Padé approximation, Comput. Methods Appl. Mech. Engrg, Vol 169, pp 263-277, 1999.

Electromagnetic Fields in Mechatronics, Electrical and Electronic Engineering
A. Krawczyk et al. (Eds.)
IOS Press, 2006

Optimum Design on Reduction of Torque Ripple for a Synchronous Reluctance Motor with Concentrated Winding using Response Surface Methodology

[*]Seong June Park [(1)], Su Jin Jeon, Jung Ho Lee

[(1)] Dept. of Electrical Eng.,Hanbat National University,
San 16-1, Dukmyung-Dong, Yuseong-Gu, Deajeon, Korea
E-mail : mll2@naver.com

***Abstract** – This paper presents an optimization procedure using Response Surface Methodology (RSM) to determine design parameters for reducing torque ripple. RSM has been achieved to use the experimental design method in combination with Finite Element Method (FEM) and well adapted to make analytical model for a complex problem considering a lot of interaction of design variables.*

1. INTRODUCTION

The Synchronous Reluctance Motor (SynRM) has advantage such as low cost and higher efficiency than induction machines. However, the vibration and noise of SynRM caused by torque ripple are relatively greater than other machines.

If stator windings of a SynRM are not a conventional distributed one but the concentrated one, the decreasing of copper loss and decreasing of the production cost due to the simplification in factory are obtained. But it is difficult to expect a good performance from concentrated winding SynRM without considering the defects of higher torque ripple, lower inductance ratio and difference (efficiency, power factor), etc. therefore, it is important to select appropriate combination of the design parameters to reduce the torque ripple.

Response surface methodology is recently been recognized as an effective optimization approach for modeling performance of electrical devices by using statistical fitting method [1].

A polynomial model is generally to be constructed to represent the relationship between the performance and design parameters in RSM. Therefore, this model can be used to predict the performance as a function of design variables, and design optimization can be carried out with much easily.

The quality of the fitted model is evaluated by checking the statistics indexes based on the data of numerical experiments. This paper deals with optimization procedure of SynRM to improve torque performance by RSM [2].

The focus of this paper is the optimum design relative to torque density, torque ripple and inductances on the basis of Stator slot number and open width of slot, teeth width, in order to improve performance and production cost problem of a SynRM.

Comparisons are given with characteristics of normal distributed winding SynRM (24slot) and those according the stator teeth, open width of slot and slot depth variation in concentrated winding SynRM (6slot). By means of these structures, anisotropy ratios up to conventional one are obtained and the consequent torque performance approaches that of state of the art (distributed winding SynRM : 24Slot).

2. ANALYSIS MODEL

2.1 Analysis model of the SynRM

Fig. 1 shows the initial design model of concentrated winding SynRM. The concentrated winding SynRM has 4 poles and 6 slots. And its stack length is 77[mm], and a radius of the rotor is 30.1[mm].

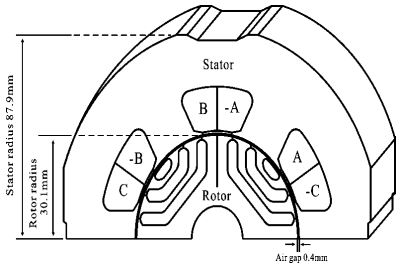

Fig. 1 The initial design model of the SynRM

2.2 Design Variables

Design variables related to torque performance in the SynRM are slot of stator, air gap, rib of rotor and flux barrier as shown in Fig. 2. Among these variables, air gap, rib width and number of flux barrier of SynRM with 6slot is the same conditions with SynRM of 24slot.

Therefore, the open width of slot, slot depth and teeth width are variables for optimum design, which is related to reduction of torque ripple production in 6slot machines. And the number 24, 6slot of stator slot is considered, because it is limited by mechanical and electrical constraint of 3-phase motor.

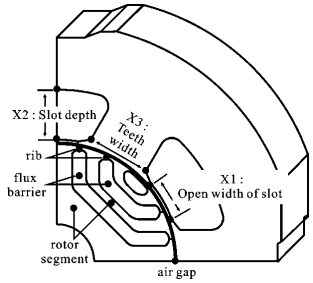

Fig. 2 The design variables of the SynRM

3. OPTIMIZATION USING THE RSM

3.1 Concept of Response Surface Methodology

The RSM seeks to find the relationship between design variable and response through statistical fitting method, which is based on the observed data from system. The response is generally obtained from real experiments or computer simulations. Therefore, 2D Finite Element Analysis is performed to obtain the data of SynRMs in this paper. It is supposed that the true response of a system η can be written as :

$$\eta = F(\zeta_1, \zeta_2, \cdots, \zeta_k) \tag{1}$$

where the variables $\zeta_1, \zeta_2, \cdots, \zeta_k$ in Eq. (1) are expressed as natural units of a measurement, so called natural variables. The form of true response function F is unknown and very complicated, so it is approximated. In many cases, the approximating function U of the function F is normally chosen to be either a first-order or a second-order polynomial model. In order to predict a curvature response more accurately, the second-order model is used in this paper. The approximating function U of true response function F is

$$U = \beta_0 + \sum_{j=1}^{k} \beta_j x_j + \sum_{j=1}^{k} \beta_{jj} x^2_j + \sum_{i \neq j}^{k} \beta_{ij} x_i x_j + \varepsilon \tag{2}$$

where β is regression coefficients, ε is a random error treated as statistical error. The observation response vector $\boldsymbol{U}$ at n data point of function U may be written in matrix notation as follows :

$$\boldsymbol{U} = \mathbf{X}\boldsymbol{\beta} + \boldsymbol{\varepsilon} \tag{3}$$

where, $\mathbf{X}$ is a matrix of the levels of the independent variables, $\boldsymbol{\beta}$ is a vector of the regression coefficients, $\boldsymbol{\varepsilon}$ is a vector of random error.

The least squares method, which is to minimize the sum of the squares of the random errors, is used to estimate unknown vector $\boldsymbol{\beta}$. The least squares function L is

$$L = \sum_{i=1}^{n} \varepsilon_i^{\,2} = \boldsymbol{\varepsilon}'\boldsymbol{\varepsilon} = (\boldsymbol{U} - \boldsymbol{X}\boldsymbol{\beta})'(\boldsymbol{U} - \boldsymbol{X}\boldsymbol{\beta}) \tag{4}$$

The estimated vector $\hat{\boldsymbol{\beta}}$ of unknown vector $\boldsymbol{\beta}$ must satisfy Eq. (5).

$$\left.\frac{\partial L}{\partial \boldsymbol{\beta}}\right|_{\hat{\boldsymbol{\beta}}} = -2\mathbf{X}'\boldsymbol{U} + 2\mathbf{X}'\mathbf{X}\hat{\boldsymbol{\beta}} = 0 \tag{5}$$

Therefore, the estimated vector $\hat{\boldsymbol{\beta}}$ can be written as (6) and the fitted response vector $\hat{\boldsymbol{U}}$ is given by (7).

$$\hat{\boldsymbol{\beta}} = (\mathbf{X}'\mathbf{X})^{-1}\mathbf{X}'\boldsymbol{U} \tag{6}$$

$$\hat{U} = \mathbf{X}\hat{\boldsymbol{\beta}} \tag{7}$$

where, $\boldsymbol{X}'$ is the transpose the matrix $\boldsymbol{X}$.

It is always necessary to examine the fitted model to ensure that it provides an adequate approximation to the true response and verify that none of the least squares regression assumptions are violated. In order to confirm adequacy of the fitted model, analysis-of-variance (ANOVA) table shown in Table I is used in this paper. In Table I, M is the total number of experiments and a is the number of parameters in the fitted model [3].

TABLE I
ANALYSIS OF VARIANCE

Source of Variation	Degree of Freedom	Sum of Squares (SS)	Mean Square (MS)
Regression	a-1	SSR	SSR/(a-1)
Residual (Error)	M-a	SSE	SSE/(M-a)
Total	M-1	SST	

There are three residual sums which play important roles in judging model adequacy ;

- The sum of squares of the residuals SSE ;
- The total sum of squares SST ;
- The regression sum of square SSR=SST-SSE

where $\mathrm{SSE} = \sum_{u=1}^{N}(\mathrm{Y}_u - \hat{\mathrm{Y}}_u)^2$; $\mathrm{SST} = \sum_{u=1}^{N}(\mathrm{Y}_u - \overline{\mathrm{Y}})^2$

(* $\mathrm{Y_u}$: observed value, $\hat{\mathrm{Y}}_\mathrm{u}$: predicted value, $\overline{\mathrm{Y}}$: average value)

The coefficient of determination, R^2, expressed by SST and SSR is

$$R^2 = \frac{\mathrm{SSR}}{\mathrm{SST}} \tag{8}$$

The adjusted coefficient of multiple determination $R_A^{\,2}$ is defined as :

$$R_A^{\,2} = 1 - \frac{\mathrm{SSE}/(\mathrm{M} - \alpha)}{\mathrm{SST}/(\mathrm{M} - 1)} \tag{9}$$

It is a measure of the proportion of the estimate of the error variance provided by the residual mean square of the error variance estimate using the total mean square. Accordingly, adequacy of the fitted model is determined by R^2 and $R_A^{\,2}$ [4].

3.2 Design of Experiments

There are many experimental designs for creation of response surface. Among them, the central composite design (CCD) is chosen to estimate interactions of design variables and curvature properties of response surface in a few times of experiments [5].

The central composite design (CCD) has been widely used for fitting a second-order response surface. Notice that the design of experiments consists of eight runs at the corner of a cubic, plus six runs at the center of its faces, plus one run at the cubic center. In terms of the coded variables the corners of the cubic are ($X1, X2, X3$)=(-1,-1,-1), (1,-1,-1), (-1,1,-1), (-1,-1,1), (1,1,-1), (1,-1,1), (-1,1,1), (1,1,1); the six face central points are at ($X1, X2, X3$)=(-1,0,0), (1,0,0), (0,-1,0), (0,1,0), (0,0,-1), (0,0,1); and the cubic central point is at ($X1, X2, X3$)=(0,0,0) as shown in Fig. 3, and the level of three design variables are shown in Table II.

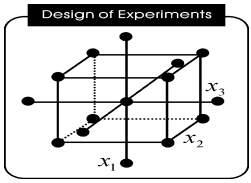

Fig. 3 Central Composite Design for the number of three design variables

TABLE II
THE LEVEL OF DESIGN VARIABLES

	Design variables	The level of design variables				
		-1.682	-1	0	-1	1.682
X1	Open width of slot	1.318	2	3	4	4.681
X2	Slot depth	12.659	13	13.5	14	14.34
X3	Teeth width	13.659	14	14.5	15	15.34

2D FEA-based simulation is used to obtain the responses with respect to the CCD experimental design. These 15 sets of design variables (X1, X2, X3) within the available domain are selected for FEA experiments to fit the second-order model. The observation data and FEA results are listed in Table III.

4. OPTIMIZAION

The purpose of this paper is to minimize the ratio of torque ripple for average torque of SynRM with 6slot using RSM. Using the estimated coefficients, the second-order predictive model can be written as follows :

$$\hat{U} = \beta_0 + \sum_{j=1}^{k} \beta_j x_j + \sum_{j=1}^{k} \beta_{jj} x^2{}_j + \sum_{i \neq j}^{k} \beta_{ij} x_i x_j + \varepsilon \tag{10}$$

where, $\beta_0, \beta_j, \beta_{jj}, \beta_{ij}$ are the coefficients, and they are shown in Table IV.

In fitted second-order polynomial of SynRM with 6slot, R^2 of 0.978 means 97.8[%] of the total variation in the ratio may be explained by the regression surface relating to the design variables. R_A^2 of 0.959 indicates that the estimate of the error variation by the residual mean square is 4.1[%] of the error variation estimate using total mean square.

Accordingly, the ratio of torque ripple for average torque obtained by RSM is compared with the result of FEM in optimal point of each model. When open width is 3.0[mm], slot depth is 13.5[mm] and teeth width is 15.341[mm] in optimal point of SynRM with 6slot, the ratio obtained by RSM is 111[%] and the result of FEM is 109.8[%] respectively. Fig. 4 shows the response surface of the ratio on the SynRM of 6-slot.

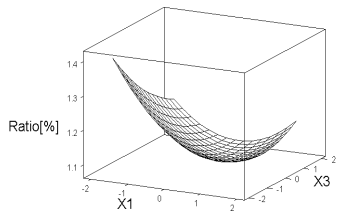

Fig. 4 Response Surface for the Ratio of 6slot

Several design solutions have been found by design strategy of Fig. 5.

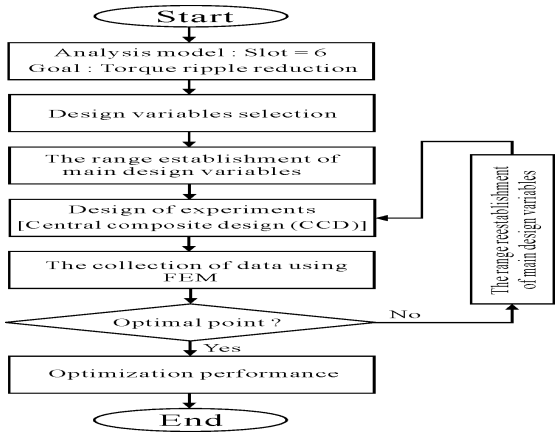

Fig. 5 The flow chart of design procedure

5. RESULTS OF DISCUSSION

The comparison with the optimized and initial ratio is shown in Table V. Fig. 6 shows configurations of optimized and initial design for 6 slot. As shown in Fig. 7, the optimized concentrated winding SynRM' torque ripples is larger than those of 24 slot because of large inductance variations due to structures. But, the values are smaller than one of initial 6 slot model. And considering decrease of copper loss and cost, in spite of more torque ripple, the optimized model should guarantee the better performance level as the conventional 24 slot model.[6]

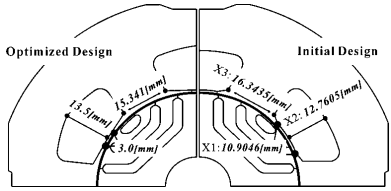

Fig. 6 Configurations of optimized and initial design for 6 slots

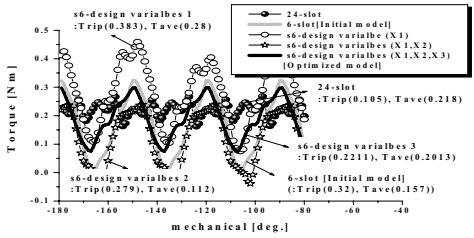

Fig. 7 Results of Torque analysis

6. CONCLUSIONS

This paper presents a RSM optimization technique in order to reduce the torque ripple of the concentrated winding SynRM. And appropriateness of RSM in machines optimization method is verified by the result of

optimized the SynRM. Therefore, RSM approach can be considered as optimization method for optimum design of SynRM and other machines. The decreasing of copper loss, a slight larger torque ripple characteristic as compared with state of the art (24 slot model) and decrasing of the production cost due to the simplification of winding in factory obtain the high industrial competitive power.

REFERENCES

[1] Y.K. Kim, Y.S. Jo, J.P. Hong : Approach to the shape optimization of racetrack type high temperature superconducting magnet using response surface methodology, Cryogenics, Vol 41, No 1, 2001, pp. 39-47.

[2] J.T. Li, Z.J. Liu, M.A. Jabbar, X.K. Gao : Design optimization for cogging torque minimization using response surface methodology, IEEE Transactions on Magnetics, Vol 40, No 2, 2004, pp.1176-1179.

[3] Raymond H. Myers and Douglas C. Montgomery, *Response Surface Methodology: Process and Product Optimization Using Design Experiments*, JOHN WILEY & SONS, 1995.

[4] A.I. Khuri and J.A. Cornell, *Response Surface: Designs and Analyzes*, New York: Marcel Dekker, 1996.

[5] S.H. Park, *Modern Design of Experiments*, Minyoungsa, 2001.

[6] J.H. Lee, D.S. Hyun : Hysteresis Analysis for the permanent magnet assisted synchronous reluctance motor by coupled FEM & preisach modeling, IEEE Transactions on Magnetics, Vol 35, No 3, 1999, pp.1203-120.

TABLE III
CENTRAL COMPOSITE DESIGN

Exper. No.	Design Variables X1 [mm]	X2 [mm]	X3 [mm]	Trip [N-m]	Tave [N-m]	Ratio [%]
1	3.0	13.5	14.5	0.2168	0.1951	1.1109
2	4.6818	13.5	14.5	0.2217	0.1992	1.1131
3	3.0	13.5	15.341	0.2211	0.2013	1.0980
4	3.0	13.5	13.659	0.2237	0.1889	1.1842
5	4.0	13.0	14.0	0.2186	0.1933	1.1305
6	2.0	13.0	15.0	0.2197	0.1940	1.1323
7	2.0	14.0	14.0	0.2313	0.1868	1.2382
8	3.0	14.341	14.5	0.2164	0.1951	1.1091
9	3.0	12.659	14.5	0.2169	0.1952	1.1110
10	4.0	14.0	15.0	0.2232	0.2013	1.1087
11	1.3182	13.5	14.5	0.2388	0.1864	1.2811
12	4.0	13.0	15.0	0.2231	0.2007	1.1116
13	2.0	13.0	14.0	0.2305	0.1862	1.2378
14	2.0	14.0	15.0	0.2208	0.1947	1.1345
15	4.0	14.0	14.0	0.2197	0.1939	1.1328

* X1 : Open width of slot, X2 : Slot depth, X3 : tooth width, Trip : Tripple, Tave : Taverage, Ratio : Trip/Tave[%]

TABLE IV
ESTIMATED COEFFICIENT OF THE ANALYSIS MODEL

Coefficients	Estimated value Trip [Nm]	Tave [Nm]	Ratio [%]
β_0	2.3045	1.0359	13.2851
β_1	-0.1409	0.0127	-0.8138
β_2	0.0088	0.0573	0.0083
β_3	-0.2644	-0.1774	-1.4521
β_{11}	0.0047	-0.0014	0.0309
β_{22}	-1.6283E-05	-0.0024	0.0008
β_{33}	0.0084	0.006	0.0447
β_{12}	-0.0002	0.0002	-0.0001
β_{13}	0.0077	-0.0002	0.0415
β_{23}	-0.0005	0.0005	-0.002

TABLE V
OPTIMIZED RESULTS

	Optimized values	Optimized Ratio [RSM]	Observed Ratio [FEM]
X1	3.0[mm]		
X2	13.5[mm]	111[%]	109.8[%]
X3	15.341[mm]		

Electromagnetic Fields in Mechatronics, Electrical and Electronic Engineering
A. Krawczyk et al. (Eds.)
IOS Press, 2006

A RESONANCE CURRENT BASED OPERATING STRATEGY FOR A VARIABLE RELUCTANCE MOTOR

Chung-How Poh, Özdemir Göl, Sam Ali

University of South Australia, GPO Box 2471, Adelaide, South Australia 5001, Australia
Ozdemir.Gol@unisa.edu.au

***Abstract*-An operating strategy for a variable reluctance motor based on the sequential excitation of phase windings has been developed. The main goal is to achieve acceptable system performance with a simple architecture and minimal hardware. Simultaneous excitation of multiple phases is avoided in the interest of better current utilisation. It would seem that the best outcome is achieved when a rectangular pulse with smoothed rising and falling edges is used for phase excitation. This is achieved by means of a resonant circuit which includes the phase winding.**

Introduction

According to [1], the power output of a variable reluctance motor is higher than that of an a.c. induction motor of a comparable size. The absence of the induced current in the torque producing mechanism makes it possible for the reluctance motor to have higher energy efficiency compared to the a.c. induction machine [2].

However, it is also known that the variable reluctance motor is not without its own drawbacks. Its torque ripple and the radiated acoustic noise are significantly higher than other motor types [3]. There have been extensive efforts to mitigate these issues, particularly the torque ripple problem [4]. Some advanced approaches reported in the literature such as ripple reduction using intelligent techniques have proven to be effective [5].

The work presented in this paper attempts to search for yet another solution to the drawbacks by a global approach. Consideration is given to the structure of the motor, its intended operating strategy and the approach taken to achieve the proposed strategy. The system is expected to demonstrate the following properties:

1) acceptable system performance
2) modest hardware requirement and low cost.

Developing an Operating Strategy

It has been shown that a major source of acoustic noise in the reluctance motor is the radial oscillation of the stator core along the axis of the excited pole winding, initiated at the point of commutation [6]. The intensity of the radiated sound depends on the extent to which the stator core is radially compressed before the collapse of the compression force. The work presented here began with a study to identify the qualitative connection between the rotor torque and the radial compression force. A model of a fictitious variable reluctance motor with a 2-2 structural configuration was created using the Finite *Element Method Magnetics, version 4.0* (*FEMM 4.0*). A script file in *Lua* language was written to enable the rotor torque as well as the radial compression force acting on the stator tooth to

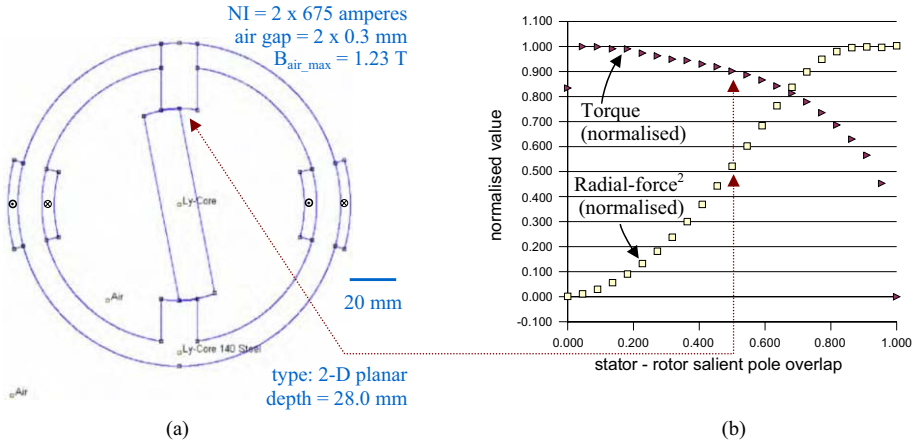

(a) (b)

Figure 1: a) The 2-2 reluctance motor. b) Torque and radial compression force as a function of overlap.

be charted against the rotor position. Fig. 1 (a) shows the fictitious 2-2 reluctance motor along with its principal data with Fig. 1 (b) giving the ensuing torque and radial force values. The upper stator salient pole is surrounded by a 50 μm air gap on both of its sides to facilitate the finite element calculation of the radial compression force. The values for the quasi-static torque and the square of the radial compression force (acoustic intensity is taken to be proportional to the square of the radial force) are given with an interval of one degree of the rotor angular position over the overlap. Overlap = 1.000 denotes the fully aligned rotor position.

The results in Fig. 1 indicate that the radial compression force increases with the overlap between the stator and the rotor tooth, while the quasi-static torque falls at an increasing rate. Hence, the torque demonstrates a negative correlation with respect to the radial compression force.

Based on these outcomes, a possible phase excitation rule is to turn on the excitation early to harvest the reluctance torque while it is relatively steady and to switch off the excitation as early as possible, before the rotor pole reaches the fully aligned position so as to minimise the radial compression force. This presupposes an excitation strategy linked to the rotor position: stator pole is excited when the rotor pole starts the overlap (in Fig. 1b, overlap = 0.000), being de-energised when the leading edge of the rotor pole reaches just past the halfway point of the stator pole (overlap = 0.500).

Use of Resonance Current with Experimental Setup

Once the stator-rotor interaction on the 2-2 structure was examined, the work proceeded to consider the issue of continuous torque generation. Since, a set of stator-rotor pole pair will only be able to contribute torque for a finite angular range, a structure with a suitable configuration will be required. On the basis of the excitation strategy discussed above, an 8-10 (stator-rotor) configuration was selected, using a graphical approach, for use experimental work. The topology for the motor obtained by finite element modelling, together with some of its key parameters, is appended to Fig. 2. as an inset. Fig. 2 depicts the calculated reluctance torque as a function of the overlap and phase current density. It is seen that the reluctance torque is more or less symmetrical around the 8-degree position, with the 18-degree position denoting the full overlap. J in the legend box is the current density in A/mm^2.

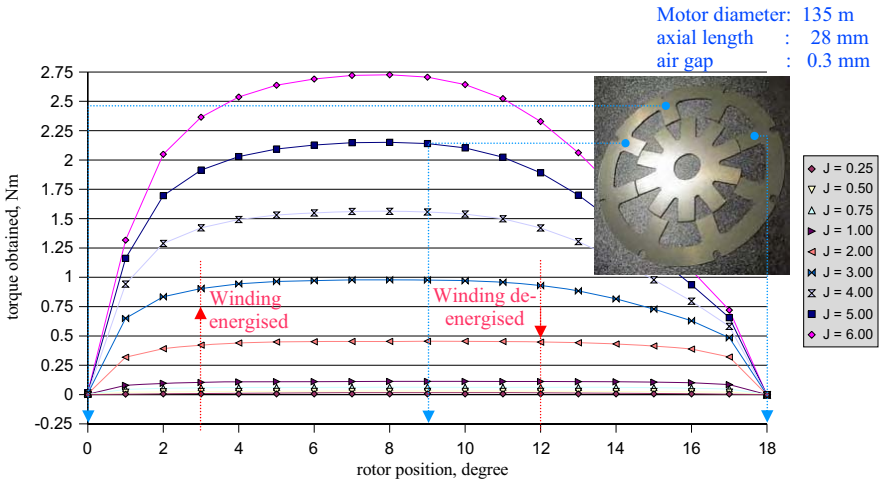

Figure 2: Reluctance torque as a function of overlap for 8-10 topology

Fig. 2 also shows that when the current is kept constant during excitation periods, the developed torque is acceptably constant with respect to the rotor position. This justifies the conclusion that the phase excitation current should approximate as closely as practicable a rectangular shape in the current-time space, if torque ripple is to be kept low. However, a step-rise edge for the current is unrealistic. A closer examination of the process reveals that a sigmoid edge in the torque-time space would result if the current edge profile was a good approximation to a sinusoid. The sigmoid edges in the torque-time space are intended to reduce the torque ripple at the points of commutation. The use of LC resonance has finally been adopted since the resultant phase current is indeed a good approximation to a sinusoid and it is produced naturally without requiring an external current source with a compiled lookup table built into the control circuitry.

Resonant Circuit Structure

The LC resonant circuit comprises the phase winding and a capacitor. The capacitor is controlled by a bi-directional triac which functions as an automatic cut-off switch once the magnitude of the discharge/charge current falls below the triac holding level. The capacitor and the phase winding are nested within four silicon controlled rectifiers (SCRs). The SCRs collectively function as an H-bridge structure so that the supply current through the phase winding can be changed alternately to match the voltage polarity of the capacitor. The H-bridge also serves to protect the d.c. supply from the capacitor when the triac is conducting and the capacitor is charged. The solid state switches are co-ordinated using a PIC16F84A (16 MHz) micro-controller. Fig. 3 illustrates the circuit structure.

The *ADC Pico 200* was used for gathering the current traces with the measurements made across the 0.1 Ω resistor. An infrared emitter-detector unit attached onto the experimental motor sensed an inkjet printed encoder disc to initiate the energising and the de-energising procedures shown in Fig. 4.

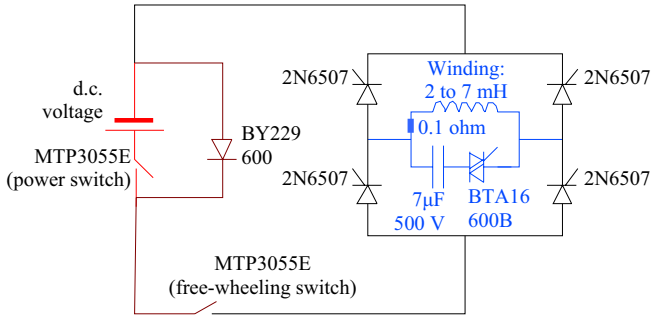

Figure 3: The circuit for realising the operating strategy.
(0.1 ohm resistor serves as a shunt for phase current measurement.)

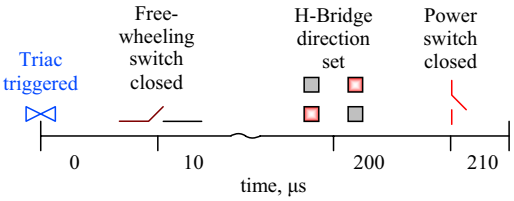

Figure 4 a): Energising procedure
(Although not illustrated, the triac triggering pulse lasts for about 120 μs to ensure that its conducting current is established above the holding level.)

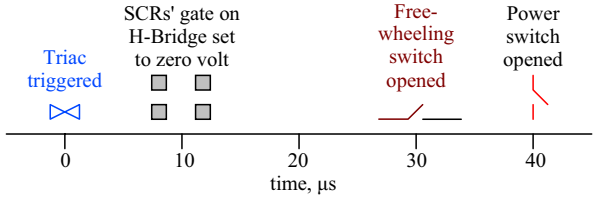

Figure 4 b): De-energising procedure.
(The triac trigger pulse lasts for about 160 μs to ensure that its current is properly established before its gate voltage is removed.)

Once the energising procedure is completed, the power switch can be driven by a pulse width modulated signal (PWM) to provide a means of torque/speed control. However, a transistor embedded within a Wheatstone bridge (or an equivalent ensemble) should be added in series with the triac to ensure a proper disconnection between the capacitor and the phase winding. It has been observed that the phase voltage across the winding in response to the PWM signal triggers the triac into conduction which affects the supply current. A 50 kHz PWM signal is used in this work for the purpose of soft starting, particularly when the input voltage is 14 volts or higher. As expected, the output voltage varies non-linearly with the duty cycle with a sharp increase in the output when the on-time/off-time ratio is approaching unity. This is due to the presence of the capacitor in parallel with the winding.

Results

The resonance current develops as expected through the phase winding when the triac is triggered using the circuit depicted in Fig. 3, as seen in Fig. 5 and 6. The d.c. supply consists of 8 lead-acid cells in series (about 16 Vdc) and the speed of rotation is 1100 rpm. Fig. 5 (a) shows the phase current when one of the four phases is driven. Fig. 5 (b) is the same current measured at a higher resolution, indicating a delay in energising the phase winding. Fig. 6 (a) shows the capacitor current during energising/de-energising cycle. As can be seen, turning-off (i.e. the de-energising procedure) takes longer than turning-on (the energising procedure) because of the parametrically variable nature of the phase inductance. The turning on and off duration are close to predictions offered by the standard LC resonance equation. Interestingly, it has been observed earlier that if the rotor was kept stationary (inductance ~ constant) the capacitor current could only reach about $^2/_3$ of the steady state current level due to energy losses within the circuit. It seems that the inductance at the point of de-energising, L_{off}, and that at the point of energising, L_{on}, should differ by about a factor of two or more to compensate for the energy dissipative effect so that the capacitor current can reach the steady state level after the triac is triggered. Fig. 6 (b) shows the current drawn from the supply, indicating that the timing for switching was appropriate since it remains virtually constant through the cycle.

The above observation allows the conclusion that the rise amplitude of the resonance current (after the triac is triggered) is affected by the L_{off}/L_{on} ratio. This ratio in turn depends on the level of saturation in the ferromagnetic core material (operating current dependent) as well as the position at which the energising procedure is initiated (in this work, the set position is at an alignment of 3º into the overlap). Fig. 7 shows the changes in the phase current pattern when the infrared emitter-detector unit was shifted so that the energising point would occur earlier (position < 3º) increasing the L_{off}/L_{on} ratio. It is observed that an increased L_{off}/L_{on} ratio causes an overshoot, both in the phase current - indicated by the shunt voltage in Fig. 7 (a) - and the developed torque, in this case calculated by importing the current values into the finite element model. Fig. 7 (b) illustrates the ensuing torque ripple behaviour at instances of commutation, which is accentuated due to high L_{off}/L_{on} ratio.

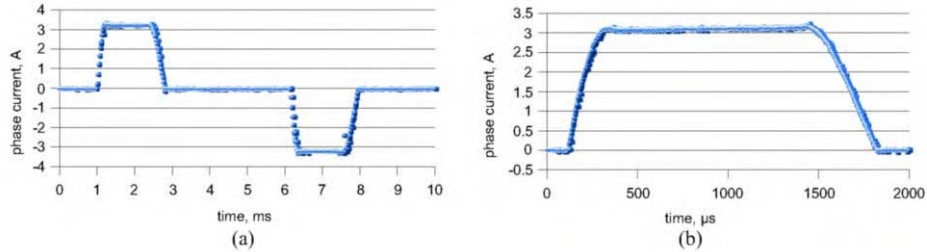

Figure 5: a) Phase current. b) Phase current measured with higher resolution.

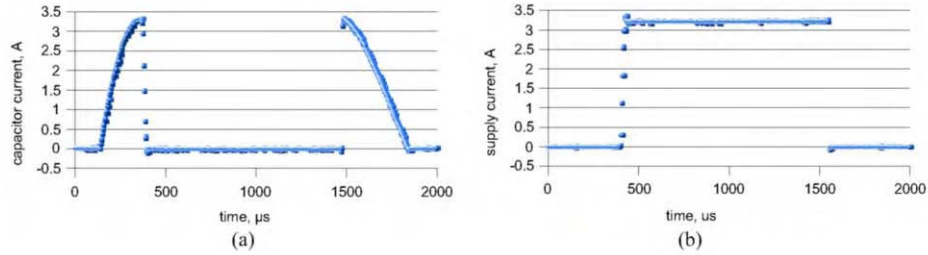

Figure 6: a) Capacitor current. b) Battery supply current.

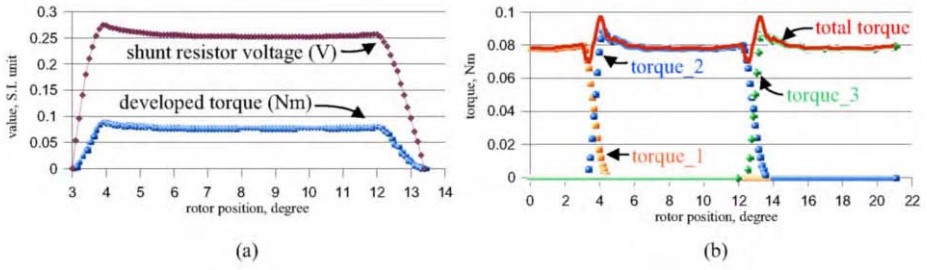

Figure 7: a) Overshoot with high L_{off}/L_{on} ratio. b) Torque ripple due to commutation.

Conclusion

The resonance current based operating strategy has been implemented in controlling a proof-of-concept variable reluctance motor with measurable success. It has been found that the extent of torque ripple is controllable by varying the angular position of the rotor at which the phase winding is energised. The proposed strategy holds the promise of reducing the ripple in the developed torque along with achieving reduced noise. The strategy proposed is attractive and merits further attention since it is based on a simple but effective circuit with a modest component count.

Acknowledgement

The authors gratefully acknowledge David Meeker, Jonathan Shewchuk and TeCGraf for making available free of charge *FEMM 4.0*, *Triangle* and *Lua* language respectively.

References

[1] I. Husain and M. Ehsani, *Torque ripple minimization in switched reluctance motor drives by PWM current control*, IEEE Transactions on Power Electronics, Vol. 11, No. 1, pp 83-88, Jan. 1996

[2] J. Larminie and J. Lowry, *Electric Vehicle Technology Explained*, Wiley, 2003, pp 175

[3] M. Sanada et al., *Novel rotor pole design of switched reluctance motors to reduce the acoutic noise*, Conf. Rec. IAS. Annu. Meet., Vol. 1, pp 107-113, 2000

[4] K. Rahman and S. Schulz, *High-performance fully digital switched reluctance motor controller for vehicle propulsion*, IEEE Trans. Ind. Appl., Vol. 38, No. 4, pp 1062-107, July/August 2002

[5] I. Agirman et al., *Adaptive torque-ripple minimization in switched reluctance motors*, IEEE Trans. Ind. Electron., Vol. 48, No. 3, pp 664-672, June 2001

[6] C. Pollock and C. Wu, *Acoustic noise cancellation techniques for switched reluctance drives*, Conf. Rec. IAS. Annu. Meet., Vol. 1, pp 448-455, 1995

Electromagnetic Fields in Mechatronics, Electrical and Electronic Engineering
A. Krawczyk et al. (Eds.)
IOS Press, 2006

HIGHER-ORDER SPATIAL FDTD SCHEMES FOR EM PROPAGATION IN DISPERSIVE MEDIA*

K.P. Prokopidis and T.D. Tsiboukis

Department of Electrical and Computer Engineering, Aristotle University of Thessaloniki,
GR-54124, Thessaloniki, Greece (E-mail: kprokopi@faraday.ee.auth.gr; tsibukis@auth.gr)

***Abstract** – A higher-order (2,N) (second-order temporal and Nth-order spatial) FDTD scheme with perfectly matched layer (PML) absorbing boundary condition (ABC) is proposed for long-distance and/or time-prolongated electromagnetic (EM) wave propagation in Debye and Lorentz media of arbitrary number of poles. The numerical dispersion relation is derived and the dispersion errors are compared with relevant techniques. The accuracy and efficiency of the suggested method is demonstrated through numerical simulations and comparisons to the original FDTD scheme and to the analytic solutions.*

Introduction

The conventional finite-difference time-domain (FDTD) method [1] has been extensively used to simulate electromagnetic (EM) wave propagation in dispersive media. Although, the FDTD algorithm has already found widespread successful applications, to ensure the accuracy of the computed spatial derivatives of the fields, a fine spatial discretisation (usually more than 10 cells per minimum wavelength) is required, increasing the memory demands. In other words, the inherent numerical dispersion and anisotropy errors render the original second-order FDTD scheme improper for long distance wave propagation or large body problems.

Higher-order (HO) FDTD algorithms have been proposed to improve the accuracy of the calculations for the above simulations. Several researchers [2-4] have studied general (2,N) (second-order temporal and Nth-order spatial) schemes only in non-dispersive media. Nevertheless, the study of EM propagation in dispersive media usually demands fine mesh resolutions and long time duration, rendering HO methods a natural choice. Some papers, [5,6] combine HO techniques with FDTD method for dispersive media in order to increase accuracy and reduce dispersion error and computational cost. Here, we propose a novel methodology, optimized in terms of additional variables, that utilizes fourth- and sixth-order accurate spatial approximations and a modified version of the Auxiliary Differential Equations (ADE) described in [7]. The dispersion errors associated with the proposed techniques are also considered. In addition, we introduce fifth- and sixth-order one-sided approximations to complete the (2,6) scheme at the interior grid points near to the boundary. Finally, we propose a new perfectly matched layer (PML) that can be placed adjacent to a dispersive medium and terminate the FDTD computational domain.

Higher-order Spatial Schemes for Dispersive media

The central difference operator $\delta_{N,\beta}$ of N-order (N : even number) has the general form

* This work was supported by IRAKLITOS-Fellowships for Research of the Aristotle University of Thessaloniki (under Grant 21765), partly funded by the E.U.

$$\delta_{N,\beta} f_n = \sum_{m=1\,(m\,\mathrm{odd})}^{N-1} c_{N,m}\left(f_{n+m/2} - f_{n-m/2}\right) \tag{1}$$

where β is one of the spatial variables (x, y, z) and m is its corresponding index. Therefore, the central finite-difference approximation to a derivative is $\partial f / \partial \beta \cong \delta_{N,\beta} f / \Delta\beta$. The coefficients $c_{N,m}$ are calculated through Taylor series expansions and are given in a closed form [8] by

$$c_{N,m} = \frac{(-1)^{\frac{m-1}{2}}}{2\left(\frac{m}{2}\right)^2} \frac{\left[(N-1)!!\right]^2}{(N-1-m)!!(N-1+m)!!}, m = 1,3,5,\ldots,N-1 \tag{2}$$

where $n!!$ is the double factorial. Applying the previous formula, the coefficients $c_{2,1} = 1$ for Yee's scheme, $c_{4,1} = 9/8$ and $c_{4,3} = -1/24$ for Fang's fourth-order scheme, and $c_{6,1} = 75/64$, $c_{6,3} = -25/384$, $c_{6,5} = 3/640$ for a sixth-order scheme are yielded.

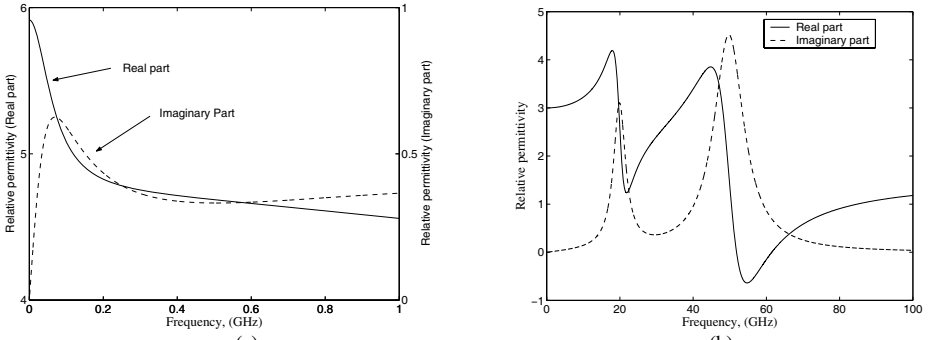

Fig.1 Complex relative permittivity of (a) a Debye medium ($\varepsilon_\infty = 4.048\varepsilon_0$, $\varepsilon_{s1} = 5.248\varepsilon_0$, $\varepsilon_{s2} = 4.715\varepsilon_0$, $\tau_1 = 2.386$ nsec, $\tau_2 = 0.09$ nsec) and (b) a Lorentz medium ($\varepsilon_s = 3\varepsilon_0$, $\varepsilon_\infty = 1.5\varepsilon_0$, $\omega_1 = 40\pi \times 10^9$ rad/sec, $\delta_1 = 0.1\omega_1$, $G_1 = 0.4$, $\omega_2 = 100\pi \times 10^9$ rad/sec, $\delta_2 = 0.1\omega_2$ $G_2 = 0.6$)

The permittivity functions of a Debye medium with M poles and a Lorentz medium with M pole pairs are expressed in the frequency domain (assuming $e^{j\omega t}$ time dependence) through the relations

$$\varepsilon_D(\omega) = \varepsilon_0 \varepsilon_{D,r}(\omega) = \varepsilon_\infty + \sum_{p=1}^{M} \frac{\varepsilon_{sp} - \varepsilon_\infty}{1 + j\omega\tau_p}, \quad \varepsilon_L(\omega) = \varepsilon_0 \varepsilon_{L,r}(\omega) = \varepsilon_\infty + (\varepsilon_s - \varepsilon_\infty) \sum_{p=1}^{M} \frac{G_p \omega_p^2}{\omega_p^2 + 2j\omega\delta_p - \omega^2} \tag{3}$$

where $\varepsilon_\infty, \varepsilon_s$ are the infinite and static frequency permittivities, τ_p is the relaxation time of the pth Debye pole, and ω_p, δ_p, G_p are the pth resonant frequency, the pth damping factor and pth pole amplitude of the Lorentz medium, respectively. The real and the imaginary parts of the relative complex permittivities for a Debye ($\varepsilon_{D,r}$) and a Lorentz ($\varepsilon_{L,r}$) medium are shown in Fig. 1. Following the methodology of [7], an additional variable is introduced for each FDTD cell. The update equation of the $\mathbf{Q}_p$ variable for the M -pole Debye medium is

$$\mathbf{Q}_p^{n+1} = \frac{2\tau_p - \Delta t}{2\tau_p + \Delta t}\mathbf{Q}_p^n + \frac{(\varepsilon_{sp} - \varepsilon_\infty)\Delta t}{2\tau_p + \Delta t}\left(\mathbf{E}^{n+1} + \mathbf{E}^n\right) \tag{4}$$

and the Ampere's law is discretised as

$$\mathbf{E}^{n+1} = c_e \mathbf{E}^n + c_m \nabla \times \mathbf{H}^{n+1/2} + 2c_m \sum_{p=1}^{M} \frac{1}{2\tau_p + \Delta t}\mathbf{Q}_p^n \tag{5}$$

where c_e and c_m are constants involving medium parameters and Δt, given by

$$c_e = \frac{2\varepsilon_\infty - \sigma\Delta t - 2\gamma}{2\varepsilon_\infty + \sigma\Delta t + 2\gamma},\ c_m = \frac{2\Delta t}{2\varepsilon_\infty + \sigma\Delta t + 2\gamma}, \text{ and } \gamma = \sum_{p=1}^{M} \frac{(\varepsilon_{sp} - \varepsilon_\infty)\Delta t}{2\tau_p + \Delta t}. \tag{6}$$

The spatial derivatives of the curl are replaced by the HO accurate approximations. Similar expressions for the Lorentz medium can easily be derived and are the following

$$\mathbf{Q}_p^{n+1} = \frac{\delta_p \Delta t - 1}{\delta_p \Delta t + 1}\mathbf{Q}_p^{n-1} + \frac{2 - (\Delta t)^2 \omega_p^2}{\delta_p \Delta t + 1}\mathbf{Q}_p^{n} + \frac{(\Delta t)^2 G_p \omega_p^2}{\delta_p \Delta t + 1}\mathbf{E}^n \tag{7}$$

$$\mathbf{E}^{n+1} = \frac{2\varepsilon_\infty - \sigma\Delta t}{2\varepsilon_\infty + \sigma\Delta t}\mathbf{E}^n + \frac{2\Delta t}{2\varepsilon_\infty + \sigma\Delta t}\nabla \times \mathbf{H}^{n+1/2} - \frac{2}{2\varepsilon_\infty + \sigma\Delta t}\sum_{p=1}^{M}(\mathbf{Q}_p^{n+1} - \mathbf{Q}_p^{n}) \tag{8}$$

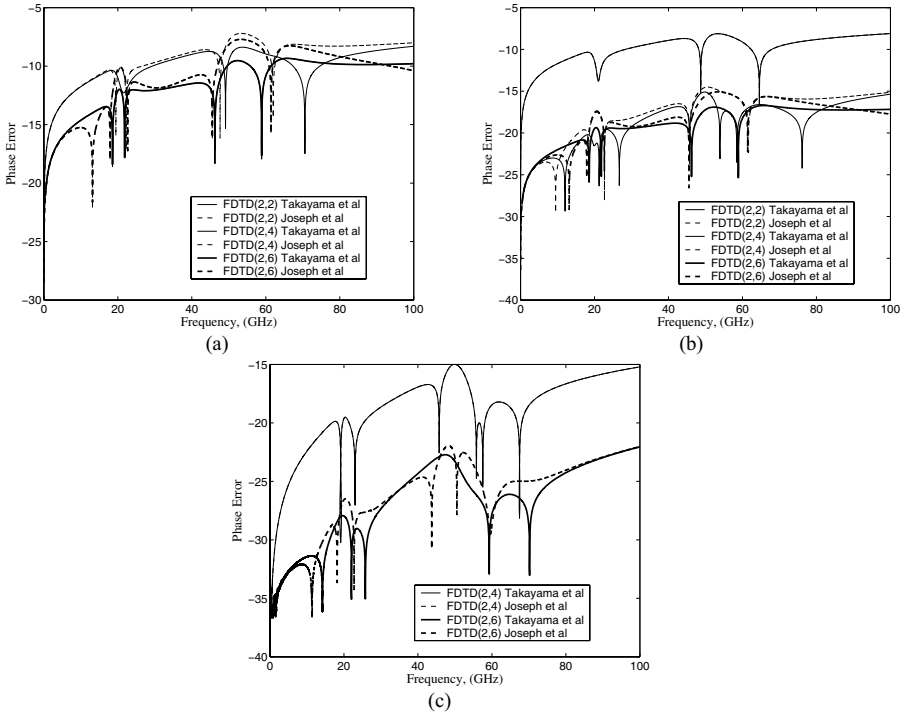

Fig.2 The phase error as a function of frequency for the Lorentz medium with parameters of Fig. 1(b) and $\Delta x = 37.5\,\mu\text{m}$ and Courant number (a) $Q = 0.4$ and (b) $Q = 0.01$ and (c) comparison of the HO schemes for very small time step ($Q = 10^{-4}$)

The HO stencils require numerical boundary conditions (except for the ABCs) at the nodes next to the electric field boundary node. For the (2,4) scheme we used the fourth- and third-order accurate one-sided approximations of [9]. However, the sixth-order stencil requires numerical conditions for four nodes next to the boundary. For the electric field node next to the boundary node we obtain, through Taylor expansions, the following fifth-order one-sided approximation

$$\left(\frac{\partial f}{\partial \beta}\right)_1 = \frac{1}{2235\Delta\beta}\left(-1689 f_{1/2} + 1005 f_{3/2} + 1430 f_{5/2} - 1110 f_{7/2} + 435 f_{9/2} - f_{11/2}\right) + \mathrm{O}((\Delta\beta)^5) \tag{9}$$

and the respective one-sided expressions for all other electric and magnetic nodes

$$\left(\frac{\partial f}{\partial \beta}\right)_{1/2} = \frac{1}{3169\Delta\beta}\left(-3254 f_0 + 1266 f_1 + 4720 f_2 - 4700 f_3 + 2730 f_4 - 866 f_5 + 2 f_6\right) + O((\Delta\beta)^6) \quad (10)$$

$$\left(\frac{\partial f}{\partial \beta}\right)_{3/2} = \frac{1}{1920\Delta\beta}\left(62 f_0 - 2061 f_1 + 1935 f_2 + 190 f_3 - 180 f_4 + 63 f_5 - 9 f_6\right) + O((\Delta\beta)^6) \quad (11)$$

$$\left(\frac{\partial f}{\partial \beta}\right)_{2} = \frac{1}{1920\Delta\beta}\left(71 f_{1/2} - 2115 f_{3/2} + 2070 f_{5/2} + 10 f_{7/2} - 45 f_{9/2} + 9 f_{11/2}\right) + O((\Delta\beta)^5). \quad (12)$$

Numerical Dispersion Relations

Suppose each field variable $\mathbf{F}$ ($\mathbf{E}$ or $\mathbf{H}$) is represented as a plane wave of the form $\mathbf{F}_0 \exp[j(\omega t - \mathbf{k}_{\text{num}} \cdot \mathbf{r})]$, where $\mathbf{k}_{\text{num}}$ is the numerical wave number given by

$$\mathbf{k}_{\text{num}} = \sum_{\beta=x,y,z} \frac{2}{\Delta\beta} \sum_{m=1(m\,\text{odd})}^{N-1} c_{N,m} \sin\left(\frac{m k_{\text{num},\beta}\,\Delta\beta}{2}\right)\mathbf{a}_\beta \quad (13)$$

where $\mathbf{a}_\beta$ is the unit vector in β-direction. In the discretised domain, we replace $\partial/\partial t$ with $j\omega_{\text{num}}$, where $\omega_{\text{num}} = 2\sin(\omega\Delta t/2)/\Delta t$, and ∇ with $-j\mathbf{k}_{\text{num}}$ in the medium's system of differential equations in order to extract the numerical permittivity ε_{num} of the medium [10]. For the Lorentz medium with M poles we find

$$\varepsilon_{\text{num}} = \varepsilon_\infty + (\varepsilon_s - \varepsilon_\infty)\sum_{p=1}^{M} \frac{G_p \omega_p^2}{\omega_p^2 + 2j\omega_{\text{num}}\delta_{\text{num}} - \omega_{\text{num}}^2} \quad (14)$$

where $\delta_{\text{num},p} = \delta_p \cos(\omega\Delta t/2)$. It is noted that the numerical permittivity function of (14) is identical to Young's method [10]. It is also observed that in Joseph's method [11], [6] $\omega_{\text{num},p} = \omega_p\sqrt{\cos(\omega\Delta t)}$ whereas in the present method $\omega_{\text{num},p} = \omega_p$. For the Debye medium it is yielded that

$$\varepsilon_{\text{num}} = \varepsilon_\infty + \sum_{p=1}^{M} 2\frac{\sin(\omega\Delta t/2) + \tau_p\omega_{\text{num}}}{\omega_{\text{num}}(\Delta t + 2\tau_p)} \frac{\varepsilon_s - \varepsilon_\infty}{1 + j\tau_p\omega_{\text{num}}/\cos(\omega\Delta t/2)} \quad (15)$$

Joseph's numerical permittivity (given in [6], [10]) is given by

$$\varepsilon_{\text{num}} = \varepsilon_\infty + \sum_{p=1}^{M} \frac{(\varepsilon_s - \varepsilon_\infty)\cos(\omega\Delta t/2)}{\cos(\omega\Delta t/2) + j\tau_p\omega_{\text{num}}} \quad (16)$$

Maxwell's equation in the discretised domain have the form

$$\left[\sigma\cos(\omega\Delta t/2) + j\omega_{\text{num}}\varepsilon_{\text{num}}\right]\mathbf{E}_0 = -j\mathbf{k}_{\text{num}} \times \mathbf{H}_0,\ \ j\omega_{\text{num}}\mu_0\mathbf{H}_0 = j\mathbf{k}_{\text{num}} \times \mathbf{E}_0 \quad (17)$$

The numerical dispersion relation is deduced from (17) and it is found to be

$$\left[\sigma\cos(\omega\Delta t/2) + j\omega_{\text{num}}\varepsilon_{\text{num}}\right] j\omega_{\text{num}}\mu_0 = -\mathbf{k}_{num} \cdot \mathbf{k}_{num} \quad (18)$$

In the following, we use the definition $\Delta t = Q\Delta x/c_0$, where Q is the so called Courant number and c_0 is the velocity of light in vacuum. In order to investigate the dispersion errors of each technique, the phase error $e_{\text{phase}} = \ln\left|\text{Re}\{k - k_{\text{num}}\}/\text{Re}\{k\}\right|$ with k the exact wavenumber, is also defined.

In Fig 2(a) the fourth- and sixth-order Joseph's FDTD schemes give the same phase error due to the high (for the HO schemes) value of the time step (the same is valid for the HO Takayama's schemes). It is also noted that second-order Joseph's and Takayama's techniques coincide and that the HO schemes do not provide serious improvement. In other words, is worthless to use HO schemes if the time step is not very small. In Fig. 2(b), the Courant number is 0.01 (although it is very small for the second-order scheme) to indicate the efficiency of the HO schemes with small time steps. In Fig. 2(c) a comparison of the fourth- and the sixth-order schemes is presented, designating the accuracy of

the last if very small time step is applied. Since in dispersive media numerical accuracy depends on how well the chosen time step resolves the shortest timescale (i.e., τ_p in a Debye medium), one has to reduce the Courant number and as a result the phase error introduced by the FDTD(2,2) scheme increases. However, in HO schemes such a reduction of the Courant number does not lead to phase error degradation as can be observed in Fig 2. In conclusion, HO schemes with very low values of the Courant number are highly precise EM solvers in dispersive media.

Perfectly Matched Layer for the Termination of Dispersive Media in HO Grids

Consider an isotropic, inhomogeneous, linear dispersive medium. The modified Maxwell's equations in the frequency domain can be written as

$$\nabla\times\tilde{\mathbf{E}}=-j\omega\mu_0\mathrm{T}\cdot\tilde{\mathbf{H}},\ \ \nabla\times\tilde{\mathbf{H}}=j\omega\left(\frac{\sigma}{j\omega}+\varepsilon(\omega)\right)\mathrm{T}\cdot\tilde{\mathbf{E}} \tag{19}$$

where $\mathrm{T}\equiv\mathrm{diag}\{\zeta_x/(\zeta_y\zeta_z),\zeta_y/(\zeta_z\zeta_x),\zeta_z/(\zeta_x\zeta_y)\}$ is the diagonal "material" tensor, including the PML conductivities and $\zeta_s=1/[\kappa_s+\sigma_s/(j\omega)]$, for $s=x,y,z$. The parameters κ_s,σ_s are assumed to be spatially variant inside the PML following polynomial profile of order n. We also introduce two additional variables $\tilde{\mathbf{R}}=\mathrm{T}\cdot\tilde{\mathbf{E}}$ and the variable $\tilde{\mathbf{S}}$ such that

$$\tilde{S}_x=\left(\zeta_x/\zeta_y\right)\tilde{E}_x,\tilde{S}_y=\left(\zeta_y/\zeta_z\right)\tilde{E}_y,\tilde{S}_z=\left(\zeta_z/\zeta_x\right)\tilde{E}_z \tag{20}$$

An additional variable $\tilde{\mathbf{B}}$ is also introduced for the magnetic fields. The finite difference equations are derived following a methodology similar to [7]. The update equation for the variable S_x is

$$S_x^{n+1}=\frac{2\kappa_z-\sigma_z\Delta t}{2\kappa_z+\sigma_z\Delta t}S_x^n+\frac{1}{2\kappa_z+\sigma_z\Delta t}\left(R_x^{n+1}-R_x^n\right) \tag{21}$$

The relations (5) and (8) can be used as the update equations of the variable $\mathbf{R}$. The other update equations are similar to (21) and are omitted here. The efficiency of proposed PML is verified in two dimensional problems. We consider the 2D TE wave propagation in a three-pole Debye medium with parameters: $\varepsilon_\infty=2.25\varepsilon_0$, $\varepsilon_{s1}=30\varepsilon_0$, $\varepsilon_{s2}=20\varepsilon_0$, $\varepsilon_{s3}=\varepsilon_0$ and $\tau_1=9.4\,\mathrm{nsec}$, $\tau_2=0.1\,\mathrm{nsec}$, $\tau_3=1\,\mu\mathrm{sec}$. We assume an FDTD grid with $\Delta x=\Delta y=0.01\,\mathrm{m}$ and $Q=0.2$ ($\Delta t=Q/c_0\sqrt{1/(\Delta x)^2+1/(\Delta y)^2}$). The global error for the FDTD(2,2) method is depicted in Fig. 3(a) and for the FDTD(2,4) method in Fig 4(b) for different values of PML thickness and for fourth- and second-order polynomial grading of the PML parameters. The global error is a function of time and is defined as $\sum_D(H_{z,\mathrm{num}}^{n+1/2}-H_{z,\mathrm{exact}}^{n+1/2})^2$, where the subscript "num" denotes the solution under examination in the computational domain D and the "exact" the solution obtained in a larger domain with no reflections in the boundaries. It is noted that the proposed PML absorbs more effectively the EM waves with a fourth-order conductivity profile and with increasing PML thickness.

Numerical Results

Firstly, the proposed schemes were tested out for the wave propagation in a homogeneous muscle, modeled as three-pole Debye medium with parameters: $\varepsilon_\infty=4.3\varepsilon_0$, $\varepsilon_{s1}=1974.3\varepsilon_0$, $\varepsilon_{s2}=35.1\varepsilon_0$, $\tau_1=1/(5.2\pi)\,\mu\mathrm{sec}$, $\tau_2=1/(680\pi)\,\mu\mathrm{sec}$, $\tau_3=1/(46\pi)\,\mathrm{n\,sec}$ and static conductivity $\sigma=0.106$ S/m. In our simulations, although the FDTD(2,2) grid was two times denser than that of the HO schemes, the solutions are almost identical as depicted in Fig. 4(a). The effectiveness of the proposed schemes is also demonstrated by considering the one-dimensional slab problem. The slab is 5 m thick and is mod-

eled as a two-pole Lorentz medium with parameters: $\varepsilon_\infty = 2.25\varepsilon_0$, $\varepsilon_s = 3\varepsilon_0$, $G_1 = 0.4$, $G_2 = 0.6$, $\omega_1 = 40\pi \times 10^7$ rad/sec, $\omega_2 = 80\pi \times 10^7$ rad/sec, $\delta_1 = 0.1\omega_1$ and $\delta_2 = 0.1\omega_2$. The transmitted electric fields, depicted in Fig. 4(b), seem to be correctly calculated though two times coarser grids were used for the HO schemes.

Conclusions

A HO FDTD technique with an unsplit field PML for the simulation of EM waves in dispersive media is introduced in this paper. The numerical dispersion relations are extracted and the introduced dispersion errors are estimated for the second-, fourth- and sixth-order schemes. Additionally, extensive numerical verification in problems with multipole Lorentz and Debye media reveals the advantages and the efficiency of the proposed method.

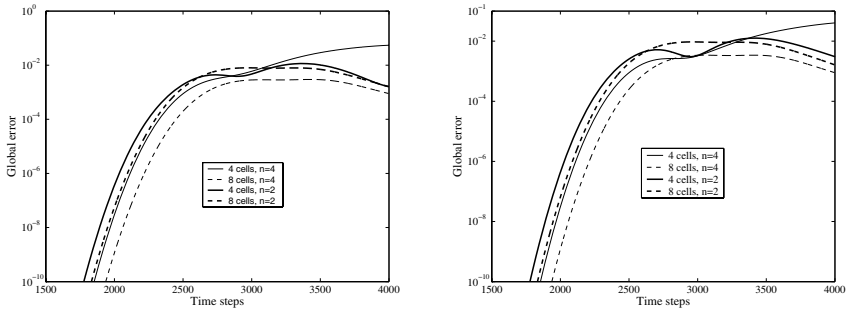

Fig.3 Global error for the (a) FDTD(2,2) and (b) FDTD(2,4) for different PML thickness and index n.

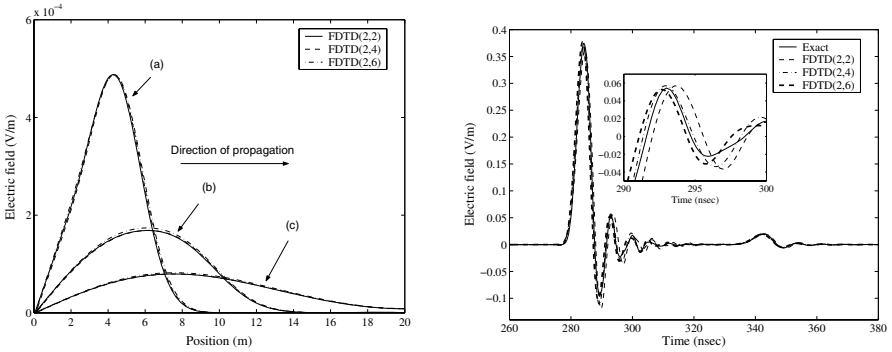

Fig.4 (a) Time history of the electric field through a three-pole Debye medium at several time steps: (i) 0.834 μsec (ii) 1.668 μsec (iii) 3.336 μsec (b) The transmitted, exact and the computed, time-domain solutions at distance 4m away from a two-pole Lorentz slab.

References

[1] A. Taflove and S. Hagness, Computational Electrodynamics: The Finite-Difference Time-Domain Method, 2nd ed. Norwood, MA: Artech House, 2000.

[2] C. W. Manry, S. L. Broschat, and J. B. Schneider, Higher-order FDTD methods for large problems, J. Applied Computational Electromagnetics Society, Vol. 10, pp 17-29, 1995.

[3] K. L. Shlager and J. B. Schneider, Comparison of the dispersion properties of higher order FDTD schemes and equivalent-sized MRTD schemes, IEEE Trans. Antennas Propagat., Vol. 52, pp 1095-1104, 2004.
[4] T. T. Zygiridis and T. D. Tsiboukis, Phase error reduction in general FDTD methods via optimum configuration of material parameters, J. Mater. Process. Technol., Vol. 161, pp 186-192, 2005.
[5] J. L. Young, A higher order FDTD method for EM propagation in a collisionless cold plasma, IEEE Trans. Antennas Propagat., Vol. 44, pp 1283-1289, 1996.
[6] K. P. Prokopidis, E. P. Kosmidou, and T. D. Tsiboukis, An FDTD algorithm for wave propagation in dispersive media using higher-order schemes, J. Electromagn. Waves Applicat., Vol. 18, pp 1171-1194, 2004.
[7] Y. Takayama and W. Klaus, Reinterpetation of the Auxiliary Differential Equation method for FDTD, IEEE Microwave Wireless Components Lett., Vol. 12, pp 102-104, 2002.
[8] B. Fornberg and M. Ghrist, Spatial finite difference approximations for wave-type equations, SIAM J. Numer. Anal., Vol. 37, pp 105-130, 1999.
[9] A. Yefet and P. G. Petropoulos, A staggered fourth-order accurate explicit finite difference scheme for the time-domain Maxwell's equations, J. Comput. Phys., Vol. 168, pp 286-315, 2001.
[10] J. L. Young, A. Kittichartphayak, Y. M. Kwork and D. Sullivan, On the dispersion errors related to $(FD)^2TD$ type schemes , IEEE Trans. Microwave Theory Tech., Vol. 43, pp 1902-1910, 1995.
[11] R. M. Joseph, S. C. Hagness, and A. Taflove, Direct time integration of Maxwell's equations in linear dispersive media with absorption for scattering and propagation of femtosecond electromagnetic pulses, Opt. Lett., Vol. 16, no. 18, pp 1412-1414, 1991.

Electromagnetic Fields in Mechatronics, Electrical and Electronic Engineering
A. Krawczyk et al. (Eds.)
IOS Press, 2006

A PERTURBATION TECHNIQUE FOR THE FINITE ELEMENT MODELLING OF NONDESTRUCTIVE EDDY CURRENT TESTING

Ruth V. Sabariego, Patrick Dular

Dept. of Electrical Engineering and Computer Science, University of Li`ege, Belgium
r.sabariego@ulg.ac.be, patrick.dular@ulg.ac.be

***Abstract** – This paper deals with a new 3D finite element scheme for nondestructive eddy-current testing (ECT) problems. It concerns a perturbation technique applied to the magnetodynamic $h-\phi$ formulation.*
The unperturbed field (in the absence of the flaw) is computed conventionally in the complete domain. The source of the perturbation problem is determined by the projection of the unperturbed field in a relatively small region around the defect that depends on the work frequency. The discretisation of this reduced domain is adapted to the size of the defect and independent of the discretisation of the complete domain. The impedance change is computed by integrating only over the defect and a layer of elements in the reduced domain that touch its boundary. As test case, we consider the second eddy current benchmark problem proposed by the WFNDEC. It involves a pancake coil scanning the inner surface of a metal tube for the detection of flaws on the outer surface.

Introduction

The nondestructive eddy-current testing (ECT) problems have been extensively studied in recent years. The ultimate goal is to determine the position and size of defects in conducting materials (inverse problem). However, a fast and accurate calculation of the probe response (forward problem) is often required for identifying the flaws from measured data. When the excitation is time-harmonic, the observed quantity is usually the impedance variation due to the presence of the defect.
Several variations of the volume integral method (VIM) have been reported in literature [1, 2]. Herein, defects can be represented by a distribution of current dipoles in its volume. A boundary element method, using VIM for describing the defect, is proposed in [3]. Only the crack is discretised. The calculations related to different probe positions are very fast. These techniques become extremely computationally expensive in case of more complicated geometries other than infinite stabs or tubes with homogeneous and linear material parameters. Another disadvantage of the method is the singularity of the Green's kernel.

The finite element method [4] allows to overcome these drawbacks. However, it may require a dense discretisation in the vicinity of the defect resulting in a large 3D mesh for the complete problem. The impedance change due to the defect is calculated as the difference of the impedance values with and without flaw. Furthermore, calculations for different probe positions are performed independently, which is time consuming.

A 3D *a*-formulation based finite element scheme that calculates directly the distortion of the eddycurrent due to a flaw is presented in [5]. Herein, the computation is split into a computation without flaw and a computation of the field distortion due to its presence. The unperturbed field (in the absence of the flaw) is calculated in a large region taking advantage of any symmetry or analytical solution, and applied as a source in the flaw for the second computation. The perturbed field can thus be determined in a reduced domain around the defect, what allows for a discretisation better adapted to the defect size, usually much smaller than the rest of the considered problem. The impedance change is computed by integrating only over the flaw region.

The present paper concerns the extension of this perturbation technique to the magnetodynamic $h - \phi$ formulation. The coupling between the scalar potential ϕ in the defect and the magnetic field h in the conductor is described in detail. Further, an expression for the impedance change is derived.

As test case, the second eddy current benchmark problem proposed by the WFNDEC [6] is considered. A study of the accuracy as a function of the extension of this reduced domain is performed.

Perturbation Method

We consider a magnetodynamic problem in a bounded domain Ω (boundary Γ) of $\mathbb{R}^3$. The governing differential equations and constitutive laws of the magnetodynamic problem in Ω are

$$\operatorname{curl} h = j, \quad \operatorname{curl} e = -\partial_t b, \quad \operatorname{div} b = 0, \quad b = \mu h, \quad j = \sigma e, \tag{1 a–e}$$

with h the magnetic field, b the magnetic flux density, e the electric field, j the current density, μ the magnetic permeability and σ the electric conductivity.

The eddy current conducting part of Ω is denoted Ω_c and the non-conducting one Ω_c^C ($\Omega = \Omega_c \cup \Omega_c^C$). Source conductors, with a given current density j_s, are comprised in $\Omega_s \subset \Omega_c^C$. A flaw Ω_f with boundary Γ_f appears in Ω_c.

Let us suppose that the flaw has different conductivity σ_f and permeability μf than the host material. It is assumed that they are linear and isotropic. Particularising (1 a) and (1 b) for the unflawed and flawed arrangements, we obtain

$$\operatorname{curl} h_u = \sigma e_u, \qquad \operatorname{curl} e_u = -\mu \partial_t h_u, \tag{2 a–b}$$

$$\operatorname{curl} h_f = \sigma_f e_f, \qquad \operatorname{curl} e_f = -\mu_f \partial_t h_f \tag{2 c–d}$$

where the subscripts u and f refer to the unflawed and flawed quantities, respectively. The source terms of the perturbed formulation are determined from the eddy-current distribution without defect.

Subtracting (2 a–b) from (2 c–d), respectively, it is easy to prove that

$$\operatorname{curl} h = \sigma_f e + j_{sf}, \qquad \operatorname{curl} e = -\mu_f \partial_t h - k_{sf}, \tag{3 a–b}$$

where $h = h_f - h_u$ and $e = e_f - e_u$ are the perturbations [5] and

$$j_{sf} = (\sigma_f - \sigma) e_u, \qquad k_{sf} = (\mu_f - \mu) \partial_t h_u, \tag{4 a–b}$$

are the incident electric and magnetic current densities that generate the perturbation of the field due to the change of σ and μ, respectively.

$h - \phi$ Magnetodynamic Formulation

Adopting the magnetic field formulation, the general expression of the magnetic field h in Ω is $h = h_s + h_r$, with h_s a source field in Ω satisfying curl $h_s = j_s$ and hr the reaction field in Ω_c. In the non-conducting regions Ω_c^C, the reaction field h_r can be derived from a scalar potential ϕ such as $h_r = -\text{grad}\ \phi$.

The $h - \phi$ magnetodynamic formulation is obtained from the weak form of the Faraday law (1 a):

$$\partial_t (\mu h, h')_\Omega + (\sigma^{-1} \operatorname{curl} h, \operatorname{curl} h')_{\Omega_c} + \langle n \times e, h' \rangle_\Gamma = 0, \quad \forall h' \in F_{h\phi}(\Omega) \tag{5}$$

where n is the outward unit normal vector on Γ, part of the boundary of Ω; $(-,-)_\Omega$ and $\langle -,- \rangle_\Gamma$ denote a volume integral in Ω and a surface integral on Γ of the product of their arguments; $F_{h\phi}(\Omega)$ is the

function space defined on Ω and containing the basis functions for h (coupled to ϕ) as well as for the test function h' [7]. The trace of e is a constraint associated with Γ (this constraint can e.g. be associated with a homogeneous Neumann boundary condition or with a global quantity) [7, 8].

For the sake of simplicity, a zero-conductivity defect Ω_f with same permeability as Ω_c is assumed hereafter for the perturbation problem. The extension of the formulation to other cases is straightforward.

The unperturbed field h_u (with $\Omega_f \subset \Omega_c$) is obtained by particularising ($h = h_u$) and solving (5). This field h_u is then projected to a reduced domain $\Omega' \subset \Omega$ around the defect. Note that projecting only h_u is not enough. This way the local current j_u = curl h_u will not be conserved. According to (4 a) with $\sigma_f = 0$, the perturbation current source j_{sf} is given by

$$j_{sf} = \operatorname{curl} h_{sf} = -\sigma e_u = -\operatorname{curl} h_u \quad \text{in } \Omega_f . \tag{6}$$

Furthermore, the trace of source field $h_{sf} = -h_u$, $n \times h_{sf}$, on Γ_f contributes to the exterior domain $\Omega' \backslash \Omega_f$. Indeed, the following interface condition has to be satisfied on Γ_f :

$$n \cdot j \,|_{\Gamma_f} = -n \cdot j_{sf} \,|_{\Gamma_f} , \tag{7}$$

which is equivalent to consider

$$n \times h \,|_{\Gamma_f} = -n \times \operatorname{grad} \phi \,|_{\Gamma_f} + n \times h_{sf} \,|_{\Gamma_f} . \tag{8}$$

The source of the perturbation problem in Ω_f is calculated through a projection method in the reduced domain Ω' as

$$(\operatorname{curl} h_{sf}, \operatorname{curl} h')_{\Omega'} + (\operatorname{curl} h_u, \operatorname{curl} h')_{\Omega'} = 0 , \quad \forall h' \in F_{h\phi}(\Omega') , \tag{9}$$

where a gauge condition using a tree-cotree method at the discrete level in Ω' is applied to ensure the uniqueness of the solution. The circulation of h_{sf} on the edges of $\Omega' \backslash \Omega_f$ is fixed to zero. For the sake of conciseness, hereafter we refer to Ω' as Ω.

The perturbation problem is completely characterised by (5) applied to the perturbation field h and taking into account (6) as follows:

$$\partial_t(\mu h, h')_\Omega + (\sigma^{-1} \operatorname{curl} h, \operatorname{curl} h')_{\Omega_c \backslash \Omega_f} + \partial_t(\mu h_{sf}, h')_\Omega + (j_{sf}, \operatorname{curl} h')_{\Omega_f} = 0 , \quad \forall h' \in F_{h\phi}(\Omega) . \tag{10}$$

Calculation Of The Impedance Variation

The impedance of the exciting coil changes and this change allows to detect and characterise the defect.

However, the change of the observed quantity is usually under 1% of the total value or even smaller in practical cases. The accurate calculation of this impedance variation ΔZ is thus crucial. Hereafter, it will be proved that ΔZ can be calculated by integrating the product of local quantities only over the flaw Ω_f and a layer of elements in $\Omega \backslash \Omega_f$ that touch the boundary Γ_f.

A suitable treatment of the surface integral term in (5) consists in naturally defining a global voltage V in a weak sense. We can define a global test function for h with a unit circulation along any current tube of the inductor so that the surface integral in (5) can be expressed as the product of a global voltage V and a unit global current I(curl h')[8].

Let us specify (5) for the unflawed problem, it holds

$$\partial_t(\mu h_u, h')_\Omega + (\sigma^{-1}\mathrm{curl}\, h_u, \mathrm{curl}\, h')_{\Omega_c} = V_u\, I(\mathrm{curl}\, h'), \quad \forall\, h' \in F_{h\phi}(\Omega). \tag{11}$$

Analogously, for the flawed problem, we can write

$$\partial_t(\mu h_f, h')_\Omega + (\sigma^{-1}\mathrm{curl}\, h_f, \mathrm{curl}\, h')_{\Omega_c\setminus\Omega_f} + (e_f, \mathrm{curl}\, h')_{\Omega_f} = V_f\, I(\mathrm{curl}\, h'), \quad \forall\, h' \in F_{h\phi}(\Omega), \tag{12}$$

where we have added the term $(e_f, \mathrm{curl}\, h')_{\Omega f}$ which is not cancelled as in the general case due to the imposed perturbation current in the flaw, i.e. $\mathrm{curl}\, h' \neq 0$ in $\Omega_f \subset \Omega_c^C$.

Choosing as test functions $h' = h_f$ in (11) and $h' = h_u$ in (12) and subtracting (11) from (12), we obtain

$$\Delta V\, I = \Delta Z\, I^2 = -(\sigma^{-1}\mathrm{curl}\, h_u, \mathrm{curl}\, h_f)_{\Omega_f} + (e_f, \mathrm{curl}\, h_u)_{\Omega_f} = (e_f, \mathrm{curl}\, h_u)_{\Omega_f}, \tag{13}$$

where the first volume integral cancels because h_f is curl-free in Ω_f and I is the real current injected in the inductor.

The perturbed electric field ef is not known in the flaw but can be calculated by means of (12) with $h' = h_{sf}$. This way $I(\mathrm{curl}\, h') = 0$ and the impedance variation ΔZ is obtained as

$$\Delta Z\, I^2 = -(e_f, \mathrm{curl}\, h_{sf})_{\Omega_f} = \partial_t(\mu(h + h_{sf}), h_{sf})_\Omega + (\sigma^{-1}\mathrm{curl}\,(h + h_{sf}), \mathrm{curl}\, h_{sf})_{\Omega_c\setminus\Omega_f}, \tag{14}$$

where the domain of integration, at the discrete level, is actually limited to Ω_f and a layer of elements in $\Omega\setminus\Omega_f$ touching Γ_f due to the definition of h_{sf}.

Application Example

As numerical example, we consider the second eddy current benchmark problem proposed by the WFNDEC [6]. It concerns an Inconel tube ($\sigma = 10^6$ S/m, inner diameter D_i = 19.69 mm, outer diameter D_o = 22.23 mm) with a defect on the outer surface and a pancake coil that scans the inner surface (Fig. 1). The flaw is t = *1mm* long in the axial direction, w = *3mm* wide in the radial direction and its depth h varies between 20% and 60% of the tube wall thickness. The coil (400 turns, inner diameter = 1 mm, outer diameter = 3 mm, height = 0.8 mm) carries an imposed sinusoidal current of 100mA and frequency f = 150 kHz. The lift-off between the center of the inferior plan of the coil and the inner surface of the tube is 0.8 mm.

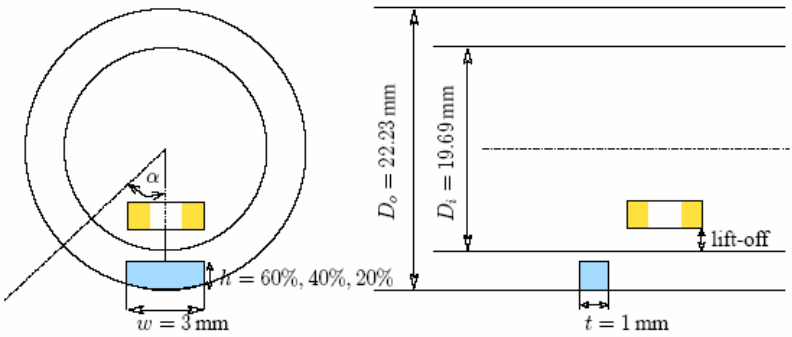

Fig. 1. Transversal (left) and longitudinal (right) cross sections of the Incodel tube with a defect on the outer surface and a pancake coil inside. The angle of rotation of the coil α is also shown.

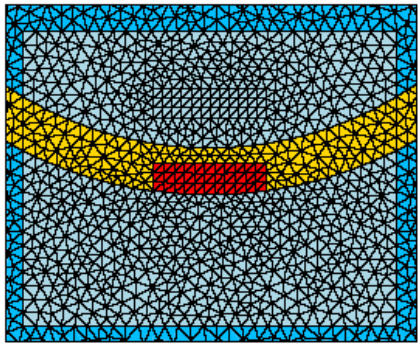

Fig. 2. Reduced domain Ω' of size $2.7\ \delta$ around the flaw used in the perturbation method. The source field is defined in the flaw, the excitation coil is taken as air.

First, we study the accuracy of the proposed method as a function of the size of the reduced domain Ω'. To this purpose, we consider a 2D model of the problem and we vary the dimensions of Ω' around the defect in terms of multiples of the skin depth $\delta = 1/\sqrt{\pi f \mu \sigma}$ = 1.3mm of the tube. We calculate the impedance variation ΔZ both in the conventional way (solving the unflawed and the flawed problem consecutively and performing the difference between two impedance values) and with the proposed perturbation method (integrating directly in a sub-domain of Ω').

In order to avoid numerical errors due to the discretisation, the conventional technique requires exactly the same mesh for the unflawed and flawed problem. Nevertheless the proposed perturbation technique can be applied using too independent meshes: a mesh of the whole domain without considering the defect and a mesh of the reduced domain without the explicit presence of the excitation coil. For the sake of a fair comparison, the error is calculated using exactly the same mesh for the two methods (Fig. 2). In the perturbation method, the source field is given by an equivalent current source in the flaw itself.

The impedance of the coil obtained for the unperturbed problem is $25.5 + i\ 210.75$. The relative error (%) in the real and imaginary parts of ΔZ is depicted in Figs. 3a and 3b, respectively. We can observe that in both cases the relative error is smaller than 1% when the distance between the border of the reduced domain and the crack is larger than $2.7\ \delta$.

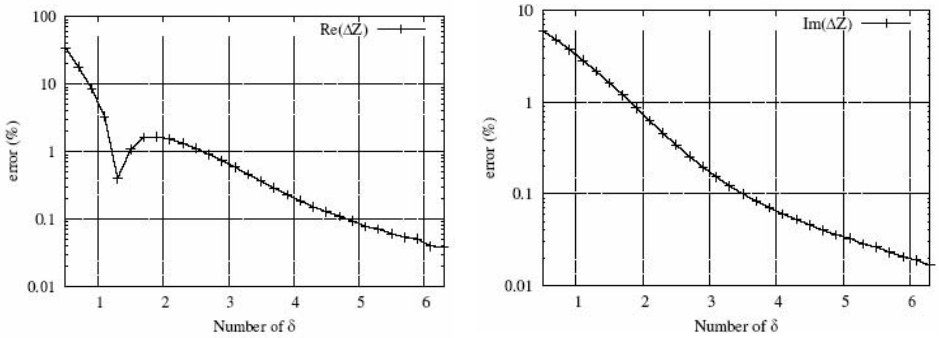

Fig. 3. Relative error (%) in the real and imaginary parts of ΔZ as a function of the dimensions of Ω', depending on a multiple of the skin depth δ.

In order to validate the numerical model, our 3D results are compared with those presented in [9]. The locus and magnitude of the impedance change for an axial scan and different depths of the flaw are represented in Figs. 4a and 4b for a rotation angle $\alpha = 0°$ and in Figs. 5a and 5b for a rotation angle $\alpha = 20°$. An excellent agreement between our results and those presented in [9] is observed.

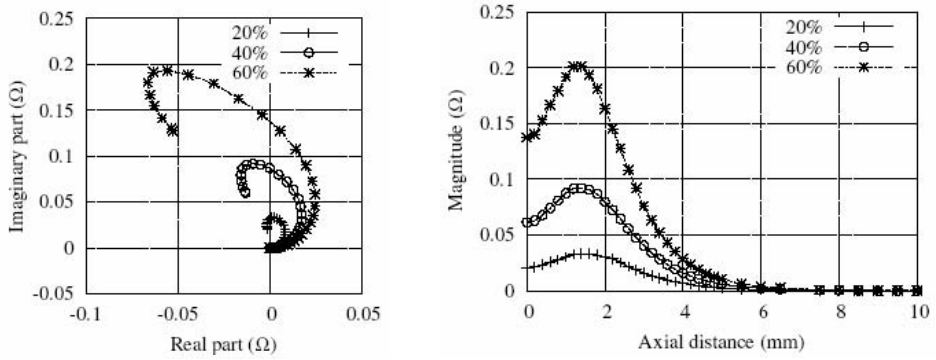

Fig. 4. Locus (left) and magnitude (right) of the impedance change ΔZ for an axial scan with $\alpha = 0°$.

Conclusions

A 3D FE perturbation technique based on the $h - \phi$ magnetodynamic formulation has been elaborated. The unperturbed field is calculated conventionally in the complete domain taking advantage of any symmetry or analytical solution (if available) and applied as a source in the flaw. Next the perturbed field is

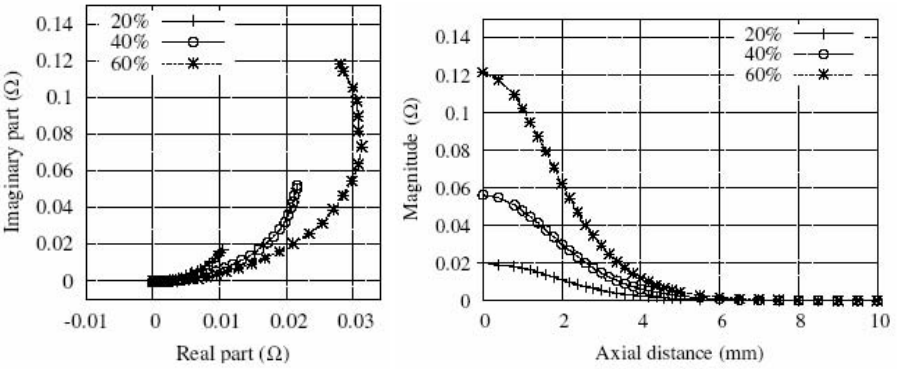

Fig. 5. Locus (left) and magnitude (right) of the impedance change ΔZ for an axial scan with $\alpha = 20°$.

determined in a reduced domain surrounding the defect. The discretisation is thus chosen independently of the dimensions of the excitation coil and the specimen under study. Furthermore, the impedance variation due to the presence of the flaw is calculated by performing an integral over the defect and a layer of elements in the exterior domain that touch its boundary.

The accuracy of the model has been evidenced by comparing the results obtained for different dimensions of the reduced domain to those achieved in the conventional way. The field distortion can

actually be neglected beyond a distance 2.7 δ around the defect. Finally, the solution of the 3D eddy current benchmark problem validates the presented perturbation scheme.

References

[1] J. R. Bowler and S. A. Jenkings, "Eddy-current probe impedance due to a volumetric flaw," *Journal of Applied Physics*, vol. 70, no. 3, pp. 1107–1114, 1991.

[2] D. Pr´emel, G. Pichenot, and T. Sollier, "Development of a 3D electromagnetic model for eddy current tubing inspection: application to the simulation of probe eccentricity," *Int. J. Appl. Electromag. Mech.*, vol. 19, no. 1-4, pp. 521–525, 2004.

[3] O. Michelsson and F. H. Uhlmann, "A boundary-integral based forward solution for eddy current nondestructive testing," *IEEE Transactions on Magnetics*, vol. 36, no. 4, pp. 756–759, 2000.

[4] N. Ida and W. Lord, "A finite element model for three-dimensional eddy current NDT phenomena," *IEEE Transactions on Magnetics*, vol. 21, no. 6, pp. 2635–2643, 1985.

[5] Z. Badics, Y. Matsumoto, K. Aoki, F. Nakayasu, M. Uesaka, and K. Miya, "An effective 3-D finite element scheme for computing electromagnetic field distorsion due to defects in eddy-current nondestructive evaluation," *IEEE Transactions on Magnetics*, vol. 33, no. 2, pp. 1012–1020, 1997.

[6] "WFNDEC, World Federation of Nondestructive Evaluation Centers," http://www.wfndec.org/.

[7] P. Dular, C. Geuzaine, and W. Legros, "A natural method for coupling magnetodynamic h-formulations and circuit equations," *IEEE Transactions on Magnetics*, vol. 35, no. 3, pp. 1626–1629, 1999.

[8] P. Dular, P. Kuo-Peng, C. Geuzaine, N. Sadowski, and J. P. A. Bastos, "Dual magnetodynamic formulations and their source fields associated with massive and stranded inductors," *IEEE Transactions on Magnetics*, vol. 36, no. 4, pp. 1293–1299, 2000.

[9] Y. Tian, Y. Li, L. Udpa, and S. S. Udpa, "Simulation of the world federation's second eddy current benchmark problem," in *Review of Progress in QNDE*, vol. 22. Plenum, New York: D. O. Thompson and D. E. Chimenti, 2002, pp. 1816–1823.

Electromagnetic Fields in Mechatronics, Electrical and Electronic Engineering
A. Krawczyk et al. (Eds.)
IOS Press, 2006

FAST ESTIMATION OF GENERATOR END REGION LOSSES WITH AN AXIPERIODIC FOURIER EXPANSION BOUNDARY ELEMENT METHOD

E. Schlemmer, B. Streibl, and F. Müller

VA TECH HYDRO GmbH & Co
Elingasse 3, A-8160 Weiz, Austria
Erwin.Schlemmer@vatech-hydro.at

Abstract **– This paper presents a method for the approximate calculation of eddy current losses in the clamping plate of large synchronous machines. The approach consists of two parts. The first of which is a harmonic model of eddy currents on a chamfered rectangular patch in cylindrical coordinates. The eddy currents on this patch are driven by the time-harmonic end region field which is calculated by a classical Biot-Savart integration of simplified stator and rotor windings. The second part consists of several refinements such as the allowance for slotted clamping plates and a better allowance for generator core, air gap and housing by an axiperiodic Boundary Element Method.**

Introduction

Analytic loss calculations in generator end regions date back to the classical works of Richter and Bödefeld/Sequenz. Examples of predominantly analytic applications can be found in [1], [2], and [3], for instance. The methods of references [4] to [11] exhibit mainly numerical characteristics. Nowadays, loss calculations are often carried out using 3D Finite Element (FE) codes. With the advent of sophisticated solid modellers, the pre- and post-processing of FE models has become much less time consuming as it was only a few years ago. Fig. 1 illustrates the complexity of a – considerably simplified - generator end region. Modes of this modest complexity are usually fully parametric and require very little user interaction. The magnetic clamping plate shows the well-known eddy current pattern due to the combined fields from the stator end winding and the field winding.

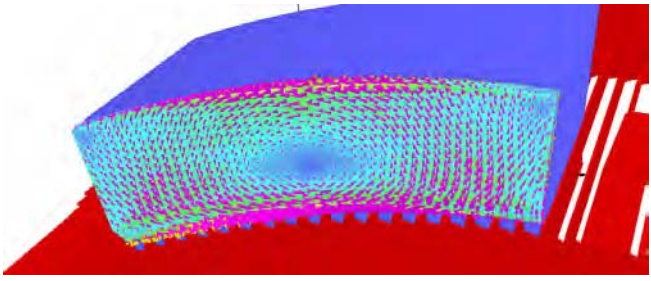

Fig. 1. Eddy current distribution on a clamping plate

Nevertheless, the effort of creating 3D FE models in the stage of tendering is not common at all. For that reason, an approximate method was implemented which allows a fast estimation of eddy current

losses in clamping plates. The method gives answers with reasonable accuracy without resorting to (commercial) numerical codes. Furthermore, it allows for different levels of approximation. A very fast approach is available for rough estimations as well as successive levels of refinement, albeit at higher computational expense. Moreover, it is important that the levels do not exhibit unsteady behaviour between each other. Simple geometric variations of the problem topology, such as radial slitting of pressure plates, are dealt with by simple analytic formulas, e.g. [12]. The nonlinearity of materials is dealt with in an appropriate way.

Approximation of the End Region

The main data structure of the program is a Fourier-decomposition of the surface current density on a polar patch (Fig. 2). Stator and rotor windings are approximated as current sheets. The influence of the stator and rotor iron can be taken into account by either conventional mirror currents or by a axiperiodic Boundary Element Method. Nonlinear material characteristics are dealt with iteratively.

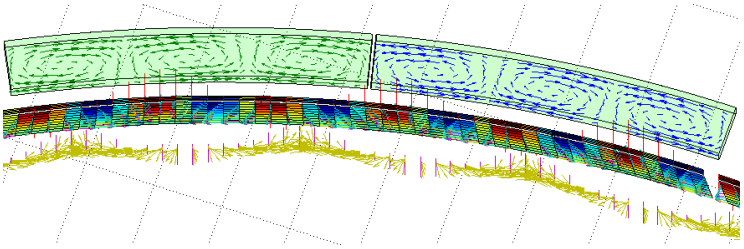

Fig. 2. Hydro generator clamping plate segments with simplified windings

End Region Windings and Eddy Current Patches

In order to be computational efficient, the classical approach of end winding representation by individual bars and mirror currents – as it is common in the computation of circulating current losses – was not applied in this context.

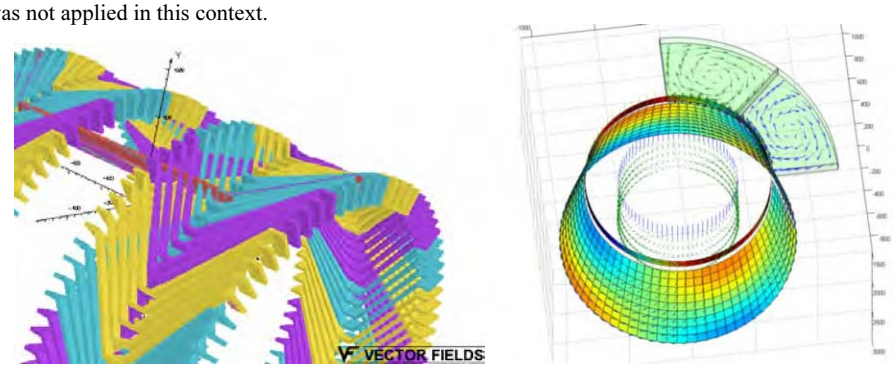

a) b)

Fig. 3. Classical approximation of the highly permeable iron core by mirror currents (a) and replacement of the end winding by current sheets (b).

Since the region of interest is relatively far away from the conductors, they can be replaced by sheets with sinusoidally distributed currents. The magnetic field from these sheets is calculated by Biot-Savart integration.The main data structure behind the modelling of eddy currents on clamping plates is a rectangular patch in cylindrical coordinates as depicted in Fig 4.

From Finite Element calculations, it can be inferred quite easily that the eddy current distribution at the surface of the patch can be described by a harmonic approach. Equations (1) and (2) perform the linear transformation between the rectilinear local coordinate system (ξ,η,ζ) and the global system (r,φ,z).

$$r(\xi)=\frac{r_1+r_2}{2}+\frac{r_2-r_1}{2}\xi \quad \Rightarrow \quad \frac{\partial}{\partial r}=\frac{2}{r_2-r_1}\frac{\partial}{\partial \xi} \tag{1}$$

$$\varphi(\eta)=\frac{\varphi_1+\varphi_2}{2}+\frac{\varphi_2-\varphi_1}{2}\eta \quad \Rightarrow \quad \frac{\partial}{\partial \varphi}=\frac{2}{\varphi_2-\varphi_1}\frac{\partial}{\partial \eta} \tag{2}$$

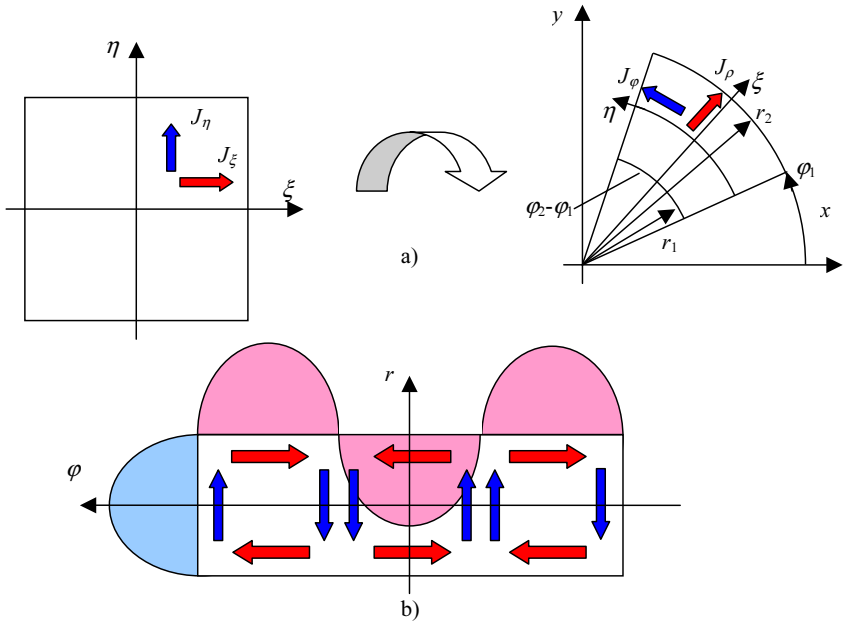

Fig. 4. Linear transformation between the local coordinate system and the global system (a); schematic representation of the fundamental eddy current distribution on a three-pole-pitch clamping plate (b).

It is assumed that the eddy current density has no component normal to the surface of the plate, i.e. the problem can be treated as a planar one in terms of the electric currents. This fact is expressed in (3). J_ρ is an abbreviation of rJ_r.

$$\operatorname{div} \mathrm{J} = \frac{1}{r}\frac{\partial\left(rJ_r\right)}{\partial r} + \frac{1}{r}\frac{\partial J_\varphi}{\partial \varphi} + \left.\frac{\partial J_z}{\partial z}\right|_{J_z=0;\frac{\partial J_z}{\partial z}=0} = \frac{1}{r}\frac{\partial\left(J_\rho\right)}{\partial r} + \frac{1}{r}\frac{\partial J_\varphi}{\partial \varphi} \tag{3}$$

In (4), the expression for the wave number is given, where ω is the angular frequency, μ stands for the permeability and σ for the conductivity of the clamping plate material. Higher order harmonics are expressed by the basic frequency ω_0 and an appropriate harmonic number ν. Non-linearity of the clamping plate material is dealt with in (4) by an analytical fitting function for the relative permeability of the material. Of course, this requires the application of an iterative scheme.

$$k = \sqrt{0.5 \cdot \omega\mu\sigma} = \sqrt{0.5 \cdot \nu\omega_0\mu\sigma} \tag{4}$$

The eddy current density on the surface of a clamping plate is approximated by the harmonic series given by (5) and (6). The axial component of the eddy current density is set to zero in the whole clamping plate. Only on the surface, this is exactly true; however, it makes the approximation much easier inside the plate.

$$J_\rho = -\sum_{i,l} J_\rho^{i,l} \cdot \cos\left(\frac{i\pi}{2}\xi\left(r,\varphi\right)\right) \cdot \sin\left(\frac{l\pi}{2}\eta\left(r,\varphi\right)\right) \cdot e^{-kz} \cdot e^{j(\omega t - kz)} \tag{5}$$

$$J_\varphi = \sum_{m,n} J_\varphi^{m,n} \cdot \sin\left(\frac{m\pi}{2}\xi\left(r,\varphi\right)\right) \cdot \cos\left(\frac{n\pi}{2}\eta\left(r,\varphi\right)\right) \cdot e^{-kz} \cdot e^{j(\omega t - kz)} \tag{6}$$

From the fact that **J** is divergence-free, it follows that the spatial behaviour of J_ρ and J_φ is restricted by (7).

$$\operatorname{div} \mathrm{J} = 0 \quad \Rightarrow \quad -\frac{1}{r}\frac{\partial\left(J_\rho\right)}{\partial r} = \frac{1}{r}\frac{\partial J_\varphi}{\partial \varphi} \quad \Rightarrow \quad \begin{cases} i = m \\ l = n \end{cases} \tag{7}$$

From (5) and (6), it can be seen how the field quantities depend on z, i.e. the direction normal to the surface. Consequently, the z-derivative of all field components F having this variation in z can be expressed according to (8).

$$F\left(r,\varphi,z\right) = F_0\left(r,\varphi\right) \cdot e^{-kz} \cdot e^{j(\omega t - kz)} \quad \Rightarrow \quad \frac{\partial F\left(r,\varphi,z\right)}{\partial z} = -\left(1+j\right)kF\left(r,\varphi,z\right) \tag{8}$$

The magnetic field on the surface of the clamping plate is described by (9) to (11). These equations give the harmonic components $\mathbf{H}^{m,n}$ for the iterative computation of the eddy currents $\mathbf{J}^{m,n}$ via the Fourier analysis of the resulting magnetic field from the windings as well as from the eddy currents.

$$H_\rho = H_r = -\sum_{m,n} H_\rho^{m,n} . \sin\left(\frac{m\pi}{2}\xi\left(r,\varphi\right)\right) \cdot \cos\left(\frac{n\pi}{2}\eta\left(r,\varphi\right)\right) \cdot e^{-kz} \cdot e^{j(\omega t - kz)} \tag{9}$$

$$H_\phi = rH_\varphi = -\sum_{m,n} H_\phi^{m,n} \cdot \cos\left(\frac{m\pi}{2}\xi\left(r,\varphi\right)\right) \cdot \sin\left(\frac{n\pi}{2}\eta\left(r,\varphi\right)\right) \cdot e^{-kz} \cdot e^{j(\omega t - kz)} \tag{10}$$

$$H_z = \sum_{m,n} H_z^{m,n} \cdot \cos\left(\frac{m\pi}{2}\xi(r,\varphi)\right) \cdot \cos\left(\frac{n\pi}{2}\eta(r,\varphi)\right) \cdot e^{-kz} \cdot e^{j(\omega t - kz)} \tag{11}$$

From the curl of H, the governing equations (12) and (13) for the calculation of the eddy currents can be found. The full development of (12) and (13) by equations (5), (6), (9) to (11) yields expressions for the individual harmonic components. This step, however, is omitted here for the sake of brevity.

$$\frac{1}{r}\frac{\partial H_z}{\partial \varphi} - \frac{\partial H_\varphi}{\partial z} = J_r \quad \Rightarrow \quad \frac{2}{\varphi_2 - \varphi_1}\frac{\partial H_z}{\partial \eta} + (1+j)\,kH_\phi = J_\rho \tag{12}$$

$$\frac{1}{r}\frac{\partial H_r}{\partial z} - \frac{\partial H_z}{\partial r} = J_\varphi \quad \Rightarrow \quad \frac{2}{r_2 - r_1}\frac{\partial H_z}{\partial \xi} + (1+j)\,kH_r = -J_\varphi \tag{13}$$

Axiperiodic Boundary Element Method

It is very well known from literature, e.g. [13], that magnetic field problems can be described via a reduced scalar potential ϕ, which allows for the presence of magnetised matter, and a solenoidal part $\mathbf{H}_S$, which comprises the effects of all currents $\mathbf{J}_S$ in the source domain Ω_S. In (14), the rotation-free source term $\nabla\phi$ and the Biot-Savart can be easily distinguished.

$$\mathrm{H} = \mathrm{H}_M + \mathrm{H}_S = -\nabla\phi + \mathrm{H}_S = -\nabla\phi + \int_{\Omega_S} \frac{\mathrm{J}_S \times \mathrm{r}}{4\pi r^3} d\Omega_S \tag{14}$$

From the continuity of the tangential component of **H** and the normal component of **B**, the interface conditions for the magnetic scalar potential ϕ on both sides of a magnetised body's boundary Γ follow immediately, cf. (15), where **t** is a tangential and **n** a normal vector to the boundary.

$$\begin{aligned} \mathrm{t}\cdot\mathrm{H}_1 = \mathrm{t}\cdot\mathrm{H}_2 \quad &\Leftrightarrow \quad \frac{\partial\phi_1}{\partial t} = \frac{\partial\phi_2}{\partial t} \quad \Rightarrow \quad \phi_1 = \phi_2 \\ \mathrm{n}\cdot\mathrm{B}_1 = \mathrm{n}\cdot\mathrm{B}_2 \quad &\Leftrightarrow \quad \mu_1\left(\mathrm{H}_S - \frac{\partial\phi_1}{\partial n}\right) = \mu_2\left(\mathrm{H}_S - \frac{\partial\phi_2}{\partial n}\right) \end{aligned} \tag{15}$$

Green's second identity, together with the interface conditions (15), gives two integral equations (16) for the determination of ϕ and its normal derivative. The index i=1 describes the situation within the magnetised body Ω_1, i=2 yields the integral equation in air, i.e. in Ω_2. Green's function is that of the three-dimensional potential problem, the magnetic scalar potential ϕ and its derivative are expanded into a Fourier series with respect to the azimuthal coordinate φ, which reflects the repetitive structure of the generator's magnetic circuit.

$$c_i\phi + (-1)^{i-1}\int_\varphi\int_\Gamma \phi(r,\varphi)\frac{\partial G}{\partial n}d\Gamma d\varphi = (-1)^{i-1}\int_\varphi\int_\Gamma G\frac{\partial\phi_i}{\partial n}(r,\varphi)\,d\Gamma d\varphi; \qquad i\in\{1,2\} \tag{16}$$

Comparisons with 3D Finite Element Solutions

For a test set of more than 40 hydro generators, comparisons between the 3D FE solution and the different levels of approximations were carried out, e.g. Fig. 5.

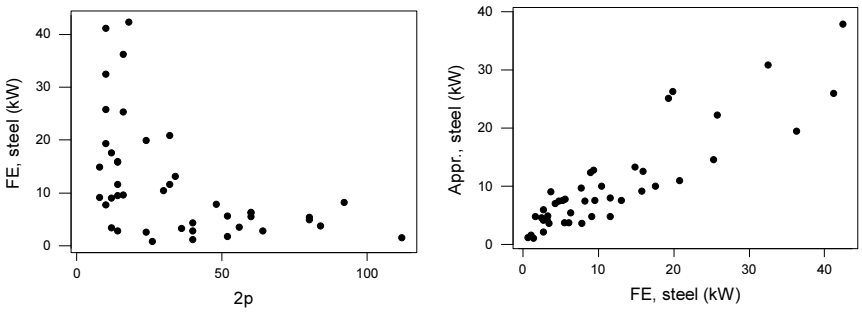

Fig. 5. Distribution of the clamping plate losses over pole number (a) and coarsest approximation (b).

Conclusions

Using a harmonic decomposition of eddy currents on a clamping plate and an axiperiodic Boundary Element Method, it is possible to achieve reasonable accuracy in the calculation of end region losses of large hydro and turbine generators.

References

[1] K. Oberretl, Streufelder, Wirbelstromverluste, Erwärmungen, Kräfte und Eisenbrand im Stirnraum von Turbogeneratoren, *E und M*, Jahrgang 80, Heft 23, pp. 539-550, 1963.

[2] R. Sikora, J. Purczynski, W. Lipinski, M. Gramz, Use of variational methods to the eddy currents calculation in thin conducting plates, *IEEE Trans. Magn*., Vol. Mag-14, No. 5, pp. 383-385, 1978.

[3] G. Traxler-Samek, Zusatzverluste im Stirnraum von Hydrogeneratoren mit Roebelstabwicklung, *PhD-Thesis*, Vienna University of Technology, 2003.

[4] V. Chechurin, Yu. Varlamov, M. Roytgarts, Surface impedance for electromagnetic field computing in large turbogenerators, *Proceedings of ICEM 2000*, pp. 1035-1037, 2000.

[5] T. Renyuan, X. Guangren, T. Lijian, Z. Danqun, X. Yi, Calculation of end region magnetic field and circulating losses for turbo-generators using a coupled field and circuit equations method, *IEEE Trans. Magn.,* Vol. 26, No. 2, pp. 497-500, 1990.

[6] G.K.M. Khan, G.W. Buckley, R.B. Bennett, N. Brooks, An integrated approach for the calculation of losses and temperatures in the end-region of large turbine generators, *IEEE Trans. Energy Conversion*, Vol. 5, No. 1, pp. 183-194, 1990.

[7] W. Krajewski, Computation of the turbogenerator end-region field using the BEM, *Archiv für Elektrotechnik*, Vol. 75, pp. 173-178, 1992.

[8] D. Xia, E.-J. Feng, The SSPFEM analysis of the eddy currents and the magnetic fields in the turbine generator end region, *Electric Machines and Power Systems*, Vol. 20, pp. 273-281, 1992.

[9] R. Sikora, K.M. Gawrylczyk, M. Gramz, S. Gratkowski, M. Ziolkowski, Magnetic field computation in the end-region of electric machines using various boundary conditions on iron surfaces, *IEEE Trans. Magn*., Vol. Mag-22, No. 3, pp. 204-207, 1986.

[10] T. Nomura, S. Maeda, Analysis of magnetic flux in stator end windings of large turbine generators using Fourier expansion, *IEEE Trans. Magn*., Vol. 26, No. 2, pp. 933-936, 1990.

[11] G. Bedrosian, M.V.K. Chari, M. Shah, G. Theodossiou, Axiperiodic finite element analysis of generator end regions, Part I – Theory, *IEEE Trans. Magn*., Vol. 25, No. 4, pp. 3067-3069, 1989.

[12] G. Strassacker, P. Strassacker, *Analytische und numerische Methoden der Feldberechnung*, B. G. Teubner, Stuttgart (1993), pp.43-49, 92-105.

[13] K. R. Richter, W. M. Rucker, Numerical foundations, integral methods and applications. In: Y. R. Crutzen et al. (eds.), *Industrial Application of Electromagnetic Computer Codes*, Kluwer, Dordrecht, (1990), pp. 29-50.

Electromagnetic Fields in Mechatronics, Electrical and Electronic Engineering
A. Krawczyk et al. (Eds.)
IOS Press, 2006

A POLAR MAGNETIZATION MODEL INSERTED IN FINITE ELEMENT METHOD SOFTWARE

E. Vinot, D. Frachon

Moving Magnet Technologies (MMT)
1 rue Christiaan Huygens, 25000 Besançon, FRANCE
evinot@movingmagnet.com, dfrachon@movingmagnet.com

Abstract *–This paper presents a model of polar magnetization which is common in small motor with permanent magnet rotor. This model is based on elliptic form and equation for the field line and has been implemented in Flux2D (finite element method software) by means of user subroutine. Then it has been validated on a magnet and use to model the torque in MMT's BLDC motor.*

Introduction

The polar magnetization (fig.1) is frequently used in small motor where the rotor is made of a bulk magnet ring. Actually, if you can magnetize efficiently the magnet ring, which supposes relatively small size, it has a lot of advantages. You do not need iron yoke neither in the rotor of your motor nor in the magnetization device. Moreover the field pattern may provide a higher field in the air gap (and thus a higher static torque) than with a radial magnetization.
To design motors with such a magnetization and to predict static and detent torque, a good model is required. In fact, it is not so easy to model polar magnetization with finite element software (magneto, amperes, Flux2D …), which has currently not the module to describe it. Hopefully, Flux2D [1] allow the users to develop his own subroutine and to "link" it to the software by means of a .dll file. This routine has a specific interface and is written in Fortran 77. Thus a routine have been written to describe a parameterized polar magnetization and this model has been used on one of our BLDC motor.

Polar Magnetization

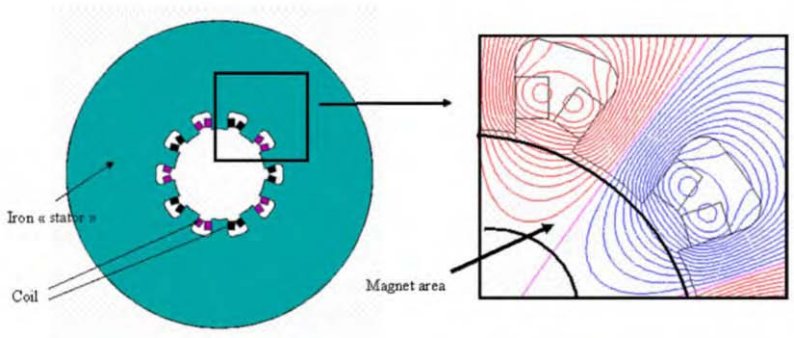

Fig 1 : Magnetizer device and polar magnetization.

A polar magnetization is easily obtained if you insert a ring magnet relatively thick (compare to the diameter) in a magnetization device without any yoke inside the magnet. The limitation is that to have a good magnetization

the magnetic field during the process has to be almost twice the coercitiv field of the magnet, thus as the magnet behave quite like air, it requires a large amount of ampere turn in the coil. This is even truer as the dimensions of the magnet grows and explains why it is especially applied to small size magnet (diameter smaller than 5 cm).
Fig 1 presents such a magnetization device (on the left), for a ten pole magnetization, and the obtained magnetization on the right.
Moreover for small size device (smaller than 50mm), the making process cost is more important than the material cost, and it may be a real advantage to have no iron yoke inside the magnet, and thus avoid a step in the making of the device. When the size increases the cost of magnetic material become too important to use such magnetization pattern, and a thinner magnet with iron yoke is economic ally better.

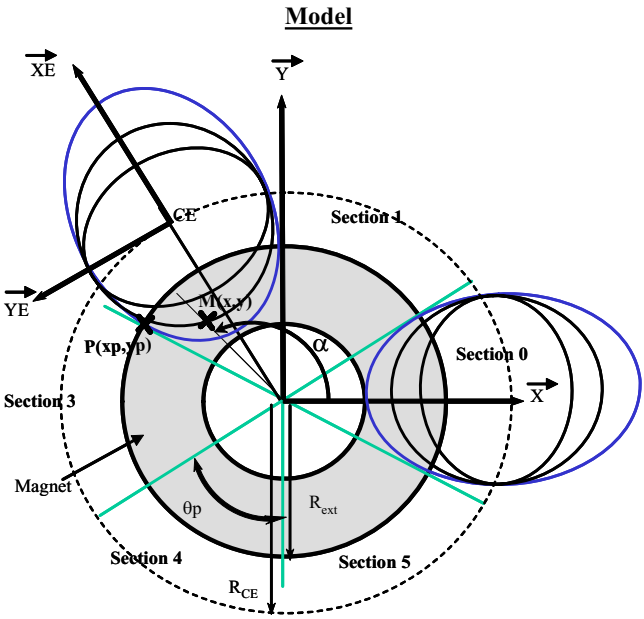

Fig 2 : Model of the magnetization

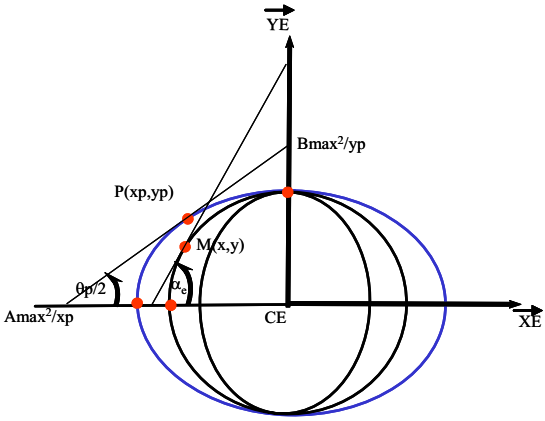

Fig 3 : Model of the magnetization in elliptic coordinate system

We can easily noted in fig 1 that the field line seems to be elliptic and are "attracted" by the iron of the magnetization device. Moreover, in the middle of the teeth, the field is tangential to the radius of the magnet. Thus, the field lines in the magnet are modeled by ellipses with the same centre (fig.2).
The parameters of the model, which can be changed without modification in the subroutine when you use the software, are the coercitiv field, the number of pole of the magnetization (6 for example in fig 2), and a parameter which is the radius of the centre of the ellipse (Fig 2), and which allows to modify its eccentricity.
In fact, as we consider that the magnet is "perfectly magnetized", which means the modulus of the coercitiv field is the same in each point and equal to H_c (module of the coercitive field depending principally of the type of the magnet: ferrite, NdFeb ...), we need to know α the angle between the magnetization and x axis in a point M(x,y).
The magnet may be separated in different section (Fig 2), which have the same pattern of magnetization (except the direction which is different for two neighbour section). The number of sections is equal to the pole number N_p, even if each section cover half of a south pole and half of a north pole, and the angle of a section is $\theta_p=360°/N_p$. Thus if you have determined the pattern of magnetization in one section, for example in section 0 (Fig 3), you can easily know the magnetization in the other section, by means of change of coordinate system .

Remember the equation of an ellipse centred in (x_{CE},y_{CE}) is given by :

$$(x-x_{CE})^2/A^2+(y-y_{CE})^2/B^2=1 \qquad (1)$$

Where A and B are respectively semi major and semi minor axes of the ellipse.
For one section the field lines are modelled by ellipses characterised by their centre CE, and their A and B parameters. It is noted that CE and B are the same for each ellipses of a section and that only A is changing depending of the ellipse and thus of the point when you are seeking the direction of the field.

A_{max} and B_{max} Determination

A_{max} and B_{max} are the parameter of the external ellipse which has the particularity to be tangent to a radius of the ring magnet in a point $P(x_P,y_P)$ (Fig 4) situated on the outer radius of the magnet and on the border of a section. That means for section 0 that P have the following coordinate in the elliptic coordinate system in CE (centre of the ellipse):

$$\begin{aligned} x_p &= R_{ext}\cos(\theta_p/2)-R_{ce} \\ y_p &= R_{ext}\sin(\theta_p/2) \end{aligned} \qquad (2)$$

The tangent in P is defined by:

$$xx_p/A_{max}^2+yy_p/B_{max}^2=1 \qquad (3)$$

And this tangent crosses the XE and YE axis in A_{max}^2/x_p and B_{max}^2/y_p , thus:

$$\tan(\theta_p/2)=|x_p|B_{max}^2/|y_p|A_{max}^2 \qquad (4)$$

Thus with (3) and (4) you determine easily A_{max} and B_{max} (respectively semi major and semi minor axis of the external ellipse):

$$\begin{aligned} A_{max} &= \sqrt{x_p^2+|x_p y_p|/\tan(\theta_p/2)} \\ B_{max} &= \sqrt{y_p^2+|x_p y_p|\tan(\theta_p/2)} \end{aligned} \qquad (5)$$

Determination of α_e

Then if you work in the elliptic coordinate system, to know the magnetization in a point $M(x_e,y_e)$, you need to know α_e angle between the tangent and the XE axis.

Knowing that $M(x_e,y_e)$ belong to an ellipse of parameter A and $B=B_{max}$:

$$x_e^2 / A^2 + y_e^2 / B_{\max}{}^2 = 1 \quad (6)$$

Thus for a point M(xe,ye) A is defined by :

$$A = \sqrt{x_e^2 B_{\max}^2 / \left(B_{\max}^2 - y_e^2\right)} \qquad (7)$$

Then with the tangent equation you define α_e :

$$\begin{aligned} & xx_e / A^2 + yy_e / B_{\max}{}^2 = 1 \\ & \Rightarrow \alpha_e = \operatorname{atan}(- x_e^2 B_{\max}^2 / A^2 y_e^2) \end{aligned} \qquad (8)$$

Determination of the coercitive field in each point of the ring

Knowing the field and especially its direction in elliptic coordinate system, it is easy for a point M(x,y) defined in absolute coordinate system to know the field in that point.
First you need to know the section to which it belongs:

$$N_s = ent\left(\frac{\theta - \theta_p / 2 - \theta_0}{\theta_p}\right) \qquad (9)$$

Where N_s is the section number, θ_0 is the angle between x axis and the center of the first section (section 0), usually equal to zéro, θ the angle between M and the x axis, and *ent()* represents the integer part of the number insert in brackets.
Then its easy to determine the coordinate of the M point in the elliptic coordinate system (XE,YE):

$$\begin{aligned} x_e &= y_i \sin\theta_{CE} + x_i \cos\theta_{CE} \\ y_e &= -x_i \sin\theta_{CE} + y_i \cos\theta_{CE} \end{aligned} \qquad (10)$$

with

$$\begin{aligned} x_i &= x - x_{CE} \\ y_i &= y - y_{CE} \\ x_{CE} &= R_{CE} \cos\theta_{CE} \\ y_{CE} &= R_{CE} \sin\theta_{CE} \\ \theta_{CE} &= \theta_0 + N_s \theta_p \end{aligned}$$

Then knowing x_e and y_e you determine A and α_e for a point M(x,y), and thus the coordinate of coercitive field (H_{cx}, H_{cy}) for this point is defined as follow :

For $A<A_{max}$:
If N_s is even :

$$\begin{aligned} H_{cx} &= H_c \cos(\alpha_e + \theta_{CE}) \\ H_{cy} &= H_c \sin(\alpha_e + \theta_{CE}) \end{aligned}$$

If Ns is odd

$$\begin{aligned} H_{cx} &= -H_c \cos(\alpha_e + \theta_{CE}) \\ H_{cy} &= -H_c \sin(\alpha_e + \theta_{CE}) \end{aligned}$$

For $A>A_{max}$:

$$H_{cx} = H_{cy} = 0$$

Where H_c is the module of the coercitive field of the magnet.

It is noted that outside of the biggest ellipse the coercitive field is equal to zero.

Result for a 10 Poles Magnetization

Fig 4 presents the field lines for a ring magnet of 8.5mm radius with a ten pole polar magnetization pattern. This magnet is placed inside an iron cylindre, separated by a small airgap.The field lines are presented for two different values of R_{CE} (25 mm and 9 mm). One should notes the importance of R_{CE} the radius of the centre of the ellipses which is a parameter you can choose, and which may be adapt to fix the eccentricity of the ellipses. A good way to choose this parameter is to measure the field versus the angle produced by the magnet in the air, to simulate this field and to adjust R_{CE} to fit the obtain curve.
It has been noted on our magnet that R_{CE} seems to be around 0.015 which means 1.76 times the radius of the magnet for a ten pole magnetization.

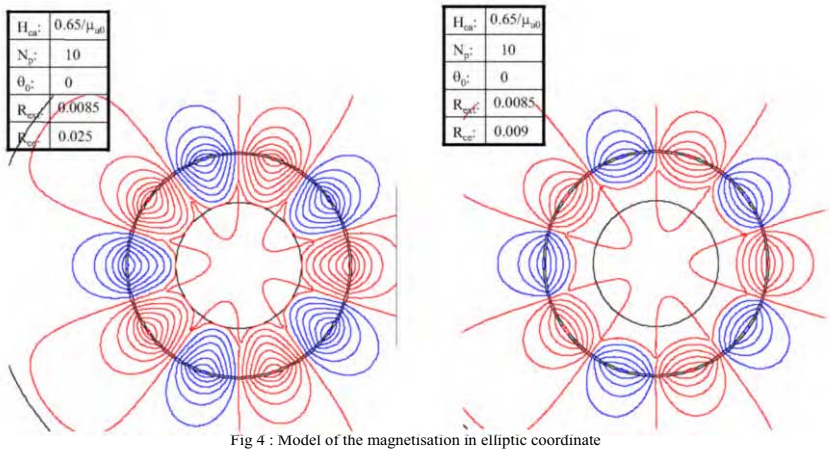

Fig 4 : Model of the magnetisation in elliptic coordinate

Application for the static torque calculation of a MMT patented motors

This model has been used for example to compare the performance of one MMT patented BLDC motors (Fig 5) for two different magnets (Fig 6):

- one 4 mm thickness magnet with polar magnetization
- one 1mm thickness magnet with radial magnetisation and 1 mm thickness iron yoke inside the magnet

Fig 5 : Our BLDC Patented motor

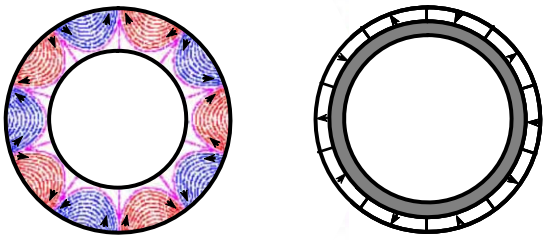

4 mm magnet
With polar magnetisation

1 mm magnet
With iron yoke inside

Fig 6 : Magnetisation pattern

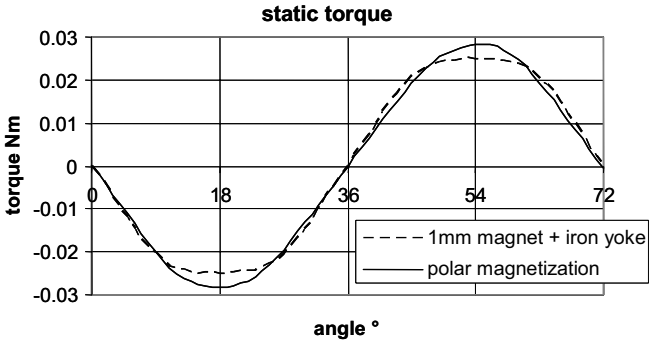

Fig 7 : Static torque versus type of magnetization.

Fig 7 presents the two phase ON static torque for a 35 mm outer diameter BLDC MMT motor. The magnet has an outer diameter of 17 mm and a 12 mm height. The remanent induction of the magnet is about 0.65T.
It is noted, that the static torque is higher with a polar magnetization.
This may be easily explained by use of the classical formula of the induction in the airgap in BLDC motors. If the permeability of iron is supposed to be infinite, the induction B_e in the airgap is given by:

$$B_e = \mu_0 H_c \frac{L}{L+e} \qquad (11)$$

where L is the length of the field line in the magnet and e the thickness of the airgap.
It is easy to understand that meaningly L is longer with polar magnetization in a 4 mm thick magnet with à 1mm thich magnet and a iron yoke.
Thus this magnetization pattern may be a good solution. It needs more magnet material than the solution with thinner magnet and iron yoke, but as there is no iron yoke the making process is simplified. Thus the cost of the rotor may be approximately the same and you have a better static torque.

Conclusion

A parameterized model of polar magnetization have been developed and implemented in Flux2D and has been used to simulate the static torque in one of our BLDC motor.
This model proves that in small device such a magnetization may be efficient in term of performance and cost.

References

[1] http://www.cedrat.com

[2] D. Prudham, “Polyphase motor, particularly for driving an indicator needle, *United States Patent 5 880 551*, March 9, 1999

Electromagnetic Fields in Mechatronics, Electrical and Electronic Engineering
A. Krawczyk et al. (Eds.)
IOS Press, 2006

AN ANALYSIS OF A MODE STIRRED CHAMBER EXCITED BY WIRES USING TLM AND FEM

Djonny Weinzierl

UNERJ – Centro Universitário de Jaraguá do Sul
Centro de Tecnologia e Artes
Rua dos Imigrantes, 500, CP 251, CEP 89254-430, Jaraguá do Sul - SC, Brazil
E-mail: Weinzierl@unerj.br

Ralf Jacobs, Arnulf Kost

BTU – Cottbus – Brandenburgische Technische Universitaet Cottbus
Lehrstuhl Allgemeine Elektrotechnik und Numerische Feldberechnung
Postfach 101344, D-03013, Cottbus, Germany
E-mails: Ralf.Jacobs@aet.tu-cottbus.de, Arnulf.Kost@aet.tu-cottbus.de

Adroaldo Raizer

UFSC – Universidade Federal de Santa Catarina
Departamento de Engenharia Elétrica
CP 476, CEP 88040-900, Florianópolis - SC, Brazil
E-mail: Raizer@eel.ufsc.br

Abstract* – *A Mode Stirred Chamber excited by wires is analysed using the Transmission Line Modelling (TLM) method. The TLM method solves the chamber problem in the time domain and computed results are compared to calculations using the Finite Element Method (FEM). Agreement with previously published Method of Moment (MoM) results will also be shown.

Introduction

Mode stirred chambers are electrically large, highly conductive enclosed cavities equipped with mechanical stirring devices. When the chamber is excited with RF energy, the resulting multi-mode electromagnetic environment can be stirred by the mechanical tuners. The cavity is employed to perform electromagnetic measurements (both emissions and immunity) on electronic equipment. The chamber mode density and the effectiveness of the mechanical tuner determine the lowest usable frequency [1].

A different method to excite and stir the fields in the chamber at low frequencies using wires has been proposed in [2]. This procedure of excitation is analysed in this work using the TLM method. As transmission lines support TEM fields, the method not only excites the common modes but also the TEM mode in the chamber. This widens the range of generated frequencies below the lowest resonance frequency [3]. In order to validate the TLM calculations, results will be compared to Finite Element computations and Method of Moment results.

Cavity Structure

Fig. 1 shows the chamber under investigation, which is excited by two transmission lines. The lines are parallel to the *z*-axis and are located at $x_1 = 0.8$m, $y_1 = 2.1$m and $x_2 = 3.2$m, $y_2 = 1.8$m. The width, height and length of the cavity are given by $a = 4.6$m, $b = 2.7$m and $c = 5.2$m, respectively. The resonance frequency is determined by:

$$f_{mnp} = \frac{1}{2\sqrt{\varepsilon\mu}}\sqrt{\left(\frac{m}{a}\right)^2 + \left(\frac{n}{b}\right)^2 + \left(\frac{p}{c}\right)^2} \tag{1}$$

where *m*, *n*, *p* determine the mode in the cavity. There is no maximum irradiation frequency, but the lowest frequency is determined by the dimensions of the chamber. Transverse electric TE_{mnp} and transverse magnetic TM_{mnp} modes can be generated in the chamber.

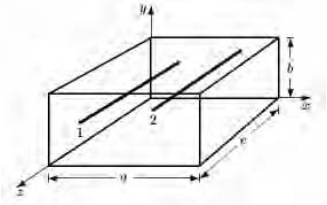

Fig. 1 – Chamber with two parallel wires.

TLM Method

The Transmission Line Modelling (TLM) method is a differential technique for the computation of electromagnetic fields. The problem domain is discretized and the fields in a subdomain are computed using a Symmetrical Condensed Node (SCN), as shown in Fig. 2(a). Each port of a SCN is associated with two voltages, and the electric and magnetic field components are calculated from these voltages by:

$$E_x = -\frac{V_1^i + V_2^i + V_9^i + V_{12}^i}{2\Delta\ell}, \qquad H_x = \frac{V_4^i + V_7^i - V_5^i - V_8^i}{2Z\Delta\ell} \tag{2}$$

$$E_y = -\frac{V_3^i + V_4^i + V_8^i + V_{11}^i}{2\Delta\ell}, \qquad H_y = \frac{V_6^i + V_9^i - V_2^i - V_{10}^i}{2Z\Delta\ell} \tag{3}$$

$$E_z = -\frac{V_5^i + V_6^i + V_7^i + V_{10}^i}{2\Delta\ell}, \qquad H_z = \frac{V_1^i + V_{11}^i - V_3^i - V_{12}^i}{2Z\Delta\ell} \tag{4}$$

respectively. V_n^i represents the incident voltage at por *n*, $\Delta\ell$ the length of the node, and *Z* the characteristic impedance of the medium. The excitation of the chamber is implemented applying magnetic fields at adjacent nodes around the wires as shown in Fig. 2(b). The path around the conducting wire is denoted *C*, $\vec{H}$ is the magnetic field at the adjacent nodes and *I* the current in the wire which is determined by Ampère's Law:

$$I = \oint_C \vec{H} \cdot d\vec{s} \tag{5}$$

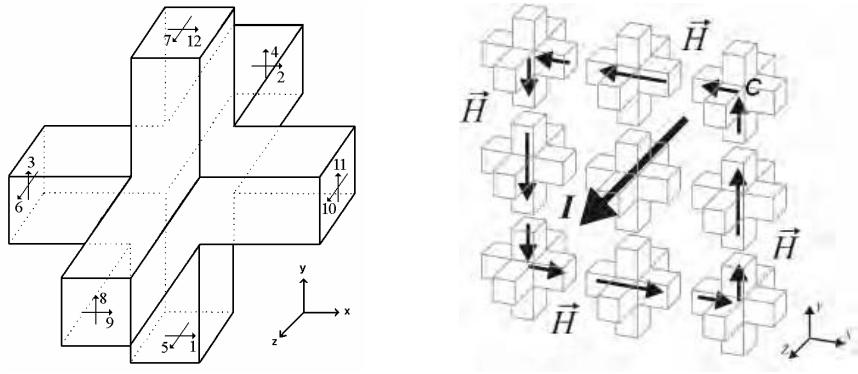

(a) (b)

Fig. 2 –Symmetrical Condensed Node (a) and Symmetrical Condensed Nodes around the wire (b).

For a *z*-directed wire equation 8 evaluates as:

$$
\begin{aligned}
I_z = {} & \frac{\Delta\ell}{2} H_x(x-1,y-1,z) + \Delta\ell H_x(x,y-1,z) + \frac{\Delta\ell}{2} H_x(x+1,y-1,z) \\
& + \frac{\Delta\ell}{2} H_y(x+1,y-1,z) + \Delta\ell H_y(x+1,y,z) + \frac{\Delta\ell}{2} H_y(x+1,y+1,z) \\
& - \frac{\Delta\ell}{2} H_x(x+1,y+1,z) - \Delta\ell H_x(x,y+1,z) - \frac{\Delta\ell}{2} H_x(x-1,y+1,z) \\
& - \frac{\Delta\ell}{2} H_y(x-1,y+1,z) - \Delta\ell H_y(x-1,y,z) - \frac{\Delta\ell}{2} H_y(x-1,y-1,z)
\end{aligned}
\tag{6}
$$

In order to implement the boundary conditions, different reflection coefficients have to be imposed on the nodes bounding the problem domain. On a perfectly conducting screen, for example, where incident waves are reflected with a phase inversion, the reflection coefficient on a boundary node must be equal to (-1). The incident voltage $V^i_{n,k+1}$ at port n of a boundary node at time step $k + 1$ is determined through the reflection coefficient Γ and the reflected voltage $V^r_{n,k}$ at time k,

$$V^i_{n,k+1} = \Gamma V^r_{n,k} \tag{7}$$

A more detailed description of the TLM method, its applications and computational requirements can be found in [4].

Finite Element Procedure

The finite element formulation is derived using the weighted residual method. Weighting the wave equation for a time-harmonic electric field $\bar{E}$ with $e^{j\omega t}$ time dependency with a set of weighting

functions $\vec{\upsilon}_i, i = 1...N$ and integrating over the cavity domain Ω, leads after application of Green's first integral theorem to:

$$\iiint_{\Omega} \frac{1}{\mu_r}\left(\nabla\times\vec{E}\right)\cdot\left(\nabla\times\vec{\upsilon}_i\right) - k_0^2\varepsilon_r\vec{E}\cdot\vec{\upsilon}_i + jk_0Z_0\sigma\vec{E}\cdot\vec{\upsilon}_i d\Omega - jk_0Z_0\iint_{\Gamma}\vec{\upsilon}_i\cdot\left[\vec{n}\times\nabla\times\vec{E}\right]d\Gamma = \\ = jk_0Z_0\iiint_{\Omega}\vec{J}\cdot\vec{\upsilon}_i d\Omega, \qquad \forall i\in\left[1,N\right] \tag{8}$$

where k_0 and Z_0 denote the wavenumber and impedance of free space, $\vec{n}$ the normal vector on the bounding surface $\Gamma = \partial\Omega$, $\vec{J}$ the current density in the wire, and the constitutive parameters σ, ε_r, μ_r the conductivity, relative permittivity and relative permeability, respectively. Approximation of the electric field $\vec{E}$ with a set of vectorial basis functions associated with the edges of the elements,

$$\vec{E} = \sum_{j=1}^{N} a_j\vec{\upsilon}_j \tag{9}$$

leads to a system of linear equations, which can be solved for the unknown coefficient a_j. The shape functions $\vec{\upsilon}_j$ are chosen to be the same as the weighting functions. The cavity domain is discretized using rectangular parallelepipeds and linear Lagrangian interpolation polynomials are employed on the elements. The wire excitation is modelled as current filament since the dimensions of the chamber and the wires are only a small fraction of operating wavelength. The current density in a wire is described by $\vec{J} = \hat{I}_k\delta(x-x_k)\delta(y-y_k)e^{-jk_0z}\vec{e}_z$, where (x_k, y_k) determine the position and $\hat{I}_k$ the current in wire *k*.

Simulated Results

Fig. 3 shows the *x, y, z*-components of the electric field along the *z*-axis at *x*=2.3m and *y*=1.0m for the chamber described before. The two wires are fed with sinusoidal current signals of frequency *f*=2.0MHz and phase difference Φ of 0° and 180°. The TLM simulations have been performed with a cell size of 5.0cm and time steps of $83.3\cdot10^{-12}$ s.

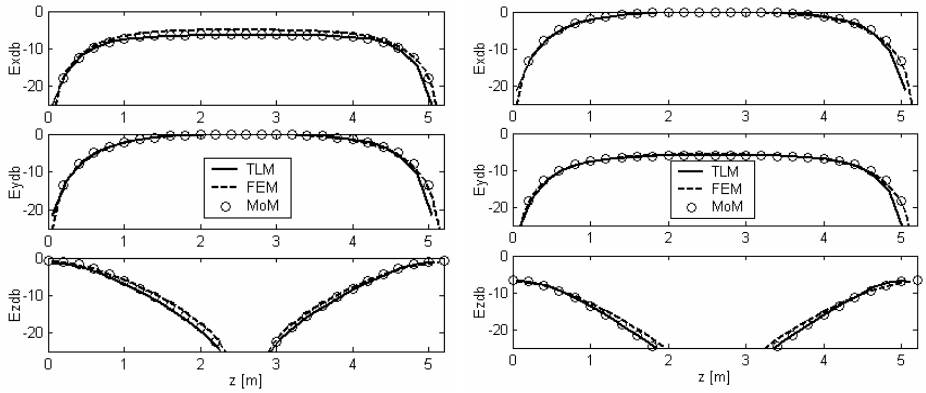

Fig. 3 – Electric field components along the *z*-axis, *f* = 2.0 MHz, Φ = 0° (a) and 180° (b).

The E_x and E_y components display a homogeneous field distribution in the center of the chamber, which yields a constant illumination of the device under test, whereas their magnitudes reflect the dependency upon the phase shift. Good agreement can be observed between the TLM calculation, the finite element (FEM) computations and Method of Moment (MoM) results from [2]. This confirms the capability of the TLM method to accurately model the field distribution in a mode stirred chamber and establishes the reliability of the procedure. Fig. 4 shows frequency dependency of the y-component of the electric field in the center of the chamber up to f=200 MHz. Both wires were excited simultaneously with a rectangular unit pulse with a duration of $83.3 \cdot 10^{-12}$ s. The resulting spectrum indicates that the lowest resonance frequency of the chamber is around 47.5 MHz. Equation 1, which is valid for a chamber without wires, yields a similar result for the TE_{101} mode, which is the mode with the lowest resonance frequency in the chamber. The efficient calculation of a spectrum is one of the advantages of the TLM method since it is a time domain method and frequency characteristics can be computed employing a Fourier transform.

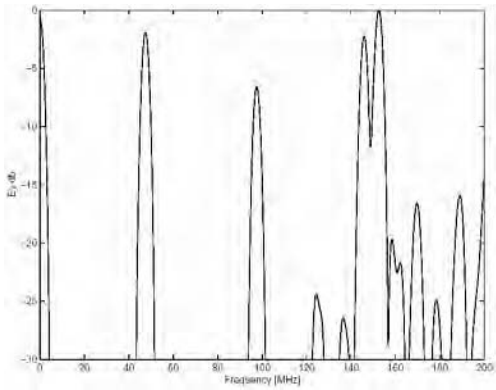

Fig. 4 – TLM computation of the y-component of the electric field in the center of the chamber.

To further investigate the properties of a mode stirred chamber excited by wires, a cell of width a=0.6m, height b=0.6m and length c=1.2m is considered. The chamber is excited by 4 wires which are parallel to the z-axis, placed at (x_1, y_1)=(0.1m, 0.1m), (x_2, y_2)=(0.5m, 0.1m), (x_3, y_3)=(0.5m, 0.5m) and (x_4, y_4)=(0.5m, 0.5m). Fig. 5(a) shows the components of the electric field along the z-axis at x=0.3m and y=0.3m. The exciting currents in all 4 wires are in phase and the operating frequency is f=10 MHz. Fig. 5(b) displays the electric field for the case that the currents in wires 2 and 4 experience a phase shift of 180°. In contrast to the 2 wire cell analysed previously, the E_x and E_y components are of the same order of magnitude. The increase of the number of wires has led to an improvement of the field homogeneity in the chamber.

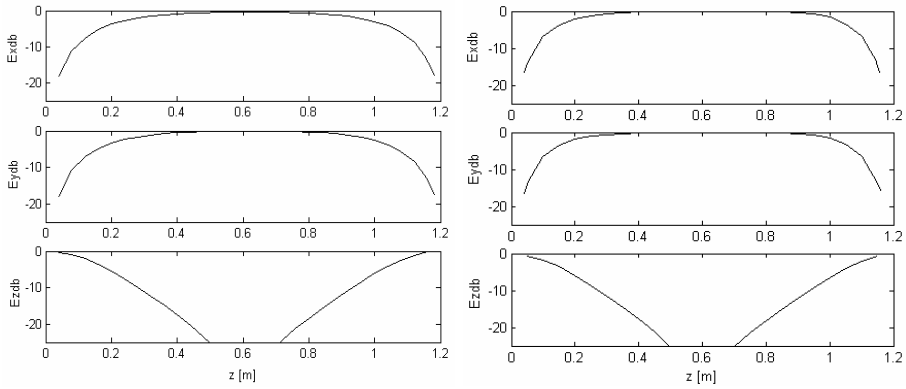

Fig. 5 – TLM Computation of the electric field along the *z*-axis for a cell excited by 4 wires, $f = 10.0$ MHz, $\Phi_1 = \Phi_2 = \Phi_3 = \Phi_4 = 0^o$ (a) and $\Phi_1 = \Phi_3 = 0^o$, $\Phi_2 = \Phi_4 = 180^o$ (b).

Conclusions

In contrast to mechanically mode stirred chambers, the wire excitation allows to set-up the TEM mode. The TEM mode lowers the minimum usable frequency of a mode stirred chamber below the lowest resonance frequency. Comparisons with FEM and MoM computations verified that the Transmission Line Modelling (TLM) method is capable of accurately predicting the field distribution in the chamber. Simulations have shown that the field homogeneity in a mode stirred chamber can be improved by increasing the number of wires in a cell.

References

[1] *Electromagnetic Compatibility (EMC), Part 4: Testing and Measurement Techniques - Section 21: Reverberation ChamberTest Methods*, International Electrical Commission, IEC 61000-4, 2000.

[2] Perini, J. and Cohen, L.S. "Extending the frequency of mode stir chambers to low frequencies." *In IEEE International Symposium on Electromagnetic Compatibility*, Washington D.C., pp. 633–637, 2000.

[3] Weinzierl, D., Raizer, A., Kost A. and Ferreira, G. S. "*An analysis of a mode stirred chamber excited by wires using the TLM method*." *In COMPEL – The International Journal for Computation and Mathematics in Electrical and Electronic Engineering*, vol. 2, no 3, pp. 770-778, 2003.

[4] Christopoulos, C. "The Transmission-Line Modelling Method TLM", IEEE Press and Oxford University Press, New York, 1996.

This page intentionally left blank

Chapter C

Applied Electromagnetism

This page intentionally left blank

Electromagnetic Fields in Mechatronics, Electrical and Electronic Engineering
A. Krawczyk et al. (Eds.)
IOS Press, 2006

Chapter C

C.0 Introductory Remarks

The third chapter constitutes the core of the ISEF conference as it is dedicated to widely understood applications. It does not mean, however, that the previous two chapters consist of the papers completely deprived of application references. The papers placed in the chapter can be grouped as follows:

- electrical machines and transformers,
- testing,
- heating and temperature field,
- various applications.

The first subgroup is a very classical subject and practically all the methods of numerical analysis started with electromagnetic field analysis in electrical machines and transformers. The structure of electrical machines and transformers is not too complicated so the first numerical approaches could have been well-tested on such structures. Of course, nowadays structures of electrical machines and transformers are more complex and their analysis more complicated but they are still simpler that those of modern applications. The particular subjects the papers deal with are typical for investigation of electrical machines and transformers, i.e. power losses, torques, end-region, skewed effect etc., thus considering them seems to be unnecessary.
The second group is poorly represented in our volume as there are many other conferences devoted to measurements and testing in electromagnetics. For this book only one paper has been accepted and it concerns insulation failure which is identified by on-line monitoring which detected slight variation of high frequency (1-100 MHz) parameters of stator winding.
The third subgroup gathers papers describing thermal problems. The problem of heating and analysis of temperature field seem to be most interesting area of electrical engineering. It is worth quoting briefly the subjects which are touched here. They are as follows:

- mathematical modelling of coupled electromagnetic and temperature fields for continual induction heating of thin non-ferrous metal strips at low frequency,
- flat two-sided induction heater applied in hot galvanizing process,
- modelling of motor with regard to temperature dependence.

The last group is connected with various applications which can be called in Latin *silva rerum*. Indeed, one can find here applications from biology to electronics. There is no doubt that the subjects should also be enumerated:

- simulation of electrical effects induced in and around biological cells in microsystems, such as dielectrophoresis or electroporation,
- bone conduction vibrator which serves for improvement of hearing impaired people,
- non-contact gear with permanent magnet,
- computer simulation of SAR distribution in human body evoked by mobile phones,
- computer simulation of electromagnetic pump for high temperature liquid metal,
- analysis of magnetic behaviour of superconducting Nb foil in linear type magnetic flux pump,
- visualization of electromagnetic phenomena inside analysed objects by coloured maps,

- design and analysis of Micro Positioning Actuator by 3-D FEM which improve its operating properties to a great extent,
- electromagnetic stirrers with an inductor generating travelling magnetic field,
- grounding system influence on Lighting Protection System analysing by means of Constrained Decision Planning,
- electromagnetic compatibility issue from the point of view of system and circuit design, component selection and Printed Circuit Board layout,
- eddy current methods of non-destructive testing for detecting defects in metallic structures,
- field analysis for tubular linear actuators with scaled geometries and regarding nonlinearity of magnetic core,
- asymmetry influence on the 1^{st}, 5^{th}, and 7^{th} harmonics in armature current in a cylindrical synchronous generator.

Electromagnetic Fields in Mechatronics, Electrical and Electronic Engineering
A. Krawczyk et al. (Eds.)
IOS Press, 2006

ELECTROMAGNETIC AND TEMPERATURE FIELDS IN CONTINUAL INDUCTION HEATING SYSTEM FOR THIN NON-FERROUS STRIPS

Jerzy Barglik

Silesian University of Technology, Krasińskiego 8, 40-019 Katowice, Poland, E-mail: jerzy.barglik@polsl.pl

***Abstract** – The paper deals with mathematical modeling of coupled electromagnetic and temperature fields for continual induction heating of thin non-ferrous metal strips of the thickness comparable with the depth of electromagnetic field penetration. For such work-pieces it is especially effective to use transverse flux induction heating system (TFIHS) which makes it possible to obtain required parameters at rather low frequencies of the field current in comparison with more often used classical induction heaters working with longitudinal magnetic field. Quite good accordance between calculation results and measurements are achieved.*

Introduction

Continual induction heating of flat, thin non-ferrous work-pieces in some technological processes like annealing belongs to modern, environment-friendly, but still rarely applied technologies. It seems that one of the reason for that is lack of experience in mathematical modeling and consequently designing of such devices. For thin, flat work-pieces of the thickness comparable with the depth of electromagnetic field penetration transverse flux induction heating system (TFIHS) is applied. It makes it possible to obtain required parameters like uniformity of temperature distribution within the work-piece and high energy efficiency at rather low frequencies of the field current in comparison with more often used classical induction heaters working with longitudinal magnetic field.

Mathematical Model

Let us consider mathematical model for calculation of weakly-coupled electromagnetic and temperature fields in a typical arrangement of the TFIHS (Fig. 1). The electromagnetic task represents an open-boundary 3D problem, but it can be treated as a typical boundary-value problem provided that we introduce artificial boundaries (shown in Fig. 1a with dashed lines) far enough from the TFIHS [1]. The electromagnetic field analyzed in 1/8 of total area is modeled by means of magnetic vector potential $\boldsymbol{A}$:

$$\operatorname{rot}\frac{1}{\mu}\operatorname{rot}\boldsymbol{A}+\gamma\frac{\partial \boldsymbol{A}}{\partial t}-\gamma\left(\boldsymbol{v}\times\operatorname{rot}\boldsymbol{A}\right)=\boldsymbol{J}_{\text{ext}} \tag{1}$$

where μ - magnetic permeability, γ – electric conductivity, v – velocity, J_{ext} – current density within the inductor.
In case when magnetic permeability μ of the core could be considered as constant equation (1)

transforms into form for phasor of magnetic vector potential $\underline{\boldsymbol{A}}$:

$$\mathrm{rot}\,\mathrm{rot}\,\underline{\boldsymbol{A}} + \mathrm{j}\omega\mu\gamma\underline{\boldsymbol{A}} - \mu\gamma\left(\boldsymbol{v}\times\mathrm{rot}\,\underline{\boldsymbol{A}}\right) = \mu\underline{\boldsymbol{J}}_{\mathrm{ext}} \tag{2}$$

where j denotes imaginary unit and ω – angular frequency of harmonic current

a)

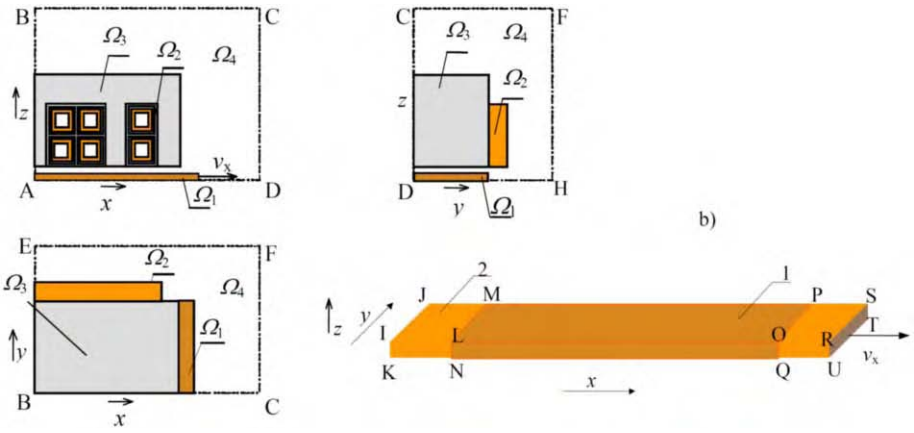

Fig.1 Calculation model of coupled electromagnetic (Fig.1a) and temperature fields (Fig.1b) $\Omega_{1=}$ strip, Ω_2 – winding, Ω_3 – magnetic core, Ω_4 = air-gap and surroundings. 1- part of the strip located in the air-gap, 2 – remaining part of the strip being outside the inductor

In sub-region Ω_1 (strip moving at a velocity v_x) equation (2) may be rewritten as

$$\mathrm{rot}\,\mathrm{rot}\,\underline{\boldsymbol{A}} + \mathrm{j}\omega\mu\gamma\underline{\boldsymbol{A}} - \mu\gamma\left(v_x,0,0\right)\times\mathrm{rot}\,\underline{\boldsymbol{A}} = 0 \tag{3}$$

Typically velocity of the strip movement in described arrangement is not too high so the third term in this equation can be neglected [2]. Consequently eddy current density $\underline{\boldsymbol{J}}_{\mathrm{eddy}}$ induced in the moving strip and specific Joule losses p_{v} are expressed by relations (4):

$$\underline{\boldsymbol{J}}_{\mathrm{eddy}} = \mathrm{j}\omega\gamma\underline{\boldsymbol{A}}, \qquad p_{\mathrm{v}} = \frac{\underline{\boldsymbol{J}}_{\mathrm{eddy}}\cdot\underline{\boldsymbol{J}}^{*}_{\mathrm{eddy}}}{\gamma} \tag{4}$$

For planes of artificial external borders (BEFC, DCFG, EGFH) taken far enough from the heating system and for the plane ABEH ($x = 0$, anti-symmetry of the field current density) condition

$$\underline{\boldsymbol{A}} = \boldsymbol{0} \tag{5}$$

however for both symmetry planes $z = 0$ (ADGH) and $y = 0$ (ABCD) condition

$$\underline{\boldsymbol{A}}\times\boldsymbol{n} = \boldsymbol{0} \tag{6}$$

are applied. Based upon known distribution of the specific Joule losses p_{v} the stationary temperature field in moving strip is calculated by means of the Kirchhoff – Fourier equation:

$$\operatorname{div}\left(\lambda \operatorname{grad} T\right) - \rho c\left(\boldsymbol{v} \operatorname{grad} T\right) = -p_{\mathrm{v}} \tag{7}$$

Length of analyzed zone of the strip is bigger than length of the inductor. The equation (7) is analyzed only in ¼ part of the sub-region. It is supplemented by the following boundary conditions :

- At the artificial input plane IJJ'K outside air-gap of the inductor

$$T\left(y,z,t\right) = T_{\mathrm{p}} \tag{8}$$

- At the artificial output plane RSTU and at the symmetry planes IRUK, KJ'TU;

$$\frac{\partial T}{\partial n} = 0\,. \tag{9}$$

- At all remaining planes (Fig. 1b) LMOP, IJML, OPRS, JSTJ'

$$-\lambda \frac{\partial T}{\partial y} = \alpha\left(T - T_{\mathrm{a}}\right) \tag{10}$$

Different values of coefficient of convective heat transfer α are put on different planes. For instance in the narrow air-gap of the inductor α is typically several times lower than an analogous coefficient outside the inductor. Due to low temperature kind of heating heat transfer by radiation is neglected. The algorithm for calculation of coupled electromagnetic and temperature fields is shown in Fig. 2.

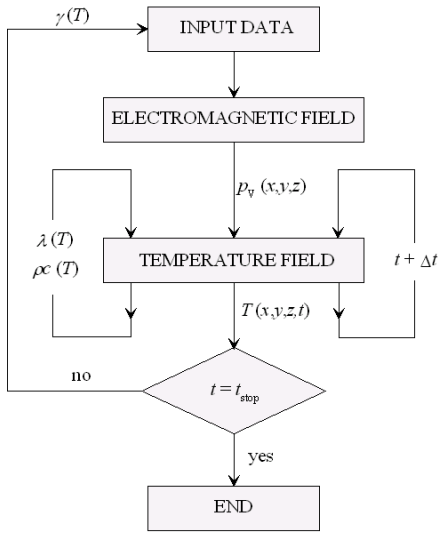

Fig. 2 Algorithm for calculation of weakly coupled electromagnetic and temperature fields

Based upon known distribution of the specific Joule losses in the strip the stationary temperature field is achieved. Temperature dependencies of the thermal conductivity λ, density ρ and specific heat c are taken into account. Electrical conductivity γ as the input parameter for the electromagnetic calculations is corrected when the average temperature within the strip changes more than by ΔT.

For $t = t_{stop}$ the calculations finish. Some more important parameters and dimensions of the TFIHS are collected in Table 1.

Table1 Parameters and dimensions of TFIHS

Inductor	current I_{ext} = 1000 A, frequency f = 50 - 2000 Hz, length, width and height (one side) respectively l_i = 0.217 m, b_i = 0.35 m, h_i = 0,08 m, air-gap a = 0.01 m
Magnetic core	width b_c = 0.25 m, relative magnetic permeability μ_r = 1000, electric conductivity γ_c = 0.
Strip:	thickness g = 0.0032 m, width b = 0.25 m, length taken to calculations l -= 0.34 m, velocity of movement v = 0.02 m/s, 0.04 m/s.
Material properties at 20°C	brass Cu60 conductivity $\gamma = 1.43 \cdot 10^7$ S/m, relative magnetic permeability μ_r = 1, density ρ = 8600 kg/m^3 , specific heat conduction λ = 144 W/m·K , specific heat c = 410 J/kg·K.
Heat transfer parameters	ambient temperature T_a = 20 °C, coefficient of convective heat transfer α =20 W/m^{2}K, (in narrow air-gap α_g =5 W/m^{2}K).

Distribution of the module of eddy currents at internal plane of the strip at mains frequency f = 50 Hz is depicted in Fig.3.

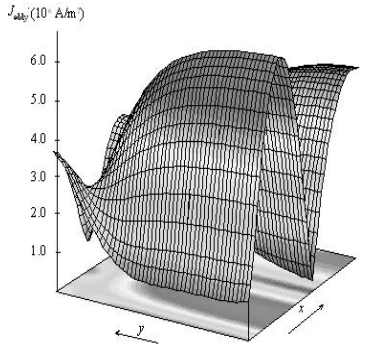

Fig. 3. Distribution of the module of eddy currents at mains frequency $f = 50$ Hz in the internal plane of flat brass strip for strip width $b = 0.25$ m

Table 2 Parameters describing distribution of the eddy-currents in the strip for three various frequencies of field current density

Module of eddy currents	Frequency [Hz]		
	50	200	2000
Average J_a (A/m^2)	$3.93 \cdot 10^6$	$8.45 \cdot 10^6$	$1.34 \cdot 10^7$
At strip axis J_o (A/m^2)	$6.736 \cdot 10^6$	$8.32 \cdot 10^6$	$1.06 \cdot 10^7$
Near edge J_b (A/m^2)	$3.751 \cdot 10^6$	$7 \cdot 10^6$	$2.24 \cdot 10^7$
Coefficient of uniformity k_J (-)	1.819	1.19	0.07

The module of eddy current density reaches its maximum ($J_{max} = 6.736 \cdot 10^6$) exactly in the middle of the strip ($y = 0$) and for $x_{max} = 0.0275$ m. Average value of the module of eddy current density is $J_a = 3.93 \cdot 10^6$ A/m^2. Let us calculate a coefficient of uniformity of eddy currents distribution k_J defined as the ratio of the module of the eddy-current density in the axis J_o and near the edge of the strip J_b characterises non-uniformity of eddy currents in the strip.

$$k_J = \left| \frac{J_o}{J_b} \right|_{x=x_{max}} \tag{11}$$

When frequency increases, the average value of the eddy current density also distinctly increases (see table 1). If we consider uniformity of eddy current distribution within the moving strip it could be noticed that it changes with frequency. For f = 200 Hz the distribution is quite uniform however for

f = 2000 Hz it becomes again non-uniform with a distinct maximum of module of eddy current density near the edges of the strip. Similar dependencies could be observed in case of the specific Joule losses produced in the strip. Particulars you can find for instance in [3-4]. Exemplary results of temperature distribution within the work-piece for two different frequencies are shown in Fig. 4

a) b)

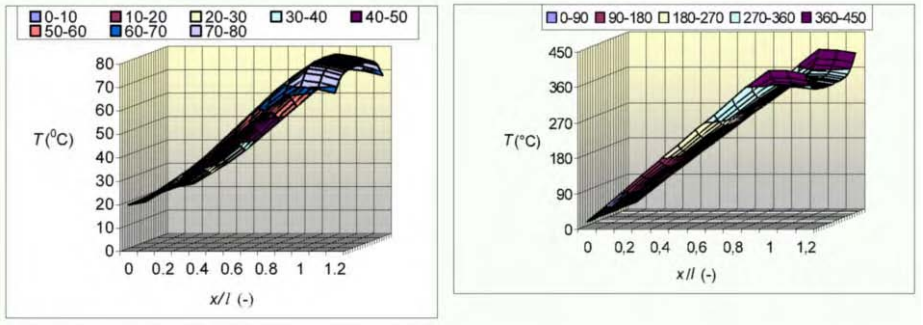

Fig. 4. Temperature distribution on the upper plane of the moving brass strip (v = 0.02 m/s) heated inductively in TFIHS supplied by the field current of frequency a) f = 50 Hz, b) f = 2000 Hz

Experimental Part

A simplified diagram of laboratory stand for measurements of the most important parameters of the TFIHS is shown and the view of the stand are shown in Fig. 5.

a) b)

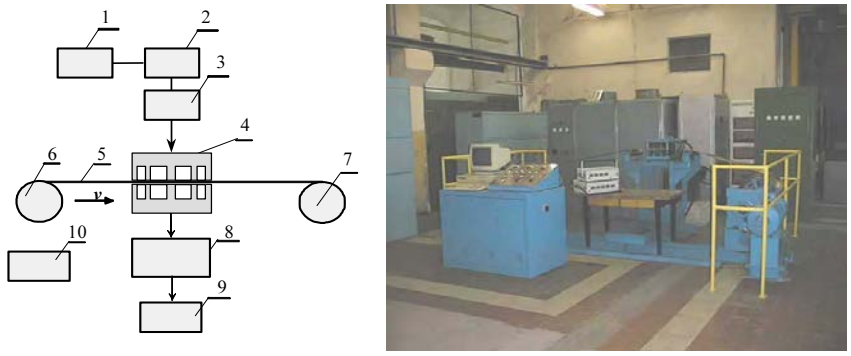

Fig. 5. Block scheme of the laboratory stand: a) block scheme b) view 1 – thyristor converter, 2 – block of capacitors, 3 – matching transformer, 4 – inductor, 5 – moving strip, 6 – uncoiling drum, 7 – coiling drum, 8 – block of measurement panels, 9 – PC as a recorder, 10 – steering desk

Temperature distributions along the width of the outlet ($x = 1.25l$) of the moving brass strip received by simulation and by measurements are shown in Fig. 6a (0.02 m/s) and in Fig. 6b (0.04 m/s).

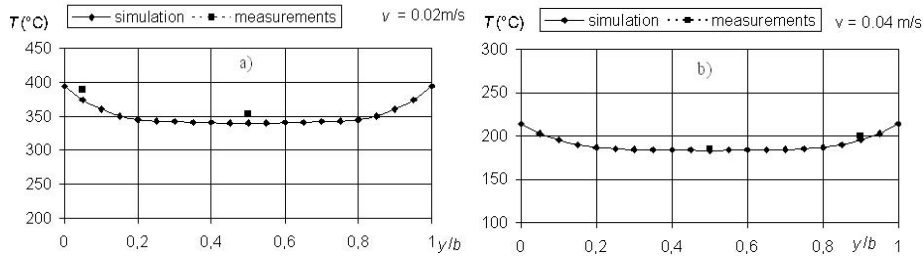

Fig. 6. Temperature distribution along width of the moving brass strip heated inductively in transverse magnetic field at frequency of the field current $f = 2000$ Hz for two different velocities of the strip movement a) - $v = 0.02$ m/s, b) - $v = 0.04$ m/s)

In both cases quite a good accordance between computations and measurements is achieved; the differences do not exceed 4.8 %.

Conclusions

3D weakly coupled electromagnetic and temperature fields in the TFIHS for thin brass strips were analysed. The eddy currents and temperature distributions within the moving work-piece were determined. The shapes of temperature curves along width of the strip for different frequencies of field current were compared. The results were discussed in order to analyse possibilities to receive requested parameters of the TFIHS. For computation of induction heating of brass strips the results were validated on a laboratory stand and a quite good accordance between calculations and measurements was achieved.

Acknowledgement

Financial support of the Polish Scientific Research Committee (grant No. 7T08B 04596C/2910) is highly acknowledged.

References

[1] Barglik J.: Induction Heating of flat Charges in Transverse Flux Field. Computer Simulation and Investigation Verification) (2002). Scientific Issues of the Silesian University of Technology. No. 65, p.120 (in Polish).
[2] Barglik J., Doležel I. and Ulrych B.: Induction Heating of Moving Bodies (1998). Acta Technica CSAV, Vol. 43, pp. 361–373.
[3] Barglik J.: Analysis of weakly-coupled electromagnetic and temperature fields in transverse flux induction heating system for non-ferromagnetic strips. Archive of Electrical Engineering. (2005) vol.1 pp.93-108
[4] Development in material science and metallurgy. Publishing House of the Silesian University of Technology. Gliwice 2005 Chapter I “Computer modeling of induction heating of thin flat non-ferrous work-pieces”. pp. 7-32 (in Polish).

Electromagnetic Fields in Mechatronics, Electrical and Electronic Engineering
A. Krawczyk et al. (Eds.)
IOS Press, 2006

PREDICTION OF CORE LOSSES IN SWITCHED RELUCTANCE MOTORS USING FINITE ELEMENT METHOD AND RAINFLOW ALGORITHM

Francis Bokose, Lieven Vandevelde and Jan A. A. Melkebeek

Electrical Energy Laboratory (EELAB)
Dept. of Electrical Energy, Systems and Automation (EESA)
Ghent University
Sint-Pietersnieuwstraat 41, B-9000 Gent, Belgium
tel. +32 9 264 34 22 – fax +32 9 264 35 82
e-mail: Francis.Bokose@UGent.be

***Abstract** – Prediction of losses in a switched reluctance motors (SRMs) is difficult due to complex flux patterns in the machine. Determination of iron losses is vital for efficient motor design. In this paper, a inite element method (FEM) coupled with a voltage supply circuitry and a control strategy is used to determine spatial and temporal distributions of flux density in the motor. Posteriori, a rainflow algorithm is used to identify major and minor loops from the distribution in order to compute hysteresis losses. Besides, classical losses are computed using a model based on the rate of change of flux density.*

Introduction

The estimation of local iron losses helps to predict hot spots in the machine structure.These losses are normally used as heat sources when modelling thermal phenonena in the machine. Ofcourse, iron losses determine the overall efficiency of the machine. However, iron loss models developed specifically for SRMs are rare. In [1] and [2], loss models were developed based on simple triangular flux waveform assumptions. In [1], the total losses were estimated, while in [2] classical and hysteresis losses are separated; the classical loss model is based on the rate of change of the flux density and the hysteresis losses are determined experimentally. However, in the context of design optimization, where machine efficiency is the target, loss minimization becomes a design goal and such modelling approaches are impracticable. In this paper, a FEM coupled with a controlled voltage supply is used to compute both spatial and temporal flux distributions. Thereafter, the classical losses are computed using a model based on the rate of change of the flux density. For hysteresis losses, a rainflow algorithm is first used to identify hysteresis loops from the flux distribution before the hysteresis loss is computed.

Finite Element Method

The motor model used in this study is a 6x4 SRM shown in Fig. 1a. The finite element method is based on the magnetic vector potential formulation and the field equation in the linear part of the motor structure is expressed in its weak form as:

$$(\nu_0 \mathbf{curl}\mathbf{A}, \mathbf{curl}\hat{\mathbf{A}})_\Omega = (\mathbf{J}, \mathbf{curl}\hat{\mathbf{A}})_{\Omega_s} \quad (1)$$

$$\mathbf{B} = \mathbf{curl}\mathbf{A} \quad (2)$$

where A and Â are the vector potential and test function respectively; ν_0 is the reluctivity of free space, B is the flux density, Ω_s, Ω are the source and problem domain respectively.

In the non-linear part of the motor, the non-linearity (saturation effect) in the iron parts of the motor is taken into account in the field formulation with a single-valued monotonic B ∨H curve. The field equation then becomes:

$$(\frac{\partial \mathbf{H}}{\partial \mathbf{B}}\mathbf{curlA}, \mathbf{curl}\hat{\mathbf{A}})_{\Omega} = (\mathbf{J}, \mathbf{curl}\hat{\mathbf{A}})_{\Omega_s} \tag{3}$$

The reluctivity tensor $\frac{\partial H}{\partial B}$ is used by the Newton-Raphson iterative process to linearize the non-linear system. This tensor is expressed as

$$\frac{\partial \mathbf{H}}{\partial \mathbf{B}} = \nu 1 + 2\frac{d\nu}{dB^2}\mathbf{BB} \tag{4}$$

where H is the magnetic field, 1 is the identity tensor.

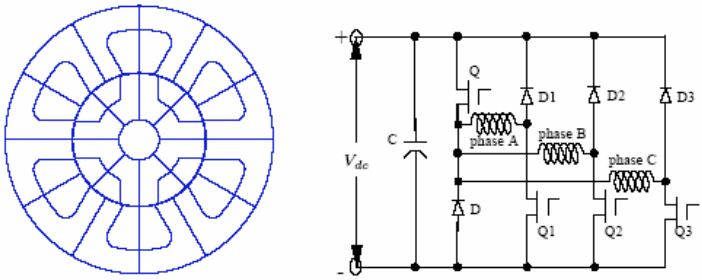

a. b.

Fig. 1. (a) a 6x4 SRM and (b) a converter

Circuit Equation

The converter shown in Fig. 1b is to supply voltage to the motor. The applied voltage $v$across the winding of each phase is linked to the field equation by the flux linkage Φ and is modelled through the vector potential as:

$$v = Ri + \frac{Nl}{S}\int_S \frac{\partial \mathbf{A}}{\partial t} dS \tag{5}$$

with $N$the total number of winding turns, $l$the stack length and $S$the total winding area.

Converter Control

In SRMs, a speed dependent control strategy is used by the converter. Current and voltage chopping modes are used to control the current at low speeds. At high speeds, a single mode regime is used.

Low Speed Operations

- *Chopping - Current Regulation Mode.* In this work, hysteresis current control is adopted for low speed operations. The switches are turned on or off according to whether the current is higher or lower than a reference current. The current is maintained within upper and lower limits of the hysteresis band. Fig. 2a shows current waveforms at 500 rpm.

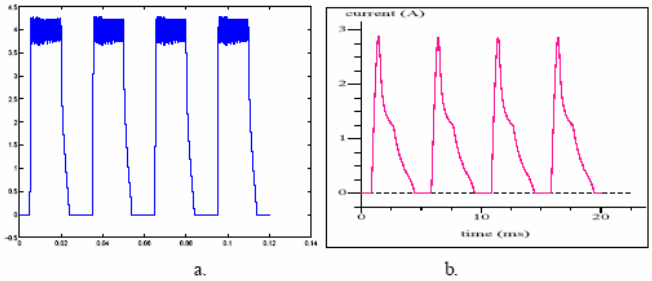

Fig. 2. (a) current waveform at 500 rpm (b) current waveform at 3000 rpm

High Speed Operations

- *Single Pulse Mode.* As the speed of the motor increases, it becomes impossible to control the current based on the previous method. This is due to the effects of back EMF and the reduced amount of time for the commutation interval. In this mode, current control is achieved by increasing the conduction period and/or adjusting the firing angles. Fig. 2b shows the current waveform at 3000 rpm.

Core Losses Computation

Iron losses are generally estimated at around 25 to 75 percent of the total electromagnetic losses (iron and copper losses) [3, 4]. In general, iron losses are divided into hysteresis, classical and excess (anomalous) losses. The eddy current and anomalous losses can be estimated based on the rate of change of magnetic flux density in the core structure [5]. However, hysteresis losses normally require complex and time-intensive models , which are unusable for practical problems like the design of electrical machines.

Hence, simplified models are often sought. The core loss models described below require the determination of both spatial and temporal distribution of the flux density in the core. The finite element method is used in this case.

Hysteresis Loss Model

Major and minor hysteresis loops characterize the hysteresis phenomenon. The minor loops appear when the rate of change of the flux density $\frac{\partial B}{\partial t}$ changes sign more than once per period. This is the case especially in applications using commutating power electronic inverters. Attempts to model minor hysteresis loops caused by distortion in the standard sinusoidal waveforms have been reported in [4, 5]. In [5], the minor hysteresis loops were taken into account by introducing a correction (distortion) factor.

The model is expressed as follows:

$$P_{hys} = \frac{k_h B_p^{\alpha}}{T}\left[1 + \frac{\beta}{B_p}\sum_{j=1}^{n}\Delta B_j\right] \quad (6)$$

The first part of the hysteresis loss equation only takes into account the major loop and is dependent on the peak flux density B_p and frequency. The second part of the equation approximates hysteresis loss due to minor loops by summing up n flux density reversals of amplitude ΔB_j . In both components, k_h, α and β represent hysteresis loss coefficients; α and β are coefficients dependent on material characteristics.
An assumption taken for this method is that all minor loops have the same area. In [4], it is stated that the problem with this method is the difficulty in determining the size and shape of ΔBj. To do so, one would require the knowledge of both the flux density and the field strength waveforms and the latter is not known a priori. However, here we use the model as it is valid when only the amplitudes are known.

Classical Loss Model

As is commonly known, most electrical machines are constructed by using laminated steel in order to reduce eddy current losses. In finite element analysis of magnetic field in such machines, the laminated core can be modelled as a solid in order to save computational time [6]. Even with such an approach, a lot of computational time is expended. In [5], the classical eddy current losses P_{cl} are estimated based on the rate of change of the flux density. This is a posteriori computation and takes relatively less time.
The model is expressed as follows:

$$P_{cl} = \frac{\sigma d^2}{12\rho}\frac{1}{T}\int_0^T \left(\frac{\partial \mathbf{B}}{\partial t}\right)^2 dt \quad (7)$$

Anomalous Loss Model

In coarse-grain materials, the anomalous eddy current loss, may become significant. Larger domain wall spacings give a non-uniform distribution of the eddy currents, causing local increases in the eddy current loss density and consequently resulting in increases in total eddy current losses. Generally, anomalous losses are estimated based on the rate of change of the flux density and are expressed as:

$$P_{exc} = \frac{k_e}{T}\int_0^T \left|\frac{\partial \mathbf{B}}{\partial t}\right|^{\frac{3}{2}} dt \quad (8)$$

Here, σ is the material conductivity, d the lamination thickness and k_e is the excess loss constant.
The anomalous losses should only be modelled if coarse grain, semi processed steel is used. Hence, the anomalous losses are neglected in this study.

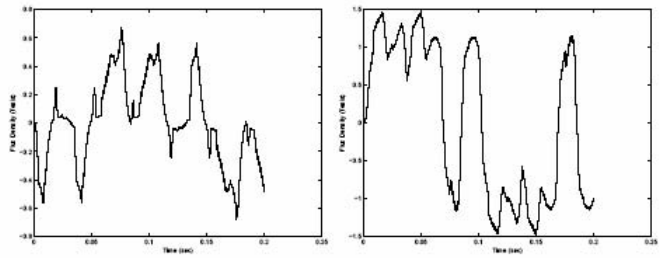

Fig. 3. (a) Rotor pole flux distribution (b) Rotor yoke flux distribution

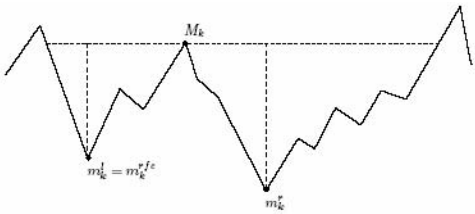

Fig. 4. Rainflow cycle definition

Hysteresis Loops Extraction by Rainflow Algorithm

As stated earlier, the switched reluctance motor displays complex patterns of flux density distributions in different parts of the machine. Examples of such patterns are shown Fig. 3a and Fig. 3b, where flux density distribution in one rotor pole (a) and one rotor yoke section (b) are shown. From the above classical loss model, the classical losses are computed based on the rate of change of the flux density. However, hysteresis losses require the identification of major and minor loops.

The rainflow method, which was first proposed in [7] and later on redefined in [8] is used here. It was designed to capture both slow and rapid variations of the load by forming cycles pairing high maxima with low minima even in the presence of intermediate extremes.

A graphical definition of a rainflow cycle is illustrated in Fig. 4, where from each local maximum M_k, one shall try to proceed in the backward (left) or forward (right) directions, with as short a downward excursion as possible [8]. The minima m_k^l to the left and m_k^r to the right are identified and the minimum representing the smallest deviation from the maximum M_k is defined as the corresponding rainflow minimum m_k^{rfc}. The k^{th} rainflow cycle is defined as (m_k^{rfc} ; M_k) and the rainflow amplitude $A^{rfc} = M_k - m_k^{rfc}$ is the amplitude of the attached hysteresis loop.

Computed Results

The results of the computations are shown in Table I and Fig 5. Only results for the range of speeds from 200-1200 rpm are shown here. In that range, hysteresis losses dominate.

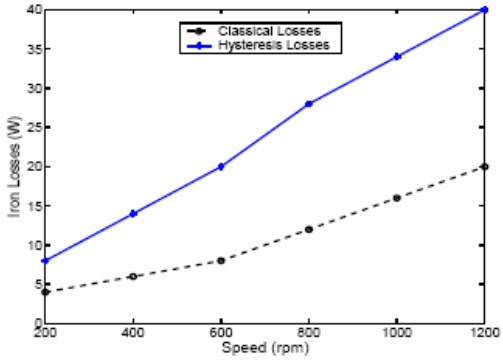

Fig. 5. Variation of Iron Losses with Speed

TABLE I
Variation of iron losses with speed

speed	P_h	P_{cl}	P_{exc}
rpm	W	W	W
200	4	8	4
400	7	14	6
600	16	20	8
800	26	28	12
1000	46	34	16
1200	65	40	20

Conclusions

A procedure for predicting core losses in switched reluctance motor has been presented. Actual flux distributions are used in this case unlike the approximations used in the cited models. Also, expensive hysteresis models are avoided and the method can be used at the design stage, especially in optimizing the efficiency of the motor.

Acknowledgement

The research was carried out in the frame of the Interuniversity Attraction Poles Programme (IAP P5/34) – Belgian Science Policy.

References

[1] P. Materu and R. Krishnan, “Estimation of switched reluctance motor losses,” *IEEE-IAS Annual Meeting*, pp. 79-90, 1988.
[2] Y. Hayashi and T.J.E.Miller, “A new approach in calculating core losses in switched reluctance motor,” *IEEEIAS*
Annual Meeting, pp. 322-348, 1995.
[3] G. Bertotti, “An improved estimation of iron losses in rotating electrical machines ,” *IEEE Transactions on Magnetics*, Vol. 27, No. 6, pp. 5007-5009, 1991.
[4] J.D. Lavers, P.P. Beringer, J. Hollitscher, “A simple method of estimating the minor loop hysteresis loss in thin laminations,” *IEEE Transactions on Magnetics*, Vol. 14, No. 5, pp. 386-388, Sept 1978.
[5] K. Atallah,Z.Q. Zhu and D. Howe, “An improved method for predicting iron losses in brushless permanent

magnet Dc drives," *IEEE Transactions on Magnetics*, Vol. 28, No. 5, pp. 2997–2998, Sept. 1992.
[6] K. Muramatsu, T. Okitsu, K. Fujitsu, F. Shimanoe, "Method of Nonlinear Magnetic Field Analysis Taking into Acount Eddy Current in Laminated Core", *IEEE Transactions on Magnetics*, Vol. 40, No. 2, pp. 896-899, March 2004.
[7] M. Matsuishi and T. Endo, "Fatique of metals subject to varying stress,"*society of mechanical engineers*, Jukvoka, Japan, 1968.
[8] I. Rychlik, "A new definition of rainflow cycle counting method,"*International Journal of Fatique*, Vol. 9, Japan, 1987

Electromagnetic Fields in Mechatronics, Electrical and Electronic Engineering
A. Krawczyk et al. (Eds.)
IOS Press, 2006

REDUCTION OF COGGING TORQUE IN A NOVEL AXIAL FLUX PERMAMENT MAGNET BLDC MOTOR

Yun-Hyun CHO, Yon-Do CHUN*, Dae-Hyun KOO* and Won-Young CHO

*Korea Electrotechonolgy Research Institute, P. O. Box 20, Changwon-si, 641-120, Korea,
Tel: +82-55-280-1427, Fax: +82-55-280-1547, Email: ydchun@keri.re.kr
Dong-A University, 840 Hadan 2 dong, Saha-gu, Busan 604-714, Korea

***Abstract** – Cogging torque, the primary ripple component in the torque generated by permanent magnet (PM) motors, is due to the slotting on the stator or rotor. This article shows the reduction of cogging torque in a novel aixal flux permament magnet (AFPM) motor through the various design schemes. 3D finite element method is used for the exact magnetic field analysis. The effects of slot shapes and skewing of slot on the cogging torque and average torque have been investigated in detail.*

Introduction

The axial flux permanent magnet (AFPM) motor has a higher power and torque per unit weight than those of a conventional motor with the same size and weight [1]-[2]. Recenty, AFPM motors have been used increasingly for various application such as electric ship, electric vehicle, and airplaine propulsion [3-4].

In general, cogging torque is a source of vibration and noise in permanent magnet (PM) machines. It is proportional to the PM flux and the reluctance variation, and it is independent of the load current. The reduction of the torque ripple has been important concern in the design of AFPM motor. The torque ripple contains both cogging torque and commutation torque components. Cogging torque occurs from the slotting on the stator or rotor of the motor, and causes the primary ripple component in the torque. There are various techniques for reducing the cogging torque in permanent magnet (PM) machines such as shoe of stator teeth, fractional pitch, change of PM magnetization shape and skewing [5-6]. However, there is a trade off relationship between the cogging torque and average torque [6]. Accordingly, it is difficult to satisfy the objectives simultaneously.

In this article, the slot shapes and the slot skewing are some main matters which affect on the cogging torque and the average torque characteristics. Therefore, it must be considered in design step of AFPM motor. In order to investigate the various design schems of AFPM, we carried out 3-D finite element anlaysis of magnetic fields with the aid of ANSYS package. The effects of slot shapes and the slot skewing on the cogging torque have been investigated in detail.

Axial Flux PM Motor Structure

Fig. 1 shows the basic structure of the slotted AFPM motor with double stator and single rotor. The rectangular-shaped teeth and fan-shaped PM in AFPM are shown in Fig. 2. Fig. 3 shows the picture of prototype AFPM motor. The motor has two stators with two sets of 3 phase stator winding. In the structure of the AFPM motor, the rotor with PM is located in the middle of the motor and the stator with exciting coils is attached on the both sides. To increase the power density of motor, Neodymium-

Iron-Boron is selected due to its high energy product. Table I shows the specifications of the AFPM motor. We proposed the innovative teeth structure. The teeth is segmented structure and assembled together with wound coils. It enables us to manufacture the motor simply and easily.

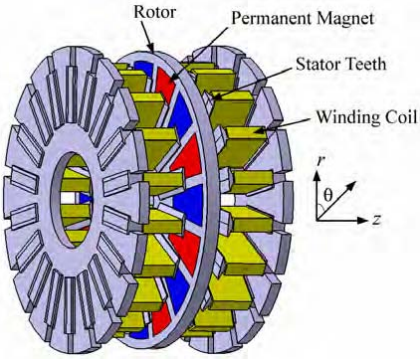

Fig. 1. The structure of AFPM motor with the innovated slot.

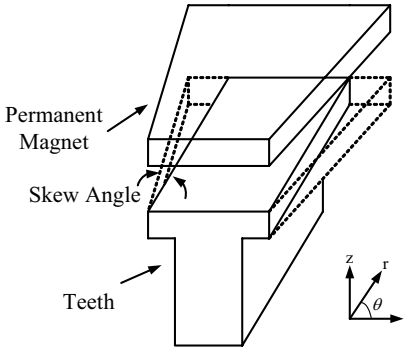

Fig. 2. Teeth and PM shape

Fig. 3. Picture of the prototype AFPM motor.

Table I. Specifications of AFPM motor

Stator		Rotor	
Slot number	18	Pole number	16
Phase	3	Inner radius	124 mm
Phase resistance	0.735 Ω	Outer radius	268 mm
Turns per phase	95	Axial length of PM	12.5 mm
Inner radius	151 mm	Remanent of PM	1.2 T
Outer radius	262 mm	PM	Nd-Fe-B
Airgap length	2 mm	Coercivity	970 kA/m

Reduction of Cogging Torque

Fig. 4 shows the stator teeth arrangement for the cogging torque reduction in AFPM motor. The teeth shapes are classified as rectangular (case 1), trapezoidal (case 2) and asymmetric skwed with 5 (case 3), 10 (case 4), 15 (case 5) [deg], respectively.

Fig. 5 shows the comparions of cogging toruqe between rectangular and trapezoidal teeth. Comparing to the rectangular shape, the peak value of cogging torque in trapezoidal shape is decreased to 35.3%.

Fig. 6 shows the comparison of cogging torque accoridng to the stator skewing angle. From the result, we can know that the increment of the skew angle decreases the cogging torque. Compare to the no skewing (case 2), the cogging torque from the case 3 to case 5 are decreased to 12%, 19.5% and 35% respectively.

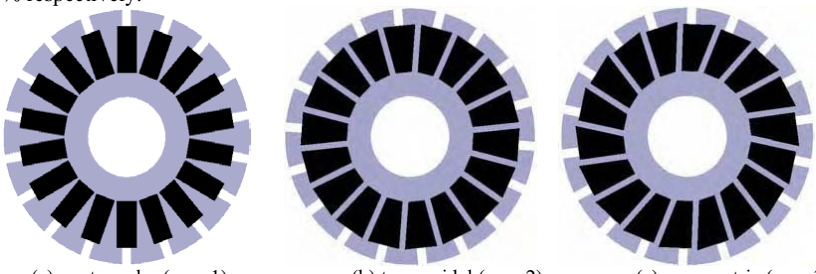

(a) rectangular (case 1) (b) trapezoidal (case 2) (c) asymmetric (case 3,4,5)

Fig. 4 Stator teeth arrangement for cogging torque reduction

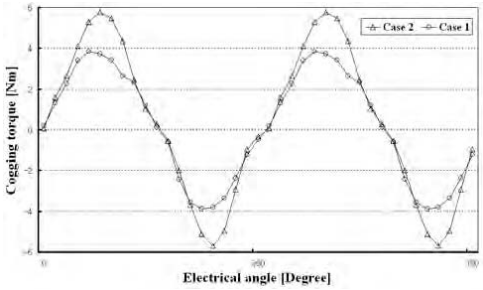

Fig. 5. Comparisons of cogging torque between rectangular and trapezoidal teeth

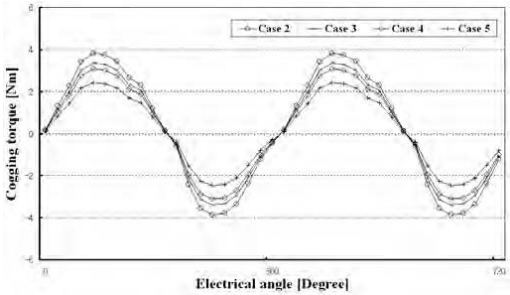

Fig. 6. Comparisons of cogging torque according to the variation of the skew angle.

Fig. 7 shows the comparison of torque characteristics according to the change of the teeth shape. Table II shows the average torque and torque ripple characteristics according to the teeth shape variation. From the cogging torque reduction point of view, we can select case 5 for the best solution. However, in order to consider the average torque and the torque ripple totally, case 4 is better than case 5.

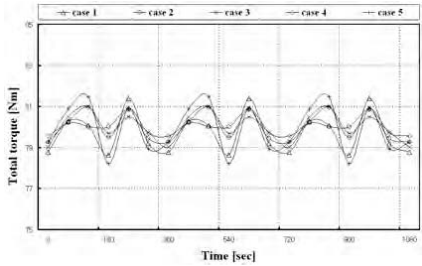

Fig. 7. Comparison of average toruqe characteristics according to the change of the teeth shape.

Table II. Average torque and torque ripple according to the teeth shape variation

	Average torque (Nm)	Torque ripple (%)
Case 1	79.66	3.45
Case 2	79.92	1.95
Case 3	80.01	2.49
Case 4	80.11	1.86
Case 5	79.91	4.05

Conclusions

In this paper, the effect of variation of design schemes is investigated for the reduction of cogging toruqe and increase of average torque. The effects of slot shapes and the slot skewing on the cogging torque have been investigated in detail. 3D FEM is used for the accurate magnetic field analysis. From the results, we can improve the cogging torque and average torque characteristics.

References

[1] M. Aydin, S. Husang, and T. A. Lipo, Optimum design and 3D finite element analysis of non-slotted and slotted internal rotor type axial flux PM disc machines, Power Engineering Society Summer Meeting, pp. 1409-1416, 2001.
[2] F. Caricchi, F. Crescimbini, O. Honorati, and E. Santini, Performance evaluation of an axial flux PM generator, Proceedings of International Conference on Electrical Machines (ICEM), pp. 761-765, 1992.
[3] R. J. Hill-Cottingham, P. C. Coles, J. F. Eastham, F. Profumo, A. Tenconi, G. Gianolio, Multi-disc axial flux stratospheric propeller drive, Proc. of IEEE IAS Annual Meeting Confrence Record 2001, vol. 3, pp. 1634-1639, 2001.
[4] F. Caricchi, F. Crescimbini, O. Honorati, Modular, axial-flux permanent magnet motor for ship propulsion drives, IEEE Trans. on Energy Conversion, vol. 14, pp. 673-679, 1999.
[5] M. Aydin, R. Qu and T. A. Lipo, Cogging torque minimizaiton technique for multiple-rotor, axial-flux, surface-mounted-PM motors: alternating magnet pole-arcs in facing rotors, IEEE Industry Applications Society Annual Meeting, Salt Lake City, 2003.
[6] Z. Q. Zhu and D. Howe, Influence of design parameters on cogging torque in permanent magnet motors, IEEE Transactions on Energy Conversion, Vol. 15, No. 4, pp. 2000.
[7] Y. D. Chun, S. Wakao, T. H. Kim, K. B. Jang and J. Lee, Multiobjective design optimization of brushless permanent magnet motor using 3D equivalent magnetic circuit network method, IEEE Transactions on Applied Superconductivity, Vol. 14, No. 2, pp. 1910-1913, 2004.

Electromagnetic Fields in Mechatronics, Electrical and Electronic Engineering
A. Krawczyk et al. (Eds.)
IOS Press, 2006

ANALYSIS OF A HYBRID METHOD FOR THE SIMULATION OF ELECTRIC FIELDS IN BIO-MEMS APPLICATIONS

Laurent De Vroey, Damien Grenier

Département d'Electricité/Université Catholique de Louvain, B-1348 Louvain-la-Neuve, Belgium
e-mail : devroey@lei.ucl.ac.be

Abstract* – *Dielectrophoresis and electroporation applications inside bio-MEMS are of growing interest and there is an important need for well-suited methods to simulate the multi-scale and multi-physics properties of those systems. In this paper, we are interested in the possibilities and limits of a hybrid analytical-numerical method for the simulation of electrical effects induced in and around biological cells in microsystems.

Introduction

The application of electric fields on biological cells within micro electromechanical systems (MEMS) is of growing interest in the field of biological and biomedical analyses.
The modelling of such systems can be difficult because of their geometrical and physical complexity. When possible, the use of simple but reliable techniques is thus desirable in order to reduce the costs in computation time and memory.
This paper deals with such a method, referred to as "hybrid". After a short description of the context, the hybrid method is introduced and the possibilities and limits of this method are presented for some cellular applications in bio-MEMS.

Context

Several electrical models exist to represent a cell in a solution. The most common model is a conducting sphere, representing the cytoplasm, surrounded by a very thin isolating layer, representing the membrane. In this article, we consider cells with an external radius R of 10 µm and a membrane thickness d of 5 nm, which is the order of magnitude for human red blood cells. The conductivity and permittivity values considered here are (fig. 1) : $\sigma_1 = 1$ S/m, $\sigma_2 = 120*10^{-12}$ S/m, $\sigma_3 = 5*10^{-4}$ S/m, $\varepsilon_1 = 640$ pF/m, $\varepsilon_2 = 44$ pF/m, $\varepsilon_3 = 640$ pF/m.

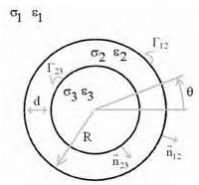

Fig. 1. Electrical scheme of a cell in a solution

Different kinds of applications are of major interest in the field of bio-MEMS. Dielectrophoresis (DEP) describes the displacement of the cells towards the area of maximum or minimum electric field, according to the frequency of the field and electric parameters of cells and medium. This makes it

possible for example to sort different types of cells. The important parameter in these applications is the voltage (or the electric field) outside the cells. Electroporation is a technique which uses electric fields as a tool to make porous the membrane surrounding the cell and to allow the insertion of various elements, such as genes or other molecules. The important parameter in these applications is the induced transmembrane voltage (TMV).

The hybrid method

Bio-MEMS applications are generally complex to model, because of their strong 3D character, their multi-scale aspects and the multi-physics couplings governing them.
In the context of cellular applications, one of the major difficulties resides in the very thin membrane, that must be treated in an adequate way while limiting the amount of calculations. The traditional finite elements method requires to mesh the membrane, which implies a very high number of nodes and calculations in and around the membrane. A complete simulation of such systems being generally too expensive, various approaches were proposed, in order to simplify the simulations (see, for example, [1,2]).
An alternative method, called "hybrid", was presented in [3] for DC applications. It is based on a simplification of the geometry, independently of the particular structure of the system studied, and which is directly compatible with a simple finite elements method.
In this paper, we extend the study to AC systems, which is the case in all the DEP applications and the majority of the electroporation applications. The frequencies $\omega/2\pi$ are generally comprised between 1kHz and 100MHz.
Using the hybrid method, a cell with a membrane is replaced by an homogeneous one. It is assumed that the magnetic effects and volumic charges are negligible, which is generally well verified, and the electrical equation of the problem is thus the Laplace equation :

$$\nabla^2 \Phi = 0 \tag{1}$$

with the following conditions at the interface Γ_{ij} between subdomains *i* and *j* (fig.1) :

$$\Phi_i = \Phi_j \quad \text{and} \quad \varepsilon_i' \frac{\partial \Phi_i}{\partial \vec{n}_{ij}} = \varepsilon_j' \frac{\partial \Phi_j}{\partial \vec{n}_{ij}} \tag{2-3}$$

with $\varepsilon_i' = \varepsilon_i - j\frac{\sigma_i}{\omega}$ and Φ is the electric potential.
In order to determine the equivalent electrical parameters of the homogeneous cell, we first consider an infinite tank and an homogeneous electric field $E = -\nabla\Phi$ at infinity, for which the Laplace equation has a finite solution. The equivalent electrical parameters are then computed in such a way that the potential on the border of the cell is the same in both models. Using the obtained equivalent parameters, the homogeneous problem can finally be solved with a finite elements method, without having to mesh the thin membrane. By doing this, the number of calculation points can be greatly reduced.
In 3D, the equivalent complex permittivity for an homogenized cell is computed as :

$$\varepsilon_{2,\text{éq}}' = \varepsilon_2' \frac{a^3 + 2\dfrac{\varepsilon_3' - \varepsilon_2'}{\varepsilon_3' + 2\varepsilon_2'}}{a^3 - \dfrac{\varepsilon_3' - \varepsilon_2'}{\varepsilon_3' + 2\varepsilon_2'}} \tag{4}$$

with a = R/(R-d). It varies between two asymptotic values in function of the frequency (fig. 2).

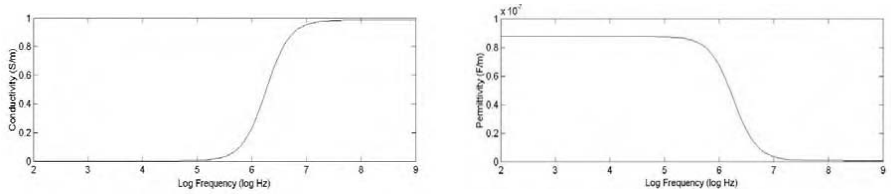

(a) (b)

Fig. 2. Equivalent conductivity (a) and permittivity (b) in function of the frequency

With the finite elements, chosen as a comparison tool for the study of the hybrid method, the resolution of the 3D problem of a cell with a thin membrane is particularly time- and memory-consuming. We thus considered the case of an increased thickness d of the membrane. The 3D results for d = 500 nm are presented below for a spherical cell in a cubic tank and a ratio $L/2R$ of 1.1 and face-to-face electrodes with Φ = ±V, respectively (fig. 3).

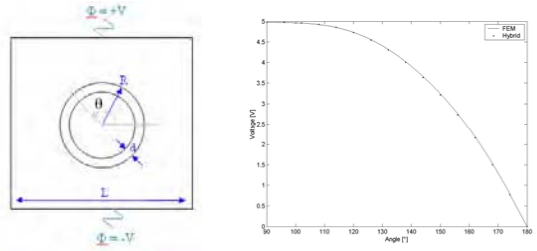

(a) (b)

Fig. 3. 3D case : general view (a); comparison of FEM and hybrid results for $\Phi(R)$, null frequency (b)

The hybrid method offers excellent 3D performances, comparable with those obtained in 2D for the same configuration [3]. The method having proved good reliability in 2D for smaller membrane thicknesses, we expect comparable performances in 3D under equivalent conditions, and we limit ourselves, in the following, to a 2D approach.

Results

Voltage computation outside a cell

We present below a comparison of the results obtained with the finite elements and the hybrid method, for various frequencies, in the case of a circular cell centred in a square tank, the two electrodes being placed face-to-face on the top and bottom edges of the tank. We limit ourselves to the observation of the voltage $\Phi(R)$ at the edge of the cell, where one can show that the differences between both methods are the largest.

Figure 4 illustrates these results for a tank with a side five times larger than the diameter of the cell. One observes in this case a very small full-scale range (FSR) error, at all the frequencies.

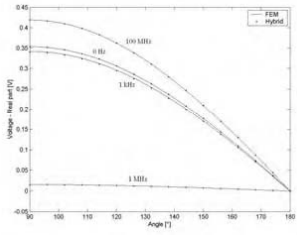

(a)

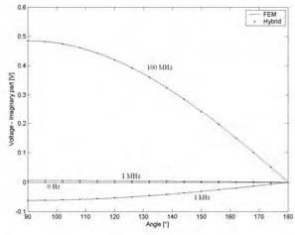

(b)

Freq	Real
0 Hz	0,08%
1 kHz	0,58%
1 MHz	2,06%
100 MHz	0,13%

Freq	*Imag*
0 Hz	*0,00%*
1 kHz	*1,08%*
1 MHz	*4,18%*
100 MHz	*0,04%*

(c)

Fig. 4. Comparison of FEM and hybrid results for $\Phi(R)$, $L/2R = 5$: real (a) and imaginary (b) parts; FSR error on amplitude (c)

Figure 5 illustrates the same results for a tank of reduced size, whose side is equal to 1.1 times the diameter of the cell. In this case, one observes a more significant difference in the results obtained by finite elements and with the hybrid method. However, the orders of magnitude remain quite good.

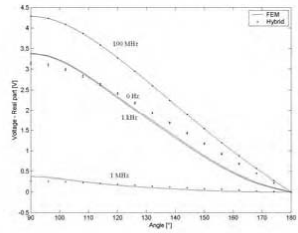

(a)

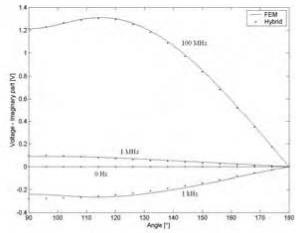

(b)

Freq	Real
0 Hz	9,22%
1 kHz	9,40%
1 MHz	26,60%
100 MHz	0,26%

Freq	*Imag*
0 Hz	*0,00%*
1 kHz	*14,74%*
1 MHz	*11,98%*
100 MHz	*1,06%*

(c)

Fig. 5. Comparison of FEM and hybrid results for $\Phi(R)$, $L/2R = 1.1$: real (a) and imaginary (b) parts ; FSR error on amplitude (c)

We are now interested in a second geometry, often met in practice, where the electrodes are located in the same plan. Figure 6 shows that the results obtained for $\Phi(R)$ with the hybrid method are not as good as in the preceding case, although the orders of magnitude are respected.

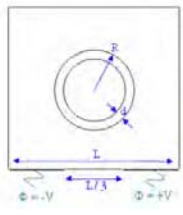

(a)

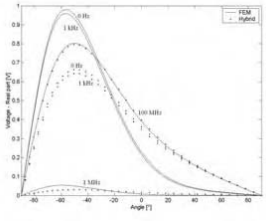

(b)

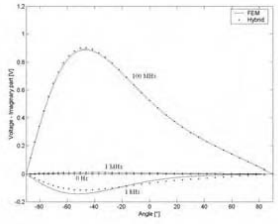

(c)

Freq	L/2R = 1.5		L/2R = 5	
	Real	*Imag*	Real	*Imag*
0 Hz	36,30%	*0,00%*	11,88%	*0,00%*
1 kHz	37,00%	*21,86%*	12,12%	*7,90%*
1 MHz	47,80%	*32,24%*	15,54%	*5,34%*
100 MHz	1,18%	*1,76%*	0,54%	*0,22%*

(d)

Fig. 6. Coplanar electrodes : general view (a); comparison of FEM and hybrid results for $\Phi(R)$, $L/2R = 1.5$: real (b) and imaginary (c) parts ; FSR error on amplitude (d)

In this case indeed, the analytical model which led to the establishment of the hybrid model by supposing an homogeneous electric field far from the cell is quite different from the real configuration. However, with this last geometry, the voltage values calculated with the hybrid method at some distance from the cell (r = 1.5R, r = 2.5R) become very close to those observed with the finite elements method. This can be seen on figure 7, which presents the voltage observed, at null frequency, at different distances with the hybrid method and the finite element method with and without cell. One can observe the influence of the cell, which is taken into account in a very satisfactory way by the hybrid method.

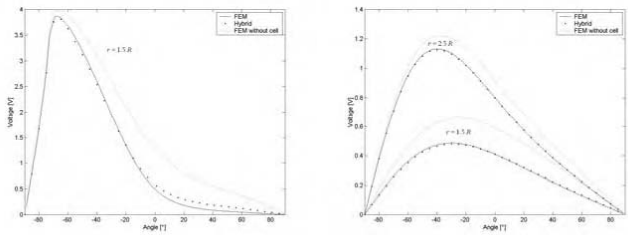

(a) (b)

Freq	L/2R = 1.5		L/2R = 5			
	r = 1.5R		r = 1.5R		r = 2.5R	
	Real	Imag	Real	Imag	Real	Imag
0 Hz	11,18%	0,00%	1,94%	*0,00%*	0,70%	*0,00%*
1 kHz	11,20%	22,72%	1,92%	*5,14%*	0,70%	*2,88%*
1 MHz	10,84%	9,50%	0,52%	*3,10%*	0,50%	*1,90%*
100 MHz	10,04%	3,88%	0,44%	*0,20%*	0,48%	*0,17%*

(c)

Fig. 7. Coplanar electrodes : comparison of FEM and hybrid results, f = 0Hz : $L/2R$ = 1.5, r = 1.5R (a) and $L/2R$ = 5, r = 1.5R and r = 2.5R (b); FSR error on amplitude (c)

Transmembrane voltage computation

In order to compute the voltage at the inner side of the membrane, we extended the hybrid method in a complementary way, by homogenizing the external medium and the membrane, in function of the inner voltage of the cell. TMV can then be obtained by combining this with the results for the outer voltage. The dimensions of the medium being a variable parameter, the determination of the equivalent parameters is geometry-dependant. The quality of the results for the inner voltage with the extended hybrid method is thus strongly related to the geometrical dimensions. In the case of figure 3a, at low frequencies (≤1kHz), the 2D inner voltage shows a high relative error but its absolute value remains low compared to the outer voltage. The error on the TMV is thus close to that on the outer voltage (fig. 5c and 8c). At high frequencies (≥100MHz), the membrane is almost transparent : it is not necessary to compute the inner voltage, which is nearly equal to the outer one. At medium frequencies, the influence of the inner voltage on the TMV is more important, but well evaluated by the extended method, as shown in figure 8a and 8b for all frequencies.

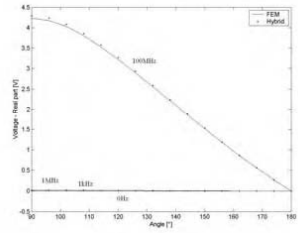

(a)

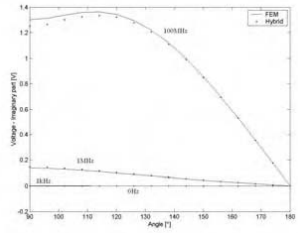

(b)

Freq	$\Phi(R)$ / Φ(electrode)				$\Phi(R\text{-}d)$ / Φ(electrode)				FSR error on TMV	
	Real		*Imag*		Real		*Imag*		Real	*Imag*
	FEM	HYB	*FEM*	*HYB*	FEM	HYB	*FEM*	*HYB*		
0 Hz	6,78E-01	6,32E-01	*0,00E+00*	*0,00E+00*	1,42E-03	3,02E-03	*0,00E+00*	*0,00E+00*	7,10%	-
1 kHz	6,74E-01	6,26E-01	*4,80E-02*	*5,60E-02*	1,44E-03	3,04E-03	*1,94E-04*	*1,36E-04*	7,40%	*17,00%*
1 MHz	7,40E-02	5,40E-02	*1,80E-02*	*2,00E-02*	4,06E-03	4,50E-03	*2,80E-02*	*3,00E-02*	28,60%	*0,70%*
100 MHz	8,56E-01	8,58E-01	*2,42E-01*	*2,40E-01*	8,56E-01	8,58E-01	*2,60E-01*	*2,50E-01*	-	-

(c)

Fig. 8. Face-to-face electrodes, $L/2R$ = 1.1: comparison of FEM and hybrid results for $\Phi(R\text{-}d)$: real (a) and imaginary (b) parts ; results for TMV = $\Phi(R)$ - $\Phi(R\text{-}d)$ (c)

Conclusion

The results at the edge of the cell are better for smaller gradients of E near the cell, this situation being closer to the computation conditions of the equivalent parameters of the homogeneous cell. This explains the better results obtained with the face-to-face electrodes configuration.
We have computed the TMV for a cell centred between two electrodes. The geometry dependence being important, the computation could be more hazardous for more general cases, and this study is on the way.
The hybrid method is well adapted for DEP applications, which are only concerned by the voltage outside the cells. The results for the external voltage, at a reasonable distance from the cell (r>1.5R), are excellent whatever the structure.
Using the hybrid method for more complex DEP applications, with other structures and physics, should allow for a substantial reduction in the calculation costs, without significant loss in quality. In particular, the method could be well suited for first computations in cellular bio-MEMS.

References

[1] C. Geuzaine, High order hybrid finite element shemes for Maxwell's equation taking thin structures and global quantities into account : PHD thesis, Université de Liège, 2001

[2] T.B. Jones, Electromechanics of particles, Cambridge University Press, 1995

[3] L. De Vroey, D. Grenier, B. Le Pioufle, Comparison of simulation methods for bio-MEMS applications, Electrimacs2005, Hammamet, april 2005

Electromagnetic Fields in Mechatronics, Electrical and Electronic Engineering
A. Krawczyk et al. (Eds.)
IOS Press, 2006

THE COMPARISON OF DIFFERENT MODELS OF INDUCTION MOTORS FOR POWER CONTROLLER SUPPLY

Maria Dems, Krzysztof Komeza

Institute of Mechatronics and Information Systems, Technical University of Lodz,
ul. Stefanowskiego 18/22, 90-924 Lodz, Poland
e-mail: mdems@p.lodz.pl, komeza@p.lodz.pl

***Abstract** – In the paper, different circuit and field-circuit mathematical models of induction motors are presented. The circuit model with varying parameters and field-circuit models, incorporating saturation effect and skin effect as well, are compared with a linear model of the induction motor, widely used in the modelling of the transient processes of the induction motors for power controller supply in the system of soft starting.*

Introduction

Linear mathematical circuit models of induction motors used often in calculations of transient processes in power and control systems disable the effect of the saturation of magnetic circuit and skin – effect in rotor bars. As it was proved in [5], such models with constant parameters give good engineering results for small motors, for steady state conditions, but these models have not been sufficiently accurate for certain large signal transient conditions such as on-line starting, for small and big machines. In the case, when the control of rotational speed is not required at the state rate but the limiting of the value of current surge and electromagnetic torque at the starting is very important, an electronic power controller is applied. This device makes it possible to optionally shape the rms. values of voltage at the terminals of the motor. The frequency of this voltage is constant and complies with the network frequency.

For these calculations, it is necessary to use the field – circuit models or the circuit model of the squirrel-cage induction motor with the multi-circuit representation of the rotor cage, incorporating saturation effect and skin effect. In this paper, the multi- circuit model and field- circuit model are compared with test results, as well as with linear mathematical models of some induction motors.

Mathematical Field-Circuit Model

The field-circuit model of the motor has been constructed assuming that the field is two-dimensional. The leakage reactance of the end connection of the stator windings has been calculated using circuit method. The clamping ring resistance has also been considered. The electromagnetic field is described, using the vector potential A and the electrical potential V in the spatial solid bars.

$$\mathrm{rot}\left(\frac{1}{\mu}\,\mathrm{rot}\,\mathbf{1_z}\,A_z\right) = -\gamma\,\mathbf{1_z}\left(\frac{\partial A_z}{\partial t} + \mathrm{grad}_z V\right) \tag{1}$$

The total current in the solid bar is determined as:

$$i = -\int_S \gamma\left(\frac{\partial A_z}{\partial t} + \Delta V\right) dS \tag{2}$$

The field in the coil area of n_c turns and the cross-sectional surface S with current i is determined as:

$$\mathrm{rot}\left(\frac{1}{\mu}\mathrm{rot}\,\mathbf{1_z}A_z\right)=\mathbf{1_z}\frac{n_c i}{S} \tag{3}$$

whereas the difference of potentials in the active part of the coil can be calculated from the equation:

$$\Delta V=\frac{n_c l}{S}\int_S\frac{\partial A_z}{\partial t}dS+n_c R_c i \tag{4}$$

where R_c is the resistance of an individual wire of the coil.

For each circuit, including the parts described with the field equations and external elements described with the resistance R_z and inductance L_z, the circuit equation has the following form:

$$u=R_z i+L_z\frac{di}{dt}+\sum_j d_j\Delta V_j \tag{5}$$

Applying this to the combination of the presented equations leads to the following system:

$$\begin{bmatrix}\mathbf{G}&\mathbf{H}&\mathbf{0}\\ \mathbf{0}&\mathbf{W}&\mathbf{D}\\ \mathbf{0}&\mathbf{D}^{\mathrm{T}}&\mathbf{R}\end{bmatrix}\begin{bmatrix}\mathbf{A}\\ \mathbf{\Delta V}\\ \mathbf{i}\end{bmatrix}+\begin{bmatrix}\mathbf{Q}&\mathbf{0}&\mathbf{0}\\ \mathbf{H}^{\mathrm{T}}&\mathbf{0}&\mathbf{0}\\ \mathbf{0}&\mathbf{0}&\mathbf{L}\end{bmatrix}\frac{\partial}{\partial t}\begin{bmatrix}\mathbf{A}\\ \mathbf{\Delta V}\\ \mathbf{i}\end{bmatrix}=\begin{bmatrix}\mathbf{J}\\ \mathbf{0}\\ \mathbf{U}\end{bmatrix} \tag{6}$$

where

$$G_{ij}=\int\frac{1}{\mu}\nabla N_i\nabla N_j dS\qquad H_{ij}=\int_k\gamma N_i dS\qquad W_{kk}=\int_k\gamma dS\qquad Q_{ij}=\int\gamma N_i N_j dS\qquad J_i=\int J_0 N_i dS$$

R and L are diagonal matrixes of the resistances and external inductances. The equations system can be presented in a more general form:

$$\mathbf{RX}+\mathbf{S}\frac{\partial\mathbf{X}}{\partial t}=\mathbf{B} \tag{7}$$

This system can be solved using differential schema with time step equal to Θ

$$\left[R(1-\Theta)-\frac{S}{\Delta t}\right]X_n+\left[R\Theta+\frac{S}{\Delta t}\right]X_{n+1}+(1-\Theta)B_n+\Theta B_{n+1}=0 \tag{8}$$

Modelling the motion of the rotor requires, at the same time, solving the mechanical equation

$$J\frac{d\Omega}{dt}=T_{em}-T_o \tag{9}$$

where Ω is the angular rotor speed, J is the moment of inertia, T_o is the load torque and T_{em} is the electromagnetic torque, based on field solution using the Maxwell's tensors method. The motion equation can be solved using Runge – Kutty's method.

The application of the field-circuit method to the modelling of the magnetic field distribution in an induction motor, taking into account the movement of the rotor, required the introduction of a special element to the model, which properly joins the unmoving and moving parts. In the applied module RM of the software packet Opera 2D, this element took the form of a gap-element. For proper modelling of air gap field distribution, which is very important due to the torque calculation using Maxwell Stress technique, three layers of elements were used in the air gap.

Mathematical Circuit Model

Linear circuit model of induction motors used often in calculations of transient processes in power and control systems disable the effect of the saturation of magnetic circuit and skin – effect in rotor bars. Such the constant parameter mathematical model, expressed in u-v co-ordinates is in the form:

$$\frac{d\Psi}{dt} = \mathbf{u} - [A]\Psi$$
$$M_e = \frac{3}{2} p\omega_k \frac{k_r}{X_{ss}\sigma}(\psi_{ur}\psi_{vs} - \psi_{us}\psi_{vr})$$
$$\frac{d\omega}{dt} = \frac{p}{J}(M_e - M_m) \tag{10}$$

As it was proved in [5], for these calculation it is necessary to use the varying parameters circuit model of the squirrel-cage induction motor with the multi-circuit representation of the rotor cage, incorporating saturation effect and skin effect, in the form [10]:

$$\frac{d}{dt}\underline{\mathbf{I}} = [\mathrm{M}]^{-1}\{\underline{\mathbf{U}} - (j\omega_s[1] - j\omega[\mathrm{K}])[\mathrm{M}]\underline{\mathbf{I}} - [\mathrm{R}]\underline{\mathbf{I}}\}$$
$$\frac{d\omega}{dt} = \frac{p^2}{J}\mathrm{Re}\{j(\frac{3}{2}L_m\sum_{i=1}^{N}\underline{\mathbf{I}}_{ri})\underline{\mathbf{I}}_s^*\} - \frac{p}{J}M_m \tag{11}$$

where: $\underline{\mathrm{U}} = (\underline{U}_s, 0, \ldots\ldots, 0)^T$ - vector voltage, $\underline{\mathrm{I}} = (\underline{I}_s, \underline{I}_{r1}, \underline{I}_{r2}, \ldots\ldots, \underline{I}_{rN})^T$ - vector current

$[\boldsymbol{M}]$, $[\boldsymbol{R}]$ - inductance and resistance matrices of the motor,

$[\boldsymbol{I}]$ = diag (1,1,.....,1) - identity matrix, $[\boldsymbol{K}]$ = diag (0,1,1,....,1)

ω_S – synchronous angular speed, ω - rotor angular speed.

The presented model can be used to calculation of the transient processes of the induction motors for power controller supply in the system of soft starting. In these cases the circuit model takes into account the real shape of rms voltage curve. The voltage curve can be approximated through different methods.

Object Of Investigation

The objects of investigation were two different types of the three-phase squirrel-cage motors:

- big power induction motor Sf 400Y6 with a rated voltage of 6 kV (star connected), rated output power 400 kW, rated rotational speed 990 rpm
- small power induction motor type Sg 90L-4 with a rated voltage of 380 V (star connected), rated output power 1,5 kW, rated rotational speed 1415 rpm.

Soft-Starting Of The Big Power Induction Motor

The results of calculation for linear voltage increase in rms value during starting time for the big power induction motor are presented in the Figures 1 and 2 for time of grow to rated value 0,05 s (case a - left figure) and 0,5 s (case b - right figure). In Figure 1 the curves of the current versus time and in Figure 2 the curves of the torque versus time during soft starting have been compared for the circuit and field-circuit models with and without saturation and skin effects. The differences in the first amplitude of the current values between different models are about 27% for case a and 17% for case b. Much bigger differences can be observed in the torque versus time curves, presented in Figure 2. The conventional model gives results that are about 30% smaller in the amplitude and its shape considerably differs from shapes calculated using multi-circuit method and field-circuit method. In Figure 3 the speed versus time curves are shown. We observe that neglecting of saturation and skin-

effect has a strong influence (up to 5 times for case a) on the time of the starting of the motor. To recapitulate, it is obvious that this simplification cannot be used for the modelling of soft-starting processes of induction motors.

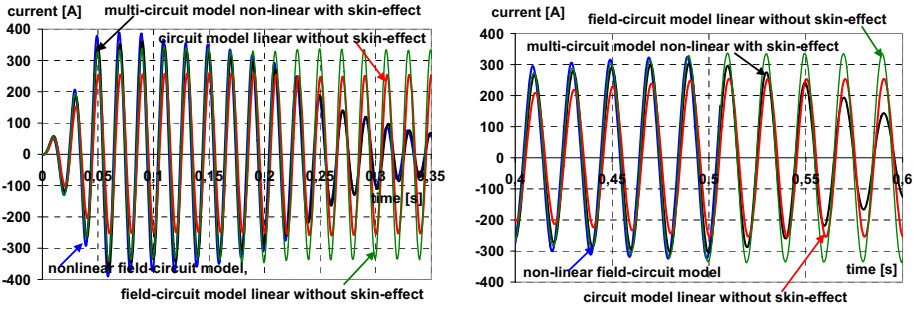

Fig. 1. Phase current versus time during soft starting for different circuit and field-circuit models of the induction motor Sf 400Y6

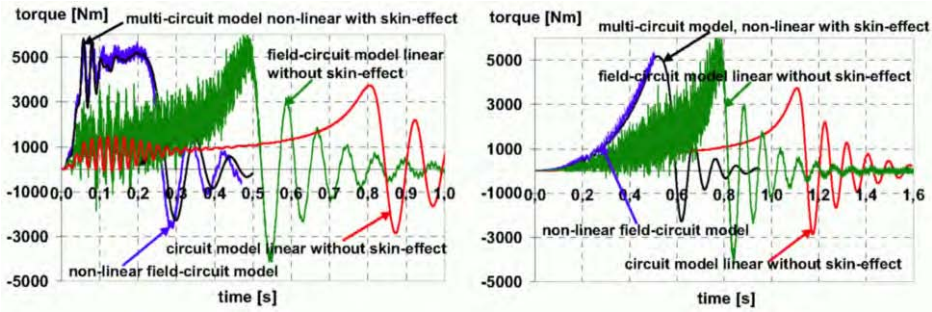

Fig. 2. Torque versus time during soft starting for different circuit and field-circuit models of the induction motor Sf 400Y6

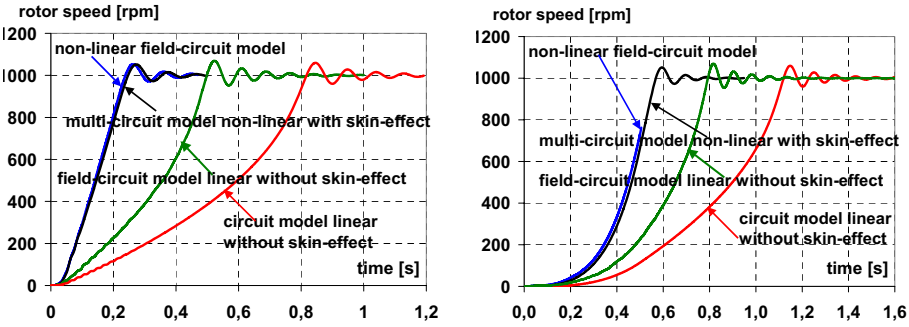

Fig. 3. Speed versus time during soft starting for different circuit and field-circuit models of the induction motor Sf 400Y6

Soft Starting Of The Small Power Induction Motor

For the small power induction motor, type Sg 90-L4, the results of calculation for: linear voltage increase in rms value during starting time for time of grow to rated value 0,1 s (case a - left figure) and measured on test for time of grow to rated value 1,6 s (case b – right figure) are presented in the Figures 4,5 and 6. The tests have been done at no-load.
In order to input as data, the required curve of voltage for case b was applied to polynomial approximation, which represented a real curve with sufficient accuracy.

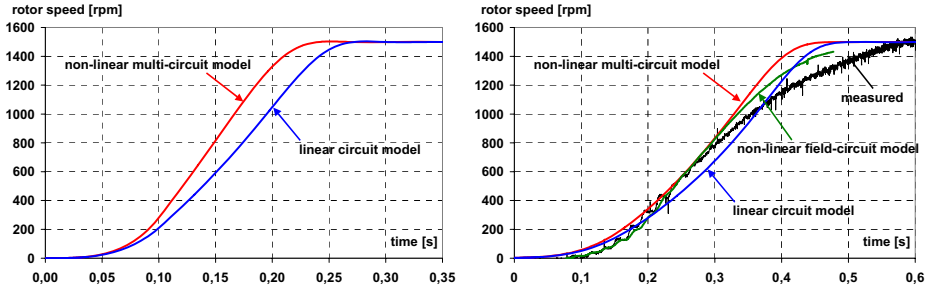

Fig. 4. The curves of the rotational speed vs. time for linear increasing of the voltage during of the time 0,1 s and for polynomial approximation of the rms. value of phase voltage vs. time.

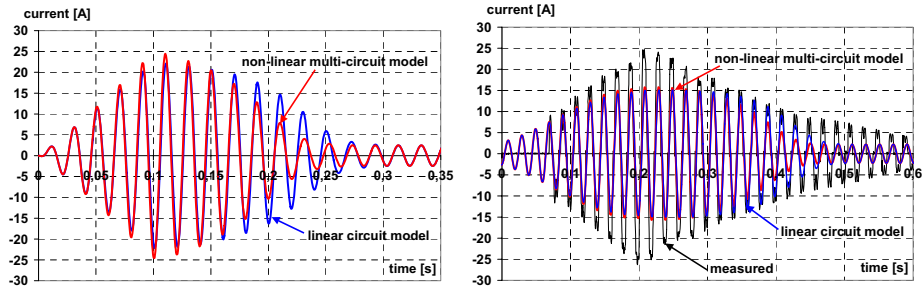

Fig. 5. The curves of the current vs. time for linear increasing of the voltage during of the time 0,1 s and for polynomial approximation of the rms. value of phase voltage vs. time.

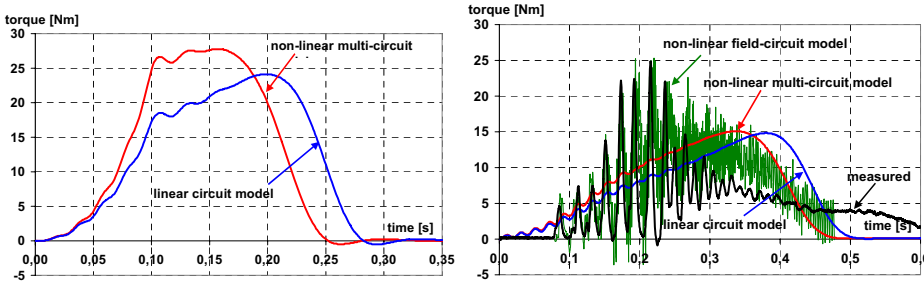

Fig. 6. The curves of dynamic electromagnetic torque vs. time for linear increasing of the voltage during of the time 0,1 s and for polynomial approximation of the rms. value of phase voltage vs. time.

Comparison of presented results with test confirm the correctness of the used circuit and field-circuit models. The results for circuit and field-circuit models without saturation and skin effects differs significantly due to problems with creating field-circuit model without skin effect. For this purpose special field-circuit model with reduced high of the rotor bar and equivalent conductivity has been included. Considerable differences between constant parameter model and models incorporated skin effect and saturation can be observe likewise for big power motor. However the differences for small power motors are smaller than the big one.

Conclusion

The two examples of induction motors have been used to illustrate the application of different models of induction machines in modelling the soft-starting processes. It has been demonstrated that models with constant parameters should not be used for this task especially for big power machines. Only the circuit model with varying parameters or field-circuit models, incorporating saturation effect and skin effect as well, can be used successfully for this purpose. Proper modelling of starting processes is crucial from the practical point of view even for small power machines.

References

[1] Brulé S., Tounzi A.: Comparison between the FEM and the Park's model to study the control of an induction machine, Proceedings ICEM'2000, Vol III, Helsinki, Finland, 28-30 august, 2000r, pp. 548-552.
[2] Dems M, Komęza K..: Circuit and Field-Circuit Analysis of Induction Motor with Power Controller Supply, International XIII Symposium Microdrives and Serwomotors, MIS'2002, Krasiczyn, Poland, 15-19 September 2002, Tom II, Vol. 2, pp. 453 -458.
[3] Dems M., Komęza K.: A comparison of circuit and field-circuit models of electromechanical transient processes of the induction motor with power controller supply, Proceedings COMPUMAG'2001, Lyon–Evian, France, 2-5 July, 2001, pp.206-207.
[4] Dems M., Komęza K.: Electromechanical transient processes of the induction motor with power controller supply, Electromotion, vol.10, no.1, January – March 2003, pp.19-25
[5] Dems M., Komęza K.: Influence of mathematical model simplifications on dynamic calculations of induction motors, , Zeszyty Naukowe Politechniki Łódzkiej,, Elektryka, wrzesień, Łódź, 2005
[6] Dems M., Komęza K.: Przebiegi elektromechaniczne silnika indukcyjnego zasilanego ze sterownika mocy wyznaczone przy pomocy modelu obwodowo - polowego, Archiwum Konferencji PTETiS nr.10,2000, IX Sympozjum "Podstawowe Problemy Energoelektroniki i Elektromechaniki" PPEE'2000, Wisła, 11 - 14. 12. 2000r., ss. 20-25.
[7] Dems M., Komęza K.: Simulations of Electromagnetic Field Distribution in an Induction Motor with Power Controller Supply, Proceedings of the XXII International Autumn Colloquium ASIS 2000,
[8] Dems M., Zadrożny J., Zadrożny J.(jr): Comparison of simulation methods of small induction motor electromechanical transients (in Polish). International XII Symposium 'Micromachines & Servodrives' MiS 2000, Kamień Śląski (Poland), September 2000
[9] Dems M.: Przebiegi elektromechaniczne silnika indukcyjnego współpracującego z układem łagodnego rozruchu, Archiwum Konferencji PTETiS nr.3, 1997, VII Sympozjum "Podstawowe Problemy Energoelektroniki i Elektromechaniki" PPEE'97, Ustroń, 17 - 20. 03. 1997r., ss. 116-121.
[10] Dems M.: Symulacja komputerowa przebiegów elektromechanicznych w silnikach indukcyjnych klatkowych, Zeszyty Naukowe no. 754, Rozprawy Naukowe, z. 229, Łódź, 1996, ss.171.
[11] Dems, M.: DYNF Software for calculation of electromagnetic transients of induction motors, Technical University of Lodz, Poland, 2003
[12] Dems, M.: STAT Software for electromagnetic design of induction motors, Technical University of Lodz, Poland, 1998.
[13] Komęza K., Dems M, Wiak S: Analysis of the influence of the assumption of equivalent saturation on starting currents in induction motor, COMPEL, The International Journal for Computation and Mathematics in Electrical and Electronic Engineering, vol 19, No. 2, 2000, pp. 463-468.
[14] Komęza K.., Dems M.: The Comparison of the Starting Characteristics of an Induction Motor for Frequency and Soft Starter Starting, Proceedings of The 8th Portuguese-Spanish Congress on Electrical Engineering, 3-5 July, 2003, Portugal. (KBN Project 8 T10A 033 20).
[15] Komęza K.: Modelling of Electromagnetic Field in Electrical Devices by Means of Finite Element Method with Hierarchical Hermitian Elements, (in Polish), Z. N. PL, nr. 724, Rozprawy Naukowe, z.216, Łódź 1995
[16] PC OPERA-2D – version 8.5, Software for electromagnetic design from VECTOR FIELDS, 2003

Electromagnetic Fields in Mechatronics, Electrical and Electronic Engineering
A. Krawczyk et al. (Eds.)
IOS Press, 2006

ON A CLASS OF SMALL DIELECTRIC MOTORS: EXPERIMENTAL RESULTS AND SHAPE DESIGN

P. Di Barba (*), E. R. Mognaschi (**), M. E. Mognaschi (*), A. Savini (*)

(*) Department of Electrical Engineering, University of Pavia, via Ferrata 1, I27100 Pavia, Italy
e-mail : di_barba@etabeta.unipv.it
eve.mognaschi@unipv.it
savini@unipv.it
phone: +39 0382 985250
fax : +39 0382 422276

(**) Department of Physics "A. Volta", University of Pavia, via Bassi 6, I27100, Pavia, Italy
e-mail : mognaschi@fisicavolta.unipv.it

Abstract* – *The torque developed by induction dielectric motors depends on the properties of the motor materials as well as on the shape of the stator. The paper reports experimental measurements of torque and speed and results of numerical shape design, which can be used to improve the construction of prototypes.

Introduction

It is known that in induction dielectric motors the torque is due to the interaction of the rotating electric field impressed by the stator electrodes with the lossy dielectric material at the surface of the rotor. Moreover, it is known that there is a dependence of the torque on the electrode shape, for a given power supply. The dependence of the torque on the electrical properties of the lossy material was studied in [1]; the effect of the motor geometry on the torque is investigated, here.

The Device

The device under investigation is represented in Fig. 1.

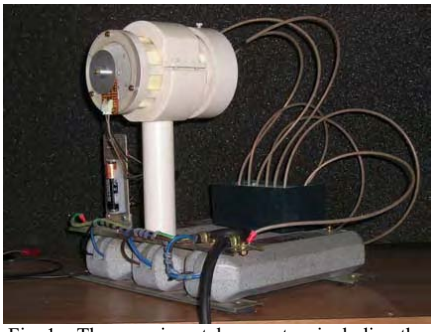

Fig. 1 – The experimental apparatus, including the device under investigation.

The stator is a hollow cylinder made of insulating material (polyvinile chloride, PVC), having an internal diameter of 57.5 mm and an axial length of 94 mm. The stator supports, on its internal surface, 72 copper electrodes with their long sides parallel to the cylinder axis and immersed in a layer of Nomex, an insulated material.
The rotor is a hollow PVC cylinder, coaxially located with respect to the stator. A paper sheet is fixed in contact with the inner surface of the rotor [2].
The 72 electrodes are sequentially connected to a three-phase power supply, of frequency equal to 50 Hz; the RMS-value phase voltage is 950 V.
From the experimental viewpoint, it has been seen that the electrical properties of the paper sheet influence both velocity and torque of the motor. In particular, the motor developed a bigger torque and was able to reach the steady-state speed when the humidity of the paper sheet was increased.

Measurements

Experimental measurements have shown that this motor can develop a maximum torque of 789 μNm depending on the degree of humidity conferred to the paper sheet; the moment of inertia I of the rotor is 1.558 10^{-6} kgm^2, the viscous friction coefficient B is 2.525 10^{-7} kgm^2s^{-1} and the static friction T_0 is 1.4 10^{-5} Nm. The latter was measured in the following way. A small pulley (radius 5 mm) was fixed to the motor axle. Across the pulley a thin silk rope was wrapped and, at the ends of the rope, two small containers were fasten, each containing some small lead shots in order to maintain the rope stretched and insure that the rope does not slip over the pulley. Starting from an equal number of lead shots in the two containers, the number in one of the two was increased until the pulley started to rotate. From the difference in the masses of the two containers the torque T_0 was determined.
In Fig. 2 one out of the ten measured curves of the angular speed vs. time is represented. At t = 0 the power supply is switched on and the rotor reaches the steady-state speed equal to 13.1 rad s^{-1} in about 2 s. At a first glance, the speed transient can be approximated by a linear dependence on time.

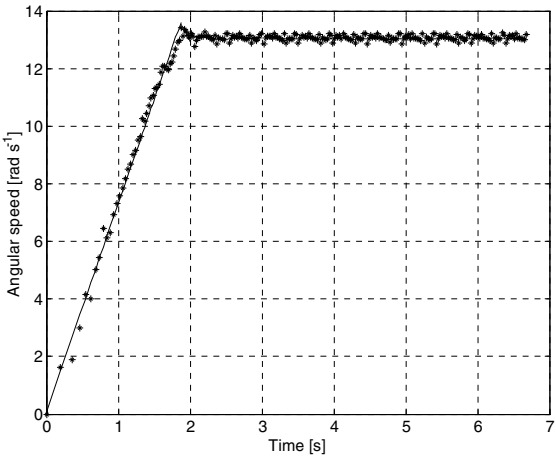

Fig. 2 – Experimental data: angular speed vs. time after switching the power supply on.

Assuming the Newton equation

$$T(t) = I\dot{\omega} + B\omega(t) + T_0 \tag{1}$$

for modelling the transient behaviour, it is possible to approximate the mechanical characteristic of the motor, i.e. the torque-speed curve, using the measured values of the angular speed $\omega(t)$ and knowing I, B and T_0. In Fig. 3 motive torque T and resistive torque $B\omega + T_0$ are represented, the intersection of the latter with the steady-state speed gives the operating point of the motor (marked by a square); in turn, the starting torque is marked by a circle.
One should be conscious that the results shown in Fig. 3 are affected by the experimental error in measuring T_0, I and $\omega(t)$ and by the numerical error in evaluating $\dot{\omega}$.

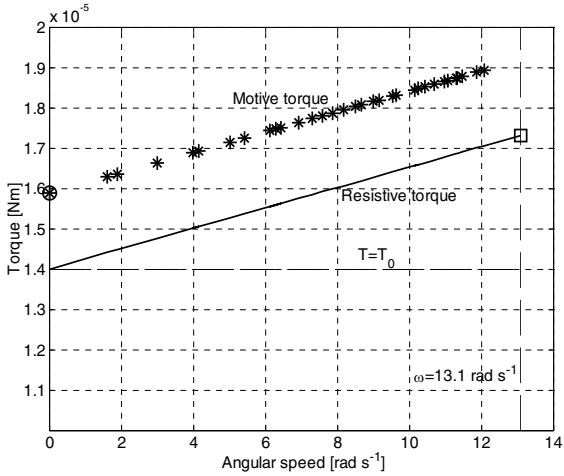

Fig. 3 – Mechanical characteristic of the motor obtained by measurements.

The linear dependence of the torque vs. the angular speed is in agreement with the theoretical behaviour given by [2]

$$T(\omega_a) \propto \frac{\omega_a \tau}{1 + \omega_a^2 \tau^2} \tag{2}$$

for $\omega_a \tau << 1$; where $\omega_a = \omega_f - \omega$ (ω_f angular speed of the field and ω angular speed of the rotor) and $\tau = \frac{\varepsilon}{\sigma}$ time constant of the rotor material. In the case considered, at the start up of the motor, one has $\omega_a \tau \cong \omega_f \tau \cong 10^{-2}$.

Field Analysis And Shape Design

To simulate the behaviour of the motor a 2D finite-element model of its cross section was considered. In Fig. 3 a detail of the finite element mesh is represented; the whole grid mesh is composed of 60,744 triangles with linear variation of potential. The electric field analysis in time-harmonic conditions was developed and the starting torque acting on the rotor was evaluated by means of the Maxwell stress tensor. To this aim, a cylindrical surface passing through the air gap and coaxially located with respect to the rotor was taken as the integration surface. A typical value of the electric field inside the paper layer in between two adjacent electrodes is $3.6\ 10^5$ V m^{-1}.
In order to maximise the starting torque, two design variables are meaningful, concerning the rotor and the stator, respectively:

1) the thickness of the paper layer;
2) the shape ratio of the electrodes, i.e. the ratio of the angular width of the electrode α to the electrode pitch β (see Fig. 4).
Finally the shape design problem could be stated this way: *let the electrical properties of the materials of the motor and its power supply be known; starting from the geometry of the experimental prototype, find the geometry that maximises the starting torque.*

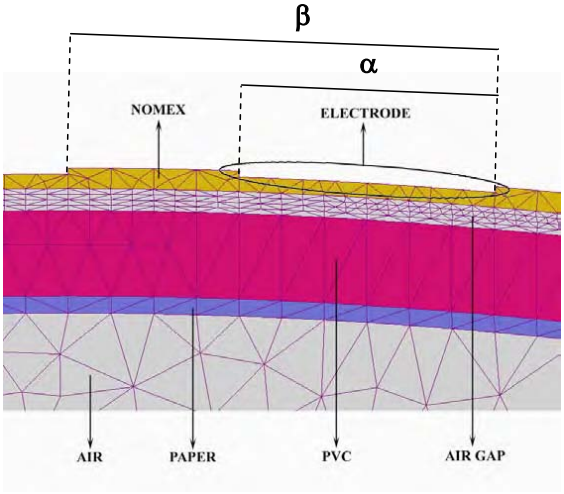

Fig. 4 – Detail of the finite element mesh.

Since in dielectric motors the torque is determined, among many factors, by the interaction of the rotating electric field with the charges induced on the rotor, it is clear that the behaviour of this kind of motors will depend mainly on the extension of the rotor surface rather than on its volume. To give an evidence to this, motors with up to five rotor disks on the same axle and stators equipped with comb electrodes were built and tested [3]. In this paper, the dependence of the motor torque on the thickness of the paper layer was simulated.

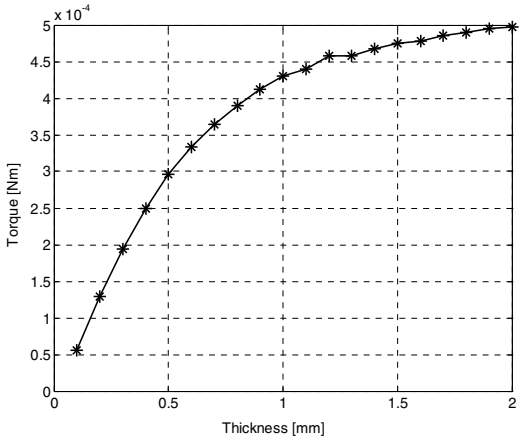

Fig. 5 – Dependence of the motor torque on the thickness of the paper layer.

In Fig 5 the dependence of the motor torque on the thickness of the paper layer is represented, after repeated finite element simulations. The relative permittivity of the paper is 3.3, while its electrical conductivity is assumed to be 10^{-8} Sm^{-1}; a starting torque comparable with that obtained from the experimental results (see Fig. 3) follows.
The shape ratio of the electrodes is 0.6 and the thickness of the paper layer is increased from 0.1 mm (prototype) to 2 mm. Up to 1 mm of thickness, the torque increases of about one order of magnitude, then, there seems to be a saturation effect. Basically, the dependence of the torque on the volume of the lossy dielectric is a secondary effect that can be appreciated for small thicknesses and there is not evidence of a maximum point within the range considered.
From a practical point of view, the changes in the thickness of the paper layer are easy to realize. A commercial paper sheet is 0.1 mm thick; for a thickness of 0.2 mm one can put a second sheet coaxially with the first and so on for the other thicknesses.
As far as the shape design of the stator is concerned, it is known from literature that in this kind of motors the torque developed is sensitive to the shape ratio of the angular width of the electrode α to the electrode pitch β (see Fig. 4) and there is an optimum value for this ratio.
The motor torque is strongly dependent on the electrical conductivity σ of the paper, as it was discussed in [1]. This property is affected by uncertainty because the degree of humidity of the paper cannot be controlled accurately. In Fig 6 the curve of the torque vs. σ, with the relative permittivity ε of the paper layer equal to 3.3, which is a reasonable value for the paper, is reported.

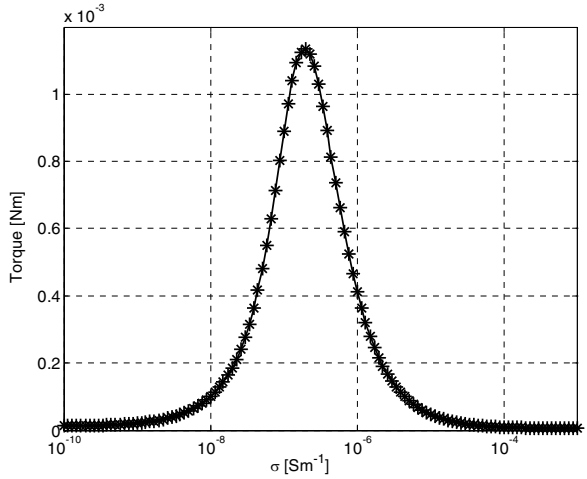

Fig. 6 – Dependence of the motor torque on the electric conductivity of the paper layer for $\varepsilon_r = 3.3$.

Considering the order of magnitude of the measured torque, it was decided to take into account the following values for σ: 10^{-7}, 5 10^{-8}, 2 10^{-8}, 10^{-8}, 10^{-9} S m^{-1}. In Fig. 7 the results of the simulations of motors with different shape ratio are reported, for the aforementioned values of σ. The relative permittivity is equal to 3.3 and the thickness of the paper layer is 0.1 mm. The shape ratio goes from 0.1 to 0.9, because of technical bounds.

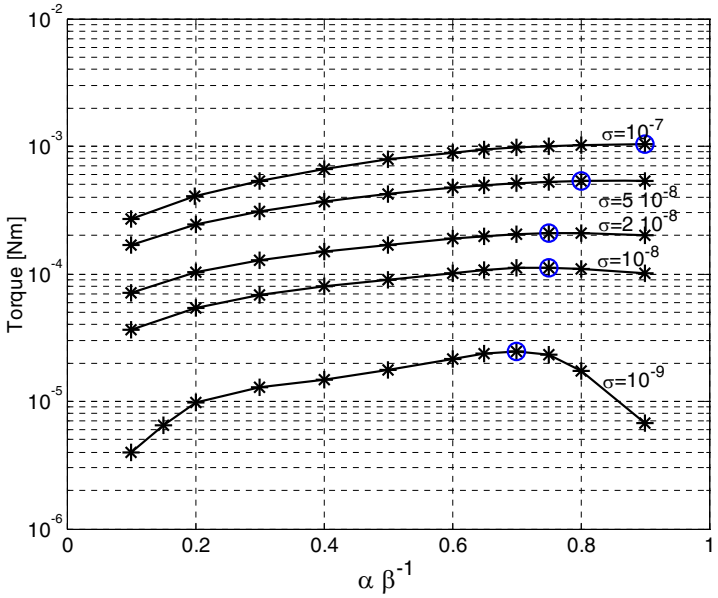

Fig. 7 – Finite element results: torque vs. shape ratio of the electrodes. The prototype corresponds to $\alpha\beta^{-1}=0.6$. The points of maximum are marked by a circle.

Each curve exhibits a point of maximum, but it does not occur always for the same shape ratio when the conductivity is varied. Nevertheless, it can be noted that the points of maximum tend to concentrate for high values of the shape ratio ($0.7 \le \alpha\beta^{-1} \le 0.9$ for $\sigma > 10^{-9}$).

Conclusion

In this paper a prototype of dielectric motor was studied. It was characterized from the electro-mechanical viewpoint on the base of experimental measurements. Then, an investigation about the shape design, based on repeated finite element simulations, was developed; accordingly, some guidelines to realize more performing prototypes are pointed out.

Acknowledgments

Thanks are due to Dr. Ing. G. Venchi for his help in measurements. The valuable help of M. Bertocchi in the realization of the last version of the motor is gratefully acknowledged.

References

[1] P. Di Barba, E. R. Mognaschi, M. E. Mognaschi, A. Savini, "Identifying material properties of a dielectric motor", Int. J. for Computation and Maths. in Electrical and Electronic Eng. COMPEL, Vol. 23, No 3, 2005.
[2] E. R. Mognaschi, J. H. Calderwood, "Asynchronous dielectric induction motor", IEE Proceedings, Vol. 137, Pt. A, No. 6, pp. 331-338, 1990.
[3] B. Bollée, "Electrostatic motors", Philips technical Review, Vol. 30, pp.178-194, 1969.

Electromagnetic Fields in Mechatronics, Electrical and Electronic Engineering
A. Krawczyk et al. (Eds.)
IOS Press, 2006

ANALYTICAL CALCULATION OF THE AIR-GAP MAGNETIC FIELD IN SALIENT-POLE THREE-PHASE SYNCHRONOUS MACHINES WITH OPEN SLOTS

Antonino Di Gerlando, Gianmaria Foglia, Roberto Perini

Dipartimento di Elettrotecnica - Politecnico di Milano, Piazza Leonardo da Vinci 32, 20133 Milano, Italy antonino.digerlando, gianmaria.foglia, roberto.perini@etec.polimi.it

Abstract *– **Nowadays, the increasing availability of powerful calculation tools makes it possible the numerical solution of very complex electromagnetic problems: nevertheless, the analytical methods present interesting advantages, both during the design and for the operation analysis of the electromechanical components. In the paper, an analytical method is presented for the evaluation of the air-gap flux density distribution in the electrical machines: this approach, particularly devoted to the analysis of slotted, salient pole synchronous machines, allows to take accurately into account the stator winding distribution, the air-gap anisotropy and the slotting field effects.***

Introduction

Presently, the increasing availability of powerful hardware and software tools makes it possible the numerical solution of very complex electromagnetic problems, generally with acceptable levels of accuracy and computing resources: thus, these opportunities have made less frequent the use of analytical approaches, usually considered difficult to be managed and suitable just for the analysis of simple configurations.
Nevertheless, the analytical methods present interesting advantages, in terms of deep insight into the electromagnetic phenomena, and as concerns their synthesis and accuracy features, both during the design and the optimisation of the electromechanical components and also for their operation analysis.
In a previous paper [2], an analytical method has been presented for the evaluation of the air-gap flux density distribution in slotted electrical machines with constant air-gap, equipped with distributed windings: with this approach, the active conductors distribution and the slotting field effects have been taken into account.
In the present paper, the method is revised and extended to slotted electrical machines, whose air-gap has a non constant width: particular reference is made to salient pole synchronous machines.
For the analysis, the following hypotheses and aspects have been considered:

- as assumed in the investigation of the constant air-gap machines, also in this case the core saturation has been considered negligible: even if we are confident in the possibility of successfully removing this limitation, for now it will be maintained, thus allowing to better concentrate the attention to the air-gap field;
- the presence of the rotor damper winding is not considered;
- in order to model the rotor and stator m.m.f.s and the anisotropy effects due to the air-gap non-uniformities (rotor saliencies, stator slotting), suited field functions are defined (basically consisting of particular p.u. flux density functions); these functions depend on winding structure, machine geometry and rotor position;
- as known, completely analytical expressions can be obtained for some of these field functions (Carter's theory of slotted structures; interpolar field of constant air-gap half-pole [1, 2]): however, also considering that the analytical solutions are known just for some particular air-gap geometries, here a different approach will be adopted, based on selected magneto-static Finite Element Method (MS-FEM) 2D simulations [3];
- the field functions will be evaluated along the circumference at half-width of the minimum air-gap: in fact, various FEM tests have shown that this is the best choice in terms of local and global waveform fidelity;

– as well known, the two-axis theory is the typical approach for the analysis of the air-gap field in the salient pole machines: here, no a priori d-q decomposition of the armature m.m.f. will be operated, because the developed field functions model directly and adequately the field distribution, whichever be the amplitude and the reciprocal orientation of the rotor and stator m.m.f.s.

Definition And Identification Of The Field Functions

The air-gap field model is based on the following decomposition:
– the air-gap flux density is obtained by suitably superposing the field effects of two ideal, distinguished situations, separately evaluated: when evaluating the rotor field functions (modelling the field-winding data and the rotor saliency), the stator is assumed without armature windings and unslotted; when evaluating the stator field functions (modelling the armature-winding data and the slotting), the rotor consists of a smoothed cylinder (with the diameter of the actual rotor at the minimum air-gap), without field windings;
– for each situation, the field effects due to anisotropy and to the winding currents are modelled separately.
In the following, each field function is defined, and the procedure for its identification is analysed in detail.

The Rotor Field Functions

The selected MS-FEM simulation suited to obtain the rotor field functions considers a p poles machine field excited in such a way to generate p/2 magnetic polarities, as illustrated for the 8-pole machine of fig.1; the analysis has been performed according to the following criteria:
– even if the conductors of the real machine are depicted, actually the stator is magnetically smoothed;
– of course, by using the suited boundary symmetry conditions along the axes 2 and 3, just a machine portion extended to one pole could be used for the analysis;
– just the zone 2 is excited, while the zone 3 is not (half of the interpolar zones are alternatively excited);
– with an arbitrary field m.m.f. M_f, the radial flux density is evaluated by FEM at half width of the minimum air-gap g, along the following arcs:
  - arc 1→2: since beyond point 2 there is an inversion of the field, this flux density B_{rI} distribution will be defined as “heteropolar”;
  - arc 1→3: since beyond point 3 the field maintains the same polarity, this flux density B_{rO} distribution will be defined as “homopolar”;
– the two arcs, of equal length, develop from the polar axis to the adjacent interpolar axes, and include the same number of equidistant, FEM sampling points;
– by referring the flux density values to the ideal flux density $B_{ir} = \mu_o \cdot M_f/g$ in the point 1, and the current position to the arc length, the curves $b_{rI}(\nu_r)$ and $b_{rO}(\nu_r)$ can be obtained (different just outside the pole shoe);
– for each p.u. abscissa ν_r, the ratio b_{rI}/b_{rO} allows to obtain the curve $\alpha_{rFEM}(\nu_r) = b_{rI}(\nu_r)/b_{rO}(\nu_r)$;
– the curve $\beta_{rFEM}(\nu_r) = b_{rO}(\nu_r)$, describing the magnetic effect of the rotor saliency, can be called “saliency” field function: one observes that it is an even function ($\beta_{rFEM}(\nu_r) = \beta_{rFEM}(-\nu_r)$), with homopolar behaviour;
– the curve $\alpha_{rFEM}(\nu_r)$, modelling the field smoothed inversion in the excited zone, is a field effect; however, it can be more suitably treated as a shaping function of the rotor m.m.f.; thus, it can be called “rotor m.m.f. smoothing” field function: it is an odd function ($\alpha_{rFEM}(\nu_r) = -\alpha_{rFEM}(-\nu_r)$), with heteropolar behaviour.

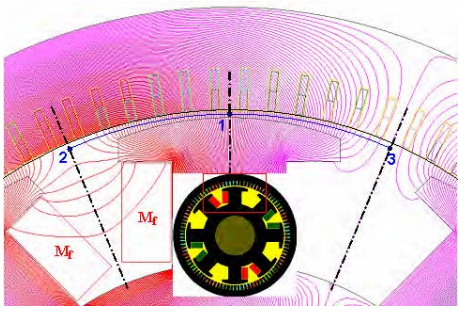

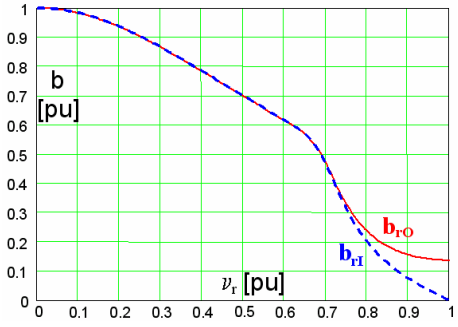

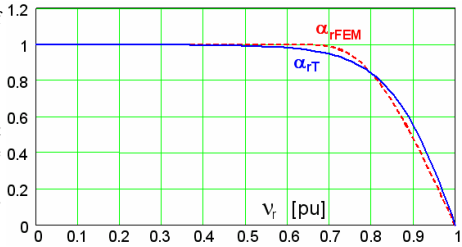

Fig.1 Selected MS-FEM analysis for the determination of the rotor field functions:
up, left: half-excited, smoothed stator, 8-pole machine, with the arcs along which to evaluate the radial flux density;
up, right: p.u. radial flux density distributions $b_{rI}(\nu_r)$ and $b_{rO}(\nu_r) = \beta_{rFEM}(\nu_r)$, along the arcs 1→2, 1→3 respectively, at half width of the minimum air-gap; flux density reference value in $\nu_r = 0$ (point 1);
down, right: curve $\alpha_{rFEM}(\nu_r) = b_{rI}(\nu_r)/b_{rO}(\nu_r)$, and its approximation by means of a hyperbolic tangent function.

It should be noted that the procedure adopted to define the rotor field functions allows for possible "interference" effects among the fields of adjacent half-poles, occurring in case of high air-gap width [1], [2].
Of course, the $\alpha_{rFEM}(\nu_r)$ and $\beta_{rFEM}(\nu_r)$ distributions have been obtained as FEM sampled points, but in order to use them, an analytical approximation of their waveform is required, taking into account their different periodicity behaviour along the machine air-gap periphery.
To this aim, even if some spline functions have been considered, they do not easily allow to obtain the periodicity behaviour, their spline interpolation is numerically heavy and their derivatives are not regular.
A different approach consists in evaluating the Fourier coefficients of the $\alpha_{rFEM}(\nu_r)$, $\beta_{rFEM}(\nu_r)$ distributions:

$$k_{\alpha r_{j_{ar}}} = (4/\pi)\cdot\int_0^{\pi/2}\alpha_{r_{FEM}}\left(\theta_e/(\pi/2)\right)\cdot\cos\left(j_{ar}\cdot\theta_e\right)\cdot d\theta_e \quad , \quad j_{ar} = 1,3,5,... \quad , \tag{1}$$

$$k_{\beta r_0} = (1/\pi)\cdot\int_0^{\pi}\beta_{r_{FEM}}\left(\theta_e/\pi\right)\cdot d\theta_e \ , \ k_{\beta r_{j_{br}}} = (2/\pi)\cdot\int_0^{\pi}\beta_{r_{FEM}}\left(\theta_e/\pi\right)\cdot\cos\left(j_{br}\cdot\theta_e\right)\cdot d\theta_e \ , \ j_{br} = 1,2,3,...,(2)$$

where $\theta_e = \nu_r \cdot \pi/2$ is the electrical angle: this approach is better, because the corresponding truncated series

$$\begin{aligned}\alpha_{r_{series}}\left(\theta_e\right) &= \sum_{j_{ar}} k_{\alpha r_{j_{ar}}}\cdot\cos\left(j_{ar}\cdot\theta_e\right), \quad j_{ar} = 1,3,5,...,j_{arM}\\ \beta_{r_{series}}\left(\theta_e\right) &= \sum_{j_{br}} k_{\beta r_{j_{br}}}\cdot\cos\left(j_{br}\cdot\theta_e\right), \quad j_{br} = 0,1,2,...,j_{brM}\end{aligned} \tag{3}$$

fit the FEM data satisfactorily (a perfect superposition is gained for $j_{arM} = j_{brM} = 39$, with regular derivatives).
Finally, in order to represent the corresponding periodicity in terms of mechanical angles θ_m, it is sufficient to rewrite eq.s (3) by expressing θ_e as $\theta_e = \theta_m\cdot(p/2)$ (with p = N° of poles).
As concerns the analytical approximation of the $\alpha_{rFEM}(\nu_r)$ distribution, by observing its shape, another approach could be adopted, trying to fit the FEM behaviour by means of a hyperbolic tangent function:

$$\alpha_{r_T}\left(\theta_e\right) = \tanh\left(h_{\alpha r}\cdot\cos\left(\theta_e\right)\right); \tag{4}$$

in (4), $h_{\alpha r}$ can be identified by imposing that $\alpha_{rFEM}(\nu_r)$ and $\alpha_{rT}(\nu_r)$ have the same area in the range ν_r = 0-1 (this condition roughly corresponds to impose the same interpolar flux, thus minimising the fitting error):

$$\int_0^1\alpha_{r_{FEM}}\left(\nu_r\right)\cdot d\nu_r = \int_0^1\tanh\left(h_{\alpha r}\cdot\cos\left(\nu_r\cdot\pi/2\right)\right)\cdot d\nu_r \ . \tag{5}$$

Finally, the dependence on the mechanical angle can be expressed as follows:

$$\alpha_{r_T}\left(\theta_m\right) = \tanh\left(h_{\alpha r}\cdot\cos\left(\theta_m\cdot p/2\right)\right). \tag{6}$$

Fig.1 shows the $\alpha_{rT}(\nu_r)$ obtained for the examined machine ($h_{\alpha r}$ = 3.940): as can be observed, the fitting result is not perfect; anyway, expression (4) is more compact and numerically simpler than the first of (3).

The Stator Field Functions

The MS-FEM simulation suited to obtain the stator field functions is shown in fig.2: a stator slotted portion is considered, excited by just one conductor. The analysis is performed according to the following criteria:
– this configuration greatly simplifies the FEM setup (no winding structure is required at this stage);
– the actual rotor has been substituted by a smoothed cylinder portion, with a constant air-gap, whose width is the minimum one, measured along the polar axis of the actual machine;
– with an arbitrary value of the slot current I_s, the radial flux density is evaluated by FEM at half air-gap width, along the arcs 1→2 (heteropolar flux density: B_{sI}) and 3→4 (homopolar flux density: B_{sO});
– the two arcs, of equal length, develop from the slots axes to the teeth axes, and include the same number of FEM sampling, equidistant, points;
– by referring the flux density values to the ideal flux density $B_{is} = \mu_o\cdot I_s/(2\cdot g)$ in the points 1 and 3 and the cur-

rent positions to the arc length, the curves $b_{sI}(\nu_s)$, $b_{sO}(\nu_s)$ follow (different just outside the tooth head);
– for each p.u. abscissa ν_s, the ratio b_{sI}/b_{sO} allows to obtain the curve $\alpha_{sFEM}(\nu_s) = b_{sI}(\nu_s)/b_{sO}(\nu_s)$;
– the curve $\beta_{sFEM}(\nu_s) = b_{sO}(\nu_s)$, describing the well known Carter's magnetic effect of the stator slotting, can be called "slotting" field function: it is an even function (homopolar behaviour: $\beta_{sFEM}(\nu_s) = \beta_{sFEM}(-\nu_s)$);
– the curve $\alpha_{sFEM}(\nu_s)$, modelling the heteropolar gradual inversion of the field in front of the slot including the current carrying conductor, can be assumed as a shaping function of the m.m.f. due to the active sides of the stator coils; thus, this curve can be called "stator m.m.f. smoothing" field function: it should be observed that it is an odd curve (heteropolar behaviour: $\alpha_{sFEM}(\nu_s) = -\alpha_{sFEM}(-\nu_s)$).

Also in this case, the procedure adopted to define the stator field functions allows for possible "interference" effects among the fields of adjacent slots, occurring in case of high air-gap width [1], [2].

Of course, also $\alpha_{sFEM}(\nu_s)$ and $\beta_{sFEM}(\nu_s)$ have been obtained as FEM evaluated points, but in order to use them, an analytical approximation of their waveform is required, taking into account their periodicity behaviour.

First of all, again, the use of interpolating field functions is unsuited to give satisfying results.

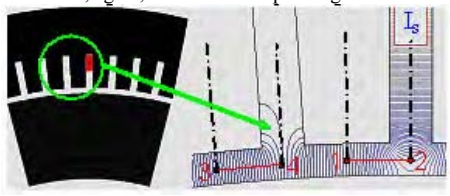

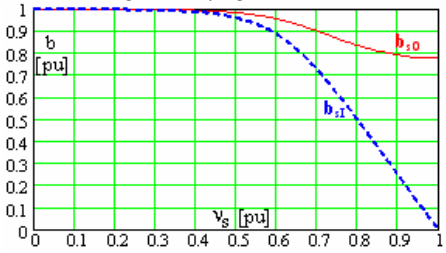

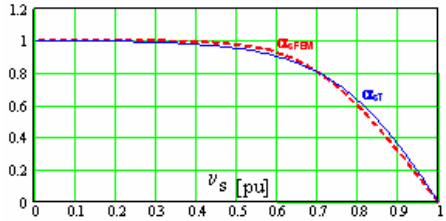

Fig.2 Selected MS-FEM analysis for the determination of the stator field functions:

up, left: machine portion of the actual stator with a cylindrical rotor (constant air-gap, equal to the air-gap measured along the polar axis of the actual machine); field map (with just one excited conductor); arcs 1→2, 3→4 (at half width air-gap) along which the radial flux density is evaluated;

up, right: p.u. radial flux density curves $b_{sI}(\nu_s) = \beta_{sFEM}(\nu_s)$ and $b_{sO}(\nu_s)$ evaluated along the arcs 1→2 and 3→4 respectively; flux density reference value in $\nu_s = 0$ (points 1, 3);

down, right: curve $\alpha_{sFEM}(\nu_s) = b_{sI}(\nu_s)/b_{sO}(\nu_s)$, and its approximation by means of a hyperbolic tangent function.

As regards the analytical implementation of the $\beta_{sFEM}(\nu_s)$ curve, it is similar to the $\beta_{rFEM}(\nu_r)$ implementation, based on a Fourier series development; indicated with n_s the total N° of stator slots, we have:

$$k_{\beta s0} = \frac{1}{\pi}\cdot\int_0^{\pi}\beta_{sFEM}(\lambda/\pi)\cdot d\lambda\ ,\quad k_{\beta s_{jbs}} = \frac{2}{\pi}\cdot\int_0^{\pi}\beta_{sFEM}(\lambda/\pi)\cdot\cos(j_{bs}\cdot\lambda)\cdot d\lambda\ ,\quad j_{bs} = 1,2,3,\ldots. \tag{7}$$

$$\beta_{s_{series}}(\theta_m) = \sum_{j_{bs}} k_{\beta s_{jbs}}\cdot\cos(j_{bs}\cdot\theta_m\cdot n_s)\ ,\qquad j_{bs} = 0,1,2,\ldots,j_{bsM}\ . \tag{8}$$

Again, the choice $j_{bsM} = 39$ allows to fit very well the $\beta_{sFEM}(\nu_s)$ curve.

Concerning the $\alpha_{sFEM}(\nu_s)$ functional implementation, fig.2 shows how the "hyperbolic tangent" approximation allows to easily fit the FEM curve. However, in order to effectively employ the $\alpha_{sFEM}(\nu_s)$ curve, the stator winding structure must be taken into account, with the corresponding m.m.f.: in the following, reference will be made to fractional slot, two-layer, stator windings, equipped with fixed, shorted-pitch coils (of course, the integer slot winding is a particular case of a fractional slot winding).

The basic winding element to be considered is the coil; regarding a generic coil (with coil pitch y_c, expressed as a number of tooth pitches), inserted in a stator with n_s slots, the m.m.f. field function of the coil is given by the curve $\alpha_c(\theta_m)$ of fig.3, where θ_m is the peripheral mechanical angle and n is the generic slot index.

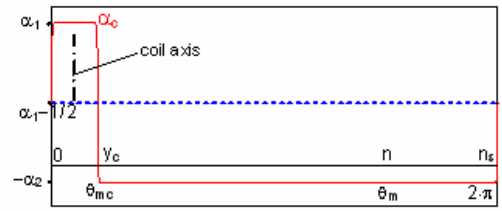

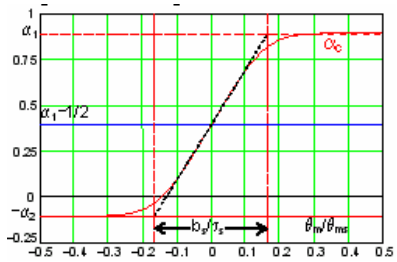

Fig.3 M.m.f. field function $\alpha_c(\theta_m)$ of a coil with pitch y_c, inserted in a stator with n_s slots; right: detail of $\alpha_c(\theta_m)$ around the origin.

Called α_1 and α_2 the levels of $\alpha_c(\theta_m)$ (absolute values, see fig.3), they must satisfy the following equations:

$$\alpha_1 + \alpha_2 = 1 \;; \qquad \alpha_1 \cdot y_c = \alpha_2 \cdot (n_s - y_c) \;: \tag{9}$$

The first equation expresses the peak-to-peak variation of $\alpha_c(\theta_m)$ around each current carrying slot; the second equation imposes the zero value of $\int\alpha_c(\theta_m)\cdot d\theta_m$ extended all along the periphery (solenoidality law); from (9), the following values follow:

$$\alpha_1 = 1 - y_c/n_s \;; \qquad \alpha_2 = y_c/n_s \;. \tag{10}$$

As shown in fig.3 right, $\alpha_c(\theta_m)$ near $\theta_m = 0$ behaves like $½\cdot\alpha_{sFEM}(\theta_m) + (\alpha_1 - ½)$; moreover, in $\theta_m = 0$ $d\alpha_c(\theta_m)/d\theta_m = 1/(\theta_{ms}\cdot b_s/\tau_s)$ occurs (where: $\theta_{ms} = 2\cdot\pi/n_s$ = slot pitch mechanical angle; τ_s = slot pitch length; b_s = slot opening width). Several FEM tests have verified this behaviour.

As regards its analytical implementation, the Fourier series appears not suited (a truncated series up to the 100th term shows "high frequency" oscillations), while the "hyperbolic tangent" curve fitting is acceptable.

To this aim, considering that $\theta_{mc} = y_c\cdot\theta_{ms}$ is the angular extension of the coil, if we apply an origin shift by $\theta_{mc}/2$ (in such a way to superpose y-axis and coil axis), this shift allows to express $\alpha_c(\theta_m)$ as follows:

$$\alpha_c(\theta_m) = \alpha_1 - 1/2\cdot\left(1 - \tanh\left(h_{\alpha s}\cdot\left(\cos(\theta_m) - \delta_c\right)\right)\right) \;. \tag{11}$$

The two unknown parameters δ_c and $h_{\alpha s}$ of (11) can be identified as follows:

– δ_c can be obtained by imposing: $\alpha_c(\theta_{mc}/2) = \alpha_1 - 1/2$, from which $\delta_c = \cos(\theta_{mc}/2) = \cos(\pi\cdot y_c/n_s)$ occurs;

– $h_{\alpha s}$ can be obtained again imposing the same area of the original curve (condition similar to (5)).

Air-Gap Field: Expressions And FEM Validation

Indicated with ξ the generic mechanical angle, measured counter-clockwise along the stator from a chosen slot, by performing a suitable superposition of the coil m.m.f. functions $\alpha_c(\xi)$ of the coils of the phase s1, one obtains the m.m.f. space distribution $M_{s1}(\xi)$:

$$M_{s1}(\xi) = \sum_{j_c} \alpha_c\left(\xi - \theta_{mc}/2 - (j_c - 1)\cdot\theta_{ms}\right)\cdot\gamma_{s1_{j_c}} \qquad j_c = 1,2,...n_{ce} \;, \tag{12}$$

where: the displacement $\theta_{mc}/2$ is introduced in such a way to position the left active side of the first coil in the origin of ξ; j_c is the coil index, extended to the N° n_{ce} of the coils of an electromagnetic cycle; γ_{s1jc} is a factor expressing the j_c^{th} coil linkage with the phase s1 ($\gamma_{s1jc} = 0$ if the coil j_c does not belong, $\gamma_{s1jc} = \pm1$, in case it does, and the sign takes into account the coil connection [4]). For the other phases, due to symmetry:

$$M_{s2}(\xi) = M_{s1}(\xi - p_e\cdot\pi/3) \;; \quad M_{s3}(\xi) = M_{s1}(\xi - 2\cdot p_e\cdot\pi/3) \;, \tag{13}$$

where p_e is the number of poles of the electromagnetic cycle of the fractional slot winding (submultiple of p).

As regards the instantaneous phase and global stator m.m.f.s, we can write:

$$m_s(\xi, i_{s1}(t), i_{s2}(t), i_{s3}(t)) = \sum_k m_{sk}(\xi, i_{sk}(t)) = \sum_k M_{sk}(\xi)\cdot(N_{tc}/a)\cdot i_{sk}(t) \qquad k = 1,2,3 \;, \tag{14}$$

where N_{tc} = N° of turns/coil, $i_{sk}(t)$ = phase current, a = N° of parallel paths. Eq. (14) includes the following stator effects: instantaneous currents; winding structure; "m.m.f. smoothing" field function $\alpha_c(\xi)$ (modelling the field gradual variation in front of the couple of slot openings of each coil).

Indicated with υ the generic mechanical angle, measured along the rotor, with respect to a rotor pole axis chosen as a reference, the rotor m.m.f. can be expressed as follows:

$$m_r(\upsilon, t) = \alpha_r(\upsilon)\cdot N_f\cdot i_r(t) \;, \tag{15}$$

where $i_r(t)$ is the rotor current, N_f is the number of field turns per pole and $\alpha_r(\upsilon)$ is the rotor "m.m.f. smoothing" field function (modelling the interpolar gradual inversion of the rotor m.m.f.).

Called $\zeta = \zeta(t)$ the rotor position (mechanical angle between rotor and stator positions), we have: $\upsilon = \xi - \zeta$. Finally, the flux density air-gap distribution (normal component at half width minimum air-gap) is given by:

$$B(\xi,\zeta,t) = (\mu_o/g)\cdot\beta_s(\xi)\cdot\beta_r(\xi-\zeta(t))\cdot\left(m_s(\xi,i_{s1}(t),i_{s2}(t),i_{s3}(t)) + m_r(\xi-\zeta(t),i_r(t))\right) \quad . \qquad (16)$$

In order to show the soundness of (16), in the following some flux density distributions will be shown (analytical-FEM comparison), for the machine of fig.4 (2-layer stator winding: p = 8; q = 29/8 slots/(pole·phase); y_c = 9): the field map refers to a loaded operating condition (torque producing and demagnetising reaction)).

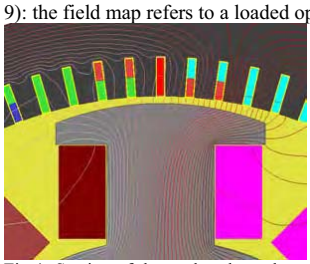

Fig.4 Section of the analysed synchronous machine: field map at loading.

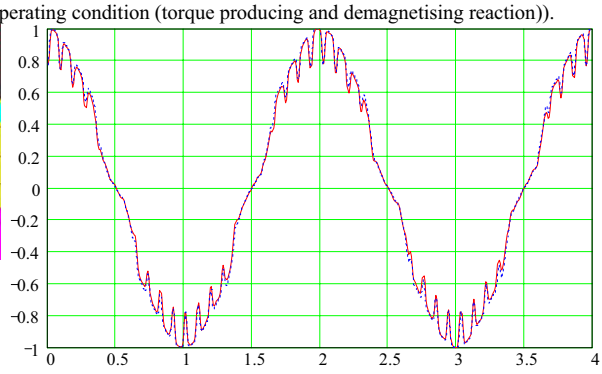

Fig.5 No-load flux density under 4 poles: (——) = analytical model; (……) = FEM (radial component).

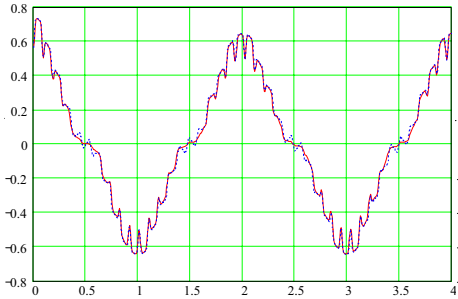

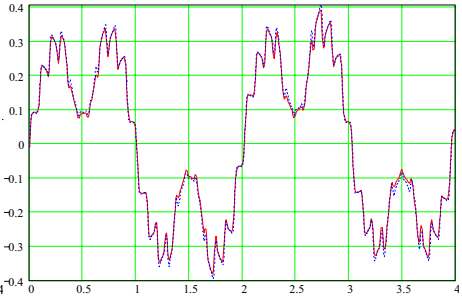

Fig.6 – Flux density distribution due to armature reaction: (——) = analytical model; (……) = FEM result (radial B) Left: d-axis reaction right: q-axis reaction.

The following remarks are valid:

- the flux density distribution in loaded conditions (see fig.7, referred to a generic reaction angle) shows the soundness of the analytical method, that correctly evaluates the field, regardless the d-q reaction decomposition;
- the fractional slot winding makes the reaction field different from one pole to the others (see fig.6);
- some local B differences can be observed in the d-axis reaction field, near the interpolar zones: the B_{FEM} oscillations are due to the leakage among teeth heads, analytically not modelled.

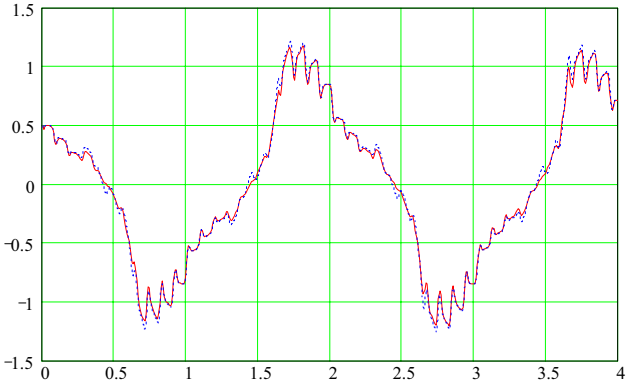

Fig.7 – Flux density distribution in loaded operation (the same of fig.4): (——) = analytical model; (……) = FEM result (radial B component).

Fig.5 shows the no-load flux density distribution; fig.6 illustrates the armature reaction along d and q axes; finally, fig.7 refers to a loaded operation in the same conditions of fig.4: apart from some small local discrepancies, the analytical approach appears well suited to correctly reconstruct the flux density radial distribution. These relevant results have been confirmed also for other synchronous machines, with different constructional and winding data and in various operating conditions.

Conclusion

An analytical method for the evaluation of the flux density distribution has been developed, suited for the design and operation analysis of salient-pole synchronous machines.
The model, up to now limited to the analysis of unsaturated machines, accurately takes into account the rotor anisotropy, the stator slotting effect and winding structure, the space and time effects of stator and rotor m.m.f.s. Selected, simplified FEM analyses allow to obtain the needed parameters of the field functions.
Some FEM simulations have validated the analytical method, with a good agreement in no-load, d and q reaction, and loaded operating conditions.
The knowledge of the air-gap field distribution, for any rotor position and current values, allows to obtain the expressions of the machine electrical parameters [4] and to calculate the e.m.f. and torque waveforms [5].

References

[1] A. Di Gerlando, G. M. Foglia: "Improved Analytical Evaluation of Air-Gap Fluxes and Forces of Ferromagnetic Smoothed and Toothed Structures and Pole Shoes", ISEF '99 Conference, Pavia, Italy, 23-25 Sept. '99, pp.224-227.

[2] A. Di Gerlando, G. M. Foglia, R. Perini: "Analytical Model of Air-Gap Magnetic Field in Doubly Slotted Electrical Machines with Distributed Windings, ISEF '03 Conference, Maribor, Slovenia, 18-20 Sept. 2003, pp.67-72.

[3] Maxwell 2D FEM code, Version 10, Ansoft Corporation, Pittsburgh, PA, USA.

[4] A. Di Gerlando, G. M. Foglia, R. Perini: "Calculation of Self and Mutual Inductances in Salient-Pole, Three-Phase Synchronous Machines with Open Slots", ISEF '05 Conference, Baiona, Spain, September 15-17, 2005.

[5] A. Di Gerlando, G. M. Foglia, R. Perini: "E.M.F. and Torque Waveform Analytical Evaluation in Salient-Pole, Three-Phase Synchronous Machines with Open Slots", ISEF '05 Conference, Baiona, Spain, September 15-17, 2005.

Electromagnetic Fields in Mechatronics, Electrical and Electronic Engineering
A. Krawczyk et al. (Eds.)
IOS Press, 2006

AN EFFICIENT BLDC WITH GEARBOX SOLUTION FOR EGR

D. Frachon, E. Vinot, G. Andrieux, J.D. Alzingre

Moving Magnet Technologies (MMT)
1 rue Christiaan Huygens, 25000 Besançon, FRANCE
dfrachon@movingmagnet.com, evinot@movingmagnet.com

***Abstract** –To reduce NOx emission, EGR (Exhaust Gas recirculation) systems are now developed in Diesel engine. The challenge in this system is to have a fast and accurate adjustment of the gas flow in the exhaust gas recirculation circuit. MMT proposes a system with a BLDC motor and a two stage gearbox. This solution is relatively simple with a good and easy position control, and good electrical performances.*

Introduction

For some years, the automotive manufacturers are strongly looking on vehicles pollution. Concerning the diesel engine, one of the most constraining problems is the NO_x emission which has to be drastically reduced. One manner to reduce this emission is the EGR (Exhaust Gas recirculation) system. EGR inject a portion of the exhaust gas back into the cylinder, so it mixes with the fuel and air (Note that the exhaust adds to the fuel and air; it doesn't replace any of it) [1-2]. The added mass in the cylinder is harder to heat up, so the combustion events have lower temperatures (600°C instead of more than 1300°C with no EGR system). Considering that above 1300°C oxygen and nitrogen rejoin to make nitrogen oxides (NO, NO_2, etc…), the EGR system reduce drastically the NO_x emission (more than 90% according manufacturer).
The main challenge with this system is to control precisely the amount of Exhaust Gas you reintroduce in the cylinder. If you reintroduce not enough gas, the temperature combustion is too hot and then NO_x are produced. If you reintroduce too much gas, the emission of carbon monoxide (CO), hydrocarbon (HC) and soot particles raise because of the lack of Oxygen. EGR system was classically made with hydraulic valve, but to respect the new norm concerning NO_x emission, you need a fast and accurate adjustment of the flow of gas in the exhaust gas recirculation circuit. Thus manufacturers are now developing electric valves.
Different systems have been developed. Pierburg proposes a linear solution based on a solenoid system [3] (this system is actually mounted on FIAT models). Siemens VDO developed a solution with DC motor and gearbox for the VW vehicles [4]. Delphi presents a rotary direct drive solution with Sonceboz ARPA [5]. This solution frequently presents a small power (ARPA or solenoid) or is really expensive (DC and gearbox). Moreover it is necessary to have a position sensor on the valve, and in the case of direct drive (solenoid or ARPA) the control position has to be really efficient. In the same time, to have a good precision whatever the gas pressure is, and to ensure the fail safe (valve closed if the electric drive is off) the motor drive is working against a spring, that means in the case of direct drive it has to provide a important torque when the valve is not moving (half open for example).

MMT's BLDC Motor Solution for EGR

MMT proposes a system with a BLDC motor (fig. 1) and a two stages gearbox for a reduction of 17. Then a motion transformation (ortation to translation) is create by means of cam. As the translation of the valve needs only a rotation smaller than 90° of the last gear, it may have teeth only on 90°.
This solution is relatively less expensive than a DC solution and the control of the position is relatively easy as the motor position is well known, our BLDC motor have a 12° step associated with a reduction of the gearbox of 17, so the resolution is 0.7°. Moreover you do not need any sensor in the valve as you know the rotor position

with the integrated hall sensors of the motor, and due to the gearbox reduction, the torque to be provided by the motor in stall position is divide by 17.
A problem with such a solution (BLDC plus gearbox), is the potential detent torque of the motor which may interfere on the accuracy of the valve position and most important may work again a stronger fail safe spring. Thus the MMT's BLDC motor is well adapted to this problem as it has quite no detent torque as it is explain in the following part.

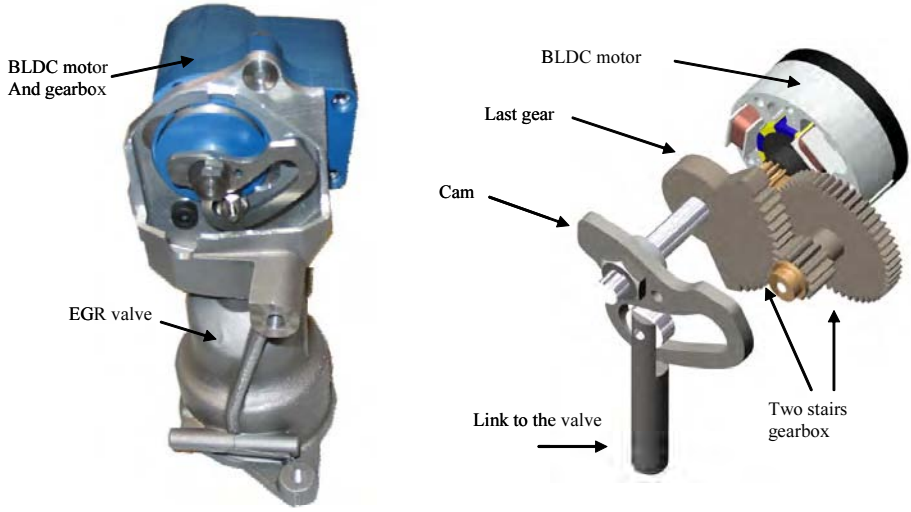

Fig 1 : EGR system and MM41 view

MMT BLDC characteristics

Fig 2 : View of a MMT typical BLDC.

Fig 2 presents a view of a structure with nine teeth on the stator and ten poles on the rotor of a MMT patented BLDC motor [6].
Due to the geometry and the position of the respective number of teeth and magnetic pole this motor presents a quite perfect sine static torque in two phase ON control mode. That means all harmonic of rank higher than 1 have been cancelled.

Considering that the even harmonics are principally due to the detent torque and the odd to the current, and assuming that in this motor the three phases are separated. Each phase is made of a coil carrying tooth, and two side teeth for flux closure (Fig 3).

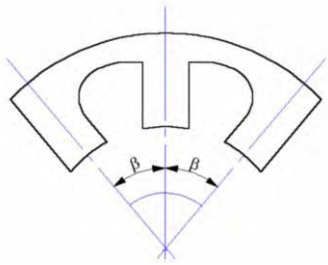

Fig 3 : One phase of the motor.

In such a structure, as the shift between the three phases is 120°, the second, forth, and eights harmonics of each phase are shift respectively by 120°, 240° and 480°, and then are cancelled each other. Only the sixth harmonic is not cancelled by the three phases structure. Thus, the angle β between each teeth of phase (Fig 3) is chosen in order to cancel this harmonic. In fact as the magnetic pole are shifted by 36° and the teeth by 40°, the torque due to each teeth is shifted by 4 mechanical degree which means 20° electrical degree. Thus, the sixth harmonic of each three teeth of a phase are shifted by 120 electrical degrees and the sixth harmonic is cancelled.
Concerning the torque with current, it is well known that the third harmonic is cancelled by a two phase ON command mode. The fifth harmonic is cancelled by the tooth angle.
Then the only harmonics that can theoretically remain in this motor are the seventh, the ninth, the tens and some on great order but of small magnitude.
The static torque measurement with current shows a really good sine torque (Fig 4) and a really small detent torque compare to the nominal static torque (3-4%) (Fig 5).

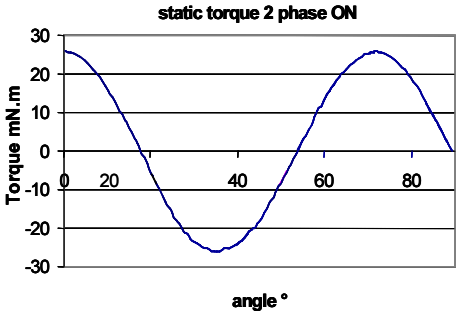

Fig 4 : 2 phase ON torque versus position, for a 35 mm diameter motor with 86 turn per coil and 1.2 Amps.

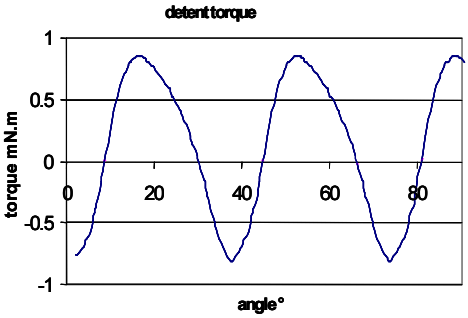

Fig 5: Detent torque.

Results

The performances are compared with those of a direct drive solution proposes with Sonceboz ARPA [5]. The force on the valve for the same electrical power of 2.8W is presented

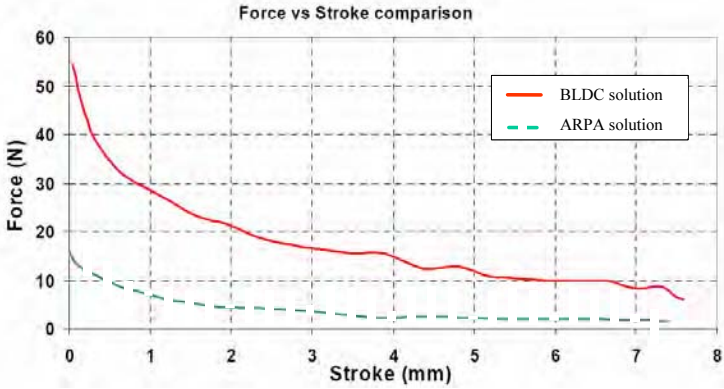

Fig 6: Force versus stroke.

It is easy to note that for the same electrical power, the solution BLDC with gearbox presents four times more force than the direct drive solution. That means for the same force required on the valve the electrical consumption will be four times smaller.
In the same time, principally due to the gearbox, the electrical consumption to keep the valve 90% open is 0.6 W with BLDC gearbox solution and 1.8W with ARPA direct drive solution.
Naturally, the dynamic of the BLDC solution is not so good, compare to ARPA solution. The time to go from the position valve 10% open to valve 90% open is 70ms compare to 23 ms, that means that the dynamic of the BLDC gearbox solution is three times slower than those of the direct drive solution. Nevertheless it seems to be correct for EGR application.

Conclusion

The challenge in the EGR system is to have as accurate positioning of the valve with a relatively good dynamic, and a low electrical power when the valve is stalled, all of this in a constraining temperature environment which may be around 125°C. For all these reasons the MMT's motor associated to a gearbox seems to be a really competitive solution; it is easy to control, exhibiting a good torque/electrical power ratio (higher than direct drive solution), and keep a good dynamic.

References

[1] http://www.allpar.com

[2] http://www.auto-innovations.com/site/dossier

[3] http://www.kolbenschmidt-pierburg.com

[4] http://www.siemensvdo.com/default.aspx?menu=PT_EGR

[5] http://www.delphi.com/pdf/e/egr_linear.pdf

[6] D. Prudham, "Polyphase motor in particular for driving the hand of a display", European patent EP 0 949 747, March 5, 2003

Electromagnetic Fields in Mechatronics, Electrical and Electronic Engineering
A. Krawczyk et al. (Eds.)
IOS Press, 2006

ESTIMATION OF OVERALL EFFICIENCY OF LINEAR INDUCTION MOTOR WITH MAGNET ROTATOR TYPE OF END-EFFECT COMPENSATOR

Nobuo Fujii, Yuichiro Ito, Takehiro Yoshihara

Department of Electrical and Electronic Systems Engineering,
Faculty of Information Science and Electrical Engineering,
Kyushu University
6-10-1, Hakozaki, Higashi-ku, Fukuoka, 812-8581, Japan
Phone & Fax number: +81-92-642-3914, e-mail: fujii@ees.kyushu-u.ac.jp

***Abstract* – The overall characteristics of linear induction motor (LIM) with the end effect compensator are studied. The compensator is the magnet rotator type and it is equipped in front of LIM. To analyze the model with linear moving and rotating magnets over the conducting plate for the compensator, the special integral equation method (IEM) and the finite element method (FEM) are used. To analyze the LIM with the compensator, the approximate two-dimensional FEM supported by the three-dimensional IEM is used. The technique made clear that the efficiency for the practical model increased by at least 3.5-3.9% by the compensator.**

1. Introduction

The use of rotating the rare-earth type of permanent magnets (PMs) has been tried to generate the induced eddy current efficiently in the conductor for its size and weight [1][2]. It may be used as an end effect compensator of linear induction motor (LIM) equipped in front of the armature of LIM to supply the compensating eddy current to the LIM region [3]. It is a long-pending subject to compensate the end-effect of LIM [4]-[6]. However, the characteristics of the magnet rotator are not clear because it is hard to analyze the eddy current model with moving and rotating magnets. In the paper, the authors show the characteristics obtained by both experimental and theoretical works. Two types of marketing tools of the finite element method (FEM) and the special integral equation method (IEM) named ELF/MAGIC for a three-dimensional (3D) dynamical magnetic field analysis are used for the numerical analysis.

2. Estimation of Characteristics of Moving Magnet Rotator

Fig. 1 shows the model of LIM with the magnet rotator type of end effect compensator. The magnet rotator moves with LIM at the moving speed of v and the rotating speed of n. The rotating speed n (1/s) is synchronized with the frequency f_1 (Hz) of armature current of LIM. That is,

$$n = 2 f_1 / p \tag{1}$$

where, p is the number of poles of the magnet rotator. Fig. 2 shows the picture of test facility. The concrete construction and dimension of the test machine for the magnet rotator is shown in Fig. 3. The test machine has four poles and 15 pieces of rare-earth type magnets for a pole are used because the

area of pole is large. Fig. 4 shows the meshing for the special 3D magnetic field analysis named ELF/MAGIC which is a kind of IEM and can deal with a dynamic problem. In the analysis, there is no need the meshing in the air gap region.

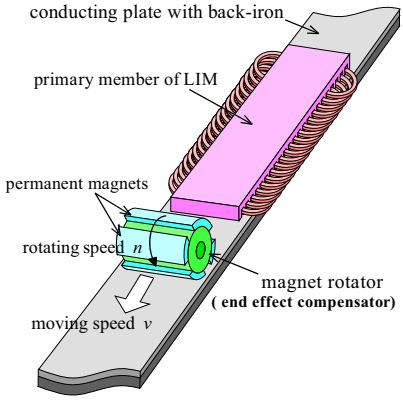

Fig. 1. Model of magnet rotator and LIM.

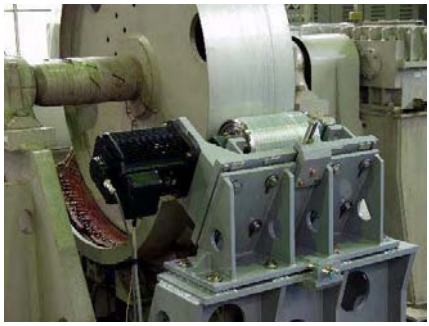

Fig. 2 Test facility.

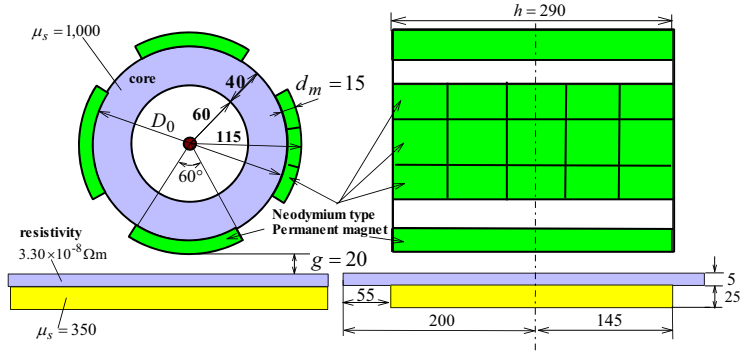

Fig. 3 Test machine of magnet rotator type of compensator.

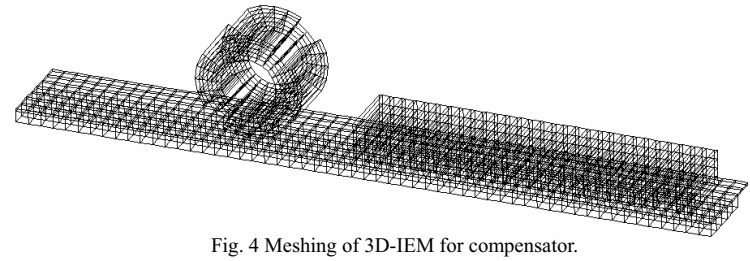

Fig. 4 Meshing of 3D-IEM for compensator.

Fig. 5 shows the flux densities at the circumference of 8mm above the surface of PM of the test machine. The measured values at several positions in the widthwise direction are plotted as they are not the same distribution. The measured distributions show that the equipping 15 magnets to form the pole are not good and the magnetic energies of some PMs are decreased. The bold line is the calculated value by the 3D-IEM, in which the remanent magnetic flux density and the coercive force of PM are determined to corresponding to the mean values of measured values. The thin line represents the calculated value when the remanent magnetic flux density and the coercive force of PM are adjusted to 1.05 magnifications respectively.

Fig. 6 shows the driving power of the magnet rotator with the rotating speed of n=10(1/s) and linear moving above the conducting plate shown in Fig. 3. P_1 is the power of motor to drive the magnet rotator. P_2 is the net power for driving the magnet rotator and it has the following relationship with the torque of T.

$$P_2 = 2\pi nT \tag{2}$$

The relation between moving speed of v and the rotating speed of n can be expressed in the following equivalent slip of s_c, using the parameters shown in Fig. 3.

$$s_c = (v_s - v)/v_s, \quad v_s = \{D_0 + 2(d_m + g)\}\pi n \tag{3}$$

In Fig. 6, the bold X represents the measured value and the circle marks are the calculated values by the 3D-IEM for PMs which have the flux density represented by the bold line in Fig. 5. The broken line with triangle marks agrees well with the measured values, which is obtained by the 3D-IEM for PMs which have the flux density represented by the thin line in Fig. 5.

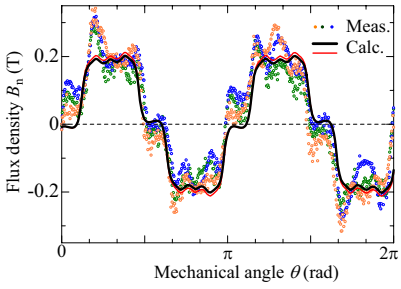

Fig. 5 Flux density of test machine for compensator.

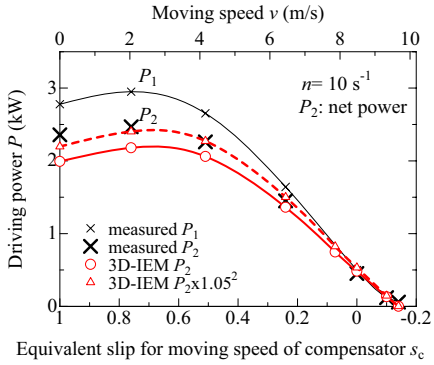

Fig. 6 Driving power of test machine for compensator.

It is very difficult to analyze the long armature LIM with the magnet rotator type compensator directly by using the 3D-IEM because it is for 3D use only and the calculating time increases sharply to enlarge the matrix almost without zero element. Then 2D-FEM analysis is used. The magnet rotator is replaced by the equivalent static winding with rotating field as shown in Fig. 7. The rotating field is made by the poly-phase (nine-phase of phase m=1 to phase m=9) current, and the current density j_c is determined to be equal to the driving power of P_2 of 3D-IEM shown by the broken line in Fig.6. Fig. 8 is the meshing for FEM on the test machine. Fig. 9 shows the comparison between the calculated values of 3D-IEM and the equivalent 2D-FEM. The result of FEM has a small error at the small slip because the magnetic pole in the model is the non-salient pole and there is little components of space

harmonics in the flux distribution of rotating field.

Fig. 10 shows the comparison of the calculated thrust of magnet rotator by the equivalent FEM to that of 3D-IEM. The difference between both calculated values will be the error due to the space and time harmonics in the flux density and the eddy current in the conducting plate.

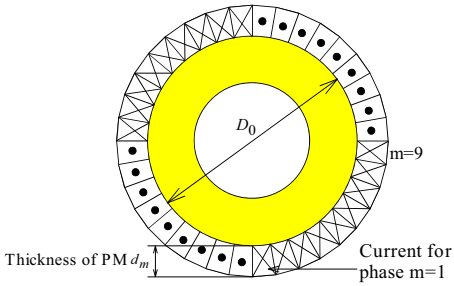

Fig. 7. Equivalent model of magnet rotator for 2-D FEM.

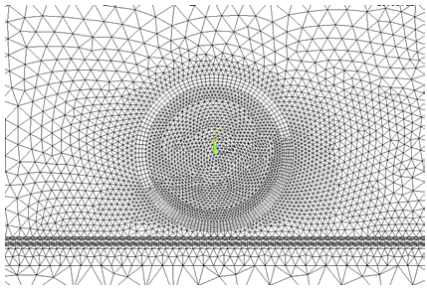

Fig. 8 Meshing of 2D-FEM for the compensator.

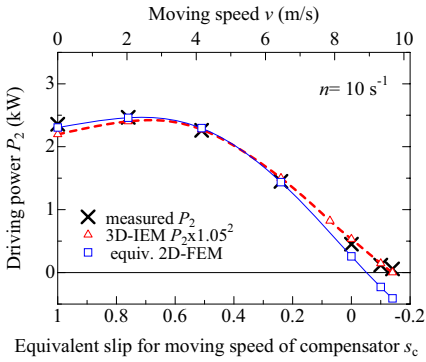

Fig. 9 Driving power for compensator.

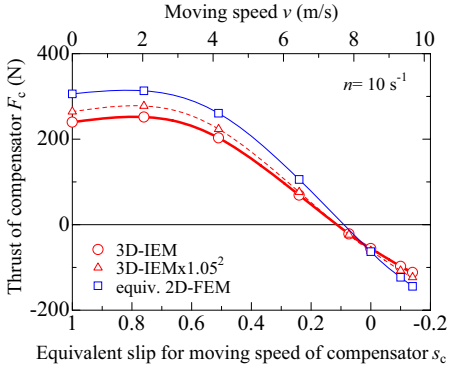

Fig.10 Thrust of compensator.

3. Estimation of Overall Efficiency of LIM with Magnet Rotator Type of Compensator

The quasi-3D analysis is done by using the 2D-FEM for the practical model of LIM with the compensator. The edge effect of transverse direction is considered with by using Russell-Norsworthy coefficient [7]. The numerical values of design parameters of LIM are shown in Table 1. The length is about 2.5m and the core of armature has 78 slots and 72 coils. The numerical values of temporary design for the equivalent compensator model are shown in Table 2. The value of equivalent current density of j_c is 5.19A/mm^2 which is determined by the calculated values of 3D-IEM.

Fig. 11 shows the meshing for the FEM analysis. Fig. 12 and Fig. 13 show the estimations of thrust and efficiency respectively. The current density of j_c for equivalent model of the magnet rotator is considered in the range changed by plus and minus 20% from the determined value. The speeds of

LIM at the operating slip s=0.17 and s=0.10 are 36.9 and 40.0km/h respectively. In the thrust shown in Fig. 12, the increase by the compensator is larger at smaller slip of 0.10. The difference between the overall thrust of LIM with the compensator and the thrust in the LIM part is a little. That is, the influence of thrust in the compensator part is a little. This shows that the influence of the estimation error shown in Fig. 10 is little.

In the efficiency shown in Fig. 13, the effect of the compensator appears at smaller slip because the end effect of LIM is larger. The overall efficiency does not increase so much although the efficiency in LIM part increases as the j_c increases because the power loss in the conducting plate in compensator region increases. The overall efficiency increases by about 3.6% at LIM slip of 0.1, although the design parameters of magnet rotator of compensator are not yet optimized.

Table 1 Values of design parameters of LIM.

Rated: Frequecy=22.0Hz, Current=208A, Capacity=396kVA
Primary member: Length of armature core=2,476mm, Width of armature core=300mm, Number of phase=3, Number of poles=8, Pole pitch=280.8mm, Slot pitch=31.2mm, Number of slots=78, Number of slots/pole/phase=3, Short-pitch factor=7/9
Mechanical clearance=12mm
Secondary member: Conductivity of conducting plate= 4.93×10^7 S/m , Width of conducting plate=360mm, Thickness of conducting plate=5.0mm, Thickness of back iron=22mm

Table 2 Values of equivalent model of end effect compensator.

Rated rotating speed=11s^{-1}, Outside diameter of core=386mm, Width of core=300mm, Number of phase=9, Number of poles=4, Thickness of conductor for equivalent current=15mm, Mechanical clearance between the rotator and the conducting plate=12mm, Mechanical clearance between the rotator and LIM core=13mm

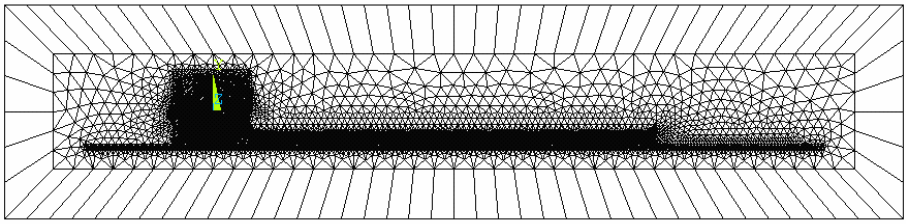

Fig. 11 Meshing of 2D-FEM analysis of practical LIM with the compensator.

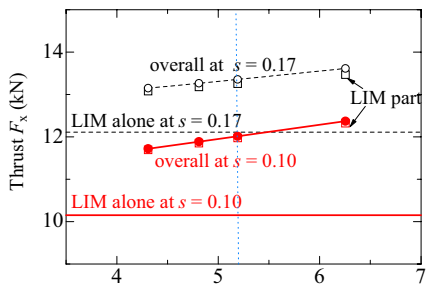

Fig. 12 Thrust for practical LIM.

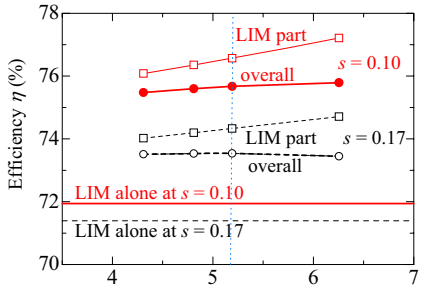

Fig. 13 Overall efficiency for the practical LIM.

4. Conclusions

It is cleared that the magnet rotator can supply the large eddy current which is useful as the compensating current for the end effect of LIM even in the small equivalent slip, where the driving power is small, although the magnet rotator is influenced by its own end effect.

The overall efficiency of LIM with the magnet rotator type of end-effect compensator can be cleared by using approximate 2D-FEM analysis with static equivalent current which is supported by the 3D-IEM analysis. The overall efficiency of the practical model increases by at least 3.5-3.9% or 4.9-5.3% in percentage around the rated speed by using the magnet rotator, at the condition that the driving torque of the magnet rotator is very small.

Acknowledgement

This work has been supported in part by the Grant-in-Aid for Scientific Research (B) from Japan Society for the Promotion of Science (No. 15360150).

References

[1] M. Kawai, H. Ariga, "Equos-lim-car," The invention, vol.89, 70 (1992)
[2] N. Fujii, M. Chida, K. Ogawa, "Three Dimensional Force of Magnet Wheel with Revolving Permanent Magnets," IEEE Trans. on Magnetics, vol.33, 4221 (1997)
[3] N. Fujii, T. Kayasuga, T. Hoshi, "Simple End Effect Compensator for Linear Induction Motor," IEEE Trans. on Magnetics, vol.38, 3270 (2002)
[4] S. Yamamura, *Theory of Linear Induction Motors*, Second Edition, University of Tokyo Press, 1978, pp.111-123, 204-206
[5] S. A. Nasar, I. Boldea, *Linear Motion Electric Machines*, John Wiley & Sons, 1976, pp.127-128
[6] N. Fujii, Y. Tanabe, Y. Ito, "Overall Characteristics of Traction Linear Induction Motor with New End-effect Compensator," Proc. of 16th Int. Conference on Electrical Machines, Krakow, Poland (Sep. 2004)
[7] R. L. Russell, K. H. Norsworthy, "Eddy Currents and Wall Losses in Screened-rotor Induction Motors," Proc.IEE, vol.105A, 163 (1958)

Electromagnetic Fields in Mechatronics, Electrical and Electronic Engineering
A. Krawczyk et al. (Eds.)
IOS Press, 2006

Investigation of Squirrel Cage Induction Motors with Semi–closed and Closed Stator Slots by a Transient Electromechanical Finite Element Technique

C. Grabner
Research and Development Motors, Siemens AG
Siemensstrasse 15, D-97616 Bad Neustadt an der Saale, Germany
grabner.christian@siemens.com

Abstract–The progress in computer science within the last years provides the opportunity of applying new methods in the optimization of asynchronous machines. A direct coupling of transient circuit equations representing additional machine parameters to a two–dimensional finite element calculation is used for the analysis of squirrel cage induction motors with semi–closed and totally closed stator slots.

1. Stator Design with Semi-Closed and Totally Closed Slots

A typical squirrel cage induction motor, which is depicted in Fig.1, has been manufactured so far with semi–closed stator slots [1-4]. Continual progress in the automation process allows the utilization of a novel stator construction, which can be characterized by a smoothed stator surface without any slots. A comparison of the usually preferred stator part with the proposed innovative design is comparatively shown in Fig.2. The suggested set–up reduces the overhang of the end winding system by about 20%.

Figure 1: A typical asynchronous norm motor.

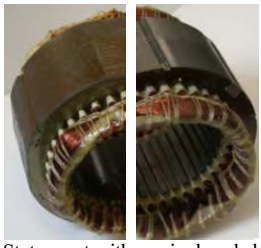

Figure 2: Stator part with semi–closed slots (right) and the novel construction without any slots (left).

The non–skewed aluminum squirrel cage rotor is also furnished with totally closed slots. The mass of the rotating part is about $m=2.9\ kg$. The stator and rotor parameter of both investigated three–phase motors listed in Tab.1 are calculated for the operating temperature level.

Table 1: Electrical parameters of both stators as well as the–inter bar parameters of the non–skewed rotor.

	Stator windings w [1]	Stator leakage resistance R_σ [Ω]	Stator leakage inductance L_σ [mH]	Rotor bar resistance R_b [μΩ]	Rotor bar inductance L_b [nH]	Rotor bar conductivity γ [MA/Vm]
Semi–closed slots	540	10.47	~ 6.4	~ 1.74	~ 22.5	~ 22.3
Without slots	540	8.69	~ 5.2	~ 1.74	~ 22.5	~ 22.3

2. Transient Electromechanical Finite Element Approach

The proposed numerical finite element approach represents parts of the machines, which are outside the modeled two–dimensional machine region, due to coupled external circuit parameters, listed in Tab.1 [5]. The analysis of the global circuit equations and the finite element algorithm is performed in the time–domain [6,7]. Thus, there are no restrictions to applied time–dependent voltage sources. Movable rotor parts as well as non–linear iron properties are also taken into account [8,9]. The magnetic field distribution itself is thereby mainly influenced by the changing rotor position. Thus, the total acting force on the rotor part is mainly governed by the actual field distribution.

The applied finite element method discretizes the considered domain Γ into a distinct number of sub–domains Γ_e using small triangular elements. The most simple and favorable finite element approach with triangular nodal shape functions N_i

$$\hat{A}^e(t) = \sum_{i=1}^{3} N_i \widetilde{A}_i^e(t) \tag{1}$$

thereby takes advantage of the primary unknown time–dependent nodal vector potential values $\widetilde{A}_i^e(t)$. Unfortunately, the approximation (1) causes some well–known difficulties along saturable material boundaries [10]. The manageable finite element diction by means of the primary unknown local vector quantity $\{\widetilde{A}^e(t)\} = \{\widetilde{A}_1^e(t),\ \ \widetilde{A}_2^e(t),\ \ \widetilde{A}_3^e(t)\}^T$ is written as

$$\sum_e \upsilon[S^e]\,\{\widetilde{A}^e(t)\} + \gamma\,[T^e]\,\frac{\partial}{\partial t}\{\widetilde{A}^e(t)\} - \{Q^e\}\,\frac{\gamma}{l_b}\,U_b(t) = \{0\}\ , \tag{2}$$

whereby the introduced matrices and vectors of one element are given with

$$S_{ij}^e = \iint\left[\frac{\partial}{\partial x}N_i\,\frac{\partial}{\partial x}N_j + \frac{\partial}{\partial y}N_i\,\frac{\partial}{\partial y}N_j\right]dxdy\ ,\quad T_{ij}^e = \iint N_i\,N_j\,dxdy\ ,\quad Q_i^e = \iint N_i\,dxdy\ . \tag{3}$$

In order to couple the field equations (2),(3) with external circuits, it is necessary to calculate the total current flow. The electrical bar current through the surface Γ_b is found by integration. Regarding the finite element notation (1), we derive the governing relation for the electrical current in one single bar with (3) and the surface Δ^e of one single element as

$$I_b(t) = \sum_{e\in\Gamma_b}\left[\Delta^e\,\frac{\gamma}{l_b}U_b(t) - \gamma\{Q^e\}^T\left\{\frac{\partial}{\partial t}\widetilde{A}^e(t)\right\}\right]\ . \tag{4}$$

The modeling of the common stator winding depicted in Fig.2 demands a distinct number of n series connected bars in order to form one single coil c as it is schematically shown in Fig.3. The small wire diameter and the high number of stator windings in Tab.1 avoid the generation of any eddy currents in each stator winding itself. Thus, each bar component in the introduced coil current vector $\{I_b(t)\} = \{I_{b1}(t)\ \ \ldots\ \ I_{bn}(t)\}^T$ of the coupled system is only consisting of contributions due to the first term in (4). Each bar in Fig.3 carries the same magnitude of the total current $I_b(t)$, but successive bars *1* to *n* carry local bar currents $I_{b1}(t)$ to $I_{bn}(t)$ in opposite directions. The leads of the coil are brought out of the finite element region depicted in Fig.3 and connected to a voltage source. Using a coil voltage vector $\{U_b(t)\} = \{U_{b1}(t)\ \ \ldots\ \ U_{bn}(t)\}^T$ we obtain

$$U_c(t) = \{d_b\}^T\,\{U_b(t)\} + R_\sigma\,I_b(t) + L_\sigma\,\frac{\partial}{\partial t}I_b(t)\,. \tag{5}$$

The important equation (5) serves to couple certain finite element regions, represented by the components $U_{b1}(t)$ to $U_{bn}(t)$, to external circuits and sources. Thereby, the changing polarity is regarded in (5) by an introduced weighting coefficient vector $\{d_b\}$ with the entries $\pm w/2$, which accounts for total acting winding number per phase given in Tab.1. The values of the resistors R_σ and the inductance L_σ in (5) can be directly taken from Tab.1.

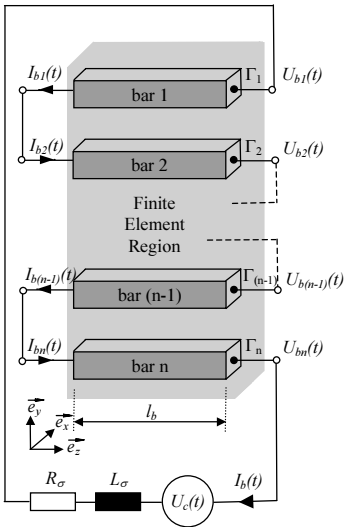

Figure 3: A number of *n*–serial connected bars are forming one stator coil.

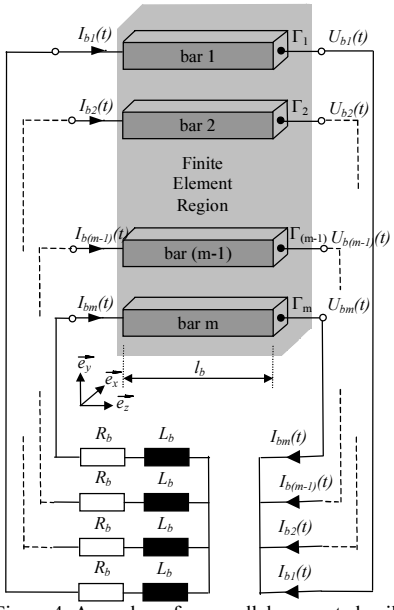

Figure 4: A number of *m*–parallel connected coils make up the squirrel cage.

The employed winding scheme for the squirrel cage rotor is shown in Fig.4. Further a number of m different coils are connected in parallel in order to form the squirrel cage. The components $I_{b1}(t)$ to $I_{bm}(t)$ of the bars in the assumed total current vector $\{I_b(t)\} = \{I_{b1}(t) \ \ldots \ I_{bm}(t)\}^T$ have to fulfill the condition $\{d_b\}^T \{I_b(t)\} = 0$ at each connection point in Fig.4, whereby all entries in the vector $\{d_b\}$ are 1. Furthermore, the coil voltage vector $\{U_c(t)\} = \{U_{c1}(t) \ \ldots \ U_{cm}(t)\}^T$ is eliminated due to the entries $U_{c1}(t)$ to $U_{cm}(t)$ between both connection points. It is assumed, that one coil (5) is only consisting of one single bar, whereby the resistors R_σ in (5) denotes the fictive resistance R_b and the inductance L_σ stands for L_b. These small end–ring and the dominating end–winding parameters of Fig.4 as well as the electrical conductivity γ of the used solid bars in (4) are summarized in Tab.1.

The basic relation of motion can be qualified with the mass m of the moving part, the actual position $\tilde{x}(t)$, the assumed speed independent damping coefficient $\lambda = 0.00045$ and the acting electro-magnetic forces $F_m(t)$ as well as the mechanical load $F_l(t)$ as

$$m \frac{\partial^2}{\partial t^2} \tilde{x}(t) + \lambda \frac{\partial}{\partial t} \tilde{x}(t) = F_m(t) - F_l(t), \quad F_m(t) = -\frac{1}{2} l_b \upsilon \left\{\tilde{A}(t)\right\}^T \left[\frac{\partial S}{\partial \tilde{x}}\right] \left\{\tilde{A}(t)\right\} . \tag{6}$$

The finite element approach (6) allows the computation of the magnetic forces, which are acting on the solid rotor body by "virtual motion" of the component under consideration. Differentiation of the assembled system matrix is straightforward since the entries N_i are simple functions of the local directions.

The field equation, the total current, the circuit equations and the equation of motion are discretized in the time domain by the usual Crank–Nicholson Method. Moreover, the field equation (2),(3) and the acceleration equation (6) are non–linear functions of the unknown vector potential $\tilde{A}(t)$ and/or the component displacement $\tilde{x}(t)$. Thus, these interrelations have to be linearized in spite of the non–linear iron behavior by applying the Newton–Raphson method.

The discretized and linearized global system is written with some abbreviations [M] and {C} by means of time–step notation as

$$\begin{bmatrix} M_{11} & M_{12} & & & M_{15} \\ M_{12}^T & M_{22} & M_{23} & & \\ & M_{23}^T & M_{33} & M_{34} & \\ & & M_{34}^T & M_{44} & \\ M_{15}^T & & & & M_{55} \end{bmatrix} \begin{Bmatrix} \{\Delta\widetilde{A}\} \\ \{\Delta U_b\} \\ \{\Delta I_b\} \\ \{\Delta U_c\} \\ \{\Delta\widetilde{x}\} \end{Bmatrix}_{k+1}^{t+\Delta t} = \begin{Bmatrix} \{C_1\} \\ \{C_2\} \\ \{C_3\} \\ \{C_4\} \\ \{C_5\} \end{Bmatrix}. \tag{7}$$

Taking account for the necessary boundary conditions the system (7) is solved for each time–step $\Delta t=0.0002s$. Thereby, the variations of the vector potential $\{\Delta\widetilde{A}\}$, the variation of the voltage vector across each bar $\{\Delta U_b\}$, the variation in the current vector in each bar $\{\Delta I_b\}$, the variation in the terminal voltage vector $\{\Delta U_c\}$ and the varying position vector $\{\Delta\widetilde{x}\}$ are obtained for each node.

3. The Steady Operational State at Rated Mechanical Load after the Transient Run-Up at Rated Voltage Supply

The stator winding system is switched on at $t_0=0.02s$ to the rated sinusoidal electrical voltage given in Tab.1 [11,12]. Main focus is put upon the arising maximal current peaks in case of saturation effects especially in the first period after switching on. The transient courses of the electrical stator coil currents are shown in Fig.5 and Fig.6 for the design with semi closed and without slots, respectively. Thereby it could be demonstrated that the maximal inrush current of the novel slot–less stator design does not exceed the limiting values in a wide range. The elapsed time to reach the steady operational state is very different depending on the design. It is obvious that the usual design with stator slots reaches the quasi–steady state within $t\approx0.13s$, whereas a much longer period of up to $t>0.2s$ is needed with the novel design. A comparison of the calculated steady state current magnitudes with the measured values in Tab2. shows a very good conformity. The mechanical speed as well as the electromagnetic torque are comparatively shown in Fig.7 and Fig.8.

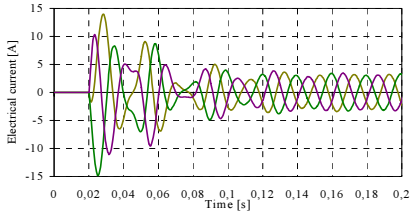

Figure 5: Numerical calculated electrical phase currents for the machine with semi–closed stator slots.

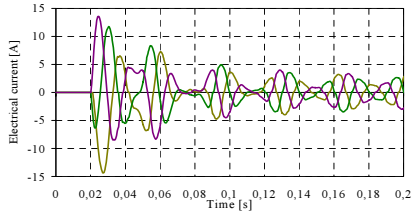

Figure 6: Numerical calculated electrical phase currents for the machine without any stator slots.

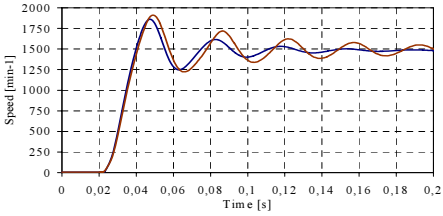

Figure 7: Mechanical speed for both machines.

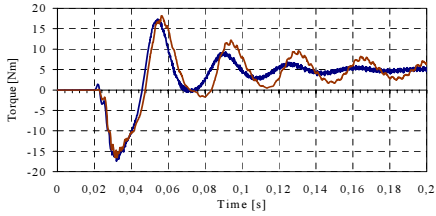

Figure 8: Electromagnetic torque for both machines.

Table 2: Measured characteristics of the investigated induction motors.

	$U_{c,eff}$ [V]	$I_{b,eff}$ [A]	cos(φ) [1]	M [Nm]	n [min^{-1}]	P_1 [W]	P_2 [W]	η [%]
Semi closed slots	400	2.01	0.79	5.15	1392	1102	750	68
Without slots	400	2.03	0.76	5.16	1389	1068	750	70

4. Determination of Losses for Different Motor Designs

4.1 Losses at steady no-load operational condition

The no-load operational condition is commonly used to segregate the iron losses from the frictional losses. Fig.9 shows the measured no–load stator currents. It is thereby remarkable that the no–load current of the investigated small motor size is approximately 75% of the rated current given in Tab.2.

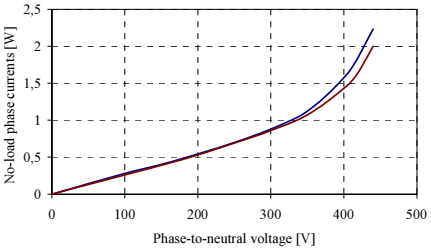

Figure 9: No-load stator current for both machines in dependency on the applied voltage.

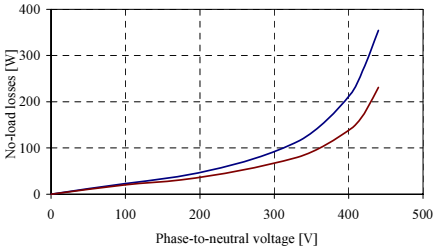

Figure 10: No-load losses for both machines in dependency on the applied voltage.

Due to the very small slip frequency, it can be assumed that the rotor losses are only of secondary interest. The stator resistance of the squirrel cage induction motor with semi–closed slots has thereby a stator resistance of about 16.9Ω per phase. The presented new stator geometry takes advantage of a novel winding assembly technology and reduced the length of the stator phase winding. Consequently, the stator resistance decreases to approximately 14.3Ω per phase. This effect is mainly responsible for the different contributions in the no–load copper losses.

If the total input power P_{10} shown in Fig.10 is reduced by the no-load stator copper losses V_{Co10} we derive the relation

$$P_{10} - V_{Co10} = V_{Frig} + V_{Iron} \,. \tag{8}$$

The assumption that the iron losses V_{Iron} are quadratic depending on the applied voltage allows separating the voltage independent frictional losses V_{Frig}. Following this idea, the constant contribution stands for the frictional losses in the mechanical bearings and for the turbulences in the airflow.

The main splitting of losses is very interesting in case of the rated source voltage. Hence, Tab.3 contains an overview for both different induction motors. It is thereby obvious that the total input power in case of the novel design without slots is much lower than it is in case of the existing motor with semi closed slots. The reduced stator resistance given at operational temperature reduces the copper losses even though the no–load current remains almost unchanged as shown in Fig.9. The appearing iron losses in Tab.3 are much lower for the proposed design.

Table 3: Losses at no-load in case of rated voltage and rated frequency.

	P_{V10} [W]	V_{Co10} [W]	V_{Frig} [W]	V_{Iron} [W]
Semi closed stator slots	211	125.7	13.5	71.8
Design without stator slots	138	87.7	13.5	36.8

4.2 Losses at steady rated-load operational condition

With the presumption that the values of the identified iron losses V_{Iron} as well as the frictional losses V_{Frig} from the previous no–load experiment are not changing even during the rated operational state, we can write the balance of power as

$$P_1 - P_2 = P_v = V_{Frig} + V_{Iron} + V_{Co1} + V_{Al2} + V_{Add} \,. \tag{9}$$

The used difference P_v of the total input power P_1 and the total output power P_2 is calculated with the measured values in Tab.2. Different copper losses V_{Co1} are produced in dependency on the stator construction, although the rated magnitudes of the stator currents are very close together, as shown in Tab.2. The term V_{Al2} in (9) typically describes the existing eddy current losses in the squirrel cage rotor and is derived with the aid of the usually rotor slip *s* from

$$V_{Al2} = s\left(P_1 - V_{Frig} - V_{Iron} - V_{Co1}\right) . \tag{10}$$

The term V_{Add} in (9) typically accounts for eddy–current losses in well–known conducting iron stator and rotor parts near the air–gap. Additional occurring inaccuracies of the measured results are also regarded in the term V_{Add} in this simplified view (9),(10) of the problem. However, the assumed additional losses V_{Add} are acting as a certain kind of balancing term in order to guarantee the exact fulfillment of the equation (9).

Table 4: Losses at rated-load in case of rated voltage and rated frequency.

	P_V [W]	V_{Frig} [W]	V_{Iron} [W]	V_{Co1} W]	V_{Al2} [W]	V_{Add} [W]
Semi closed stator slots	352	13.5	71.8	206.8	58.3	1.6
Design without stator slots	318	13.5	36.8	176.6	62.3	28.8

The generated losses V_{Co1} of the proposed machine design with smoothed stator boundary in Tab.4 are about 30W lower than for the usual design. Of course, the omitted effect of the load dependency of the generated iron losses in Tab.4 may be responsible for some inaccuracies in the used description (9). However, in particular the iron losses V_{Iron} are reduced by about 35W. Unfortunately, the additional rotor losses are increasing by about 27W.

5. Conclusions

The proposed finite element approach for the transient electromechanical analysis of the squirrel cage induction motor has been verified by some experiments. It has been shown, that the novel stator design without the usually used slotted stator structure generates less copper losses in the stator part, as well as less iron losses in the steady operational state. Moreover, the presented design reduces the undesired losses and increases the efficiency. Unfortunately, the power factor decreases a little bit, whereas the magnitude of the stator current is kept almost constant.

References

[1] T. Bödefeld and H. Sequenz, *Elektrische Maschinen,* Springer: Wien / New York, 1942.
[2] T. Königshofer, *Die Praktische Berechnung Elektrischer Maschinen,* Technischer Verlag Herbert Cram: Berlin, 1959.
[3] T. Königshofer, *Die Wicklungen Elektrischer Maschinen,* Technischer Verlag Herbert Cram: Berlin, 1969.
[4] X. Klamt, *Bemessung Elektrischer Maschinen,* Springer: Wien / New York, 1973.
[5] P. P. Silvester, *Finite Elements for Electrical Engineers,* Kluwer Publisher: Boston / London / Dortrecht, 1995.
[6] J. S. Salon, *Finite Element Analysis of Electrical Machines,* Cambridge University Press: Cambridge, 1996.
[7] K. J. Bins, P. J. Lawrenson and C. W. Trowbridge, *The Analytical and Numerical Solution of Electric and Magnetic Fields,* John Wiley & Sons: Chichester, 1992.
[8] Basim Istfan, *Extensions to the Finite Element Method for Nonlinear Magnetic Field Problems*, *PhD Thesis,* Rensselaer Polytechnic Institute, New York, 1987.
[9] M.J. DeBortoli, *Extensions to the Finite Element Method for the Electromechanical Analysis of Electrical Machines*, *PhD Thesis,* Rensselaer Polytechnic Institute, New York, 1992.
[10] O. Biro, K. Preis and K. R. Richter, "On the Use of the Magnetic Vector Potential in the Nodal and Edge Finite Element Analysis of 3D Magnetostatic Problems," *IEEE Transactions on Magnetics,* vol. 32, no. 5, 1996.
[11] R. DeWeerdt, E. Tuinman, K. Haymeyer and R. Belmans, "Finite Element Analysis of Steady State Behavior of Squirrel Cage Induction Motors Compared with Measurements," *IEEE Transactions on Magnetics,* vol. 33, no. 2, March 1997.
[12] S. Krikor, I. A. Mohammed and F. A. Abbood, "Finite Element Analysis of a Balanced Three Phase Induction Motor with a Narrow Shunt Bridge of the Rotor Bars," *International Conference on Electrical Machines,* Warschau, 2004.

Electromagnetic Fields in Mechatronics, Electrical and Electronic Engineering
A. Krawczyk et al. (Eds.)
IOS Press, 2006

Determination Of Radial And Axial Magnetic Flux Density In Pmsm(S)

J.A. Güemes, A.M. Iraolagoitia and J.I. Del Hoyo

University of the Basque Country, Escuela Universitaria de Ingeniería Técnica Industrial
Plaza de la Casilla 3, 48012 Bilbao, Spain, joseantonio.guemes@ehu.es

***Abstract** – This paper presents a practical approach for determining the radial and axial magnetic flux density of permanent magnet synchronous motors (PMSM). The analysis is carried out by means of finite element calculations by utilizing three-dimensional (3D) models. The proposed method constitutes an industrial application to the design and modeling of this type of electric machines and mainly it is useful to calculate the end winding reactance.*

Background

Permanent magnet AC motors are usually divided in two major groups: first, the brushless DC motors (BLDC) which have trapezoidal emf waveforms, and second, the permanent magnet synchronous motors (PMSM) which have sinusoidal emf waveforms.
The interest for PMSM is currently increasing in a wide area of applications. There are mainly two reasons for this trend: first, the efficiency and low rotor losses of the PMSM, and second, the falling prices of magnets, in particular NdFeB alloys.
The electric machine simulation using the finite element method is considered a very important tool for the calculation engineer as it allows getting to know with a quite good approximation the different machine parameters, as well as its behavior under extreme working conditions.
Electrical machines are usually represented, in electrical engineering, by means of their equivalent circuit. The knowledge of the different parameters of the equivalent circuit allows us to know the behavior of the machine, by applying the laws of electrical circuits.
The use of the finite element method, as a calculation and simulation tool during the design process of the motor, let us, on the one hand, know its behavior and, on the other hand, model it by means of an equivalent circuit.
A very important parameter of the equivalent circuit of the machine is the synchronous reactance, which as is well-known can be calculated as addition of armature reaction reactance, leakage reactance (magnetic core) and end-winding reactance.
Armature reaction reactance and leakage reactance can be calculated by simulating the motor behavior by means of two-dimensional (2D) plane models (no-load and load analysis).
By considering that in the end winding zones, flux is canalized mainly through air, support and frame of the motor and that end-windings are usually constituted by a straight side and another circular concentric-with-the-axis-of-the-machine side, end winding reactance can be calculated by means de 2D models [1]. First we analyzed by means of a 2D-plane model the straight side of the windings (conductors parallel to the machine axis) and afterwards by means of the 2D-axisimetric models, the circular side of the windings are considered.
This method needs to analyze a great number of axisymmetric models because in each circular tract, the conductor number and also of currents is different.

The development of finite element software and improvements in the performance of PCs as calculation tools mean that we can now solve systems with more equations than just a few years ago, and do so more quickly. With 3D-solid modeling techniques, we can use finite element models with end windings of any shape.
In view of the foregoing, this paper presents a method, in which only a single test using FEM needs to be performed, for calculating, on the one had, the radial and axial magnetic flux density and, on the other hand, the end winding reactance.

Motor

According to the previous data we have a motor with the following characteristics:

- Three-phase motor
- Controller device input voltage: 400 V
- Frequency of the controller device input voltage:50 Hz
- Frequency of the motor input voltage: 12.5 Hz
- Power rating (referred to 12.5 Hz): 5 kW
- Speed rating (referred to 12.5 Hz): 125 rpm
- Number of permanent magnets: 12
- Number of stator slots: 72.

Figure 1 show one-quarter of the cross section of the motor.

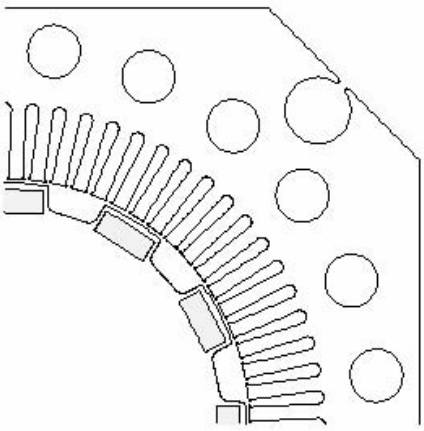

Fig.1 One-quarter of motor geometry

Model

The model utilized comprises 30º (a polar pitch) of the half of the motor axial length. The space of air surrounding the motor has to be taken into account too (see Fig. 2).

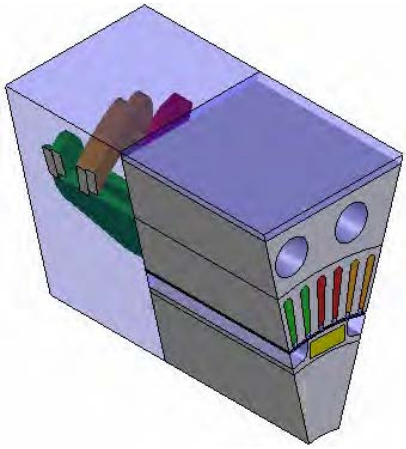

Fig.2 Model

Figure 3 shows the finite element mesh used.

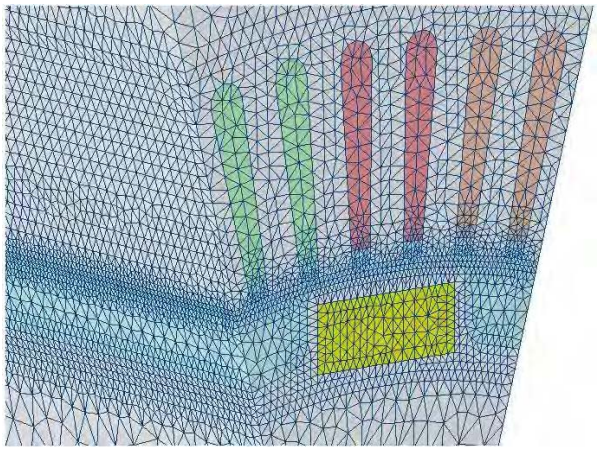

Fig.3 Finite element mesh (zoom)

The material property has been established as follows:

- For the air and copper (stator windings) by means of the magnetic permeability.
- For the stator and rotor magnetic core sheet, by means of its BH curve.
- For the permanent magnets, by means of the its coercive force and magnetic permeability.

Results

Figure 4 shows the map of magnetic flux density obtained once that the np-load analysis has been carried out (only the half of the occupation of a polar pitch is shown).

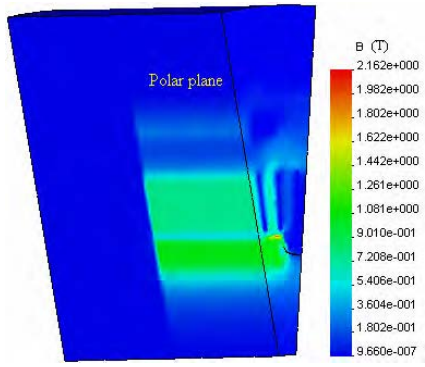

Fig.4 Magnetic flux density for the right half of the model shown in Fig. 2

Figure 5 shows the map of magnetic flux density for $0 < B < 0.01$ T. We can see that the maximum figure of the magnetic flux density in the end winding region is located in the area close to the air gap.

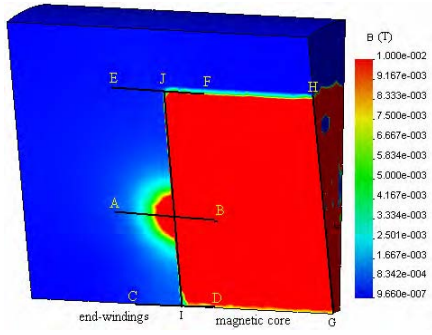

Fig.5 Magnetic flux density ($0 < B < 0.01$ T)

Figure 6 shows the magnetic flux density along of a straight line on axial direction, placed in the middle of the air gap and in a polar plane, with a distance of 40 mm to both sides of the contour of the body of the motor (line AB in Fig. 5). The active length of the machine is 250 mm.

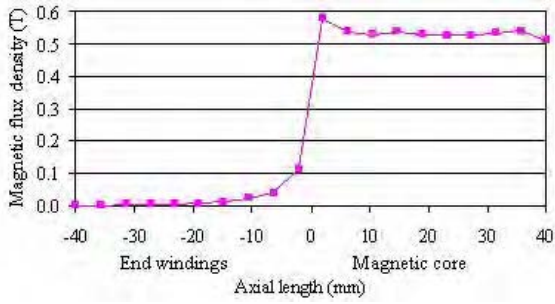

Fig.6 Magnetic flux density (air gap)

Figure 7 shows the magnetic flux density in the line CD (inner rotor radius) and EF (outer stator radius) of the Fig 5.

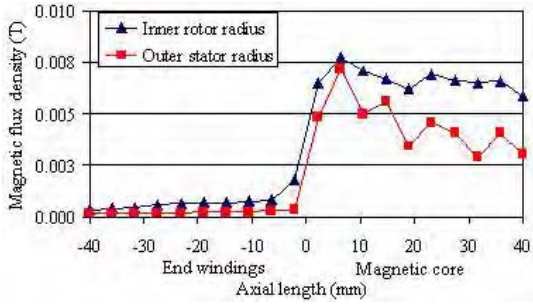

Fig.7 Magnetic flux density

Figure 8 shows the magnetic flux density in the line GH (centre of the motor) and IJ (boundary of the body of the motor) of the Fig 5. The shaft diameter is 100 mm.

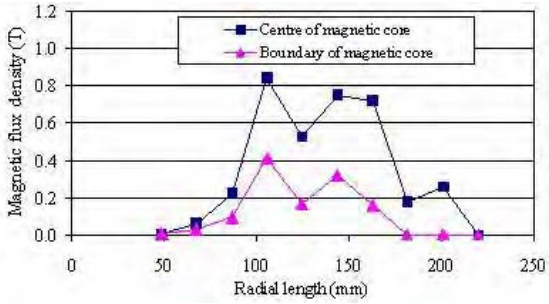

Fig. 8 Magnetic flux density (radial)

End winding reactance

One the input energy of the model (W_m) is obtained, the end-winding energy (W_{ew}) can be calculated by means of the following expression:

$$W_{ew} = 24\left(W_m - W_1\right) \tag{1}$$

Where W_1 is the input energy calculated in the simulation of the motor behavior without end-windings. This is the model used for calculate the armature reaction reactance and leakage reactance.

Finally the end winding reactance is calculated by means of the following equation:

$$X_{ew} = \frac{4\pi f W_{ew}}{3I^2} \tag{2}$$

This reactance has been compared with the reactance calculated by means of the following equation (traditional method) [2]:

$$X_{ew} = 4\pi f \cdot p \cdot n_{pf} \cdot Z_n^2 \cdot \lambda_{cb} \cdot L \tag{3}$$

Where:

- f: frequency;
- p: number of pole pair
- n_{pf}: number of slots per pole and phase
- Z_n: number of wires per slot
- λ_{cb} permeance per unit of length

Table I, shows the winding head reactance calculated by means of equations indicated above.

Table I. End winding reactance

Method	X_{ew} (Ω)
Proposed in this paper (2)	0.57
Classical method (3)	0,44

Conclusions

The behavior of a PMSM has been studied and the end-winding reactance has been calculated.
In this paper, a method was provided to compare the axial and radial magnetic flux density of a PMSM.
The result obtained are good if are compared with those calculated by the traditional method.
The method proposed, which has been tried and tested, can be used for calculated the end-winding reactance in PMSM(s) with windings of any shape.
The results of the method presented in this paper are good in comparison with those obtained by means of classical method..

The method may prove highly useful in determining precise formulas applied to calculating, on the one hand, the radial and axial magnetic flux density and, on the other hand, the end winding reactance.

References

[1] J.A. Güemes and J.I. del Hoyo, "A new equivalent circuit for three-phase induction motors", Proc. ICEM, pp. 402-406, 2000

[2] J. Corrales Martín, "Cálculo industrial de máquinas eléctricas. Tomo I". Marcombo Bouxareu Editores. Barcelona 1982, pp 239 and 262.

[3] Chang-Chou Hwang and Y. H. Cho, "Effects of leakage flux on magnetic fields on interior permanent magnet synchronous motors". IEEE Trans. on Magnetics, vol 37, pp. 3021-3024, 2001.

[4] J. Engström, "Effects of axial leakage on torque performance in PM machines", Proc. ICEM, 2002.

[5] A. Cavagnino, M. Lazzari, F. Profumo, and A. Tenconi, "A comparation between the axial flux and the radial flux structures for PM synchronous motors", IEEE Trans. on Industry Applications, vol. 38, no.6, pp.1517-1524, 2002.

[6] A. K. Adnanes, "Torque analysis of permanent magnet sysnchonous motors", Conf. Power Electronics spcialists, pp. 695-701, 1991

[7] A. Taieb Brahimi, A. Foggia and G. Meunier, "End winding reactance computation using a 3D finite element program", IEEE Trans. Magnetics, vol. 29, no. 2, pp. 1411-1414, 1993.

Electromagnetic Fields in Mechatronics, Electrical and Electronic Engineering
A. Krawczyk et al. (Eds.)
IOS Press, 2006

DEVELOPMENT OF A BONE CONDUCTION VIBRATOR FOR HEARING IMPAIRED PERSONS USED FOR PORTABLE ACOUSTIC DEVICE

Sang-Moon Hwang[1], Hong-Joo Lee[1], Joong-Hak Kwon[1], Young-Chang Yang[1], Gun-Yong Hwang[2]

[1]School of Mechanical Engineering, Pusan National University, Kumjung-Ku,Busan 609-735, Korea,
E-mail: shwang@pusan.ac.kr, honz75@pusan.ac.kr, focar@pusan.ac.kr, yyc@pusan.ac.kr
[2]School of Network and Information Engineering, Youngsan University,Kyoungnam 626-847, Korea,
E-mail: gyhwang@ysu.ac.kr

Abstract *– One of the important parts in multimedia era is acoustic ones. With increased demand of smallest multimedia products such as personal digital assistant (PDA) and mobile phones, it is necessary to develop acoustic devices which have higher performance and smaller size. Acoustic parts with various functions are developed by customer's demands. One of the important functions is hearing aid function for hearing impaired persons. This paper introduces a bone conduction vibrator (BCV) for hearing impaired persons to use portable acoustic device without additional devices. For vibration analysis of the BCV, electromagnetic, mechanical and their coupling effects are considered for the analysis. This paper shows that the development of design and analysis technique by finite element method (FEM) of BCV.*

Introduction

Technologies related to human communication have long been considered as driving force for the realization of information society. The ultimate purpose of communication and information technology is to promote human welfare in the modern society. Therefore, all the relevant benefits from the modern society have to be shared not only with the normal but also with those who are physically handicapped for the full realization of human welfare. For hardness of hearing, gradual hearing impairment seems to be natural in the process of aging. Senile hearing impairment rate is on the steady rise in an aging society preventing those groups of people from participation in social activities. Therefore, particular concern needs to be paid for those who are auditory impaired to improve their lives with the modern communication technology [1].

BCV is a device using born conduction mechanism that can help auditory impaired people to hear sound without any extra hearing aid. However, this mechanism has not been used widely due to lower sound amplitude compared to the conventional ones. In this paper, design and analysis technique by FEM are presented for the development of BCV adopting both air conduction and born conduction mechanism for the elimination of those technical bottlenecks that the former types could not solved.

Method of Analysis

Fig 1 shows a schematic of BCV presented in this paper. A top plate helps to concentrate most of the magnetic flux within the permanent magnet into the narrow radial gap. A time varying current from an amplifier drive is fed into a voice coil attached to a suspension. Axial force exerted on the suspension causes translation motion of vibration plate along the central axis producing bone conduction sound. In design of this system, electromagnetic

and mechanical field needs to be considered. This paper deals with design processes for the two fields respectively.

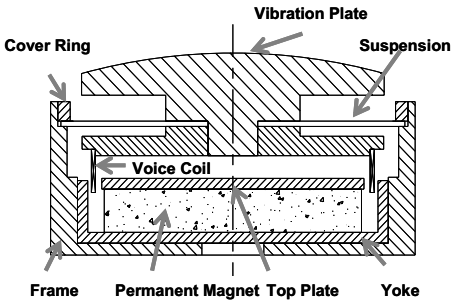

Fig.1 Schematic of BCV

Electromagnetic System

For the electromagnetic field analysis, a two dimensional (2-D) FEM model can be implemented utilizing axisymmetric boundary conditions. The governing equation describing the electromagnetic system can be derived from Maxwell's equations. The magnetic flux density can be expressed as the curl of the magnetic vector potential of $\{A\}$ as in

$$\{B\} = \nabla \times \{A\} \quad (1)$$

A quasistatic model can be used when the magnetic wavelength is much larger than the geometric dimensions of structure. For the quasistatic problem, magnetic field can be described by the partial differential equation as:

$$\nabla \times \left(\frac{1}{\mu} \nabla \times \{A\} \right) = \{J\} \quad (2)$$

where $\{J\}$ and μ denote the current density and the permeability, respectively. Coil current can be also determined by solving the voltage equation of the equivalent circuit as in Eq. (3), where V, R, I, and L denote applied voltage (DC 0.1V), coil resistance (8Ω), coil current, and inductance, respectively. The voice coil motion generates the back electromotive force, $Bl\dot{z}$, where l and $\dot{z}$ are the voice coil length and the voice coil velocity. It should be noted that the back electromotive force and inductance can be obtained by electromagnetic field analysis. The magnetic force resulting from the interaction between the magnetic field and the total electric currents in the conductive parts of the dynamic receiver system can be expressed in Eq. (4) [2], [3].

$$V = IR + L\frac{dI}{dt} + Bl\dot{z} \quad (3)$$

$$F_{coil} = \oint Idl \times B \quad (4)$$

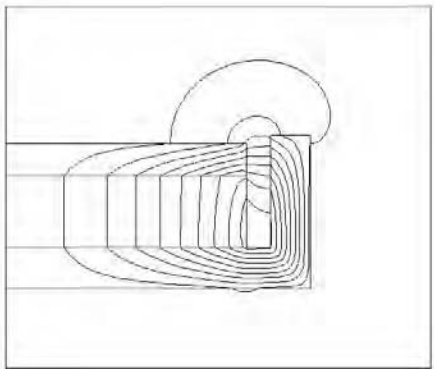

Fig.2 Flux line of BCV

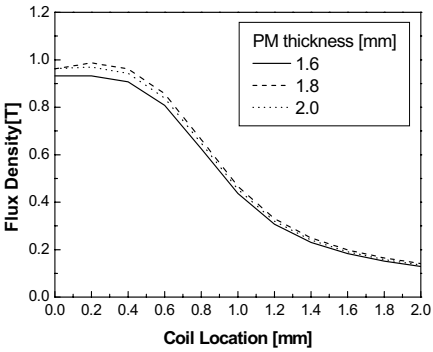

Fig.3 Distribution of flux density at voice coil

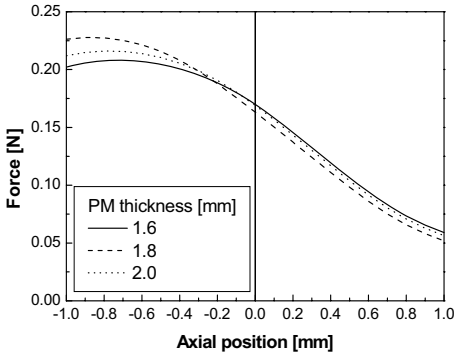

Fig.4 Magnetic force

Fig 2 shows 2-D magnetic flux line at near airgap of a device. Fig 3 shows a distribution of magnetic flux density from the top to the bottom of coil. Fig 4 shows a variation of magnetic force exerted on voice coil as it translates along the central axis. In comparison between Fig 3 and 4, it can be noted that flux density and magnetic force show their maximum values when permanent magnet (PM) thickness is 1.8mm.

Mechanical System

The mechanical model of the vibrator including voice coil can also be developed using FEM. Displacement and velocity of the vibrator can be obtained by solving mechanical vibration equation as in Eq. (5), where [M], [C], [K] and $\{F_{coil}(t)\}$ denote mass matrix, damping coefficient matrix, stiffness coefficient matrix and magnetic exciting forces acting on voice coil, respectively [3].

$$[M]\{\ddot{z}\}+[C]\{\dot{z}\}+[K]\{z\}=\{F_{coil}(t)\} \quad (5)$$

Fig 5 delineates a set of shapes for vibration plates and suspensions selected for mechanical design. Analytical results for each type are respectively plotted in Fig 6 and 7, showing variation of displacement and acceleration vs. frequency.

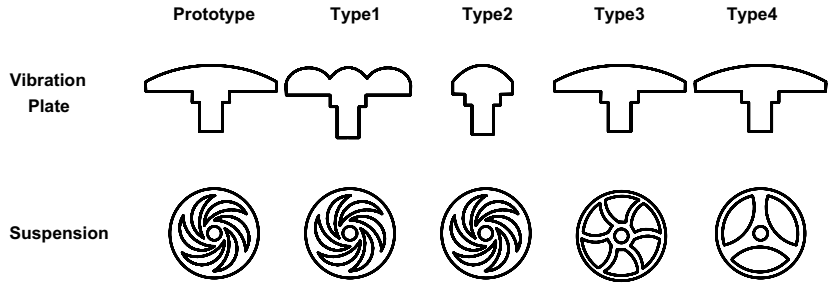

Fig.5 Shapes of vibration plate and suspension

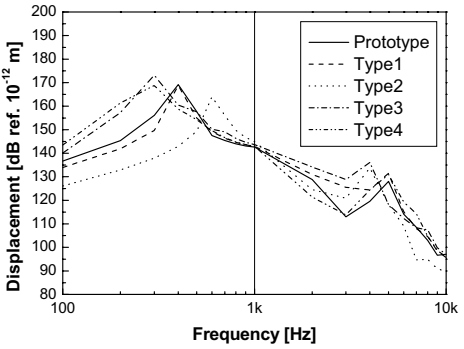

Fig.6 Displacement of vibrators

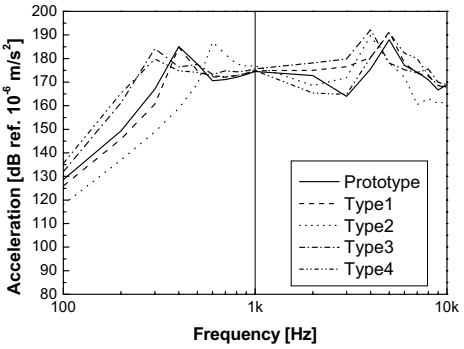

Fig.7 Acceleration of vibrators

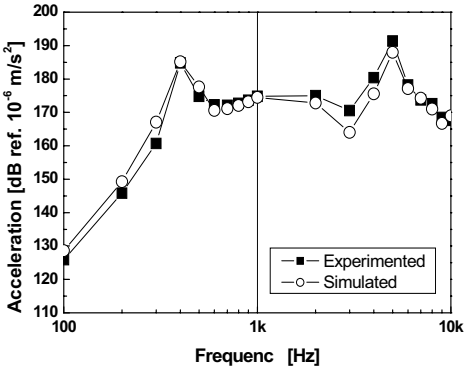

Fig.8 Acceleration of experimented and simulated vibrators

For the prevention of mechanical interference between vibration plate and top plate, the maximum displacement is restrained by dimensional design to provide a sufficient axial clearance (about 1mm) while performance of

bone conductor vibrator is heavily dependent on acceleration. Considering all factors, it can be noted that vibration plate of type 1 and suspension of type 3 is the most efficient design.

The maximum displacement and the rms value of acceleration for each type are written in Table 1.

In this paper, acceleration is measured directly from a miniature accelerometer attached to the vibration plate. The purpose of this experiment is solely for the prediction of BCV. This paper focuses mainly on the development of design and analysis technique for the given system rather than on performance enhancement. Validity of analysis is confirmed by experiment and the results are plotted in Fig 8 with comparison of simulated model and prototype.

Table. 1

Displacement and acceleration of devices

	Prototype	Type1	Type2	Type3	Type4
Displacement Max. [dB ref. 10^{-12}m/s^2]	169.1	168.8	163.9	173.2	168.8
Acceleration Rms. [dB ref. 10^{-6}m/s^2]	178.9	181.7	180.3	182.5	181.5

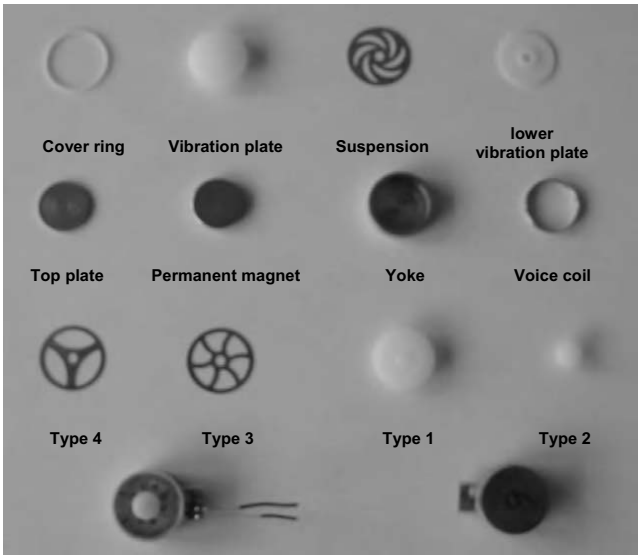

Fig.9 Photograph of the BCV

Conclusion

The design and development of a high performance BCV by the electromagnetic and mechanical system analysis has been a main issue of this paper. One of the advantages of this type of receiver is that users can communicate more efficiently at the noisy environment and even at the state of a long time communication there is not much stress on the users' auditory sense. Moreover, the communication for auditorily handicapped persons is available and applied products of the BCV can be developed for people who have difficulty in hearing.

At the electromagnetic system, it is designed to maximize magnetic flux density and magnetic force by setting up thickness of the PM, top plate, and yoke as design parameters. It is also designed to maximize acceleration of the vibration plate at the mechanical system by establishing the shape of the vibration plate and suspension as design parameters. For a realistic application, it is designed that the maximum displacement of the vibration part is in the range of 1mm (180dB ref. 10-12m) because there exists the limitation of space between top plate and suspension. Magnetic flux density and magnetic force is maximized when thickness of the PM is 1.8mm. Acceleration is maximized when the vibration plate is type 1 and the suspension is type 3 at Fig 5. Fig 9 shows photograph of the BCV.

A research on the sound quality of the BCV has not been sufficiently made now so that there should be a more research on the distribution of acceleration relative to the audible frequency.

Acknowledgment

This work was supported by a Korea Science and Engineering Foundation Grant No. R05-2003-000-10640-0.

References

[1] Birch. T. S. et al., Microengineered systems for the hearing impared, IEE Colloquium on, pp. 2/1-2/5, 31 Jan 1996

[2] T. J. Kim et al., Analysis of Vibration for Permanent Magnet Motors Considering Mechanical and Magnetic Coupling Effects, IEEE Trans. on Magnetics, Vol. 36, No. 4, pp. 1346-1350, July 2000

[3] S. M. Hwang et al., Development of Solenoid-Type Vibrators Used for Mobile Phones, IEEE Trans. on Magnetics, Vol. 39, No. 5, pp. 3262-3264, Sep. 2003

Electromagnetic Fields in Mechatronics, Electrical and Electronic Engineering
A. Krawczyk et al. (Eds.)
IOS Press, 2006

FINITE ELEMENT ANALYSIS FOR THE DIAGNOSIS OF BROKEN ROTOR BARS IN 3-PHASE INDUCTION MACHINES

Joya Kappatou*, Claude Marchand, Adel Razek****

* University of Patras
Department of Electrical and Computer Engineering
Electromechanical Energy Conversion Laboratory
26500 RION PATRAS, Greece
E-mail : joya@ee.upatras.gr

** Laboratoire de Génie Electrique de Paris / SPEE labs,
CNRS UMR 8507, Supelec, Université Paris VI, Université Paris XI
Plateau de Moulon, F 91192 Gif sur Yvette

Abstract **–** ***In this paper a study of an induction machine under both healthy and broken rotor bars condition, taking into account the non linearity of the magnetic materials, the operating point and the rate of degradation of the machine has been done. The results show that the measurement of the external field on the surface of an induction machine can be used to characterize its healthiness.***

I. Introduction

As known, the three-phase squirrel cage induction motor is the most widely used electrical machine in the industry. Due to possible serious repercussions a breakdown of the machine either on the manufacturing process, on goods and services or on the safety of people, many investigations regarding the induction machine faults and the diagnostic methods used to detect them are developed. Lot of contributions can be found in the bibliography during the last two decades [1-7].

The most prevalent failures in induction machines include broken rotor bars and end ring connectors, stator faults, eccentricity and bearing faults. The well-known consequences of such faults are unbalanced phase voltages and line currents, torque pulsations, mechanical vibrations and excessive heating.

The observation of the characteristic fault symptoms for the monitoring of the machines has introduced the use of additional instrumentation and sophisticated signal processing techniques. In case of variable speed drives the additional cost needed is relatively small. The advanced control techniques of electrical machines, such as vector control, require the use of sensors (position, speed, current) and enhanced digital controllers (DSP), which permit the implementation of powerful observers and estimators. On the other hand there are applications, such as constant speed drive systems, which are connected directly to the network and they do not include such instrumentation. For these cases, non-invasive detection and diagnosis techniques will be developed. A well known non-invasive technique for the fault diagnosis is the monitoring and processing of the stator currents to detect harmonics characteristics for the various types of faults.

Besides the current harmonics and torque pulsations, the magnetic field leakage, on the outside surface of the stator, can also feature the operating point of the machine and can be used

for the detection of internal faults. The exterior leakage magnetic field can be easily detected using magnetic sensors and this technique can be applied in cases of constant speed drive systems, as mentioned above, during on-site maintenance operation.

The present paper deals with the effect of cage faults on the performance and characteristics of the machine using a 2D finite element model of an induction machine. The current harmonics and torque pulsations, as well as the magnetic field leakage on the surface of the stator, are calculated in the presence of fault in comparison with healthy case.

II. The 2D Numerical Analysis

To study the influence of broken bars on motor performances, a magnetic investigation by a 2D finite element analysis is carried out. A transient eddy current solver, accounting for the rotation of rotor and the consideration of the non-linear characteristics of the magnetic material (BH curve), is used.

The numerical analysis is based on a magnetic vector potential formulation, which consists in solving the differential equation:

$$\nabla\times\left(\nu\nabla\times\vec{A}\right)=\vec{J}_S-\sigma\frac{\partial\vec{A}}{\partial t} \tag{1}$$

where

$\vec{A}$ is the magnetic potential
μ is the magnetic permeability
σ the electric conductivity
J_S the current density

The stator windings are fed from sinusoidal varying voltage sources V, which are connected via external circuits to the model: a resistor R, an inductor L (which can represents the flux leakage). Solving the following equation, the current in each phase is obtained.

$$V=RI+L\frac{\partial I}{\partial t}+\frac{\partial\phi}{\partial t} \tag{2}$$

$$\text{with } \phi=\oint\vec{A}d\vec{l} \text{ and } I=\iint\vec{J}_S.d\vec{S}$$

The used software permits to perform the calculation for both the healthy and the faulty case over the smallest symmetrical part of the machine model, which in our case is 180 degrees of the complete model.

The data of the considered induction machine are:

P=5 kW, 230/240 V- 50 Hz, 36 stator slots, 48 rotor slots, 4 poles.

III. Simulation Results

The aim of the magnetic analysis is to compare the behaviour of the machine among the healthy case and the faulty case with broken rotor bars [7]. All the calculations assume the velocity of the rotor constant at 1400 rpm and the stator windings fed with sinusoidal voltages.

III.1. Case of 5 broken bars

The flux density distribution in the cross section of the machine for the healthy case is shown in figure 1. The impact of the faulty cage can be clearly observed. Figure 2 shows the modification of the vector potential in the air gap: an asymmetry of the waveform is evident, the magnitude is modified and harmonics are generated.

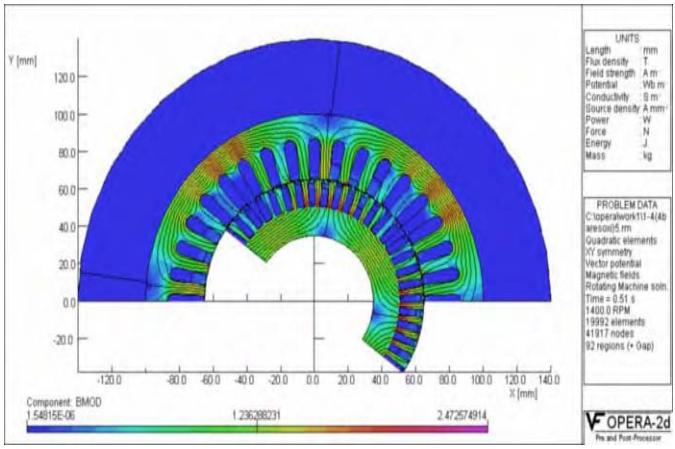

Fig. 1. Flux density distribution and flux lines in the healthy case.

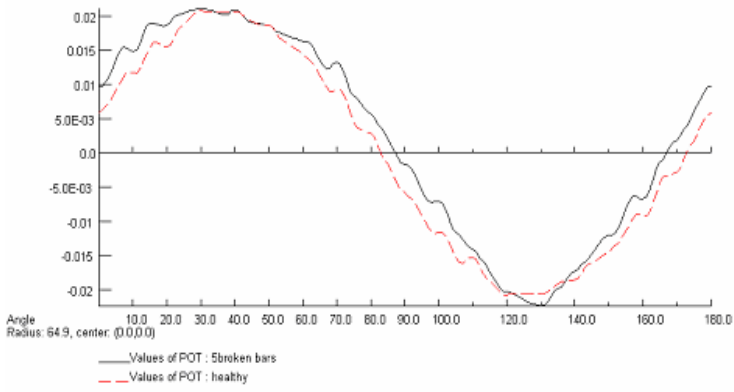

Fig. 2. Potential, in Wb/m, in the midle of the airgap of the machine.

To make an on line supervision of such system, electromagnetic variables have to be observed directly by measurements or by using signal processing calculations on the measured sensor signals. The figures 3 and 4 show the influence of the fault on the stator current and torque waveforms. The repercussion is mainly identifiable on the average value of the torque but also on the current harmonics.

However when advanced control techniques are not required, the specific permanent equipment necessary for the monitoring (sensors, digital controller) becomes in these conditions very expensive and not conceivable. Then, only a non-invasive technique has to be implement to make the supervision with external signal, namely the leakage magnetic field closed to the machine outside surface. This field can be representative of the magnetic state of the machine and allows the detection of faults.

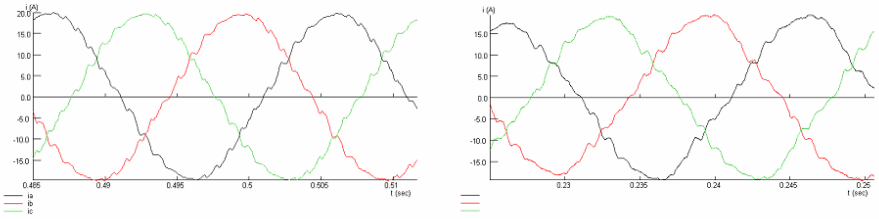

healthy condition *5 broken rotor bars condition*

Fig. 3. Stator phase currents

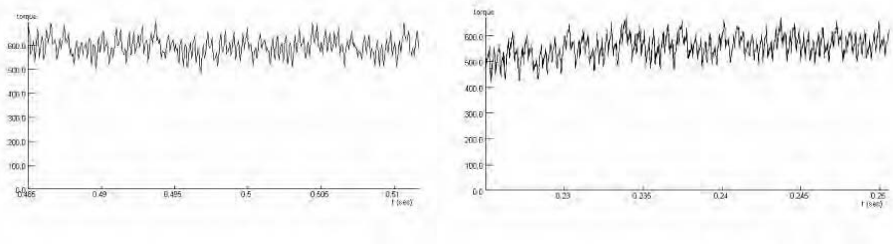

healthy condition *5 broken rotor bars condition*

Fig. 4. Torque, in Nm/m, for the case of healthy machine

The figure 5 shows the instantaneous distribution of the radial component of B outside the stator in the cases of the healthy and faulty rotor.

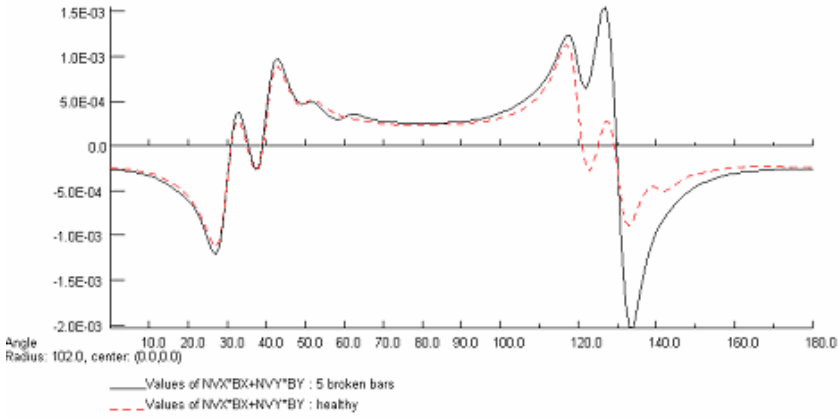

Fig. 5. Distribution of the radial component of B, in T, outside the stator.

Consequently, the layout of magnetic sensors to the periphery of the machine must be able to inform us in real time about the state of the machine. However, it is necessary to evaluate the sensitivity of the method with respect to the damage of the machine and to the operating point.

III.2. Influence of the degree of damage

In the last section the case of Five broken bars has been analysed using a non linear model. In this section the influence of the degree of damage (number of broken bars) is presented. The figure 6 shows their influence on the surface magnetic field. Due to the time consuming software, these calculations have been conducted using a linear model of the machine.

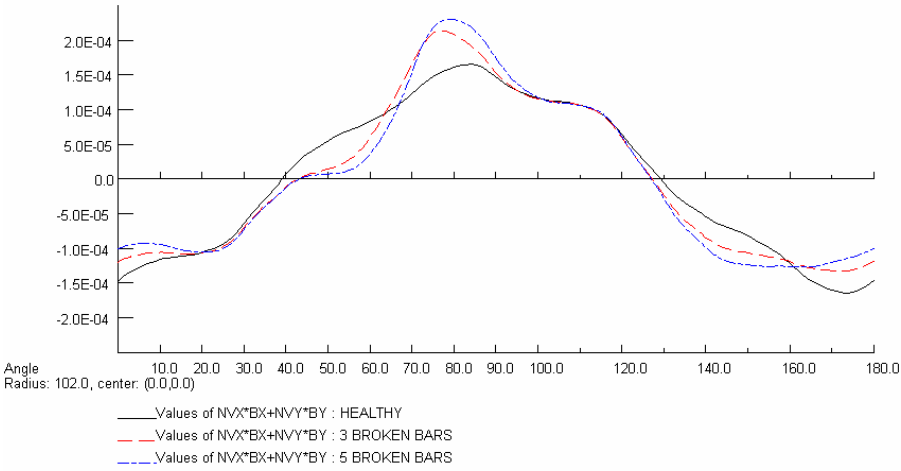

Fig. 6. Distribution of the radial component of the inductio, outside the stator for: the healthy case and for the cases of 3 and 5 broken bars.

The results neglecting the magnetic saturation are far from those considering no linear magnetic circuit (see figure 5). Nevertheless the effect of degradation (number of broken bars) on the external field measurement is undeniable. Consequently, the obtained outcomes show that the leakage field observation can be used to characterise healthiness of an induction machine.

IV. Conclusion

In this paper, the obtained results show that the measurement of the external field on the surface of a induction machine can be used to characterize its healthiness. A thorough study, taking into account the non linearity of the magnetic materials, the operating point and the rate of degradation of the machine makes it possible to consider the solution of the inverse problem aiming to the monitoring and the diagnosis of induction machines connected directly to the electrical supply network.

References

[1] Richard J. Povinelli, John F. Bangura, , Nabeel A. O. Demerdash, and Ronald H. Brown "Diagnostics of Bar and End-Ring Connector Breakage Faults in Polyphase Induction Motors Through a Novel Dual Track of Time-Series Data Mining and Time-Stepping Coupled FE-State Space Modeling" IEEE TRANS. ON ENERGY CONVERSION, VOL. 17, NO. 1, March 2002.

[2] Behrooz Mirafzal,Nabeel. A. O. Demerdash " Induction Machine Broken-Bar Fault Diagnosis Using the Rotor Magnetic Field Space-Vector Orientation" IEEE TRANS. ON INDUSTRY APPLICATIONS, VOL. 40, NO. 2, March/April 2004.

[3] Masoud Haji, Hamid A. Toliyat "Pattern Recognition—A Technique for Induction Machines Rotor Broken Bar Detection" IEEE TRANS. ON ENERGY CONVERSION, VOL. 16, NO. 4, December 2001

[4] Humberto Henao, Claudia Martis, Gérard-André Capolino "An Equivalent Internal Circuit of the Induction Machine for Advanced Spectral Analysis" IEEE TRANS. ON INDUSTRY APPLICATIONS, VOL. 40, NO. 3, May/June 2004

[5] Zhenxing Liu, Xianggen Yin, Zhe Zhang, Deshu Chen, Wei Chen "Online Rotor Mixed Fault Diagnosis Way Based on Spectrum Analysis of Instantaneous Power in Squirrel Cage Induction Motors" IEEE TRANS. ON ENERGY CONVERSION, VOL. 19, NO. 3, September 2004

[6] Carla C. Martins Cunha, Renato O. C. Lyra, Braz Cardoso Filho « Simulation and analysis of induction machines with rotor asymmetries » IEEE TRANS. ON INDUSTRY APPLICATIONS, VOL. 41, NO. 1, Jan./Febr. 2005

[7] Rastko Fiser, Stanislav Ferkolj "Application of a finite element method to predict damaged induction motor perfomance" IEEE TRANS. ON MAGNETICS, VOL. 37, NO. 5, September 2001.

Electromagnetic Fields in Mechatronics, Electrical and Electronic Engineering
A. Krawczyk et al. (Eds.)
IOS Press, 2006

LEVITATION FORCE ANALYSIS ACTING ON SLIDING CONDUCTOR BY 3-D FINITE ELEMENT METHOD

Yoshihiro Kawase*, Tadashi Yamaguchi*, Takafumi Eguchi*, Takayuki Kobayashi*, Osamu Noro, Koji Hashimoto** and Yuji Shindo****

*Department of Information Science, Gifu University, 1-1 Yanagido, Gifu, 501-1193, Japan
E-mail: kawase@info.gifu-u.ac.jp
**Kawasaki Heavy Industries, 1-1 Kawasaki-cho, Akashi, 673-8666, Japan
E-mail: noro@tech.khi.co.jp

Abstract **- *In this paper, we calculated the dynamic levitation force of a sliding levitation system quantitatively using the 3-D finite element method taking into account the eddy currents. The speed characteristics of the levitation force of the sliding levitation system are investigated.***

Introduction

Sliding levitation system is a kind of transform systems, in which a conductor moves very fast in the alternating magnet fields and the levitation force generates in the conductor.

In this paper, we calculated the levitation force acting on the sliding conductor using the 3-D dynamic finite element method taking into account the eddy currents[1][2], and investigated the speed characteristics of the levitation force acting on the sliding conductor.

Analyzed Method

The fundamental equations of the magnetic field can be written using the magnetic vector potential $\boldsymbol{A}$ and the electric scalar potential ϕ as follows:

$$\mathrm{rot}(\nu\ \mathrm{rot}\boldsymbol{A}) = \boldsymbol{J}_e + \mathrm{rot}\,\nu_0 M\ ,\ \boldsymbol{J}_e = -\sigma\left(\frac{\partial \boldsymbol{A}}{\partial \mathrm{t}} + \mathrm{grad}\,\phi\right),\ \mathrm{div}\,\boldsymbol{J}_e = 0 \qquad (1)$$

where ν is the reluctivity, $\boldsymbol{J}_e$ is the eddy current density, ν_0 is the reluctivity of vacuum, σ is the conductivity, and $\boldsymbol{M}$ is the magnetization.

Mesh Modification Method

In this analysis, the following procedure is carried out in order to express the sliding conductor movement using the 3-D finite element method.

First of all, the initial mesh is prepared as shown in Fig. 1 (a). Then, the mesh is divided into two areas as shown in Fig. 1 (b). One is the moving-area and another is the stationary-area. The finite elements in the moving-area are moved according to the conductor movement as shown in Fig. 1 (c). The overhang of the moving-area from the stationary-area is cut out and is connected to opposite side of the moving-area as shown in Fig. 1 (d). Finally, the moving-area is connected to the stationary-area as shown in Fig. 1 (e).

Analyzed Model and Condition

Fig. 2 shows the principle of levitation force generation. In the sliding levitation system, many magnets set in line, the magnetic poles of which are changed alternately. In such a case, if a conductor moves very fast over the magnets, the magnetic field generated by the magnets set in line seems like alternating magnetic field from the point of view of the conductor. Therefore, eddy current generates in the conductor, and the levitation force is generated by the eddy current and the magnetic field. Fig. 3 shows the analyzed model of a sliding levitation system. This model is consisted of a sliding conductor and magnetic parts (permanent magnets and yokes). The sliding conductor is consisted of two conductors as shown in Fig. 2 (c). It is assumed that the sliding conductor moves fast by the external force. Fig. 4 shows the 3-D finite element mesh except the air. Table I shows the analysis conditions. The analyzed region is 1/2 of the whole region because of the symmetry. The electromagnetic force acting on the sliding conductor is calculated as the Lorentz force.

Results and Discussion

Levitation Force Acting on Sliding Conductor

In this section, the sliding conductor is analyzed in case that the speed is v_0 m/s. Fig. 5 shows the distributions of eddy current density vectors in the sliding conductor. It is found that there are large eddy current density vectors between the poles of permanent magnets, and those vectors gradually decrease toward the direction of movement.

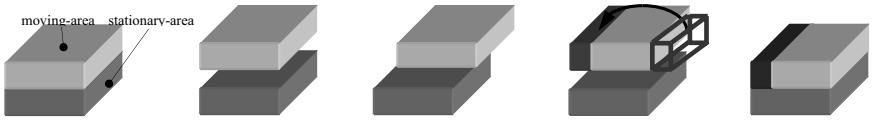

(a) initial mesh (b) separating mesh (c) moving mesh (d) connection (e) mesh after connection

Fig. 1. Mesh modification method.

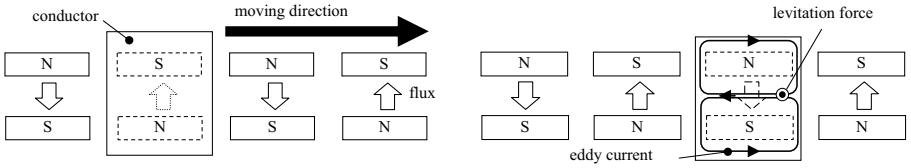

(a) initial state (b) conductor is slid.

Fig. 2. Principle of levitation force generation.

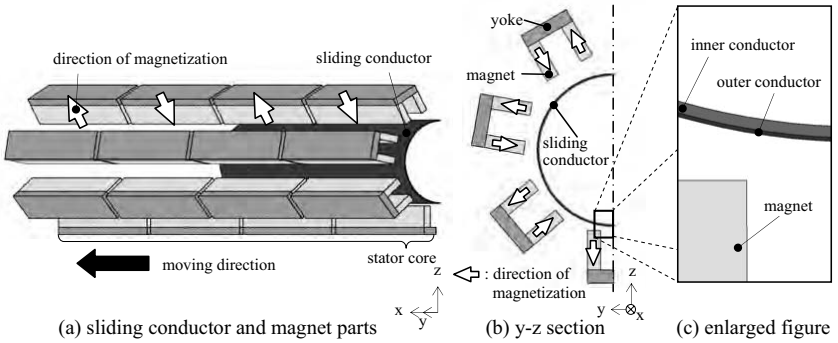

(a) sliding conductor and magnet parts (b) y-z section (c) enlarged figure

Fig. 3. Analyzed model (1/2 region).

Figs. 6 (a) and (b) show the distributions of flux density vectors and Lorentz force vectors at the section α as shown in Fig. 5, respectively. It is found that there are large Lorentz force vectors in the lower part of the sliding conductor, because the eddy current density vectors are large in the lower part of the sliding conductor as shown in Fig. 5.

Fig. 7 shows the calculated levitation force waveform. f_0 is the average value of the levitation force at the steady state. It is found that the calculated levitation force becomes steady state after about 50 steps.

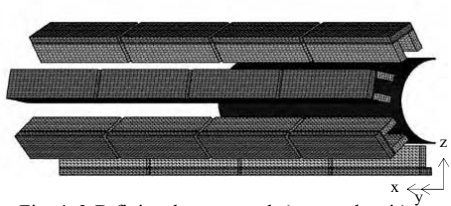

Fig. 4. 3-D finite element mesh (except the air).

TABLE I
Analysis Conditions

Magnetization of magnet (T)		1.0
Conductivity (S/m)	Outer conductor	5.77×10^7
	Inner conductor	3.80×10^7

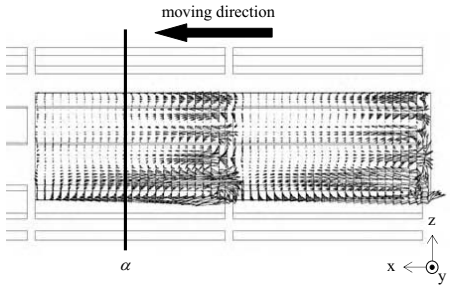

Fig. 5. Distributions of eddy current density vectors ($v = v_0$ (m/s)).

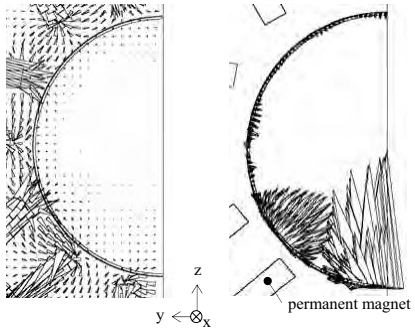

(a) flux density vectors (b) Lorentz force vectors.

Fig. 6. Distributions of flux density vectors and Lorentz force vectors.

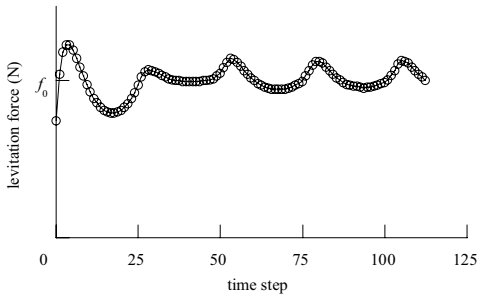

Fig. 7. Levitation force waveform.

Effect of Speed on Levitation Force

Fig. 8 shows the distributions of flux density vectors at the section α (see Fig. 5) in case that the speed is $v_0/6$, v_0 and $2.5v_0$ m/s. From these figures, it is found that the flux density vectors inside of the sliding conductor are small as the speed is large, because the reaction field of eddy currents in the sliding conductor increase as the speed is large. Fig. 9 shows the distributions of Lorentz force vectors at the section α in case that the speed is $v_0/6$, v_0 and $2.5v_0$ m/s. From these figures, it is found that the Lorentz force vectors, when the speed is v_0 m/s, are larger than those when the speed is $2.5v_0$ m/s, because the flux in the sliding conductor decreases by the reaction field of eddy currents. Fig. 10 shows the effect of speed on the levitation force. From this figure, the levitation force waveforms are different depending on the speed. Fig. 11 shows the average value of the levitation force characteristics at the steady state on various speeds. It is found that the average value of the levitation force increases from 0 to v_0 m/s, because the eddy currents are large as the speed becomes fast. However, the levitation force decreases when the conductor moves faster than v_0 m/s, because the eddy currents decrease the magnetic flux in the moving conductor by the skin effects.

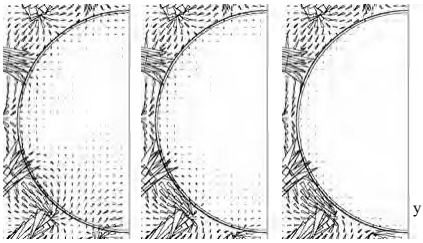

(a) $v = v_0/6$ (m/s) (b) $v = v_0$ (m/s) (c) $v = 2.5v_0$ (m/s)

Fig. 8. Distributions of flux density vectors.

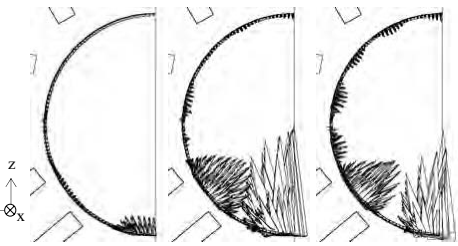

(a) $v = v_0/6$ (m/s) (b) $v = v_0$ (m/s) (c) $v = 2.5v_0$ (m/s)

Fig. 9. Distributions of Lorentz force vectors.

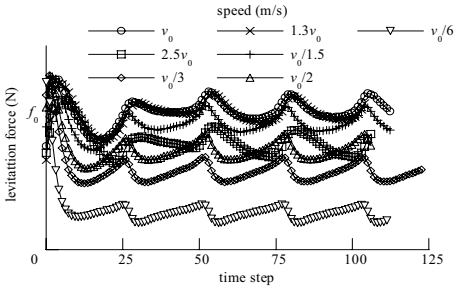

Fig. 10. Levitation force waveform.

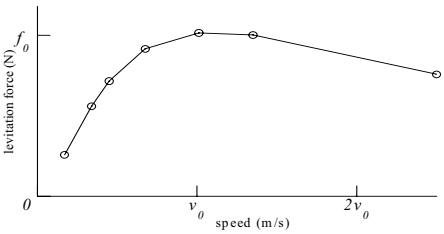

Fig. 11. Average value of levitation force characteristics.

Conclusion

In this paper, the levitation force of sliding conductor is calculated circumstantially, and the effects of speed on levitation force are clarified. It is found that levitation force has the maximum value at v_0 m/s, because the eddy currents decrease the magnetic flux in the moving conductor by the skin effects when the conductor moves faster than v_0 m/s.

References

[1] Y. Kawase and S. Ito, *New Practical Analysis of Electrical and Electric Apparatus by 3-D Finite Element Method*, Morikita Publishing Co., 1997

[2] T. Ota, Y. Kawase, K. Hirata and Y. Mitsutake, "3-D Eddy Current Analysis of Linear Solenoid Using A New Auto Mesh Coupling Method," *Trans. IEE of Japan*, Vol. 119-D, No.11, pp. 1393-1400, Nov., 1999.

Electromagnetic Fields in Mechatronics, Electrical and Electronic Engineering
A. Krawczyk et al. (Eds.)
IOS Press, 2006

EXPERIMENTAL VERIFICATION OF THE 3D VOLTAGE DRIVEN EDGE ELEMENTS MODEL OF A FRACTIONAL POWER INDUCTION MOTOR

Krzysztof Komeza, Sławomir Wiak, Maria Dems and Paweł Jastrzabek

Institute of Mechatronics and Information Systems, Technical University of Lodz,
ul. Stefanowskiego 18/22, 90-924 Lodz, Poland
e-mail: komeza@p.lodz.pl ,wiakslaw@p.lodz.pl, mdems@p.lodz.pl, pjastrza@pf.pl

Abstract *– In the paper, a three-dimensional analysis, using a voltage driven edge elements model, of the electromagnetic field of a fractional power induction motor is presented. The results of this analysis for different models were compared with experiments. The skewing effect of the rotor slots was taken into account using solid modelling of the motor.*

Introduction

Induction motors are usually investigated using a 2D method according to the proportions of the outer motor diameter and core length. For the fractional power motors this proportion is not large, hence a more interesting 3D analysis, especially that the skewing effect of the rotor bars can be described properly only using a 3D analysis. The 3D or 2D models of the motor are always the results of approximations of real field distributions with the finite element shape function so neither of them are error free. It is very important from the practical point of view to observe the differences between solutions for different models and discretization densities. In the paper, the results of 3D calculations are compared with experimental results.

Mathematical Model

Induction motor phase winding, excited from a voltage source V_p, can be described using the Kirchoff closed-loop voltage expression

$$\mathrm{V_p} = R_p I_p + \frac{d\Psi_p}{dt} \tag{1}$$

where R_p is the lumped resistance of the filamentary phase winding, $\frac{d\Psi}{dt}$ is phase induced voltage produced by variation of the magnetic flux Ψ_p linking that winding.
The electromagnetic field in motor volume can be obtained using the magnetic vector potential. The magnetic vector potential is defined by the expression

$$\mathbf{B} = \mathrm{curl}\,\mathbf{A} \tag{2}$$

The phase induced voltage about a closed winding path l_p linked with magnetic flux Ψ_p can be expressed in terms of magnetic vector potential. This is accomplished by the use of (2), to permit writing the induced voltage as follows

$$\frac{d\Psi_p}{dt} = \frac{d}{dt}\int_{S_p}\mathbf{B}\cdot d\mathbf{S} = \frac{d}{dt}\int_{S_p} curl\mathbf{A}\cdot d\mathbf{S} = \frac{d}{dt}\oint_{l_p}\mathbf{A}\cdot d\mathbf{l} \tag{3}$$

on applying Stokes's theorem to obtain the final result. Thus it follows that induced voltage can be determined by a variation of integrals of the vector magnetic potential on the winding path.
Therefore the natural choice for solution of the voltage driven windings is a use of tetrahedral edge elements for vector potential approximation.

The vector potential approximation is given in terms of a summation of the edge contribution a_i weighted by the vector shape function w_i for the six element edges.

$$\mathbf{A}^{(e)}(x,y,z) = \sum_{i=1}^{6} a_i \mathbf{w_i} \tag{4}$$

The unknown edge contributions are the line integrals along the edges

$$a_i = \int_{l_i} \mathbf{A} \cdot d\mathbf{l} \tag{5}$$

and the $\mathbf{w_m}$ is the vector basis function defined for the edge i spanned between vertices k and l as

$$\mathbf{w_i} = N_k \, grad \; N_l - N_l grad \; N_k$$

where N_k and N_l are classical piecewise polynomial shape functions associated with nodes k and l respectively, usually given in terms of barycentric coordinates.

$$N_k(x,y,z) = L_k(x,y,z) = \frac{volume(P,V_l,V_m,V_n)}{volume \; of \; tetrahedron} \tag{6}$$

where P is a point at (x,y,z) and V_l, V_m and V_m are vertices of the tetrahedron.

The shape functions $\mathbf{w_i}$ are called the Whitney 1-forms. The circulation of the $\mathbf{w_i}$ along the edge i is equal 1 and zero along the other five edges of the element.

The approximation given by (4) have the following properties:

- the tangential component of the vector potential is continuous across facets and the normal component is discontinuous,
- the divergence of **A** equals zero within the element, so the Coulomb gauge is naturally satisfied,
- magnetic flux density **B** = curl **A** has normal continuity across the facets and is constant in element

$$\mathbf{B} = curl \; \mathbf{A} = curl \left(\sum_{i=1}^{6} a_i \mathbf{w}_i \right) = 2 \sum_{i=1}^{6} \left(grad \; N_l \times grad \; N_k \right) a_i \tag{7}$$

For eddy-current free regions, including those with filamentary windings, the magnetic field is described by

$$curl\left(\nu \; curl \mathbf{A}\right) = \mathbf{J_p} \tag{8}$$

where ν is the reluctivity and $\mathbf{J_p}$ is the current density.

The winding current I_p in (1) is represented using the winding current density

$$\mathbf{J_p} = \frac{n_p}{S_p} I_p \mathbf{n_p} \tag{9}$$

where np is the number of turns, Sp is the cross-section of the winding's coil and **ns** is the unit tangential vector along the direction of the phase winding.

For conducting regions based on Faraday's Law and relation (2) the following can be obtained

$$curl \mathbf{E} = -curl \frac{\partial \mathbf{A}}{\partial t} \tag{10}$$

and by the integration of both sides

$$\mathbf{E} = -\frac{\partial \mathbf{A}}{\partial t} - grad \Phi \tag{11}$$

where Φ is the electric scalar potential.

The eddy currents in the conducting regions are equal to

$$\mathbf{J_e} = \sigma \mathbf{E} \tag{12}$$

Connecting (8),(11) and (12) leads to the equation

$$curl\left(\nu\ curl\mathbf{A}\right) = -\sigma\left(\frac{\partial \mathbf{A}}{\partial t} + grad\Phi\right) \tag{13}$$

Adding electric scalar as the second unknown value in (13) necessitates the introduction of an additional equation. This equation is commonly obtained from the current continuity condition for eddy currents (neglecting displacement current).

$$div\mathbf{J}_e = 0 \tag{14}$$

Incorporating (11) and (12) into the second equation is

$$div\left(-\sigma\left(\frac{\partial \mathbf{A}}{\partial t} + grad\Phi\right)\right) = 0 \tag{15}$$

The Galerkin procedure and the weighted residual method are used to transform the partial differential equation to a discretized set of non-linear algebraic equations. Boundary conditions and interface conditions should also be embedded in these equations.

Magnetic vector potential connected with electric scalar potential representation of electromagnetic field in electrical machines is obviously more expensive than the magnetic scalar potentials Ψ-Φ. However for the voltage driven model, scalar potentials are very inconvenient due to problems with the calculation of the flux linked with the phase winding. In principle, the use of scalar description is always less expensive than the vector one. The magnetic scalar potential can be used to describe the magnetic field in non-conducting materials.

$$\begin{aligned} &-div\ \left(\mu\ grad\ \Psi\right) = 0 \\ &grad\ \Psi \cdot grad\ \mu\ +\ \mu\ \nabla^2\Psi = 0\ \ . \end{aligned} \tag{16}$$

Application of reduced magnetic scalar potential Φ provides the basis for accounting the presence of the forced currents of known distribution in non-conducting areas. The magnetic field strength can be expressed as the sum of three components

$$\mathbf{H} = \mathbf{H}_s + \mathbf{H}_m + \mathbf{H}_e \tag{17}$$

from the first $\mathbf{H_S}$ is the magnetic field strength obtained as a result of the source's current flow in the air ($\mu=\mu_0$), the second $\mathbf{H_m}$ is a result of the existence of a ferromagnetic material in the surroundings and the last $\mathbf{H_e}$ is a result of the existence of some conducting material in the surroundings.

Using the Biot-Savart law, the formula for the first component becomes:

$$\mathbf{H}_s = \frac{1}{\mu_0}\mathbf{B} = \int_V \frac{\mathbf{J} \times \mathbf{1}_r}{4\,\pi\,r^2}\,dv \tag{18}$$

The last two components can be described using the aforementioned reduced magnetic scalar potential Φ.

$$\mathbf{H}_m + \mathbf{H}_e = -\,\mathrm{grad}\,\Phi \tag{19}$$

Resultant magnetic field strength takes the form:

$$\mathbf{H} = \int_V \frac{\mathbf{J} \times \mathbf{1}_r}{4\,\pi\,r^3}\,dv\ -\ \mathrm{grad}\,\Phi \tag{20}$$

Using this description, the magnetic vector potential must still be used in the conducting area. The effect of reducing the number of equations and calculation time due to the use of scalar potentials instead of a vector one is lowered by the time needed to calculate the $\mathbf{H_s}$ component (18) on the total-reduce scalar border in the case of a complicated winding's shape.

Analysis

The object of investigation was the three-phase induction squirrel-cage motor of 380 V (star connected) with rated output power 0,37 kW. Table 1 shows the specification of the motor.

Table. 1 Specification of analysed motor

Diameter of Rotor and Stator	60,5 mm, 106 mm	Number of series turns in stator winding	612
Air gap length	0,25 mm	Rotor winding	Aluminium Cage
Core Length	56 mm	Number of stator and rotor slots	24, 18
Number of phase and poles	3 phases, 4 poles	Depth of Secondary Slot	10,56 mm
Primary Winding Resistance	21 Ω	Rotor cage skew	one slot pitch
Primary Winding Pitch	Single layer, 5/6 short pitch		

The presented motor was used to study the influence of the representation of the windings on the results for voltage driven model and to compare the results of edge element methods with vector potential and nodal element methods with scalar potentials representations of the motor. Finally both models were compared with experimental results. Because the real winding produces some extra effects connected to coil-ends, the simplified model for 3D calculation was taken into account, consisting of one coil of the winding only. The winding coil was represented by a different number (from 1 to 4) of standard Modeller (Opera 3D pre-processor) constant perimeter ends (cpe) coils. Each coil can be represented by different number of elementary filaments. During mesh generation, the mesh generator ensures that the edges of the elements lie along the representative filaments in the coil. During the analysis, the vector potential along the edges was integrated to compute the flux linked to the winding. Therefore an appropriate mesh density is needed for proper representation of windings filaments.

Case A one “cpe” coil one filament Case B two “cpe” coils two filaments

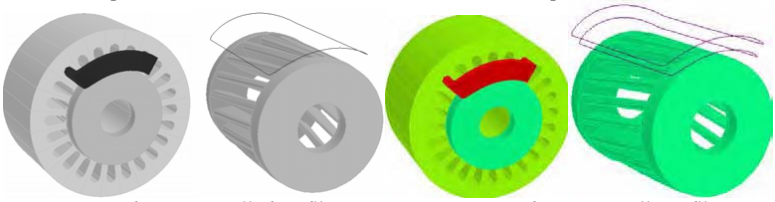

Case C four “cpe” coils four filament Case D four “cpe” coils 36 filaments

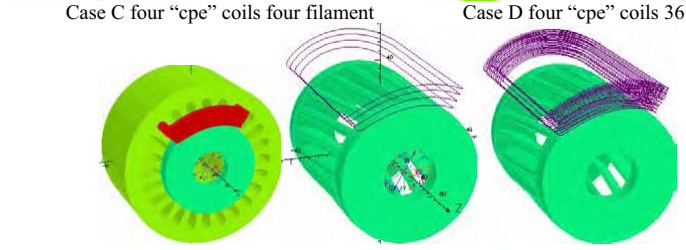

Fig.1 The simplified 3D models of the investigated motor with different coil representation

In order to compare different 3D computation results, the starting conditions were taken into account. For voltage excitation (77,78 V), the coil current and power losses in rotor cage were investigated.

Analysis of the presented cases show that integral values like coil current or power losses are not very sensitive to discretization density and representations with four filaments in case C produces adequate results.

Table. 2 Comparison of different coil representations

Case	Number of elements	Coil current A	Deviation from case D %	Power losses in rotor cage W	Deviation from case D %
D	2072000	8.36		48.304	
C	2072000	8.23	-1.54	48.7	0.82
B	680235	8.64	3.33	50.984	4.69
B	2072000	8.51	1.81	49.138	-3.62
A	680235	8.19	-2.01	45.53	-7.34

In Fig. 2, the complete model of the motor is shown. The stator windings overlap each other at the coil-ends because the real shape of the winding's outhangs is very complicated. Nevertheless, the amount of currents in the coil-ends region is equal to the real one.

voltage driven model current driven model

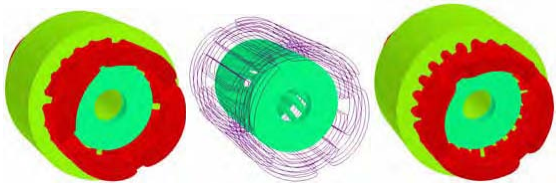

Fig.2. The complete 3D models of the investigated motor

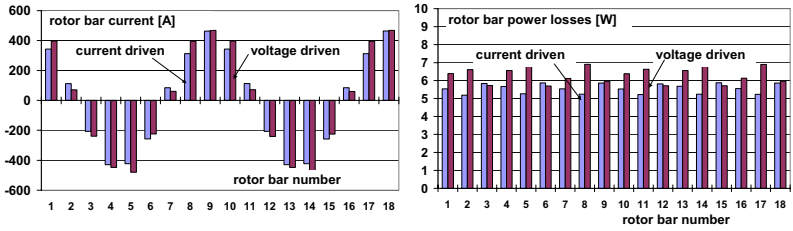

Fig.3. Comparison of results for current and voltage driven models

As can be seen in Fig. 3, although the results obtained with current and voltage driven models differ slightly, the discretisation and representation of the conductive region are the same.

In Fig. 4, the comparison of motor phase currents, measured and calculated using the voltage driven model, is presented. The discrepancies between calculation and measurements have a source partly in the technology of production of fractional power motors where proper air gap length is obtain through rotor turning.

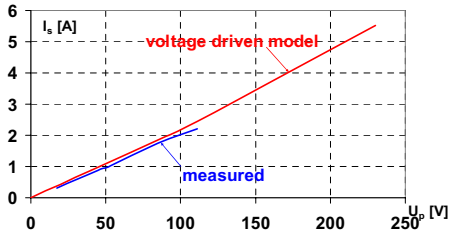

Fig.4. Comparison of measured and calculated using voltage driven model's values of starting currents

In Fig. 5, the comparison of rotor power losses, measured and calculated using voltage driven and current driven models, is presented. The accuracy for the voltage driven model is a little bit better even

though for the current driven model, the stator currents have been taken from measurements. The time of calculation for the voltage driven model is 1.8 times shorter than the current one, despite the number of equations is 20% lower. The reason for this is a large amount of time needed to calculate source magnetic field strength on the reduced-total scalar potential's boundaries in the case of complicatedly shaped windings.

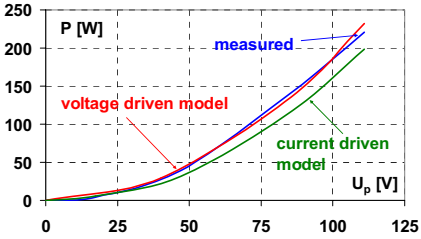

Fig.5. Comparison of measured and calculated, using voltage driven and current driven models, values of rotor power losses at starting

Conclusion

The obtained results of using 3D voltage driven edge elements for modelling of fractional power induction motors shows the possibility of efficient investigation of analysed objects especially at start-up. Experimental verification shows that the method is adequately accurate especially for calculation of rotor power losses. Comparison with widely used current driven models exploiting scalar potentials demonstrates that vector potential edge elements are, in this case, more efficient due to shorter calculation time and slightly better accuracy.

References

[1] Nakata, T., Takahashi, N., Fujiwara, K. and Ahagon, A. (1988), „ 3-D finite element method for analysing magnetic fields in electrical machines excited from voltage sources", IEEE Transaction on Magnetics, vol. 24, no. 6, pp 2582-2584.

[2] Bossavit, A., (1988), "Whitney forms: a class of finite elements for three-dimensional computations in electromagnetism", IEE Proceedings, Vol. 135, Pt. A, No. 8, pp 493-500

[3] Emson, C.R.I., Trowbridge, C.W., (1988), "Transient 3D eddy currents using modified magnetic vector potentials and magnetic scalar potentials", IEEE Transaction on Magnetics, vol. 24, no. 1, pp 86-89.

[4] Bouissou, S., Piriou, F., (1994), "Comparison between two formulation in terms of potential for the coupling of magnetic and electric circuit equations", IEE Proceedings. – Science Measurements Technology, Vol. 141, No. 6, pp 486-490.

[5] Lai, H.C., Leonard, P.J., Rodger, D., Allen, N., (1997), "3D finite element dynamic simulation of electrical machines coupled to external circuits", IEEE Transaction on Magnetics, vol. 33, no. 2, pp 2010-2013.

[6] Pinho, A.C., Sadowski, N., Kuo-Peng, P.,Bastos, J.P.A., Batistela, N.J., (1998), „A general method for coupling electronic circuits with 3D electromagnetic fields", IEEE Transaction on Magnetics, vol. 34, no. 5, pp 3166-3169.

[7] Dems M., Leśniewska E., Komęza K., Wiak S. (1998), "Finite-element method accuracy in three-dimensional field analysis of induction motors", Electromotion, vol.5, no.3, pp.103-106.

[8] Golovanov, C., Marechal, Y., Meunier, G., (1998), „3D edge element based formulation coupled to electric circuits", IEEE Transaction on Magnetics, vol. 34, no. 5, pp 3162-3165.

[9] Wiak S., Komęza K., (1999), "Field/Torque modelling of Electromagnetic Devices by Use of Opera-3D Code", International Workshop on Electric Machines, Prague, 8-9 September, pp. 12-24

[10] Demenko, A., (2002), "Representation of windings in the 3-D finite element description of electromagnetic converters", IEE Proceedings. – Science Measurements Technology, Vol. 149, No. 5, pp 186-189.

[11] Xu, E.X., Simkin, J., (2004), " Total and reduced magnetic vector potentials and electrical scalar potential for eddy current calculation", IEEE Transaction on Magnetics, vol. 40, no. 2, pp 938-940.

[12] Biro, O., Preis, K., Buchgraber, G., Ticar, I., (2004), „Voltage-driven coils in finte-elements formulations using a current vector and a magnetic scalar potential", IEEE Transaction on Magnetics, vol. 40, no. 2, pp 1286-1289

[13] OPERA-3D– version 10.5, Software for electromagnetic design from VECTOR FIELDS

Electromagnetic Fields in Mechatronics, Electrical and Electronic Engineering
A. Krawczyk et al. (Eds.)
IOS Press, 2006

ANALYSIS OF INDUCTION HEATING PROCESS IN HOT GALVANIZING LINE OF STEEL SHEETS

K.Kurek[1], M.Niklewicz[1], W. Koszuta[2]

[1]Electrotechnology Department, Silesian University of Technology,
Krasinskiego 8, 40-019 Katowice, Poland, krzysztof.kurek@polsl.pl
[2]Mittal Steel Poland, unit Swietochlowice, Metalowcow 5, 41-600 Swietochlowice

***Abstract** – Analysis of work of a flat two-sided induction heater has been presented in the paper. The analyzed heater type is applied in the hot galvanizing process of flat heaters where it is used to achieve the temperature growth of galvanized steel sheets. In order to enable achieving proper temperature growth the knowledge of influence of such parameters as supplying frequency and thickness of the heated steel sheets is necessary. The calculations have been carried out using a stationary model. Due to big velocity of a heated strip skipping the movement factor can lead to some mistakes. To assess their significance results obtained for a model taking the movement factor into consideration have also been presented.*

Introduction

Hot galvanizing is one of the most popular technologies preventing steel elements from corrosion. The continuous method is used for galvanizing of steel sheets and wires. This process the scheme of which has been shown in Fig. 1 is carried out on the complex lines equipped in large number of devices [1].

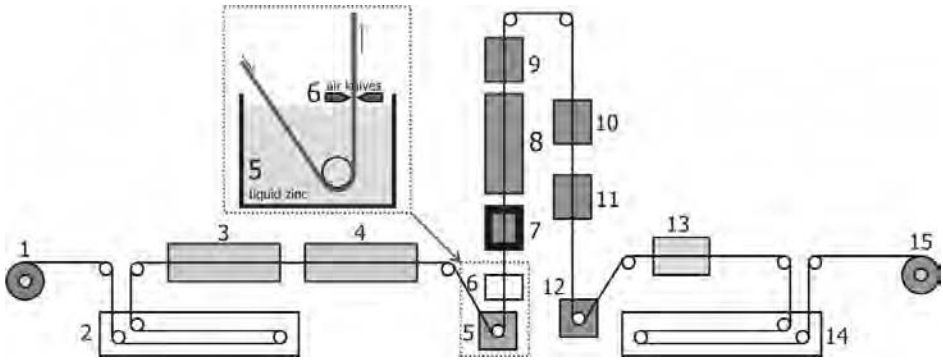

Fig.1. Simplified scheme of hot galvanizing lines. Designations: 1-decoiler, 2-strip input accumulator, 3-system of surface preparation, 4-system of annealing furnaces, 5-galvanizing pot, 6-air knives, 7-induction heater, 8-gas heater, 9,10,11-air coolers, 12-water cooler, 13-system of final treatment, 14- strip output accumulator, 15-coiler

The process is carried out in different ways in order to obtain products of highest quality and maximally suited for recipients. Differences between them are in temperatures reached during the particular production stages, speed of strip movement, chemical constitution of the bath, presence of finishing processes et al. Additional heat treatment is applied in one type of the galvanizing technology of steel strips called galvannealing [2][3]. This is an additional treatment of strip that has already been coated in the galvanizing pot. Such action leads to properties alteration of the obtained coat. The coat despite significant increase of alloy layers has good weldability, is well suited for putting painting coats, has good anti-corrosion resistance and can be deeply drawn. Because of these advantages the galvanized steel sheets are widely used in the automotive industry and can also be noticed in the household goods.

Two types of heaters are the most used in the galvannealing process: the induction one and the gas one. The induction heater is used for increasing temperature while the gas one for keeping the steel sheets in the set temperature. The induction heater has flat winding placed on both sides of the charge. The inductor is supplied from the transistorized inverter which is a source of current of between ten and twenty to several hundreds kHz. The heater is steered by setting the quantity of current flowing through the inductor. Its operation however is in changing conditions because of changing supplying frequency and thickness of the galvanized steel sheet. The changing conditions of operation cause changes of strip output temperature. In order to keep it on the set level required by the process the knowledge of the influence on the heating process of the mentioned above parameters: supplying frequency and steel sheet thickness is necessary.

Calculation model

The calculation model has been worked out in order to make the analysis of the work of induction heater (Fig. 2a) in different operation conditions. It is shown in Fig. 2b.

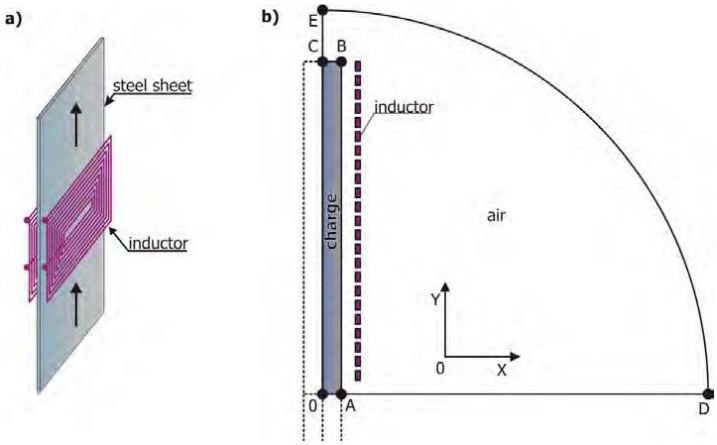

Fig. 2. Induction heater used in production process (a) and worked out calculation model (b)

The calculation model consists of the following elements: a charge (steel), inductor coils (copper) and surrounding air. The basic geometrical parameters and material properties have been put into Table 1 and 2. The heating time has been assumed at 3 seconds which corresponds to velocity of 30 m/min. The calculations has been done for three thicknesses of the charge (1 mm, 1,5 mm and 2 mm) and three supplying frequencies (f_1 = 50 kHz, f_2 = 100 kHz, f_3 = 200 kHz).

Table 1. Model geometrical dimensions

charge height *	750 mm
charge thickness *	0,50 mm (variant G1), 0,75 mm (variant G2), 1,00 mm (variant G3)
distance charge-inductor	7,50 mm (variant G1), 7,25 mm (variant G2), 7,00 mm (variant G3)
inductor coil height	25 mm
inductor coil width	10 mm
distance between coils	5 mm
number of inductor coils*	24

* - ½ real quantities/numbers

Table 2. Material properties

steel	electrical conductivity	σ	$4 \cdot 10^6$ S/m
	magnetic permeability	μ	500
	thermal conductivity	λ	48 W/(m·K)
	accumulativity	ρc	$2{,}75 \cdot 10^6$ J/(m^3·K)
	convection factor*	α_k	15 W/(m^2·K)
	emissivity*	ε	0,20
inductor	electrical conductivity	σ	$55 \cdot 10^6$ S/m
	magnetic permeability	μ	1
air			properties of vacuum have been assumed

* conditions of heat exchange have been assumed as for zinc

The calculations of electromagnetical and thermal fields have been carried out using the computer program Flux 2D. The program is based on the finite elements method. A pair of potentials is used for the electromagnetic field calculations: vector potential of magnetic field $\boldsymbol{A}$ and scalar potential of electric field V as in the following equations [4]:

$$j\omega\sigma \boldsymbol{A} + \mathrm{rot}\left(\frac{1}{\mu} \cdot \mathrm{rot}\, \boldsymbol{A}\right) = \boldsymbol{J} \tag{1}$$

where: ω – pulsation, σ – conductivity, μ – magnetic permeability, $\boldsymbol{A}$ – magnetic vector potential, $\boldsymbol{J}$ – source current density.

The Dirichlet's boundary condition A=0 (Fig.2) has been defined on the border of the calculation area.The thermal field calculations contain the charge area and the Fourier-Kirchoff's equation is applied:

$$\nabla(\lambda \nabla T) = \rho c \frac{\partial T}{\partial t} - w \tag{2}$$

where: T – temperature, λ - thermal conductivity, $w = \sigma\omega^2 \underline{A}\underline{A}^*$ - volume density of power.

The exchange of heat with the environment on the charge surface happens through convection and radiation and has been taken into account with a following boundary condition:

$$-\lambda \frac{\partial T}{\partial \mathrm{n}} = \alpha_k \cdot (T - \mathrm{T_{ac}}) + \varepsilon \cdot \mathrm{C}_0 \cdot (T^4 - \mathrm{T_{ar}^4}) \tag{3}$$

where: T – temperature, $\mathrm{T_{ac,r}}$ – temperature of convection and radiation environment, α_k – convection coefficient, ε – emissivity, C_0 –Stephan – Boltzman's constant.

The numerical calculations for the assumed frequencies and geometrical dimensions required using a computer equipped with a quick processor and big enough Random Access Memory. It is caused by big differences between dimensions of penetration depth of electromagnetical field into the elements of charge and inductor as well as big size of the examined object. With frequencies in the range of several hundred kHz the penetration depth of the field can be below 0,1 mm, which means that for object size expressed in meters the number of elements of the net enabling precise calculations can be higher than five hundred thousand elements.

Calculation results

The temperature distributions on the charge surface have been compared to assess the influence of steel sheet thickness supplying frequency on the heating process. Fig. 3 shows temperature distributions depending on the charge thickness and comparison of electrical efficiency of the system with frequency 100 kHz.

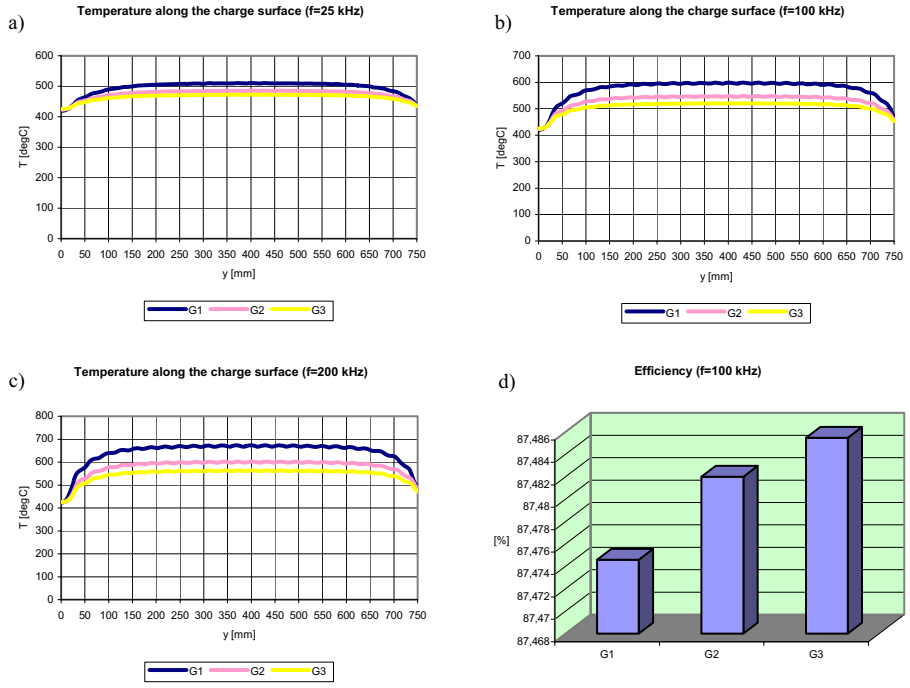

Fig. 3. Charge surface temperature (a, b, c) and electrical efficiency of system (d)

The influence of inductor supplying frequency on the obtained temperature distribution on the charge surface and electrical efficiency of the heater is shown in the following diagrams (Fig. 4).

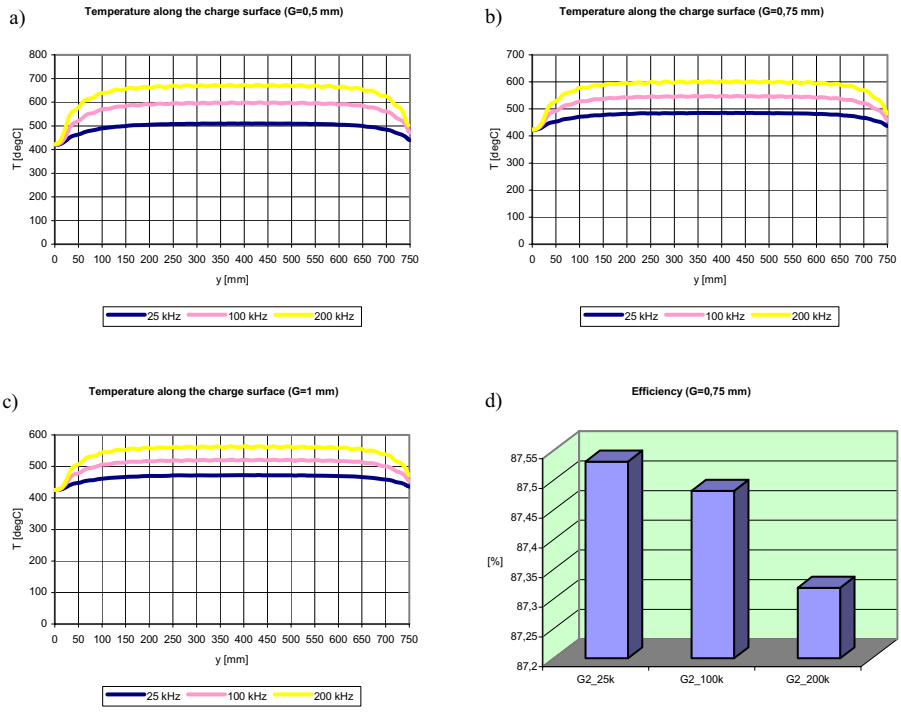

Fig. 4. Charge surface temperature (a, b, c) and electrical efficiency of system (d)

Assessment of movement influence on obtained results

A stationary model of induction heater has been used in the presented analysis. However in real conditions the charge moves inside the inductor with velocities up to 100 m/min. Not taking movement factor into account makes the obtained results somewhat erroneous. A simulation of a heater's model using the stationary model and the model taking movement into account [5] has been made in order to assess the size of this error. Calculations were carried out according to the following equations:

$$\nabla \times \left(\frac{1}{\mu} \nabla \times \boldsymbol{A} \right) = \boldsymbol{J} - \sigma \left(\frac{\partial \boldsymbol{A}}{\partial \boldsymbol{t}} + \mathbf{v} \times \nabla \times \boldsymbol{A} \right) \tag{4}$$

$$\nabla \left(\lambda \nabla T \right) = \rho c \left(\frac{\partial T}{\partial t} + \mathbf{v} \cdot \nabla T \right) - w \tag{5}$$

where: $\mathbf{v}$ – charge's velocity.

Comparison of obtained results is shown in Fig. 5.

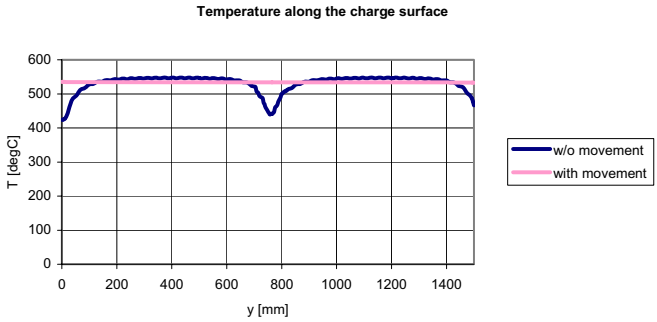

Fig. 5. Comparison of temperature on the charge surface using stationary model and model taking movement into account

Conclusions

The obtained calculation results enabled the assessment of changing parameters (charge thickness and frequency) influence on the heating process of steel strip. The carried out analysis shows that during heating of strips of bigger thickness the inductor's current needs to be supplied with higher current (Fig. 3a, b, c) in order to have comparable heating effect. Increasing frequency leads to heating the charge to higher temperature (Fig. 4a, b, c). This change requires also the correction of power source supplying the inductor when obtaining the charge set temperature at the inductor's exit is needed. Electrical efficiency analysis proved that supplying frequency and charge thickness does not lead to its noticeable changes (Fig. 3d, 4d).

The observed relation can be of significant help in operation of the considered induction heater in industry conditions.

The analysis is simplified by using the model not taking movement into account for calculations however it leads to some mistakes. On the basis of temperature distribution comparison on the charge surface obtained using the stationary model and the model taking movement into account (Fig. 5) it can be said that the differences in obtained temperature are not significant. This conclusion is true for the substantial length of the charge where the difference in temperature in both cases was not more than 15°C. Considerable differences occur only in the outermost parts of the charge, which can be acceptable in some kinds of research.

Literature

[1] M. Niklewicz: Examination of the temperature distribution in a steel strip during hot dip galvanizing process. VI Międzynarodowa Sesja Studencka "Materiały i Technologie XXI Wieku", Katowice, 2004, pp 137-142.
[2] A. R. Marder: The metallurgy of zinc-coated steel. Progress in materials science 45, pp 191-271.
[3] P. Maab, P. Pieibker: Cynkowanie ogniowe. Wydawnictwo Placet, Warszawa 2003.
[4] Flux2D v.9.1 User's guide. Cedrat-Grenoble France 2004.
[5] K. Kurek: Modelowanie procesu nagrzewania indukcyjnego wsadu w przelocie. Zeszyty Naukowe Politechniki Świętokrzyskiej – Elektryka nr 36. Kielce 2000, pp 215-222.

Electromagnetic Fields in Mechatronics, Electrical and Electronic Engineering
A. Krawczyk et al. (Eds.)
IOS Press, 2006

VERIFICATION OF AXI-PERIODIC ANALYSIS WITH 3D-FEA AND CALCULATION OF EDDY CURRENT LOSS OF FLUX SHIELD IN THE LARGE TURBO GENERATOR USING AXI-PERIODIC ANALYSIS

S. O. Kwon, Hyuk Nam, B. Y. Choi, J. P. Hong, *Senior Member, IEEE*

Dept. Electrical Eng., Changwon Nat'l Univ., Changwon. Gyeongnam, 641-773 Korea
LG Electronics.
Doosanheavy Industires and Construction Co., Ltd.
(kso1975@changwon.ac.kr)

Abstract *–Axi-periodic analysis for end region of large turbine generator is studied and verified by 3D-FEA in this paper. Verification is done by comparing three components of flux densities from axi-periodic analysis and 3D FEA in static field, and the comparison shows some differences, and the cause of those differences are studied. Even though, the differences, considering computation time and effort for modeling of 3D FEA, the errors would be acceptable for initial design of large turbine generator. Then, axi-periodic analysis is extended to time harmonic field for its application. From the time harmonic field analysis, the effect of flux shield and eddy current loss in the flux shield for power angles are presented.*

Introduction

As a quasi 3-dimensional analysis, axi-periodic analysis is applied to the magnetic field for the end region of large turbine generator in [1] - [6]. Since axi-periodic analysis provides 3-dimensional flux distributions with 2-dimensional finite element modeling, it reduces computation time and efforts greatly comparing to 3D FEA. Many researches, applications, and verifications for axi-periodic analysis have been done since 1970's. However, the verifications are made only by measurements in small regions because measurements of flux density in the end region are limited in practical aspects.

Therefore, axi-periodic analysis is verified by 3D-FEA in this paper. Three components of flux densities from axi-periodic analysis and 3D FEA are compared in static field. To do that, 3D FEA model is constructed precisely including stator end windings based on an actual large turbine generator.

Axi-periodic formulations for time harmonic field using magnetic vector potential is firstly set for the field analysis. Then, three components of flux densitis from axi-periodic analysis are compared to that from 3D FEA in the static field. The comparison shows differences, and the cause of the error is studied. In spite of the differences, considering computation time and effort for modeling of 3D FEA, the errors would be acceptable for initial design of large turbine generator.

Axi-periodic analysis is extended to time harmonic field for its application. In time harmonic field analysis, eddy current loss in flux shield for load condition is calculated, and flux distribution due to the eddy current in flux shield is presented.

In the large turbine generator (ratings of 500MW or over), leakage flux in the stator end windings is the major design limitation of capacity due to the thermal effect caused by eddy current in stator end [1], [2]. The eddy current on the stator end region is mainly produced by axial component of leakage flux of stator and rotor end windings, and to prevent the axial flux impinging to the stator end, the flux

shield made of copper is placed in the stator end region of large turbine generator. Due to the eddy current on the flux shield, leakage flux cannot go through the stator end region, and temperature in the flux shield can be high. However, flux shield is made of copper having high thermal conductivity, therefore, cooling can be easy comparing laminated stator core.

Analysis Theory

In order to apply the finite element method to an axi-periodic model, following assumptions are made:[3]

a) Slot effects are not considered
b) Displacement current is ignored.
c) Magnetic material is isotropic with infinite permeability.
d) The analysis model is axi-symmetric.
e) Current density in rotor and stator windings are assumed to be consist of axial and circumferential components with sinusoidal distributions along axial and circumferential direction respectively.

Governing equations using vector potential for time harmonic fields are (1) and (2).

$$\nabla \times (\nu \nabla \times \vec{A}) = -\sigma(\frac{\partial \vec{A}}{\partial t} + \nabla \phi) + \vec{J}_o \tag{1}$$

$$\nabla \cdot (\sigma \frac{\partial \vec{A}}{\partial t} + \sigma \nabla \phi) = 0 \tag{2}$$

where, ν , $\vec{A}$, σ , ϕ , and $\vec{J}_o$ is magnetic reluctivity, magnetic vector potential, conductivity, electric scalar potential, and current density respectively.

Weighting function (W_i) and shape function (N_i) for Galerkin formulation are (3) and (4) respectively, and residuals are represented in (5) and (6).

$$W_i = N_i(r,z)e^{jp\theta} \tag{3}$$

$$N_i(r,\theta,z) = N_i(r,z)e^{-jp\theta} \tag{4}$$

$$R = -\int \nabla(N_i e^{jp\theta}) \times (\nu \nabla \times \vec{A}) dv + j\omega\sigma \int (N_i e^{jp\theta}) \vec{A} dv + \sigma \int (N_i e^{jp\theta}) \nabla \phi dv - \int (N_i e^{jp\theta}) \vec{J}_o dv \tag{5}$$

$$R_\phi = -\int \nabla(N_i e^{jp\theta}) \cdot (j\omega\sigma \vec{A} + \sigma \nabla \phi) dv \tag{6}$$

Using N_i, magnetic vector potentials and electric scalar potentials are represented in r-z plane by (7) – (10).

$$A_r(r,\theta,z) = \sum_k A_r^{\,k} N_k(r,z) e^{-jp\theta} \tag{7}$$

$$A_\theta(r,\theta,z) = \sum_k A_\theta^{\,k} N_k(r,z) e^{-jp\theta} \tag{8}$$

$$A_z(r,\theta,z) = \sum_k A_z^{\,k} N_k(r,z) e^{-jp\theta} \tag{9}$$

$$\phi(r,\theta,z) = \sum_k \phi_k N_k(r,z) e^{-jp\theta} \tag{10}$$

Current distributions in conductors are represented by (11) - (13).

$$J_{or}(r,\theta,z) = J_r(r,z) e^{-jp\theta} \tag{11}$$

$$J_{o\theta}(r,\theta,z) = J_{\theta}(r,z)e^{-jp\theta} \tag{12}$$

$$J_{oz}(r,\theta,z) = J_{z}(r,z)e^{-jp\theta} \tag{13}$$

Analysis Model

3D analysis model of 800MW turbine generator is shown in Fig. 3. Based on the periodicity and symmetry, 1/4 model is used for 3D FEA. Commercial software, Flux-3D, is used and analysis is performed in magneto static field. Field variable of 3D FEA is magnetic scalar potential; armature windings are modeled with non-meshed coils. 3D FEA model is precisely constructed considering stepped core and end step of stator as well as stator end windings, but non-magnetic retaining ring of rotor and flange of stator core are not considered. For stator end windings, coordinates of the windings are obtained from actual generator and one top and bottom coils consist of 10 segments of coils. 420,000 of elements are used and it takes 5 hours for single step with Pentium IV and 2GB RAM.

Axi-periodic analysis model is shown in Fig. 2, non-magnetic flange is not considered in the analysis and modeled region represents when a-phase is peaking. To make the comparison easy, only stator windings are excited for both analysis models. Fundamental component of current is applied to the stator and rotor end windings for the analysis. Total number of elements is 14,000, and it takes about 30 seconds for single step.

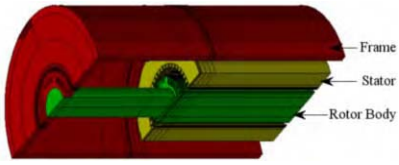

(a) Cross section of large turbine generator (1/4 model)

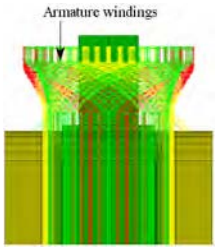

(b) Armature winding

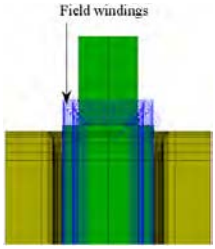

(c) Field winding

Fig. 1 3D FEA analysis model

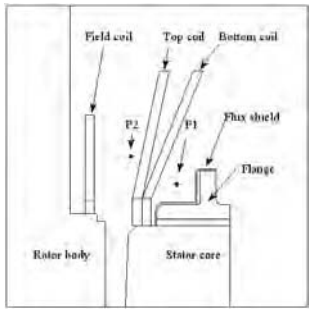

Fig. 2 Axi-periodic analysis model

Analysis Result And Comparison

Three components of flux densities (B_r, B_θ, B_z) from axi-periodic analysis are compared to those from 3D FEA in Fig. 3, flux densities from axi-periodic analysis agree well with 3D FEA except B_θ at P1. It is expected that the error is caused by the assumption of sinusoidal current distribution in axi-periodic analysis. Therefore, the current distribution in the stator end region is studied.

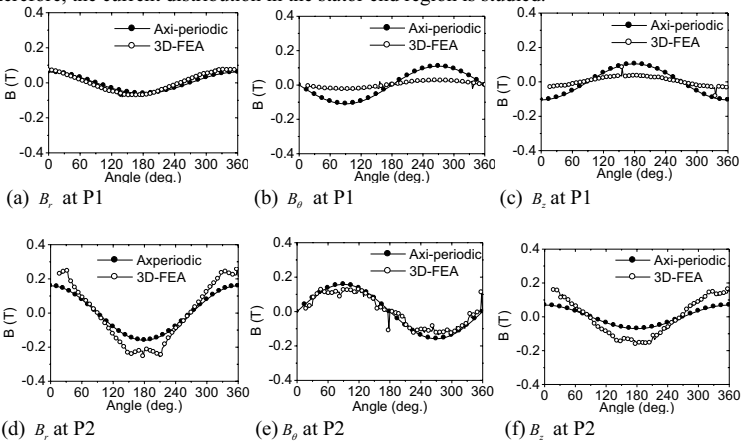

Fig. 3 Comparison of flux densities from axi-periodic analysis and 3D FEA

Current distribution in end windings

To find out the cause of differences between axi-periodic analysis and 3D FEA, current distribution in the stator end winding according to current phase angle, 3-phase stator end windings is studied. In order to compare the current distributions of axi-periodic analysis model and 3D FEA stator end windings, stator windings are represented as shown in Fig. 4, where solid lines represent coils going out from stator slots, and dot lines represent coil going into stator slots. Coils on the right side of slots are top coil and on the left side are bottom coil. Peak value of 3-phase current is set to 1. When a-phase current is peaking, I_θ, and I_z along line L1 and L2 are calculated and compared to sine and

cosine function in Fig.5.

In Fig. 3 (b), the compassion shows a big difference. The difference is caused by the I_z current and this is shown in Fig. 5 (b), where I_z producing B_θ in the 3D FEA model is zero, while that in axi-periodic model has some value.

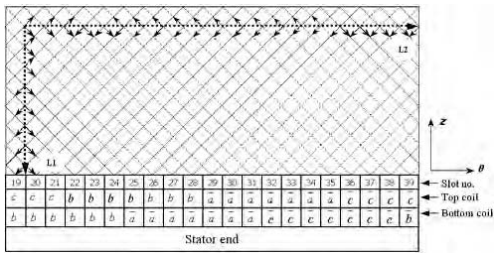

Fig. 4 Current distribution on the stator end winding

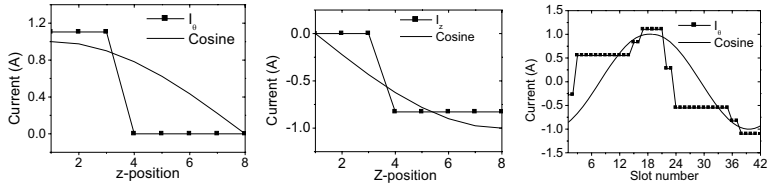

(a) I_θ along L1 (b) I_z along L1 (c) I_θ along L2

Fig. 5 Estimation of current distribution on the stator end windings

Applications

Eddy current loss in the flux shield is calculated using (14), where, p_e^k, k, J_e^k, and σ^k are the eddy current loss in flux shield, harmonic order, eddy current density, conductivity in flux shield respectively. Only fundamental component of eddy current density is considered in this paper.

$$p_e^k = \frac{1}{2}\mathrm{Re}\left[\int_v \frac{J_e^k \cdot J_e^{k*}}{\sigma^k}\right] \quad , \; P_e = \sum_k p_e^k \;[\mathrm{W}] \tag{14}$$

In Fig. 6, (a) shows the eddy current loss in the flux shield for power angle. For the leading power angles, field from rotor windings and stator windings are additive, on the contrary, field are subtractive in lagging power angle. Therefore, higher eddy current loss is produced in the leading power angle than lagging power angle.

In Fig. 6, (b) flux distribution due to the eddy current in the flux shield at no load is shown. Because of eddy current in the flux shield, flux caused by end windings tends to take other paths around flux shield. In the figure, four corners in the flux shield show high flux densities, therefore it can be said that the flux density on the surface of flux shield represents the eddy current distributions. Therefore, in the figure, regions of high flux density have high eddy current density, and high temperature is expected.

The effect of flux shield is shown in Fig. 7. When the frequency is 0Hz, that is DC field, flux caused by end windings goes to the stator end directly, therefore, the flux shield does not work. However, when the frequency is 60Hz, eddy current is induced in the flux shield and flux caused by end

windings cannot go through stator end directly.

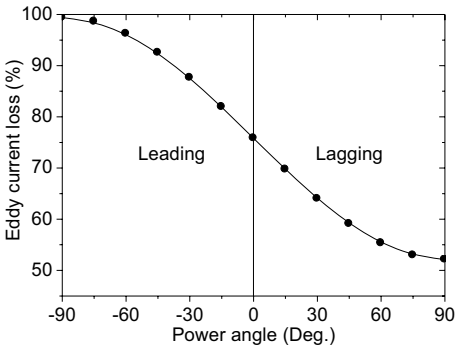

(a) Eddy current loss for load conditions

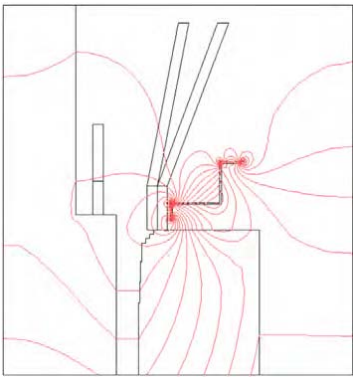

(b) Flux caused by eddy current in the flux shield

Fig. 6 Eddy current loss of the flux shield and flux distribution due to eddy current in flux shield

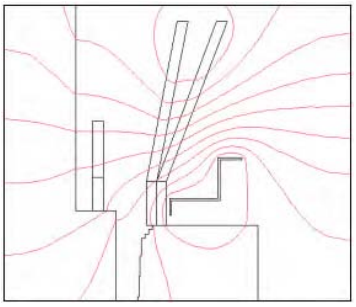

(a) Flux distribution at 60Hz

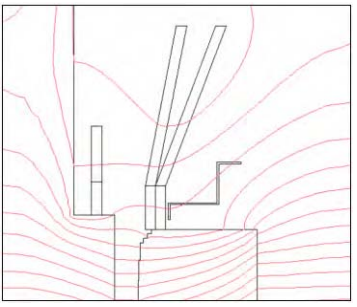

(b) Flux distribution at 0Hz

Fig. 7 Flux distribution for frequencies

Conclusion

Axi-periodic analysis for magnetic field of end region in large turbine generator is studied and verified by 3D FEA in this paper. Due to the differences between the sinusoidal current distribution and the actual one, comparison of flux distribution on the end region shows the differences, and the difference is proved by the comparison of current distribution on the stator endwindings. In spite of the error of axi-periodic analysis, considering the effort and calculation time for 3D FEA, the error would be acceptable for initial design of large turbine generator. For the applications of the axi-periodic analysis, the effect of flux shield on the flux distribution of end region is shown and eddy current loss of flux shield is calculated for power angle, and the application can be extended to the geometry design of flux shield, stepped core, calculation of force in the end windings.

References

[1] G.K.M. Khan, G.W. Buckley, R.B. Bennett, N. Brooks, "An Integrated Approach for the Calculation of Losses and Temperatures in the End-region of Large Turbine Generators", *IEEE Trans. on Energy Conv.,* Vol.5, No. 1, March 1990.

[2] Kaoru Ito, Tadashi Tokumasu, Susumu Nagano, Makoto Tari, Shin-ichi Doi, "SIMULATION FOR DESIGN PURPOSE OF MAGNETIC FIELDS IN TURBINE-DRIVEN GENERATOR END REGION", *Trans*. *on Power Apparatus and Systems*, Vol. PAS-99, No. 4 July/Aug 1980.

[3] Sheppard J. Salon, "Finite element analysis of electrical machines", Kluwer academic publishers, 1995.

[4] G.K.M Khan, G.W.Buckley, N. Brooks, "Calculation of forces and stresses on generator end–windings- part I: Forces", *IEEE Trans. Energy Conv.,* vol.4, No. 4, December 1989.

[5] V. Varbero, G. Dal Mut, G. Grigoli, M. Santamaria, "Axisymmetric analysis and experimental measurements of magnetic field in the end region of a turbine generator", *IEEE Tran. on Magn.,* vol. MAG-19, no. 6, November, 1983.

[6] Gary Bedrosian, M.V.K. Chan, Manoj Shah, George Theodossiou, "AXIPERIODIC FINITE ELEMENT ANALYSIS OF GENERATOR END REGIONS PART I - THEORY", *IEEE Trans .on Magnetics*, vol. 25, No. 4, July 1989.

Electromagnetic Fields in Mechatronics, Electrical and Electronic Engineering
A. Krawczyk et al. (Eds.)
IOS Press, 2006

EFFICIENCY EVALUATION OF PMASYNRM VS. SYNRM USING COUPLED FEM & PREISACH MODELING

Rae Hwa Lee[(1)], **Young Jin Jang** [(2)], **Jung Ho Lee** [(3)]

Dept. of Electrical Eng., Hanbat National University, Dukmyung-Dong, Yuseong-Gu, Deajeon, Korea
[(1)] E-mail: naezone0850@naver.com
[(2)] E-mail: jyj6936@naver.com
[(3)] E-mail: limotor@hanbat.ac.kr

***Abstract** – This paper deal with the efficiency evaluations in a Synchronous reluctance motor(SynRM) Vs. PMASynRM using a coupled transient finite element method(FEM) and preisach modeling, which is presented to analyze the characteristics under the effect of saturation and hysteresis loss.The focus of this paper is the efficiency evaluation relative to hysteresis loss, copper loss, etc. On the basis of load condition in a SynRM and PMASynRM. Computer simulation and experimental result for the efficiency using dynamometer shoe the propriety of the proposed method.*

1. INTRODUCTION

In high-speed applications of a SynRM, hysteresis loss can become the major cause of power dissipation. Therefore, whereas in other kinds of machines a rough estimation of hysteresis loss can be accepted, their importance in a SynRM justifies a greater effort in calculating them more precisely.

The preisach model is now generally accepted to be a powerful hysteresis model, and is therefore intensively studied [1]-[3]. By adding proper quantity of permanent magnets the torque density and power factor of SynRM can be greatly increased. It is called Permanent Magnet Assisted Synchronous Reluctance Motor (PMASynRM).

But, it must be that PMASynRM is more saturated than SynRM, due to the additional magnet flux density. In this paper, a coupled finite element analysis and Preisach modeling for a PMASynRM and SynRM are presented and characteristics analysis and efficiency evaluations are performed under the effect of saturation and hysteresis loss. The focus of this paper is the efficiency evaluation relative to hysteresis loss, copper loss, etc. On the basis of load condition in a SynRM and PMASynRM.

Also, TMS320C31 DSP installed experimental device and dynamometer are equipped and experiments are performed. Computer simulation and experimental results for efficiency show the propriety of the proposed a coupled finite element analysis and Preisach model.

2. Modeling and Principle of PMASynRM

2.1 Principles of PMASynRM For High Power Application

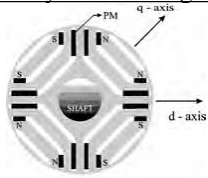

Fig.1 Rotor cross-section of PMASynRM

A cross-sectional view of a PMASynRM is shown in Fig. 1. A normal synchronous reluctance motor runs at a somewhat poorer power factor than the induction motor. This problem can be alleviated by inserting permanent magnets between rotor segments.

2.2 Governing Equation of PMASynRM and SynRM

Maxwell's equations can be written as

$$\nabla \times \vec{H} = \vec{J}_0 \tag{1}$$

$$\nabla \cdot \vec{B} = 0 \tag{2}$$

$$\vec{B} = \frac{1}{\upsilon_0}\vec{H} + \vec{M} \qquad \vec{B} = \frac{1}{\upsilon_0}\vec{H} + \vec{M}_{PM} \tag{3}$$

Where, $\vec{M}$, $\vec{M}_{PM}$ are the magnetization of magnetic material and permanent magnet with respect to the magnetic intensity $\vec{H}$. $\vec{M}_{PM}$ is removed in a SynRM. The magnetic vector potential $\vec{A}$ and the equivalent magnetizing current $\vec{J}_m$, $\vec{J}_{PMm}$ are expressed as follows

$$\vec{B} = \nabla \times \vec{A} \tag{4}$$

$$\vec{J}_m = \upsilon_0(\nabla \times \vec{M}),\ \vec{J}_{PMm} = \upsilon_0(\nabla \times \vec{M}_{PM}) \tag{5}$$

The governing equation derived from (1)-(5), is given by

$$\upsilon_0(\nabla \times \nabla \times \vec{A}) = \vec{J}_0 + \vec{J}_m + \vec{J}_{PMm} \tag{6}$$

2.3 System Matrix

The system matrix can be written as

$$[K^{(e)}]\{A^{(e)}\} + \{F^{(e)}\} + \{M^{(e)}\} + \{M_{PM}{}^{(e)}\} = 0 \tag{7}$$

The overall model is therefore described by the matrix as follows

$$[K]\{A\} + \{F\} + \{M\} + \{M_{PM}\} = 0 \tag{8}$$

2.4 Application of Preisach's Model

The magnetization M can be expressed as a scalar model, because the rotor rotates according to the input current angle θ synchronously. Therefore, it can be supposed that the domain in stator is an alternating field with reference to x axis and y axis. B and H of the domain in rotor is constant and is a rotating field, but it is an alternating field with reference to x axis and y axis, also [4]-[6]. It is natural that M, H which is calculated on the same axis has a same vector direction

$$M(t) = \iint_{\alpha \geq \beta} \mu(\alpha,\beta)\gamma_{\alpha\beta}(H(t))d\alpha d\beta \tag{9}$$

$$= \iint_{S^+(t)} \mu(\alpha,\beta)d\alpha d\beta - \iint_{S^-(t)} \mu(\alpha,\beta)d\alpha d\beta$$

A more convenient treatment of this model is also to substitute the Everett plane for Preisach's one as shown in (10).

$$E(\alpha,\beta) = \iint_{\alpha \geq \beta} \mu(\alpha,\beta)\gamma_{\alpha\beta}(H(t))d\alpha d\beta \tag{10}$$

In the Everett plane, the distributions of M, which is accepted from experimental data of material S40 and ferrite magnet, are Gaussian ones.

3. Result and Discussion

Fig. 2, 3 show the torque characteristics of SynRM and PMASynRM at load 8kg-cm, 12kg-cm, respectively. Fig. 4, 5 shows i-λ loci characteristics according to each load conditions characteristics of SynRM and PMASynRM, respectively.

Whereas average torque density has the same values according to the same load conditions, torque ripples of SynRM are larger than those of PMASynRM as shown in Fig. 2, 3.

The q-axis inductance can be made to approach zero in PMASynRM, theoretically. The compensating flux can normally be obtained by ferrite magnets since L_q is sufficiently low. Whereas L_d is decreased by only saturation, L_q is decreased by additional counteracting the flux of P.M. in PMASynRM. Therefore, the higher currents of a SynRM for the same torque density of PMASynRM, the higher current magnitude as shown in Fig. 4 and this is the reason of high torque ripple of SynRM.

Experimental Comparisons are given with efficiency and currents angle characteristics of normal Synchronous reluctance motor (SynRM) and those of PMASynRM according to load as shown in Fig. 5.

The hysteresis loss can be calculated by the area of the i-λ loci times the frequency (66.7 Hz), and the copper loss can be calculated by the resistance times rms value square of phase current.

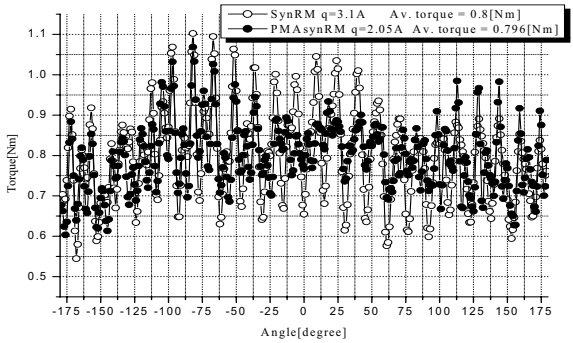

Fig.2 Torque characteristics of SynRM & PMASynRM (load : 8 kg cm)

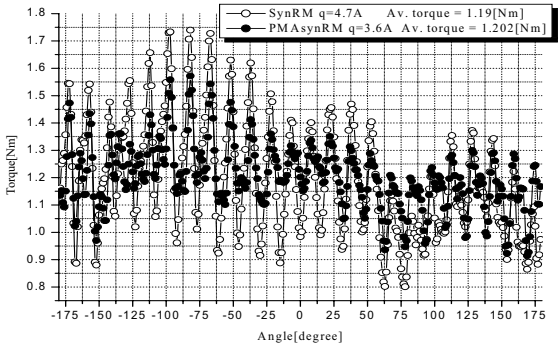

Fig.3 Torque characteristics of SynRM & PMASynRM (load : 12 kg cm)

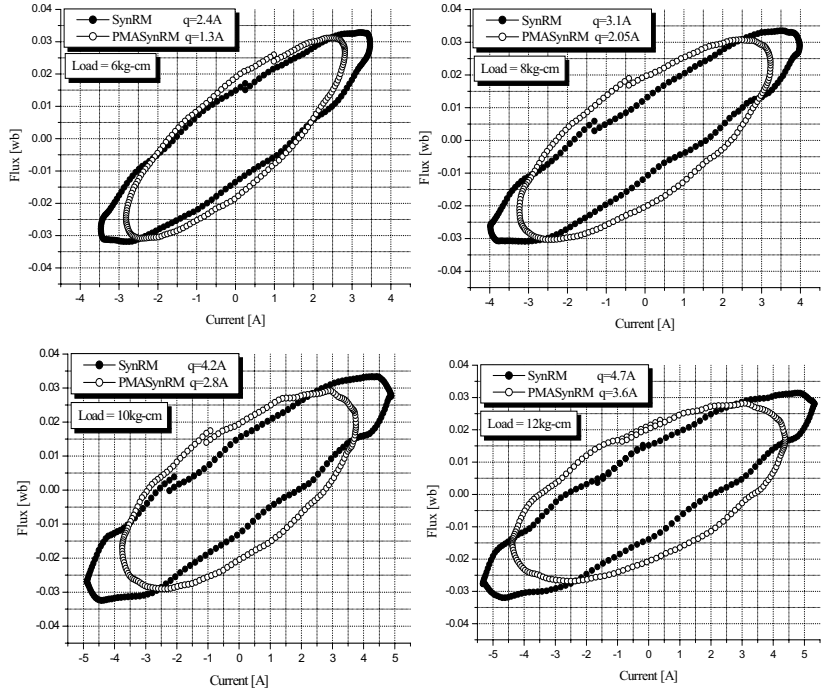

Fig .4 i-λ loci in each load condition

Other losses are the eddy current loss, mechanical loss and the stray load loss, etc. These losses are denoted in TABLE I. Output powers in simulation are the same with that developed in experimental test. Therefore, phase currents are similar to the experimental phase current.

Fig. 6 shows the each loss ratio to the total loss in each load condition. Whereas in hysteresis loss increasing current due to the increasing load should be enlarged, their rate in a core loss should be reduced at higher efficiency condition. However, the copper loss increasing rate of SynRM are lager than those of PMASynRM because of high current for the same torque dissipations, as shown in Fig. 2, 3, TABLE I.

TABLE I.
COMPARISON OF LOSS IN SYNRM AND PMASYNRM

Load (kg-cm)	Efficiency (%)	Hy. Loss (W)	Copper Loss (W)	Other losses (W)	Phase current (A)
		SynRM			
6	83	12.3	19.4	8.6	3.85
8	81	14.6	25.2	15.1	3.74
10	86.2	16.3	30.1	14.6	4.05
12	86.5	18.6	37.9	15.7	4.56
		PMASynRM			
6	83.7	16.3	14.1	5.6	3.46
8	84.7	17.7	17.9	9.45	3.9
10	85.7	18.3	20.1	12.52	4.14
12	86.8	21.3	25.2	9.47	4.63

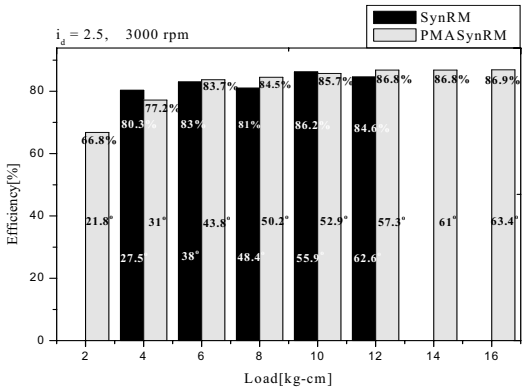

Fig. 5 Efficiency, current angle and runaway point of PMASynRM and SynRM according to load in experimental test

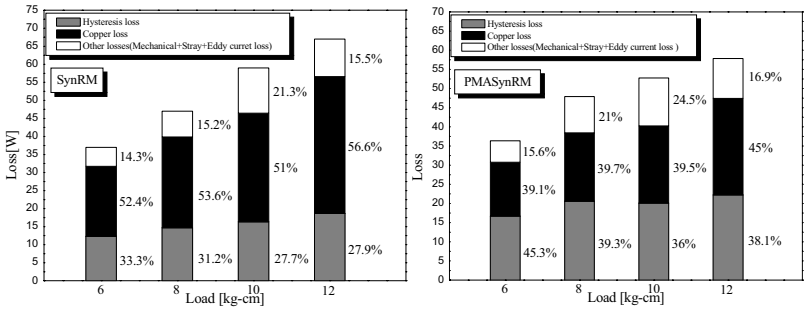

Fig. 6 Loss analysis in each load condition of SynRM and PMASynRM

Whereas the hysteresis loss rate of PMASynRM has the higher percentage than those of SynRM, the hysteresis loss values have similar those.

For the purpose of the reason analysis, the hysteresis responses analysis of teeth and yoke element in PMASynRM and SynRM is performed, when current i_d is 4[A], 25Hz (the same condition).

From the analysis results, we can see that the magnitude of hysteresis in stator teeth is larger than those in yoke as shown in Fig 7 ,8.

And it can be found that PMASynRM is more saturated than SynRM, but have similar hysteresis characteristics in spite of inserting a permanent magnet.

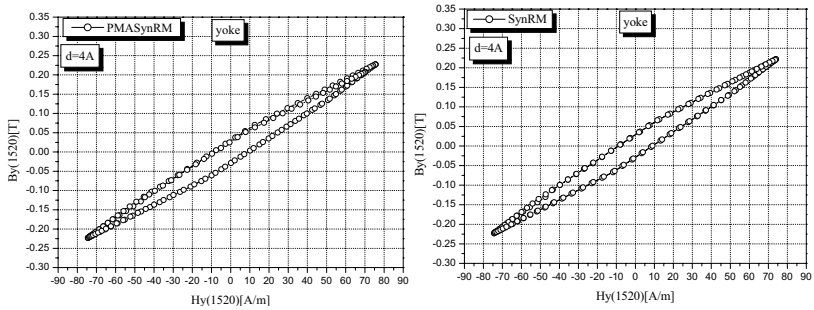

Fig. 7 B-H Curve in a yoke of PMASynRM and SynRM

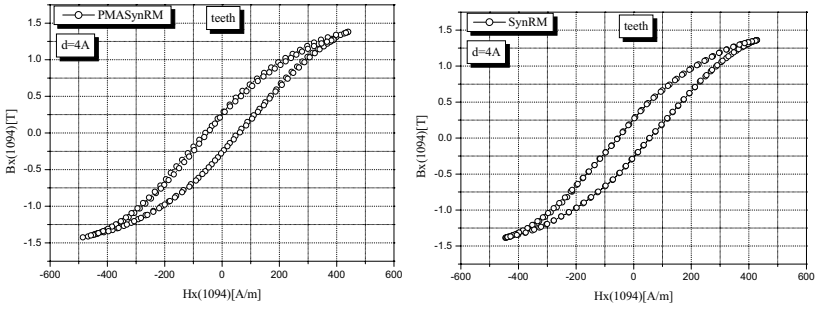

Fig. 8 B-H Curve in teeth of PMASynRM and SynRM

4. Conclusions

A characteristic analysis method has been proposed, which is suited for efficiency evaluation of machines with magnetic non-linearity.

The i-λ loci which is total hysteresis loss, copper loss of a SynRM and PMASynRM(except mechanical loss, eddy current loss, stray load loss which are other losses in this paper) are investigated quantitatively on the basis of the proposed analysis method and the experimental test.

In the PMASynRM, L_q was reduced by inserting permanent magnets in the direction of counteracting q axis flux, which results in increased L_d-L_q and L_d/L_q.

Also, the increased L_d-L_q and L_d/L_q can help improve torque density and power factor.

And It is confirmed that the PMASynRM result in high output power performance through experimental and theoretical (numerical analysis) proof.

Being developed an analysis method combined with a problem of vibration, eddy current loss it is surely possible for more precise analysis of an efficiency and power factor of electromagnetic machine and is useful to the change of a motor's structure, material and the development of control algorithm for high efficiency performance.

References

[1] A. Ivanyi, Hysteresis Models in Electromagnetic Computation, AKADEMIAI KIADO, BUDAPEST
[2] I. D. Mayeroyz, "Mathematical Models of Hysteresis." *IEEE Trans. Magn*, Vol. 22, No.5, pp.603-608 Sept. 1986
[3] A. Visintin, Differential models of hysteresis, Applied Methematical Sciences, Springer, 1994.
[4] J. H. Lee, D. S. Hyun, "Hysteresis Analysis for permanent Magnet Assisted Synchronous Reluctance Motor by Coupled FEM & Priesach Modelling", *IEEE Trans. Magn.,* Vol. 35, No. 5, pp. 1203-1206. May 1999.
[5] J. H. Lee, J. C. Kim, D. S. Hyun, "Effect of Magnet on Ld and Lq Inductance of Permanent Magnet Assisted Synchronous Reluctance Motor", *IEEE Tranl. Magn*., Vol.35, No. 5, pp. 1199-1202, May 1999.
[6] J. H. Lee, J. C. Kim, D. S. Hyun, "Dynamic Characteristic Analysis of Synchronous Reluctance Motor Considering Saturation and Iron Loss by FEM", *IEEE Trans. Magn*., Vol. 34, No. 5, pp. 2629-2632, Sep. 1998.

Electromagnetic Fields in Mechatronics, Electrical and Electronic Engineering
A. Krawczyk et al. (Eds.)
IOS Press, 2006

MAGNETICFIELD ANALYSIS OF NON-CONTACT MAGNETIC GEAR BY USING EQUIVALENT MAGNETIZATION CURRENT

[1]Sang-Ho Lee, [1]Soon-O Kwon, [1]Jung-Pyo Hong, [2]Young-Kyun Kim, and [3]Kyung-Ho Ha

[1]Dept. of Electrical Eng., Changwon Nat'l Univ., Changwon, Gyeongnam, Korea
[2]Digital Appliance Business SAMSUNG ELECTRONICS CO.,LTD. Gyeonggi,Korea
[3]Electrical Steel Research Team of Technical Research Lab., POSCO, Gyeongbuk, Korea
E-mail : tapaya@korea.com, jphong@sarim.changwon.ac.kr, youngkyoun.kim@samsung.com, khha@posco.co.kr

***Abstract** – This paper deals with the analysis method for finding the characteristic of non-contact gears. The permanent magnet of the magnet gear is changed into the equivalent magnetizing current (EMC). And then, the flux density is calculated by Biot-Sarvart law from the current in a closed circuit. The torque of the magnet gear is obtained from the relation between flux density and magnetization current. The proposed analytical method is easier and simpler than the 3-dimensional Finite Element Analysis (3D FEA). The analysis results are compared with the experiment and the numerical analysis results.*

Introduction

The conventional conveyor used in semiconductor manufacture adopts belts and various mechanical gears for power transfer from a drive source, and raise dust due to contact. Therefore, some special cleaning mechanisms are demanded for the reason. Recently, permanent magnets, owing to the development of various high-grade magnetic materials, are widely used in many applications such as motors, sensors, actuators, PM torques, etc. [1]. The non-contact gear using permanent magnets could be an attractive transmission mechanism for the conveyor system because it does not generate any dust.

Magnet gear consists of driven and driving skewed permanent magnets, like the helical type gear shape. The respective axes of the upper magnet and the lower magnet intersect each other perpendicularly and the respective peripheral surfaces are close to each other, but not in contact with each other, separated by a relatively small air gap. The torque is produced by the electromagnetic phenomenon between two permanent magnets. The permanent magnet with skew mounted at a 90 ($^{\circ}$) changes the transmission for direction without any direct contact.

A characteristic analysis is very important to investigate the influences of main parameters related to the performance of the before designing it [2]. The magnet gear demands the 3-dimensional analysis. The popular method for 3D electromagnetic problems is 3D Finite Element Analysis, which is still powerful. However, the numerical method has some disadvantages, such as great computing time, complicated process and unsuitableness for the initial design stages.

Therefore, an alternative method should be considered, the analytical approach based on the concept of the EMC could be useful for the design and analysis of the non-contact gear with permanent magnet. In this paper, the simplest EMC method coupled with Biot-Sarvart law is proposed to solve the 3-D electromagnetic problem. The permanent magnet is changed into the equivalent magnetization surface current [3-4], and the flux density is computed by Biot-Sarvart law from the calculated surface current. Then, the magnetic torque of the gear is obtained from the relation between flux density and the

magnetization current. First, for the validity of the analysis method, the flux density of the cylinder and square permanent magnet is analyzed by the proposed method, which is compared with the analysis results calculated by the numerical method. Secondly, the characteristic of the magnet gear is investigated and compared with the experiments. From the proposed method, characteristics of the magnet gear can be easily obtained.

Analysis Model

Fig. 1 shows the relative position of each magnet in the magnet gear. The analysis model has two skewed permanent magnets that is the driving and driven permanent magnet, respectively. The each permanent magnet is fixed on two shafts crossed at right angle. The magnet gear has a space between two permanent magnets for the non-contact drive. The function of upper permanent magnet is to the running gear and the lower is to the passive gear. With the help of the skew in the permanent magnet, the driven magnet can be smoothly rotated according to the rotation of the driving magnet.

The magnetic material is a ring type of Nd-sintered magnet. The residual flux density of 1.2 (T) magnetized at radial direction is used to design the magnet gear. The shafts are inserted into the hole of two permanent magnets. The normal component of the non-skewed model is a sine-wave distribution and the lateral flux leakage along axial direction is larger than that of the skewed model, which is due to the effect of skew. Material is the stainless steel. The permeability of the medium is an air, which allows the permanent magnet to be replaced as the EMC. This is due to the non-magnetic material with non-saturation characteristics.

Analysis Process

The magnetic flux density at P due to a rectangular loop carrying current J_{md}, as shown in Fig. 2, is calculated by using the Biot-Sarvart law. The resultant flux density at the field point is the sum of that caused by four sides of the current from J_{md1} to J_{md4}. Finally, the Lorentz force is used to find the magnetic force by the source element, which is obtained by the product of the resultant flux density and the conducting element dl at P.

Step 1) Mesh generation of two permanent magnets
Step 2) Calculation of equivalent magnetizing current of each element [3,4]
Step 3) Set one element and determines the flux density B at a set point caused by all source elements n that carry a magnetization current by applying the Biot-Sarvart law as follows [5]:

$$d\vec{B}_i^e = \frac{\mu_0 I_i^e}{4\pi}\left(\frac{d\vec{l}_i^{\,e} \times \vec{a}_{i\,r}^{\,e}}{R_i^{e^2}}\right) \tag{1}$$

$$\vec{B} = \sum_{e=1}^{n}\sum_{i=1}^{4} d\vec{B}_i^e \tag{2}$$

where dB is the flux density caused by only a single side in the rectangular current loop . a_r is the unit vector directed from the source point to the field point, R is the vector from the source element dl to the field point, I is the magnetization current replaced by the permanent magnet. dl is the length of the source element. n is number of elements of analysis model. i is the four side in the rectangular current loop.

Step 4) Calculate the magnetic force on the set point by applying the Lorentz force to the resultant magnetic field and the magnetization current at field point, which is expressed as:

$$d\vec{F}^{e} = I^{e} d\vec{l} \times d\vec{B}^{e} \tag{3}$$

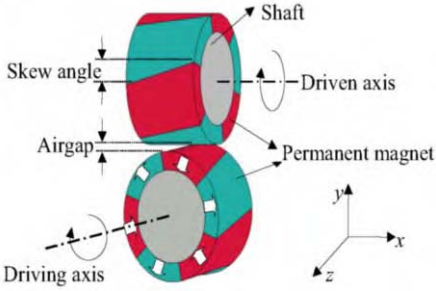

Fig. 1. Configuration of magnet gear permanent magnets (upper: running gear; lower: passive gear).

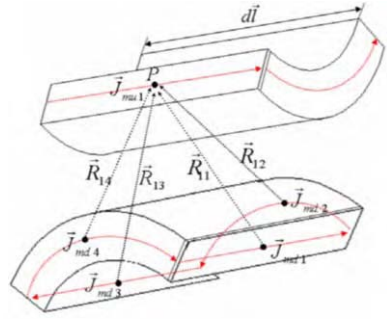

Fig. 2. The magnetic flux density at *P* due to rectangular loop carrying current.

Step 5) Repeat from Step 3 to Step 4 for all elements to obtain the force acting on the permanent magnet

$$\vec{F} = \sum_{e=1}^{n} d\vec{F}^{e} \tag{4}$$

From the above procedures, the magnetic torque is calculated by the cross product of the magnet radius vector and the force vector acting on the observed permanent magnet.

Analysis Results

Rectangular type permanent magnet

The residual flux density of the permanent magnet is 1.2 (T). The magnet has a width 30(mm), height 10, length 30 (mm) and y-axis magnetization. Fig. 3 shows the flux density distribution on the surface of the permanent magnet along the x-axis at height 11 (mm). The calculated results by Biot-Sarvart law, of normal and tangential component are matched with that obtained by 3D FEA.

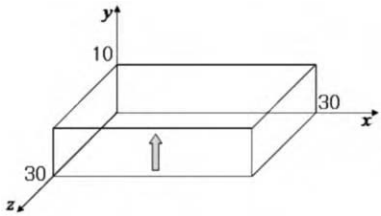

(a) Rectangular type permanent (unit : mm)

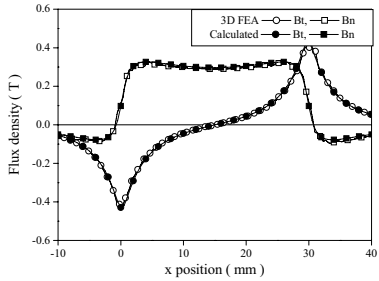

(b) Flux density distribution.

Fig. 3. Flux density distribution comparison obtained by the proposed method and 3-D FEA.

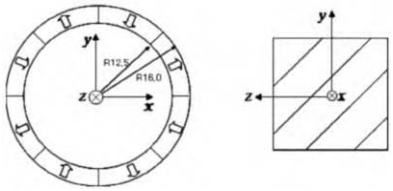

(a) front view. (b) side view.

Fig. 4. Configuration of cylinder type permanent magnet with skew.

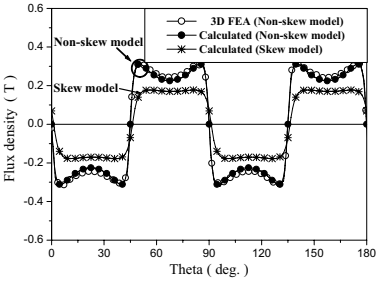

Fig. 5. Flux density of normal component.

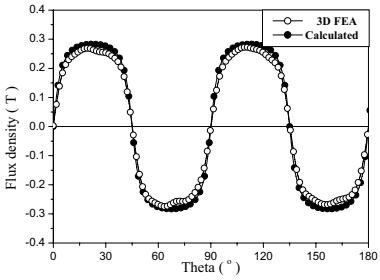

Fig. 6. Flux density of axial component.

Cylinder Type Permanent Magnet

The cylinder type permanent magnet is used for the verification of the analysis method, as shown in Fig. 4. The residual flux density is 1.2 (T). The permanent magnet has eight poles and the skew angle of 45 (°). Fig. 5 shows the flux density distribution of normal component along the surface in the middle of the permanent magnet length, which calculated using the analytic and numerical method. The normal component of the skewed model is a sine-wave distribution due to the effect of skew. Fig. 6 shows the flux density distribution of axial component at the edge of permanent magnet. The lateral

leakage fluxes exist in both ends of the permanent magnet. The analysis results by the proposed agree well with that calculated by 3D FEA.

Magnet gear

The analysis model consists of two permanent magnets that is the same dimension plotted on Fig. 4 and material properties. The air gap between the driven and the driving permanent magnet is 0.5 (mm). The magnet gear is divided into 20000 elements to apply the proposed method.

Fig. 7 shows flux density distribution in air gap between two permanent magnets according to the position of driving permanent magnet. The position related to two permanent magnets has an effect on the magnet torque. When the driving permanent magnet is placed in 22.5 (°) of the driven permanent magnet ahead of aligned position, the flux density is distorted and has a large tangential component. This position can lead to a maximum torque. The black square line presents the flux density when only one permanent magnet exists.

Fig. 8 presents that the variation of magnetic torque varying with rotation angles of the driving magnet is calculated by the proposed method. The torque maximum at 22.5 (°) is 4.18 (kgf.cm). Furthermore, to examine the validity of the analysis method, the magnetic torque of the magnet gear is calculated by the 3D FEA and measured by an experimental unit. The number of element of the analysis region is 229070 for 3D FEA. For the magnetic field analysis, the element is a tetrahedron having four nodes. The mesh generation and the magnetic flux distribution vector are plotted on Fig. 9.

Fig. 10 shows the experiment unit is made to measure the torque of the magnet gear by load cell, two permanent magnets and indicator. The shaft material is a stainless steel. The indicator displays the magnetic toque value. The measured torque is 3.98 (kgf.cm). In Fig. 8, when compared with data sets at the maximum torque, the results between the calculated and measured values are nearly similar. In this way, the calculation programs used in this study are suitable to design the magnet gear.

Conclusions

In this paper, the improved analytical approach is proposed to analyze the 3D electromagnetic problem. This technique based on the EMC method has been coupled with Biot-Sarvart law. It was verified that the analytical simulation results have a good agreement with both experimental results and 3D FEA analysis results. The proposed method can effectively and exactly predict the performance of the magnet gear and will effectively assist the initial design of the magnet gear and other machines with 3D electromagnetic phenomenon**.**

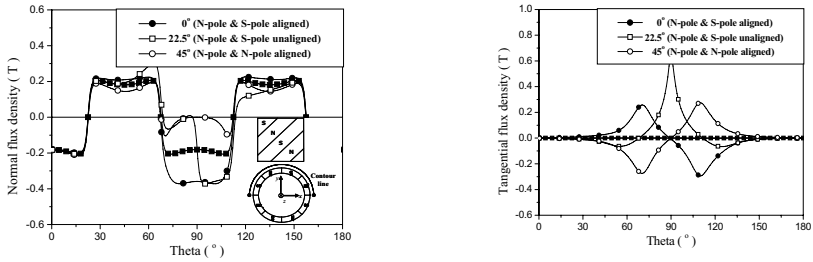

(a) Normal flux density distribution. (b) Tangential flux density.

Fig. 7. Flux density distribution in the air gap with the driving permanent magnet.

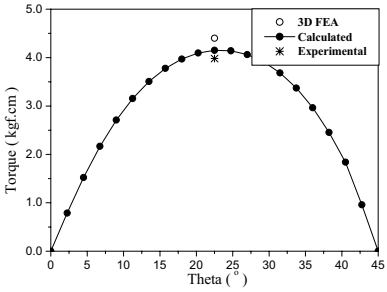

Fig. 8. Comparison of magnetic torque.

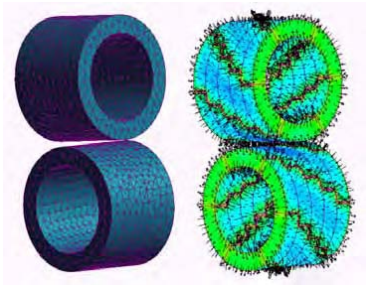

Fig. 9. Mesh generation and flux distribution arrow plot.

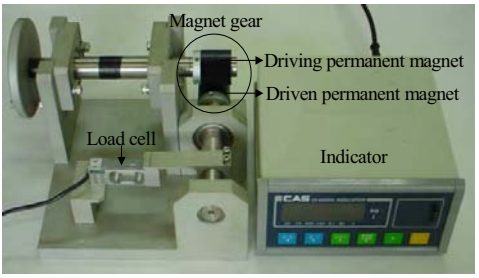

Fig. 10. Experiment unit for measuring the magnetic torque of magnet gear.

ACKNOWLEDGMENT

This work was financially supported by MOCIE through IERC program.

REFERENCES

[1] In-Soung Jung, *et al*., "Magnetization modeling of a bonded magnet for performance calculation of inner-rotor type BLDC motor," *IEEE Tans. on Magn*., Vol. 37, No. 4, pp. 2810-2813, 2001.

[2] K. H. Ha, Y. J. Oh, J. P. Hong and Y. J. Oh, "Design and Character Analysis of Non-Contact Magnet Gear for Conveyor by Using Permanent Magnet," *Proceeding of IEEE-IAS'2002,* Pittsburg, USA, Vol., May 2003.

[3] G. H. Kang, J. P. Hong and G. T. Kim, "Design and Analysis of Slot less-Type Permanent Magnet Linear Brushless Motor by Using Equivalent Magnetizing Current," *IEEE Trans. on Ind. Applicant.*, Vol. 37, No. 5, 2002.

[4] K. C. Lim, J. P. Hong and G. T. Kim, "The Novel Technique Considering Slot Effect by Equivalent Magnetizing Current," *IEEE Trans. on Magn*., Vol. 35, No. 5, 1999.

[5] William H. Hayt, *Engineering Electromangetics*, MacGraw Hill, 1989.

Electromagnetic Fields in Mechatronics, Electrical and Electronic Engineering
A. Krawczyk et al. (Eds.)
IOS Press, 2006

NEW APPROACH TO APPLYING CAPACITANCE CONTROL IN THE MAIN INSULATION OF HV INSTRUMENT TRANSFORMERS

Lesniewska Elzbieta

Department of Applied Electrical Engineering & Instrument Transformers
Technical University of Lodz,
ul. Stefanowskiego 18/22, 90-924 Lodz, POLAND E-mail: elalesni@p.lodz.pl

Abstract – The new method of placing electrostatic shields inside the paper-oil insulation to obtain a uniform electrostatic field is presented in this paper. The new construction is simpler for production processes and is less labour consuming and decreases the cost of an insulation system.

Introduction

Very often, similarly as with the bushings, the capacitance control is applied in HV current transformers with a primary winding U-type or δ-type. Capacitance control has been used in main paper-oil insulation of HV instrument transformers for many years. In this case, the electrostatic shields pass through the whole main insulation of the primary winding as shown in Fig 1. Capacitance control, aluminium electric shields placed between the paper layers, enables uniform field distribution in insulation especially in cylindrical parts. These shields and the insulation make up the system of capacitors. The field distribution depends on the value of this capacitance and can be controlled by the parameters of the electric shields to protect the main insulation. The application of capacitance control is also necessary because the requirements concerning the electric strength and partial discharges of the system. The paper insulation is divided into thin layers, which increase its electric strength. The field distribution must be uniform on the boundary of solid insulation and inside it as well.

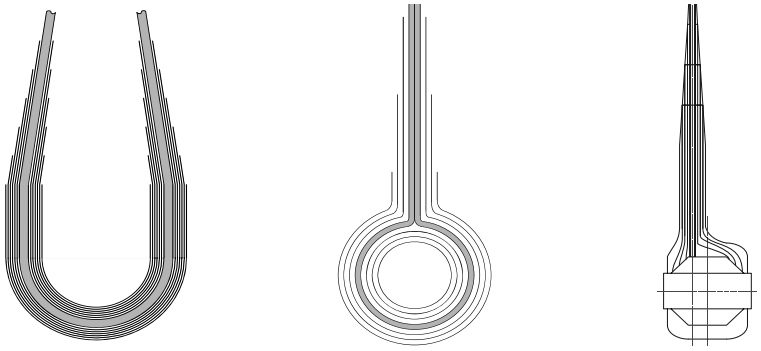

Fig.1 System of main shield in main insulation of the primary winding of current transformers with primary windings U-type or δ-type and in a voltage transformer

As applied in practice, construction solutions of capacitance control, in the main insulation of the lead conductor of the primary coils in HV voltage transformers, the electrostatic shields came into the HV coil and were joined to the layers at specifically determined electric potentials.

The application of these solutions of the capacitance control gives satisfactory results but is found to be labour-consuming and increases the cost of insulation.

The Mathematical Model

The distribution of potentials in any paper-oil main insulation and, as a result, the distribution of electric field strength is determined by the capacitance between the electrostatic shields.
The author's software, SHIELDS, was used to optimise the number, dimension and position of each electrostatic control shield in the insulation of the instrument transformer. Criteria of choosing the parameters of the electrostatic shields were: not exceeding the permissible electric field strength, uniform distribution of the electric field strength in the axis direction and the minimum difference of its value in the radius direction. The criterion of the SHIELDS' iterative procedure of choosing the radius of the main and intermediate shields is the same difference of potential between the main shields and between the intermediate shields.

The electric field in an insulation system (after introducing the scalar electric potential $\mathbf{E} = -\nabla V$ where $\mathbf{E}$ is the electric field strength) is described by Laplace's equation

$$\nabla^2 V = 0 \qquad (1)$$

with Neuman's and Dirichlet's boundary conditions. Applying the commercial software OPERA3D based on the numerical finite element method makes it possible to solve this equation and estimate the field distribution. In electrostatic fields electrode surfaces will obviously have assigned potential boundary conditions (V=constant value).

The Analysis of Electric Field Distribution

Modern current transformers have an "inverse construction" which means that the cores and windings are in the head. The HV terminals are on the top and the LV terminals are at the bottom. Therefore, the secondary windings of the current transformer and the endings of them at potential zero must all be insulated. In this case, the whole casing with cores and secondary windings must be insulated (Fig.2). This has proved to be costly, labour-consuming and very difficult to design and make.

a) b)

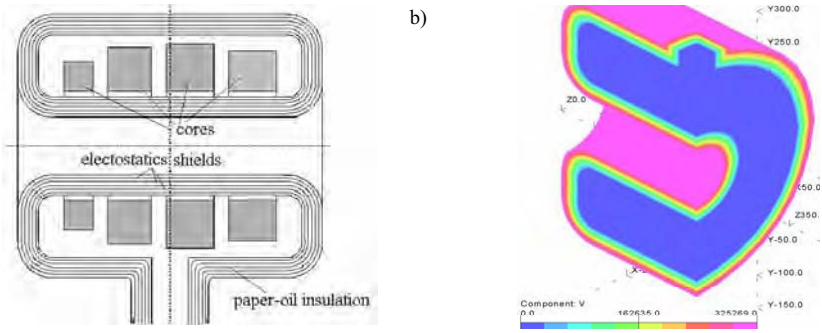

Fig.2 The casing with cores and paper-oil insulation with electrostatic shields and distribution of electric potential inside paper-oil insulation of the casing

In this new approach, the casing with cores or HV coil can be insulated separately and the electric shields, which do not pass through the insulation, are only placed in the cylindrical part of insulation at the edge of the insulation. It requires very accurate computations of the parameters of electrostatic shields and determination of electric field distribution especially where the shields begin. The electrostatic shield can not begin simultaneously and the position of their beginnings must be computed to obtain an optimal field distribution. Fig.3 shows how the shields should be wound in paper-oil insulation. The beginning of the main electrostatic shields are inside the paper insulation and in this part there are not any problems with surface discharges as on a boundary of solid insulation but is very important to eliminate any non- homogeneousness in this region.

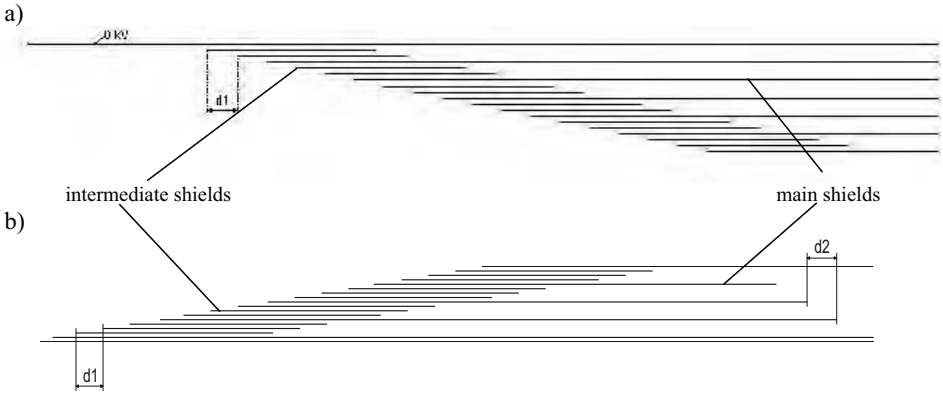

Fig.3 The difference between an old (a) and new (b) method of placing electrostatic shields

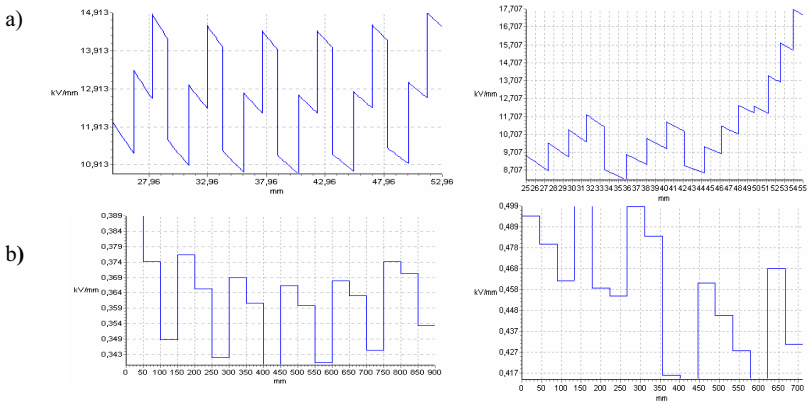

Fig.4 Distribution of the electric field strength in the insulation system with capacitance control for an old (left hand column) and new (right hand column) method of placing electrostatic shields
a) in the axis direction and b) in the radius direction

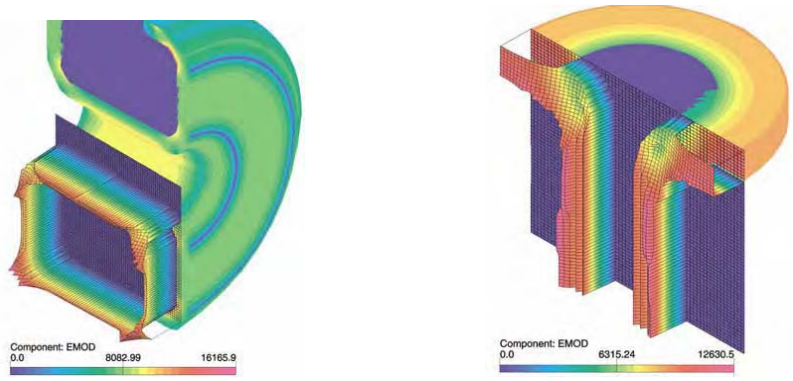

Fig.5 Distribution of electric field strength [V/mm] inside paper-oil insulation
a) of the casing with cores and paper-oil insulation without electrostatic shields
b) of the pipe with the endings of the secondary windings in the place where the shields begin

Application of this new method opens up the possibility of joining different insulation material, for example paper-oil insulation and epoxide resin. Some constructional solutions of current transformers of "inverse construction" insulation using joining material were considered. For example, casing with cores may be insulated by epoxide resin (without electrostatic shields) and the pipe with endings of secondary windings may be insulated by paper-oil insulation with capacitance control.

The difference between paper-oil insulation and joined insulation lies in the fact that electrostatic shields must be somewhat shorter because of joining and this causes an increase of electric field strength in paper-oil insulation from 12.6kV/mm to 15.8kV/mm. The introduction of these two kinds of insulating materials caused a further increase of electric field strength to 17.5kV/mm.

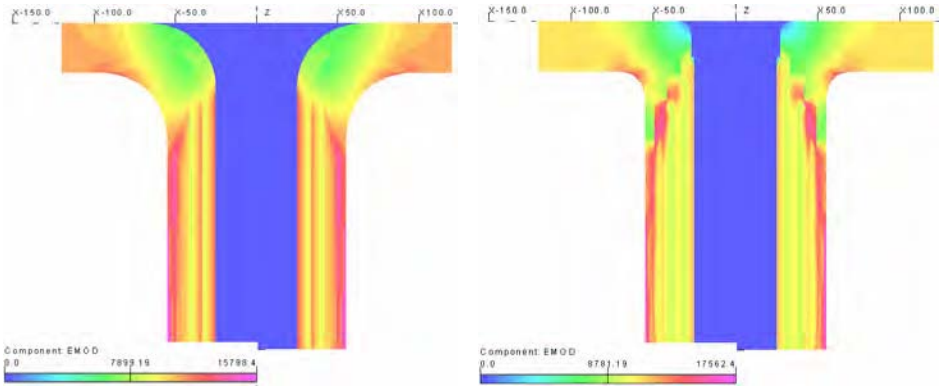

Fig.6 Distribution of electric field strength [V/mm] inside paper-oil insulation in the place where the shields begin for two different versions with joining paper-oil and epoxide resin insulation

The main problem in this case is the use of proper technology in joining both forms of insulation so as to prevent the existence of oil between paper-oil and epoxide resin insulation which can cause break of insulation.

The next problem was with the insulation of the casing because electric strength of paper oil insulation (70÷80kV/mm) is four times larger than that of epoxide resin (19÷26kV/mm). It was necessary to change the construction of casing, to enlargen the radius of the casing's corners (from 22 to 40mm) and to obtain a larger thickness of insulation resulting in a lessening of electric field strength to 16kV/mm at assumption the same external dimensions.

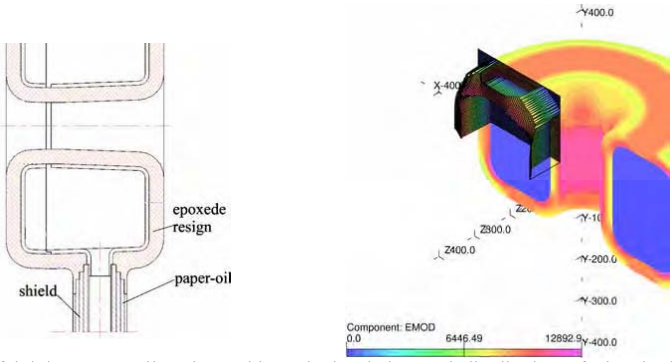

Fig.7 Diagram of joining paper-oil and epoxide resin insulation and distribution of electric field strength [V/mm] inside epoxide resin insulation for versions with casing corners 40mm joining paper-oil and epoxide resin insulation

The next example, the main insulation of HV coil of voltage transformer (Fig. 8) was considered.
In this new approach, the HV coil is insulated separately and the shields are only placed in the cylindrical part of insulation.
All of the designed prototypes of the current and voltage transformer presented in this paper were built and successfully passed all HV tests.

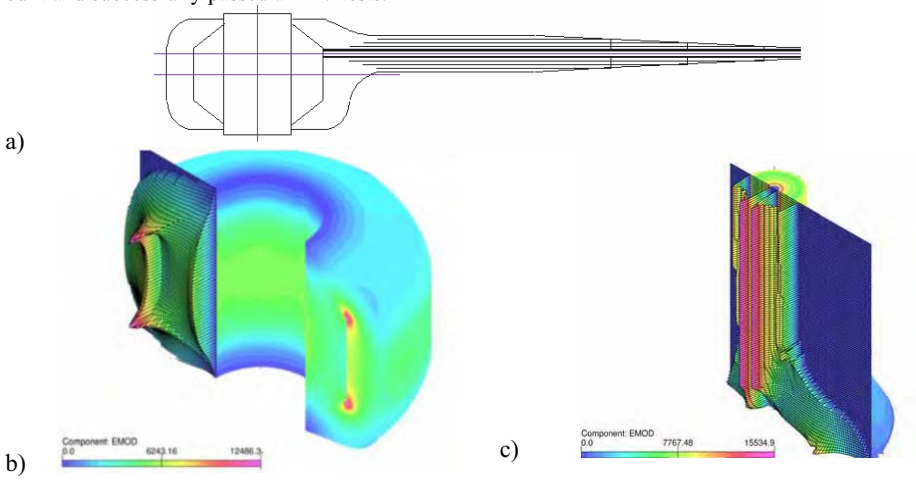

Fig.8 New method of placing electrostatic shields applied in main insulation of HV voltage transformer and electric field distribution in this case
a) diagram of placing the electrostatic shields
b) of the HV voltage coil - primary winding of the voltage transformer
c) of the of lead conductor of HV coil in the place where the shields begin

Conclusions

The new method creates the possibility of applying this construction as well for main isolation of the inverse construction of HV current transformers as for HV voltage transformers. This construction is simpler for production processes and may be automated. It is not so labour consuming and decreases the cost of the insulation especially for an "inverse construction" of a current transformer. Also, this method opens up the possibility of joining different insulation material. This proposed solution of a new approach to capacitance control was applied in a real-life model of HV instrument transformer and has successfully passed all HV tests.

References

[1] Leśniewska E., Main insulation with capacitance control of HV instrument transformer, patent application 22.05. 2001 P-347701 (in Polish)
[2] A. Koszmider, J. Olak and Z. Piotrowski, "Current Transformers", WNT, Warsaw, 1985 (in Polish)
[3] E. Lesniewska, The Use of 3D Electric Field Analysis and the Analytical Approach for Improvement of a Combined Instrument Transformer Insulation System, IEEE Transaction on Magnetics, vol. 38, no 2, March 2002, pp. 1233-1236
[4] W. Kalat, "Determination of optimised lengths of control shields in paper-oil insulation of a HV current transformer", Proceedings of the 5th Symposium for the Simulation of Dynamic Processes, 1988, pp.81-88 (in Polish)
[5] M. Griejsuch, G. Kuczynski, D. Kaplan, and G. Miesserman "The paper-oil insulation in HV constructions", Moskwa 1963, pp.39-52 (in Russian)
[6] Lesniewska E.: Estimation of the Electric Strength of Insulation System of an HV Combined Instrument Transformer Using 3D Analysis, The International Journal for Computation and Mathematics in Electrical and Electronic Engineering COMPEL Vol.19, No 2, 2000, pp. 488-494
[7] Lesniewska E.: Application of 3D Field Analysis for Modelling the Electric Field Distribution in Ceramic Insulator of HV Combined Instrument Transformer, ELSEVIER, Journal of Electrostatics, vol. 51-52, 2001, pp 610-617

Electromagnetic Fields in Mechatronics, Electrical and Electronic Engineering
A. Krawczyk et al. (Eds.)
IOS Press, 2006

A STUDY OF MAGNETIC FLUX DENSITY HARMONICS IN A THREE PHASE SQUIRREL-CAGE INDUCTION MACHINE AT IDEAL NO-LOAD CONDITION

T. Marčič[1], M. Hadžiselimović[2], I. Zagradišnik[2], B. Štumberger[2]

[1]TECES, Development centre for electrical machines
Gosposvetska cesta 84, 2000 Maribor, Slovenia, e-mail: marcic@teces.si
[2]Faculty of Electrical Engineering and Computer Science, University of Maribor
Smetanova ulica 17, 2000 Maribor, Slovenia, e-mail: miralem.h@uni-mb.si

***Abstract** – The paper presents a comparison between measured and calculated results of harmonic analysis of the air-gap's magnetic flux density in a three phase squirrel-cage induction machine. The comparison is made in order to evaluate the accuracy of a multi-slice finite element model which is intended to be used in analyzing the effect of skewing of rotor bars. The presented comparison is focused on higher order harmonics, mainly slot harmonics. In conclusion, the paper also discusses how the geometry of used measurement coils influences the harmonic spectrum of the induced voltage.*

Introduction

A previously published paper [1] presented a comparison between characteristics of a four pole three phase squirrel-cage induction motor with different number of rotor slots.
A multi-slice finite element model of the machine was developed to study how skewing of rotor bars influences the harmonic contents of the machine's air gap magnetic flux density. Since higher harmonics are closely related to parasitic torques which cause torque dips in torque-speed curves [2], the study of air-gap magnetic flux density harmonic spectrum is essential.
Higher harmonics are classified as a consequence of the saturation of magnetic paths, the non-sinusoidal distribution of the MMF in the air gap caused by the stator and rotor winding and the reluctivity of the air gap due to stator and rotor slotting (i.e. slot harmonics). The order of predominant slot harmonics ν depends on the number of slots Q and the number of poles p of the induction machine as in (1), where $k = \pm 1, \pm 2, \pm 3, \ldots$, the subscript r stands for rotor and s stands for stator.

$$\nu_{r(s)} = k\frac{Q_{r(s)}}{p} + 1 \tag{1}$$

The aim of the proposed paper is to evaluate how results from finite element analyses correspond to measured values, thus evaluating accuracy of the finite element model. The paper presents a comparison between harmonic contents of magnetic flux density evaluated using finite element analyses and measurements by using measurement coils placed in the machine in a different manner. Measurement coils spanned one pole pitch. One coil was put into stator slots, the other three were placed in the air-gap area, i.e. pasted on stator teeth.

Machine Details, Measurement Of Induced Voltages And Evaluation Of Magnetic Flux Density Harmonics

Measurements and FEM calculations were conducted on an AC servomotor, i.e. a three phase squirrel-cage induction motor, with a four pole stator winding in star connection. The stator had 36 slots. The rotor was skewed for one stator slot pitch and had 34 slots. Both, stator and rotor slots were semi-closed. The machine had a shaft height of 132 mm, a core length of 230 mm and an air-gap of 0,5 mm. The used magnetic material was a non oriented fully-processed steel with the standard designation M530-50A, of 0,5 mm thickness and maximal total losses of 5,3 W/kg at 1,5 T.

Measuring coils enabled the measurement of voltages, induced by the flux of one pole pitch. Thus, coils spanned 9 stator teeth in width.

Coil A was put in stator slots, its axial length equaled the axial length of the stator yoke. Coils B, C and D were pasted on stator teeth. Coil C was skewed in the same manner as was the rotor, thus sensing the air-gap flux as if the rotor was not skewed. Coils B and C had an axial length of 1/2 of the stator yoke (l_{Fe}). Coils A, B and C had 1 turn. Coil D had 4 turns and its axial length was 1/16 of the stator yoke. Coils B, C and D were placed in the center of the stator yoke.

The time-varying flux, which induced the measured voltage in a measuring coil, was obtained by using a numerical integration technique. The magnetic flux density was then calculated by knowing the appropriate coil cross-section. Harmonic spectrums of the calculated magnetic flux densities were obtained by using Fast Fourier Transformation.

Measured Voltage Waveforms And Magnetic Flux Density Harmonic Spectrums

Under ideal no-load conditions, induced voltages in the measuring coils were measured at rated voltage, rated frequency and a resolution of $20\ \mu\mathrm{s}$. Ideal no-load conditions were assured by driving the tested induction motor by a synchronous reluctance motor. Both motors were fed from the same power supply, thus ensuring the same supply frequency for both machines.

Fig. 1 through Fig. 4 present waveforms of the measured voltages, induced in the measuring coils A, B, C and D.

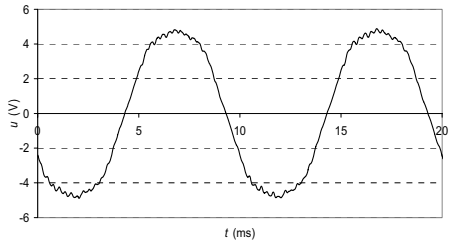

Fig. 1 Induced voltage in measuring coil A (placed in stator slots, $l = l_{Fe}$)

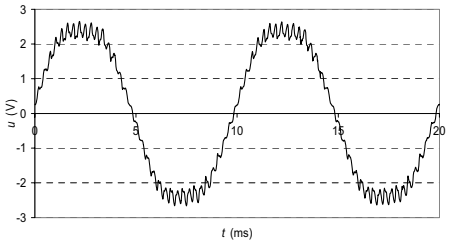

Fig. 2 Induced voltage in measuring coil B (pasted on stator teeth, $l = l_{\mathrm{Fe}}/2$)

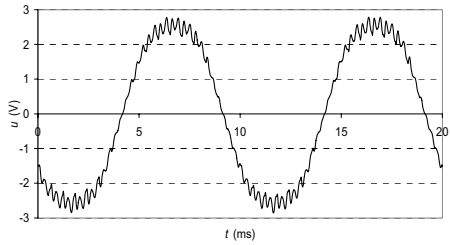

Fig. 3 Induced voltage in measuring coil C (pasted on stator teeth, skewed, $l = l_{\mathrm{Fe}}/2$)

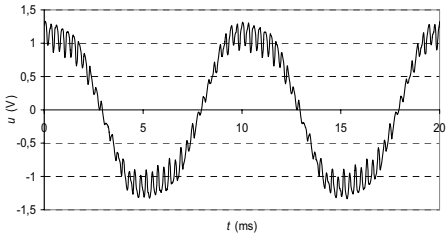

Fig. 4 Induced voltage in measuring coil D (pasted on stator teeth, $l = l_{\mathrm{Fe}}/16$)

Fig. 5 through Fig. 8 present harmonic spectrums of measured voltages.

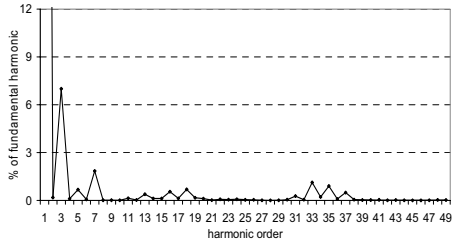

Fig. 5 Harmonic spectrum of induced voltage in measuring coil A, where the fundamental harmonic equaled 5,06 V

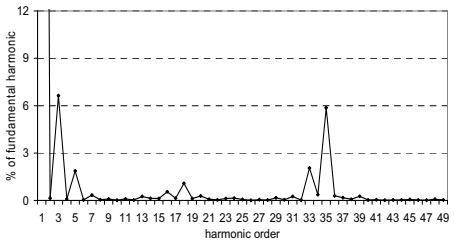

Fig. 6 Harmonic spectrum of induced voltage in measuring coil B, where the fundamental harmonic equaled 2,54 V

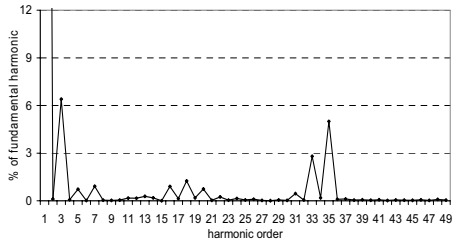

Fig. 7 Harmonic spectrum of induced voltage in measuring coil C, where the fundamental harmonic equaled 2,73 V

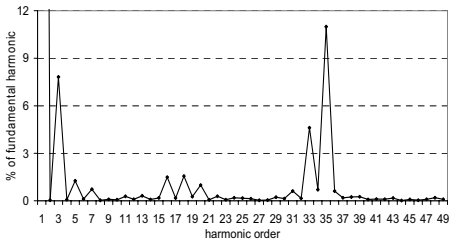

Fig. 8 Harmonic spectrum of induced voltage in measuring coil D, where the fundamental harmonic equaled 1,24 V

Fig. 9 through Fig. 12 present harmonic spectrums of the magnetic flux density evaluated from induced voltages in measuring coils A, B, C and D.

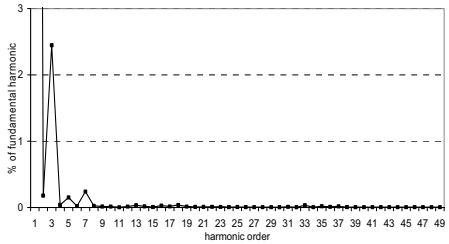

Fig. 9 Harmonic spectrum of magnetic flux-density evaluated by coil A (placed in stator slots, $l = l_{Fe}$), where the fundamental harmonic equaled 0,609 T

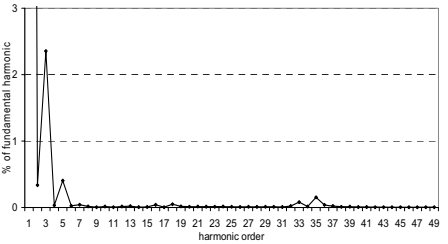

Fig. 10 Harmonic spectrum of magnetic flux-density evaluated by coil B (pasted on stator teeth, $l = l_{\mathrm{Fe}}/2$), where the fundamental harmonic equaled 0,624 T

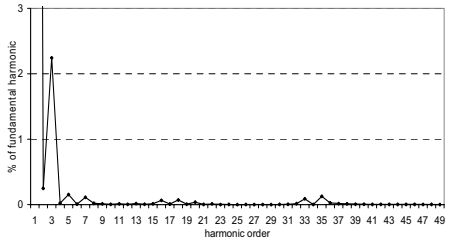

Fig. 11 Harmonic spectrum of magnetic flux-density evaluated by coil C (pasted on stator teeth, skewed, $l = l_{\mathrm{Fe}}/2$), where the fundamental harmonic equaled 0,650 T

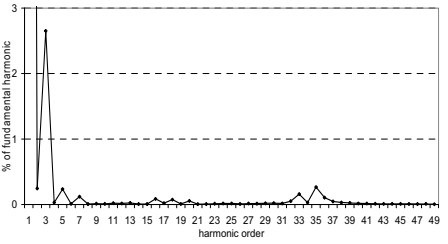

Fig. 12 Harmonic spectrum of magnetic flux-density evaluated by coil D (pasted on stator teeth, $l = l_{\mathrm{Fe}}/16$), where the fundamental harmonic equaled 0,594 T

Magnetic Flux Density Harmonic Spectrums From 2D FEM Analyses

Static 2D FEM calculations of the described motor under ideal no-load conditions were performed by using a FEM software package (Ansys). The flux of one pole pitch was calculated by subtracting values of magnetic vector potential under two stator teeth (under an angle of one pole pitch) and multiplying this with the machine's stack length. Magnetic field densities were calculated by dividing the flux with the area of one machine pole.
Fig. 13 shows the nodes that were used to read values of magnetic vector potential. The nodes in question were in the middle of the air-gap.

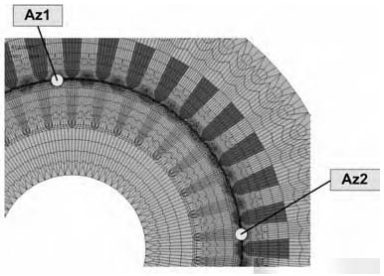

Fig. 13 Nodes that were used to read values of magnetic vector potential

Fig. 14 presents the harmonic spectrum of the magnetic flux density obtained from the magnetic flux. The full line (a) presents the harmonic spectrum of magnetic flux density in the case of alignment of stator and rotor tooth (at node Az1) at the start of rotation. The dashed line (b) presents the harmonic spectrum of magnetic flux density when the stator and rotor tooth are not aligned (at node Az1) at the start of rotation.

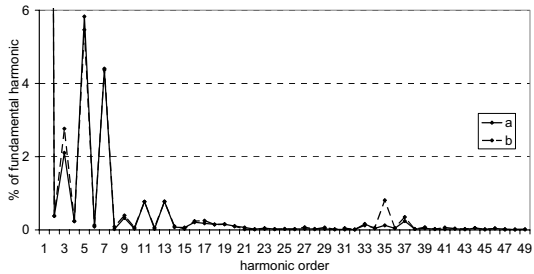

Fig. 14 Harmonic spectrum of the magnetic flux density obtained from the magnetic flux, where the fundamental harmonic equaled in case (a) 0,648 T and in case (b) 0,652 T (a - alignment of stator and rotor tooth, b - stator and rotor tooth are not aligned at the start of rotation)

Magnetic Flux Density Harmonic Spectrums From Multi-Slice FEM Analyses

The multi-slice finite element model was developed to study how skewing of rotor bars influences the harmonic contents of the machine's air gap magnetic flux density.
The machine's magnetic field was calculated in 11 different starting positions of the rotor (the angle between the first and last position equaled one stator slot pitch). In all of these calculations the same current waveforms were used. Read values of magnetic vector potential were then averaged over all positions and the magnetic flux density was evaluated by using the above described procedure.
Fig. 15 presents the harmonic spectrum of the magnetic flux density obtained from the magnetic flux, when the rotor is skewed for one stator slot pitch.

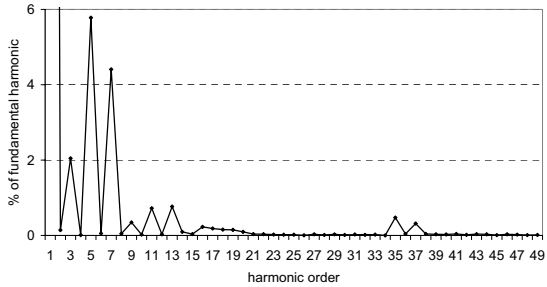

Fig. 15 Harmonic spectrum of the magnetic flux density obtained from the magnetic flux, where the fundamental harmonic equaled 0,705 T

Conclusion

Harmonic spectrums of measured induced voltages and magnetic flux-densities differ because of the placement of measuring coils and their axial length. The larger the measuring coil is the grater is the influence of the leakage flux from the winding ends. Therefore, with the increase of the coil cross-section the damping of higher harmonics also increases. All of these can be observed from Fig. 1 through Fig. 12. Harmonic spectrums of measured induced voltages in measuring coils B, C and D do not include the 37^{th} harmonic (stator slot harmonic), because they are put directly onto stator teeth. Despite the large area of the measuring coil A, the harmonic spectrum of measured induced voltage in this coil includes all slot harmonics (16^{th}, 17^{th}, 18^{th}, 19^{th}, 33^{rd}, 35^{th}, 37^{th}). A comparison of harmonic spectrums of measured induced voltages in coil B and C (Fig. 6 and Fig. 7) illustrates how skewing influences higher harmonics. In Fig. 6 the value of the 16^{th}, 18^{th} and the 33^{rd} harmonic is lower than in Fig. 7, although Fig. 6 shows a higher value of the 35^{th} harmonic than in Fig. 7.

Harmonic spectrums from 2D FEM analyses (Fig. 14) include all slot harmonics (16^{th}, 17^{th}, 18^{th}, 19^{th}, 33^{rd}, 35^{th}, 37^{th}). By using a multi-slice FEM analysis the effect of rotor skewing could be taken into account. Harmonic spectrums from multi-slice FEM analysis showed (Fig. 15) that in the case of rotor skewing for one stator slot division the 33^{rd} rotor slot harmonic could be eliminated.

Harmonic spectrums of results from FEM analyses show good agreement in the order of predominant higher harmonics. The fundamental harmonic values of magnetic flux densities show also a good agreement with measured values. Therefore, the multi-slice model can be used in the analysis of skewing effects on the harmonic content of the air-gap magnetic flux density (also machine behavior at different load conditions). Nevertheless, multi-slice FEM analyses can not include the damping of higher harmonics in the end rings of the rotor's squirrel cage.

References

[1] T. Marčič, M. Hadžiselimović, I. Zagradišnik, M. Gajzer, Rotor slot number influence on the characteristics of three phase squirrel-cage induction motors, Conference proceedings of 16th International conference on electrical machines ICEM 2004, Cracow, Poland

[2] I. Zagradišnik, B. Slemnik, Električni rotacijski stroji, Maribor: Tiskarna tehniških fakultet, 2001, pp. 107 - 109

Electromagnetic Fields in Mechatronics, Electrical and Electronic Engineering
A. Krawczyk et al. (Eds.)
IOS Press, 2006

IRON LOSS CHARACTERISTICS OF SKEWED INDUCTION MOTOR USING 3-D FINITE ELEMENT METHOD

Tatsuya Masuda*, Yoshihiro Kawase, Tadashi Yamaguchi**, Hitoshi Yonezawa** and Toshiyuki Yano****

*Aichi Electric Co.,Ltd., 1, Aichi-cho, Kasugai, 486-8666, Japan
E-mail: masuda.tatsuya@adkk.co.jp
**Department of Information Science, Gifu University, 1-1, Yanagido, Gifu, 501-1193, Japan
E-mail: kawase@info.gifu-u.ac.jp

***Abstract* - This paper describes the iron loss characteristics analysis of a skewed induction motor by the 3-D Finite Element Method (FEM) with a new mesh modification method for skewed motors. The accuracy of the iron loss analysis and the effects of the iron loss on the skew are quantitatively clarified by comparing the 2-D and 3-D results.**

Introduction

The accurate estimation of iron loss of skewed induction motors is desired for environmental problems. Especially, it is important for the high efficient design of motors to clarify the iron loss (the eddy current loss and the hysteresis loss) using the 3-D Finite Element Method (FEM), because it is difficult to obtain the accurate value of the iron loss in experiments.

In time-stepping analysis of an induction motor by the FEM, it is necessary to shorten the interval of electrical angle ($\Delta\omega t$) in order to obtain the accurate value of iron loss because of the harmonic components of the magnetic flux in the cores. However, if $\Delta\omega t$ is shorter, the CPU time becomes longer. Therefore, it is very important to study the effects of $\Delta\omega t$ on the iron loss analysis.

In this paper, we analyze the iron loss of a skewed induction motor with the 3-D FEM with a new mesh modification method for skewed motors in order to estimate the iron loss accurately. Then, we study the effects of $\Delta\omega t$ and skew on the iron loss. Furthermore, the analytic accuracy of the iron loss is quantitatively clarified by comparing the iron loss of the skewed motor with that of the no-skewed motor in the 2-D and 3-D FEM.

Method of Analysis

Magnetic Field Analysis: The fundamental equations of the magnetic field can be written using the magnetic vector potential $\boldsymbol{A}$ and the scalar potential ϕ as follows [1]:

$$\mathrm{rot}(\nu\,\mathrm{rot}\boldsymbol{A}) = \boldsymbol{J}_0 + \boldsymbol{J}_e,\quad \boldsymbol{J}_e = -\sigma\left(\frac{\partial \boldsymbol{A}}{\partial t} + \mathrm{grad}\phi\right),\quad \mathrm{div}\boldsymbol{J}_e = 0 \tag{1}$$

where ν is the reluctivity, $\boldsymbol{J}_0$ is the exciting current density, $\boldsymbol{J}_e$ is the eddy current density, and σ is the conductivity.

New Mesh Modification Method for Skewed Motors: Our new developed mesh modification method for the skewed motor analysis is carried out as follows [2]:

First of all, the conventional 3-D mesh for the motor analysis is prepared, which is without skew and is made by building up the 2-D mesh as shown in Fig. 1 (a). The air gap between the stator and the rotor is divided into two areas. One is the air gap of rotor region, and another is that of stator region.

Next, the elements in the air gap of the rotor region are deleted as shown in Fig. 1 (b). Then, the rotor is skewed as shown in Fig. 1 (c). The elements in the air gap of rotor region are generated with the auto-mesh generator in the Delaunay method. At last, the skewed rotor region and the stator region are connected each other with the new air gap of the rotor region as shown in Fig. 1 (d).

In our method, the auto-mesh generator is essential, however, it is used for only making the initial mesh because the new rotor region in Fig. 1 (d) can be rotated with the conventional mesh modification method for motor analysis. Therefore, the computational cost for the mesh modification is very small.

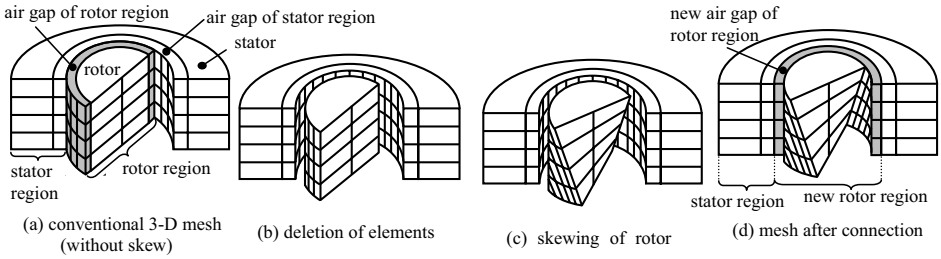

Fig.1. Process of skewed initial mesh creation.

Calculation of Iron Loss: The eddy current loss W_{ed} in the laminated cores is estimated as follows [3]:

$$W_{ed} = \frac{K_e D}{2\pi^2} \int_{iron} \frac{1}{N} \sum_{k=1}^{N} \left\{ \left(\frac{B_r^{k+1} - B_r^{k}}{\Delta t} \right)^2 + \left(\frac{B_\theta^{k+1} - B_\theta^{k}}{\Delta t} \right)^2 + \left(\frac{B_z^{k+1} - B_z^{k}}{\Delta t} \right)^2 \right\} dv \tag{2}$$

where K_e is the coefficient of the eddy current loss which is the experimental constant by the Epstein frame, D is the density of the steel sheet, N is the number of time step per one time period, B_r, B_θ and B_z are the flux density of the radial direction, the rotation direction and the z-direction, respectively.

The hysteresis loss W_{hy} taking into account the major and minor loops can be estimated as follows [3]:

$$W_{hy} = \frac{K_h D}{T} \sum_{i=1}^{NE} \frac{\Delta V_i}{2} \left(\sum_{j=1}^{Npr^i} \left(B_{mr}{}^{ij} \right)^2 + \sum_{j=1}^{Np\theta^i} \left(B_{m\theta}{}^{ij} \right)^2 + \sum_{j=1}^{Npz^i} \left(B_{mz}{}^{ij} \right)^2 \right) \tag{3}$$

where K_h is the coefficient of the hysteresis loss which is the experimental constant by the Epstein frame, T is the period of analysis time, NE is the number of the elements in the steel sheet and ΔV_i is the volume of the i-th element. $N_{pr}{}^i$, $N_{p\theta}{}^i$ and $N_{pz}{}^i$ are the number of the maximum or minimum value of the flux density of the radial direction, the rotation direction and the z-direction of the i-th element, respectively. $B_{mr}{}^{ij}$, $B_{m\theta}{}^{ij}$ and $B_{mz}{}^{ij}$ are the amplitude of the flux density of major and minor hysteresis loops of the radial direction, the rotation direction and the z-direction, respectively.

Analyzed Model and Conditions

Fig. 2 shows the analyzed model of a squirrel-cage induction motor, the rotor of which is skewed with two rotor slot pitch. Table 1 shows $\Delta\omega t$ (Δt) of each model. In this paper, the aim of this analysis is to obtain how analytical results of the iron loss are affected in case that we change $\Delta\omega t$. We calculate the skewed model in case that $\Delta\omega t$=5 and 20 degree. The no-skewed models in both the 2-D and the 3-D are analyzed to compare the results with that of skewed models. $\Delta\omega t$ of the 2-D analysis is very small enough to calculate the iron loss accurately. Table 2 shows the analyzed conditions. The conductivity of secondary conductor in the 2-D model is different from that in the 3-D model to take into account the effect of end-ring in the 2-D analysis.

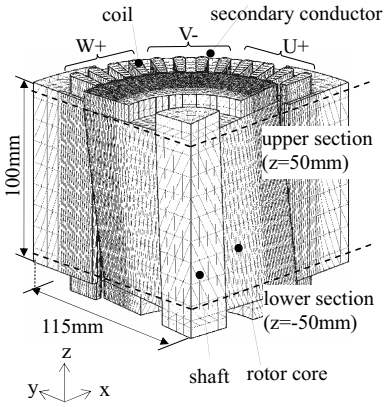

Fig.2. Analyzed model (skewed model).

Table 1. $\Delta\omega t$ (Δt) of each model

		$\Delta\omega t$ (deg.)	Δt (ms)
3-D FEM	2 rotor slot pitch skew	20	0.9259
		5	0.2315
	no-skew	5	0.2315
2-D FEM	no-skew	2	0.09259

Table 2. Analyzed conditions

Number of poles		4
Line voltage (V)		230
Coil turn (turn)		130(=32+33+33+32)
Resistance of coil (Ω/phase)		0.4496
Frequency of line voltage (Hz)		60
Rotor speed (min^{-1})		1,200
Slip		0.333
Conductivity of secondary conductor (S/m)	3-D FEM	2.116×10^7
	2-D FEM	1.557×10^7

Results and Discussion

Fig. 3 shows the waveforms of the flux density in the surface of stator teeth. From this figure, differences are found between the waveforms in the lower section and those in the upper section due to the skew. From Fig. 3 (a), it is also found that there are a lot of harmonic components in the surface of stator and rotor teeth. On the other hand, in Fig. 3 (b), the waveforms have less harmonic components because $\Delta\omega t$ is not short enough.

Fig. 4 shows the contours of iron loss in case that $\Delta\omega t$ =5 degree. From Fig. 4 (a), it is found that there is a lot of hysteresis loss in the surface of stator and rotor teeth because there is much harmonic

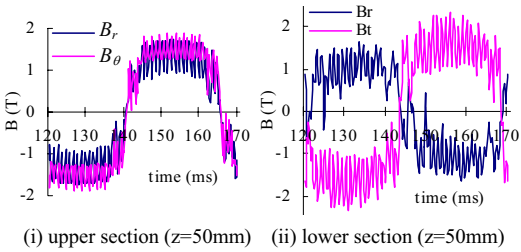

(a) $\Delta\omega t$ = 5 deg.

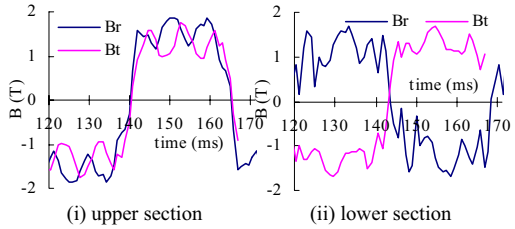

(b) $\Delta\omega t$ = 20 deg.

Fig.3. Waveforms of flux density.

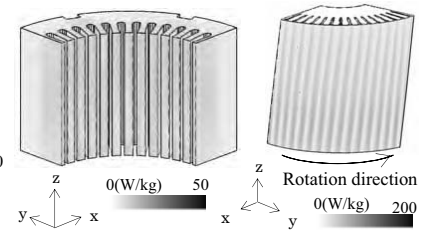

(a) hysteresis loss

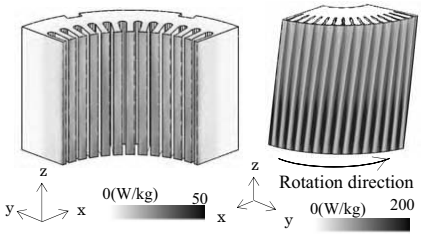

(b) eddy current loss

Fig.4. Contours of iron loss ($\Delta\omega t$ = 5 deg.).

components in the surface of the cores. It is also found that the hysteresis loss density at the lower part in the surface of the rotor is larger than that at the upper part. From Fig. 4 (b), it is clarified that the eddy current loss is found more than the hysteresis loss especially on the surface.

Fig. 5 shows the calculated iron losses. In skewed models, the hysteresis loss becomes slightly large and the eddy current loss becomes much large if $\Delta\omega t$ is shortened. You can see the reasons in Fig. 3 (a). It is that the hysteresis loss is hardly affected by harmonic components. On the other hand, the eddy current loss is remarkably affected. Therefore, the calculation of the eddy current loss needs to be set $\Delta\omega t$ very short.

The hysteresis loss is almost the same between the 3-D no-skewed model in case that $\Delta\omega t$=5 degree and the 2-D model in case that $\Delta\omega t$=2 degree. On the other hand, the eddy current loss in the 3-D model is smaller than that in the 2-D model. Consequently, if $\Delta\omega t$ is set such a short interval as 5 degree, it is expected that the hysteresis loss of skewed models can be calculated properly. However, the eddy current loss under that condition is estimated less than the actual value.

Table 3 shows the discretization data and CPU time. Much CPU time is needed even if our new mesh modification method is used.

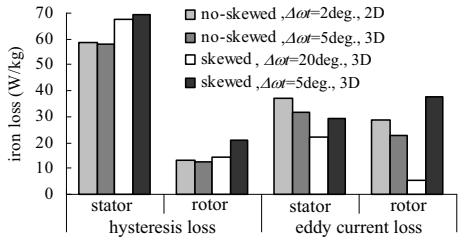

Fig.5. Comparison of iron loss.

Table 3. Discretization Data and CPU Time (skewed model, $\Delta\omega t$ =5deg.)

Number of elements	366,327
Number of nodes	66,609
Number of edges	445,973
Number of unknown variables	435,959
Average number of non-linear iterations	12.1
Number of time steps	504
Total CPU time (hours)	2,182

Computer used: Pentium 4 (2.8GHz) PC

Conclusions

In this paper, we analyzed the eddy current loss and the hysteresis loss of a skewed induction motor by the 3-D FEM using a new mesh modification method for skewed motors in order to estimate the iron loss. In this model, the eddy current loss is changed very much and the hysteresis loss is changed a little by $\Delta\omega t$. And, we clarified that the iron loss of the skewed model is large compared with that of the no-skewed model. Furthermore, in this case, it is clarified that the hysteresis loss of skewed models can be calculated properly in case that $\Delta\omega t$=5 degree. However, it is also clarified that the eddy current loss under this condition is estimated less than the actual value.

References

[1] Y. Kawase and S. Ito, *New Practical Analysis of Electrical and Electronic Apparatus by 3-D Finite Element Method*. Tokyo, Japan: Morikita Publishing, 1997.

[2] T. Yamaguchi, Y. Kawase and S. Sano, "3-D Finite Element Analysis of Skewed Squirrel Induction Motor", *IEEE Trans. Magn*, vol. 40, pp. 969-972, March 2004.

[3] K. Yamazaki, "Efficiency Analysis of Induction Motor Considering Rotor and Stator Surface Loss Caused by Rotor Movement," *International Journal of Applied Electromagnetics and Mechanics*, vol.13, no.1, pp. 229-234, 2001/2002.

Electromagnetic Fields in Mechatronics, Electrical and Electronic Engineering
A. Krawczyk et al. (Eds.)
IOS Press, 2006

DYNAMIC MODEL OF PMSM BASED ON 2D FEM FLUX AND TORQUE COMPUTATION

L. Melcescu, M. Covrig, V. Bostan, A. Fociuc

POLITEHNICA University of Bucharest, Electrical Machines and Drives Department,
313 Splaiul Independenței, Bucharest, Romania
leonard@amotion.pub.ro, m_covrig@amotion.pub.ro, vali_bostan@yahoo.com, andreea_fociuc@forus.ro

***Abstract** – Simulation of the functioning of electrical systems and numerical modelling of electromechanical equipment are modern means of design electrical engineers increasingly use. A numeric Simulink model is suggested in the paper, allowing the simulation of the permanent magnets synchronous machines functioning both in motor and generator regimes. The model has been developed on basis of the results obtained from the 2D numerical modelling of the magnetic field in the machine. The accuracy of this model is checked by means of comparing the results of the simulation to the results of the real life experiment.*

Introduction

Dynamic models of permanent magnets synchronous machines, PMSM, are usually implemented based on the assumption that the flux established by the permanent magnets in the stator is sinusoidal. These models operate with inductances that may be considerate variable with saturation [1-2].
This paper proposes a phase coordinate dynamic model, which uses the phase fluxes and torque values previously computed with the finite element method. For all possible machine states that are determined from different rotor position and phase current values in chosen intervals, a series of 2D magnetostatic field problem is solved.
Since this dynamic model is approximates to the real machines more closely, it is a good tool for electric drives design. The model takes into account the magnetic nonlinearity and the slots influence and may consider the skewed yokes, if applicable. It was designed in order to have the possibility to connect with power electronics blocks from SimPowerSystem Simulink Toolbox [7].

The Circuit Model

In the phase voltage equations, (1), u_k, i_k, e_k, represent the phase value of winding voltage, current and back-emf induced by phase flux, R is the resistance and L_σ is the leakage inductances of the overhung winding.

$$u_k = Ri_k + L_\sigma \frac{di_k}{dt} - e_k, \qquad k = A, B, C \tag{1}$$

We assume that the phase fluxes dependence with stator currents and rotor position is known: $\Psi_k=\Psi_k(i_A, i_B, i_C, \theta)$, $k=A,B,C$. The Y stator winding

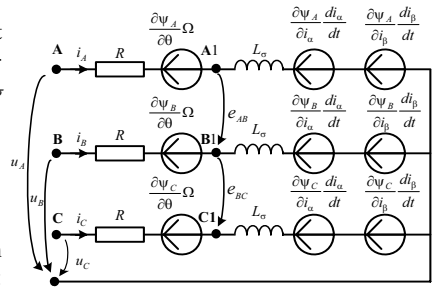

Fig.1. Three-phase circuit of PMSM

connection allows the reduction the number of initial variables by substituting the phase currents i_A, i_B, i_C, with i_α, i_β, spatial phasor components of stator current. The fluxes derivates are computed through partial derivate (2):

$$\begin{aligned} i_\alpha &= 2/3\left[\cos(0)i_A + \cos(2\pi/3)i_B + \cos(4\pi/3)i_C\right] \\ i_\beta &= 2/3\left[\sin(0)i_A + \sin(2\pi/3)i_B + \sin(4\pi/3)i_C\right] \end{aligned} \tag{2}$$

In the equivalent PMSM diagram in Fig. 1, which resulted from equation (1), the emf components are highlighted on each phase, and they were calculated through partial derivatives of the fluxes (3):

$$-e_k = \frac{d\psi_k(i_\alpha, i_\beta, \theta)}{dt} = \frac{\partial\psi_k}{\partial i_\alpha}\frac{di_\alpha}{dt} + \frac{\partial\psi_k}{\partial i_\beta}\frac{di_\beta}{dt} + \frac{\partial\psi_k}{\partial\theta}\Omega\,. \tag{3}$$

In this diagram, points A_1, B_1, C_1, separate the circuit elements whose voltage depend on the currents derivates. The voltages e_{AB} and e_{BC}, between the points A_1, B_1 and B_1 C_1 have the following expressions (4):

$$\begin{aligned} e_{AB} &= \left(\frac{\partial\psi_A}{\partial i_\alpha} - \frac{\partial\psi_B}{\partial i_\alpha}\right)\frac{di_\alpha}{dt} + \left(\frac{\partial\psi_A}{\partial i_\beta} - \frac{\partial\psi_B}{\partial i_\beta}\right)\frac{di_\beta}{dt} + L_\sigma\left(\frac{di_A}{dt} - \frac{di_B}{dt}\right) \\ e_{BC} &= \left(\frac{\partial\psi_B}{\partial i_\alpha} - \frac{\partial\psi_C}{\partial i_\alpha}\right)\frac{di_\alpha}{dt} + \left(\frac{\partial\psi_B}{\partial i_\beta} - \frac{\partial\psi_C}{\partial i_\beta}\right)\frac{di_\beta}{dt} + L_\sigma\left(\frac{di_B}{dt} - \frac{di_C}{dt}\right) \end{aligned}. \tag{4}$$

Taking into account equations (2) and the relation between the phase currents, $i_a+i_b+i_c=0$, imposed by the Y connection, and using the following notations $\Psi_{AB}=\Psi_A-\Psi_B$ and $\Psi_{BC}=\Psi_B-\Psi_C$, the above mentioned voltages (4) can be expressed based only on two currents i_a and i_c:

$$\begin{bmatrix} e_{AB} \\ e_{BC} \end{bmatrix} = \begin{bmatrix} \frac{\partial\psi_{AB}}{\partial i_\alpha} - \frac{\sqrt{3}}{3}\frac{\partial\psi_{AB}}{\partial i_\beta} + 2L_\sigma & \frac{2\sqrt{3}}{3}\frac{\partial\psi_{AB}}{\partial i_\beta} + L_\sigma \\ \frac{\partial\psi_{BC}}{\partial i_\alpha} - \frac{\sqrt{3}}{3}\frac{\partial\psi_{BC}}{\partial i_\beta} - L_\sigma & -\frac{2\sqrt{3}}{3}\frac{\partial\psi_{BC}}{\partial i_\beta} - 2L_\sigma \end{bmatrix} \frac{d}{dt}\begin{bmatrix} i_A \\ i_C \end{bmatrix} = \begin{bmatrix} M_{11} & M_{12} \\ M_{21} & M_{22} \end{bmatrix} \frac{d}{dt}\begin{bmatrix} i_A \\ i_C \end{bmatrix} = M\frac{d}{dt}\begin{bmatrix} i_A \\ i_C \end{bmatrix} \tag{5}$$

By means of adding the mechanical equations to (5), a differential equation system, (6), is obtained, which will be integrated into Simulink. The state variables of the system will be: i_a, i_c, Ω and θ.

$$\begin{cases} \dfrac{di_A}{dt} = \dfrac{e_{AB}M_{22} - e_{BC}M_{12}}{M_{11}M_{22} - M_{12}M_{21}} & \text{a)} \\ \dfrac{di_C}{dt} = \dfrac{e_{BC}M_{11} - e_{AB}M_{21}}{M_{11}M_{22} - M_{12}M_{21}} & \text{b)} \\ \dfrac{d\Omega}{dt} = \dfrac{1}{J}\left[T_e(i_\alpha, i_\beta, \theta) - T_l - F\Omega\right] & \text{c)} \\ \dfrac{d\theta}{dt} = \Omega & \text{d)} \end{cases} \tag{6}$$

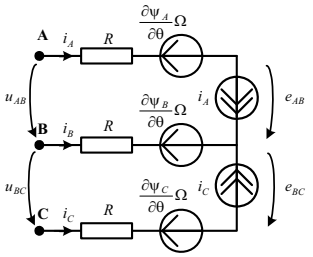

Fig.2. Equivalent circuit of the three-phase PMSM

Through applying the second Kirchhoff theorem, the voltages e_{AB} and e_{BC} can be expressed based on the line voltages and the emf

voltages induced by the movement of the rotor:

$$\begin{aligned} e_{AB} &= u_{AB} - R\left(2i_A + i_C\right) - \left(\frac{\partial \psi_A}{\partial \theta} - \frac{\partial \psi_B}{\partial \theta}\right)\Omega \\ e_{BC} &= u_{BC} + R\left(i_A + 2i_C\right) - \left(\frac{\partial \psi_B}{\partial \theta} - \frac{\partial \psi_C}{\partial \theta}\right)\Omega \end{aligned} \quad (7)$$

The implementation of the dynamic model is made starting from the equivalent diagram in Fig. 2, obtained through the replacement of the circuit part limited by points A_1, B_1, and C_1 in Fig. 1, with two remote controlled current sources, i_α and i_c whose values are known after solving the equation system (6).

Computing the Fluxes and Torque Dependences with Rotor Position and Currents by FEM Analyses of Electromagnetic Field

For a given rotor position and time, the 2D magnetostatic field in a cross-section is computed by FEM in MATLAB environment using PDE Toolbox functions [5]. The maximal current value establishes the domain that must be considered for the variation of the i_α, and i_β stator currents. The sources of the magnetic field, represented by the currents densities are computed by means of equations (2) and the relation $i_a+i_b+i_c=0$, imposed by the Y winding connection. Due to the periodical structure, it is sufficient to consider only half a pole-pitch rotor movement. For the studied six poles PMSM, the flux density chart and the equiflux lines of the magnetic field for load condition are presented in Fig. 3. The interdependence of fluxes, currents and rotor position, necessary for a dynamic model, is obtained from the numerical solution of magnetic field problems, solved

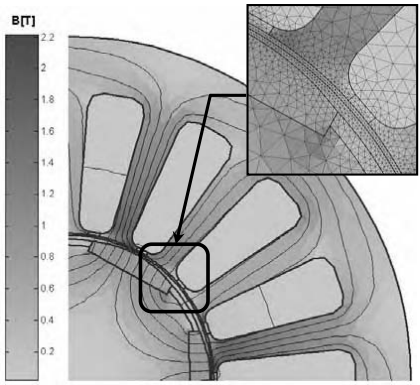

Fig. 3 The 2D FEM results in cross sections

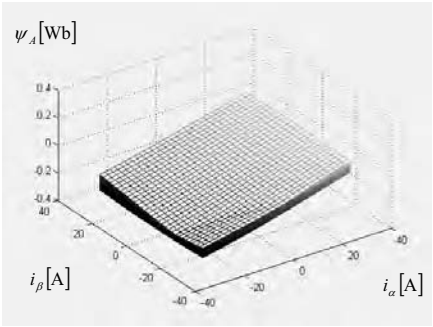

(a)

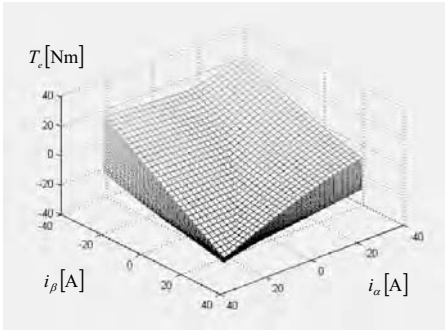

(b)

Fig. 4. The families of surfaces resulting from FEM. (a) phase *A* flux. $\Psi_A=\Psi_A(i_\alpha, i_\beta)|\theta\in[0\div30]$. (b) electromagnetic torque $T_e=T_e(i_\alpha, i_\beta)|\theta\in[0\div30]$.

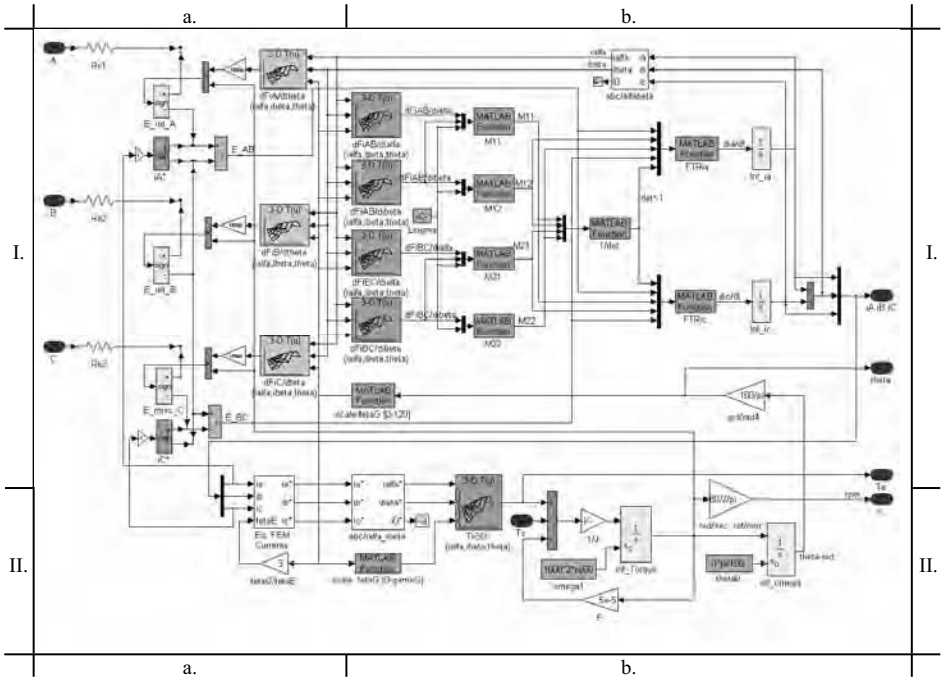

Fig.5. The MATLAB Simulink Model of Permanent Magnet Synchronous Machines

for all possible current values and positions in the selected domains. Also, by means of the virtual magnetic work method, the electromagnetic torque is computed [3]. Moreover, as the dependences of fluxes and the torque with rotor position are known, by making an average of the computed values along the yoke length, this method may be applied in the case of skewed stator as well. For the investigated PMSM, the surfaces families dependences of the phase *A* flux, $\Psi_k=\Psi_k\ (i_\alpha, i_\beta, \theta)$, and electromagnetic torque $T_e=T_e\ (i_\alpha, i_\beta, \theta)$ are plotted in Fig.4.

Dynamic Model

The model of the synchronous machine, in Fig. 5, is partially made up of components taken from SimPowerSystem toolbox, and partially of blocks from the Simulink main library. The *Look-up table* blocks contain the three-dimensional matrices of the partial derivates of fluxes, the torque values matrix depending on the position θ of the rotor and on the currents i_α and i_β, computed using relation (2), in accordance with the known i_a and i_c.

The diagram from Fig. 2 is implemented in the I.a. zone, from Fig 5. In each phase circuit there is a resistance and a remote voltage source corresponding to the emf voltage induced by the rotor movement: $(\partial\psi_k / \partial\theta)\Omega$. There is a remote controlled current source in both circuit phases *a* and *c*.

The voltages from those current sources are transferred to the I.b. zone of the diagram that corresponds to the equations (6a-b). The partial derivates of the fluxes Ψ_{AB} and Ψ_{BC}, with respect to the currents i_α and i_β, provided by the *Look-up table* blocks, are used for the computation of the elements in matrix *M*, (5).

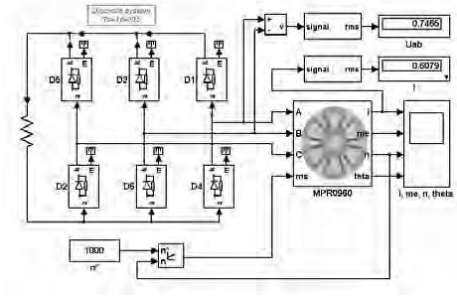

Fig. 6. Block diagram for generator regime with rectifier bridge and resistive load

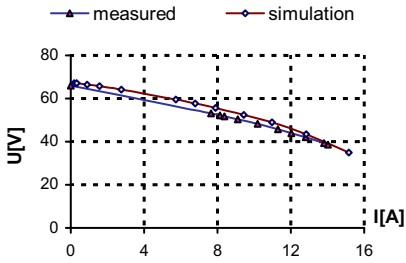

Fig.7. Phase to phase voltage vs. current at n=1000 rpm

The blocks corresponding to the equations of the movement of the rotor (6c-d) are placed in the lower part of the diagram, in zone II. The access in the electromagnetic torque *Look-up table* is possible through some blocks that scale the entrance values. They are correlated with the way in which the torque values were accumulated, considering the recurrence of the magnetic phenomena.

Model Validation

In order to evaluate the method, the PM synchronous machine with following rated data: P_N = 4 kW, M_N = 9.6 Nm, I_N = 9.3 A, M_{0m} = 16 Nm, I_{0m} = 14.9 A, k_E = 65 V/krpm, K_T = 1.075 Nm/A, was analysed. In this section of the paper the simulations results and the experimental results are presented comparatively. The experimental tests were performed on two identical coupled synchronous machines, one functioning as motor, fed from an inverter in a speed control loop, and the other functioning as generator, with resitive load coupled by a rectifier bridge. A power analyser was used to record the evolutions in time for the currents and for the line voltages.
The diagram generator simulation, Fig.6, contains the model for the synchronous machine with permanent magnets from Fig. 5, under the *MPR0960* mask. The computed phase to phase voltage versus current curve at n = 1000 rmp, plotted in Fig. 7 is similare to the experimetal curve. A comparison between the measured and the simulated results of terminal voltage and current waveform, and of its harmonic analyses, for I = 10.19 A load current, is presented in Fig. 8.

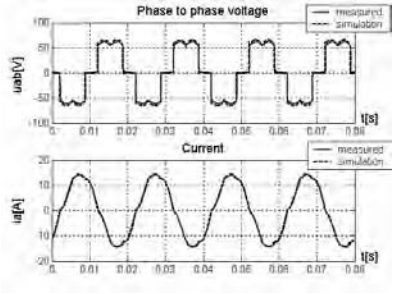

(a)

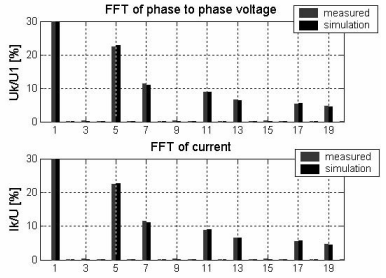

(b)

Fig. 8. Measured and calculated phase to phase voltage and current in generator regime with rectifier bridge and resistive load. (a) Time dependence. (b) Harmonic analyses.

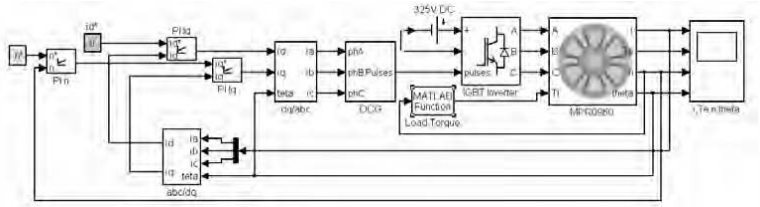

Fig. 9 Motor speed control block diagram

The testing of the model in motor regime was performed in a classical speed control drive, Fig. 9. The time-dependent variations of the currents and of the rotor speed trekking the reference speed are presented in Fig. 10. If the recordings for the measured currents, when reversing the speed, are compared to the simulated results, Fig. 11, it can be easily noticed that the simulated phenomenon is faster than the real one. The difference is caused by the discordance between the regulator coefficients.

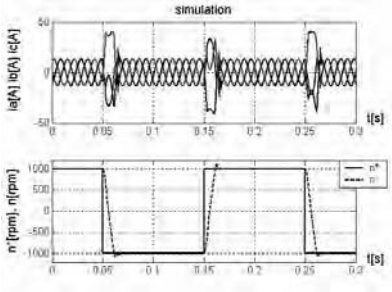

Fig. 10. Simulation results of motor reversing

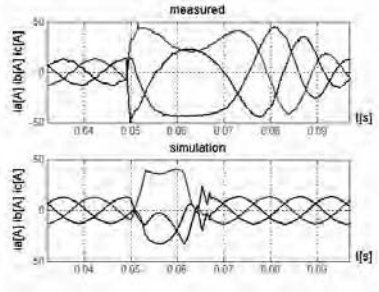

Fig. 11. Currents measured and calculated at speed reversal

Conclusions

The proposed method provides a dynamic model that considers the magnetic nonlinearity, the influence of the slots and the possible skewed yokes. In order to reduce the computation effort for finding the phase fluxes and torque matrices, the periodical structure of machines is exploited. The model is a good tool for electric drive simulations, and this method is more effective than FEM analyses using the time-stepping technique [4]. The implementation of the dynamic model in the same software with FEM of magnetic field computation is a good way to correlate the design of the electric machines, power electronics and drive systems.

References

[1] Chee-Mun Ong, “Dynamic Simulation of Electric Machines”, Prentice-Hall, New Jersey, 1998.
[2] I. Boldea, S.A. Nasar, Electric Drives, Spring 1998,Timisoara, Romania,Lexington, Ky., USA
[3] Gh. Mândru, M Rădulescu, Numerical Analyses of Electromagnetic Field, Ed. Dacia, Cluj-Napoca, 1986.
[4] F. David, O. Craiu, M. Covrig, L. Melcescu, Finite Element Study of the Induction Motor Transient Regime, Proc. of. ELECTROMOTION '97, Cluj-Napoca, Romania, pp. 111-115, 1997.
[5] MATLAB©, Partial Differential Equation Toolbox User’s Guide, The MathWorks, Inc., 1995.
[6] TransÉnergie Technologies, SimPowerSystems for Use with Simulink® User’s Guide”, Hydro-Québec, and The MathWorks, Inc., 2002.

Electromagnetic Fields in Mechatronics, Electrical and Electronic Engineering
A. Krawczyk et al. (Eds.)
IOS Press, 2006

THE INFLUENCE OF THE ELECTROMAGNETIC WAVE POLARIZATION ON SAR IN HUMAN BODY MODEL

Arkadiusz Miaskowski[*], Andrzej Krawczyk[**]

[*]Electrotechnical Institute , Pozaryskiego 28, 04-703 Warsaw, Poland, a.miaskowski@iel.waw.pl
**Central Institute for Labour Protection, Warsaw, Poland

***Abstract** – The paper is aimed at computer simulation of SAR distribution in human body dedicated to the investigation of how SAR distribution depends on polarizations. The simulation is based on FDTD calculations of the whole-body averaged SAR in an anatomically realistic voxel model of the human body. SAR values are presented for 900 MHz, 1800 MHz, 2400 MHz for plane wave exposure.*

Introduction

The increasing use of wireless portable communication devices has created public concern about their safety, in spite of the fact that many reports show no substantive scientific evidence of a long-term public health hazard. On the other hand available experimental evidence indicates that the exposure of resting humans to electromagnetic field (EMF) for about 30 min produces the whole-body SAR in amount of 1 to 4 W kg^{-1} , that causes a body temperature to increase of approximately 1 ^{0}C [1]. In tissue, SAR is proportional to the square of internal electric field strength ($|\boldsymbol{E}|^2$) and complex conductivity $\sigma^*=\sigma+\omega\varepsilon_0\varepsilon_r''(\omega)$ and its values depend on the following factors:

1) the incident field parameters, i.e. the frequency, intensity, polarization,

2) the characteristic of the exposed body, i.e., its size and internal and external geometry, and electric properties of the various tissues,

3) ground effects and reflector effect of other object in the field near the exposed body.

In this paper authors investigated how SAR distribution depends on polarizations using model based on Human Visible Project developed by U.S. National Library of Medicine [2]. The model consists of approximately 18 millions voxels, each of dimension 3mm, fulfilling the phantom of an adult, segmented into 42 tissue types, as shown in Fig 1. Dielectric properties of tissues were described by the Cole–Cole approximation (Eq. 1-2)[3] for considered frequencies, i.e., 900 MHZ, 1800 MHz, 2400 MHz, with the parameters given by Gabriel [4].

$$\varepsilon'(\omega) = \varepsilon_\infty + (\varepsilon_s - \varepsilon_\infty)\frac{1 + (\omega\tau_0)^{1-\alpha}\sin\frac{1}{2}\alpha\pi}{1 + 2(\omega\tau_0)^{1-\alpha}\sin\frac{1}{2}\alpha\pi + (\omega\tau_0)^{2(1-\alpha)}} \tag{1}$$

$$\varepsilon''(\omega) = (\varepsilon_s - \varepsilon_\infty)\frac{(\omega\tau_0)^{1-\alpha}\cos\frac{1}{2}\alpha\pi}{1 + 2(\omega\tau_0)^{1-\alpha}\sin\frac{1}{2}\alpha\pi + (\omega\tau_0)^{2(1-\alpha)}} \tag{2}$$

where: α determines the spread of relaxation frequencies within the tissue (i.e., the higher α is, the more spread are the relaxation frequencies), ε_∞ is the high frequency relative permittivity, ε_s is the low frequency relative permittivity.

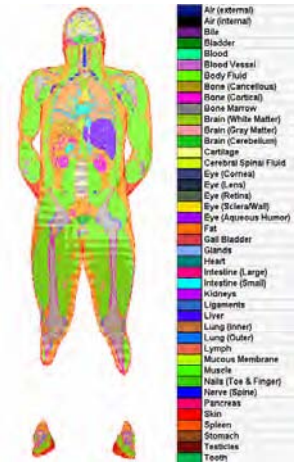

Fig.1 Human realistic model: 42 tissues anatomically correct

Results

In order to investigate influence of polarization on SAR, authors considered twelve situations as shown in Fig. 2 [5].

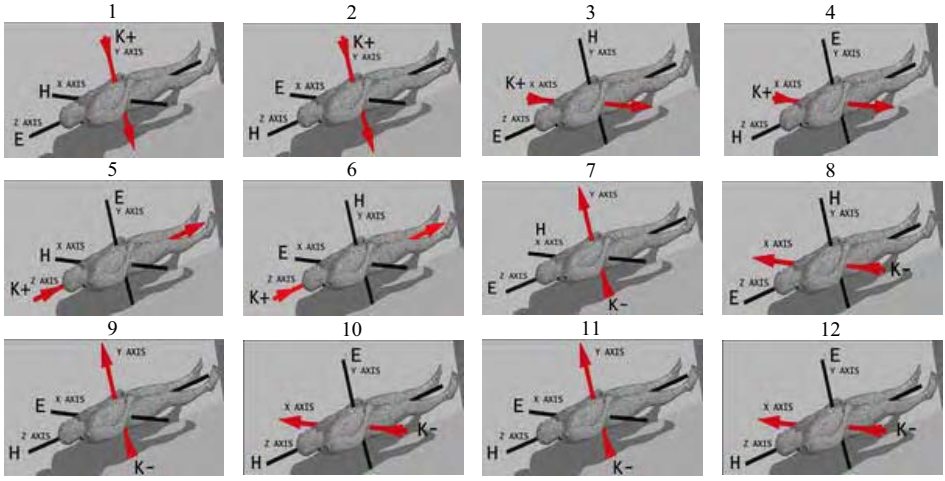

Fig. 2. Twelve different polarizations

Results of calculations are shown in Table I.

TABLE I. Result of calculations of whole-body SAR

Frequency [MHz]	Polarization	SAR [W/kg]
900	1	0.0624
1800	1	0.0588
2400	1	0.0552
900	2	0.04
1800	2	0.038
2400	2	0.0361
900	3	0.0596
1800	3	0.0643
2400	3	0.063
900	4	0.0506
1800	4	0.0461
2400	4	0.0451
900	5	0.0373
1800	5	0.0223
2400	5	0.0231
900	6	0.0352
1800	6	0.0241
2400	6	0.0233

Frequency [MHz]	Polarization	SAR [W/kg]
900	7	0.0638
1800	7	0.0568
2400	7	0.0526
900	8	0.041
1800	8	0.0384
2400	8	0.0359
900	9	0.0619
1800	9	0.0604
2400	9	0.0583
900	10	0.0512
1800	10	0.0461
2400	10	0.0448
900	11	0.0326
1800	11	0.0229
2400	11	0.0227
900	12	0.0351
1800	12	0.0212
2400	12	0.0225

As it can be seen from Table 1 the worst case is polarization “3” where SAR value is 0.0643 W kg^{-1} for 1800 MHz. In Fig. 3-4 maxSAR [W/kg] distribution in body model for polarization ”3” is shown.

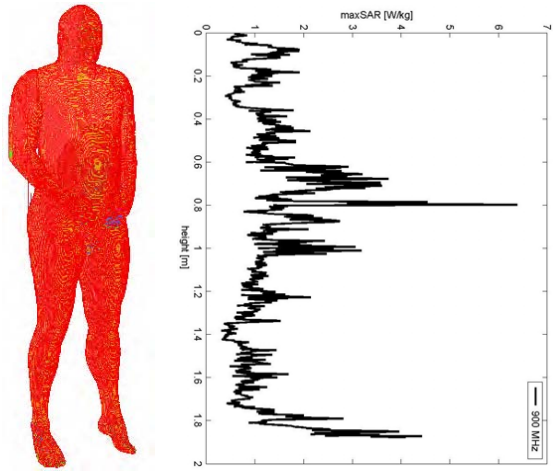

Fig.3 maxSAR distribution in body model for polarization “3” for 900 MHz

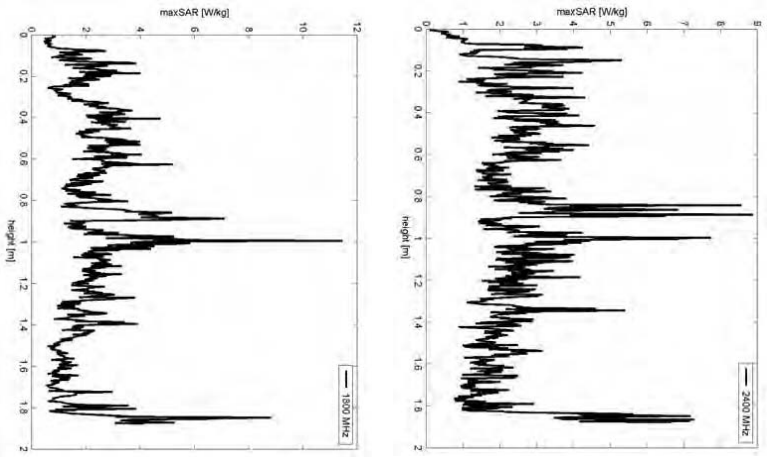

Fig.4 maxSAR distribution in body model for polarization "3" for 1800 MHz (left) and 2400 MHz (right)

Conclusion

According to the results we can find out that when the long axis of the human body is parallel to the electric field vector, and under plane-wave exposure conditions (i.e., far-field exposure), whole-body SAR reaches maximal values (as shown in Figure 2 and in the Table I). In general, exposure to a uniform (plane-wave) electromagnetic field reveals in a highly non-uniform deposition and distribution of energy within the body, which must be assessed by computer dosimetry as shown in this paper or by measurement using phantoms.

References

[1] International Commission on Non-Ionizing Radiation Protection, Guidelines for limiting exposure to time-varying electric, magnetic, and electromagnetic fields (up to 300 GHz), Health Physics Society, 1998

[2] http://www.nlm.nih.gov/research/visible/visible_human.html

[3] Cole, K.S. and Cole, R.H., Dispersion and absorption in dielectrics, J. Chem. Phys., 1941, pp. 341-351

[4] Gabriel C, Compilation of the Dielectric Properties of Body Tissues at RF and Microwave Frequencies, Brooks Air Force Base, report no AL./OE-TR-1996-0037,1996

[5] Finite Difference Time Domain Front-end Utility developed by D. LeBlack, D. Hatcher, R. Post (http://www.brooks.af.mil/NHRC/nhrc.h)

Electromagnetic Fields in Mechatronics, Electrical and Electronic Engineering
A. Krawczyk et al. (Eds.)
IOS Press, 2006

3D FEM SIMULATION OF AN ELECTROMAGNETIC PUMP USING ANSYS AND EXPERIMENTAL VALIDATION

Daniel Moríñigo[a,b], Mª Ángeles Rodríguez[a], Rafael Cuesta[a], Jose Antonio Maroto[a], Ana Rivas[a], David Escudero[a]

[a] Cidaut, Research and Development Centre in Transport & Energy, Technological Park of Boecillo, Valladolid, Spain, danmor@cidaut.es
[b] Dpt. of Electrical Engineering, University of Valladolid, Spain

***Abstract** – The experimental study of an electromagnetic pump for high temperature liquid metal shows many technical inconveniences, and economical disadvantages. Simulation can be a more reasonable alternative from the technical and economical point of view. But, in order for the simulation to be considered reliable, it must be experimentally validated. In this paper we present the experimental validation of ANSYS® code for the electromagnetic simulation of a liquid metal pump, whose principle and working process are described.*

1. Introduction

The experimental study of an electromagnetic pump shows a number of technical inconveniences and economic disadvantages. In order to operate an electromagnetic pump with molten aluminium, a large facility with many different devices, monitoring equipment, safety measures and specially trained personnel are required. As an example, we can mention the pre-heat oven, crucible, melting furnace, adjustable power supply, PLC, etc. And all these bulky devices need a huge space. For a small laboratory, the investment in space and money is very high if the main aim is only to study the operation of a pump from an electromagnetic point of view. In a recent article [1], the authors used a solid secondary in an electromagnetic pump only for the purpose of studying electromagnetism and obtaining a general idea of the thrust provided by the pump. So, from the technical point of view, if the electromagnetism of the pump is the aim of the study, it is enough to use a test bed with a solid secondary. When we say that working with high temperature liquid metals present 'technical inconveniences', we mean that a lot of work must be done, during a long period of time, to tune all the required facilities and check all safety measures. Working with a solid secondary is faster, considerably cheaper, safer and the results can be extrapolated to liquid secondary [2].

An electromagnetic pump is a magnetohydrodynamic device. Magnetohydrodynamics (MHD) is the theory of interaction of electrically conductive fluids with magnetic fields. It is important in many engineering problems, such as molten metal pumping and finds application in geophysics and astronomy [3]. Our study is focused on an AC electromagnetic pump used in low pressure and gravity casting. The governing equations of the pumping action are: Maxwell equations for electromagnetism and one model for fluid-dynamics, such as the k-ε model. The simulation of the electromagnetic pump requires the simultaneous solving of the electromagnetic problem and the fluid dynamics problem. When the magnetic Reynolds number is low, the velocity of the fluid has little influence on the magnetic flux density [4], whereas the flow can be strongly governed by the magnetic field [5]. Therefore, both fields are considered uncoupled. This simplified frame applies to industrial processes such as pumping, stirring, metal treatment, etc.

Consequently, the process of simulation is less complicated. Nevertheless, the first step of the simulation requires solving the electromagnetic problem. The molten fluid, secondary of the pump, can be considered as a solid. The resulting Lorentz force field is incorporated as a volume force source into the k-ε model, that can be solved independently from the electromagnetic problem, as long as there is not magnetic coupling. So this method may require the use of two codes to solve the complete MHD simulation [5, 6]: one code for the electromagnetic simulation: ANSYS®, FLUX3D®, etc., and a second code for the fluid dynamics simulation: FLUENT®, PHOENICS®, etc. The functioning of an electromagnetic pump has been simulated at CIDAUT using ANSYS® and FLUENT®. The aim of this paper is to present the work concerning the electromagnetic simulation and its experimental validation by means of force measurement exerted by the MHD pump on an aluminium solid secondary, in substitution of the channel carrying molten metal [1, 7]. The pump subject of this study is of the magnetodynamic type [8], and it is used industrially in low pressure counter-gravitational casting processes.

2. Electromagnetic Pump Operating Principle

The pump is made up of two elements which are series-connected (figure 1): a transformer and a C-shape electromagnet. The secondary of the transformer is a channel carrying molten metal encased in non-electrical conductive ceramic walls. When the primary coil is fed with a single-phase AC voltage, an electric current is induced in the molten metal (figure 2 a). The electromagnet produces a magnetic flux density field in a specific section of the channel of molten metal, known as *slot*, and perpendicular to the induced electric current (figure 2 b). The cross product (1) of the current density field induced in the molten metal, J, and the magnetic flux density field, B, produces a three-dimensional field of electromagnetic volumetric forces, F, distributed along the channel, which provides the pumping action on the molten metal.

$$\vec{F} = \vec{J} \times \vec{B} \tag{1}$$

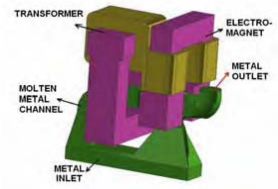

Fig.1 Physical construction of the electromagnetic pump with all ceramic shapes deleted.

(a) (b)

Fig.2 Electromagnetic pump operating principle.

3. Experimental Section

3.1 ANSYS® simulation procedure

The simulations have been carried out in the ANSYS® FEM commercial code, which provides with a number of 3-D elements to perform electromagnetic simulations. The selection of the right element to model the pump components was the first problem we encountered because not all available elements are suitable to represent permeable materials along with non-permeable. For this reason, we studied all different types of 3-D magnetic field elements available (geometry, material properties, loads, analysis types, output data...) and we verified that the SOLID117 element allows carrying out low-frequency simulations involving ferromagnetic and non-ferromagnetic materials.

This element is based on the edge-flux formulation, which associates degrees of freedom (DOFs) with element edges rather than element nodes. The element is defined by 20 nodes. The electromagnetic pump mesh was created manually using the HYPERMESH® program. The model consisted of approximately 130.000 hexahedral elements (figure 3) and was imported into ANSYS®. The electromagnetic pump mesh contains four different elements to represent: air, aluminium channel, magnetic cores and coils of the transformer and electromagnet. The solid channel, used for the validation, was built using the 7075T651 aluminium alloy, and therefore, we used the properties of this alloy to model the channel in ANSYS®. The rest of elements of the pump were modelled according to the real materials used in normal operating conditions: M19 steel for the transformer and electromagnet cores, and anodized aluminium for the coils.

Prior to specifying the model boundary conditions, DOFs of the different model elements must be selected. Each type of element has different DOFs, depending on its role in the model. For instance, DOFs are different if the electrical current is imposed or induced. The boundary conditions specified in the model are the electric currents that flow through the transformer and electromagnet coils (50 Hz AC single-phase).

The ANSYS® simulation provides the following variables of interest: electrical current density in the solid channel, magnetic flux density and the electromagnetic force field in all nodes and centroids of the mesh elements. The electromagnetic force field is three-dimensional and these forces are distributed all along the channel. As was to be expected, the maximum force values are produced in the slot, due to the fact that the cross section in this region is narrower than in the rest of the channel, and therefore the current density is also greater. In addition, this region of the channel is contained in the air-gap of the electromagnet, where the magnetic flux density has the maximum values.

Results from one of the simulations of the electromagnetic pump are shown in figure 4, where the forces in Newtons produced over the finite elements of the channel can be observed. The sum by components of these forces along the channel (considered as rigid solid) is the variable that we used to compare with the experimental tests.

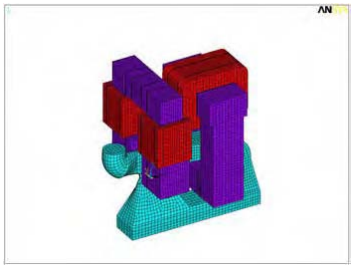

Fig.3 Mesh of the pump. Air elements are not shown.

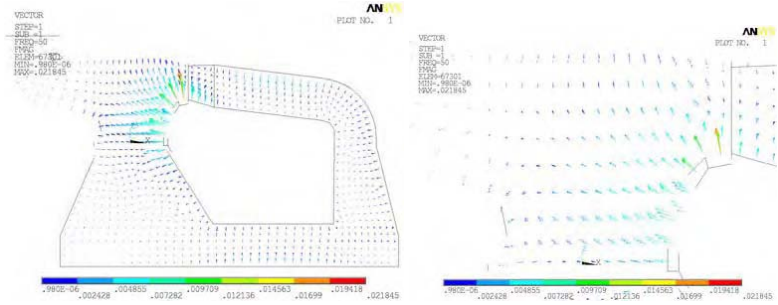

Fig.4 Electromagnetic forces from simulation expressed in Newtons.

3.2 Test Bed

The main aim of this work was the validation of the electromagnetic pump simulation with experimental tests, using the whole force exerted on the secondary of the pump. For this reason, we designed a test bed using a solid secondary in substitution of the channel carrying molten aluminium (figure 5). This solid channel, made out of the same alloy considered in the simulation (7075T651), was placed exactly in the same position that it would be occupied by the liquid metal in the real pump (figure 6). The rest of the elements used were the original parts of the pump.

The physical variable that was used to compare the experimental results with the simulation results is the force exerted on the solid channel when the coils of the electromagnet and the transformer are fed by a variable toroidal single-phase autotransformer. Two load cells were used to measure the force (figure 5). One of the cells measured the horizontal component of the force, and the other the vertical one. When the pump was under operating conditions, the load cells measured force variations with respect the standstill position.

The pump has a vertical symmetry plane. The component of the force perpendicular to this plane was dismissed in the experimental and simulation results, because it was symmetrical with respect to this plane and hence the sum gave a null resultant.

In all laboratory tests, the electrical current and the signals from the load cells were registered using a PC-based data acquisition system (DAQ) from National Instruments (PCI 6024E, Labview).

Fig.5 Solid secondary that substitutes the channel carrying molten aluminium.

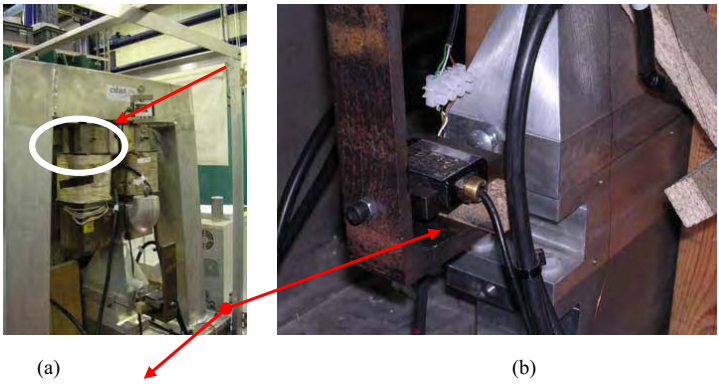

(a) (b)

Fig.6 Test bed. The position of the load cells is shown.

4. Results and Discussion

During the laboratory tests, the pump was fed with a single-phase, 50 Hz electric current, whose RMS value was measured. Simultaneously, using a PC-based DAQ system, the output signals of the two load sensors were registered. The electromagnetic force is time-dependent with a frequency which is double the line frequency (100 Hz in this particular case). With the DAQ system, the whole force signals were registered, but in order to compare simulation and experimental results, it was necessary to calculate the mean value of the force sinusoidal signals. The module (F) of the propulsion force exerted on the solid channel was calculated (2) from the mean values of the two components of the measured force.

$$F = \sqrt{F_{vertical}^2 + F_{horizontal}^2} \tag{2}$$

A set of laboratory tests for different values of the electric current were carried out. Next, the operation of the pump was simulated with ANSYS® under the same current values measured in the tests. The whole force on the channel was calculated by summing up the electromagnetic force components in all element centroids, provided by the ANSYS® simulation.

The results from both laboratory tests and simulations are shown graphically in figure 7. In figure 7 (a), it is represented the whole force, expressed in Newtons, as a function of the RMS value of the electrical supply current of the pump. The relative error, comparing the simulation with respect to the laboratory tests, is represented in figure 7 (b).

The obtained relative error is within a ±5% range. Therefore, we consider that the simulation results agree, extremely accurately, with the real electromagnetic performance of the pump, considering the secondary of it as a rigid solid.

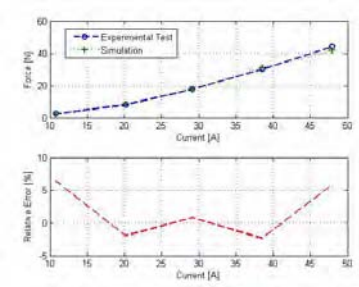

(a)

(b)

Fig.7 Comparison of simulation and experimental results.

5. Conclusions

In this paper, it can be concluded that ANSYS® is a powerful and useful tool for the electromagnetic simulation of the MHD pump. The test bed built with a solid secondary allowed the experimental validation of the electromagnetic simulation using the relationship between the whole force exerted on the solid channel with the electric supply current. It can also be said that the obtained results are satisfactory. Simulation error range, compared with test bed results, is within ± 5% band.

We intend to present the results of the complete pump simulation, including fluid-dynamic calculations, in future papers.

References

[1] Tsutom Ando, Kazuyuki Ueno, Shoji Taniguchi, and Toshiyuki Takagi, Induction pump for high-temperature molten metals using rotating twisted magnetic field: Thrust measurement experiment with solid conductors, IEEE Transactions on Magnetics, Vol. 38, 1789-1796, 2002.

[2] Tsutomu Ando, Kazuyuki Ueno, Shoji Taniguchi, and Toshiyuki Takagi, Induction pump for high-temperature molten metals using rotating twisted magnetic field: molten gallium experiment, IEEE Transactions on Magnetics, Vol. 40, 1846-1857, 2004.

[3] R. Moreau, Magnetohydrodynamics, Kluwer Acadmic Publishers, 1990.

[4] P.A. Davidson, An introduction to magnetohydrodynamics, Cambridge: Cambridge University Press, 2001.

[5] Michael Hughes, Computational Magnetohydrodynamics, London: University of Greenwich, Doctoral Thesis, 1994.

[6] K. A. Periclous, The Development and Validation of Computational MHD Techniques for the Modelling of Metal Production Processes, Fifth International Pamir Conference on Fundamental and Applied MHD, Vol. 1, L21-L26, 2002.

[7] Lluís Massagués, Aportaciones al estudio de los motores de inducción magnetohidrodinámica, Barcelona: Universidad Politécnica de Cataluña, Doctoral Thesis, 2001.

[8] V. P. Polishchuk, Industrial use of magnetodynamic devices, Vol. 11, No. 1, 93-102, 1975.

Electromagnetic Fields in Mechatronics, Electrical and Electronic Engineering
A. Krawczyk et al. (Eds.)
IOS Press, 2006

MAGNETIC BEHAVIOUR OF SUPERCONDUCTING FOIL UTILIZED FOR LINEAR-TYPE MAGNETIC FLUX PUMP

Taketsune Nakamura, Yoondo Chung and Tsutomu Hoshino

Department of Electrical Engineering, Graduate School of Engineering, Kyoto University,
Kyoto-Daigaku Katsura, Nishikyo-Ku, Kyoto 615-8510, JAPAN
E-mail: tk_naka@kuee.kyoto-u.ac.jp

Abstract *– Magnetic behaviour of superconducting Nb foil, which is utilized for the proposed linear-type magnetic flux pump, was investigated based on 3D FEM analysis. The superconducting (nonlinear) J-E expressions were taken into account for the precise analysis. It was found that there exists the appropriate range of the DC bias current for the realisation of the travelling magnetic field. The value of the travelling magnetic flux was also found to be frequency dependent, and almost shielded over around 50 Hz. These findings are important for the optimal design of the superconducting flux pump for the compensation of the current decay in the superconducting magnets.*

Introduction

Superconducting magnet is one of the most powerful tool for the realisation of high magnetic field. For instance, Nuclear Magnetic Resonance (NMR) as well as Magnetic Resonance Imaging (MRI) analyzer is commercialized with the use of such magnets. NMR and MRI applications, however, need extremely stable magnetic field with respect to time in order to obtain the high resolution signals. In an ideal case, this stable current can be realised by using ”true” superconducting magnet that has really zero resistivity in the superconducting loop, i.e., persistent current mode. From the practical point of view, on the contrary, the contact resistance between the superconducting coil and the current leads exists, and such resistance results in the current decay. Furthermore, thermal relaxation such as so-called flux creep phenomenon [1] in the superconducting materials cause also intrinsic and slight current decay in the magnets. Therefore, the compensator for such current decrement is crucial for the high performance systems. In order to realise such compensation, the magnetic flux pump has been proposed and developed by Iwasa et al., at MIT, USA [2-4]. On the other hand, we have proposed the linear-type magnetic flux pump (LTMFP) as an another type of the compensator [5], and then demonstrated the compensation performance of the current decay by the experiment [6]. For the effective and optimal operation of the system, on the other hand, the nonlinear relationship among the AC current, DC bias current, and the driving frequency has to be clarified.

In this study, the magnetic behaviour of the superconducting Nb foil, which is utilized for the above-mentioned flux pump, is analysed based on the 3D finite element method. Nonlinear *J-E* expression of the Nb foil is taken into account in order for the precise analysis. Dependences of the DC bias current and driving frequency upon the magnetic behaviour are to be presented and discussed.

Basic Principle of Linear-type Magnetic Flux Pump

In this chapter, basic principle of the superconducting LTMFP is explained based on Fig. 1. A superconducting Nb foil, 20 μm in thickness for our system, and the superconducting Niobium

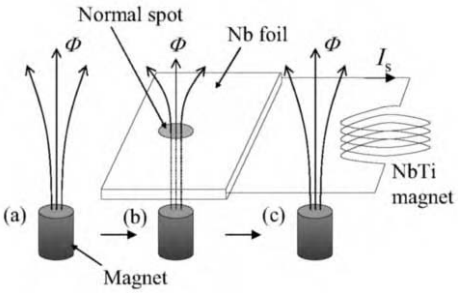

Fig. 1 Basic principle of linear-type magnetic flux pump. Term 'normal spot' denotes the region of the magnetic flux Φ invaded in the superconducting Nb foil. By moving the magnet from (a) to (c), the current I_s increases because the magnetic flux Φ are pumped in the superconducting loop.

-titanium alloy (NbTi) magnet are connected each other for the formation of the superconducting closed loop. When both of Nb foil and NbTi magnet are truely in the superconducting state, the current I_s will flow without any energy dissipation, i.e., persistent current mode. However, the practical current slightly decay due to the aforementioned reasons. Then, this current decay is compensated by using the LTMFP. That is, by moving the magnet from (a) to (b), the magnetic flux Φ invades in the superconducting Nb foil. The flux invaded region is locally in the normal conducting state, and this region is called 'normal spot'. It should be noted that other area except for the normal spot in the Nb foil remain to be in the superconducting state, i.e., zero resistance. When the normal spot passes through the Nb foil by moving the magnet from (b) to (c), the flux Φ is pumped in the superconducting loop. Therefore, the current I_s can be compensated by repeating the procedures (a)-(c).

Analysis Method

Fabricated Linear-type Magnetic Flux Pump

Practical travelling magnetic field is produced by using the AC windings as shown in Fig. 2 [5,6]. The superconducting Nb foil is placed at the air-gap in between the iron teeth and the yoke. The AC coils are wound at the iron teeth with the 3-phase and 4-pole configuration. DC bias coil is also installed in order to move up the air-gap magnetic field, for the monopolar magnetic field.

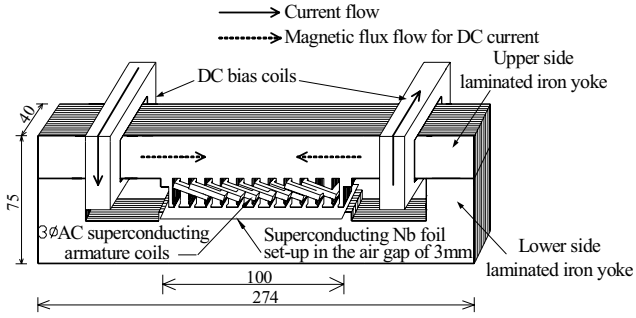

Fig. 2 Structure of fabricated linear-type magnetic flux pump [5,6].

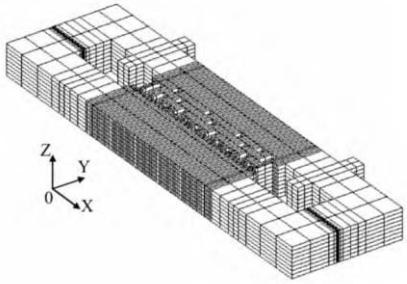

Fig. 3 3D FEM analysis model. Upper half of the fabricated flux pump (Fig. 2) along the z-axis is modelled for symmetry, and natural boundary condition is set at this surface.

Analysis Model and Method

The fabricated LTMFP (Fig. 2) is directly modelled for the FEM analysis of the magnetic behaviour in the superconducting Nb foil (Fig. 3). By using the symmetry of the electromagnetic field, upper half of the flux pump along the z-axis is only modelled, and then the natural boundary condition is set at this surface. For the current density, J, vs. electric field, E, (J-E) constitutive relation, the commonly used power-law curve is introduced as follows,

$$\boldsymbol{E} = E_0 \left(\frac{J}{J_c(B)} \right)^n \frac{\boldsymbol{J}}{J} \tag{1}$$

where, boldface shows the vector. The parameter E_0 denotes the electric field criterion for the definition of critical current density J_c, which is varied as a function of the magnetic field B. As can be seen in Eq. (1), the direction of $\boldsymbol{E}$ is considered to be same with that of $\boldsymbol{J}$. Typical values of J_c for superconducting Nb is expressed from the reference [7] as follows:

$$J_c(B) = 2 \times 10^9 - 4.77 \times 10^9 \cdot B \quad [\mathrm{A/m^2}] \tag{2}$$

The value of the power-law index n is unclear here, and then we select 10 as an adequately large value. Eqs. (1) and (2) is introduced for the superconducting Nb foil, and the analysis is carried out by means of 3D finite element method.

Results and Discussion

Dependency of DC Bias Current

Fig. 4 shows the contour plots of magnetic flux density in the superconducting Nb foil in a travelling magnetic field, for the electrical angles θ at 0, π/2, π, (3/2)π and 2π, respectively. The analyses are performed for the conditions of driving frequency f= 10 Hz, AC current I_{AC}= 1 A_{rms}, and for different DC bias currents I_{DC} at 10 and 400 mA, respectively. The upper-most surface of each

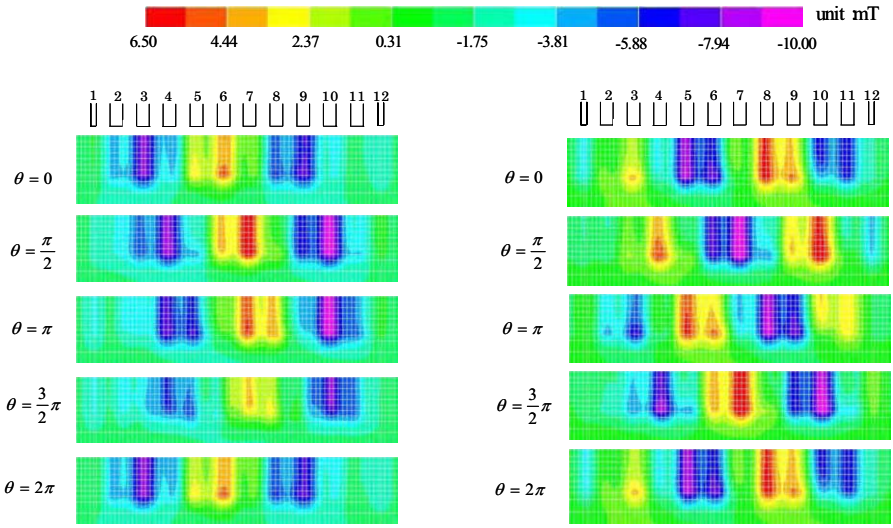

(a) I_{DC}= 10 mA (b) I_{DC}= 400 mA

Fig. 4 Contour plots of magnetic flux density in the Nb foil for different electrical angles θ (I_{AC}= 1 A_{rms}, f= 10 Hz). The positions of the iron teeth at the primary side are also illustrated with numbers. Upper-most surface of each figure is the symmetrical plane.

figure is the symmetrical plane, and then the half of the foil is only shown in the figures. The positions of the iron teeth at the primary side are also illustrated for reference by numbering from left (1) to right (12). As can be easily seen, the magnetic fluxes invade in the foil for all figures depending on the electrical angle θ and the teeth position. In case of I_{DC}= 10 mA, however, the magnetic fluxes move only locally in between three or four numbers of teeth (see Fig. 4(a)). This means that the moving magnetic fluxes are not realised at this small bias current, and then this local movement of the fluxes results in the energy dissipation. On the other hand, when the bias current increases up to 400 mA, for instance, the moving magnetic fluxes are clearly realised as shown in the figure (b). In this case, the Nb foil surely works for the the flux pumping. This is due to the magnetic field dependence of the *J-E* relations in the Nb foil, i.e., the movement of the magnetic fluxes are confined in the local area. The superconducting Nb foil, however, transits to the normal conducting state if the bias current is so large.

This has already been confirmed by the analysis, and the superconducting loop is no more maintained in this case. Therefore, the appropriate range of the DC bias current exists for the realisation of the pumping function.

Dependency of Driving Frequency

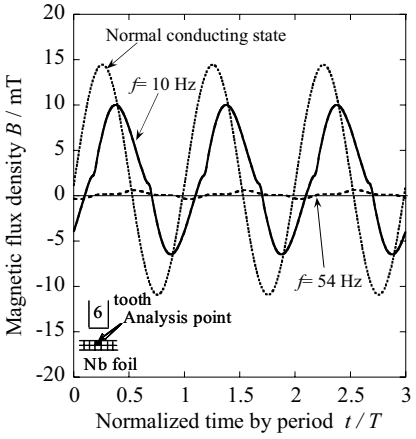

(a) Temporal variations

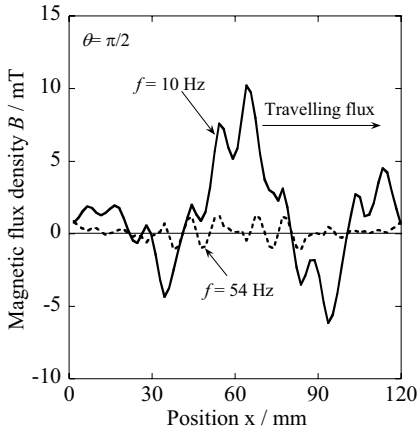

(b) Spatial variations

Fig.5 Temporal and spatial variations of the magnetic flux density in Nb foil at 10 Hz and 54 Hz, respectively. Analysis position for figure (a) is illustrated in the inset (see Fig. 4 for the number 6 of the tooth). The electrical angle θ for figure (b) is $\pi/2$.

Next, the dependency of the driving frequency upon the magnetic behaviour of the Nb foil is investigated. In this section, the AC current I_{AC} and the DC bias current I_{DC} are set to 1 A_{rms} and 400 mA, respectively. Fig. 5(a) shows the temporal variations of the magnetic flux density at the uppermost surface of the superconducitng Nb foil just below the tooth No. 6 (see the inset). The time t is normalised by the period $T(=1/f)$. For comparison, the waveform in the normal conducting state (not superconducting) is also plotted in figure (a) (no frequency dependence for normal conducting state).

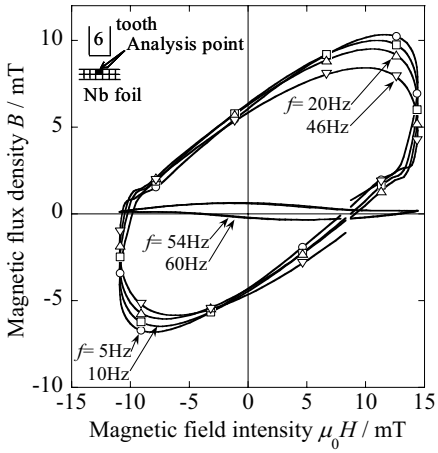

Fig.6 Frequency dependence of hysteresis loops for a travelling magnetic field in the superconducting Nb foil. Analysis point is illustrated in the inset (see Fig. 4 for the tooth number 6).

The waveform at f= 10 Hz is delayed compared to the normal conducting state in figure (a), and this is because of the shielding effect of the superconducting Nb foil. In other words, the equivalently inductive component is induced by this shielding current. Further, the waveform for this frequency is distorted due to the nonlinear *J-E* curves. In case of f= 54 Hz, on the contrary, the magnetic flux is almost shielded. That is, the time constant for the magnetic variation in the Nb foil is larer than the travelling speed of the magnetic field, and then the magnetic field is almost shielded in this frequency range. The spatial distributions of the magnetic flux density in the Nb foil are also plotted for θ= π/2 in figure (b). As can be seen, although the waveform for f= 10 Hz realise the travelling waveform, that for f= 54 Hz is almost shielded no dependence of the position in the Nb foil. Therefore, the magneric field is not able to invade in the Nb foil if the driving frequency is high.

In order to see the frequency dependence in more detail, the hysteresis loops in a travelling magnetic field are plotted for different driving frequencies in Fig. 6. The hysteresis loops are observed surely because of the nonlinear *J-E* relations. As shown, the higher the driving frequency is, the smaller the peak value of the hysteresis loop is, from f= 5 to 46 Hz. Moreover, when the driving frequency is higher than 46 Hz, e.g., 54 Hz, 60 Hz, the hysteresis loop is not formed and show almost perfect diamagnetic behaviour. Then, the threshold frequency for shielding in this analysis is around 50 Hz. Namely, there exists the upper limit of the driving frequency for the pumping action depending on the material property, i.e., magnetic field dependent *J-E* characteristics.

Conclusion

In this paper, the magnetic behaviour of the superconducting Nb foil, which is utilized for the linear-type magnetic flux pump, was examined based on the 3D finite element method. It was found that the appropriate range of the DC bias current exists for the realisation of the travelling magnetic flux. It was also found that the pumping rate is frequency dependent, and then almost shielded at around 50 Hz. This is because of the magnetic field dependent *J-E* relations. These results are important for the optimal design of the flux pump.

Acknowledgements

We would like to thank Prof. Emeritus Itsuya Muta for giving us an idea about linear-type magnetic flux pump. We are also grateful to Mr. Takashi Teramoto for performing FEM analysis. This work has been supported in part by the 21st Century COE Program (No. 14213201) in Japan.

References

[1] M. Tinkham, Introduction to Superconductivity (second edition), McGraw-Hill, 1996, pp 148-190
[2] Y. Iwasa, Microampere flux pump for superconducting NMR magnets part 1; basic concept and microtesla flux measurement, Cryogenics, Vol. 41, pp 385-391, 2001
[3] S.K. Jeong, H. Lee and Y. Iwasa, Superconducting flux pump for high temperature superconductor insert coils of NMR Magnets, Advances in Cryogenic Engineering, Vol. 48, pp 305-312, 2002
[4] H. Lee, H.M. Kim and Y. Iwasa, A flux pump for NMR Magnts, IEEE Transactions on Applied Superconductivity, Vol. 13, No. 2, pp 1640-1643, 2003
[5] Y. Chung, I. Muta, T. Hoshino, T. Nakamura and M.H. Sohn, Design and performance of compensator for decremental persistent in HTS magnets using linear type magnetic flux pump, Cryogenics, Vol. 44, No. 11, pp 839-844, 2004
[6] Y. Chung, I. Muta, T. Hoshino and T. Nakamura, Characteristics of a persistent current compensator for superconducting NMR magnets using linear type magnetic flux pump, IEEE Transactions on Applied Superconductivity, Vol. 15, No. 2, pp 1338-1341, 2005
[7] R.P. Huebener, R.T. Kampwirth, R.L. Martin, T.W. Barbee Jr. and R.B. Zubeck, Critical current density in superconducting niobium films, Journal of Low Temperature Physics, Vol. 19, pp 247-258, 1975

Electromagnetic Fields in Mechatronics, Electrical and Electronic Engineering
A. Krawczyk et al. (Eds.)
IOS Press, 2006

THE QUICK METHOD OF THE COLOURED MAPS FOR THE FIELDS VISUALISATION

CNRT Futurelec 2 –outils de calcul (Interface- post traitement)
Napieralska-Juszczak Ewa*, Krolewiak Adam*, Napieralski Piotr**

*Universite d'Artois, FSA, LSEE, Technoparc Futura, 62400 Bethune, France
e-mail: krol@isc.lodz.pl , napieralska@univ-artois.fr, ** Institute of Computer Science, TUL, Lodz, Poland

***Abstract** – The coloured maps method allows to display the field distributions in the from of scaled colours. The authors have developing two methods that allow to improve the visibility of the transfer, make possible analysing the phenomenon inside the object, improve the conditions of the space exploration, visualize in the real time. In both methods are created objects allowing to record the results of the calculations needed to the following stages of the visualisation. For the drawing the library DirectX was used. The ways of classifying and recording the data permit to fully use the possibilities of this graphic library.*

1. Introduction

The coloured maps method is one of the oldest and most frequently used for data fields visualization. This method allows to display the field distributions either on the outer surfaces of the device or on the cutting plane (predefined device cross-section) in the from of scaled colours. The method is very useful in two-dimensional scalar fields visualization. Moreover, thanks to pictorial features it could be also used in vector field presentations while one vector parameter is selected. This method is applicable in the case of two and as well three-dimensional field visualization. In standard cases, the coloured maps are usually defined for the outer surfaces of the examined model device. Coloured map can be also drawn on the defined cutting plane (cross section) by user, while the cutting plane is chosen arbitrary basing on user experience. In the literature it is possible to find some authors proposals based on extracting (defining) the set of parallel cutting planes, set up in constant distance between them, to be extracted from output graphic data. Such a proposed methodology allows to change to observation point, and the position of the "displayed object" as well. In order to examine the field distribution on particular surface, the user could interactively remove any coloured map. Moreover, it is also possible to generate the sub-sequential animation the sequence of maps for defined constant distances between maps and time intervals [2,3]. Applying this method we exploit the data files, imported from CAD package, in any format with stored geometry of the object, data of mesh, and values of searched function results in fixed nodes of the mesh. Defining any cutting plane is based on introducing projection each elementary mesh element on this plane. In order to provide enough fast method of building coloured maps the method of flat mesh generation is based originating the data from FEM. The authors have succeeded developing the above briefly described method proposing more efficient (effective) analysis of field distributions obtained by use of sophisticated CAD software. The idea of the elaborated method consists of two stages. In the first, we define interactively the sequence of coloured map drawings for the set of cutting planes, and defined axis. The proposed methodology is efficient and useful in quick examining of the character of vector field distribution in

the searched volume. The quality of coloured map drawings, obtained by exploiting the first method, are fully satisfactory for rough estimation of field gradient in all volume. The second step of proposed methodology is a little slower, but the map is much more precisely drawn, which is an advantage for final vector analysis. Thanks to the proposed methodology of fast flat mesh generation for the surface map it is possible in both cases to in generate the current coloured map from any distance and angle. Moreover, the maps are drawn into the context of examined device, exactly in the place concerned with the presented field distribution. The device is presented as semi-transparent solid.

2. Data Formats And Structures

The electric, magnetic and electromagnetic fields are defined either by integral or by partial differential equations[1], in which unknowns can be scalar potentials, vector potentials or even both types. The most frequently used method in field calculation is the Finite Element Method (FEM), which idea lies in replacing the continuum Ω by the set of of elementary volumes $\Omega^{(e)}$, called the finite element. The FEM analysis results are usually presented in the table form of text or in graphical form. Following this methodology user could obtain the text files with explicitly described relationship between nodes' coordinates, mesh elements and field vectors. It is obvious, that obtained values are not the original FEM results, but they are obtained either by interpolation or approximation procedure. Such a methodology does not give the user possibility to control the calculation procedure. Moreover, the user has no knowledge about volume division during the mesh generating. Than, the user has no control on calculation process nor he knows the original volume division by finite elements mesh. The methods concerning both the graphical FEM results' presentation and its interactive analysis, required creation of own neutral data structures and objects storing the data of the fields. The above presented short survey of FEM methodology confirm necessity to elaborate a new efficient methodology of visualization of vector quantities. This new methodology, proposed and elaborated by authors, implies from necessity of interactive design. We construct our own "structures", called "neutral structures", and objects responsible for storing the field quantities, which are imported from filed packages thanks to our dedicated drivers. These structures should be independent of FEM elementary volumes and structures commonly used in graphic methodology, which are exploited in surface presentation of the objects. From the other hand they should guarantee the compromise between the necessity of processing the large set of data and CPU time.

The base data type proposed by the authors is the structure called *MYVERT*. The object *MYVERT* presents the nodes of imported mesh, integrating the information about node position at the space with the field value in this point. *MYVERT* contains the following components: *Vert* -- the vector determining spatial position (x,y,z) of the node, *Index* - the index of the node, *ElementInd*- the table of elements' indices, sharing given node (represented by the object), *FEMVect*- the vector of the field, *FEMVal* - the scalar of the field.

The next data type is the structure called *MYEEM*. It contains the following components (Fig.2): *Index* – index of the finite element in the mesh, *NodeInd* – the table of given element's indices, *FEMVect* – field's vector in the element, *FEMVal* – field's scalar value in the element, *VectPos* – the coordinates of element's mass center, *NodeMax* and *NodeMin* – adequately maximum and minimum fields' scalar values in elements . *NodeMax* and *NodeMin* are used in the algorithm of fast element's verification during equi-potential surface extraction.

MYVERT	`typedef struct _MYVERT`	MYELEM	`typedef struct __MYELEM`
Index		*Index*	{

Vert	{	*VectPos*	UINT Index;
FEMVect	UINT Index; D3DVECTOR Vert;	*FEMVect*	D3DVECTOR VectPos;
FEMVal	D3DVECTOR FEMVect;	*FEMVal*	D3DVECTOR FEMVect;
ElementInd[]	double FEMVal; LPMYELEM ElementInd; } MYVERT, *LPMYVERT;	*NodeInd[]*	double FEMVal;
		NodeMax	double FEMVal;
		NodeMin	MYVERT NodeInd[8]; double NodeMax, NodeMin; } MYELEM, *LPMYELEM;

Fig. 1 The structure describing the nodes of the final elements mesh (MYVERT) and structure designed for the description of volume elements in the finite elements mesh (MYELEM).

The structure MYVERT and MYELEM allow to store the results of FEM mesh generation. The most important feature, and advantage of each structure, is that both structures are independent of the shape of each element (tetrahedron, cube, hexahedron), type of the mesh (homogeneous, heterogeneous), and form of field presentation (scalars or vectors, field values in nodes or in elements). For the flexibility of structures' application, the kind of the objects' set storing is of great importance. The object *MYVERT* and *MYELEM* are both stored in the one dimensional tables: *MYVERTTab* – for nodes, and *MYLEMTab* – for elements. Such simple way of storing data allows to keep structures independent from source data, and gives the universality and flexibility of proposed methodology.

3. The coloured maps in VR system

In case when discreet set of volume data is given as the source for coloured map generation it is necessary to create two-dimensional data mesh for the surface map. In the simplest case the set of field data contains the nodes set of cube finite elements. The set is written in one-dimensional table. *MYVERTTab[],* which stores the objects of *MYVERT* type. The elements of the table are sorted basing on the rule, that it can be treated as three-dimensional table *MYVERTTab3D[L][M][N],* numbered l=0,1,..,L, m=0,1,...,M, n=0,1,...,N. The node data (l,m,n) could be obtained by call of the function *MYVERTGetElem*(l,m,n). If the mesh of fields data is suitably thick then the cutting plane p=const. (where p=x, y or z) can be identified by index k=const of the table *MYVERTTab3D[L][M][N]* (where k=l, m or n) corresponding to the nearest value p=const.:

$$k = \mathrm{int}\left(\frac{p_{\min} + p}{\left[\frac{p_{\max} - p_{\min}}{K} \right]} \right), \tag{1}$$

where: $<p_{mim} - p_{max}>$ - the range of p coordinate in *MYVERTTab3D* table,
K=L, M or N,
int() – function approximating its argument to the nearest integer value
In the case of irregular mesh with tetrahedron elements, the author proposed the method for fast definition of the cutting surface for coloured map creation. It depends on describing the coloured map

surface by indexes of tetrahedron finite elements cut by given surface. For the example, the finite element is cut by surface *y=const* if sum *S*:

$$S = \sum_{i=0}^{4} sign(y_i'), \tag{2}$$

where: $y_i' = y_i - y$,
sing() – signum function examined the sign of parameter

where $y_i' < 0$,
where
where $sign(y_i') = \begin{cases} -1 & y_i' = 0, \\ 0 & y_i' > 0. \\ 1 & \end{cases}$
meets the conditions: -4< S < 4

Testing the condition (2) for each element of the mesh containing a large number of finite elements (typical FEM mesh) could cause significant decrease of the speed of coloured map creation or even impossibility of generating maps in real time on interactively chosen surfaces. To accelerate this process the authors proposed to limit examined volume to the area around the plane *p=const*. In order to fulfil such a procedure the coloured plane map could be moved along each axis, while the range W_i is predefined (see Fig. 2).

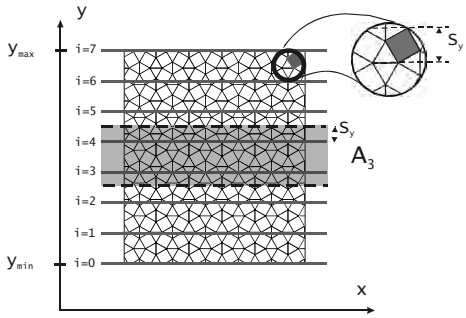

Fig. 2 The volume division into n ranges to optimise intersecting the field results by the plane.

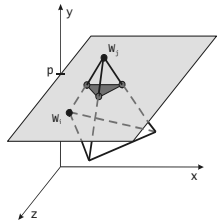

Fig. 3. Determination of intersection points of cutting plane with tetrahedron finite elements.

$$W_i = \left\{ V(x,y,z) : i \cdot dy - sy < y < (i+1) \cdot dy + sy, i \in (0,...,n-1), dy = \frac{Y_{\max} - Y_{\min}}{n} \right\}, \tag{3}$$

where: Y_{min}, Y_{max} – the extreme values of Y coordinates of three-dimensional data mesh.
n – assumed number of mesh divisions along Y axe.
sy – the largest dimension of element in Y direction.

The division along the other axes is done in the same way. For each of range W_i the table of specially selected finite elements is created. The element is chosen to be included into the table when all of its nodes $V(x,y,z)$ belong to W_i. After cutting such a prepared mesh by plane *y=p* it is easy to determine which of areas W_i contains the cutting plane:

$$i * dy < p < (i+1) * dy, \tag{4}$$

so

$$i = \text{int}(\frac{p}{dy} - 0{,}5). \tag{5}$$

The condition –4 < S < 4 is checked only for those finite elements, which indexes *i* belong to the table assigned with area W_i. Thanks to that methodology the data set of elements to be searched is reduced,

even a few times lees. Then, the triangle (product of intersecting the elements with the plane) is created for each element located in current searched area and fulfil the condition: -4 < S < 4. The triangle is formed by finding the points in which the plane cuts the edges $\{V_i(x_i, y_i, z_i)$, $V_j(x_j, y_j, z_j)\}$ of the element. The condition which should be fulfilled for cutting point to exist is $sign(y_i^{'}) + sign(y_j^{'}) = 0$. For the edges fulfilling this condition the cutting point with the plane $y=p$ has the coordinates determined by equations:

$$x = \left[p - \frac{y_i}{x_i} * \left(\frac{x_i - x_j}{y_i - y_j} \right) \right] * \left(\frac{x_i - x_j}{y_i - y_j} \right) \quad , \quad y = p \quad , \quad z = \left[P - \frac{y_i}{z_i} * \left(\frac{z_i - z_j}{y_i - y_j} \right) \right] * \left(\frac{z_i - z_j}{y_i - y_j} \right) \quad (6).$$

The points generated by cutting plane are stored in the structure of *vector<MYVERT>* type together with interpolated field values, when the triangle is stored in vector *vector<MYFACE>*. The particular components of the *MYFACE* structure contain: *Index* – the triangle index, *VertInd[]* – the table of triangle nodes indexes, *FEMVal* – the scalar field values in finite element (from which the triangle is created).

Authors propose two methods of coloured maps drawing then implementing them by exploiting DirectX graphical library. This methodology could be very useful by exploiting DirectX library or other graphical libraries. The possibilities are connected with hardware maintaining of triangle's generating and displaying. The table of triangle contains two-dimensional data mesh generated for chosen plane on basis of spatial set of field data. The simplest way of creating the coloured map lies in drawing subsequent triangles from the table. Each of drawn triangle is filled out with colour, which is the result of mapping the field values *FEMVal* to the index in applied colours scale. The hardware supporting the triangles' drawing in DirectX assure such speed of coloured map creation, that almost whole calculation cost concerns the generation of the table containing triangles. This methodology is different than classic method of coloured map creation process, in which the edges between colour strips are appointed by isolines. In our method the edges are appointed by the mesh of triangles, where each triangle has assigned its colour according to the colour scale. Such coloured map gives a user the view of field distribution, which can could be treated as working good quality visualization, useful for preliminary field analysis. In the case of high density mesh the discrepancies in map drawing are practically invisible, especially from any distance. The user observes sharp edges of coloured map mainly when approaches the map to see its details (Fig. 4a). Due to the high speed of the method one could draw the map interactively, transposing it along one of the axes.

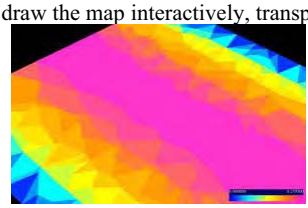

a)

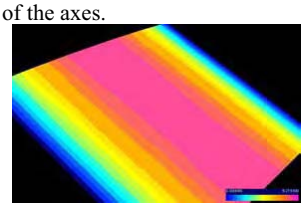

b)

Fig. 4 The coloured map drawings
a) with simplified method depended on filling out the triangle with the colour
b) on basis of isolines and painting algorithm. One picture from stereo pair (left eye)

Authors have also elaborated the method of coloured map creation based on isolines, giving the precise view of field distributions (Fig. 4b). Following this methodology, similar to the previous method, the table of triangles is created, but coloured map is drawn on the basis of field values assigned to the nodes of triangle mesh rather than to whole triangles. To fill out the plane with coloures, the value of isoline is calculated from the following formula, and then painting algorithm was used:

$$A_i = A_{i-1} + \Delta A, \quad i=1,2,\ldots,n, \qquad (7)$$

where: $\Delta A = \frac{A_{\max} - A_{\min}}{n}$,

A_{min}, A_{max} - Respectively maximum and minimum field values. $A_0 = A_{min}$,

In the first the whole surface of the map is covered with colour corresponding to A_{min}. In the next step the coloured areas enclosed to isoline i=1,2,…,n, are created, so that the i area partially covers the areas drawn for isolines featuring with indices lesser than i.

To determine the outline of isoline i the values of field V in the nodes of triangle are compared with value V_i on isoline. The following three cases can be defined (Fig. 6):

1. For all vertices $V>V_i$ – the triangle is outside of area enclosed by isoline.
2. For all vertices $V \leq V_i$ – the triangle is inside the area
3. The part of vertices meets the condition $V>V_i$ the remaining ones $V \leq V_i$ – the isoline goes through the triangle.

In first case the triangle is rejected, in second one the triangle is added entirely to the *IDirectD3DRMObjectBuilder* graphical object representing the isoline i.

The third case requires the triangle to be cut off to the edge of isoline, and then the triangle is added to the graphical object (Fig. 6). For this purpose the points of intersection of the isolines and triangle edges are calculated. The points with the vertices fulfilling the condition $A \leq A_i$ creates the needed polygon. In the special border case when isoline is on the edge of triangle the polygon is reduced to the line.

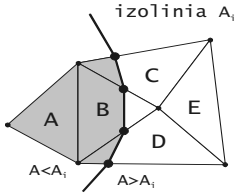

Fig. 5 Creating i isosurface for painting algorithm

As a rule several or dozen isolines are created, when the number of triangles is significantly larger. Therefore it is recommended to create n empty graphical object of *IDirectD3DRMObjectBuilder* type (n is a number of isolines). These objects are filled in successive way during single pass through the triangle mesh. Then the objects can be drawn consecutively with colours assigned to individual isolines. Such map has high quality of presentation, because it shows exactly the field's distribution. The time needed to create such coloured map is longer than in previous method, but significantly shortest than in classical method, where the isoline is calculated with differential equation. In both cases short drawing time of current map allows its interactive observation from different points and direction in the space.

4. Conclusions

The methods, proposed and elaborated by authors, has been tested and successfully applied to objects visualization (vector graphics) in 3D space. The main goal of the proposed methodology is focused on creating the joined methods, based on the stereoscopy visibility, interactive design, and virtual entering to interior of the object and its efficient exploration. The idea of the elaborated method consists of two stages:

- In the first stage, our effort is focused on quick analysis of huge number of graphic data without demand of high resolution in order to select interesting graph, then to be analyzed precisely in the next stage. This could be even done as on-line procedure. The above is the advantage of the proposed methodology in the reference to classical 3D vector presentation,

- In the second stage, selected graph could be displayed and analyzed with high resolution demand of the displayed object. This analysis is usually done as off-line procedure.

This method is proposed due to commonly used the plane graphic presentation, which is too weak method for 3D vector graphics. Moreover the classical method will not give a enough good orientation in the analyzed space. The proposed method allows defining a free shape volume with predefined transparency of each wall by the user, moreover free rotation of each volume is also available. Our method, defined as quick cutting planes method, allows a dynamic generation of colour bit-maps (see Fig. 6). As the first preliminary estimation (approximation), obtained colour bit-maps, does not give enough smooth edges of each colour. The observed smoothing process of each colour edge is strictly related to the mesh density. The obtained figure resolution is fully satisfactory for the first step of plane selection, then to be displayed by exploiting the second method.

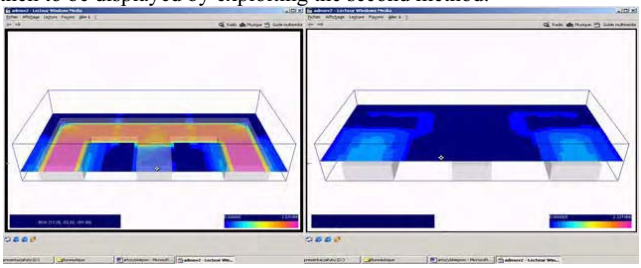

Fig .6 The The coloured map drawing with simplified method depended on filling out the triangle with the colored map.

The results and times obtained thanks to the program we have created have been compared with results obtained thanks to some other visualization programs. As to conclude, the submitted methods of presenting three dimensional field thanks to the dynamically generated coloured maps allows to create an instrument thanks to whom the classic methods of coloured maps become an efficient way of analyzing spatial data, but also easy and friendly in use.

ACKNOWLEDGMENT

This work in supported by the program "Futurelec 2" supervised by the French national center of technological research (CNRT) on electrical engineering. This program, including EDF and Framatome ANP, is sponsored by the region "Nord - Pas de Calais", the French ministry (FRT) and the European funds (FEDER).

References

[1]D.A.Bowman, D.Koller, L.F.Hodges. A A Methodology for the Evaluation of Travel Techniques for Immersive Virtual Environment. College of Computing Graphics, Visualisation and Usability Center, Atlanta (USA), 1997

[2] A.Bossavit Computational Electromagnetism. San Diego, Acad Press, 1998

[3] L.Chin-Feng, Y.Don-Lin, Y-Ch. Chung A marching voxels method for surface rendering of volume data. Computer Graphics, pp 306-311, 2001

[4] Adam Krolewiak, Ewa Napieralska – Juszczak , Maria Pietruszka “The Methods of Interaction and Data Analyze in the Visualization System for Electromagnetic Fields”, XI Int. Symp. On Electromagnetic Fields, ISEF 2003, pp27-32, vol1, Slovenia, sept 2003

[5] Adam Krolewiak, Ewa Napieralska – Juszczak , Maria Pietruszka "The stereoskopy vizualization in the 3D presentation system of the electromagnetic fields”. Proc of ICEM 2004, Krakow, Poland

[6] B.Akka “Writing stereoscopic software for stereo Graphics Systems using Microsoft Windows OpenGL.”, Documentation of Stereo Graphics Corporation, 1998

[7] P.Cigoni, P.Marino, C.Montani, E.Puppo, R.Scopigno Multiresolution Representation and Visualisation of Volume Data. IEEE Trans V&CG, 3(4), pp 352-369, 1997

Electromagnetic Fields in Mechatronics, Electrical and Electronic Engineering
A. Krawczyk et al. (Eds.)
IOS Press, 2006

Analytical Calculation of Magnetic Field Distribution in Brushless DC Permanent Magnet Motors

Hacer Öztura

Dokuz Eylül University
Electrical and Electronics Eng. Dept.
35160 Kaynaklar Buca İzmir Turkey
hacer.oztura@deu.edu.tr

Abstract: ***A general analytical technique predicts the magnetic field distribution in brushless permanent magnet machines equipped with surface-mounted magnets. It accounts for the effects of both the magnets and the stator windings, for slotted motors. The technique is based on two-dimensional models in polar coordinates and solves the governing Laplacian / quasi-Poissonian field equations in air gap magnet regions. The paper validates results of the analytical models by two-dimension finite element analyses.***

1. Introduction

Significant advances in technologies power electronic devices and digital control strategies necessitate development in design and analysis techniques for electrical drive systems, for which the analysis of the magnetic field distribution throughout the electrical machine is fundamental. For the truly prediction of performance parameters –torque, back-emf, stator and rotor losses, winding inductances, demagnetization, noise, etc– of brushless permanent magnet motors, an accurate magnetic field distribution knowledge is a prerequisite.

In this paper is described an improved two-dimensional analytical technique for predicting the magnetic field distribution in internal rotor radial-field motor topologies. The z-directed magnetic vector potential is analyzed for the different field regions and for steady-state operation. Based here upon all quantities of potential interest with respect to motor performance prediction are deduced from the 2D field distribution. A two-dimensional model in polar coordinates is formulated at [1]. However, approximated relative recoil permeability of the permanent magnet is usually insufficient for accurately predicting the flux density. The model using the Laplacian/quasi Poissonian field equations in the air gap/magnet region was introduced by [2-4]. This study also extends the analytical model for predicting the magnetic field produced by the stator windings together radial magnetization of magnet.

2. Mathematical Model

Figure 1 represents an interior permanent magnet motor. Different region of exmined motor are indicated in Figure 1.

Figure 1 examined motor geometry

The magnetic field equations for each regions can be given in terms of the coupled vectors B and H [5,6].

$$\vec{B}_I = \mu_0 \vec{H}_I \quad \& \quad \vec{B}_{II} = \mu_0 \mu_r \vec{H}_{II} + \mu_0 \vec{M} \tag{1}$$

Where M is the residual magnetization vector. Subscript I shows the air-spaces and similarly II shows the permanent magnet. If the magnet have a linear second-quadrant demagnetization curve, the amplitude of the magnetization vector M is given

$$M = \frac{B_r}{\mu_0} \tag{2}$$

In polar coordinates, this magnetization vector is given by

$$\vec{M} = \vec{M}_r \vec{r} + \vec{M}_\theta \vec{\theta} \tag{3}$$

In this motor, permanent magnet has a radial magnetization and its waveform of the magnetization components are shown in Figure 2.

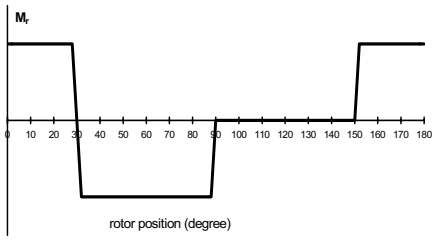

(a)

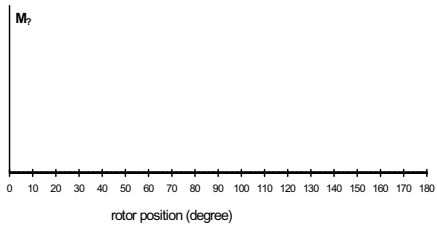

(b)

Figure 2. Waveforms of magnetization components M_r & M_θ

Magnetization vector components can be expressed as Fourier series, [6] i.e..,

$$M_r = \sum_{n=1,3,..}^{\infty} M_{rn} Cos(np\theta) \quad \& \quad M_\theta = \sum_{n=1,3,..}^{\infty} M_{\theta n} Sin(np\theta) \tag{4}$$

Where while $M_{\theta n}$ component equal to zero, the other can be given;

$$M_{rn} = 2\frac{B_r}{\mu_0}\alpha_p \frac{\sin\dfrac{n\pi\alpha_p}{2}}{\dfrac{n\pi\alpha_p}{2}} \tag{5}$$

Where α_p is the magnet pole-arc to pole pitch ratio.

To calculate the airgap field distribution as analytically, the following assumptions are made;

- end-effects are ignored,
- the rotor and stator core is infinitely permeable,
- the permanent magnets have a linear demagnetization curve.

The scalar magnetic potential function φ can be given [6,7];

$$H_r = -\frac{\partial\varphi}{\partial r} \quad \& \quad H_\theta = -\frac{1}{r}\frac{\partial\varphi}{\partial\theta} \tag{6}$$

While the scalar magnetic potential distribution in the airgap is obtained by Laplacian equation, in the permanent magnet regions it is obtained by the quasi-Poissonian equation.

The field distribution produced by multipole magnets mounted on the surface of rotor is calculated by;

$$\frac{\partial^2\varphi_I}{\partial r^2} + \frac{1}{r}\frac{\partial\varphi_I}{\partial r} + \frac{1}{r^2}\frac{\partial^2\varphi_I}{\partial\theta^2} = 0 \quad \& \quad \frac{\partial^2\varphi_{II}}{\partial r^2} + \frac{1}{r}\frac{\partial\varphi_{II}}{\partial r} + \frac{1}{r^2}\frac{\partial^2\varphi_{II}}{\partial\theta^2} = \frac{1}{\mu_r} div\vec{M} \tag{7}$$

The divergance of the magnetization vector for the magnet region can be written by using Fourier series expantion;

$$div\vec{M} = \frac{M_r}{r} + \frac{\partial M_r}{\partial r} + \frac{1}{r}\frac{\partial M_\theta}{\partial\theta} = \sum_{n=1,3,..}^{\infty}\frac{1}{r}M_n Cos(np\theta) \tag{8}$$

The general solutions of equation (7) are obtained in the airgap and magnet as;

$$\varphi_I(r,\theta) = \sum_{n=1,3,..}^{\infty}(A_{nI}r^{np} + B_{nI}r^{-np})Cos(np\theta)$$

$$\varphi_{II}(r,\theta) = \sum_{n=1,3,..}^{\infty}(A_{nII}r^{np} + B_{nII}r^{-np})Cos(np\theta) + \sum_{n=1,3,..}^{\infty}\frac{M_n}{\mu_r\left[1-(np)^2\right]}rCos(np\theta) \tag{9}$$

Where A_{nI}, A_{nII}, B_{nI}, and B_{nII} are constant obtained by applying boundary conditions. The complete solution for the magnetic field components in the airgap & magnet regions can be calculated from the general solution of Laplacian/quasi-Poissonian equations and under the specifeid bondary conditions.

$$B_{rI}(r,\theta) = \sum_{n=1,3,..}^{\infty}K_B(n)f_{Br}(r)Cos(np\theta) \quad \& \quad B_{\theta I}(r,\theta) = \sum_{n=1,3,..}^{\infty}K_B(n)f_{B\theta}(r)Sin(np\theta) \tag{10}$$

Where

$$f_{Br}(r) = 1 + \left(\frac{R_s}{r}\right)^2 \quad \& \quad f_{B\theta}(r) = -1 + \left(\frac{R_s}{r}\right)^2$$

$$K_B(n) = \frac{\mu_0 M_n}{2\mu_r} \frac{A_n\left(\frac{R_m}{R_s}\right)^2 - A_n\left(\frac{R_r}{R_s}\right)^2 + \left(\frac{R_r}{R_s}\right)^2 \ln\left(\frac{R_m}{R_s}\right)^2}{\frac{\mu_r+1}{\mu_r}\left\{1-\left(\frac{R_r}{R_s}\right)^2\right\} - \frac{\mu_r-1}{\mu_r}\left\{\left(\frac{R_m}{R_s}\right)^2 - \left(\frac{R_r}{R_s}\right)^2\right\}} \tag{11}$$

Where R_r, R_s, and R_m are the radius of the rotor, stator, and magnet respectively.

To verify the analytical results 2-D finite element analysis are used. This numerical calculation is made with 2 degree steps. The airgap flux density results are shown in Figure 3.

By using similar procedure, flux density formulation is obtained for permanent magnet region as;

$$B_{rII}(r,\theta) = \frac{\mu_0 M_n}{2}\left(\frac{A_n\left(\frac{R_m}{R_s}\right)^2 + \ln\left(\frac{R_m}{R_r}\right)\left\{\frac{\mu_r+1}{\mu_r}\left(\frac{R_r}{R_s}\right)^2 - \frac{\mu_r-1}{\mu_r}\left(\frac{R_r}{R_m}\right)^2\right\}}{\frac{\mu_r+1}{\mu_r}\left[1-\left(\frac{R_r}{R_s}\right)^2\right] - \frac{\mu_r-1}{\mu_r}\left[\left(\frac{R_m}{R_s}\right)^2 - \left(\frac{R_r}{R_m}\right)^2\right]}\right) Cos\theta$$

$$B_{\theta II}(r,\theta) = \frac{-\mu_0 M_n}{2}\left(\frac{A_n\left(\frac{R_m}{R_s}\right)^2 + \ln\left(\frac{R_m}{R_r}\right)\left\{\frac{\mu_r+1}{\mu_r}\left(\frac{R_r}{R_s}\right)^2 - \frac{\mu_r-1}{\mu_r}\left(\frac{R_r}{R_m}\right)^2\right\}}{\frac{\mu_r+1}{\mu_r}\left[1-\left(\frac{R_r}{R_s}\right)^2\right] - \frac{\mu_r-1}{\mu_r}\left[\left(\frac{R_m}{R_s}\right)^2 - \left(\frac{R_r}{R_m}\right)^2\right]}\right) Sin\theta \tag{12}$$

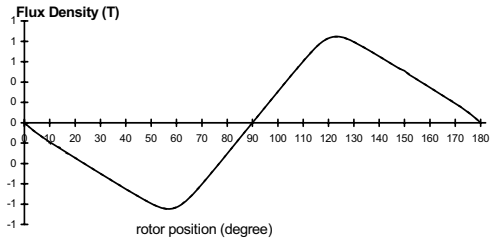

Figure 3. Waveforms of flux density at the air gap.

Conclusions

Whilst numerical methods for field computation, such as finite elements, also provide an accurate means of determining the flux distribution, with due account of saturation etc., they are often time consuming and do not provide nearly as much insight as analytical solutions into the underlying

behavior. Therefore an alternative analytical technique is proposed. It is a prerequisite for force calculations, for the prediction of the back-emf waveform and the prediction of torque-speed characteristics. Moreover electromagnetic design synthesis benefits significantly from a two-dimensional analytical method for predicting the magnetic field distribution.

References:

[1] N. Boules, "Prediction of no-load flux density distribution in permanent magnet machines", IEEE Trans. Ind. Applications, Vol. IA-21, pp.633-643, July-Aug. 1985.
[2] Z.Q. Zhu, D. Howe, E. Bolte, & B. Ackermann, "Instantaneous magnetic field distribution in brushless permanent magnet dc motors, Part I: open-circuit field", IEEE Trans. Magnetic, Vol. 29, pp.124-135, Jan. 1993
[3] K. F. Rasmussen, "Analytical prediction of magnetic field from surface mounted permanent magnet motor" Proc. Int. Electrical Machines and Drives Conference, Seattle WA, 1999, pp. 34-36
[4] Z.Q. Zhu & D. Howe, "Instantaneous magnetic field distribution in brushless permanent magnet dc motors, Part II: armature reaction field", IEEE Trans. Magnetic, Vol. 29, pp.136-142, Jan. 1993
[5] Z.Q. Zhu & D. Howe, "Instantaneous magnetic field distribution in brushless permanent magnet dc motors, Part III: effect of stator slotting", IEEE Trans. Magnetic, Vol. 29, pp.143-151, Jan. 1993
[6] E. Bolte & J. Peschke, "Magnetic Field Distribution in Radial-Field Brushless Permanent Magnet Motors" pp426-30, ICEM 5-8 September 2004 Cracow, Poland
[7] Z. P. Xia, Z. Q. Zhu, & D. Howe, "Analytical Magnetic Field analysis of Halbac Magnetized Permanent-Magnet Machines", IEEETrans. Magnetics Vol. 40, pp.1864-72, July 2004

Electromagnetic Fields in Mechatronics, Electrical and Electronic Engineering
A. Krawczyk et al. (Eds.)
IOS Press, 2006

ON-LINE TESTING OF AC MOTOR FOR PREDICTIVE MAINTENANCE

Frederic Perisse, Daniel Roger, IEEE Member, Claude Saligot

LSEE – Université d'Artois, Technoparc Futura, 62400 BETHUNE, France
Frederic.Perisse@iut-geii.univ-artois.fr

Abstract* – *Insulation failure is one of the major causes of electrical machine destruction. The proposed paper shows that it is now possible to perform on-line monitoring of AC machines by detecting slight variations of high frequency parameters of stator windings. The system is based on low-level magnetic field measurements in the vicinity of the machine in the 1-10MHz range. The paper describes an on-line monitoring system, able to detect slight variations of high frequency characteristics of stator windings that depends on machine insulation aging.

Introduction

The paper proposes a new principle which can be used to observe the insulation aging on a working machine. It is based on the on-line measurement of the machine winding high frequency characteristics. Experiments on thermal accelerated aging of magnet wire show that the capacitance, measured between two enamelled wires increases along the life of specimens. This change is significant enough, to obtain substantial information about the quality of the winding. Considering an entire machine, turn to turn capacitance changes yield a modification of high frequency characteristics of windings. The on-line monitoring system consists of injecting in the machine winding a signal close to the resonance frequency, which depends on winding inter-turn capacitances, and observing the consequences of its slight variations on the external magnetic field. We propose an on-line method contrary to the classic off-line diagnosis methods which require a human intervention [1-4]. The on-line method based on partial discharges are not adapted to machines supplyed by PWM inverter [5, 6].

Thermal Accelerated Aging of Twisted Pairs

The thermal accelerated aging has been performed on a twisted pair specimen obtained from a Magnebond® CAB-200 which is a polyesterimide (THEIC) enameled copper wire over-coated with polyamide-imide, and the final layer is a polyamide aromatic bondcoat. The thermal index is 210°C and the diameter 1.37 mm. The specimens were built following the IEC 60851-5 standard procedure. Fig. 1 presents such a specimen.

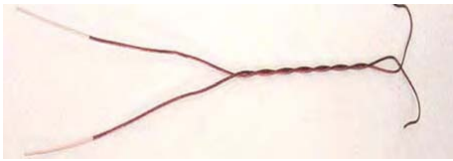

Fig. 1. A twisted pair specimen.

A set of 180 specimens was stressed by high temperature (270°C) during 12 cycles of sixty hours, according to the indications of the IEC 60216-1, 2, and 3 standards. After each cycle the capacitance (C) of the twisted specimens was measured with an Agilent 4294A precision impedance analyzer. Fig. 2 shows the evolution of the mean value of the capacitance of the twisted pair during accelerated aging and the standard deviation.

The capacitance value increases throughout the expected life time. The strong increase measured after the first cycle can be explained by the presence of the external thermal bondcoat of the CAB 200 magnet wire. Nevertheless the aging process on the twisted pair can still be easily observed after the first cycle.

After each cycle, 60 specimens are also submitted to the standard test that consists of applying 400V, 50Hz during one minute and observing if the specimen will survive. This test was performed in order to get the probability of failure on rated voltage. In other words this test is used to get the two-parameter Weibull distribution.

The Weibull cumulative failure distribution function is:

$$F(t) = 1 - \exp\left(-\left(\frac{t-\gamma}{\eta}\right)^{\beta}\right) \text{ when } t \geq \gamma \quad (1)$$

where β, γ, η are coefficients dependent on the material studied, in our case γ=0, β=3.912 and η=574 h. These values have been determined by the reliability software Relex® which analyses the experimental data obtained with the set of 60 specimens. The corresponding curve is presented in Fig. 3.

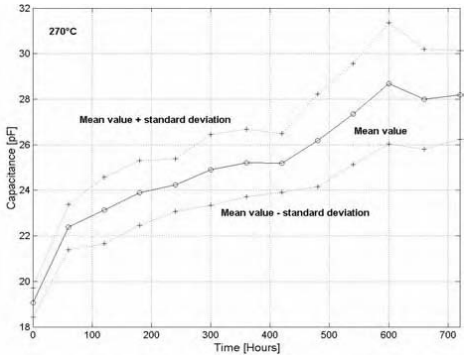

Fig. 2. Capacitance evolution due to thermal aging.

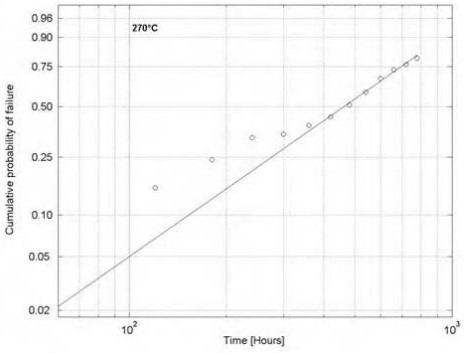

Fig. 3. Weibull plot of the cumulative probability of failure.

The analysis of Fig. 2 and Fig. 3 shows that a correlation can be made between the twisted pair specimen capacitance and the probability of failure of the insulation layer at nominal voltage. The variation of the capacitance of the twisted pair can be considered as a measurable sign of the enamelled copper wire insulation aging.

On-line Monitoring System

The synopsis of monitoring system is represent at Fig. 4. The spectrum of measured signal (magnetic field or injected current) of a running machine has many low frequency spectrum lines up to several kilohertz that correspond to slotting effects but has no natural lines in the range of 1–10MHz that corresponds to stator winding resonances.
To detect such phenomena a high frequency low-level signal is injected in the stator, the corresponding high frequency magnetic field or current are measured. The high frequency injection system contains an inductance which allows obtaining a series resonance at chosen frequency. A synchronous detector keeps only the information corresponding to the injected signal and rejects the noise. This system allows detecting high frequency winding resonance when the machine is working. Phase variation, at a given frequency chosen near a winding resonance, is caused by the evolution of the winding turn to turn capacitance. Estimation of the remaining life time of the stator winding could be performed by comparison between this measurement and the evolution law of capacitance changes studied in the accelerated aging experiments made on the same enamelled wire.

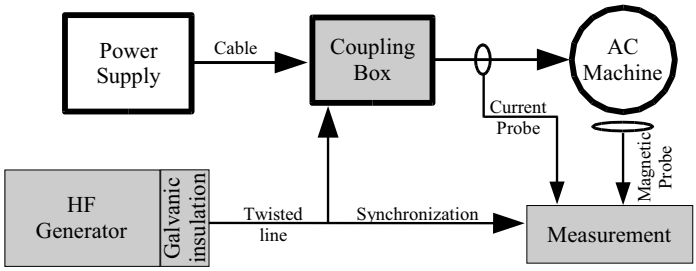

Fig. 4. Synopsis of monitoring system.

Equivalent Circuit of the Complete System

Fig. 5 represents the equivalent circuit of the complete system. It consists of tree main part:

- Model of the AC motor
- Power supply and cable
- Coupling box, High frequency generator and twisted line

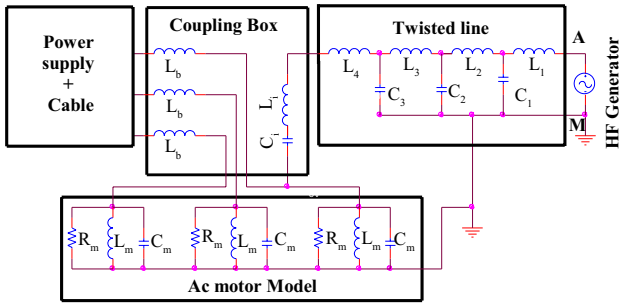

Fig. 5. Equivalent circuit of complete system.

AC Motor Model

The experimental investigations are made on a 4kW standard induction machine fed by an industrial PWM inverter which switching frequency is 12kHz. For a frequency range from 1kHz to 10MHz, a simple parallel RLC equivalent circuit represents roughly the machine winding frequency behavior [7]. We represent one phase by an RLC parallel notice Rm, Lm, Cm.

Injection System

The signal injection circuit consists of a HF generator, a line made of a twisted line represented by a classic propagation line, a coupling capacitor and an injection inductance. Coupling capacitor and injection inductance are placed in a coupling box which is placed near AC machine.
The coupling capacitor (Ci) function is to provide large impedance at inverter switching frequency (12 kHz) and a low impedance at chosen series frequency (≈1MHz). A 1 nF/1000 V polypropylene film capacitor is chosen, its impedance is 13kΩ at 12kHz and 156Ω at 1MHz.
The injection inductance allows choosing the system working frequency which must be close to the series resonance. Equation 2 represents the impedance of a single ac motor phase with the injection inductance and coupling capacitor. This expression allows determining the impedance at any frequency of this system.

$$Z = \frac{1}{\frac{1}{R_m} - \frac{1}{i.L_m.\omega} + i.C_m.\omega} + i.L_i.\omega - \frac{i}{C_i.\omega} \qquad (2)$$

Where: Z = Complex Impedance
R_m, L_m, C_m = element of AC motor parallel equivalent (Ω, H, F)
L_i = Injection inductance (H), Ci = Coupling capacitor (F), ω = Frequency (rd/s)
This expression allows to calculate differential of Z modulus. The solution of dZ/dω=0 yields the resonances. Then it is possible to find an expression function of ω and L_i. Fig. 6 represents the evolution of injection inductance versus frequency.

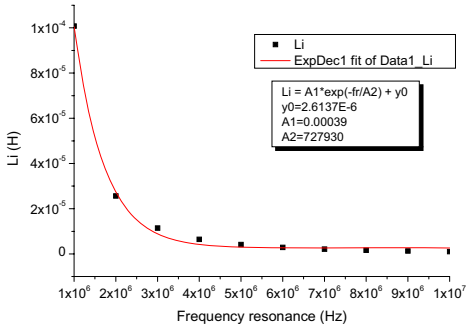

Fig. 6. L_i value versus frequency resonance.

For the application, L_i = 54µH was chosen, which fixes frequency resonance (fr) at 1.38MHz. This calculus allows to choose approximately the wanted resonance frequency. However this frequency is slightly modified by the twisted line and coupling inductance L_b. This modification is taken into account afterward.

Power Supply and Cable

The influence of power supply and cable is negligible considering the choice of the coupling inductance L_b. These inductances are chosen to separate at high frequency the power supply and the injection system. This inductance is calculated to obtain high impedance of power supply line at frequency resonance.

Parameter Values of Equivalent Circuit

Values of the principal elements of the model:

Injection system and twisted pair: $L_i = 54\mu H$, $C_i = 1nF$, $L_4 = 0.5\mu H$, $L_3 = 1\mu H$, $L_2 = 1.5\mu H$, $L_1 = 2.5\mu H$, $C_3 = 50pF$, $C_2 = 80pF$, $C_1 = 100pF$.

Coupling inductance: $L_b = 300\mu H$

AC motor model: $R_m = 2.515k\Omega$, $L_m = 9.36mH$, $C_m = 329pF$.

Exploitation of Equivalent Circuit

Model Validation

Fig. 7 shows the comparison between measurement and simulation of impedance. The impedance measurement between A and M (Fig. 5) are compared to the simulation. A good correlation is obtain which enables to validate the suggested model. Fig. 8 and 9 represent a zoom of impedance and phase, the value of simulate resonance frequency is $fr_0 = 1.35MHz$ (working frequency).

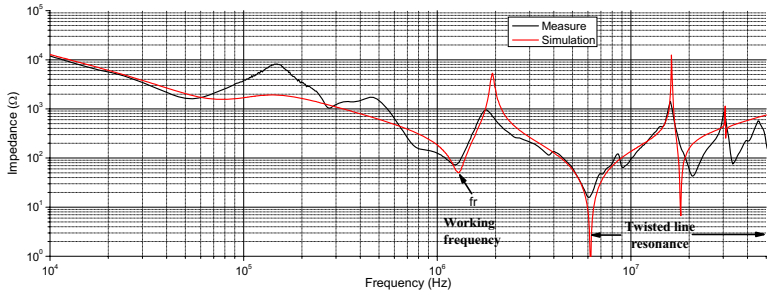

Fig. 7. Impedance versus frequency

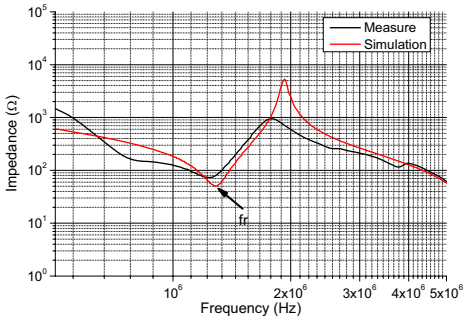

Fig. 8. Impedance versus frequency

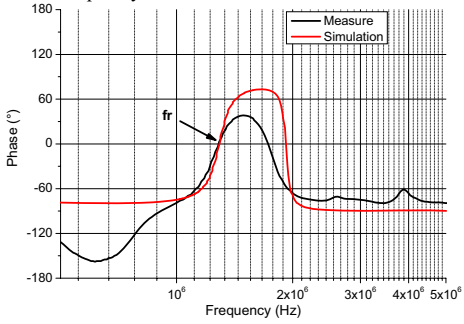

Fig. 9. Phase versus frequency

Influence of AC Motor Aging

Aging of AC motor leads to a variation of the turn to turn capacitance [7]. These variations influence the resonance frequency fr. A variation of 30% of the winding capacitance (Cm) of AC machine is simulated. This variation induces a modification of the resonance frequency Fr. Fig. 10 shows this variation, and Fig. 11 shows the slip of the impedance at fr_0.

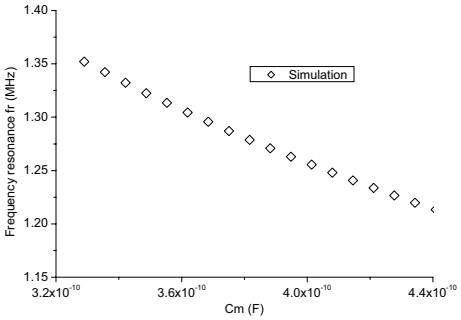

Fig. 10. Frequency resonance versus Cm

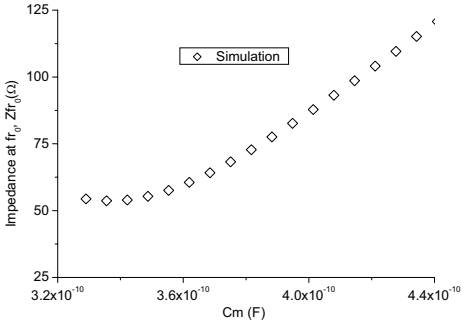

Fig. 11. Impedance at fr_0 versus Cm

Method of Measurement

The aging of the machine can be determined by two types of simple measurements :

1. By the research of the frequency of resonance which is a function of the capacitance of the engine. This frequency can be determined by the measurement of the following parameters:
   - Phase, maximum of current, maximum of magnetic field, minimum of impedance
2. For the frequency resonance fr_0, by the measurement of parameters functions of Cm:
   - Current, magnetic field, impedance

These various measurements can be performed out easily and in an autonomous way. Fig. 12 shows an example of, voltage, current and magnetic field measurements at fr_0. One can calculate phase delay and or signal amplitude to determine evolution of stator capacitance (Cm).

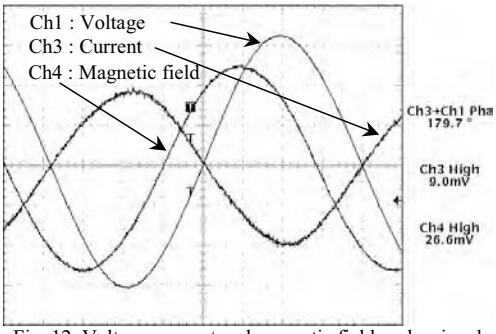

Fig. 12. Voltage, current and magnetic field probe signal

Conclusion

Experimentations on accelerated aging of the magnet wire insulation show that the winding inter-turn capacitance increases [7]. This variation causes a slip in the winding resonance frequencies. To provide an on-line monitoring, the novel system injects a low level high frequency signal in the stator winding. High frequency measurement of phase, current, impedance or magnetic field allows to determine the variation of the winding inter-turn capacitances. With a proper knowledge and a database concerning the dielectric aging process, this information can be linked to the probability of failure of the inter-turn insulation. This method can be implemented easily, even on applications already existing. The possible choice of measurements (current, magnetic field) allows to adapt the system according to the various working conditions.

References

[1] G.C .Stone, E.A. Boulter, I. Culbert, H. Dhirani, *Electrical Insulation for Rotating Machines,* IEEE Press Series on Power Engineering

[2] Robert Fournié, *Les isolants en électrotechnique, Essais, Mécanismes de dégradation. Applications industrielle*s, Editions Eyrolles, Paris, 1990

[3] C. Neacsu, P. Bidan, T. Lebey and M. Valentin, "Presentation of a new off line test procedure for low voltage rotating machines fed by adjustable speed drives (ASD)" *VIII IEEE Int. Technical Proceedings of Power Electronics Congress CIEP 2002*, 20-24 Oct. 2002, pp. 9 – 14.

[4] P. Bidan, T. Lebey, and C. Neacsu, "Development of a new off-line test procedure for low voltage rotating machines fed by adjustable speed drives (ASD)", *IEEE Trans. Dielectrics and Electrical Insulation,* Vol. 10, No. 1, Feb. 2003, pp. 168 – 175

[5] A. Mbaye, F. Grigorescu, T. Lebey, and Bui Ai; "Existence of partial discharges in low-voltage induction machines supplied by PWM drives*," IEEE Trans. Dielectrics and Electrical Insulation*, Vol. 3, No 4, Aug. 1996, pp. 554 – 560.

[6] D. Fabiani, G.C. Montanari, and A. Contin, "Aging acceleration of insulating materials for electrical machine windings supplied by PWM in the presence and in the absence of partial discharges", *IEEE 7th International Conference on Solid Dielectrics*, ICSD01, 25-29 June 2001, pp. 283 – 286.

[7] P. Werynski, R. Corton, D. Roger and J.F. Brudny, " On-line monitoring of insulation aging in AC motors fed by PWM inverters" *IEEE Int. Electric machines and drives Conf.,* IEMDC05, 15 - 18 May 2005, pp. 1942-1948.

Electromagnetic Fields in Mechatronics, Electrical and Electronic Engineering
A. Krawczyk et al. (Eds.)
IOS Press, 2006

DESIGN AND ANALYSIS OF MICRO POSITIONING ACTUATOR USING THREE DIMENSIONAL FINITE ELEMENT METHOD

Jong-Seok Rho, Chang-Hwan Lee, and Hyun-Kyo Jung

School of Electrical Engineering and Computer Science, Seoul National University, Kwanak-gu, Seoul, Korea.
(phone: +82-2-880-7262; fax: +82-2-878-1452; e-mail: zzong@elecmech.snu.ac.kr)

Abstract *– **In this research, the Micro Positioning Actuator(MPA), which is more effective precise ositioning actuator than the existent one is proposed. We suggest the design and analysis methodology of the MPA by the precise examination of the working principle and using three dimensional Finite Element Method(3-D FEM). We also prototyped the mechanical system and the driving circuit of the MPA. Finally, it is verified that the suggested MPA is more effective precise positioning actuator than most of the existent one. And the proposed design and analysis methodology is validated by comparing their outcomes with experimental data.***

Introduction

Most of the existent precise positioning actuator has problems. That is the largeness of size, the much consumption of energy, and the large production and maintenance cost [1]-[5]. To address these problems, we propose the MPA in this research. The proposed MPA has the merits such as, small in size, low in energy consumption, and very cheap in production and maintenance cost.

We also propose the design and analysis methodology of the MPA by the precise examination of the working principle and using 3-D FEM. This design and analysis methodology can be applicable to many other kinds of machine, which uses same working principle. Such as the miniaturized micro robot of Aoyama, the precise positioning mechanism of T.Higuchi, the micro impact drive mechanism of O.Ohmichi, and etc [1]-[7]. But, the design and simulation methodology of those machines is not proposed, yet [1]-[8]. As a result, it needs much time and cost to design that. To solve these problems, we propose the design and analysis methodology of the MPA by the precise examination of the working principle and using 3-D FEM.

Also, we prototyped the mechanical system and the driving circuit of the MPA. Finally, it is verified that the proposed MPA is more effective precise positioning actuator than most of the existent ones. And, the proposed design and analysis methodology is validated by comparing their outcomes with experimental data.

Prototype of the MPA

Fig.1 shows the prototype of the MPA. The specification of the MPA is tabulated in Table.1. Three electrical input square waves with 90 degree phase difference are needed to operate the MPA. Fig.2 shows the flow chart of the driving circuit. Fig.3 illustrates the result of output waves from the driving circuit for the MPA. Fig.4 displays the whole system of the MPA.

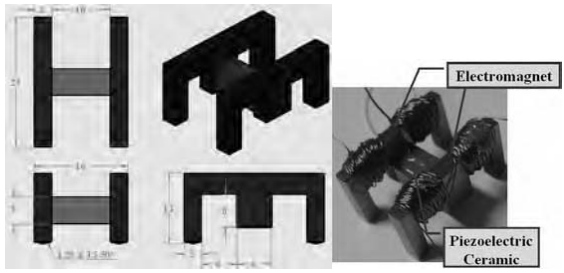

Fig.1 Protopype of the MPA [mm]

TABLE.1 Specification of The MPA

Kinds	Value
Total weight	13 [g]
Piezoelectric ceramic	NEC/TOKIN AE0505D08
Coil diameter	0.2 [mm]
Number of coil turns	150 [turn]

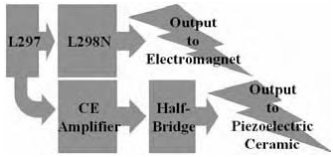

Fig.2 Flow chart of the driving circuit for the MPA.

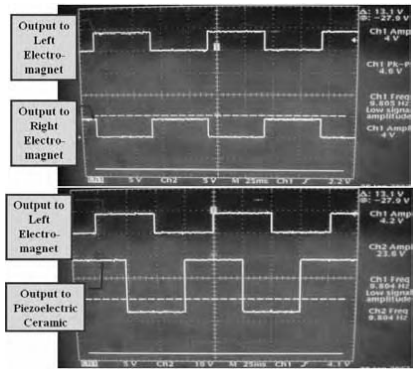

Fig.3 Result of output waves from the driving circuit for the MPA.

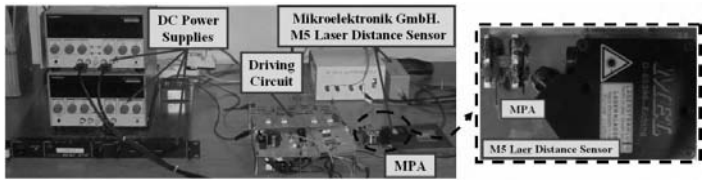

Fig.4 Whole system of the MPA.

Finite element Formulation for Analysis of the MPA

The matrix equations of (1) and (2) are base for the derivation of finite element formulation, which relate mechanical and electrical quantities in piezoelectric media [8],[9].

$$T = c^E S - e^t E \qquad (1)$$
$$D = eS + \varepsilon^S E \qquad (2)$$

where,
T: vector of mechanical stresses
S: vector of mechanical strains
E: vector of electric field
D: vector of dielectric displacement
C^E: mechanical stiffness matrix for constant electric field E
ε^S: permittivity matrix for constant mechanical strain S
e: piezoelectric matrix; superscript t means transposed.

The matrix equations (3) and (4) can be obtained from the Hamilton's variation [8], [9].

$$M\ddot{u} + D_{uu}\dot{u} + K_{uu}u + K_{u\Phi}\Phi = F_B + F_S + F_P \qquad (3)$$
$$K^t{}_{u\Phi}u - K_{\Phi\Phi}\Phi = Q_S + Q_p \qquad (4)$$

where,
$\dot{u}, \ddot{u}$: velocities, accelerations
Φ : electrical potentials
M : mass matrix
D_{uu} : mechanical damping matrix
K_{uu} : mechanical stiffness matrix
$K_{u\Phi}$: piezoelectric coupling matrix
$K_{\Phi\Phi}$: dielectric stiffness matrix
F_B, F_S, F_P : mechanical body, surface, point forces
Q_S, Q_P: electrical surface, point charges.

For the transient analysis of the MPA with the solution at time $t+\Delta t$, (3) and (4) can be modified as follows :

$$M\ddot{u}_{t+\Delta t} + D_{uu}\dot{u}_{t+\Delta}t + K_{uu}u_{t+\Delta t} + K_{u\Phi}\Phi_{t+\Delta}t = F_B + F_S + F_P \qquad (5)$$
$$K^t{}_{u\Phi}u_{t+\Delta t} + K_{\Phi\Phi}\Phi_{t+\Delta t} = Q_S + Q_p \qquad (6)$$

where,
Δt : fracture of the time step
$t+\Delta t$: time of solution.

The backward-difference formulas with errors of order $(\Delta t)^2$ are derived from the Taylor series expansion, as follow [10]:

$$\ddot{u}_{t+\Delta t} = \left(\frac{-u_{t-2\Delta t} + 4u_{t-\Delta t} - 5u_t + 2u_{t+\Delta t}}{\Delta t^2} \right) \qquad (7)$$
$$\dot{u}_{t+\Delta t} = \left(\frac{u_{t-\Delta t} - 4u_t + 3u_{t+\Delta t}}{2\Delta t} \right). \qquad (8)$$

By applying (7) and (8) to (5) and (6), the governing equations, which are used in this research, for transient analysis of the MPA are derived as follow :

$$M\left(\frac{-u_{t-2\Delta t} + 4u_{t-\Delta t} - 5u_t + 2u_{t+\Delta t}}{\Delta t^2} \right) + D_{uu}\left(\frac{u_{t-\Delta t} - 4u_t + 3u_{t+\Delta t}}{2\Delta t} \right) + K_{uu}u_{t+\Delta t} + K_{u\Phi}\Phi_{t+\Delta t} = F_B + F_S + F \qquad (9)$$

$$K^{t}{}_{u\Phi}U_{t+\Delta t} + K_{\Phi\Phi}\Phi_{t+\Delta t} = Q_S + Q_p \cdot \qquad (10)$$

Characteristic Analysis and Experimental Results of the MPA

Fig.5 shows the transient analysis result of the MPA by using 3-D FEM. Fig.6 shows the one cycle displacement comparison between the experimental data and simulated ones of the MPA. The results of the simulation almost agreed with the experimental ones. This proved that the 3-D FEM routine used in this research was correct. From Fig.5 and Fig.6, it is also verified that the designed MPA has no problems for the proper motion.

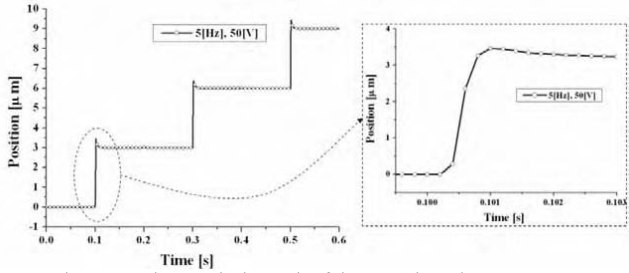

Fig.5. Transient analysis result of the MPA by using 3-D FEM.

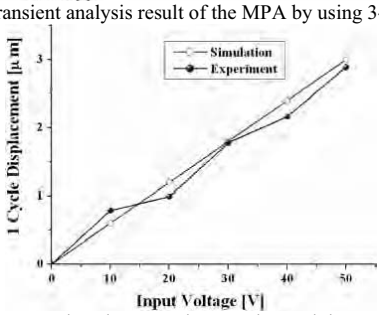

Fig.6 One cycle displacement comparison between the experimental data and simulated ones of the MPA.

Design of the Electromagnet

It is important that the electromagnet, which is attaching to the steel plate, must not be slid by the expansion or contraction of the piezoelectric ceramic. Therefore, the maximum resistible horizontal force of the attaching electromagnet by the electromagnetic force must larger than the receiving horizontal reactive force. Theses force relations can be induced from the “Equation of Motion”, which explains the force equilibrium of horizontal direction [11],[12]. But, the maximum resistible horizontal force must not so much larger than the receiving horizontal reactive force. If then the MPA do not operates properly with some problems. The main reason of those problems is due to the residual magnetic flux of the electromagnet [13],[14]. From above mentioned theories of the mechanical and the electrical, we can derive design and analysis methodology of the MPA as follows.

Fig.7 shows the free-body diagram of the MPA at the attaching electromagnet.

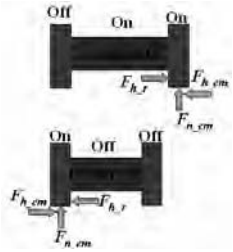

Fig.7 Free-body diagram of the MPA at the attaching electromagnet.

The maximum resistible horizontal force of the attaching electromagnet is as follows :

$$F_{h\_em} = \mu \times F_{n\_em} \qquad (11)$$

where,

F_{h_em} : maximum resistible horizontal force of the attaching electromagnet

μ : coefficient of the static friction

F_{n_em} : normal force which is generated by the electromagnet.

The receiving horizontal reactive force at the attaching electromagnet is as follows :

$$F_{h\_r} = \left(m_{em} + \frac{m_p}{2} \right) \times a \qquad (12)$$

where,

F_{h_r} : receiving horizontal reactive force at the attaching electromagnet

m_p : mass of piezoelectric ceramic

m_{em} : mass of one electromagnet

a : acceleration of slipping electromagnet.

As mentioned above, it is important that electromagnet, which is attaching to the steel plate, must not be slid by the expansion or contraction of the piezoelectric ceramic. Therefore, the maximum resistible horizontal force of the attaching electromagnet by the electromagnetic force must larger than the receiving horizontal reactive force, as follows :

$$F_{h\_em} > F_{h\_r} \qquad (13).$$

But, the maximum resistible horizontal force must not so much larger than the receiving horizontal reactive force. If then the MPA do not operates properly with some problems. Such problems can be happened as, the sliding of the attaching electromagnet or the attaching of the detaching one to the steel plate. The main reason of those problems is due to the residual magnetic flux of the electromagnet. To avoid these problems, the maximum resistible horizontal force must larger than the receiving horizontal reactive force optimally. Therefore, the optimal electrical source has to be applied to the electromagnet according to the varying electrical source of the piezoelectric ceramic. In this reason, the mutual relation between the maximum resistible horizontal force and the receiving horizontal reactive one is analyzed by using FEM in this research. Considering these relations, such parameters as the dimensions of electromagnet, the number of coil turns, and the electrical input source of the coil according to the varying source of the piezoelectric ceramic are determined.

At first, the maximum received horizontal reactive force at the electromagnet is analyzed by 3D-FEM about time step. Fig.8 shows the transient analysis results of a received horizontal reactive force at the electromagnet by using FEM. In this case, the maximum received horizontal reactive force, during the operation of the MPA, is about 0.576 [N]. The electrical input source 5[Hz] and 50[V] is the maximum value for the operation of the MPA in this research. Therefore, the maximum received horizontal reactive force 0.576 [N] at the electromagnet is the maximum one of the MPA. From these results, the electromagnets can be designed by using FEM. The

dimensions of electromagnet, the number of coil turns, and the maximum electrical input source of the coil are designed by FEM. The designed results are shown in Fig.1. Fig.9 shows the analysis result of finally designed electromagnet at the maximum input current 0.55[A] using FEM. In this case, the maximum resistible horizontal force of the attaching electromagnet by the electromagnetic force is 0.688[N]. Also, the optimal electrical input sources to the coil are designed according to the varying electrical source of the piezoelectric ceramic by using FEM. The results are shown in Fig.10.

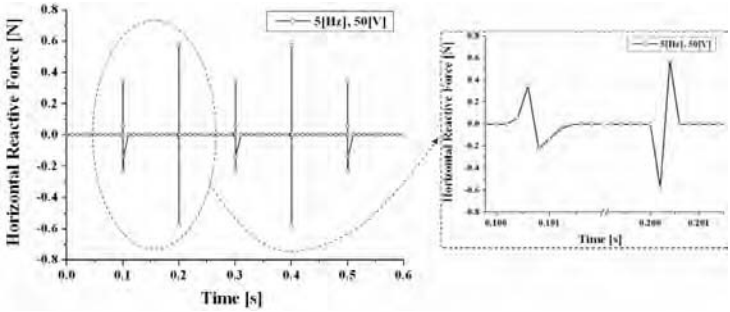

Fig.8 Transient analysis result of a received horizontal reactive force at the electromagnet by using FEM.

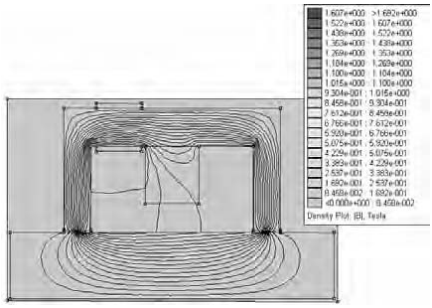

Fig.9 Analysis result of finally designed electromagnet at the maximum input current 0.55[A] using FEM.

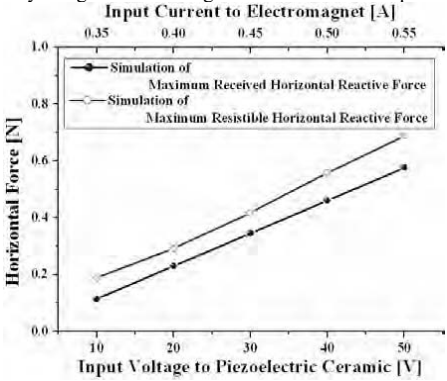

Fig.10 Analysis result of the maximum received and resistible horizontal reactive forces at the electromagnet by using FEM.

Conclusion

It is important to note that in this research the MPA is proposed and verified as the more effective precise positioning actuator than most existent one in aspect of size, energy, and cost. It is also noteworthy that the design and analysis methodology of the MPA is proposed and validated through comparison with experimental data. And, this methodology can be applicable to many other kinds of actuators, which uses same working principle.

References

[1] K. Uchino, and Jayne R. Giniwicz, "Micromechatronics," Marcel Dekker, Inc. New York/Basel, 2002, ch.6.
[2] Toshiiku Sashida and Takashi Kenjo, "An Introduction to Ultrasonic Motors," Clarendon Press, Oxford, 1993
[3] S. Ueha, Y. Tomikawa, M. Kurosawa, and N. Nakamura, "Ultrasonic Motors: Theory and Applications," Clarendon Press. Oxford, 1993, ch. 5.
[4] H.Aoyama and A.Hayashi, Multiple Micro Robots for Desktop Precise Production , Proc. Of 1st Conf. of EUSPEN, (BREMENN) pp. 60-63, 1999
[5] Ohmi Fuchiwaki and Hisayuki Aoyama, "Micromanipulation by Miniature Robots in a SEM Vacuum Chamber," *Journal of Robotics and Mechatronics*, Vol.14, No.3, 2002.
[6] Higuchi, T., Yamagata, Y., Furutani, K., Kudoh, K., "Precise Positioning Mechanism Utilizing Rapid Deformations of Piezoelectric Elements," *IEEE transaction on Micro Electro Mechanical Systems*, Pages:197-202,11-14,Feb.1990.
[7] Ohmichi, O., Yamagata, Y., Higuchi, T., "Micro Impact Drive Mechanisms using Optically Excited Thermal Expansion" *IEEE transaction on Microelectromechanical Systems*, Vol. 6, Issue: 3, pp.200 – 207, Sept. 1997.
[8] Jong-Seok Rho, Byung-Jai Kim, Chang-Hwan Lee, Hyun-Woo Joo and Hyun-Kyo Jung, "Design and Characteristic Analysis of L1B4 Ultrasonic Motor Considering Contact Mechanism," *IEEE Transactions on Ultrasonics, Ferroelectrics and Frequency Control.*, to be published.
[9] Reinhard Lerch, "Simulation of Piezoelectric Devices by Two- and ThreeDimensioanl Finite Elements," *IEEE Transactions on Ultrasonics, Ferroelectrics and Frequency Control*, vol. 37, pp. 233-247, May 1990.
[10] Klaus A.Hoffmann, and Steve T. Chiang, "Computational Fluid Dynamics For Engineers," vol. 1, Engineering Education System^{TM} : Wichita, Kansas, USA, 1993, ch. 2.
[11] Singiresu S.Rao, "Mchanical Vibrations," 3nd ed. Addison-wesley publishing company, 1995.
[12] Daniel J. Inman, " Engineering Vibration," Pearson Education Korea, 2000.
[13] David K.Cheng, "Field and Wave Electromagnetics," 2nd ed. Addison Wesley, publishing company, 1989.
[14] Mulukutla S.Sarma, "Electric Machines," 2nd ed. West publishing company, 1994.

Electromagnetic Fields in Mechatronics, Electrical and Electronic Engineering
A. Krawczyk et al. (Eds.)
IOS Press, 2006

ELECTROMAGNETIC STIRRING IN THE PROCESS OF CONTINUOUS CASTING OF STEEL INGOTS

Czesław SAJDAK[*], Sławomir GOLAK[*], Alicja KUREK[*], Artur MAZUR[**], Roman PRZYŁUCKI[*]

*Department of Electrotechnology, Silesian University of Technology, 40-282 Katowice, Krasinskiego 8, Poland, czesław.sajdak@polsl.pl
** Stanisław Staszic Institute of Ferrous Metallurgy, 44-101 Gliwice, K.Miarki 12, Poland, amazur@imz.gliwice.pl

Abstract **- *The object of the examination are electromagnetic stirrers with an inductor generating travelling magnetic field, used for stirring liquid steel in the secondary cooling zone. The analysis of stirring process has a complex character. It deals with the electromagnetic (electromagnetic forces), thermokinetic (ingot solidification) and hydrodynamic (velocity of liquid metal) problems. For 2D models the following were determined electromagnetic forces acting on liquid ingot core, thickness and temperature of solidified layer of the ingot and velocity of stirred metal. Commercial computer programmes (FLUX, FLUENT, CalcoMOS) and author's programmes were used for the calculation.***

Introduction

Electromagnetic stirrers constitute the standard equipment of modern technological processes for continuous casting of steel [1-3]. Such devices are installed in the primary cooling zone (MEMS type), and in the secondary cooling zone: directly under the mould (SEMS type), as well as in places where liquid phase participation is not big (FEMS type) (Fig.1). Usually in the continuous casting of steel there are 2 or 3 stirrers. Liquid metal movement is caused by the inductors generating travelling, rotating or travelling–rotating field. Inductor windings are supplied by alternating, two or three phase current, often of lowered frequency (f <50 Hz). Putting liquid metal into motion during the ingot solidification causes, among others, decrease of centre segregation and axial porosity, as well as number of pores and punctures in sub surface zone. The final effect is the limitation of ingot defects thus improvement of their quality.
Distribution of density components of electromagnetic forces, velocities and direction of travelling or rotating fields determines the character and effectiveness of stirring (Fig.2). They, however depend on frequency of the current supplying the inductor, pole pitch and number of inductor pole pairs, current intensity and number of inductor phases and inductor construction. In case of stirring in secondary cooling zone, the place where the stirrer is mounted is important, as the liquid phase participation of continuous ingot changes (diminishes) together with the increase of distance from the mould.
The object of the examination presented in this paper are the electromagnetic stirrers with flat and cylindrical inductors generating travelling field, used for stirring liquid steel in the secondary cooling zone. The analysis of stirring process has a complex character. It deals with electromagnetic (electromagnetic forces), thermokinetic (ingot solidification) and hydrodynamic (velocity distribution of liquid metal) problems (Fig.3). Commercial computer programmes (FLUX, FLUENT, CalcoMOS) [4-6] and author's programmes were used for the calculation. Presented results constitute

part of the research work conducted within the grant [7], in which these problems are analysed in models 1D, 2D and 3 D.

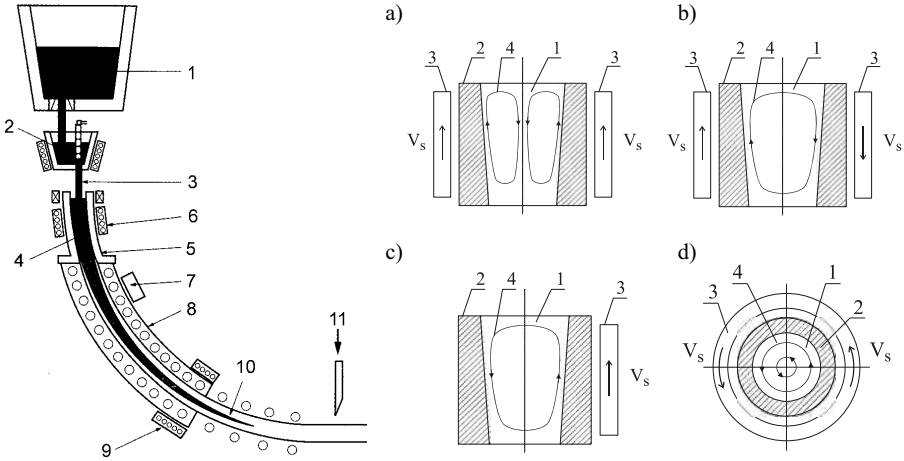

Fig.1 (left) Electromagnetic stirrers in the continuous casting of steel (1 – main ladle, 2 – tundish, 3 – immersion nozzle, 4 – liquid metal, 5 – mould, 6 – MEMS stirrer, 7 – SEMS stirrer, 8 – secondary cooling zone and guiding rollers, 9 – FEMS stirrer, 10 – solidified metal layer, 11- cutting [2])

Fig.2 (right) Liquid metal – types of movement (a - flat or cylindrical inductors, directions of travelling fields – the same, b – two side flat inductors, directions of travelling fields – the opposite, c – one side flat inductor, d – cylindrical inductor generating rotating field, 1 – ingot liquid core (liquid phase), 2 – solidified layer (solid phase), 3 – inductor, 4 – movement of liquid metal, v_s - synchronous velocity)

The Analysis Of Physical Fields

In the analysed process of electromagnetic stirring, physical fields: electromagnetic, thermokinetic and hydrodynamic - are treated as separated. Such simplification is justified because:

- cooling and casting conditions (temperature of liquid metal, casting velocity, cooling intensity) are very stable,
- influence of electromagnetic field (induction heating of ingot, generating liquid metal movement) on heat exchange and ingot solidification is insignificant,
- velocity of stirred metal is small (about 1 m/s), so rotation (motional) current can be neglected in electromagnetic field equations,
- in a given place where stirrers are mounted, temperature distributions and thickness of solidified layer do not change significantly. Material properties of steel (electrical conductivity, viscosity, density, thermal conductivity etc.) can thus be treated as not changed in a given place of ingot.

The analysis aiming at the determination of the most important parameters of stirrers and stirring process, covers the following stages (Fig 3):

- taking input data (ingot dimensions, chemical composition of steel, temperature of liquid steel, casting velocity, cooling parameters, type of stirrer and its basic dimensions etc.),
- determining temperature distribution in the ingot and thickness of solidified outer layer of the ingot along all ingot height (model 2D or 3D),
- calculating the distribution of electromagnetic field in the ingot in part with the stirrer (model 1D, 2D or 3D),

- determining the distribution of liquid metal velocity which undergoes stirring (model 2D or 3D),
- calculating electric parameters of the stirrer (power, supply voltage, power factor etc).

If the obtained results do not meet the expectations and operating requirements (especially distribution and the value of liquid metal velocity) the repetition of a given stage of calculations takes place, with changed input data. Methodology of determining parameters of stirrers is discussed in paper [7].

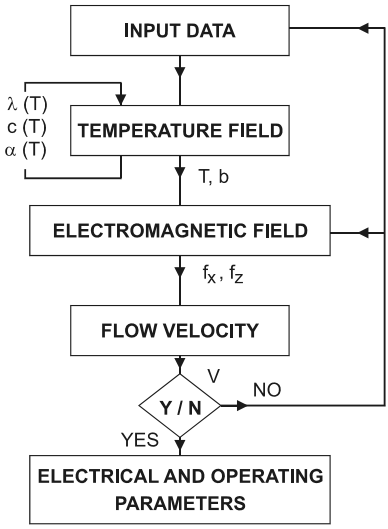

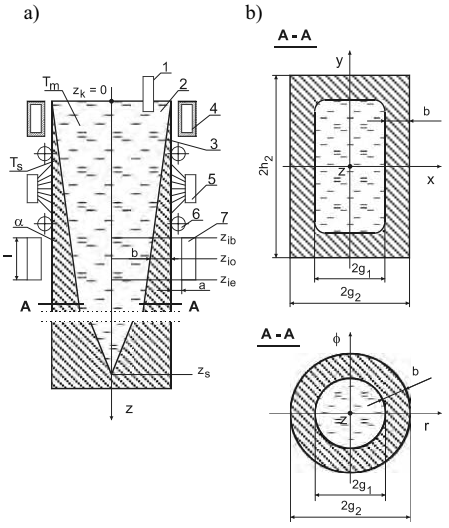

Fig.3 (left) Calculation diagram of the parameters of electromagnetic stirrers

Fig.4 (right) Model of ingot for the calculation of temperature and thickness of solidified layer (a – longitudinal section of the ingot, b – cross section of the slab and cylindrical ingot, 1 – immersion nozzle, 2 – liquid metal, 3 – solidified layer, 4 – mould, 5 – water cooling, 6 – guiding rollers, 7 – inductor, T_m - liquid metal temperature, T_s – solidified layer temperature, z_k - level of liquid metal in the mould ($z_k = 0$), z_s – length of solidification zone)

Exemplary calculation results presented in this paper deal with casting of the following ingots:

a) rectangular ingots made of 06JA steel, with dimensions $2g_2 \cdot 2h_2 = 175 \cdot 950$ mm (liquid steel temperature $T_m = 1551$°C): casting velocity $v_c = 0.0283$ m/s – ingot In1a, $v_c = 0.0317$ m/s – ingot In1b,
b) rectangular ingot made of 18G2A steel with dimensions $2g_2 \cdot 2h_2 = 140 \cdot 165$ mm (casting velocity $v_c = 0.0358$ m/s, liquid steel temperature $T_m = 1550$°C) (ingot In2),
c) cylindrical ingot made of 18G2A steel of diameter $2g_2 = 170$ mm (casting velocity $v_c = 0.028$ m/s, liquid steel temperature $T_m = 1544$°C) (ingot In3).

Temperature Field. Thickness Of Solidified Layer

Temperature field in the continuously casted ingot can be determined after solving the equation of thermal conduction, with boundary conditions which take into account changeable of effective heat transfer coefficient and latent heat. Calculation were done with the use of commercial computer programme CalcoMOS (finite elements method 2D) [6] and the author's programme (analytical method 1D)[8,9]. The advantage of CalcoMOS programme is possibility of taking into consideration the ingot movement and continuous access of liquid metal to the mould.

It was assumed that effective heat transfer coefficient α changes along the height of the ingot (Fig.4), is different in particular cooling zones – primary (mould) and secondary (zones 3 – 7). Values of coefficients α, lengths of cooling zones and other data necessary for the calculation of analysed cases (ingots In1a, In1b, In2, In3) are presented in paper [7]. Non-linear dependence of material properties upon temperature was allowed for in CalcoMOS programme; their mean values for mean temperatures - in author's programme.

As a result of calculations (by means of numerical and analytical method) the following can be obtained thickness of solidified layer of the ingot (participation of solid phase), temperature distribution and mean temperatures in solidified layer and in ingot liquid core.

It is necessary to know the values of solidified layer thickness and temperature distribution in the ingot to be able to perform further calculations – electromagnetic and hydrodynamic ones (Fig.3).

Fig.5 shows changes in solidified layer thickness of ingots for analysed examples of continuous casting, both in the function of distance from the level of liquid metal in the mould (Fig.5a) and casting time (Fig.5b) (programme CalcoMOS). Further discussion of the calculation results was carried out in paper [7]. It was proved that, among others, calculation of solidified layer thickness when the dependence:

$$b = K\sqrt{t} = K_1\sqrt{z_k}$$

where: K, K_1 – solidification coefficients, z_k – distance from meniscus, t – time,
is used can feature an error reaching even tens of %.

a) b)

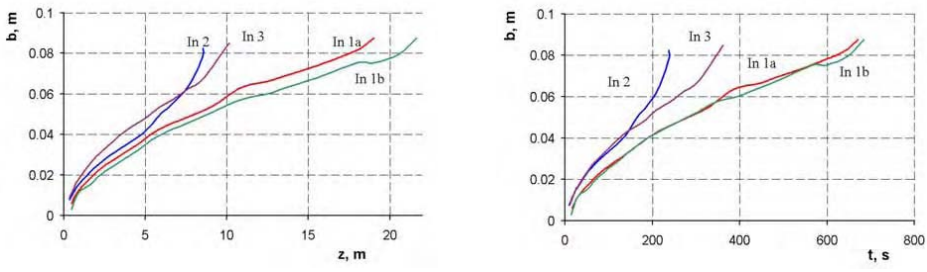

Fig.5 Changes of solidified layer thickness in the function of distance from the mould (a) and solidification time (b)

Electromagnetic Field

In the developed methodology of the electromagnetic stirring process analysis at continuous casting [7], the calculation of basic values of electromagnetic field were divided into two stages:

- stage I (initial) in which Maxwell's equations is solved analytically in model 1D or quasi-2D. Dependencies determining electromagnetic forces acting on liquid metal are used in the initial

choice of supply current frequency and pole pitch of the inductor. Components of the electromagnetic forces density f_x and f_z are presented in the form $f_{x,z} = f_{x,z}(x)$ (model 1D[8]), $f_{x,z} = f_{x,z}(x,z)$ or as $f_{x,z} = f_{x,z}(x) \exp(-kz^2)$ (models quasi-2D [7-9]). The results of that stage can be the base for determining approximate velocity distribution of liquid metal in the ingot.

- stage II (final) in which on the basis of numerical solution of vector potential equations in model 2D or 3D, vectors of electromagnetic field are determined; they are used for calculation of electromagnetic forces, velocity of liquid metal and electrical parameters of stirrers.

For the calculations in the first stage, author's programmes are used (models 1D [7,8] or quasi-2D [7-9]), in the second stage - programme FLUX2D or FLUX3D.

Fig.6 shows exemplary dependencies of total electromagnetic force acting in the axis z (relative value, non-dimensional [9]) upon parameters ω_{rm} and α_r (model 1D) for rectangular ingot, whilst

$$\omega_{rm} = \omega\mu_0\sigma_m g_2^2 = 2\pi f\mu_0\sigma_m g_2^2 , \quad \alpha_r = \frac{\pi}{\tau} g_2$$

where: τ – pole pitch, f – frequency, μ_0 - magnetic permeability of free space, σ_m - electrical conductivity of liquid metal, $2g_2$ - ingot thickness or diameter.

Directions of the travelling fields of the inductors are opposite (Fig 2b). It was assumed that: $a_r = 0.3$, $b_r = 0.2$, $\sigma_{rs} = 1.1$ (Fig.6a) and $a_r = 0.3$, $b_r = 0.7$, $\sigma_{rs} = 1.3$ (Fig.6b), whilst

$$a_r = \frac{a}{g_2}, \qquad b_r = \frac{b}{g_2}, \qquad \sigma_{rs} = \frac{\sigma_s}{\sigma_m}$$

where: a, b, g_2 – dimensions (Fig.4), σ_s – electrical conductivity of solid phase. Thickness of solidified layer b and mean temperatures of liquid metal and solidified layer were calculated by means of CalcoMOS programme. Characteristics presented in Fig.6 are used at the initial choice of current frequency which supplies inductor f and the pole pitch τ of the inductor.

For the same values a_r , b_r , σ_{rs} (Fig.6a) and for $\alpha_r = 1$, changes in the densities of electromagnetic forces f_{rz} were determined (relative values, non-dimensional [8]) along the coordinates $x_r = x/g_2$ (Fig.7). Description of applied calculation methods are shown in paper [7]. Results obtained when programme FLUX2D was used are also presented there.

a) b)

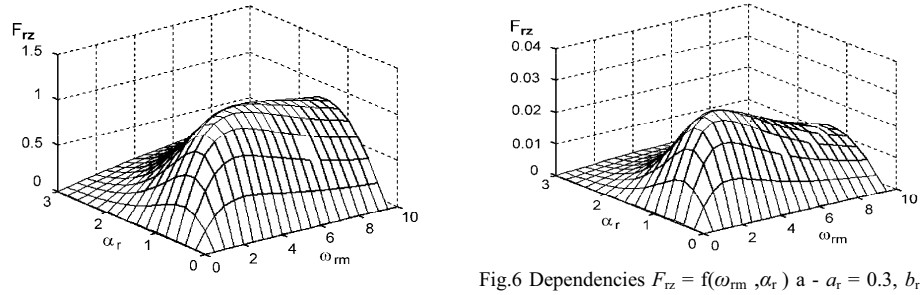

Fig.6 Dependencies $F_{rz} = f(\omega_{rm}, \alpha_r)$ a - $a_r = 0.3$, $b_r = 0.2$, $\sigma_{rs} = 1.1$, b - $a_r = 0.3$, $b_r = 0.7$, $\sigma_{rs} = 1.3$

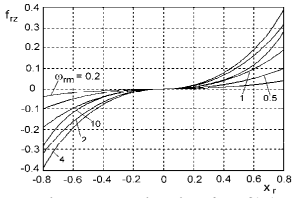

Fig.7 Dependencies $f_{rz} = f(x_r)$

Velocity Distribution Of The Liquid Metal

At the stage of mathematical modelling (computer simulation) efficiency of electromagnetic stirring is estimated on the basis of determined velocity distribution of the liquid metal (velocity value, range of stirring – depth and the height of stirring zone). Intensity of stirring can be changed by selecting type of the stirrer (Fig.2), its dimensions, number of pole pairs, pitch pole and supply parameters – frequency and current intensity of the inductor.

Velocity distribution of the liquid metal in ingot core were calculated by means of programme FLUENT (model 2D) [5,7]. Fig.8 shows exemplary results obtained for the stirrers with the flat inductors generating a travelling fields in the same direction (Fig.2a). Inductors are placed in the distance z_{io} = 4.32 m (z' = 0, Fig.8) from the level of liquid metal in the mould (Fig.4). It was assumed that in temperature T_m = 1550°C, for ingot In1a, density of liquid steel is ρ = 7007 kg/m^3, its dynamic viscosity is $v = 6.387 \cdot 10^{-3}$ Ns/m^2 (a_r = 0.229, b_r = 0.354; σ_{rs} = 1.104).

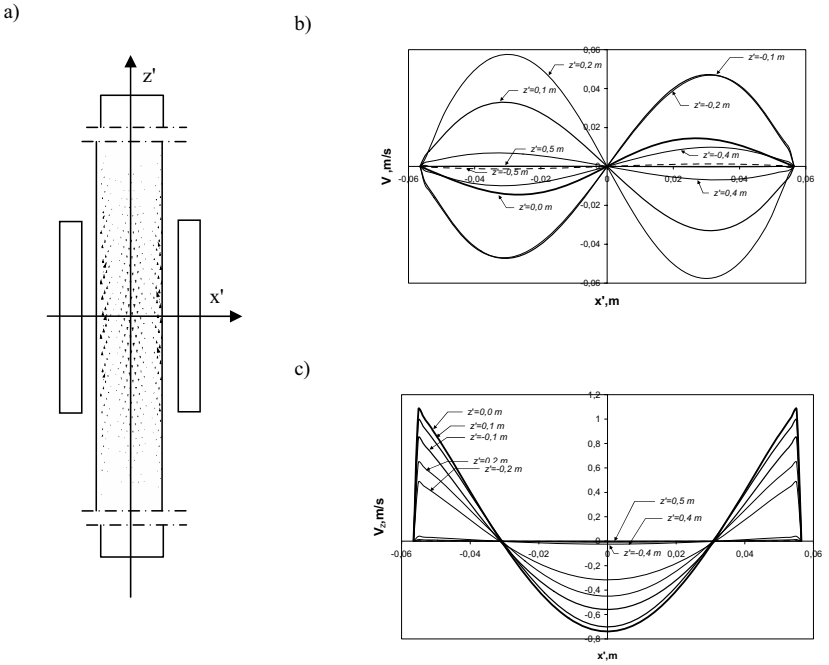

Fig.8 Velocity distribution of liquid metal at the same direction of travelling fields (Fig.2a)

The research has been done within the project no 4T08B 043 23, financed by Ministry of Science and Information Society Technologies (Poland).

References

[1] J.J. Moore et al., The application of electromagnetic stirring (EMS) in the continuous casting of steel, Continuous Castings, vol.3, Iron & Steel Society of AIME, 1984
[2] J. Lucas J., Electromagnetic induction and electric conduction in industry, Centre Français de l'Electricite, 1997
[3] K. Fujisaki, In-mold electromagnetic stirring in continuous casting, IEEE Transactions on Industry Applications, 37(2001), 4, 1098-1104
[4] FLUX2D v.7.40 User's guide. Cedrat, Grenoble France 1999
[5] www.fluent.com
[6] http://www.calcom.ch/HomeWebCalcom/index.html
[7] C. Sajdak, Mathematical models and simulation of liquid steel and non-ferrous metals stirring processes, Grant No 4T08B 043 23 (2003-2005) (in Polish)
[8] C. Sajdak, A. Kurek, R. Kadzimierz, The choice of construction and parameters of electromagnetic stirrers used in continuous casting of ingots, Hutnik-Wiadomości Hutnicze, 9/2004, 458-464 (in Polish)
[9] C. Sajdak, Calculation of parameters of electromagnetic stirrers applied in the secondary cooling zone at continuous casting of steel, Acta Metallurgica Slovaca,10, 2004, 420-429

Electromagnetic Fields in Mechatronics, Electrical and Electronic Engineering
A. Krawczyk et al. (Eds.)
IOS Press, 2006

PERMANENT MAGNET MOTOR WITH EMBEDDED MAGNETS AND FLUX BARRIERS

Pia Salminen, Markku Niemelä and Juha Pyrhönen

Lappeenranta University of Technology, Department of Electrical Engineering
P.O.Box 20, 53851 Lappeenranta, Finland, pia.salminen@lut.fi

Abstract - It was studied the effect of flux barriers on the flux density waveform and on the torque developed by several different permanent magnet synchronous motors. The rotor types studied have permanent magnets embedded inside the rotor. The magnets of one pole shoe are placed in V position. The embedded magnet rotor "pole shoes" encourage the quadrature armature reaction, which may be harmful with respect to the motor performance. Different kinds of flux barriers were designed and computed with finite element method, using Cedrat's Flux2D software.

Introduction

Permanent magnets can be buried in the rotor axially, radially or tangentially. Some advantages of embedded permanent magnet machines are that, in low speed the iron losses are often small, the rotor constructions are actually simple – the rectangular magnets are easy to mount into the holes of the rotor, the air-gap flux density may reach high values and the air-gap flux density can be easily made sinusoidal, which makes it possible to achieve a very low torque ripple or cogging torque. The electromagnetic torque T of a permanent magnet synchronous motor can be analytically calculated using the load angle δ_a, the stator phase voltage U_s, the PM induced electromotive force E_{PM} and the d- and q-axis inductances

$$T = \frac{m}{2\pi n_s}\left[\frac{E_{PM}U_s}{\omega L_d}\sin(\delta_a) + \frac{U_s^2}{2}\left(\frac{1}{\omega L_q} - \frac{1}{\omega L_d}\right)\sin(2\delta_a)\right] \quad (1)$$

The direct axis inductance L_d is in a significant way dependent on the permanent magnet material and the d-axis geometry. The q-axis inductance L_q typically becomes larger than L_d in the case of embedded magnet motors. This means that the maximum torque of the salient pole PM motor is reached with a power angle δ_a larger than $\pi/2$. According to Eq. (1) the maximum torque is inversely proportional to inductances: the smaller the inductances are the higher is the maximum torque. [1]

The embedded magnet structures in this study are designed using the criteria explained in [1]. In literature there are studies concerning embedded permanent magnet machines with one flux barrier [2,5] and with several barriers [3,4]. Bianchi and Bolognani [4] have studied an interior (embedded) permanent magnet motor, IPM with a segmented rotor, where the rotor structure is similar to synchronous reluctance rotor designs. The main idea was to reduce the q-axis inductance. Their motor design was proven to have a good performance in the flux weakening area and it was capable to give a high torque, but below the base speed the segmented IPM motors deliver a smaller torque than IPMs. Thereby it was in the authors' interest to study the behaviour of the embedded permanent magnet motors with flux barriers.

Static Computations

Different types of rotor structures were designed for a 45 kW 10-pole machine. At first, the finite element analysis, FEA was performed at no-load for an embedded V magnet structure, in which the pole consists of two embedded rectangular magnets. For all the machines the same amount of magnet material was used. It was assumed that the iron must be at least 2.5 mm wide in the iron bridges of the rotor pole to maintain the mechanical strength. It was studied several variations of flux barriers some of them are shown in Fig. 1. The motor structures studied were:

A. No flux barriers and a 1/cosine formed air-gap. Magnets in V-position.
B. 1 flux barrier (max. width 5 mm) and a 1/cosine formed air-gap. Magnets in V-position.
C. 1 flux barrier (max. width 5 mm) and a 1/cosine formed air-gap. Magnets in V-position.
D. 1 flux barrier (max. width 3 mm) and a 1/cosine formed air-gap. Magnets in V-position.
E. 8 flux barriers and a 1/cosine formed air-gap. Magnets in V-position.
F. No flux barriers and a 1/cosine formed air-gap. Magnets in W-position.
G. 5 flux barriers, barriers designed along the no-load flux lines. Magnets in V-position.

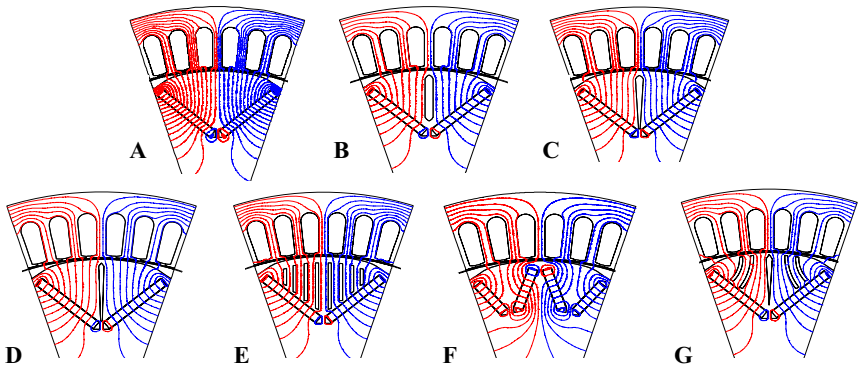

Fig. 1 The motor geometries and the flux lines, obtained from Flux2D at no-load.

A steady state calculation was performed using FEA. Constant phase currents were applied to the stator slots and the rotor was rotated step-by-step over one pole pitch. Fig. 2 shows the torque curves as a function of the rotor angle for the different 10-pole motors.

The maximum torque is achieved at a load angle higher than 90 degrees for the embedded V-magnets; this can be explained through the reluctance difference between the d- and q-axis. Forming the rotor pole and using several flux barriers diminished this armature reaction. As 8 flux barriers were used, the obtained curvature became more symmetrical. The motors with one flux barrier gave high maximum torque values, too. The pole shoe of the motor F was constructured using smaller permanent magnets than in the other motors. The torque curvature produced was unsymmetrical and thereby it may lead to unbalanced motor operation.

In Fig. 2 b) are shown the flux lines of Motor A, C and E at rated load. In the basic structure A there exist a very heavy quadrature armature reaction, which causes that in some pole areas the flux lines travel from a stator tooth to the rotor iron and then back to another stator tooth without passing the rotor magnets. This kind of tangential flux may not be useful in the torque production and thereby it was decided to design some air flux barriers for the quadrature flux.

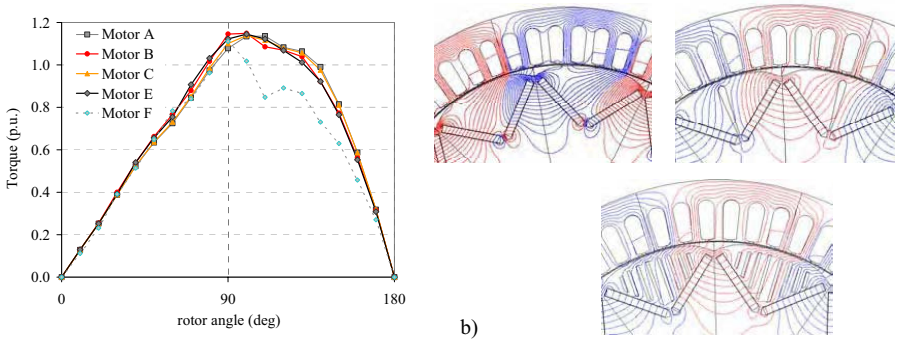

Fig. 2 a) The torque as a function of the rotor angle (with respect to the current) with steady currents in slots. The constructions of the machines described in this figure are: motor A has no flux barriers, motor B with 1 flux barrier, motor C with 1 flux barrier, motor E with 8 flux barriers and cosine formed rotor surface with magnets in V-position and motor E with magnets in W-position. Fig. 2. b) The geometries of motors A, C and E and their flux lines obtained from Flux2D at rated load.

Transient Computations with voltage supplies

Transient magnetic computations were performed with finite element program Flux2D by Cedrat. The computations were carried out with circuit couplings. A set of voltage driven computations with different load angles were performed for the motors. It was used a purely sinusoidal voltage supplies with 368 V terminal voltage. From these computations the pull-out torque and the rated load angle were solved. The torque ripple peak-to-peak values were also solved out from these computations. The ripples of embedded magnet machines equipped with flux barriers tend to have higher ripples than the machine topologies without flux barriers.

In table I are presented the machine data needed for computations and on the right side is presented the V-magnet motor topology C. The air gap in FEA was divided in three layers. The magnet material used in computations was Neorem's 495a100a. The remanent flux density B_r of the magnet material used was 1.1 T and the coercivity ${}_BH_C$ was 830 kA/m.

Table I The machine data needed for finite element computations.

Parameter	Symbol	Value
Shaft power	P	45 kW
Speed	n	600 rpm
Rated torque	T	716 Nm
Pole pair number	p	5
Stator stack length	L	270
The number of slots	Q	60
The number of slots per phase and per pole	q	2
Phase resistance	R_1	0.12 ohm
Terminal voltage	U	368 V
Frequency	f	50 Hz
Number of winding turns in phase	N_{ph}	80

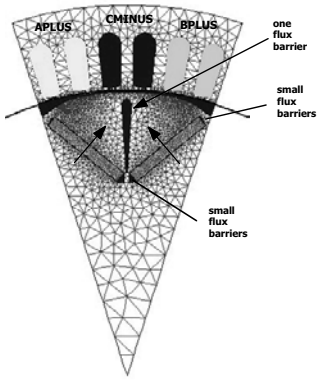

The armature reaction affects indirectly the torque by saturating the machine and decreasing the q-axis inductance, as a result of which the reluctance torque of the embedded permanent magnet machine decreases. [1] According to the flux density distributions from FEA, in Fig. 3, it can be seen that the armature reaction is reduces by using flux barriers. In Fig 3 are shown the flux density distributions of the V-magnet motor at rated load for machines A, C and E. It is also presented the flux distribution at no-load, to show the effect of magnets. The armature reaction in motor A is larger than the armature reaction seen from the flux densities of motor C and E, which both have flux barriers.

The flux densities and their harmonic contents were analysed, too. Multiplies of the 6^{th} harmonic can be seen, e.g. 12^{th} and 18^{th}. The multiplies of the 6^{th} harmonic are lower in case of motor A (without flux barriers) than with the other machines with flux barriers as shown in Fig. 3 b).

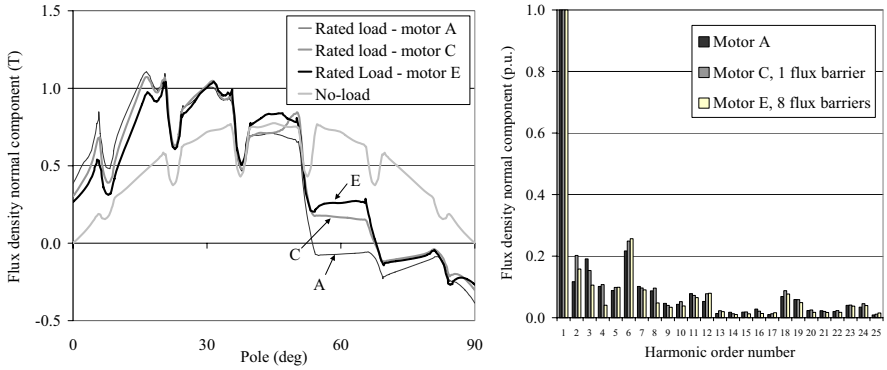

Fig. 3 a) The air-gap flux density distribution under one pole in the embedded magnet structures. Thicker grey line; only the magnets. Thin black line; motor A at rated load. Thick grey line; motor C at rated load. Thick black line; motor E at rated load. b) The harmonic components of the flux density normal component at load for motors A, C (1 flux barrier) and E (8 flux barriers).

In Fig. 4 are presented torque curves and current curves as a function of the load angles for some V-magnet motors: motor A (basic structure) and for motor C with one flux barrier. The curves are obtained from voltage driven FEA computations.

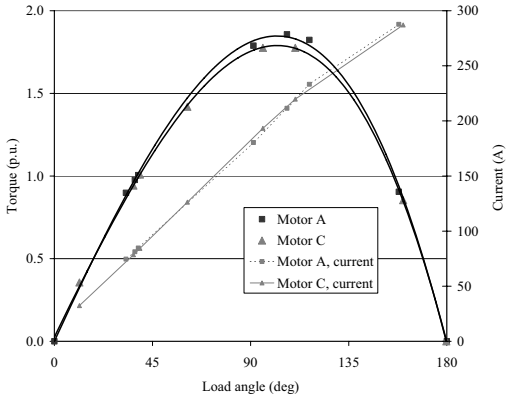

Fig. 4 The torque curves and current curves of the V-magnet motor A and C as a function of the load angle.

Table II Results from voltage driven computations: The motors C and D have one flux barrier in the middle of the pole shoe. The flux barrier of the motor D is higher and narrower than the flux barrier of motor C.

	Rated torque (Nm)	Rated Current (A)	Pull out torque (p.u.)
Motor A, No flux barriers	716	84.7	1.86
Motor C, One flux barrier	716	84.3	1.8
Motor D, One flux barrier	716	79.5	1.88
Motor E, 8 flux barriers	716	86.0	1.8
Motor G, 5 flux barrier	716	87.5	1.8

From the results shown in table II, it can be seen that the basic version under study, motor A, without flux barriers produces 1.86 p.u. pull-out torque and the rated current of the motor is 84.7 A. This motor type may utilise all the rotor pole iron, because there are no extra air holes e.g. flux barriers in the rotor. The narrow and thin flux barrier of structure D gave a good performance. The rated current 79.5 A is smaller and the pull-out torque of motor D is slightly higher than with other motors. As motor E was analysed, it was noticed that it has a lower power factor than the other motor types studied here. When observing the flux lines at rated load – it may be seen that there are leakage flux routes. A part of the flux created by permanent magnets and the rated current vanishes from the torque production. The idea of several flux barriers might work with flux barriers designed according to flux lines at no-load and therefore it was designed motor G, which has 5 flux barriers. [3] According to FEA the behaviour of that motor was also similar to earlier versions, not much difference in the pull-out torque. So, changing the q-axis inductance with flux barriers did not give a higher pull-out torque in these 45 kW, 600 rpm motors.

Analyses

The torque production capability and the inductances were studied closer. According to the finite element analysis the torque developed with flux barriers or without flux barriers was about the same. Thereby it was analyzed the d-axis and q-axis inductances, the saliency ratio L_d/L_q of the motors investigated. The amount of L_d was kept as a constant 1 p.u. and the amount of L_q was changed from $0.5L_d$ to $2L_d$. Eq. (1) was used to compute the torque as a function of load angle and the results are shown in Fig. 5.

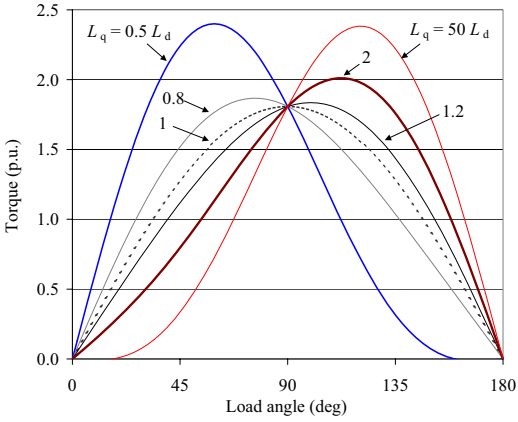

Fig. 5 Torque as a function of load angle when d-axis inductance L_d is kept as a constant 1 p.u. and the q-axis inductance L_q varies from $0.5L_d$ to $2L_d$. Torque is computed with Eq. (1). In traditional salient-pole synchronous machines typically $L_d/L_q \cong 2$.

It was assumed that other parameters in Eq. (1) remain constants although the quadrature inductance L_q is changed. From the torque curves, in Fig 7, it may be seen that when L_d equals to L_q the pull-out torque is 1.8 p.u. The analytical results were similar to the FEA results, e.g. the pull-out torque from FEA varied from 1.8 to 1.9 p.u. as L_q varied from $0.8L_d$ to $1.5L_d$.

So, reducing the q-axis inductance by 20% or increasing it by 50% with the flux barriers does not give much difference to the torque. It is needed a larger difference between the d-axis and q-axis inductances, if a higher pull-out torque is wanted. Reducing L_q to $0.5L_d$ would give a pull-out torque of 2.4 p.u. To achieve the same torque by increasing L_q then L_q should be increased up to $50L_d$ to achieve a pull-out torque of 2.4 p.u.

Conclusion

The flux barriers guide the flux to the air gap, reduce the quadrature armature reaction and they increase the useful flux density in the air gap, especially at higher loads. It was found that a machine equipped with a rotor structure with one flux barrier might have smaller rated current and a slightly higher pull-out torque than a machine without any flux barriers in the rotor. The improvement in this machine type studied was not very big. It was noticed that the flux barriers have clearly some impact to armature reaction, but it didn't affect too much to the pull-out torque as the supply voltage and the machine speed were kept as constants.

The difference of the pull-out torque and the torque ripple between the different motor structures – with or without flux barriers – is actually quite small. The aim of having flux barriers in an embedded motor was to change the inductances. The idea was to reduce the q-axis inductance in order to reduce the armature reaction and thereby it was assumed to gain a higher maximum torque. The results show only a small difference in the torque production capability. It was found that the q-axis inductance should be reduced significantly to achieve a high pull-out torque.

References

[1] Heikkilä, T. Permanent magnet synchronous motor for industrial inverter applications –analysis and design, Dissertation, Acta Universitatis Lappeenrantaensis 134, ISBN 951-764-699-2, Finland, 2002.

[2] Thelin, P., Nee, H.-P. Suggestions regarding the pole-number of inverter-fed PM-synchronous motors with buried magnets. Power Electronics and Variable Speed Drives, IEE, 1998, p. 544 – 547.

[3] Bianchi, N., Bolognani, S. Performance analysis of an IPM Motor with segmented rotor for flux-weakening applications. International Conference on Electrical Machines and Drives, IEE, 1999.

[4] Bianchi, N., Bolognani, S. Interior PM Synchronous Motor for High Performance Applications. Power Conversion Conference, IEEE, Proceedings Vol. 1, PCC-Osaka, 2002.

[5] Ionel, D.M., Eastham, J.F., Betzer, T. Finite Element Analysis Of A Novel Brushless DC Motor With Flux Barriers, IEEE Transactions on magnetics, Vol. 31, no. 6, 1995.

Electromagnetic Fields in Mechatronics, Electrical and Electronic Engineering
A. Krawczyk et al. (Eds.)
IOS Press, 2006

EVALUATION OF THE GROUNDING SYSTEM INFLUENCE ON FIELD COORDINATION STUDIES APPLIED TO LPS OPTIMIZATION

Carlos Antonio França Sartori, and José Roberto Cardoso

Escola Politécnica da Universidade de São Paulo, Departamento de Engenharia Elétrica PEA/EPUSP
Av. Prof. Luciano Gualberto Trav. 3, 158. O5508-900. São Paulo, SP. Brazil.
sartori@pucsp.br; cardoso@pea.usp.br

Antonio Orlandi
University of L'Aquila.
Dept. of Electrical Engineering
67040 Poggio di Roio, L'Aquila, Italy.
orlandi@ing.univaq.it.

Yves Marèchal
Laboratoire d'Electrotechnique de Grenoble,
ENSIEG BP 46. 38402 Saint Martin d'Heres,
France. Yves.Marechal@leg.ensieg.inpg.fr

Abstract*- This paper presents an evaluation of the grounding system influence on a Lightning Protection System (LPS) optimization process, in which the Constrained Decision Planning method is applied. The evaluation approach is based on the Field Coordination studies that take into account the resulting magnetic field effects in the regions where the equipment will be placed and the relating threshold levels. The induced magnetic flux is evaluated by time-domain simulations, and the concepts of "safe area" and "connectivity index" are used as measures of this procedure.

I. Introduction

The search for the Lightning Protection System (LPS) configuration that maximizes the regions inside the building, in which the specified threshold levels are satisfied, is a very important topic of the LPS design. Basically, it should be mentioned that the induced effects on the electric and electronic equipment installed inside buildings depend on the electromagnetic field radiated by the LPS, and on the equipment immunity levels. Thus, the elements of a LPS, like down-conductors, horizontal equipotential rings, and the ones concerning the grounding system assume an important role on the resulting electromagnetic environment when a building is directly struck by lightning. This design topic is called "Field Coordination", and it is discussed in previous works [1]-[5]. The authors propose the use of a Constrained Decision Planning tool to optimize the field profile in the regions where the equipment will be placed, and the concepts of "safe area" and "connectivity", as measures of this procedure [5]. The magnetic flux density is evaluated by time-domain simulation based on a methodology that has already been developed and validated by the authors [1], [2]. The influence of the down-conductors and horizontal equipotential rings are evaluated, assuming the configuration of grounding system as a pre-defined one. In this paper, although the same optimization method is applied, an evaluation of the grounding system influence on the optimization process is carried out. These new results are emphasized, allowing the authors to draw some important and suitable conclusions for LPS designer decisions.

II. Methodology

a. General Assumptions

The optimization approach used in this work is similar to the one presented in [5]. The same steps are carried out in order to optimize a LPS, but here it is considered different pre-selected grounding systems.
Concerning the grounding system model, a grid of conductors interconnected by rods can be used as a model. The resulting elementary grounding system cell is represented by: the earth resistance of the vertical rods, and by the transversal conductance of the horizontal conductors that can be assumed as a load to a transmission line, represented by its characteristic impedance. The soil is assumed homogeneous, and the electrical parameters and the characteristic impedance are evaluated based on analytical formulas [7]-[9]. The voltage response of the cells can be obtained by the general expressions, similar to the ones used to calculate the cell response situated above the ground [1],[2]. The ionization is considered, and its model follows the one presented in [10], similar to the well-known Korsuncev´s process: The earth resistance of the vertical rods is represented by a nonlinear resistance that depends on the instantaneous injected current, on its geometrical length, and on the soil resistivity. The so-called "Oettle expression" presents the relationship between the critical breakdown gradient of the soil and the soil resistivity. The magnetic field is evaluated based on the time-varying dipole theory and on the method of images. The lightning stroke is simulated by an ideal unidirectional current source injected in the structure, not taking into account the lightning channel [1]-[5].

b. Optimization Approach

The optimization approach here used is based on the so-called Constrained Decision Planning method. Basically, the proposed approach is a heuristic-guided search technique that uses a hierarchical structure that applies to planning problems with multiple goals that require constraint satisfaction [11]. It is based on the “Depth Search Algorithm” in which, starting from a given initial goal, it triggers the solution search process. In this work, the initial goal corresponds to the identification of the points of the space that satisfy the pre-established thresholds. For a better understanding, it follows a brief description of the main steps and definition used in the proposed approach. The optimization approach is based on the following steps:
1. Calculation of the magnetic flux density at pre-selected points “P(z, x, y)” of the regions under analysis, for each LPS configuration, taken into consideration the different grounding systems, based on the method presented in [1], [2];
2. Organization of the maximum magnetic flux density values “Bmax” as the input data set for the interpolation process, function of the number of down-conductors “Nd” and rings “Nr” of the LPS;
3. Generation of extra maximum magnetic flux density values through a multidimensional data interpolation. For this purpose, the authors have applied the Kriging one [12];
4. Determination of the safe areas, and the connectivity indexes concerning the threshold values, using as constraint to the aforementioned interpolated values of the maximum magnetic flux density, and
5. Finally, the selection of LPS, i.e., the best arrangement of “Nd” and “Nr” that maximizes the physical extension of the connective SA regions taking into account also the dimensions posed by the Standards.
Concerning the aforementioned indexes, they were firstly presented in [4], and [5]. The concept of safe area is defined as the total area in the region of interest, resulting from the sum of the elementary areas where the induced magnetic field is less than the pre-specified threshold level [4]. In fact, it will be only a suitable index for optimization of LPS, if its shape and area satisfy the geometrical layout criteria for equipment and cables. Thus, the "Connectivity Index" is introduced, and defined as the number of "common edges" of the elementary safe areas in this region: This index evaluates how connected the elementary safe areas are, and it helps us to avoid choosing the arrangement where "spots" in the region under analysis may occur [5].

c. Formulation: Basic Equations

As it was previously presented, the first step of this methodology consists in subdividing the considered structure in three-dimensional cells, each of them corresponding to a junction of transmission lines belonging to the axis z, x, and y, resulting in cells formed by one central node, and six series ones. The grounding system is considered

as an extension of the building structure, and a grid of conductors interconnected by rods [1],[2].

Response of the Cells and Current Distribution

The voltage and current wave propagation on each transmission line of the cell are related to the per-unit-length line parameters, inductance L and capacitance C, and the reflected and incident currents are obtained from the solution of the transmission lines equations. The discretized form of the currents along line "n", at the instant "k", is expressed by (1) and (2).

$$ {}_k\left[I_n^r(z,x,y)\right]=\left[\frac{1}{Z_n}\right]SR^D\,{}_k\left[V_n^r(z,x,y)\right] \tag{1}$$

$$ {}_k\left[I_n^i(z,x,y)\right]=\left[\frac{1}{Z_n}\right]\left[C(I,J)\right]SR^D\,{}_{k-1}\left[V_n^r(z,x,y,\Delta l)\right] \tag{2}$$

In these equations, "*Zn*" is the characteristic impedance of the line "*n*", and SR^D is a unitary scattering factor that will be positive or negative depending on the position and direction of the reflected-wave propagation. The space and time are represented in terms of discrete units, Δl and Δt, which are related by the speed of light "c". The variable Δl is the length between two series nodes of the cell; and $\Delta t = \Delta l/2c$ is the propagation time along each branch of the cell and it is assumed as the time step of the calculation. For an instant of time *"t", t = kΔl/2c.*The matrix *C(I,J)* is the *Connection-Matrix* that relates incident and reflected impulses. The reflected and incident voltage impulses on lines "*n*" is given by (3):

$$ {}_k\left|V_n^r(z,x,y)\right|=\left[\sigma(i,j)\right]_{k-2}\left|V_n^i(z,x,y)\right| \tag{3}$$

The matrix $\sigma(I,J)$, is the transmission coefficients matrix, where the coefficients σ_h and, σ_v are the transmission coefficients of lines 1-4 and 5-6, respectively the horizontal and vertical ones. When the central node $P_0(z, x, y)$ of the cell is the point struck by lightning, the value of the lightning pulse current at the instant $(k-1)$, must be added in (1). Concerning the characteristic impedance of the transmission lines, they are calculated through traditional formulas given by literature [8], [9].

Grounding System

A grid of conductors interconnected by rods models the grounding system. The Fig. 1 shows the resulting elementary grounding system cell: the earth resistance of the vertical rods "R_{gh}", and the transversal conductance of the horizontal conductors "G_{ge}" are represented as a load to transmission lines, which characteristic impedance is "Z_c". The soil is assumed as homogeneous, and the electrical parameters and the characteristic impedance are evaluated based on an approach similar to the ones presented in [7], [8].
Thus, the voltage response of the cells can be obtained by applying the general expression (3), but assuming $V_5^i(z,x,y)=0$. The reflected voltages regarding the central node and the lines "*n*" of the cell are then calculated by:

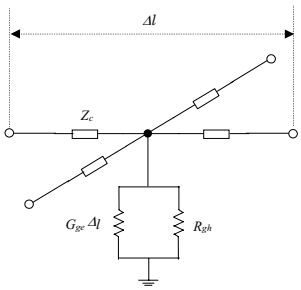

Fig. 1 - Simplified model used for the grounding system.

$$ {}_kV_N^{r,n} = \sigma_h^{at} \sum_{m=1}^{n_h} {}_{k-1}V_m^i - {}_{k-1}V_n^i + \sum_{m=5}^{6} \sigma_m^{at}\, {}_{k-1}V_m^i \tag{4} $$

The transmission coefficients in (4) will be noted by $\sigma_v(n=5)=\sigma_5^{at}$, $\sigma_v(n=6)=\sigma_6^{at}$, and $\sigma_h=\sigma_h^{at}$. When the grounding system is a single vertical rod, the resulting expressions will be (5) and (6), depending on the node in contact with the soil, the central or the series one, respectively:

$$ {}_kV_N^{r,n} = \left(\sigma_6^{at} - 1\right)_{k-1}V_6^i = \left(R_{gh} - Z_v / R_{gh} + Z_v\right)_{k-1}V_6^i \tag{5} $$

$$ {}_kV_5^i = \left(R_{gh} - Z_v / R_{gh} + Z_v\right)_{k-1}V_5^r \tag{6} $$

Ionization Model

The ionization phenomena tend to cause lower values of earth resistance due to the increased contact area of the electrode with the surrounding soil material. In this work, the ionization model follows the one presented in [10], similar to the well-known Korsuncev's process. The earth resistance of the vertical rods is represented by a nonlinear resistance that dependence on the instantaneous injected current "I (kA)", on the geometrical length *"s* (m*)",* and on the soil resistivity *"*$\rho\,(\Omega\mathrm{m})$*":*

$$ R_{gh} = 0.2631\rho^{0.6918} s^{-0.3836} \left(I/E_0\right)^{-0.3082} \tag{7} $$

The parameter E_0 (kV/m) is the critical breakdown gradient of the soil, and the so-called "Oettle expression" presents the relationship between "E_0" and the soil resistivity:

$$ E_0 = 241\rho^{0,215} \tag{8} $$

Moreover, it is assumed, as general criteria, that the ionization begins immediately after reaching the critical breakdown gradient, the independence of the electric field calculation concerning the horizontal or vertical conductor position, as well as the per-unit-length inductance of the horizontal conductors "L_{ge}" not varying with the ionization. The affecting parameters, like the capacitance "C_{ge}" and the conductance "G_{ge}" presented in [7], are evaluated assuming "$r=r_{eq}$", the resulting equivalent radius:

$$ r_{eq} = \rho\left(I/2\pi\, \Delta l E_o\right) \tag{9} $$

In that case, the propagation time and the relating characteristic impedance are obtained by [8]:

$$ Z_c = L_{ge}\Delta l / \Delta t \text{ , where } \Delta t = \Delta l \sqrt{L_{ge} C_{ge}} \tag{10} $$

It should be emphasized that, in order to keep the synchronism among the cells in the two different media, air and soil, a time-delay regarding the highest and lowest time propagation values is applied.

The Magnetic Flux Density

The magnetic flux density due to the distribution of current dipole I_0 along each of the conductors of the LPS is obtained after integrating (11) and adding (12). The method of images applies.

$$ \frac{\mu_0 I_0 r}{4\pi R^3}\, d\xi' \,, t\rangle\, R/c + \xi'/v \tag{11} $$

$$ \frac{\mu_0 I_0\, r}{4\pi c\left[\left(\xi-\xi'\right)^2 + r^2\right]} \frac{1}{\left(\dfrac{1}{v} + \dfrac{\left|\xi-\xi'\right|}{c\left[\left(\xi-\xi'\right)^2 + r^2\right]^{1/2}}\right)} \left(t\rangle \frac{R}{c} + \frac{\xi'}{v}\right) \tag{12} $$

The relating geometrical factors are: R, the evaluating point distance from the current pulse dipole, and r, the Cartesian system origin distance from the projection of $P(z,x,y)$ on the perpendicular plane to the current

propagation axe (ξ). The time ($R/c + \xi'/v$) is the retarded time, c and v are the light and the current propagation speed, ξ' is the current dipole coordinate, and μ_0 is the permeability of the vacuum. It should be noticed that the absolute value in the denominator of (12) takes into account the influence of the observer position related to the wave front of the current pulse that is particularly important when high structures are under analysis [5].

III. Application and Results

In order to illustrate the proposed methodology, we show some results related to a grounding system formed by vertical rods, connected to the down-conductors, part of a LPS of a building which dimensions are 12m x 12m x 13.5m. The basic structures is the same used in [4], in which the lighting striking point is represented as the origin of the system $P(0,0,0)$, and the plane α_n as the regions that were evaluated.

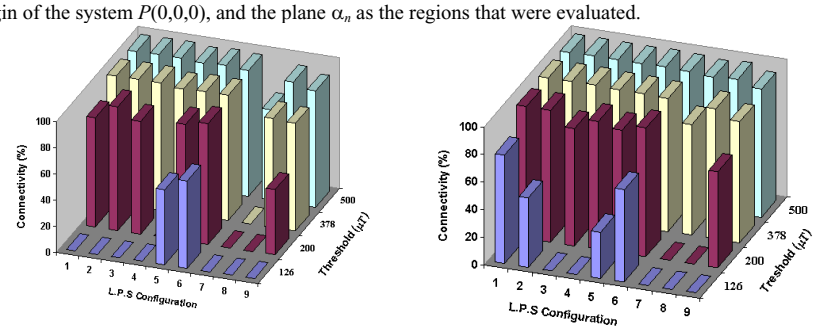

Fig 2 – Connectivity index (%) as a function L.P.S and threshold levels (μT), for the earth resistances R=5Ω (Left) and R=80Ω (Right) , Plane α (y = −5,0m), and Asymmetric Scenario.

Basically, it was considered nine LPS configurations, assuming the striking points at the center (symmetric scenario) and at the corner (asymmetric scenario) of the building, the soil resistivity equal to 200Ωm, and the equivalent earth resistance values varying from 5 Ω to 100 Ω. The authors also adopted the diameter of the LPS conductors (down-conductors and rings) d=0.015m, and I_0 =10.0kA, τ_1 =0.25μs, τ_2 =2.5μs, and n =2 as typical values for the lightning current waveshape, the same used in previous work. Regarding the LPS configurations, the LPS 1, 2, 3 are the ones related to the number of rings Nr varying from 1 to 3, and the number of down-conductors N_d equal to 4. Similarly, the LPS 4, 5 and 6, and LPS 7, 8 and 9 are related to N_d equal to 8, and 16, respectively. The LPS down-conductors are equally spaced, and the "y coordinates" of the horizontal rings are y= -6, for Nr=1, y= -3 and –9, for Nr=2, and y= -3, -6 and -9, for Nr=3. An extensive analysis was carried out, considering the influence of the earth system characteristics on the electromagnetic environment inside the LPS configurations. First, we would like to emphasize the influence of the striking point on the resulting field profile, and on the connectivity indexes: In the symmetric scenario, there is a tendency to link the highest indexes to the most complex LPS. On the other hand, if an asymmetric scenario is considered, a remarkable variation and non-uniformity of the index values are observed, and the tendency is quite the opposite. Although for some particular configuration and threshold levels the indexes do not follow this trend, it can be mentioned as a general behavior even if different earth system characteristic are taken into account. These comments are similar to the ones that have already been presented by the authors in [5]. It is illustrated by Fig. 2, where two values of earth resistances 5Ω and 80Ω are considered. Regarding the influence of the earth resistance on the LPS performance, it was observed as general tendency that the highest indexes are related to the highest values of earth resistance. It can be explained, if one considers that the transmission lines coefficients of the cells that connect the down-conductors and the rods of the grounding system vary with this parameter. Moreover, it should be notice that, the time-derivative of the current affects, directly, the values of the magnetic flux density [1], [2]. Fig. 3 presents the evaluation of the connectivity index, considering a strike on the corner of the building protected by a LPS configuration with one ring and four down-conductors. The influence of the earth resistance and the aforementioned tendency can be easily realized in this example. Although asymmetric scenarios takes a very important part in the search process, and the authors have selected and presented some results concerning this scenario, the decision about the best arrangement of the LPS that maximizes the physical extension of the

connective safe areas should take into account the resulting electromagnetic environment in the region under analysis. Therefore, all the scenarios should be considered in the field coordination studies.

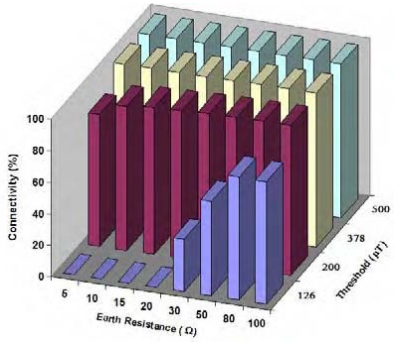

Fig 3 – Connectivity index (%) as a function of earth resistance (Ω) and threshold levels (μT).
LPS 1, Plane α (y = −5,0m), and Asymmetric Scenario.

IV. Conclusion

This paper presented the application of the Constrain Decision Planning Method on the LPS optimization in which the influence of the grounding system influence is emphasized. The formulation, the concepts of field coordination, and the main aspects and definitions of the optimization process were briefly explained, and a basic structure was selected as case study. An extensive analysis was carried out based on simulations, and some selected results were presented. The influences of striking point, the complexity of the LPS, and the earth system characteristics influence on the LPS electromagnetic environment were discussed. Although, it was possible to obtain some direct conclusions regarding the influence of the aforementioned variables on the LPS performance, a remarkable variation and non-uniformity of the index values were observed. Therefore, these new results allow us to draw some important and suitable conclusions, showing that the proposed methodology can be helpful for LPS designers.

References

[1] C. A. F. Sartori and J. R. Cardoso, "EMC Aspects in a Steel Structure Struck by Lightning," *1995 IEEE International Symposium on EMC, Atlanta - GA, USA*, Proceedings, pp. 248-252, August 1995.
[2] C. A. F. Sartori, J. R. Cardoso and A. Orlandi, "Transient Induced Voltage Computation in a High Building struck by Lightning," *IEEE Transactions on Magnetics*, v.34, n.5, pp. 2815-18, Sept. 1998.
[3] A. Orlandi, C. Mazzetti, Z. Flisowski and M. Yarmarkin, "Systematic Approach for the Analysis of the Electromagnetic Environment inside a Building during Lightning Strike," *IEEE Transactions on Electromagnetic Compatibility*, v.40, n.4, pp. 521-34, Nov. 1998.
[4] C. A. F. Sartori, A. Orlandi and G. Antonini, "Optimization of the LPS Configuration for Minimization of the Radiated Electromagnetic Field," *2000 IEEE International Symposium on EMC, Washington DC, USA*, Proceedings, pp. 248-252, August 2000.
[5] C. A. F. Sartori, A. Orlandi, J. R. Cardoso, G. Antonini and C. C. Barioni, "Constrained decision planning applied to field profile optimization in LPS of structures directly struck by lightning," *IEEE Transactions on Magnetics*, v.38, n.2, pp. 757-760, 2002.
[7] E. D. Sunde, Earth conduction effects in transmission systems. New York, D. Van Nostrand Company Inc., 1949.
[8] Kuffel, E. and Zaengl, W.S., High voltage engineering – Fundamentals, Pergamon Press, chap. 3, pp. 152-94: Measurement of high voltages, 1970.
[9] Ametani, A. et al., "Frequency-dependent Impedance of Vertical Conductors and a Multiconductor Tower Model," IEE Proc. - Gener. Transm. Distrib., v.141, n. 4, pp. 339-345, July 1994.
[10] W. A. Chisholm and W. Janischewskyj, "Lightning surge response of ground electrodes," *IEEE Transactions on Power Delivery*, v.4, n.2, pp.1329-37, April. 1989.
[11] C. Petrie, "Constrained Decision Revision," 1992 National Conference on Artificial Intelligence, San Jose - CA, USA. Proceedings, July 1992.
[12] N. A. C. Cressie, "The origin of Kriging," Mathematical Geology, v.22, pp. 239-252. 1990.

Electromagnetic Fields in Mechatronics, Electrical and Electronic Engineering
A. Krawczyk et al. (Eds.)
IOS Press, 2006

DESIGN PROCEDURE OF BEARINGLESS HIGH-SPEED PERMANENT MAGNET MOTORS

T. Schneider, A. Binder, L. Chen

Department of Electrical Energy Conversion, Darmstadt University of Technology,
Landgraf-Georg-Strasse 4, 64283 Darmstadt, Germany
tschneider@ew.tu-darmstadt.de

***Abstract** – This paper focuses on the design of bearingless high-speed permanent magnet motors. These motors can be an alternative to magnetically suspended motors using active magnetic bearings. Starting with an introduction to the required design formulas, the design procedure is explained. As an example, a 40 kW bearingless motor spinning at 40000 rpm is calculated. This design is based on an existing high-speed motor using active magnetic bearings. Finite Element calculations are used to verify the single design steps.*

Introduction

High-speed electrical machines cannot be mechanically suspended using conventional ball bearings. Magnetic levitation is a way to overcome this problem [1, 2]. The spinning rotor of the machine hovers freely within a magnetic field. Active magnetic bearings can be placed on either side of the motor shaft and use a controlled direct current to achieve stable levitation conditions. However, active magnetic bearings tend to elongate the motor design, which causes additional problems in terms of lower resonance frequencies of the shaft. Furthermore, these bearings require a direct current supply, which necessitates a special power converter and specially designed non-standard iron sheets. As an alternative, there is also a possibility to integrate the generation of levitating forces into the motor itself. In a so-called bearingless motor, the motor is equipped not only with a single three-phase winding with a certain pole pair number p_1 to generate torque, but with an additional three-phase winding of different pole pair number $p_2 = p_1 \pm 1$ to be capable of producing lateral forces. Fig. 1 shows a comparison of the design principles of magnetically levitating rotors equipped with active magnetic bearings (Fig. 1a) and as a bearingless arrangement (Fig. 1b). In the latter case, the motor is split into two half-motors with half the rated output power each, in order to provide two independent suspension points.

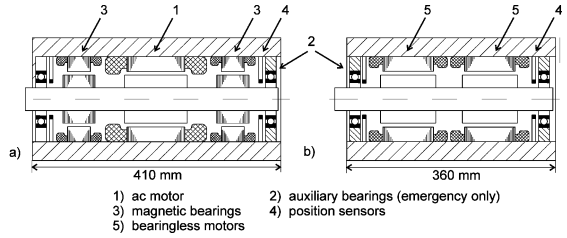

Fig. 1: a) Sketch of a magnetically suspended rotor with active magnetic bearings (40 kW, 40000 min^{-1}), b) Bearingless motor arrangement

Theory of Force Generation in Bearingless Motors

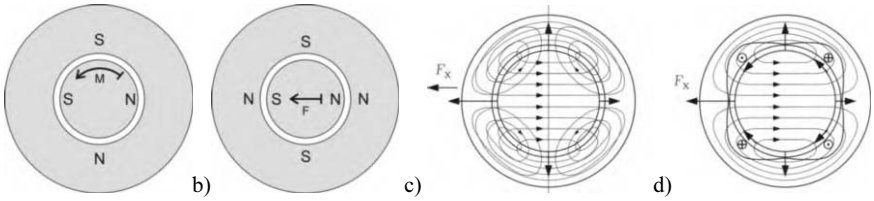

Fig. 2: a) Torque and b) lateral force generation in a bearingless motor
c) Generation of *MAXWELL* and d) *LORENTZ* forces [4]

In [3], the effect of lateral forces in an electric machine, caused by the interaction of magnetic air gap fields with p and $p \pm 1$ pole pairs, has first been described. Nowadays, modern power electronics permit the utilization of this principle to generate and control lateral forces, which can be used to provide a non-contact suspension of the rotor. Fig. 2 shows the general idea of a bearingless motor. In this example, a two-pole rotor is assumed, so that a two-pole stator field is able to generate torque (Fig. 2a)). A combination of a two-pole rotor field with a four-pole stator field will generate a lateral force, as shown in Fig. 2b). The direction of the force can be controlled by the orientation of the stator field with respect to the rotor angular position. In fact, both *MAXWELL* and *LORENTZ* forces contribute to the generation of lateral forces, so that a more detailed investigation of the force generation is necessary. Fig. 2c) shows the generation of *MAXWELL* forces, caused by the superposition of a two pole rotor field B_1, which can be excited by permanent magnets, and a four pole stator field B_2, excited by a four pole current loading A_2. This flux distribution leads to an increase of flux density in the left part of the air gap, whereas the flux density in the right part of the air gap in weakened, thus causing a magnetic force F_x pointing to the left. Both flux densities are sinusoidally distributed along the rotor circumference angle α and rotate with ω_1 and ω_2 according to (1), (2). The phase angles φ_1 and φ_2 can be chosen arbitrarily and can be used to control the direction of the force. In the following, only the fundamentals are considered.

$$B_1(\alpha,t) = \hat{B}_1 \cos(p_1\alpha - \omega_1 t - \varphi_1) \tag{1}$$

$$B_2(\alpha,t) = \hat{B}_2 \sin(p_2\alpha - \omega_2 t - \varphi_2), \qquad A_2(r_s,\alpha,t) = \hat{A}_2 \cos(p_2\alpha - \omega_2 t - \varphi_2) \tag{2}$$

Assuming non-saturated iron, the superposition of these flux densities gives the air gap flux density

$$B_\delta(\alpha,t) = B_1 + B_2 = \hat{B}_1 \cos(p_1\alpha - \omega_1 t - \varphi_1) + \hat{B}_2 \sin(p_2\alpha - \omega_2 t - \varphi_2). \tag{3}$$

The force can be calculated using *MAXWELL*'s attraction:

$$F_M = \frac{B_\delta^2}{2\cdot\mu_0}\cdot A \quad \Rightarrow \quad d\vec{F}_M = \frac{B_\delta^2(\alpha)}{2\cdot\mu_0}\cdot d\vec{A} = \frac{B_\delta^2(\alpha)}{2\cdot\mu_0}\cdot l_{Fe}\cdot r_s \cdot d\alpha \cdot \vec{e}_r \tag{4}$$

In Fig. 2c), also the current loading A_2, which excites the four pole flux in Fig. 2c), will generate lateral forces according to *LORENTZ'* law. The *LORENTZ* force $\vec{F}_L^*$ is acting on the current carrying conductor, but the rotor experiences the same force $\vec{F}_L$ with opposite direction:

$$\begin{aligned} \vec{F}_L^* = I\cdot(\vec{l}_{Fe}\times\vec{B}) \quad \Rightarrow \quad d\vec{F}_L &= -d\vec{F}_L^* = -dI\cdot(\vec{l}_{Fe}\times\vec{B}_1) = -A_2(\alpha)\cdot r_s\cdot d\alpha\cdot(\vec{l}_{Fe}\times\vec{B}_1(\alpha)) \\ &= -A_2(\alpha)\cdot r_s\cdot l_{Fe}\cdot B_1(\alpha)\cdot(-\vec{e}_\varphi)\cdot d\alpha \end{aligned} \tag{5}$$

Integrating (4) and (5) from 0 to 2π will lead to the total forces. These integrals are 0 for all combinations of $p_1$and p_2, except for $p_2 = p_1 \pm 1$. The time dependant components vanish, if $\omega_1 = \omega_2$. Both *MAXWELL* and *LORENTZ* forces act on the rotor. For $p_2 = p_1 + 1$, they have the same direction and can be added, for $p_2 = p_1 - 1$, they have to be subtracted to get to total force [5]:

$$p_2 = p_1 \pm 1: \qquad \vec{F} = \begin{pmatrix} F_x \\ F_y \end{pmatrix} = \vec{F}_M + \vec{F}_L = \pi l_{Fe} r_s \left[\frac{\hat{B}_1 \hat{B}_2}{2\mu_0} \begin{pmatrix} \sin(\varphi_1 - \varphi_2) \\ \cos(\varphi_1 - \varphi_2) \end{pmatrix} \pm \frac{\hat{B}_1 \hat{A}_2}{2} \begin{pmatrix} \sin(\varphi_1 - \varphi_2) \\ \cos(\varphi_1 - \varphi_2) \end{pmatrix} \right] \tag{6}$$

Therefore, the first case with $p_2 = p_1 + 1$ is considered to be the best choice for the construction of a bearingless motor. Equ. (6) can be further transformed to obtain an equation, which will be the basis for the levitation winding design. Expressing B_2 by A_2 and considering only the maximum force that can be generated in one direction ($\sin(\varphi_1 - \varphi_2) = 1$), we can determine the current loading A_2 which is required to generate a certain desired force F.

$$\hat{B}_2 = \sqrt{2} \frac{2 r_s k_{w,2} \mu_0}{2 p_2 \delta} A_2 \quad \Rightarrow \quad F = \pi l_{Fe} r_s \frac{\hat{B}_1}{\sqrt{2}} A_2 \left(\frac{2 r_s k_{w,2}}{2 p_2 \delta} + 1 \right) \tag{7}$$

Design of a Bearingless Motor

As an example for the design of a bearingless motor, an existing permanent magnet synchronous machine (PMSM) with magnetic bearings [2, 6], is redesigned in bearingless technology. This four pole motor ($p_1 = 2$) with water jacket cooling has a rated output power of $P_N = 40$ kW at rated speed of $n_N = 40000$ rpm. Standard IEC 100/4.944 sheets with outer diameter $d_a = 150$ mm, inner diameter $d_i = 90$ mm and $Q = 36$ slots are used. A design procedure overview is shown in Fig. 3.

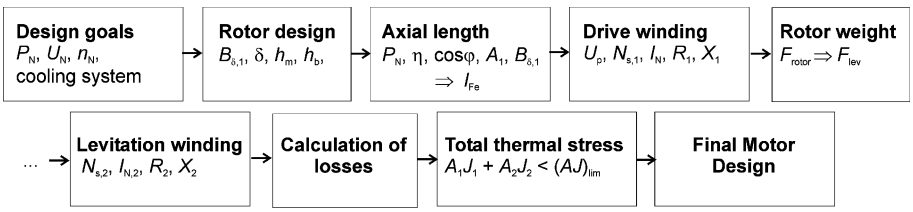

Fig. 3: Flow chart for a bearingless motor design

Motor Parameters

According to Fig. 1b), each bearingless motor needs to provide half the total output power. Therefore, two bearingless motors with 20 kW each must be designed. Rated speed is $n_N = 40000$ rpm and the motor is supposed to be operated by a standard three-phase ($m = 3$) 400 V inverter, giving a maximum phase voltage of $U_1 = 230$ V (r.m.s.).

Design Of The Magnetic Circuit

First of all, the magnetic circuit must be designed in order to specify the fundamental air gap flux density B_δ. In high speed machines, this value is chosen to be rather small, as iron losses P_{Fe} are proportional to $B^2 \cdot f^{1.8}$. Stator frequency will be very high for high rotational speed, e.g. $f_N = n \cdot p = 1333$ Hz for a four pole machine spinning at $n = 40000$ rpm, so the only way to limit iron losses is to operate with a rather low fundamental air gap flux density of about 0.5 T. The air gap in a surface

mounted magnet PMSM is rather big, as a carbon fibre bandage is required to assure structural integrity at high speed. The design of the bandage is not explained here, but can be found in [7]. A mechanical air gap of δ_{mech} = 1 mm and a bandage height of h_b = 5 mm lead to a total magnetic air gap of δ = 6 mm. Choosing NdFeB magnets with characteristics as shown in Table 1, a magnet height of h_m = 4.5 mm leads to a fundamental air gap flux density of $B_{\delta,1}$ = 0.51 T. The magnets are segmented to limit eddy current losses. 15 magnets per pole are used with 100% pole coverage ratio (no inter-pole gap). The magnet height can be analytically determined using

$$h_m = \frac{\mu_m \delta \frac{4}{\pi} B_{\delta,1}(r = r_m)}{B_R - \frac{4}{\pi} B_{\delta,1}(r = r_m)} \cdot k_s \cdot k_{fr}, \qquad k_s = \frac{r_m}{r_m - h_m}, \qquad k_{fr} \cong \frac{\tau_p(r = r_m)}{\tau_p(r = r_m) - \frac{4 \cdot \delta}{\pi}} \tag{8}$$

with $B_{\delta,1}(r = r_m)$ being the fundamental air gap flux density at the magnet surface, μ_m the relative magnet permeability, τ_p the pole pitch and k_s and k_{fr} representing the influence of segmented magnets with gaps in between and air gap leakage flux ("fringing"). For the geometry considered here, both factors are approximately $k_s = k_{fr}$ = 1.1. The fundamental air gap flux density of $B_{\delta,1}$ = 0.51 T is also verified by FE calculations (Fig. 5). The rotor data is summarised in Table 1.

Table 1: Rotor dimensions and parameters

Remanence flux density	B_R (80°C)	1,233 T
Coercive force	H_{CB} (80°C)	956 kA/m
Number of rotor pole pairs	p_1	2
Stator bore diameter	d_i=2·r_s	90 mm
Mechanical air gap	δ_{mech}	1 mm
Bandage height	h_b	5 mm
Magnet height	h_m	4,5 mm
Fundamental air gap flux density	$B_{\delta,1}$	0,51 T

Design Of The Drive Winding

Before designing the levitation winding, which will be placed together with the drive winding in the same slots, first of all the axial iron length l_{Fe} of the machine needs to be determined. Therefore, a reduced current loading A_1 = 220 A/cm for the drive winding is aimed in order to provide enough thermal margin for the additional levitation winding. Using a single layer winding with two slots per pole and phase, the winding factor is $k_{w,1}$ = 0.96. For a desired output power of P_N = 20 kW and estimated efficiency of η = 0.9, cosφ = 0.9, the iron length can be determined as

$$l_{Fe} = \frac{P_N}{\eta \cdot \cos\varphi \cdot \frac{\pi^2}{\sqrt{2}} \cdot k_{w,1} \cdot \hat{B}_1 \cdot A_1 \cdot n \cdot d_i^2} = 0.06\,\text{m} \tag{9}$$

Starting with this axial length of the machine, the stator winding parameters can be determined, which are summarised in Table 2. With this winding arrangement, the drive winding occupies $A_{slot,1}$ = 39 mm² of the slot area (slot filling factor k_{slot} = 0.4), which is 48.7% of the total slot area of A_{slot} = 80.1 mm². The drive winding is placed on the slot bottom to increase the slot stray inductance. This helps to limit the sudden short circuit current, which is critical in high speed machines in terms of demagnetisation of the permanent magnets.

Design Of The Levitation Winding

The remaining slot area of $A_{slot,2}$ = 41.1 mm² can now be filled with the second winding with p_2 pole pairs, which will be responsible for the generation of lateral forces. The weight of the rotor of each

half motor needs to be calculated taking into account the total length comprising of the active iron length l_{Fe} and overhang projection h_b. In the existing PMSM, which is used as a benchmark, the overhang projection is h_b = 35 mm on each side, which is also taken as a realistic value for this

Table 2: Key drive winding parameters

Number of pole pairs	p_1	2
Number of slots per pole and phase	$q_1 = Q/(2mp_1)$	3
Winding factor (single layer)	$k_{w,1}$	0.96
Number of turns per phase	$N_1 \cong 0.9 \cdot U_s / (\sqrt{2}\pi \cdot f \cdot k_{w,1} \cdot 2/\pi \cdot \tau_{p,1} \cdot l_{Fe} \cdot B_{\delta,1})$	24
Number of parallel branches	a_1	2
Number of turns per coil	$N_{c,1} = a_1 \cdot N_{s,1} / (p_1 \cdot q_1)$	8
Back e.m.f. (r.m.s.)	$U_p = \sqrt{2}\pi \cdot f \cdot N_s \cdot k_{w,1} \cdot 2/\pi \cdot \tau_{p,1} \cdot l_{Fe} \cdot B_{\delta,1}$	190,3 V
Rated current (r.m.s.)	$I_{N,1} = P_{el,N} / (3 \cdot U_p)$	38.93 A
Current loading	$A_1 = 2 \cdot m \cdot N_{s,1} \cdot I_{s,1} / (2 \cdot p_1 \cdot \tau_{p,1})$	197 A/cm
Current density	J_1	10 A/mm²

bearingless design. With the mass densities of iron ρ_{Fe} = 7800 kg/m³, magnet ρ_m = 8400 kg/m³ and the carbon fibre bandage ρ_b = 1800 kg/mm³, the rotor mass per half motor is calculated as m_r = 4.89 kg, which corresponds to a weight force of F_r = 48 N. In applications such as compressors, which do not cause any additional lateral forces, the lateral force only needs to overcome the rotor weight and forces caused by rotor eccentricity during take off. Here, it is sufficient to provide 2…3 times the rotor weight as steady state lift force. Therefore, a steady state levitation force of $F_{lev} = 3 \cdot F_r$ = 144 N is aspired. The related current loading A_2 is determined according to (7). Based on this current loading A_2, the 6 pole ($p_2 = p_1 + 1$) levitation winding can be designed (Table 3).

Table 3: Key levitation winding parameters

Current loading	$A_2 = F_{lev} / (\pi \cdot l_{Fe} \cdot r_s \cdot \hat{B}_1 / \sqrt{2} \cdot (2 \cdot r_s / 2 \cdot p_2 \cdot \delta) + 1)$	192,3 A/cm
Rated levitation current (r.m.s.)	$I_{N,2}$	19 A
Number of turns per phase	$N_{s,2} = A_2 \cdot 2 \cdot p_2 \cdot \tau_{p2} / (2 \cdot m \cdot I_{N,2})$	48
Number of turns per coil	$N_{c,2} = N_{s,2} / (p_2 \cdot q_2)$	8
Current density	$J_2 = I_{N,2} / q_{Cu,2} = I_{N,2} \cdot N_{c,2} / (A_{slot,2} \cdot k_{slot})$	9.25 A/mm²

FE-Calculations

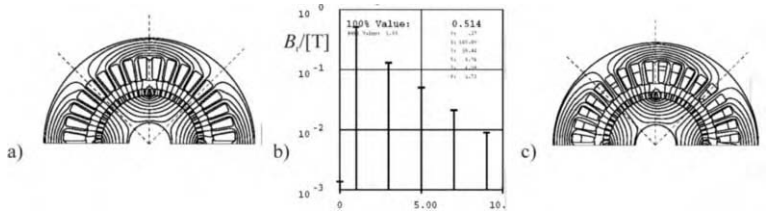

Fig. 5: a) FE model of the bearingless motor, no-load flux lines, b) Radial air gap flux density harmonics at no-load, $B_{\delta,1}$ = 0.514 T, c) Flux lines for rated torque and force.

In order to verify the design, FE calculations with programme code FEMAG are used. For no-load and load investigations, a reduced model of only 180° can be employed due to symmetry, but for force calculation, the entire motor needs to be modelled. The comparison of design goals and FE results (Table 4) show only a very small deviation from the desired analytical values as the iron saturation level has been kept low.

Table 4: Comparison of analytical calculations and FE results

Quantity	Analytical design value	FE verification Result	Deviation
No load air gap lux density $B_{\delta,1}$	0.51 T	0.514 T	0.8 %
Rated shaft torque M_N	5.31 Nm	5.41 Nm	1.9 %
Rated lateral force F_N	144 N	144 N	0 %

Predicted Motor Performance

Special attention needs to be paid to sudden short circuit current demagnetisation, which is always critical in high-speed machines with small inductances. Analytical calculation of the peak sudden short circuit current ($\hat{I}_{sc} = 413\,\mathrm{A}$) and impressing it to the FE model revealed that the motor is well protected against demagnetization. For the calculation of losses, only the resistive losses, iron losses and air friction losses are considered (Table 5). For a more detailed investigation additional losses such as eddy current losses in the magnets or load dependent iron losses need to be taken into consideration [6]. The total thermal stress is $\sum A \cdot J = 3750\,\mathrm{A/cm} \cdot \mathrm{A/mm^2}$, which is very high, but still feasible with water jacket cooling.

Table 5: Parameters of the bearingless permanent magnet motor, at n = 40000 min^{-1}

Torque generation			
Output power P_N	20.9 kW	Stator impedance $X_{s,1}$	1.15 Ω
Rated voltage $U_{N,1}$	200 V	Losses $P_{d,1}=P_{Cu,1}+P_{Fe}+P_{fr,air}$	1.3 kW
Rated current $I_{N,1}$	38.93 A	Efficiency η	0.94
AC Stator resistance $R_{s1,ac,145°C}$	0.12 Ω	Drive winding power factor cosφ_1	0.97
Force generation			
Rated lateral force F_N	144 N	Levitation copper losses $P_{Cu,2}$	187 W
Rated levitation voltage $U_{N,2}$	55.8 V	Levitation winding power factor cosφ_2	0.06
Rated levitation current $I_{N,2}$	19 A		

Conclusion

The parameters of the bearingless motor described above show that bearingless motors can be an alternative to the established magnetic bearing technology. They offer the opportunity to replace dc current sources by cheaper standard three-phase inverters. Standard iron sheets for electrical machines can be employed instead of especially designed sheets for magnetic bearings. The total axial length in this example is reduced by 12% (Fig. 1). Future work will include production and testing of a prototype, so that the above calculations can also be verified by measurements.

References

[1] Schweitzer, G.: *Magnetic Bearings*, Springer, Heidelberg, 1989

[2] Klohr, M.; Binder, A.: *Bemessung und Simulation eines magnetgelagerten Permanentmagnetantriebs (MAGPERM) 40kW, 40.000 min^{-1}*, 4. Workshop Magnetlagertechnik, Kassel – Zittau, p. 18-24, 1999

[3] Sequenz, H.: *Die Wicklungen Elektrischer Maschinen*, Volume 3, Springer Verlag Vienna, 1954

[4] Schoeb, R.: *Beiträge zur lagerlosen Asynchronmaschine*, PhD Thesis, ETH Zürich, 1993

[5] Bikle, U.: *Die Auslegung lagerloser Induktionsmaschinen*, PhD Thesis ETH Zürich, 1999

[6] Binder, A.; Klohr, M.; Schneider, T.: *Losses in high speed permanent magnet motor with magnetic levitation for 40000/min, 40 kW*, Proc. of the 16th Int. Conf. on Electrical Machines, ICEM 2004, Vol. 1, p. 93-94, (full version 6 pages on CD-ROM), Krakow, Poland, 5.-8.9.2004

[7] Binder, A.; Schneider, T.; Klohr, M.: *Fixation of buried and surface mounted magnets in high-speed PM synchronous motors*, Proc. IEEE-IAS Annual Meeting, Hong Kong, 2.-6. Oct. 2005 (to appear)

Electromagnetic Fields in Mechatronics, Electrical and Electronic Engineering
A. Krawczyk et al. (Eds.)
IOS Press, 2006

STRUCTURE-DYNAMIC SIMULATION OF AN INDUCTION FURNACE WITH RESPECT TO FLUID-SOLID INTERACTION OF LIQUID METAL AND CRUCIBLE

M. C. Schöning, D. van Riesen, H. Brunnberg, K. Hameyer

Institute of Electrical Machines, RWTH Aachen University
Schinkelstraße 4, D-52062 Aachen, Germany
Marc.Schoening@iem.rwth-aachen.de

***Abstract** – Induction furnaces are used for melting purposes of electrically conducting material such as steel or aluminium. Due to the high power consumption of such devices evoking strong vibrations, the electromagnetically excited acoustic noise states an important criteria for their design. This paper presents an approach for the structure-dynamic simulation of an induction furnace representing the basis for the acoustic computation. The presented approach is performing an electromagnetic simulation taking eddy currents in the coils and in the melt into account. The resulting Lorentz forces are transformed to a structure-dynamic model capturing the approximation of the interaction between the liquid metal and the crucible. The simulation procedure is terminated computing the body sound and airborne sound.*

Introduction

The simulation is performed by means of the Finite-Element Method (FEM). In the first step, the Lorentz forces are computed. The resulting forces are transformed to a structure-dynamic model consisting of first order hexahedral elements. With this model the harmonic response analysis is performed determining the dynamic behaviour of the induction furnace caused by the Lorentz forces. Based on the deformation an acoustic simulation is performed to calculate the body sound and airborne sound.

Electromagnetic Simulation

Due to the sinusoidal currents in the coils, a time-harmonic approach is used. The coil windings are water-cooled solid conductors. Therefore, the coils are considered as eddy current regions. The melt is assumed to be an eddy current region as well. For the computation, an edge-element formulation with two vector potentials $(\vec{A},\vec{T})$ is applied [2][3]. In order to reduce the computation time, a symmetric cut out of 30° is sufficient to model the furnace. The Lorentz force density is defined by:

$$\vec{f}(t) = \left(\vec{J}(t) \times \vec{B}(t)\right) \quad . \tag{1}$$

The force density becomes maximal, when the fields are perpendicular to each other. Assuming a rotationally symmetric geometry, the current density $\vec{J}(t)$ has a pure circular component and the flux density $\vec{B}(t)$ has an axial and a radial component:

$$\vec{f}_{=}(t) = \vec{J} \times \vec{B} = \begin{pmatrix} 0 \\ J_{\varphi} \\ 0 \end{pmatrix} \times \begin{pmatrix} B_r \\ 0 \\ B_z \end{pmatrix} = \begin{pmatrix} J_{\varphi} \cdot B_z \\ 0 \\ -J_{\varphi} \cdot B_r \end{pmatrix} \quad . \tag{2}$$

As equation (2) shows, the force has no circular component. Applying the product rule to (1) yields by using (2):

$$f(t) = \frac{1}{2} \cdot \hat{J}_{\varphi} \cdot \left[\underbrace{\begin{pmatrix} \hat{B}_Z \cdot \sin(2\omega t + \varphi_J + \varphi_{B_Z}) \\ 0 \\ \hat{B}_r \cdot \sin(2\omega t + \varphi_J + \varphi_{B_r}) \end{pmatrix}}_{\textit{Alternating Component}} + \underbrace{\begin{pmatrix} \hat{B}_Z \cdot \sin(\varphi_J - \varphi_{B_Z}) \\ 0 \\ \hat{B}_r \cdot \sin(\varphi_J - \varphi_{B_r}) \end{pmatrix}}_{\textit{Static Component}} \right] . \qquad (3)$$

The static component is important for the flow computation in the melt and the coupled calculation of the surface curvature of the bath. The alternating component leads to an oscillation amplitude resulting in sonic radiation. Therefore, both components are required for the simulation. Fig. 1a) shows the resulting flux-density distribution and Fig. 1b) shows the Lorentz-force density distribution.

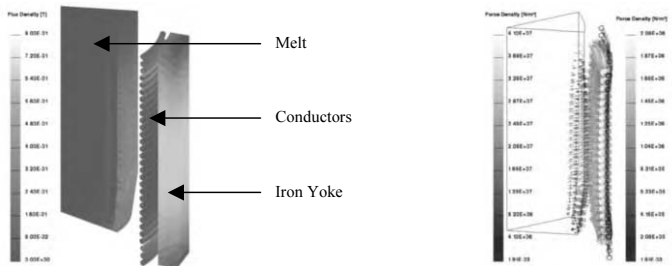

a) Flux density distribution. b) Force density distribution.

Fig. 1: Results of the electromagnetic simulation.

Structure-Dynamic Simulation

The smallest symmetry of the relevant structure-dynamic components of the furnace is 180°. The applied forces determined by the electromagnetic computation are transformed to this mechanical model. There are two approaches to simulate the structure-dynamic behaviour of a geometry. The first is a modal analysis followed by a modal superposition computation and the second is a harmonic analysis (Fig. 7). The advantage of the modal analysis and modal superposition is the short computation time, disadvantage is the necessity for symmetric system matrices. In case of the induction furnace regarding fluid-solid interaction, which results in a dense stiffness matrix [1], a full harmonic response analysis is required. The Helmholtz equation describes the distribution of oscillations in a material:

$$\Delta \underline{p} + k^2 \underline{p} = 0 , \qquad (4)$$

where $k = \frac{\omega}{c}$ represents the wave number. Equation (4) is multiplied by a change of pressure δp and integrated over the volume V. Applying Gauss theorem leads to the following equation:

$$\frac{1}{c^2} \cdot \int_V \delta p \cdot \frac{\partial^2 p}{\partial t^2} dV + \int_V \nabla \cdot (\delta p \cdot \nabla p) dV = \int_S \delta p \cdot \nabla p \, d\vec{S} = \int_S \delta p \cdot \nabla p \cdot \vec{n}_S \, dS. \qquad (5)$$

S is the surface of the boundary layer and $\vec{n}_S$ the corresponding normal vector. The relation between the pressure $\underline{p}$ (melt) and the deformation $\underline{u}$ (structure) is given by:

$$\Delta \underline{p} \cdot \vec{n}_S = -p_0 \cdot \omega^2 \underline{\vec{u}} \cdot \vec{n}_S . \qquad (6)$$

This yields the discretrised lossy wave equation:

$$\underline{M}^p \cdot \ddot{\underline{p}} + \underline{C}^p \cdot \dot{\underline{p}} + \underline{K}^p \cdot \underline{p} + p_0 \cdot \underline{R}^T \cdot \ddot{\underline{u}} = 0. \tag{7}$$

$\underline{K}^p$ is the stiffness matrix, $\underline{C}^p$ is the damping matrix and $\underline{M}^p$ is the mass matrix of the fluid material. $\underline{R}$ is the coupling matrix for the fluid-solid interaction. The pressure node vector is represented by $\underline{p}$ and the deformation node vector is represented by $\underline{u}$. Finally a common formulation regarding the deformation of the structure and the behaviour of the fluid material is required:

$$\underline{K}^u \cdot \underline{u} + \underline{C}^u \cdot \dot{\underline{u}} + \underline{M}^u \cdot \ddot{\underline{u}} - \underline{R} \cdot \underline{p} = \underline{G}. \tag{8}$$

In equation (8), $\underline{G}$ represents the global load vector. The other matrix notations are similar to equation (7) but they are related to the solid material. Equation (7) and (8) are combined describing the field problem for the calculation of the fluid-solid interaction:

$$\begin{bmatrix} \underline{M}^u & 0 \\ \underline{M}^{fs} & \underline{M}^p \end{bmatrix} \cdot \begin{pmatrix} \ddot{\underline{u}} \\ \ddot{\underline{p}} \end{pmatrix} + \begin{bmatrix} \underline{C}^u & 0 \\ 0 & \underline{C}^p \end{bmatrix} \cdot \begin{pmatrix} \dot{\underline{u}} \\ \dot{\underline{p}} \end{pmatrix} + \begin{bmatrix} \underline{K}^u & \underline{K}^{fs} \\ 0 & \underline{K}^p \end{bmatrix} \cdot \begin{pmatrix} \underline{u} \\ \underline{p} \end{pmatrix} = \begin{pmatrix} \underline{G} \\ \underline{0} \end{pmatrix}. \tag{9}$$

$\underline{M}^{fs}$ is defined as $p_0 \underline{R}^T$ and $\underline{K}^{fs}$ as $-\underline{R}$. Equation (6) is to be solved for each single frequency in range from 0 Hz to 2000 Hz. Two examples of the resulting deformation are shown in Fig. 2.

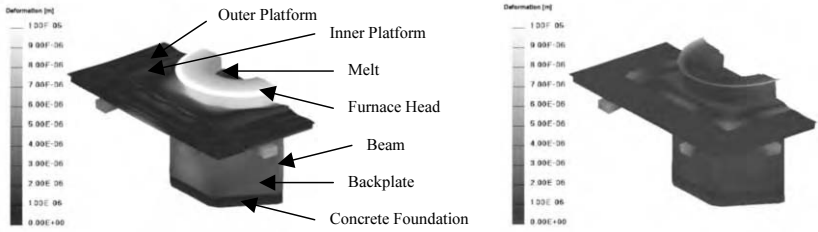

a) Real component of deformation at 306 Hz. b) Real component of deformation at 470 Hz.

Fig. 2: Results of the structure-dynamic simulation.

The deformation at the boundary layer of the melt is shown in Fig. 3.

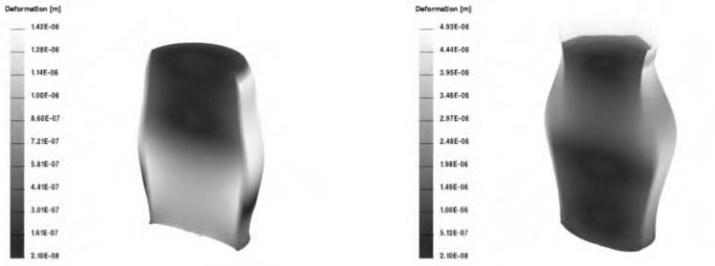

a) Real component of deformation of the melt. b) Imaginary component of deformation of the melt.

Fig. 3: Results of structural-dynamic simulation in the melt.

Acoustic Simulation

The body sound is calculated by means of the following equation [4]:

$$L_{Sh^2} = 10\log\left(\frac{\Omega^2 \sum_{p=1}^{N_{el}} \int_{S_p} \left|v^{(p)}(\Omega)\cdot n^{(p)}\right|^2 dS}{S_0 {h_0}^2}\right). \qquad (10)$$

The body sound calculation with its short computation time is a well suited method to identify problematic frequencies. Fig. 4 shows the results for the induction furnace in range from 0 Hz to 2000 Hz.

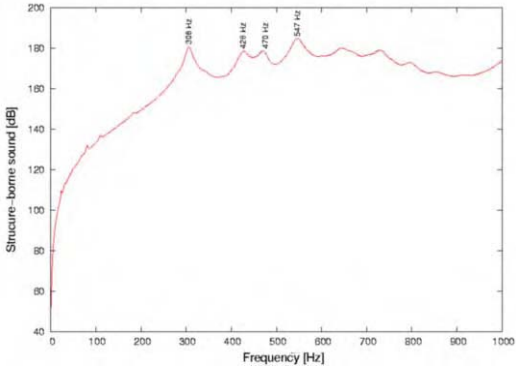

Fig. 4: Results of the structure-borne sound computation.

For the identified peaks, an airborne sound simulation is performed employing a Boundary-Element model consisting only of the surface of the induction furnace.

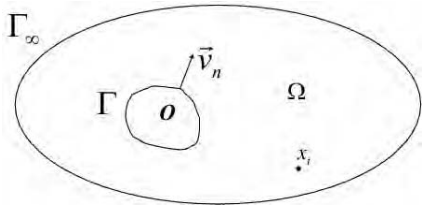

Fig. 5: Derivation of the integral equation.

Fig. 5 shows the basic approach to derive the integral equation needed for the airborne sound simulation. Γ represents a flat surface with a distinct normal vector of the irradiating object ***o***. Ω marks the surrounding area, with Γ_∞ the border in infinity. Starting with the Helmholtz equation (4), which describe the sound pressure in the area Ω, a weighting function is introduced resulting in

$$u^* = \frac{e^{-jkr}}{4\cdot\pi\cdot r} \qquad (11)$$

for an isotropic medium in the three-dimensional case. The computation leads to the final equation:

$$c_i \cdot \underline{p}(x_i) + \int_\Gamma \underline{p} \cdot \frac{\partial u^*}{\partial n} d\Gamma = -j\omega\rho \cdot \int_\Gamma u^* \underline{v}\, d\Gamma \quad . \tag{12}$$

The coefficient c_i is defined as:

$$c_i = \begin{cases} 0, & x_i \in O \\ \dfrac{\theta_i}{4\pi}, & x_i \in \Gamma \\ 1, & x_i \in \Omega \end{cases} \tag{13}$$

and the sound particle velocity is defined as

$$\underline{v} = \frac{1}{j\omega\rho} \cdot \frac{\partial \underline{p}}{\partial n} \cdot \vec{e}_n \quad . \tag{14}$$

In Fig. 6, the irradiated sound level at 306 Hz and 428 Hz are shown. From the sound level distribution, the components of the induction furnace can be classified acoustically. Therefore, the acoustic behaviour of each single component can be optimized. Besides the sound level distribution the sound power is calculated. Therefore, the sound intensity is computated on a spherical seat surrounding the induction furnace. Afterwards an integration over the spherical seat is required. To obtain a decibel value, the following equation is used:

$$L_W = 10 \log\left(\frac{P}{P_0}\right) \quad . \tag{15}$$

P_0 is defined as $10^{-12} W$. The sound power is utilised to compare the different frequencies generally. At 306 Hz, the sound power is 76,095 dB. At 428 Hz, the sound power is 68,287 dB. Compared with the body sound calculation, the value at 306 Hz is also higher then the value at 428 Hz.

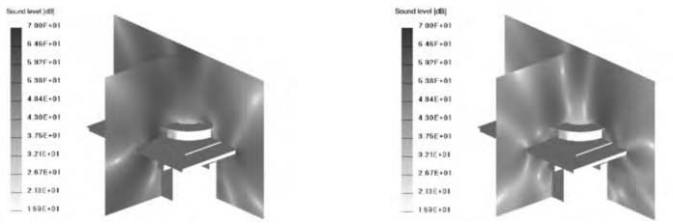

a) Airborne sound at 306 Hz. b) Airborne sound at 428 Hz.

Fig. 6: Results of the acoustic simulation.

Conclusions

The computation chain, presented in this paper represents a well suited approach to determine the structure-dynamic behaviour and the irradiated sound of induction furnaces considering the interaction of liquid metal and the crucible. To reduce computation time all possible symmetries are utilised. Thereby, the body-sound computation provides the possibility to evaluate the acoustic behaviour of the furnace with only marginal

calculation time. Due to large computational effort, the acoustic simulation is performed only for the identified peaks of the body-sound calculation. In Fig. 7, the dependencies of the computation steps are shown.

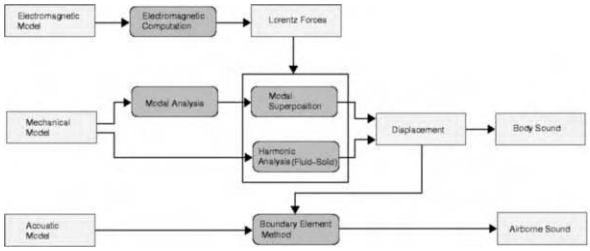

Fig. 7: Computation chain.

Different modifications are made to the induction furnace, and simulations of these variants are performed to reduce the irradiated sound of the furnace. At first, a rubber buffer between inner and outer platform is implemented. In addition the material density of the concrete as well as the thickness of the back plate, of the platform and of the beams are varied. The results (Fig. 8) show that a rubber buffer decreases the sound power significantly. Doubling the back plate thickness reduces the irradiated sound up to 480 Hz. Since the current frequency can reach 250 Hz depending on the melt level, the frequency of the resulting force is 500 Hz. Therefore, this variant is not appropriate for a completely filled induction furnace. At last, decreasing the concrete density reduces the sound power over the complete examined frequency spectrum marginally. All other simulated variants do not enhance the acoustic behaviour of the induction furnace.

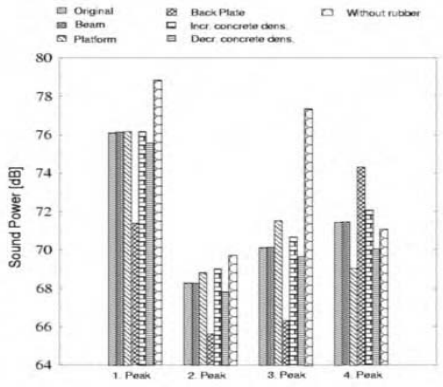

Fig. 8: Results of different modifications.

References

[1] W. Kanok-Nukulchai, B. T. Tam. *Structure Fluid Interaction Model of Tuned Liquid Dampers*, International Journal for Numerical Methods in Engineering, Vol. 46, pp 1541-1558, 1999.

[2] O. Bíró, *Edge element formulations of eddy current problems*, Computational Methods in Applied Mechanics Eng., vol. 169, pp. 391-405, 1999.

[3] D. van Riesen, G. Henneberger, *Combining electrical and mechanical analysis in an object-oriented package for the coupled calculation of an induction furnace*, Proceedings of the 10th International Symposium on Numerical Field Calculation in Electrical Engineering, IGTE, Graz, pp 76-77, September 2002.

[4] F. G. Kollmann, *Maschinenakustik*, Berlin, Springer Verlag, 2000.

Electromagnetic Fields in Mechatronics, Electrical and Electronic Engineering
A. Krawczyk et al. (Eds.)
IOS Press, 2006

PCB DESIGN ASPECTS IN DISTRIBUTED CONTROL ARCHITECTURES FOR POWER ELECTRONICS

V. Serrao, A. Di Napoli, L. Solero

University ROMA TRE - DIMI
Department of Mechanical and Industrial Engineering
Via della Vasca Navale, 79 - 00146 Roma, Italy
Email: serrao@uniroma3.it

***Abstract* - This paper deals with electromagnetic compatibility (EMC) issue from the point of view of system and circuit design, component selection and PCB (Printed Circuit Board) layout. Particularly, the design and realization of a measures acquisition board intended for use in several control applications of power electronic converters and electric drives is presented. In this work we intend to investigate the EMC/EMI issues related to the PCB layout design with particular attention to the grounding management; the PCB design is related to the distributed control architecture concept and experimental results are achieved from a prototypal system realized on purpose.**

Introduction

In every application concerning either a process or an equipment control, the measures acquisition is a basic topic; in fact, in order to achieve a control system that works effectively, the measures have to be performed with the adequate high degree of accuracy (depending on the specific case) and transmitted in the right way. As it is well known, electromagnetic interference (EMI) is a major problem in modern electronic circuits, specially in the digital ones; the fast clock speeds and rapid edge rates needed in many PCB designs require proper management of board level design, layout and signal connections in order to minimize EMI. High speed switching has the capability of producing electromagnetic waves that generate resonance, power/ground bounce, simultaneous switching noise, reflections, and coupling between traces and power/ground planes. Furthermore, the analog nature of our physical world and the growing need of processing continuous functions in the digital domain place even more stringent performance demands on mixed-signal PCB layouts, particularly when there are very noisy devices (such in power electronics applications).
In this work, explaining our data acquisition system design, we intend to investigate the EMC/EMI issue related to the PCB design; the major guidelines to be followed and the implications in power electronics systems are then outlined. The first step is the introduction of the concept of the distributed control architecture; then the functional block scheme, the design and the characterization of the related schematics are described; finally the PCB is realized and tested.

Distributed Control Architecture

Most of the high and medium power converters have a centralized control architecture (shown in Fig. 1a) in which all of the control and monitoring functions are performed by a single, centralized controller; this approach exhibits several drawbacks, such as poor system modularity, limited system

flexibility and reconfigurability, large number of point-to-point links and interconnections with a resulting underutilization of the transmission media [1].

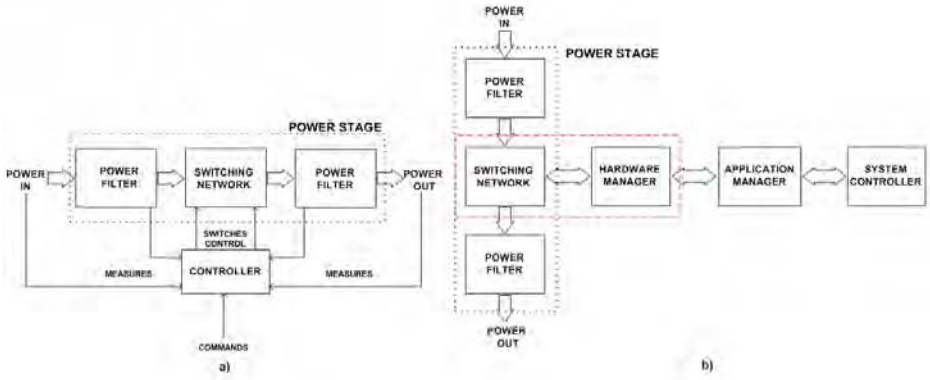

Fig. 1 a) Centralized and b) Distributed control architecture of a generic power switching converter

Today's power conversion system instead, have a distributed control architecture; to minimize the number of interconnections between the different blocks and to provide enough flexibility and modularity, we can divide the control section of a generic converter in three subsections (as depicted in Fig. 1b). The "Hardware Manager" performs a low-level hardware-oriented control tasks, as the PWM (*Pulse Width Modulation*) generation, the switches protection or the blanking time management; the "Application Manager" performs a high-level application-related regulation (in terms of current and voltage for example) of an inverter or a dc/dc converter; the "System Controller" has less specific tasks as monitoring one or more electric drives. In this way we have three different control units that have to communicate each other and so it arise the need for a proper transmission system.

Nowadays we have designed, realized and tested a generic measures acquisition system that can be used for the application manager of a general power electronic converter; analyzing some different types of converters (dc/dc, ac/dc and dc/ac) we have deduced that four measures (for example three currents and one voltage) are sufficient for any generic control function of an electric drive and the selection of the control variables can however change without having to alter the measures acquisition system architecture.

Measures Acquisition System

The switching frequency increase in power devices has allowed the construction of denser and less expensive converters, but has also increased the high frequency noise (common mode and differential) that causes EMI. Even if power electronic converters switching frequency is not very high (about tens of kHz), due to the high values of currents and voltages (up to hundreds of Amperes and Volts), the noise originated in the power conversion stage can considerably disturb the measures system mode of operation, degrading in this way the whole control system performances. For this reason, in power electronics applications usually a remote control is performed; the control system is not in the immediate vicinity of the electric drives and so it is built up of two boards: one for the measures acquisition (PCB_A on the converter side) and one for the control functions (PCB_B on the controller side).

In Fig. 2 it is illustrated the simplified functional blocks scheme of the proposed two control boards. Starting from general DAS (*Data Acquisition System*) configurations, by choosing the main features of

the project, we have outlined the basic shape of the two boards. First of all we have chosen as application manager a DSP (ADSP21992) evaluation board from Analog Devices; then, for the communication link between the two boards, we have decided for a serial I/O interface accomplished by means of the SPI (*Serial Peripheral Interface*) Motorola industrial standard that, with only four wires allows a full-duplex, serial and synchronous transmission between two or more SPI-compatible devices.

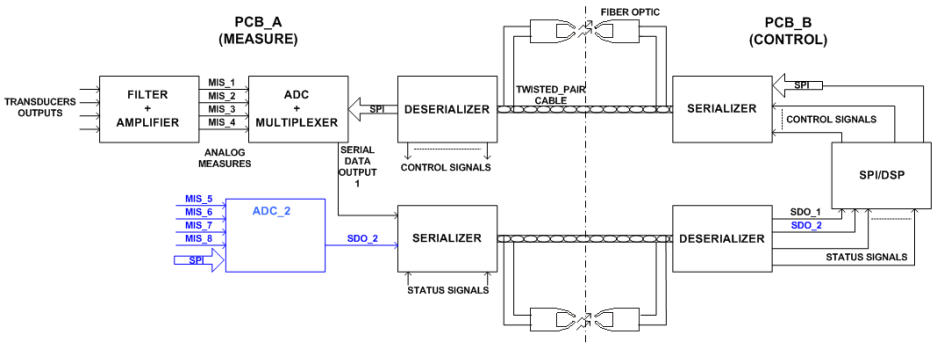

Fig.2 Simplified functional blocks scheme of the measure acquisition system

In order to minimize the number of transmitted signals (and thus the number of the connection cables) between the measures system and the control system (achieving a really serial transmission path), we have added two couples of Ser/Des (Serializer/Deserializer) devices; with a compression factor of 10, the system parallel data rate (10 ÷ 40 MHz) is translated in a useful serial data rate between 100 and 400 Mbps; as well as the serializing/deserializing tasks, these components turn the single-ended input signals into the LVDS (*Low-Voltage Differential Signaling*) standard format so improving the communication system EMC/EMI performances.

A very high serial transmission frequency implies design problems related to the link reliability and to its capability of being immune and/or to generate noise. In the case of electrical transmission (cable), to reduce the emissions, a differential media (for example a twisted-pair cable) can be used; an alternative solution is the use of a fiber-optic communication link. In our project we have thought to allow the system user to choose the transmission media (electrical or optical) best suited for his application in terms of transmission frequency, distance and reliability.

The components selection is another step that considerably affects the PCB design performances; we spent a lot of attention to the ICs (*Integrated Circuit*) package (all SMD: *Surface Mount Device*) and pinout with the purpose of PCB size reduction and PCB layout simplification. At last, we considered as a basic issue the EMC/EMI, crosstalk, reflection and signal integrity problems prevention.

PCB Layout

The PCBs realization starts with the schematic diagrams drawing and then the PCBs layout follows. A PCB layout is the physical realization of a circuit design, aimed to minimizing EMC/EMI and Signal Integrity (crosstalk, reflections, transmission lines) problems and to optimizing interconnection between the circuit elements. In the following the main steps of a good PCB layout are shortly described; the final layout is however highly dependent on the number of devices in the circuit, on the types of the devices (analog, digital and mixed-signal) and on the environment in which the final product will be located.

The first step is the PCB stack-up that is the layers configuration inside the PCB; it is a determining factor in the EMC performance of the final product. A good stack-up can be in fact very effective in

reducing the radiations emitted by both the PCB closed loops (current loop related to the differential mode emissions) and the cables connected to the board (single-ended mode emissions). The main aspects to deal with are the layers number, the planes number and type (ground/power plane), the layers pattern and their relative distance. In the layers number choice several parameters must be taken in account as the number and the frequency of signals to be drawn, the specifications in terms of emissions and finally the whole board costs. It is obvious that a multi-layer board can be more efficient in its EMC problems prevention but often another parameter (for example the cost) can be more stringent. In our design we have decided to use a four layers PCB; it seemed to be the right balance between the board costs and its EMC performances.
Components placement has two main targets, the functional blocks physical isolation and the traces length minimization. The functional blocks physical isolation works to assure that the switching noise generated by digital circuitry is not coupled into the analog signal path (the same for transmitter and receiver circuits); the traces length minimization has the purpose of reducing the current loops area.
As the number of layers and planes are decided, the management of the implementation of the reference planes (ground and power planes) must be planned. First of all, ground noise problems are more difficult to deal with than power supply noise problems because analog signals are most typically referenced to ground and, for the power supply noise suppression you can use other techniques such as the power supply by-passing and decoupling. If the circuit has a “minimum” (that is defined by the PCB designer) amount of digital circuitry, a single ground plane and a single power plane may be appropriate. When both analog and digital circuits are present and only one ground (and power) plane is provided, the proper grounding strategy must be decided; the main two approaches are either the splitting planes (Fig. 3a) or the partitioned planes (Fig. 3b).

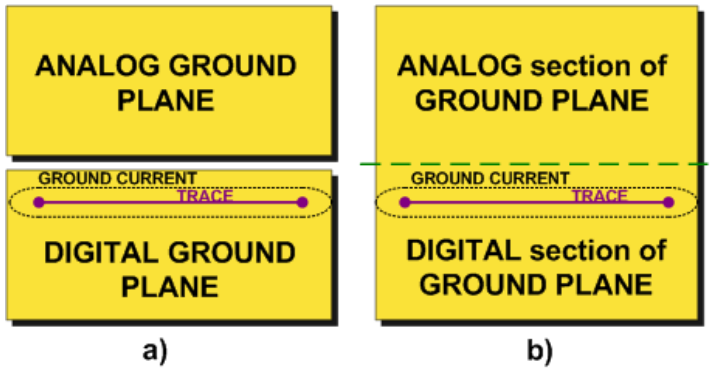

Fig.3 Different grounding strategies: a) Physical isolation (split plane); b) Partitioning

In the first case, to isolate the analog ground from the digital ground, both of them sharing the same plane, the ground plane can be split in two sections (analog and digital) physically separated each other by means of a slot in the plane without having any overlaps. With this method some problems arise specially in large complex systems; one major issue is related to traces routed over the split in the plane: in these cases radiation and crosstalk will increase dramatically because the current return path is broken and the current loop area is boosted. The planes should have one-point connection in order to form a bridge; by routing all the traces which share the analog and digital ground planes in order that they cross at this bridge, a current return path directly underneath each trace is provided, thereby producing a very small loop area.
The second technique is based on the concept that HF (*High Frequency*) currents want to return on a plane directly underneath the signal trace since it is the lowest impedance (and inductance) path, regardless of the plane type (power or ground); the current will spread out slightly in the plane, but

will otherwise stay under the trace. So, component placement, partitioning and a routing discipline can be the keys to succeed in laying out a mixed-signal PCB; in this case only one ground plane partitioned in analog and digital sections is used. If analog signals are routed only in the analog section of the board and digital signals are routed only in the digital section of the board (on all layers) the digital return currents will not flow in the analog section of the ground plane but will remain under the digital signal trace not corrupting the analog circuitry.
The final step in the PCB layout is the routing; the problems related to this stage are the same depicted previously for the PCB layout (EMC/EMI and Signal Integrity) with a particular care for crosstalk (magnetic and capacitive coupling), reflections, ringing, impedance control and signal terminations (especially for high frequency signals); besides, some rules for corner and differential signals tracing must be followed and it is also significant the routing order, the trace width choice and the vias positioning.

Experimental Results

Measures acquisition PCB and control PCB have been manufactured and they are shown in Fig. 4a with a cable connection.

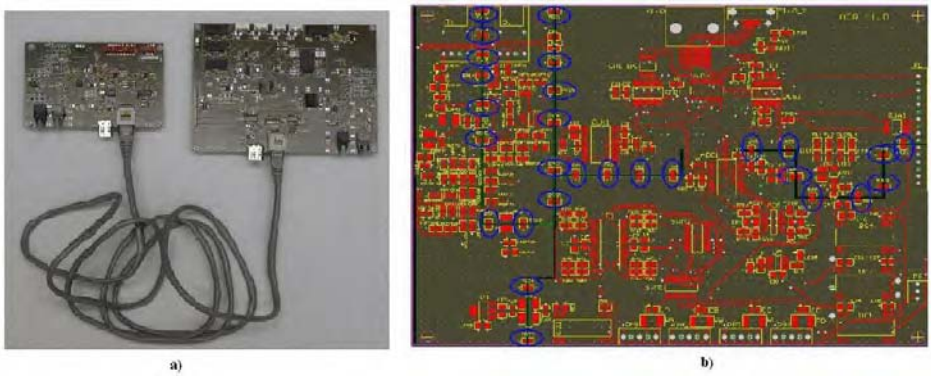

Fig.4 a) Measures acquisition and control PCBs; b) PCB layout: splitting vs partitioning

Since nowadays the EMC predictive techniques (software simulations) are not still enough effective, EMC experimental tests have to be executed. Full compliance measurements require a great effort to get the best accuracy and repeatability, a qualified OATS (*Open Area Test Site*) and instrumentation that meets the requirements set forth in the European or International Directives (as CISPR 16); this can be very expensive. Precompliance measurements are intended to give an approximation of the EMC performance of the EUT (*Equipment Under Test*) and are more straightforward and less expensive to perform than full compliance ones. For our purpose this preliminary precompliance testing is assumed to be adequate.
Because during our PCBs layout design we were still sceptical about using a single partitioned ground plane on our mixed-signal PCB instead of a split plane, as suggested by several authors [2], we have performed an experiment for determining the better choice between the two grounding techniques. We have split our ground plane in digital, analog and optical ground planes thus accomplishing the split planes configuration. However it is possible to move to the partitioned planes configuration by soldering zero ohm resistors (marked with a blue ellipse in Fig. 4b) on the pads between the slots at intervals of ½ inch; in this way in fact, the different ground planes are connected together forming a single partitioned ground plane.

For both the configuration (Case A: Split plane and Case B: Partitioned plane) we have performed radiated emission testing in the frequency range between 30 MHz and 1 GHz, in a semi-anechoic chamber with a distance of 3 m between the EUT and the broadcast antenna connected to the EMI receiver. We have executed different tests with a parallel transmission rate of 10 MHz, 20 MHz and 40 MHz, varying the antenna's height and polarization and the EUT position (rotating) till determining the maximum emissions condition.
In Fig. 5a and 5b the experimental results obtained in Case A and B respectively, in the frequency range from 30 MHz to 300 MHz and for a transmission frequency of 10 MHz (to get as close as possible the far field condition) are shown for a direct comparison.

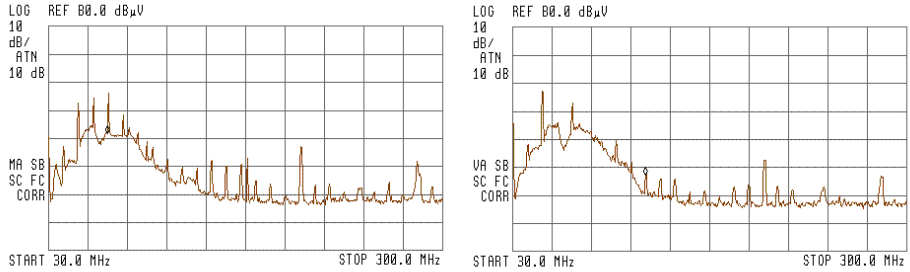

Fig.5 Radiated emission testing a) Case A (Split plane); b) Case B (Partitioned plane)

During these tests we have detected only few differences between the two test conditions; in Case B (partitioning) the radiated emissions from the two boards are slightly lower than in Case A (splitting) but this result is not so relevant.

Conclusions

In this paper a measures acquisition system suitable to be used in a wide range of applications in power electronics and electric drives has been investigated from an EMC point of view, with particular attention to the grounding management; the concept of the distributed control architecture has been introduced, then the functional block scheme, the design and the characterization of the related schematics has been described; finally the PCB has been realized and tested. The proposed boards have been realized in order to test the two main grounding strategies (split and partitioned ground planes) and their relationships with the EMC performance of the EUT. At the moment we have performed radiated emission testing and we have no detected great difference between the two different solutions. Future developments will concern other experimental validations to evaluate the system overall EMC performances in different modes of operation and varying the environment in which the system works; in fact, as it is well known, this is often the more relevant feature that affects the equipment EMC behaviour (especially in a noisy site like in power electronics applications).

Reference

[1] I. Celanovic, A Distributed Digital Control Architecture for Power Electronics Systems, Master of Science Thesis, Virginia Tech, 2000, pp 1-19
[2] Henry Ott Consultants, PCB Stack-up; Partitioning and layout of a mixed-signal PCB; Slots in ground plane, http://hottconsultants.com
[3] W. Kester, Mixed-signal and DSP design techniques, Analog Devices, 2000
[4] D. Brooks, Splitting Planes for Speed and Power, CPM Media publication (Printed Circuit Design), 2000
[5] http://www.intetron.com, EMC Tip
[6] Lattice Semiconductor Corporation, AN 6012-01: Analog Layout and Grounding Techniques http://www.latticesemi.com, 1999

Electromagnetic Fields in Mechatronics, Electrical and Electronic Engineering
A. Krawczyk et al. (Eds.)
IOS Press, 2006

THE MAGNETIC NETWORK MODELING OF A PERMANENT MAGNET MOTOR WITH CONSIDERATION OF THE SATURATION AND HEATING EFFECTS

S. Srairi, J. Farook, A. Djerdir, A. Miraoui

Research Laboratory in Electronics, Electrical engineering and Systems (LEES), which is a joint Research Unit of the University of Technology of Belfort-Monbéliard (UTBM) and the University of Franche-Comté (UFC) with the INRETS (n° LRE-T 31).
LEES-UTBM (Bat.F), Rue Ernest THIERRY-MIEG, F90010 Belfort.
Tel: 33 (0)3.84.58.36.29 – Fax: 33 (0)3.84.58.36.36
E-mail:salim.srairi@utbm.fr, abdesslam.Djerdir@utbm.fr & abdellatif.miraoui@utbm.fr

Abstract*—this work gives a semi analytical model for the design of a permanent magnet actuator having a reversed structure. Indeed the permeance network has been used to establish an equivalent network scheme for witch the physical parameters are depending on both saturation and heating effects. First, the motor has been simulated under the flux 2D software which is based on the finite element method. Then the reluctance network has been used to check out the semi-analytical model. In the second part the proposed method is verified by experimental testing. Finally, the authors explain the modeling of the motor with saturation effect and introduce the temperature dependences with adding the corresponding analytical expression.

I. Introduction

The presented magnetic network model of the synchronous motor with permanent magnet and a reversed construction allows the analysis of the field distribution and the calculation of its significant performance parameters. In order to obtain a good compromise accuracy- computation time we have used the permeance network method to solve the magnetic equations of electromagnetic system. The permeance model has great potential as an analysis tool in research, in particular, in the operational simulation of an electrical machine. A simple model can solve simulation accurately enough more quickly than a FE model [2]. So, we firstly established the equivalent reluctance network of the studied motor afterwards, we started a simulating study with the well known FE software, flux 2d. This simulation step allows expressing the permeance of the air-gap region with a high accuracy. The other permeances of the motor are computed by using the geometrical and material characteristics of the stator and the rotor armatures. In order to check out the validity of our model we first started a comparative study with the flux 2d software. After the proposed method is verified by experimental testing. After describing the 2D geometry of the studied machine and its main characteristics we explain the used methodology to obtain the reluctance network. Thus, we give simulation result showing the validity of the proposed model.

II. Geometry of the Studied Motor

The studied electrical motor is a synchronous permanent magnet one for which the classical disposition of the stator and the rotor are inverted "reversed structure".The later is available at the L2ES laboratory and it is integrated in a bicycle wheel "engine-wheel" [3]. The figure 1 shows the transverse cross section of six pair of poles of the motor. For reasons of symmetry and by neglecting the extremity effects the only study of this part of geometry is sufficient to totally model the motor. The main characteristics of the studied motor are given in the table 1. Its stator and its rotor consist of soft ferromagnetic materials, unlike the magnets which are hard ferromagnetic materials, their remanent induction is weak and their relative permeability is high (from 100 to 10000 according to material).

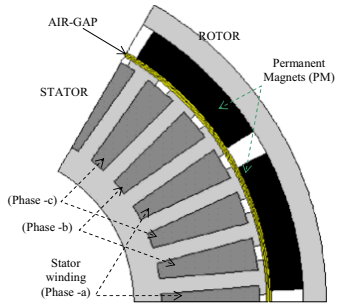

Fig.1. 2D transverse cross section of the studied motor

TABLE 1. MAIN CARATERISTICS OF THE MOTOR

Nominal power	(w)	200
Torque Max	(N.m)	25
Rotating speed	(rpm)	200
Nominal running	(A)	8.33
number of pair of poles		p=6
number of notches		36
Nominal torque	(N.m)	9.55

III. Permeance Network Modeling

The searched network of permeances traducing the studied motor behaviours is a single-phase equivalent circuit. The magnetic equivalent circuit method is based on decomposition of the electromagnetic field into flux tubes, each tube is characterized by its permeance [2]. The main permeances are computed along the main-flux paths and the leakage permeances are computed along the leakage-flux paths. The values of the permeance components in all regions are defined at no-load operating mode. By the use of FE simulation. The flux density in the air-gape region has been defined as a function of the angular position of the rotor regarding to the stator. Furthermore, the different flux paths have been defined accurately in the single-phase equivalent circuit. The values of these permeances have been calculated from averaging formulae for every single leakage-flux path.

Two categories of permeances exist depending on the fact that they are constant or variables with respect to the rotor position. Only the air-gap permeance depends on the rotor position. The values of the permeance components in all regions are defined at no-load operating mode.

The constant permeances concern the different peaces of the motor having an unchanged geometry and material characteristics whatever the rotor position. The stator and rotor steels as well as the permanent magnets pemeances are making a part of this category. So, these permeances are defined by a cylindrical portion having over a length l an opening angle α and a thickness defined by internal and external radius namely r_{int} and r_{iext}. Thus the stator and rotor permeances Pr,s as the permanent magnets ones Pa, are expressed as follows [8]:

$$P_{r,s} = \mu \frac{l.ln\left(\frac{r_{ext}}{r_{int}}\right)}{\alpha} \quad (1)$$

$$P_a = \mu \frac{l.\alpha}{ln\left(\frac{r_{ext}}{r_{int}}\right)} \quad (2)$$

After applying these expressions on the studied motor we obtained its constants permeances corresponding to the principle flux paths seen through one FE simulation in the no- loaded operating mode. The Table2 gives their values and where they are located inside the machine.

TABLE 2 CONSTANT PERMEANCES OF THE STUDIED MACHINE

Permeance index	Location in the machine	Value (H)
P1	Rotor steel permeance	**4.5593×10^{-6}**
P2	Permanent magnet (PM) permeance	**2.8611×10^{-7}**
P3	Leakage permeance between PM poles	**8.26×10^{-8}**
P5	Leakage permeance between stator tooth's	**3.694×10^{-8}**
P6	Permeance of one stator tooth	**1.666×10^{-4}**
P7	**Stator steel permeance**	**$1{,}02302\times10^{-4}$**

Because of the electromagnetic energy is exchanged in the air gap region, its permeance is very delicate to compute. Moreover, one must take into account the rotor motion to evaluate this permeance. Two strategies are generally used to achieve this calculation, Ostovic [6] or the finite element models [1]. So, in this study we chose to use the FE model for reasons of accuracy. Then, the permeance in the air-gap region has been defined as a function of the angular position of the rotor regarding to the stator, see Fig. 2. This computation is very difficult and requires a long time of operating of the FE software. So, the obtained point number of the permeance is generally small and not sufficient especially for doing a derivative operation. Indeed, when one needs to compute the electromagnetic torque or EMF its necessary to derive the permeance according to the time. So, this problem has been solved by interpolating the original permeance list of values with a continuous and derivative function.

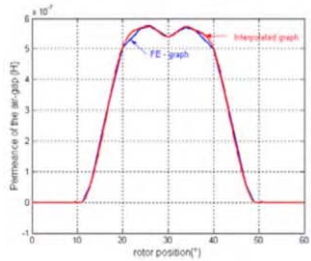

Fig.2. Evolution of the air-gap permeance according to the rotor position

A. The equivalent permeance network

The above computations lead to the equivalent single-phase permeances network given on the Fig3.

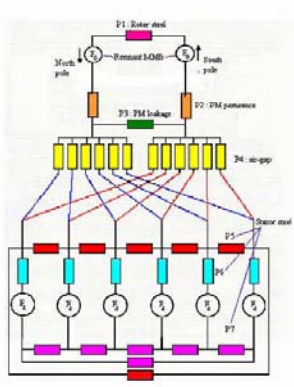

Fig. 3. The equivalent permeance network of the studied machine

In a way completely similar to the electric circuits, a magnetic circuit or a network of permeances can be seen like a group of magnetic branches. In network of permeances a magnetic tooth is composed by a permeance in series with a MMF of tooth. The latter may be easily calculated using a linear combination of the various MMF of slots. The other magnetic branches consist of simple permeances containing a possible source of MMF mounted in series which could be of a permanent magnet. In order to complete the network of permeances modelling one must compute all the flux values of branches and all the magnetic potentials of the nodes. The nodes and stitch laws allows establishing algebraic relations in each magnetic branch of the circuit of Fig.3. For each magnetic tooth we obtain the relation (3),

$$U_{dj} - U_{a_j} = Fd_j + \frac{\phi_j}{P_j} \quad (3),$$

and for the permanent magnets we have,

$$U_{dj} - U_{a_j} = Fa_j + \frac{\phi_j}{P_j} \quad (4),$$

so, for the entire magnetic branch we have,

$$U_{d\,j} - U_{a_j} = \frac{\phi_j}{P_j} \tag{5}$$

where, U_{dj} and U_{aj} are respectively the magnetic potentials of the starting and arrival nods of the branch j, P_j is the perméance of the branch j, ϕ_j is the flux density in the branch $_j$ and F_{dj} and F_{aj} are respectively the MMFs of tooth due to the compensation of the ampere turns and the permanent magnet.

When scanning all the nodes of the circuit we obtain a matrix relationship between the MMFs of the different braches *[F]* and the magnetic potentials of different nodes *[U]* through the invertible permeance matrix *[G]*. So, for a given power supply of the stator windings we can compute by a simple inversion, all the magnetic potentials *[U]* and thus the corresponding flux densities, the EMFs and the torque of the machine.

$$[G]\cdot[U] = [F] \Rightarrow [U] = [G]\cdot[F] \tag{6}$$

We notice that the studied magnetic circuit has 15 nodes and 33 branches. Thus, the dimension of the matrix equation (6) is equal to 14.

IV. Simulation and Validations Tests

In this stage of study we discuss the validation of the proposed model .The figures 4 shows the EMF of the first phase of the studied motor (the EMFs of the two other phases have the same waveforms but they are out of phased with an angle of $\pm 2\pi/9$ regarding to the first one). It can be seen that the obtained results from our modeling have a good agreement with the FE and measurements ones.

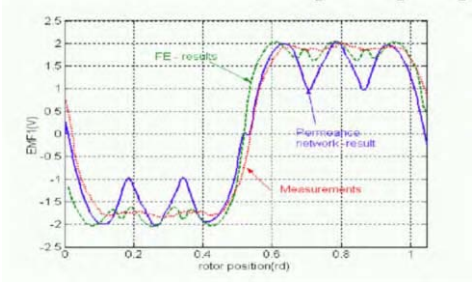

Fig. 4. EMF waveform

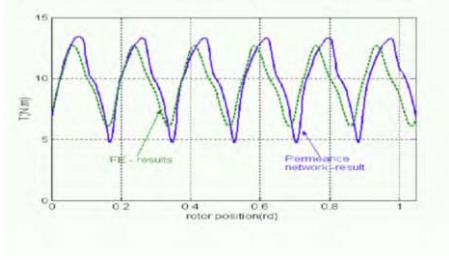

Fig. 5. Dynamic torque

The Fig. 5 presents the variation of the electromagnetic torques according to the mechanical position. The latter are issued from the permeance and the FE models but also from measurements [6]. We also conclude that the torque given by the permeance model has a good correlation with the ones obtained through the FE model and the measurements.

V. Permeance Network Modeling with Considerating the Saturation and Heating Effects

In order to take into account the saturation effect we generate the variation of the relative permeability of material according to induction. It thus each permeance, which composes a network can reproduce this phenomenon. To describe the variation of the relative permeability of a material, we chouse to use the better approximation formula suggested by Marrocco [4].

$$\frac{1}{\mu_r} = \varepsilon + (c-\varepsilon) * \frac{B^{2*\alpha}}{B^{2*\alpha} + \tau} \quad (7)$$

With, ε, c, α and τ are coefficients identified by using the real B(H) curve of different materials of the motor.

The increase in the temperature involves losses of magnetization; any rise of temperature involves a lowering of the curve of demagnetization. This effect is responsible for the reversible losses of magnetization and it is, modeled by a coefficient of temperature α_{mg} intervening in the modification of the remnant induction of the magnet as given in the equation (8) [5].

$$B_{mg} = B_r * (1 - \alpha_{mg} * \Delta\theta_{mg}) \quad (8)$$

With $\Delta\theta_{mg}$ is heating variation according to the ambient temperature.

The figures 6 and 7 show respectively the magnetudes of the the magnetic field along the air-gap of the motor obtained respectively from the permeance model and FE model. We remark that the magnetic fields in air-gap region have a maximal value of 0.95T and the waveforms have the same global time variations. This result is satisfactory, the peaks seen in the FE are mainly due to the tangent component of the permanent magnet and the armatures notches

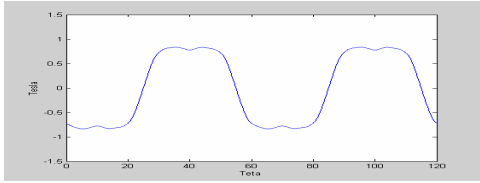

Fig. 6. Radial magnetic field – permeances model

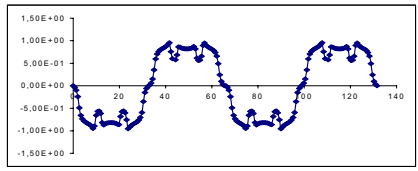

Fig. 7. Radial magnetic field – FE model

VI. Conclusions

This work leads to propose an interesting model of the based on the methodology of the permeances network. A good agreement has been seen between our results and those obtained by a finite element method. The main advantage of the proposed model is the consideration of the saturation and heating effects but also its simplicity and its fast execution regarding to the FE ones. Furthermore, the proposed model may be used as well in a design process as in a control scheme.

VII. References

[1] Hervé Roisse, “Contribution à la modélisation des systèmes électrotechniques par la méthode des réseaux de perméance couples. Application aux machines synchrone à aimants permanents”, PHD, University of Lille, 1998.

[2] Jarmo Perho “Reluctance Network for Analysing Induction Machines”, PHD, Helsinki University of Technology, 2002.

[3] C.Espanet “ Modélisation et conception optimal de moteur sans balais à structure inversée.Application au moteur- roue” Thèse de doctorat université de franche comté Belfort, janvier 1999.

[4] A.Marroco “Analyse numérique des problèmes en électrotechnique” Ann. Sc Math, Québec, Vol .1, p271-296,1977

[5] P.Brissonneau“Aimants permanents- principe et circuits magnétique” technique de l’ingénieur, D2090, pp1-20, D2091, pp1-2

[6] V. Ostovic, “Dynamic of saturated electric machines”, New-York, Springer-Vertag 1989.

[7] A-O, N’diaye, “Compensation active des ondulations de couple d’un moteur synchrone à aimants permanents”, PHD, University of Franche-Comté, 2002

[8] Jacek, F.G. Gieras and J.P. Zbigniview, “Linear synchronous motors”, Transportation and Automation Systems, CRC, 2000.

Electromagnetic Fields in Mechatronics, Electrical and Electronic Engineering
A. Krawczyk et al. (Eds.)
IOS Press, 2006

OPTIMIZATION OF EXCITER COILS IN EDDY CURRENT TRANSDUCER FOR TESTING THICK CONDUCTING PLATES

Krzysztof Stawicki, Stanisław Gratkowski

Chair of Theoretical Electrotechnics and Computer Science,
Szczecin University of Technology, al. Piastów 17, 70-310 Szczecin, Poland, e-mail: ks@ps.pl

***Abstract** – Eddy-current methods of non-destructive testing are used extensively for detecting defects in metallic structures. In this paper an optimization procedure based on a genetic algorithm is presented to choose parameters of the exciter in an eddy current transducer developed at the Szczecin University of Technology, Szczecin, Poland. Some numerical results, as well as results of measurements are given.*

Introduction

The eddy current transducer under study is shown in Fig. 1a. The transducer consists of two exciting coils connected differentially. Between these coils, around a ferrite core, a pick-up coil is placed. The system of coils is located inside an electromagnetic screen made of aluminum. The plate under test is placed below the transducer which has a compensating, conductive replaceable ring made of the same material as the tested object. If there is no influence of a defect, the transducer is in equilibrium. The defect causes changes in eddy currents and results in non-zero output signal from the pick-up coil. Figure 1b shows an example of measurement results obtained for different frequencies of the exciting current. It can be seen that the exciting frequency strongly influences the output signal.

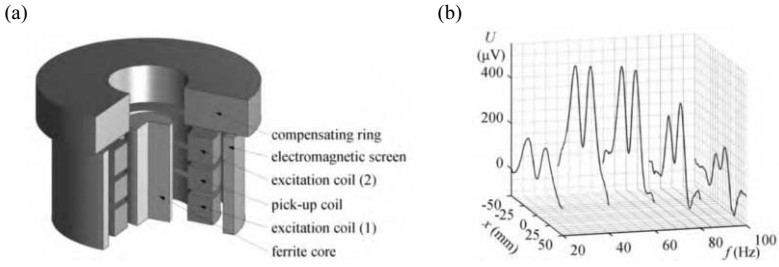

Fig. 1 Eddy current transducer for testing plates (a) and exemplary results of measurements (b)

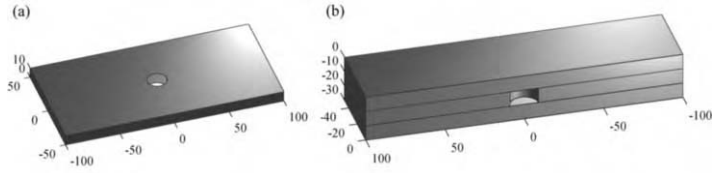

Fig. 2 Tested objects: (a) plate with a flaw, (b) a stack of plates

The test specimen used for the study is a stack of aluminum plates 10 mm thick (Fig. 2), from which one has a flaw in the form of a hole 5 mm or 9 mm in diameter. This plate was placed between two unflawed plates or under them. The transducer was moved over the tested specimen along a straight line parallel to the longer edge of the plate.

Analysis

We are looking for defects at the bottom of thick conducting plates.
If the flaw is represented by a loss of material, then no eddy current is induced at the site where the flaw occurs. Such a flaw may be modeled by a current of the same intensity as that induced in the unflawed plate but of the opposite direction. The former and the latter current superimposed yield a zero-valued current density at defect location (Fig. 3).

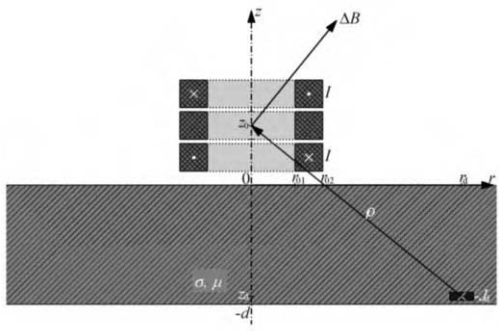

Fig. 3 Eddy current transducer and tested plate

The change in magnetic flux density caused by the occurring flaw may be defined in terms of current density. Of the magnetic flux density components only one is usually measured B_z, the increment of which may be defined according to the Biot-Savart law as [1]:

$$\Delta B_z = \frac{\mu_0}{4\pi} \int_{V_d} \frac{J_d r_d}{\rho^3} \, \mathrm{d}V \,, \tag{1}$$

where: J_d – current density in the unflawed plate, in the flaw region, ρ – distance from the flaw to the point of measurement, r_d – radial distance from the flow to the point of measurement, V_d – flaw volume.
This estimated magnetic flux density produced by the defect does not include the higher order multipol moments arising from the complex eddy current flow around the flaw. During the measurements the transducer is being moved over the plate, and the mutual arrangements of the flaw and the transducer are changing. The ratio r_d/ρ^3 reaches its maximum for

$$r_d = \frac{z_0 - z_d}{\sqrt{2}}, \tag{2}$$

where: z_0 – transducer location height, z_d – depth at which the flaw is searched.

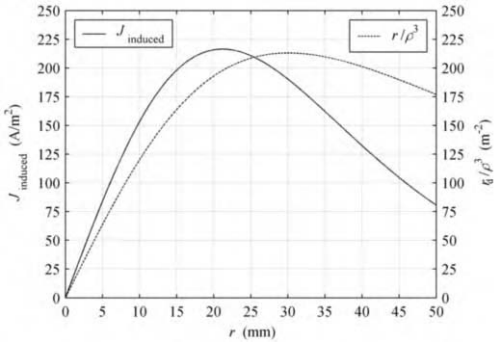

Fig. 4 Eddy current density distribution and ratio r_d/ρ^3 distribution

At the bottom of the plate the maximum of the current density occurs under the coil winding, i.e. for r within the range from r_{01} to r_{02}. The maximum is shifted toward greater values of r, as the plate thickness increases. The situation is the most advantageous when the integrand is maximal. This is the case when the maximum of the ratio r_d/ρ^3 and the maximum of the current density are matched. This condition, however, was not fulfilled for the transducer used in tests (Fig. 4). Hence, the effectiveness of testing may be improved only by increasing the density of the current induced at the bottom of the plate. For a fixed transducer position, the effect of the flaw on the magnetic flux density is the greater, the greater is the density of the current induced in the plate at the defect location. For the transducer employed in tests, the only tunable parameter that exerts an influence on test results, is the supply current frequency, which has a profound impact on the current density, thus on the magnetic flux density. Fig. 5 shows changes in the magnetic flux density ΔB_z evaluated from eq. (1) that are caused by a small flaw at the bottom of the plate tested.

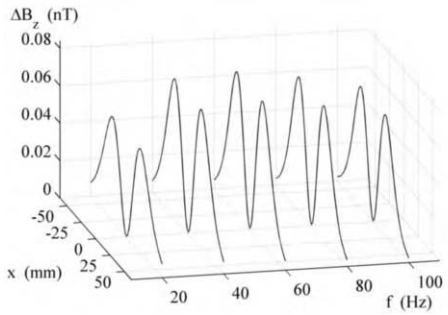

Fig. 5 Calculated changes in magnetic flux density

Optimization Procedure

In this paper a genetic algorithm technique is proposed to find optimal parameters of the excitation system. The flow chart of the optimization procedure is shown in Fig. 6.

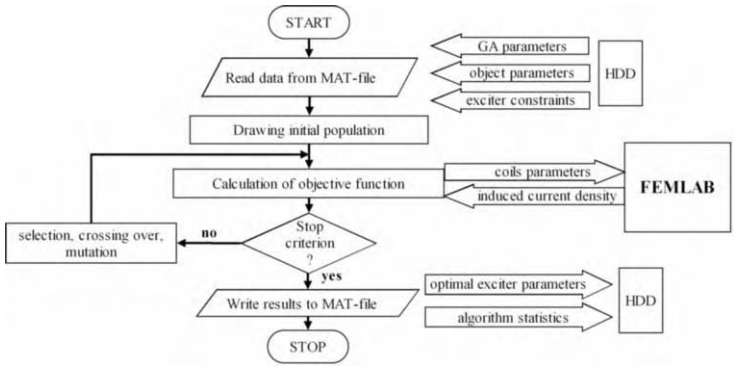

Fig. 6 Flow chart of optimization procedure based on genetic algorithm

After the program has started the following data are read in from a file: genetic algorithm parameters, object parameters and exciter constraints.

In the second step an initial population is drawn. The algorithms encode each parameter of the transducer into a sequence called a *gene*. A string of genes builds a *chromosome*. The chromosome is an artificial creature which represents a single point in a space of all possible search points. The set of creatures constitutes a *population*. In this case, parameters of the problem are encoded in the chromosome as a finite length string over a binary alphabet.

In the third step the value of objective function is calculated. Sensitivity to defects depends on eddy current density at defect location, no matter what kind of magnetic field sensors are used. When designing the exciter to test thick plates, its shape should be optimized and measurements are to be taken at different frequencies. Therefore, the objective function is simply the eddy current density induced at the bottom of the plates. In our case, eddy current density is computed in FEMLAB.

In the fourth step the program checks whether the condition for its stopping is fulfilled, i.e. whether the maximal current density value obtained in the present generation is identical to or is smaller than those obtained during the former iterations. If not, the best creatures are duplicated, paired off, crossed and sometimes mutated. By this means, the next generation is created, and the program returns to the third step. In every generation a new population is created as a result of crossing the best chromosomes from a previous generation. In this way population of individuals evolves towards better solutions. If the condition for computation stopping is fulfilled, then the optimal exciter parameters are written to a file, and the program is terminated.

Results

Figure 1a shows our general purpose transducer. Parameters of transducer are as follows: inner radius of coils r_{01} = 11 mm, outer radius r_{02} = 18 mm, height of coils h = 7 mm, diameter of ferrite core d_c = 12 mm, height of core h_c = 26 mm, inner radius of aluminum screen r_1 = 21 mm, outer radius of screen r_2 = 24 mm, height of screen h_s = 26 mm, inner radius of compensating ring r_{r1} = 10 mm, outer radius of ring r_{r2} = 30 mm, height of ring h_r = 30 mm. For these parameters we can expect good results in detecting flaws up to 15 mm beneath the surface of the plate. However, when looking for defects at the bottom of 30 mm aluminum plate the optimal parameters of the excitation system are quite different.

Example 1

The excitation coils have been optimized under the assumption that they must go into the existing casing, and must be wound up with wire of the same length as coils in a universal transducer. Parameters of optimized excitation coils are as follows: inner radius r_{01} = 6.8 mm, outer radius r_{02} = 20 mm, height of coils h = 4 mm, frequency f = 55 Hz (Fig. 7a). As a result of optimization we obtained a 20% greater current density. Comparison of induced current density at the bottom and inside the plate, for universal and optimized excitation coils is given in Fig. 6b for frequencies from 1 Hz up to 150 Hz.

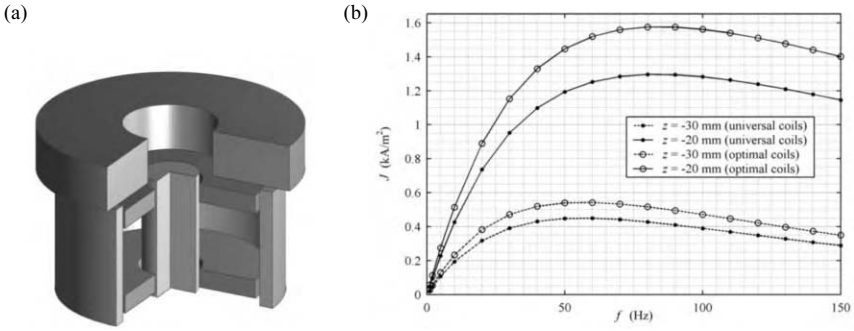

Fig. 7 Eddy current device with optimized coils (a) and results of calculations of induced current density in the plate (b)

Magnetic flux density caused by the flaw is also by about 20 % greater. Figure 8 presents results of evaluated changes for frequencies from 20 Hz to 100 Hz and for the optimal frequency f_{opt} = 55 Hz. Changes in magnetic flux density were computed under the assumption that the flaw is shaped like a cylinder being 1 mm high, the base of which has 4 mm in diameter. It was also assumed the flaw is located at the bottom of the plate. The measurements were taken by the pick-up coil situated at a point at the height of z_0 = 13.5 mm.

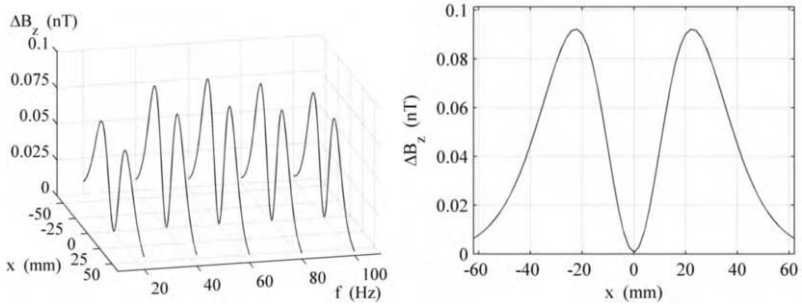

Fig. 8 Calculated changes in magnetic flux density for f = 20 - 100 Hz and for f_{opt} = 55 Hz

Example 2

Insertion of z_d = -30 mm for the depth at which the flaw is searched for, and z_0 = 13.5 mm for the height at which the pick-up coil is positioned into eq.(2) gives r_d = 30.76 mm. In optimizing the exciter parameters to detect flaws in a thick aluminum plate, the dimensions of exciting coils should be chosen in such a way, as to induce currents of greatest densities in the scoured area. Since the existing screen has smaller dimensions, we have decided to suit them to the coil dimensions. In this example the inner radius of the screen is chosen in such a way as to be by 1 mm greater than the outer radius of the coil. Parameters of optimized excitation coils are as follows: inner radius r_{01} = 14.9 mm, outer radius r_{02} = 34.9 mm, height of coils h = 1.4 mm, inner radius of the aluminum screen r_1 = 35.9 mm, outer radius of ring r_{r2} = 44 mm, frequency f = 45 Hz.
The geometry of the transducer with exciting coils chosen to detect flaws in a 30 mm thick aluminum plate is depicted in Fig. 9.

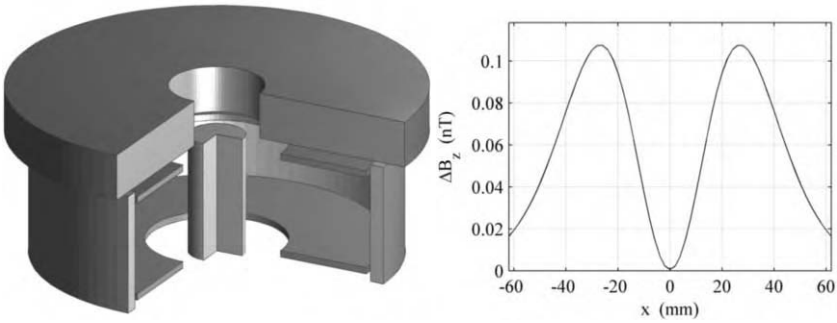

Fig. 9 Optimized eddy current transducer and calculated changes in magnetic flux density for f_{opt} = 45 Hz

Conclusions

A genetic algorithm has been implemented in MATLAB, coupled with FEMLAB and applied to the design of the excitation system in eddy-current testing of conducting plates. The use of GA techniques for this kind of problems ensures that an optimal solution may be found efficiently. The optimum frequency and dimensions of the eddy current excitation system for testing of conducting plates can be selected after trial-and-error tests. Much time can be saved by using the analysis given in this paper.

Acknowledgment
This work was supported by Polish State Committee for Scientific Research (KBN) under grants 4T10A 068 25 (2003–2005) and 4T10A 024 24 (2003-2006).

References
[1] J.R. Claycomb, N. Tralshawala, J.H. Miller Jr, “Theoretical investigation of eddy-current induction for nondestructive evaluation by superconducting quantum interference devices”, IEEE Transactions on Magnetics, vol. 36, no. 1, pp.292-298, (January 2000)
[2] R. Sikora, T. Chady, S. Gratkowski, M. Komorowski, K. Stawicki, “Eddy current testing of thick aluminum plates with hidden cracks” *Review of Progress in Quantitative Nondestructive Evaluation”, American Institute of Physics,* QNDE’2002 Conference Proceedings, vol. 22A, pp.427-434, New York, 2003
[3] K. Stawicki, “Choice of parameters of the exciter in eddy current non-destructive testing” (in Polish), *Ph.D. Thesis*, Szczecin University of Technology, Electrical Engineering Faculty, Szczecin, Poland, 2005

Electromagnetic Fields in Mechatronics, Electrical and Electronic Engineering
A. Krawczyk et al. (Eds.)
IOS Press, 2006

THE IMPACT OF MAGNETICALLY NONLINEAR IRON CORE CHARACTERISTICS ON RESPONSES OF A THREE-PHASE POWER TRANSFORMER DYNAMIC MODEL

Gorazd Štumberger, Sebastijan Seme, Klemen Deželak, Boštjan Polajžer, Matej Toman, Drago Dolinar

University of Maribor, Faculty of Electrical Engineering and Computer Science
Smetanova 17, 2000 Maribor, Slovenia, gorazd.stumberger@uni-mb.si

***Abstract** – This work analyses the impact of magnetically nonlinear iron core characteristics on responses calculated by a three-phase power transformer dynamic model. The iron core characteristics are determined in different way. Their impact on calculated responses is evaluated by the comparison of calculated responses with the measured ones. Results presented in the paper show that a very good agreement between the measured results and the calculated ones can be achieved only if the complete harmonic content of measured currents is used for determining magnetically nonlinear iron core characteristics of the transformer.*

Introduction

The finite element models of electromagnetic devices can provide us with a very accurate distribution of electromagnetic fields, but they are too complex and require too much computational effort to be appropriate for computation and analysis of power system transients. The program packages developed for computation of power system transients, like EMTP, ATP, PSCAD, and Matlab with library SimPowerSystem, normally use lumped parameter dynamic models of electromagnetic devices. These models can be completed by magnetically nonlinear characteristics of electromagnetic devices in order to achieve better agreement between measured and calculated results. Electromagnetic devices are usually composed of magnetic materials with different magnetic properties. The properties of the magnetic material are normally described by the permeability tensor, while the magnetically nonlinear properties of the complete electromagnetic device can be described by the current-dependent characteristics of flux linkages $\psi(i)$. These characteristics can be incorporated into dynamic models of electromagnetic devices as nonlinear iron core models [1][2].

A power transformer is one of the most important power system elements. Its iron core behaves magnetically nonlinearly. In order to achieve better agreement between the measured responses and those calculated by the power transformer dynamic model, the power transformer dynamic model can be completed by magnetically nonlinear iron core characteristic $\psi(i)$. This characteristic is normally determined from measured active power and RMS values of currents and voltages at no-load applying calculation of impedances. Unfortunately, the $\psi(i)$ characteristic determined in this way is incorrect due to the neglected higher harmonic components in the no-load currents [3].

In this work, the $\psi(i)$ characteristic of tested three-phase transformer is determined by the standard method [4,5] using RMS values and by an alternative experimental method [3] which considers complete harmonic spectrum of the no-load currents. The impact of magnetically nonlinear iron core characteristics determined by both methods on behavior of the three-phase power transformer dynamic model is evaluated by the comparison of measured results with the calculated ones.

Determining Magnetically Nonlinear Iron Core Characteristic

This section describes standard and alternative methods for determining magnetically nonlinear characteristics of a three-phase transformer iron core. Magnetic nonlinearities of the iron core are normally given in the form of current dependent characteristic of flux linkages $\psi(i)$. The characteristics determined by standard and alternative method are compared at the end of this section.

Standard method

The standard method is described in [4] and [5]. The no-load test of the tested three-phase transformer is performed at different terminal voltages. For each test the active power and the RMS values of applied voltage and corresponding currents are measured. Although the no-load current contains higher harmonic components, the complete RMS value of the no-load current is assigned exclusively to the fundamental harmonic component. In this way an equivalent fundamental harmonic component current is defined [4]. Its RMS value is the same as the RMS value of the measured current while its phase angle is selected in such a way that the equivalent current and the applied voltage fundamental harmonic component produce fundamental harmonic component active power equal to the measured active power. The impedance Z, resistance R, reactance X, inductance L and flux linkage ψ are calculated by (1):

$$Z=\frac{U}{I};\qquad R=\frac{P}{I^2};\qquad X=\sqrt{Z^2-R^2};\qquad L=\frac{X}{2\pi f};\qquad \psi(\sqrt{2}I)=L\sqrt{2}I \tag{1}$$

where P is the per phase fundamental harmonic component active power, U is the RMS value of line voltage fundamental harmonic component, I is the RMS value of equivalent line current while f is the frequency.

Authors in [3] reported that the flux linkage characteristics $\psi(i)$ determined by the described method are incorrect due to the incorrectly considered higher harmonic components in the no-load current. Also, the operating range in which the $\psi(i)$ characteristic can be determined by this method is insufficient. Even if the maximal allowed voltage is applied during the no-load test, the corresponding no-load current reaches in the best case around ten percents of the rated current. Fig. 1 shows measured voltage $u(t)$ and current $i(t)$, current fundamental harmonic component $i_1(t)$, fundamental harmonic component equivalent current $i_{1e}(t)$, and current and voltage amplitude spectra I_h and U_h, where h denotes harmonic component.

It is evident form Fig. 1, that the maximal value of measured current $i(t)$ is much higher than that of equivalent current $i_{1e}(t)$ which leads to too steep $\psi(i)$ characteristic determined by this method. In order to evaluate the impact of incorrectly considered higher harmonic components in the no-load current on determined $\psi(i)$ characteristic an alternative method is introduced.

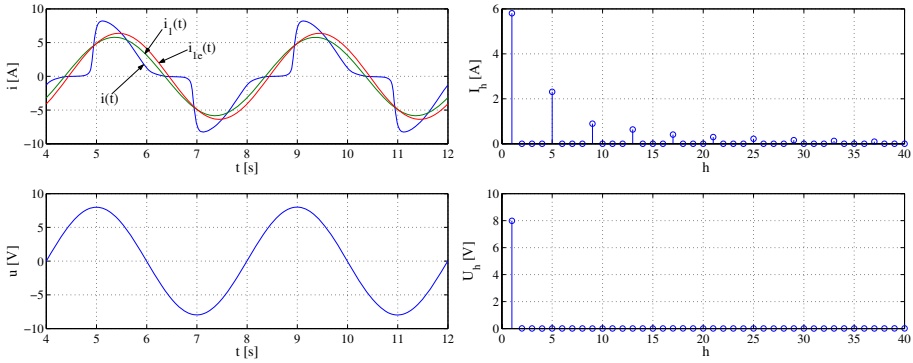

Fig.1: Measured current $i(t)$ and voltage $u(t)$, fundamental harmonic component of the measured current $i_1(t)$, equivalent fundamental harmonic component current $i_{1e}(t)$, and current $I_h(h)$ and voltage $U_h(h)$ amplitude spectra given as functions of harmonic component h.

Alternative method

This method uses instantaneous values of measured no-load current $i(t)$ and applied voltage $u(t)$ to determine the magnetically nonlinear characteristic $\psi(i)$. The characteristic $\psi(t)$ is determined by numerical integration (2), while the characteristic $\psi(i)$ is obtained by presenting $\psi(t)$ as a function of $i(t)$. R is the resistance while $\psi(t=0)$ is the initial condition due to remanent flux.

$$\psi(t) = \int_0^t \left[u(\tau) - Ri(\tau)\right] d\tau \quad + \quad \psi(t=0) \tag{2}$$

During the no-load test voltage and current are measured in only one phase winding. The current range in which the $\psi(i)$ characteristic is determined by this method can be extended even over the rated current value if sinusoidal or stepwise changing voltage with low frequency and amplitude is applied during the no-load test.

Comparison of obtained magnetically nonlinear characteristics

At no-load the tested three-phase core type laboratory transformer with rated data 3500 VA, Yd5 690/400 V, was supplied with different voltages which were increased in steps up to 20% over the rated value at nominal frequency of 50 Hz. Fig. 2 a) shows $\psi(i)$ characteristics in the form of hysteresis loops determined by the alternative method. The end points of individual hysteresis loops form an unique $\psi(i)$ characteristic determined by the alternative method. It is shown in Fig. 2 b) together with the $\psi(i)$ characteristic determined by the standard method. The same measured currents and voltages were used for determining both characteristics. The results presented show that the $\psi(i)$ characteristic determined by the standard method is too steep due to incorrectly considered higher

harmonic components in the equivalent current. Measured current $i(t)$ shown in Fig.1 has higher maximal value than the equivalent current $i_{1e}(t)$.

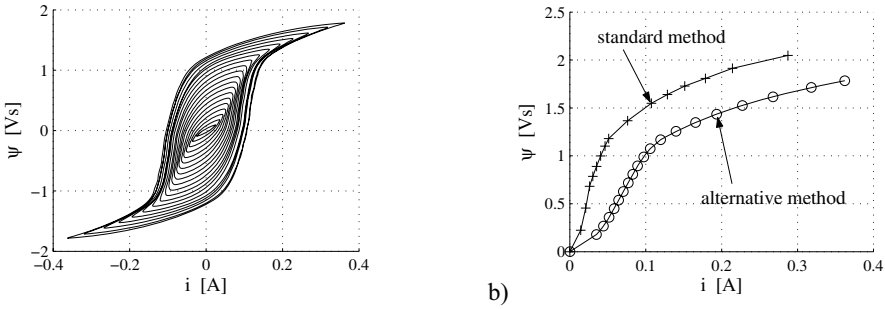

Fig.2: Characteristics $\psi(i)$ in the form of hysteresis loops determined by numerical integration a) and unique $\psi(i)$ characteristics determined by standard and alternative methods at 50 Hz b).

Characteristics presented in Fig. 2 covers less than 10% of the nominal current which is insufficient. In order to determine $\psi(i)$ characteristic also for higher saturation levels, the tested transformer was feed with sinusoidal voltages from a linear amplifier at 0.25 Hz. The maximal amplitude of the applied voltage and corresponding current are shown in Fig. 1. The $\psi(i)$ characteristic determined by the alternative method at 0.25 Hz is shown in Fig. 3.

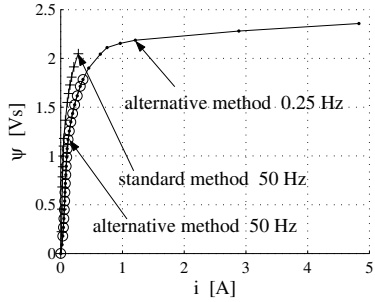

Fig.3: Characteristics $\psi(i)$ determined by standard method at 50 Hz and by alternative method at frequencies 0.25 and 50 Hz.

Results

The impact of $\psi(i)$ characteristics on currents calculated by the transformer dynamic model is evaluated by the comparison of measured results with the calculated ones. The $\psi(i)$ characteristics determined by the standard and alternative methods shown in Fig. 3 were included into three phase transformer dynamic model from library SimPowerSystem, which is a part of program package

Matlab/Simulink. Figs. 4 to 6 show measured and calculated line currents i_{l1}, i_{l2} and i_{l3} in the case of unloaded transformer switch-on and in steady state operation at no-load. The terminals of wye connected windings of tested transformer were supplied by nominal voltages.

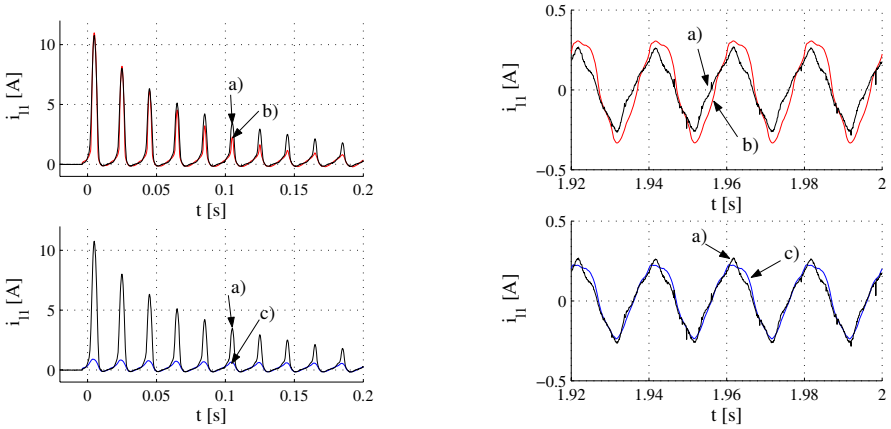

Fig. 4: Line current i_{l1} during switch-on and in steady state: a) measured; b) calculated - $\psi(i)$ characteristic determined by alternative method; c) calculated - $\psi(i)$ characteristic determined by standard method.

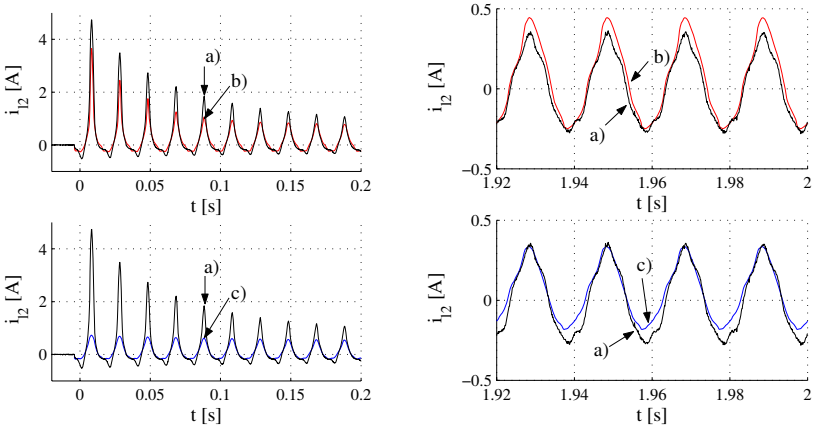

Fig. 5: Line current i_{l2} during switch-on and in steady state: a) measured; b) calculated - $\psi(i)$ characteristic determined by alternative method; c) calculated - $\psi(i)$ characteristic determined by standard method.

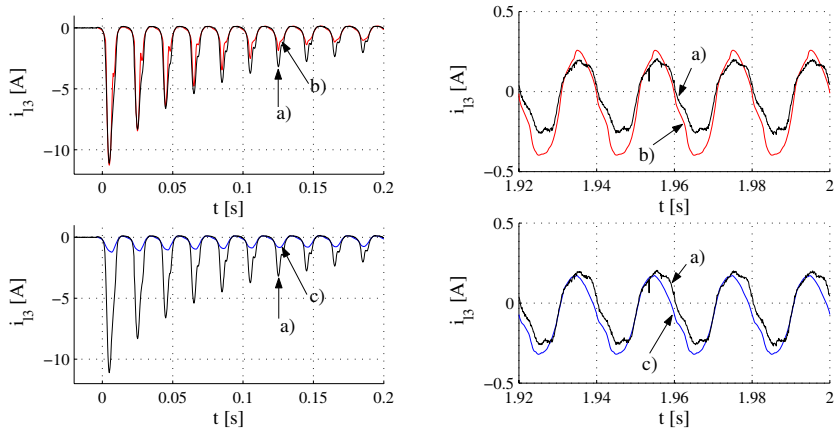

Fig. 6: Line current i_{l3} during switch-on and in steady state: a) measured; b) calculated - $\psi(i)$ characteristic determined by alternative method; c) calculated - $\psi(i)$ characteristic determined by standard method.

Conclusion

If characteristic $\psi(i)$ determined by the alternative method is used in dynamic transformer model, then the agreement between measured and calculated line currents is good in the cases of switch-on and no-load operation. The use of $\psi(i)$ characteristic determined by the standard method in the dynamic transformer model gives acceptable results only in the case of no-load operation. However, in the case of switch-on a substantial difference between the measured and calculated currents can be seen.

References

[1] G. Štumberger, B. Štumberger, D. Dolinar, Magnetically nonlinear and anisotropic core model of synchronous reluctance motor, *Journal of Magnetism and Magnetic Materials*, 254-255, 2003, pp. 618-620

[2] G. Štumberger, B. Štumberger, D. Dolinar, Identification of linear synchronous reluctance motor parameters, *IEEE Transactions. On Industry Applications*, vol. 40, no 5, 2004, pp. 1317-1324

[3] S. Calabro, F. Coppadoro, S. Crepaz, The measurement of the magnetization characteristics of large power transformers and reactors through d.c. excitation, *IEEE Transactions on Power Delivery,* PWRD-1, no. 4, 1986, pp. 224-232

[4] A.E. Fitzgerald, C. Kingsley, *Electric Machinery*, McGraw-Hill, New York, 1961.

[5] C.V. Jones, *The unified theory of electrical machines*, Butterworths, London, 1967

Electromagnetic Fields in Mechatronics, Electrical and Electronic Engineering
A. Krawczyk et al. (Eds.)
IOS Press, 2006

ELECTROMAGNETIC PARAMETERS SIMILARITY FOR SCALED GEOMETRIES OF LINEAR ACTUATORS

B. Tomczuk[*] **K. Zakrzewski**[**] **M. Sobol**[*]

[*]Technical University of Opole, Dept. of Electr. Eng. & Automatic Control,
ul.Luboszycka 7, 45-036 Opole, Poland, e-mail: tomczuk@po.opole.pl

[**]Technical University of Lodz, Institute of Mechatronics and Information Systems
ul.Stefanowskiego 18/22, 90-924 Lodz, Poland, e-mail: zakrzew@.p.lodz.pl

***Abstract* - Some investigations of the field analysis for tubular linear actuators with scaled geometries are described. The rules to create static characteristics for the devices, with open magnetic circuit have been given. Including nonlinearity of the actuator magnetic cores, magnetic field problems were also considered. The obtained results compose the characteristics for the scaling actuators with open and closed magnetic system, as well. They were developed as a practical design tool. For the device in real scale, the calculated results have been compared with the measured ones, and a good conformity has been obtained.**

I. Introduction

Electrical actuators with linear motion are widely used in special electric drives [1], [2], [3]. They have different constructions. Open - as well as closed magnetic structures make up the two main groups of such devices. In this work we investigated both of them. However, through lack of the prototype with closed magnetic circuit, the measurement verification has been done for the open one.

Prior publications of the authors [4], [7] provide a description for scale modeling of transformers. In this work, a new approach, as scaling laws set, for the scaled structures of the actuators with magnetically linear circuit e.g. open system, is presented. We report magnetic field investigations of the tubular linear actuators with scaled geometries. Thus, the static characteristics for the integral parameters of the scaled devices are given.

II. Rules for Parameters Calculating of the Actuators with Magnetically Linear Circuit

After geometrical scaling of an electrical device, the linear dimensions l of the full-scale model (original) turn into the dimensions l_1 of the scaled one, naturally. It applies to coil linear dimensions $s=l_{c1}/l_c$, and the ferromagnetic core $s=l_{F1}/l_F$, as well. Similarly, we can scale a quantity X of the original to the scale-model X_1. The scale factor $m_X=X_1/X$ is obvious for transformation [6] of the quantity.

From Maxwell's equations we obtain that the scale factors are valid for the geometrical transformation if they hold the conditions of electrodynamic similarity [6].

$$m_\varepsilon m_\mu m_f^2 s^2 = 1, \qquad m_\sigma m_\mu m_f s^2 = 1, \qquad \frac{m_f s}{m_H} = 1 \tag{1}$$

If we neglect the displacement currents in dielectrics, only the two last equations must be held.

Keeping the same number N of the coil wires in an actuator, and including the geometric similarity rules [4], [7], the cross-section S_w of each wire is changed by the scale factor s^2. When we keep at a constant level of the current value, the current density is considerably increasing while the cross section is shrinking, $J_{w1} > J_w$. Thus, one should make additional winding cooling.

When we change the whole cross section S_c of the coil, we can keep the same number of turns $N_1=N$, or fits other turn number, certainly. In the second case, to secure the same current value (in each wire), with variation of the scale s, we must change the number of turns $N_1= s^2N$. The ampere-turns of the coil are obviously not the same:

$$\Theta_1 = I_1N_1 = s^2IN = s^2\Theta \tag{2}$$

It is convenient transformation, because we conserve the average value of the current density in coil cross-section. The current density value within the all cross-sections of the coil wires is the same:

$$J_{c1} = I_1N_1/S_{c1} = s^2 IN /(s^2 S_c) = J_c \tag{3}$$

The same scale factor s, (as for the scaled coil) is assumed for the magnetic core, naturally, and the iron cross-section is scaled according the expression $S_{F1} =s^2S_F$. Having regarded Ampere's law for the original and for the model we can write, respectively

$$IN = H_F l_F \quad , \quad I_1N_1 = H_{F1}l_{F1} \tag{4}$$

Including (4), and equality $l_{F1} = sl_F$, the ampereturns of the model amount to

$$\Theta_1 =I_1N_1 = s^2 IN = s\, H_{F1}l_F \tag{5}$$

From the above, taking into account (4), we obtain relation for field intensity in magnetically linear systems

$$H_{F1} = s\, H_F \tag{6}$$

The magnetic flux value, in scaled cross-section of the core iron, is determined according to

$$\Phi_1 = B_1S_{F1} = sB\, s^2S_F = s^3\Phi \tag{7}$$

The flux linkage and the inductance, which is calculated from the definition formula $L=\Psi/I$, (of all winding wires) and the inductance are equal to, respectively

$$\Psi_1 = \Phi_1N_1 = s^5\Psi \quad , \quad L_1 = s^5L \tag{8}$$

From magnetic energy, we can also calculate the magnetic force on the actuator mover $F_1 = s^4F$.

III. Field Analyses for Magnetically Nonlinear Models

Using magnetic vector potential ($\vec{A}$) formulation, the axis-symmetrical magnetic field was described in form of the simple elliptic equation in cylindrical coordinates r and z

$$\frac{\partial}{\partial r}\left[\nu(B)\left(\frac{\partial A}{\partial r}+\frac{A}{r}\right)\right]+\frac{\partial}{\partial z}\left[\nu(B)\frac{\partial A}{\partial z}\right] = -J \tag{9}$$

The magnetic material permeability is characterized by the nonlinear reluctivity function $\nu(\boldsymbol{B})$. Thus, the B/H ought to be included in the calculations. For the tubular actuators we can assume that the potential has only the A_θ component [2], [5].

From the A_θ values, the magnetic flux density components can be calculated

$$B_r = -\frac{\partial A_\theta}{\partial z}, \quad B_z = \frac{\partial A_\theta}{\partial r}+\frac{A_\theta}{r} \tag{10}$$

In Fig. 1, the magnetic flux density maps and flux lines in the upper part of the halved actuator, with the mover ejected towards right from the central position, have been presented. The distribution of the field lines relates the enlarged (s=2) actuator with the closed magnetic system. Contrary, in Fig. 2 the field lines, for the open magnetic system, are presented. The flux density maps and field lines are given only in the actuator vicinity. Thus the boundary lines are not visible. The figures concern the magnetic fields excited by relatively small current value (I=1A) in the excitation winding.

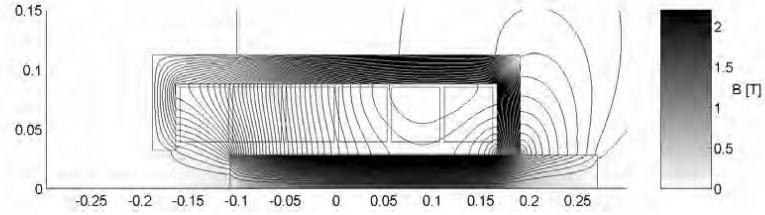

Fig. 1. Flux density map and field lines for the scaled (enlargement s=2) actuator (I=1A)

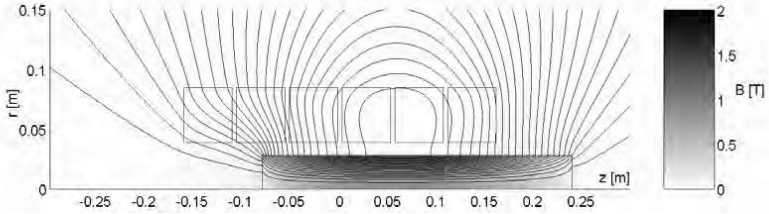

Fig. 2. Actuator with open magnetic circuit (s=2, I=1A)

IV. Recalculation of the Flux Density Values in the Scaled Actuator and Measurement Verification

In this work we verified the calculation results (by the experimental tests) for the actuator with open magnetic circuit. The magnetic flux density components have been measured (by means of a hallotron probe) at many points of the magnetic field area. Some measurement lines, along which the verification has been done, are presented in Fig. 3. In the figure we depicted halved (along axis of symmetry) actuator with the mover ejected from excitation winding. We measured the flux density components at many accessible points of the actuator structure. In this work we present some values, which were measured in the vicinity of the mover (armature) inside the stator (section A–A'). The measurements consider the rms current value I=1 A in the excitation winding of the stator.

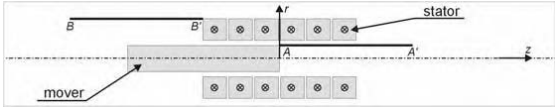

Fig. 3. The measurement lines for the mover ejected from excitation winding (I=1A)

In Fig. 4, the magnetic flux density components, obtained from the calculations and the measurements have been compared. The values, related to the scaled up model, were recalculated (circles) to the original (continuous line). As the excitation current is relatively small (I=1 A), the field lines cross magnetically linear system. Field intensity can be recalculated by expression (6). Flux density values B in the scaled object were obtained by multiplication of the field intensity $\vec{H}$ by the magnetic permeability value.

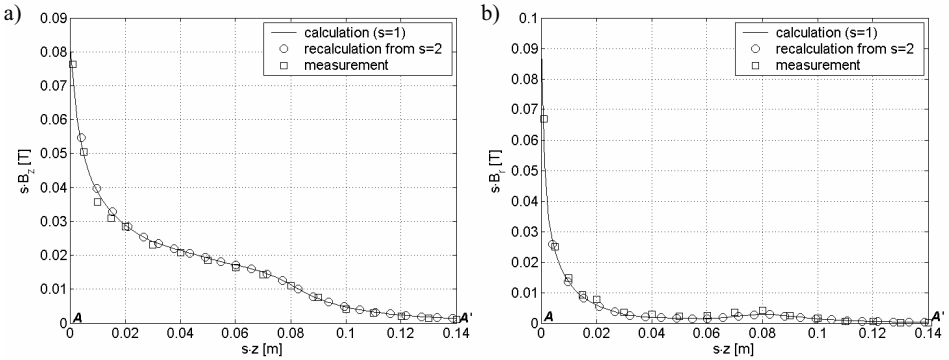

Fig. 4. The recalculated B_z and B_r components along the line *A–A'* (current value *I*=1A)

For high excitation current (e.g. *I*=8A) in the actuator winding of the actuator, with open or closed magnetic circuits, the *B* values have to be recalculated with the magnetization curve of the core iron. Some recalculated flux density values are given at points of the segment *C–C'* (Fig. 5). It is visible (Fig. 6), that the values, which are denoted by the circles, correspond with those obtained for the full-scaled actuator (*s*=1). Due to high current and saturation of the core, the values recalculated by the scale factor (Sec. II) differ very much from those recalculated by the proper characteristic. Thus, we must look for the *B* values at the proper nonlinear part of the B/H curve, for the $I_1 = sI$ current value.

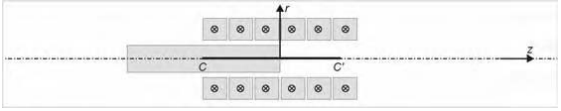

Fig. 5. The measurement line for the mover ejected from the excitation winding (*I*=8A)

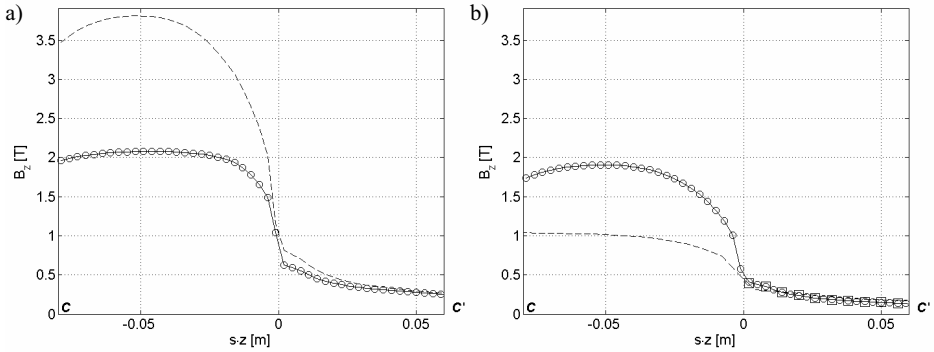

Fig. 6. B_z components at the points of the segment *C–C'* (current value *I*=8A)

a) enlarged object (*s*=2)
   —— scaled object (s=2)
   O recalculated from original (*s*=1)
   - - - improper linear recalculation from original

b) full scaled object (s=1)
   —— original (s=1)
   O recalculated from scaled (*s*=2) object
   - - - improper linear recalculation from *s*=2
   □ measurements

V. Nonlinear Characteristics of the Field Integral Parameters

Many pieces of field analysis have been performed and integral parameters have been determined for the scaled objects. In this work we created the characteristics of the actuator with the scale factors equal to 1, 1/5, 1/2, 2 and 5, respectively. Some curves for scaling by s=2 are given, in this paper.

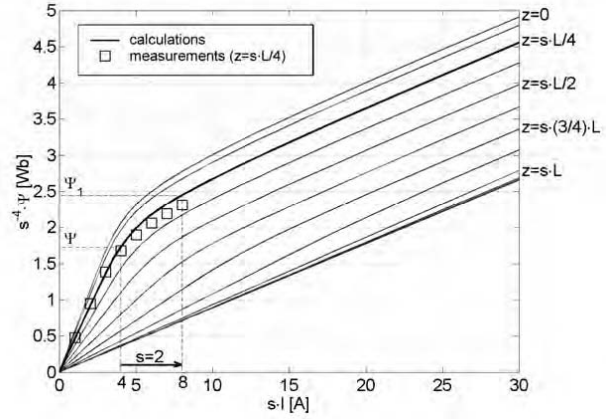

Fig. 7. Flux linkage divided by the fourth power of the scale factor, verso the scaled current value

The important parameter, i.e. flux linkage (Ψ) of the scaled actuator, has been calculated. Using the Ψ/I curve (Fig. 7), we have also determined the inductances L of the windings for the scaled devices. Using the characteristics it is possible to determine a scaled coil inductance. We must multiply (by the factor s) the current value in the full-scaled coil. Then, one can read of (from the curve, Fig. 7) value of the flux linkage divided by the fourth power of the scale factor s. Each curve concerns one position of the mover. For the full-scale actuator the mover is ejected by a quarter of its length from the excitation winding. If the mover is put deep (within the winding), the Ψ line is naturally up than for the mover ejected from the coil. For high values of the excitation current, the ferromagnetic parts are almost completely saturated, and the Ψ changes nearly linearly with the current variation (Fig. 7).

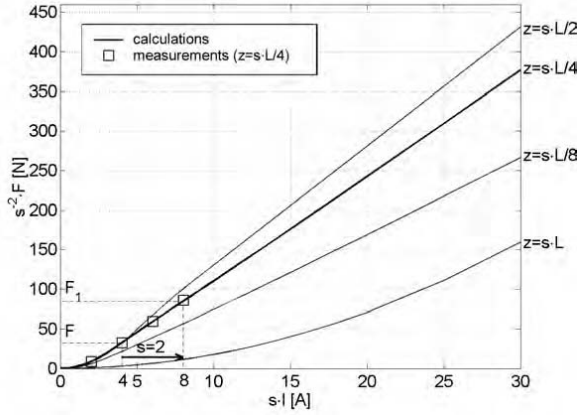

Fig. 8. Force values divided by the second power of the scale factor, verso the scaled current value

In Fig. 8, the values of the magnetic force are divided by the second power of a scale factor, and the current values are multiplied by the factor. Each graph deals with one position of the mover. For the full-scale actuator, the mover is ejected by a quarter of its length from the excitation winding.

The graphs of the flux linkage (Fig. 7) and the magnetic force (Fig. 8) have been drawn after magnetic field analyses (for the full-scale actuator only). The values for the scaled objects can be obtained using the curves. The quantities F and Ψ can be found (from the curves) for the current value $I_1 = sI$.

Conclusions

Under scaling the nonlinear electromagnetic systems, like the actuators, we have to change the number turns or to keep the magnetic intensity factor m_H=1 to unity. The second case is very difficult for realization. Thus, we have proposed to carry out the first one, and maintain the current value in each wire of winding.

The goal of this work was to give the way for static parameters determination of the scaled actuators. One must underline, that according to the approach presented here we can obtain the parameters without reiterated field analysis. For magnetically linear system the scale factors are given. For saturation of the actuator magnetic system some diagrams have to be used. The integral values of the magnetic field, obtained from the calculations, were compared with those obtained from measurements, which is not presented here.

When we have characteristics for the full-scaled object (original), we can use them for recalculating of the field values without numerical modeling of the scaled objects, repeatedly. The **e**xperimental results have been compared with the calculated ones. The recalculated magnetic flux density values were checked by the measurements, and a good agreement was obtained.

The presented approach can be applied for the analysis of the actuator operation, and the method can be used for designing of all electromagnetic devices.

References

[1] M. T. Thompson, R. D. Thornton, A. Kondoleon, “Flux Canceling Electrodynamic Maglev Suspension: part II Test Results and Scaling Laws”, IEEE Trans. on Magn., New York, USA, Vol. 35, No. 3, pp. 1964-1975, 1999

[2] B. Tomczuk, M. Sobol, “Field Analysis of the Magnetic Systems for Tubular Linear Reluctance Motors (TLRM)”, IEEE Trans. on Magn., New York, USA, Vol. 41, No. 4, pp. 1300-1305, April 2005

[3] B. Tomczuk, M. Sobol, “Analysis of Tubular Linear Reluctance Motor (TLRM) under Various Voltage Supplying”, ICEM 2004, Proc. of The XVth International Conference on Electrical Machines, Cracow, Poland, pp. 1099-1100, September 5-8, 2004

[4] B. Tomczuk, K. Zakrzewski, A. Waindok, “Scale-models in Computer Aided Design of Transformers”, ISEF'2003, Proc. of The XIth International Symposium on Electromagnetic Fields in Electrical Engineering, Maribor, Slovenia, September 18-20, pp. 869-872, 2003

[5] B. Tomczuk, M. Sobol, “Time Analysis of an Oscillating Motor”, EPNC’2002, Proc. of The XVIIth International Symposium on Electromagnetic Phenomena in Nonlinear Circuits, Leuven/Poznań, Belgium, pp. 23-26, July 1-3, 2002

[6] K. Zakrzewski, “Physical Modelling of Leakage Field and Stray Losses in Steel Constructional Parts of Electrotechnical Devices”, Archive. für Elektrotechnik, No. 69, pp. 129-135, 1986

[7] K. Zakrzewski, B. Tomczuk, A. Waindok, “Nonlinear Scaled Models in 3-D Calculation of Transformer Magnetic Circuits”, COMPEL - The International Journal for Computation and Mathematics in Electrical and Electronic Engineering, MCB University Press Limited, England, 2005, (in printing)

Electromagnetic Fields in Mechatronics, Electrical and Electronic Engineering
A. Krawczyk et al. (Eds.)
IOS Press, 2006

ANALYSIS BY FINITE ELEMENT METHOD OF THE CROSSTALK COMPENSATION PROCEDURES FOR CURRENT TRANSDUCERS

Usón A., Artal J.S., Letosa J., Arcega F.J. and Samplón M.

Department of Electrical Engineering. Escuela Universitaria de Ingeniería Técnica Industrial.
University of Zaragoza, Campus Rio Ebro. María de Luna nº 3.
Edificio Torres Quevedo, 50018. Zaragoza, Spain.
E-mail: auson@unizar.es, jsartal@unizar.es, jletosa@unizar.es, arcegafj@unizar.es and msamplon@unizar.es

Abstract - ***The present paper intends to analyse and compare three methods of measuring electrical current by modern sensors. These methods are important because they allow the compensation of crosstalk errors associated to the use of several busbars in the vicinity. The selected measuring systems have in common that they can be verified easily by experimental setup. In this way, the accuracy and the uncertainty associated to each method in function of the variations of the electric current in the conductors has been evaluated. Moreover the position of the sensors around the conductor in order to improve the response has been studied. All these situations have been simulated by the Finite Element Method (FEM) and have been measured and verified in our Laboratory of Electrical Metrology (LME) accredited by ENAC, the Spanish Accreditation System in the frame of the EA (European Accreditation).***

1. Introduction

The aim of this paper is to study and compare several modern methods of measuring high currents (circular sensor arrays [1], linear equations [2] and stable point [3]) and the compensation of crosstalk errors originated by the current carried by near conductors [4], [5] under normal working conditions. In this way, a comparison between the uncertainties associated to the three studied methods -values numerically calculated with the modelization by Finite Element Method- and the magnetic flux of an infinite straight line calculated theoretically by the Biot-Savart law has been done. Simulations have been developed using the commercial software OPERA-3D of Vector Fields for low frequency fields (50Hz).

The system analysed consists, see figure 1, of a single circuit with currents flowing through two straight conductors of rectangular section (5 x 40 mm). One of the bars is placed in the centre of the measuring toroidal core, where the different sensors are positioned in function of the selected measuring method. The two parallel conductors have the same geometry and the perpendicular distance between them is $d = 50mm$. The geometrical characteristics of the core are the following: inner and outer radius $R_{IN} = 25mm$, $R_{EX} = 39mm$ and height $h = 25,4mm$. The core used is a commercial non-linear iron powder toroidal core (yellow-white) ref. T300-26D of Micrometal Inc. Magnetic flux through a cross-sections of the torus was chosen as the result from the numerical calculations as the response of a current transducer and measurement errors were evaluated.

Figure 2 shows the magnetic flux, obtained by simulation, for the different angles of the toroidal core in the case of a rectangular conductor in the inner and the complete system constituted by two bus bars, one in the inner and the other one outside the torus and carrying the same current in the same sense for both conductors. Both graphics are compared with the value of the magnetic flux obtained in the ideal model. In the three cases shown, the current carried by each conductor is $I_{CIN} = I_{CEX} = 300A$ and the relative permeability of the core is $\mu = 213$. The ideal magnetic flux corresponds to the one obtained theoretically for an infinite straight cable and for the

data of our problem gives a value of 147,76μWb. In the other side, the magnetic flux due to the alone inner bus bar varies between 147,03μWb and 148,20μWb. It corresponds to a maximal deviation of 0,494% with respect to the ideal. In the case of the two parallel bus bars, the magnetic flux shows a greater variation, due to the crosstalk, the influence of the external conductor in the magnetic material of the sensor. It varies between 138,02μWb and 151,07μWb. It corresponds to a maximal deviation 6,591% with respect to the ideal model. This paper shows the technical development accomplished by the research group in uncertainties of measurements.

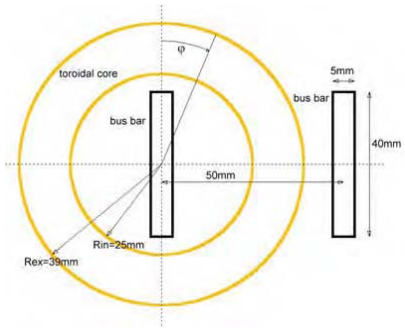

Fig 1. Illustration of the experimental model.

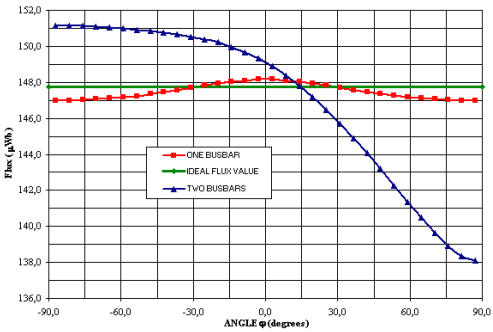

Fig 2. Magnetic flux measured with one and two bus bars, versus the angle φ of the sensor $I_{CIN} = I_{CEX} = 300A$.

Figures 3 and 4 show -in color contour map format- the influence of a near external current ($I_{CEX} = 300A$) in the magnetic flux in the inner of the torus (where the sensors are situated) originated by an internal current ($I_{CIN} = 150A$, $I_{CIN} = 0A$). The computer simulations by FEM have allowed to estimate the errors associated to the magnetic flux in each studied method with respect to the ideal situation, analyzing in all cases the influence of the current in the measuring system. In this way, the errors associated to the computational analysis have been estimated under 0,14%. Another possible source of error in the measurement comes from the uncertainty in the positioning of the sensors around the conductor: small variations with respect to the suitable angle give rise to non negligible errors in the different methods of measurement based on numerical compensation [2], [3].

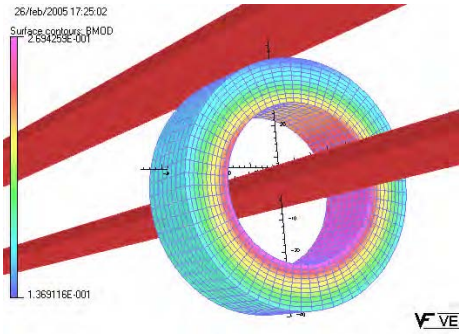

Fig 3. Simulation of the single circuit model with two conductor, $I_{CIN} = 150A$; $I_{CEX} = 300A$.

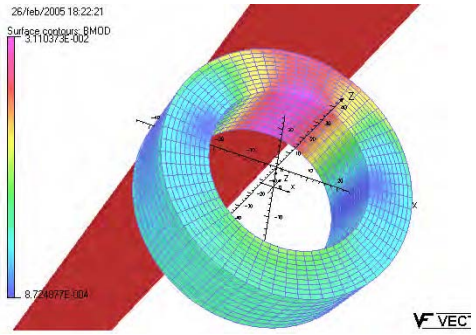

Fig 4. Influence or current near to conductor, $I_{CIN} = 0A$; $I_{CEX} = 300A$.

2. Comparison Between Methods Of Measuring Current

In this paragraph the different methods for current measurement analysed (based in the measure of the magnetic field) and the obtained results are described briefly. These methods present, as fundamental characteristic, the compensation of the crosstalk error associated to the influence of the currents in the vicinity of the sensor. For each one of the studied method, the error in the value of the current measured, originated by an angular positioning, will be determined. In this work the errors introduced by the sensors have not been taken into account, considering the sensors as ideals.

Sensor Array's [1]. Sensors are distributed uniformly around the circle whose centre is the centre of the rectangular conductor , see figure 5 A. Two arrays constituted by 4 and 8 sensors have been calculated and the uncertainties associated to the angular positioning of the sensors in each one of the two proposed systems have been determined. The angular rotation affects in the same way to all sensors, because they are mechanically fixed all together.

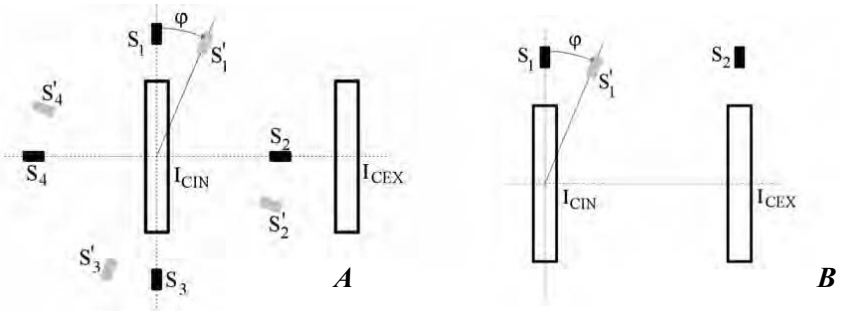

Fig 5. *Geometrical situation of the sensors in the studied cases:*
A) Method based in an array of 4 sensors. B) Method of linear equations

Linear Equation [2]. The sensors are situated parallel to the rectangular conductors. In this way the compensation is established by calculating, in analytical way, the influence of the magnetic field originated by the external current I_{CEX} in the measurement of the flux created by the current carried by the internal conductor I_{CIN}. So $\Phi_1 = aI_{CIN} + bI_{CEX}$, and for calculating the coefficients a and b is enough to calculate the contribution to the flux Φ_1 of each one of the currents I_{CIN} e I_{CEX}. The main advantage of this method is the easy implementation of the experimental setup. (See figure 5B)

Stable Point [3]. This method consist in situating the sensor in the point of intersection of the lines of the magnetic flux, as shown in the figure 2, obtained by the circulation of current in only one conductor ($I_{CEX} = 0$) and the existence of both currents ($I_{CEX} \neq 0$).This point has immunity with respect to modifications of the external current (all the curves converge in that point independently of the current carried by the external conductor). The main disadvantage of the method is that a previous numerical calculation of the point is needed. In our model this point is situated at $\varphi = 9{,}755^{o}$, as shown in the figure 5B, this position is related with the geometry of the model and the magnetical properties of the surroundings of the conductors and the torus. In the method of stable point only one sensor S'_1 is used.

The figure 6 represents the relative error produced by the different methods with respect to the angular position of the sensor. As can be appreciated the method more insensible to this position is the sensor array whose results are improved with the number of used sensors. Logic results because there is a better approximation to the Ampere's law. In fact with an array of 8 sensors the obtained errors are below of the estimated one's by the simulation program.
With respect to the rest, for $I_{CIN} = 2 \times I_{CEX}$ and considering a maximum admissible error of $\Delta\varepsilon = \pm 0{,}5\%$, case represented in the figure 6, it can be seen that the maximum angular variation associated to each model. The

method of linear equations has a margin of operation of $\varphi \leq +14{,}853^{o}$ while the method of the stable point allows a margin of $+8{,}180^{o} \leq \varphi \leq +30{,}285^{o}$.

The table I presents a comparison between the studied measurement methods, showing the maximum error ε_{MAX} and the ratio between the flux variation and the theoretical flux $\Delta\Phi/\Phi_T$ in the different methods. If this points to a better operation of the method of the linear equations in front of the method of the stable point, the bigger sensibility of the first method with respect to the variations of the external current originates that in practice the performance of both methods is comparable. In particular, with the same admissible error of $\Delta\varepsilon = \pm 0{,}5\%$ but in the case of $I_{CEX} = 2 \times I_{CIN}$, the angular position in the method of linear equations $-4{,}958^{o} \leq \varphi \leq +4{,}466^{o}$ is superior to the interval obtained for the method of the stable point $+9{,}314^{o} \leq \varphi \leq +16{,}497^{o}$.

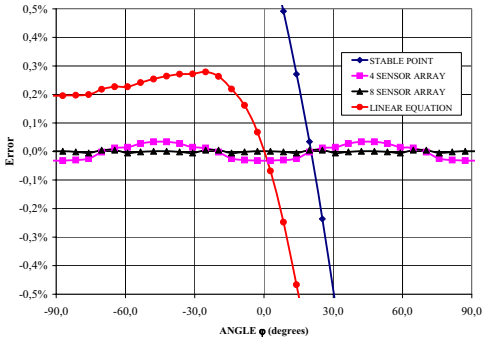

Fig 6. Current errors versus the angular position of the sensor for the different method, $I_{CIN} = 300A$; $I_{CEX} = 150A$.

RATIO CURRENT	$I_{CIN} = 2 \times I_{CEX}$; $I_{CIN} = 300A$	
THEORETICAL FLUX Φ_T	147,7602μWb	
PROCEDURES	$\Delta\Phi/\Phi_T$	MAXIMUM ERROR ε_{MAX}
SENSOR ARRAY (4 POINT)	0,068%	+0,034%
SENSOR ARRAY (8 POINT)	0,01%	+0,0051%
LINEAR EQUATION	4,29%	-4,0142%
STABLE POINT	4,31%	-3,192%

***Table I.** Comparison among the crosstalk compensation procedures.*

3. Conclusions

The present study contributes to improve the knowledge about the uncertainty sources in current measurements based on sensor or transducers. Furthermore, it explores the possibilities of using FEM simulations to reduce the experimental arrangements needed for calibrating these devices. Consequently this work is devoted to help the metrology authorities and instrumentation manufacturers to develop new rules for calibration devices and new procedures to characterize the precision of the equipment.

The computer simulations by FEM have allowed to estimate the errors associated to the magnetic flux in each studied method with respect to the ideal situation, analyzing in all cases the influence of the current in the measuring system. On the other hand, it is observed that this phenomenon is lower in the method based in sensor array [1] due to his axial symmetry (better approximation to a current transformer). But it is important to consider that this method is more expensive as higher is the number of sensors used in the array. This fact does not affect to the other two methods.

Acknowledgements

This paper has been developed with the financial support of the University of Zaragoza (Program 2001-02), Ibercaja (Research Program 2003) and the Diputación General de Aragón (Emergent Research Group 2004/2005).

References

[1]. Luca Di Rienzo, Renzo Bazzochi and Angelo Manara. "*Circular Arrays of Magnetic Sensors for Current Measurement*". IEEE Transactions on Instrumentation and Measurement, Vol. 50, nº 5, pp 1093 to 1096. October 2001.
[2]. P. Niewczas, W. Iain Madden, W. Craig Michie, A. Cruden and J.R. McDonald. "*Magnetic Crosstalk Compensation for an Optical Current Transducer*". IEEE Transactions on Instrumentation and Measurement, Vol. 50, nº 5, pp 1071 to 1075. October 2001.
[3]. M. Samplón, J.S. Artal, J. Letosa, A. Usón and F.J. Arcega "*Evaluation of Errors associated with Crosstalk Magnetic Fields using Finite Element Method in High Electrical Current Measurement*". Internacional Conference on Renewable Energy and Power Quality, ICREPQ 2005.
[4]. M. Imamura, M. Nakahara, T. Yamaguchi and S. Tamura. "*Analysis of Magnetic Fields due to Three-phase bus bar Current for the Design of an Optical Current Transformer*". IEEE Transactions on Magnetic, Vol. 34, nº 4, pp 2274 to 2279. July 1998.
[5]. J. Letosa, J. S. Artal, F. J. Arcega, M. Samplón, and A. Usón. "*Modelization of Current Sensors by Finite Elements Method*". Elsevier Science Ltd. Measurement, Vol 35, issue 3, pp 233 to 241. April 2004.

Electromagnetic Fields in Mechatronics, Electrical and Electronic Engineering
A. Krawczyk et al. (Eds.)
IOS Press, 2006

INFLUENCE OF THE SYNCHRONOUS CYLINDRICAL MACHINE DAMPING CAGE ON CONTENT OF HIGHER HARMONICS IN ARMATURE CURRENTS DURING CO-OPERATION WITH THE DISTORTED AND ASYMMETRICAL ELECTRIC POWER SYSTEM

Sławomir Wiak[1], Roman Nadolski [2], Krzysztof Ludwinek[2], Jan Staszak[2]

[1] Institute of Mechatronics and Information Systems, Lodz Technical University,
ul. Stefanowskiego 18/22, 90-924 Lodz, Poland, e-mail: wiakslaw@p.lodz.pl
[2] Chair of Electrical Machines, Kielce Technical University,
Al. 1000-Lecia P. P. 7, 25 – 134 Kielce, Poland
e-mail: r.nadolski@tu.kielce.pl, k.ludwinek@tu.kielce.pl, j.staszak@tu.kielce.pl

Abstract *- The paper presents the results of asymmetry influence of the first, fifth and seventh harmonics of power supply on contents of higher harmonics in armature currents in a cylindrical synchronous generator with and without damping cage. In calculations of the total armature currents the superposition method for the first, fifth and seventh higher harmonics of positive- and negative-sequence voltages have been used. Obtained in numerical calculations results have been confirmed in experimental verification.*

Introduction

Electromagnetic properties of a synchronous machine in large stage depend on presence of the damping cage. The dumping cage in dynamic states allows on shortening many transients' stages e.g. the hunting [3]. Determination of the damping cage influence on higher harmonic contents in armature currents in synchronous cylindrical generators is possible by means of magnitude and phase characteristics of synchronous machine spectral impedance. The way of validation of the frequency characteristics by means ot the standstill frequency response (SSFR) test has been described in paper [4].

Frequency characteristics of the magnitude $L_d(j\omega)$, $L_q(j\omega)$ and phase $\varphi_d(j\omega)$, $\varphi_q(j\omega)$ of the spectral impedance in d-axis and q-axis for two constructional rotor structures for the examined synchronous generator rated data as follows: $P_N = 8.5$ kW, $U_N = 380$ V (windings connected in star), $I_N = 15.25$ A, $n_N = 3000$ obr/min, $\cos\varphi_N = 0.85$ with and without damping cage are presented in Fig. 1 ÷ Fig. 4. Frequency characteristics of spectral impedance in d-axis with shorted field winding are presented in Figure 1. In d-axis, in case of synchronous machine harmonics voltage supplying with shorted field winding, it is visible the small difference in course of determined magnitude characteristics for the two constructional rotor structure: with damping cage and without damping cage. Obvious conclusion results from here, that for harmonics supply voltages the influence of the presence or lack of damping cage in relation to influences shunt of the field winding and solid iron of the rotor in d-axis is small. From the course of the phase – Fig. 1 in d axis, we can see that for higher frequencies dominates considerably the real over the imaginary part of the impedance. This means, that for examined synchronous machine, the phase angle between components of the currents and voltages for higher harmonics in d-axis is equal to about 10^odag. If to determined spectral impedance $L_d(j\omega)$ add the

resistance of armature winding, the phase angle between components of the currents and voltages for higher harmonics is smaller then 10^{o}dag.

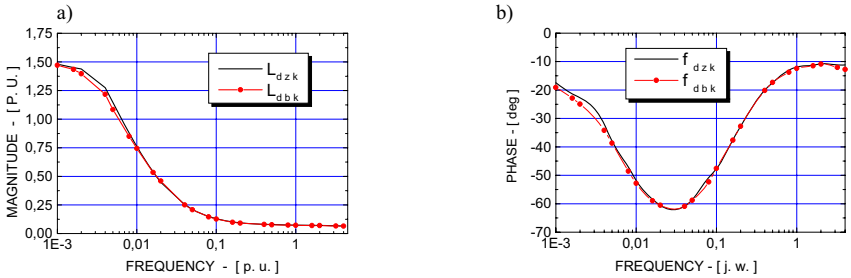

Fig. 1. Frequency characteristics of spectral impedance in d-axis with shorted field winding for the two constructional rotor structure: L_{dzk} – with damping cage, L_{dbk} – without damping cage a) magnitude, b) phase.

The courses of spectral impedance for two constructional rotor structure of examined synchronous machine in d-axis with open field winding $L_{d0}(j\omega)$ are presented in Fig. 2.

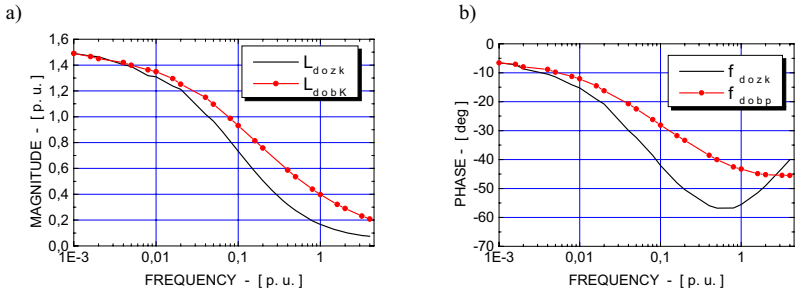

Fig. 2. Frequency characteristics of spectral impedance in d-axis for two constructional rotor structure with opened field winding L_{dozk} – with damping cage, L_{dobk} – without damping cage a) magnitude, b) phase

The courses of the spectral impedance $L_{d0}(j\omega)$ in d-axis for two constructional rotor structure with open field winding shows the large influence of shunting effect of the damping cage already for small frequencies.

From comparison of the shape of the spectral impedance courses in d-axis with shorted and opened field winding (shown in Fig. 1 and Fig. 2) we can state, that for higher frequencies of supply voltages the decrease of spectral impedance magnitude values get out of shunting influence of the damping cage, solid iron and field circuit.

In Fig. 3 the courses of spectral impedance frequency characteristics in q-axis are shown. For the higher frequency supply voltages similarly like in longitudinal axis also and in transverse axis the presence of the damping cage and solid iron decrease the magnitude values of the spectral impedance Fig. 3.a. From the course of the phase – Fig. 3.b in q-axis it is possibly to conclude, that for higher frequencies the ratio of the imaginary component to the real component of the spectral impedance is equal to 4. This means, that for examined synchronous machine, the phase angle between components of the currents and voltages for higher harmonics in q-axis is more then 30^{o} than in d axis.

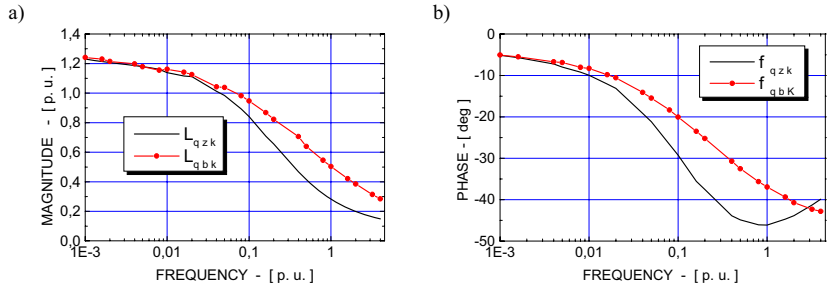

Fig. 3. Frequency characteristics of spectral impedance in q-axis for two constructional rotor structure: L_{qzk} – with damping cage, L_{qbk} – without damping cage a) magnitude, b) phase

In Fig. 4 the courses of spectral impedance frequency characteristics in d-axis are shown in conclusion of the courses in Fig. 1 ÷ Fig. 3: without damping cage and opened field winding L_{dobk}, with damping cage and opened field winding – L_{dozk}, with damping cage and shorted field winding – L_{dzk}.

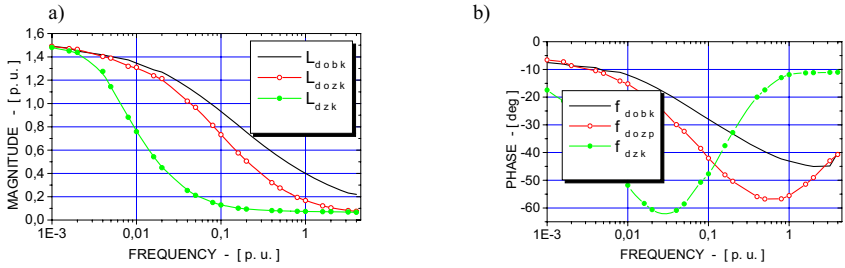

Fig. 4. Frequency characteristics of spectral impedance in d-axis a) magnitude, b) phase

The characteristics of the spectral impedance show, that both the constructional rotor structure as well as the way of damping circuits representation in equivalent electrical network have got large influence on cylindrical synchronous machine electromagnetic properties. The damping cage presence in the rotor slots causes: the decrease of spectral impedance magnitude as well as the decrease of minimum phase characteristic and its shift in direction of lower frequencies.

From the courses of magnitude characteristics of spectral impedance obtained with measurements taking into account the real rotor structure we can state, that for higher harmonics supply voltages greater than 50 Hz (harmonics order n > 1) it can be assumed that in d-axis $L_{dn} = L_d$" ($X_{dn} = X_d$" – sub-transient impedance in d axis). Whereas similar assumption in q-axis is possible only for the higher harmonics supply voltages greater than 350 Hz (harmonics order n > 7) in other words $L_{qn} = L_q$" ($X_{qn} = X_q$"- sub-transient impedance w q axis). For the frequency lower than 350 Hz assumption $L_{qn} = L_q$" causes considerable mistakes. For example with damping cage, the value L_{q2} for 100 Hz is equal to 0.19 [p. u.] but for 250 Hz – $L_{q5} = 0.12$ [p. u.].

From the shown courses of the spectral impedance magnitude characteristics we can see the difference between values of spectral impedance in d and q axes, it means that the investigated synchronous machine has got the considerable asymmetry of the magnetic circuit. The value of the impedance is equal to $L_d = 1.5$ [p. u.] and $L_q = 1.25$ [p. u.] respectively. We can see the difference between values of spectral impedance magnitude in d and q axes for frequency greater than 50 Hz. Difference between the values of the magnitudes and the asymmetry of magnetic circuit especially for 5 harmonics (250 Hz) and for 7 harmonics (350 Hz) have got an influence on the shapes of the armature current courses. Moreover, about shape of armature currents in examined synchronous machine for the frequency

supply voltages greater than or equal to 100 Hz, the shunting circuits of the damping cage and solid iron in d and q axes as well as shunting circuit of the field winding in d-axis have been decided.

Mathematical Modelling Of Synchronous Generator

Basing on the determined frequency characteristics shown in Fig. 1 ÷ Fig. 4, the distributed parameters equivalent circuit with and without damping cage has been calculated [5]. The value of the parameters were as follows:

- for the constructional structure of the rotor with damping cage: $R_a = 0.024$, $L_\sigma = 0.042$, $L_{ad} = 1.459$, $L_{aq} = 1.208$, $L_{ekd} = 0.0076$, $L_{ekq} = 0.038$, $R_{ed} = 0.021$, $R_{eq} = 0.025$, $R_{kd} = 0.190$, $R_{kq} = 0.399$, $R_f = 0.011$, $L_{f\sigma} = 0.038$, $T_{ed} = 0.026$, $T_{eq} = 0.010$.
- for the constructional structure of the rotor without damping cage: $R_a = 0.024$, $L_\sigma = 0.042$, $L_{ad} = 1.459$, $L_{aq} = 1.208$, $L_{ekd} = 0.0082$, $L_{ekq} = 0.026$, $R_{ed} = 0.025$, $R_{eq} = 0.023$, $R_{kd} = 1.497$, $R_{kq} = 2.12$, $R_f = 0.0105$, $L_{f\sigma} = 0.034$, $T_{ed} = 0.022$, $T_{eq} = 0.007$.

The time constants are in [s] but R, L parameters are in [p. u.] referred to the magnitude of synchronous generator rated impedance Z_N. The equivalent circuit parameters of the synchronous generator in d and q axes are shown in fig. 5.

a)

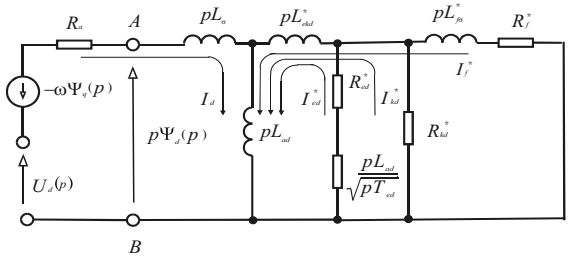

b)

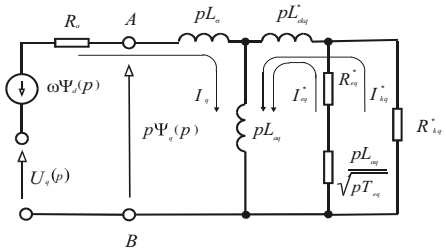

Fig. 5. Equivalent circuit parameters for the synchronous generator a) in d axis, b) in q axes

To calculate the armature currents in d and q axes coming from higher harmonic supply of positive-sequence voltages (1) and negative-sequence voltages (2) taking into account the equivalent circuit parameters shown in Fig. 5 is required as well as determination of higher harmonics voltages in longitudinal axis $u_{d(1,\,2)}(p_n)$ and in transverse axis $u_{q(1,\,2)}(p_n)$ and the values of the spectral impedance. Determination of the harmonics voltages $u_{d(1,\,2)}(p_n$ in d and $u_{q(1,\,2)}(p_n$ in q axes have been presented in [2]. The values of the spectral impedance are depended on the determined parameters of investigated synchronous generator, frequency and slips calculated for higher harmonic supply of positive- and negative-sequence voltages. Above mentioned dependencies in detail have been presented in [1, 2]. Influence of frequency of higher harmonic supply and taking into account the direction of rotor motion (with $\Omega_m = \omega_1$ = cons.) in relation to revolving of positive- and negative-sequence supply voltages

cause, that the values of spectral impedance (with rotor motion) can be determined taking into account the equivalent circuits shown in Fig. 5 and as well as through replacement in operator's place differentiation $p = jv\omega_1 = j\omega$ new operator $p_n = jn\omega_l \pm j\omega$. Whereas, for the slips of higher harmonic supply of positive-sequence voltages order 6N + 1 and negative-sequence voltages order 6N – 1 has been accepted $p_n = jn\omega_l - j\omega$. Moreover, for the slips of higher harmonic supply of positive-sequence voltages order 6N – 1 and negative-sequence voltages order 6N + 1 has been accepted $p_n = jn\omega_l + j\omega$.

Simulating Harmonics in Armature Currents for Synchronous Machines with and without Damping Cage

For the supply voltages measured in Laboratory of Electrical Machines in Kielce Technical University the calculations of armature currents with taking into account the mathematical model of the examined synchronous machine with and without damping cage have been carried out in Matlab. The rms harmonic values and the initial phase angles used in calculations are given in Tab. 1. In field circuit (Fig. 5) was added resistance R_{fd} = 0.0117 [p. u.]. The additional resistor has been used during experiment to adjust value of the field current equal to I_f= 3.35A and power angle ϑ equal to 0.5 rad.

Table 1. The rms harmonic values and the initial phase angles

Harmonics n	U_{An} [V]	φ_{uAn} [rad]	U_{Bn} [V]	φ_{uBn} [rad]	U_{Cn} [V]	φ_{uCn} [rad]
1	215.83	2.43	215.59	3.80	218.13	4.55
5	2.44	2.90	3.20	5.27	2.04	1.22
7	1.73	4.13	1.62	2.19	1.97	6.24

For the supply voltages given in Table 1, the armature currents for the individual harmonics positive- and negative-sequence supply voltages with and without damping cage have been calculated. The results of the simulations of armature current courses for the individual harmonics positive- and negative-sequence supply voltages are shown in Fig. 6.

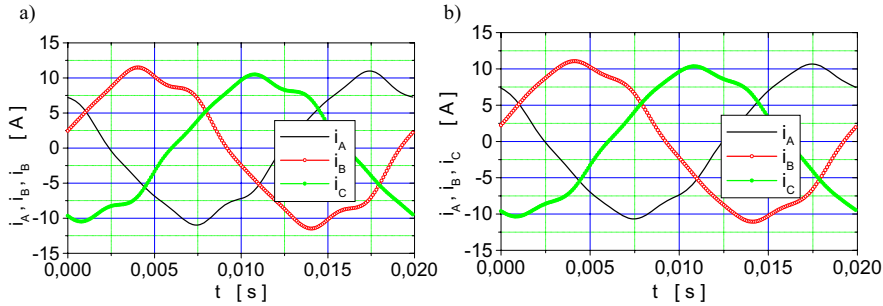

Fig. 6. Armature current courses for the individual harmonics positive- and negative-sequence supply voltages: a) with damping cage, b) without damping cage

The maximal value (amplitude) of individual harmonics in courses of armature currents shown in Fig 6, with damping cage are given in Table 2 and without damping cage are given in Table 3. Moreover, in Tables 2 and 3 are given IHD_{Ik} (Individual Harmonic Distortion) and THD_{Ik} (Total Harmonic Distortion).

Table 2. Individual harmonics in courses of armature currents with damping cage

Harmonics n	I_{mAn} [A]	I_{mBn} [A]	I_{mCn} [A]	IHD_{IA} [%]	IHD_{IB} [%]	IHD_{IC} [%]	THD_{IA} [%]	THD_{IB} [%]	THD_{IC} [%]
1	10.17	10.85	9.96	100	100	100	6.55	7.07	6.29
3	0.08	0.09	0.02	0.78	0.75	0.80			

5	0.59	0.71	0.52	5.80	6.54	5.22			
7	0.30	0.28	0.34	2.95	2.58	3.41			
9	0.006	0.006	0.006	0.06	0.05	0.06			

Table 3. Individual harmonics in courses of armature currents without damping cage

Harmonics n	I_{mAn} [A]	I_{mBn} [A]	I_{mCn} [A]	IHD_{IA} [%]	IHD_{IB} [%]	IHD_{IC} [%]	THD_{IA} [%]	THD_{IB} [%]	THD_{IC} [%]
1	10.21	10.73	10.04	100	100	100	3.82	4.11	3.81
3	0.06	0.06	0.02	0.55	0.52	0.21			
5	0.31	0.39	0.30	3.06	3.56	2.96			
7	0.23	0.21	0.25	2.22	1.98	2.39			

Removing the damping cage cause reduction about 48% harmonic contents in courses of armature currents. Percentage participation of 3, 5, 7 and 9 harmonic in armature currents in individual phases k = A, B and C with damping cage (index zk) without damping cage (index bk) are shown in Fig. 7.

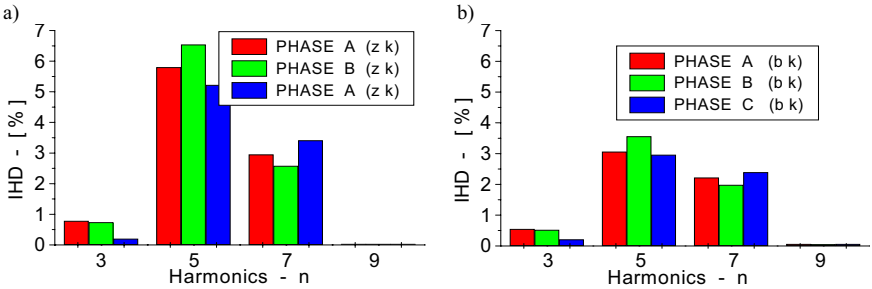

Fig. 7. Percentage participation of 3, 5, 7 and 9 harmonic in armature currents: a) with damping cage, b) without damping cage

From carried out simulations result, that during supplying 5 and 7 harmonic positive- and negative-sequence and 1 harmonic negative-sequence supply voltages without damping cage, in armature current courses decease of participation of 3, 5, 7 and 9 harmonic positive- and negative-sequence harmonics. In individual phases of armature currents also decrease THD_{Ik} The decrease of THD_{Ik} (without damping cage) is due to increase of investigated synchronous generator impedance for higher harmonics (Fig. 1 ÷ Fig. 4).

Experimental Verification

Registration of steady–state phase current waveforms for the examined synchronous generator ($\omega = \omega_1 = \text{const}$) in the individual phases of armature windings in case of the co-operation between the synchronous generator and the distorted and asymmetrical electric power system taking into account the real rotor structure (damping cage, solid iron and field winding) has been carried out. The generator rated data were as follows: $S_N = 10$ kVA, $U_N = 380$ V (Y), $n_N = 3000$ r/min, $\cos\varphi_N = 0.85$, $\Delta P_N = 940$W. The field winding was supplied by means of battery of accumulators and additional resistance R_{fd} to adjust value of the field current equal to $I_f = 3.35$A and power angle ϑ equal to 0.5 rad, what corresponds to the simulations. Registered courses of armature currents are shown in Fig. 8.a. In Fig. 8.b are shown the results obtained from theoretical analysis. Fig. 8.b is presented to compare the simulations to the real time courses presented in Fig. 8.a.

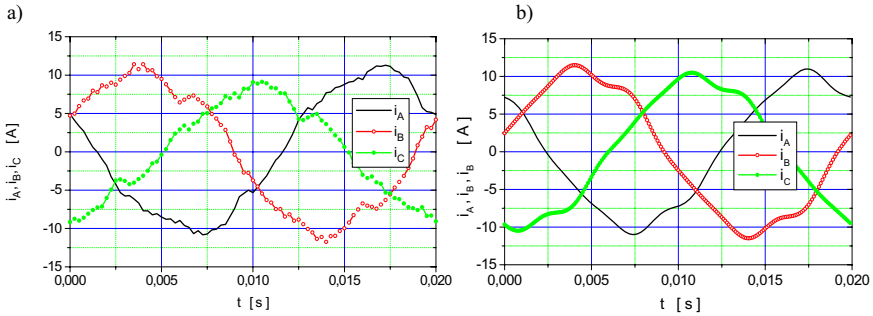

Fig. 8. Armature current courses: a) registered in measurement set, b) obtained in simulations.

Analysis of individual harmonic contents in the courses obtained in theoretical and experimental verification with the help of Fouriera's series has been carried out. The most important contents harmonic, which appear in registered courses are given in Table 4, while calculated theoretically in Table 5. Moreover, in Table 4 and Table 5 harmonics participation IHD_{Ik} in individual phases in relation to armature current fundamental components (fundamental harmonic) is compared. Whereas, THD_{Ik} only for harmonics given in Table 4 and Table 5 is calculated.

Table 4. The most important contents harmonic in registered courses

Harmonics n	I_{An} [A]	I_{Bn} [A]	I_{Cn} [A]	IHD_{IAn} [%]	IHD_{IBn} [%]	IHD_{ICn} [%]	THD_{IA} [%]	THD_{IB} [%]	THD_{IC} [%]
1	7.34	7.62	6.55	100	100	100			
3	0.11	0.11	0.07	1.50	1.44	1.07			
5	0.40	0.59	0.41	5.45	7.74	6.26	6.22	8.53	7.65
7	0.19	0.25	0.28	2.59	3.28	4.27			
9	0.004	0.004	0.004	0.05	0.05	0.06			

Table 5. The most important contents harmonic calculated theoretically

Harmonics n	I_{An} [A]	I_{Bn} [A]	I_{Cn} [A]	IHD_{IAn} [%]	IHD_{IBn} [%]	IHD_{ICn} [%]	THD_{IA} [%]	THD_{IB} [%]	THD_{IC} [%]
1	7.19	7.67	6.89	100	100	100			
3	0.06	0.06	0.02	0.83	0.78	0.29			
5	0.40	0.55	0.37	5.56	7.17	5.37	6.33	7.76	6.41
7	0.21	0.22	0.24	2.92	2.87	3.48			
9	0.004	0.004	0.004	0.05	0.05	0.06			

Comparison of individual contents 3, 5, 7 and 9 harmonics in armature currents registered in measurement set and obtained in simulations are presented in Fig. 9.

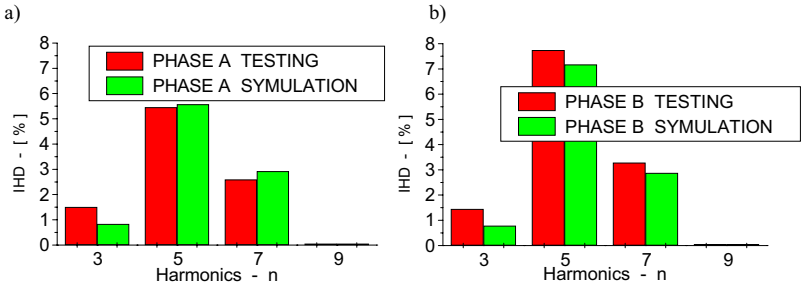

c)

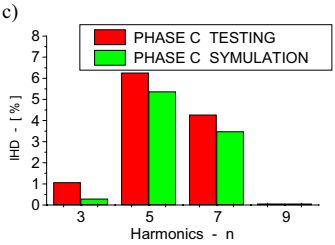

Fig. 9. Comparison of individual contents 3, 5, 7 and 9 harmonics in armature currents registered in measurement set and obtained in simulations

In presented comparison of harmonic contents in armature currents we can state large convergence among harmonic contents obtained in simulations and in measurement set. It confirms usefulness of frequency characteristics and on the base of the characteristics determined equivalent circuit parameter with distributed parameters in analysis of harmonic contents in armature currents for different constructional rotor structures. For construction of rotor structure without damping cage, the experimental verification have not been conducted because of large convergence among values of harmonics obtained in simulations and in measurement set (for construction of rotor structure with damping cage).

Conclusion

The paper presents simulations of constructional rotor structure influence on content of higher harmonics in armature currents in a cylindrical synchronous generator with and without damping cage. Simulations of the armature current courses for the asymmetry of the first, fifth and seventh harmonics of power supply have been carried out. From conducted simulations in the paper results, that removing the damping cage causes reduction about 48% contents of harmonics in armature current courses. It means, that the stronger influence of the damping cage the higher contents of harmonics in armature currents for the same values of power supply voltages. Because all synchronous machines are equipped with damping cage, therefore it is necessary limitation of harmonics amplitude in power supply.

References

[1] Ludwinek K.: Model of synchronous machine for co-operation with distortion and asymmetrical electric power system (in Polish). Kielce Technical University. Elektryka 42 2005, Poland

[2] Ludwinek K., Nadolski R., Staszak: J. Nonsinusoidal and asymmetrical influence of electric power system on field voltages and currents waveforms of synchronous machine (in Polish). 39th International Symposium on Electrical Machines, SME'2003, Gdańsk-Jurata, Poland.

[3] Nadolski R. Transient states modelling in turbogenerator with taking into account reaction of solid iron (in Polish) Monograph. ZN Kielce Technical University, 1998, Poland.

[4] Nadolski R., Staszak J., Ludwinek K.: Evaluation of electric machinery parameters by standstill frequency response test (in Polish). Metrology and measuring systems, Vol. V, No. 3 1998, Poland.

[5] Nadolski R., Staszak J., Ludwinek K.: Influence of damping cage on magnitude and phase characteristics of synchronous machine spectral impedance (in Polish), 35th International Symposium on Electrical Machines, SME'1999, Kazimierz Dolny, PNPW No. 111, Poland.

[6] Nadolski R., Staszak J.: Equivalent circuit analysis of solid rotor turbogenerator. Archives of Electrical Engineering, Vol. XLIII, No. 2, 1994, Poland.

[7] Muszyński R., Load limit for AC machines, transformers and lines due to the nonsinusoidality (in Polish). IX International Symposium PPEE'2000 – Wisła, Poland.

Electromagnetic Fields in Mechatronics, Electrical and Electronic Engineering
A. Krawczyk et al. (Eds.)
IOS Press, 2006

ANALYSIS OF PROXIMITY LOSSES IN A BRUSHLESS PERMANENT MAGNET MOTOR

Rafal Wrobel, Phil Mellor, Neville McNeill

University of Bristol, Department of Electrical and Electronic Engineering, Merchant Venturers Building, Woodland Road, Bristol, BS8 1UB, UK, P.H.Mellor@bristol.ac.uk, R.Wrobel@bristol.ac.uk

***Abstract* – This paper presents a finite element investigation into the proximity losses in brushless AC permanent magnet motors used in hybrid/electric vehicle applications. The proximity effect in winding conductors is as a result of eddy-currents caused by magnetic fields generated by nearby conductors. This paper considers the influence of the conductor shape and disposition on the losses for a given stator lamination. Several structures of the winding are analysed and compared in respect to the loss and AC resistance. The analysis shows that the proximity losses can be significantly reduced through an appropriate choice of conductor shape and winding technique. An experimental winding test bench is used to validate the calculated results.**

Introduction

The output power of an electrical machine is ultimately limited by the maximum temperature of the windings. To realise a high output for a given frame size it is necessary to both reduce the level of copper loss and improve the thermal path between the winding and the external coolant. The copper loss can be reduced by increasing the volume of copper in the winding (packing factor). In practice the choice of conductor size and the winding physical layout can significantly influence the overall loss, particularly at high speeds where eddy current effects are more prominent. There are two different phenomena that contribute to the total eddy-current losses: the skin effect and the proximity effect. The skin effect is the tendency for high-frequency currents to flow on the surface of a conductor and can be mitigated through the use of smaller conductor strands. The proximity effect is the tendency for current to flow in other undesirable patterns that form localised current loops or concentrated distributions due to the presence of a magnetic field generated by nearby conductors [1-4]. Both of these are well-known current-displacement effects within electrical machines. However, little attention has been paid to considering proximity effects in brushless permanent magnet machines. Whilst the effect is often mitigated through the use of multi-stranded Litz wire, this has its own drawbacks as a result of the relatively poor thermal performance, low packing factor and high cost. In brushless AC traction motors used in hybrid/electric vehicle applications these effects can be considerable and are a consequence of the high maximum operating frequencies and the high levels of slot leakage flux present in typical high specific output designs. This paper presents an analysis of proximity losses through the use of the finite element method (FEM) where each conductor is coupled via an external circuit. The calculations are carried out for a worst case condition – a winding short circuit at maximum rotational speed – and are representative of a machine operating in the field weakened regime. Several winding structures are analysed and compared in respect to the loss and AC

resistance. The calculated results show that the proximity losses can be significantly reduced using selected profiles of copper wire and winding techniques.

Prototype motor used in the investigation

The research has been applied to the design of a surface-mounted brushless traction permanent magnet motor for a hybrid vehicle application. To minimise the overall system weight the machine is required to operate at a high speed. The basic structure of the original motor is shown in Fig. 1 and comprises a concentrically wound twelve-slot stator and an eight-pole rotor magnetisation. In the original design a high copper packing factor is realised through the use of a segmented stator construction and a multi-stranded parallel winding.

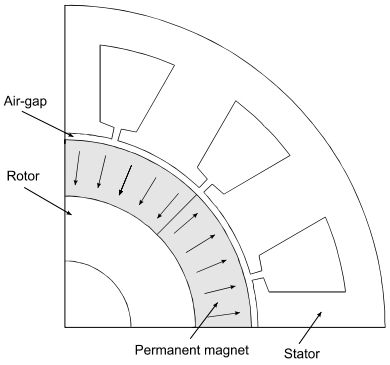

Fig. 1. Structure of the traction motor

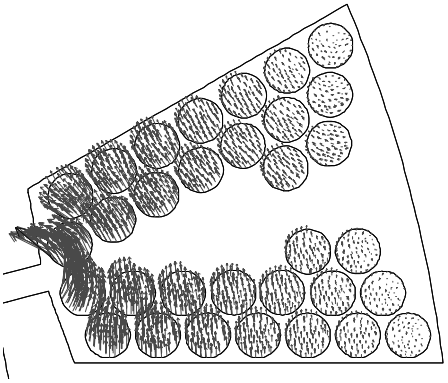

Fig. 2. Circulation of the magnetic flux in the motor winding (short-circuit, n = 6000rpm)

FEM analysis

The analysis of the proximity loss is carried out using a two-dimensional discrete time step finite element (FE) method where each conductor is coupled via an external circuit. Due to symmetry the calculation area is limited to one quarter of the motor cross-section (see Fig. 1). The conductor currents are solved for a winding short circuit over a range of rotor speeds. This short circuit is a worst case condition and is representative of a machine operating in the field weakened regime. Several winding structures are analysed and compared in respect to the loss and AC resistance. The power loss in the winding regions is determined from the Joules loss from which an equivalent bulk value of the AC winding resistance is found:

$$P = \rho \iiint_V J^2 dV = l\rho \iint_S J^2 dS = R_{ac} i_{rms}^2 \tag{1}$$

where: R_{ac} is the AC resistance and i_{rms} is the RMS value of the short-circuit current.

Results

Fig. 2 illustrates an example of circulation of the magnetic flux in the winding during a short-circuit. The distribution of the magnetic flux causes eddy-currents, which circulate in a direction parallel to the motor axis. The highest eddy-currents are induced close to the tooth opening. Fig. 3 presents the winding layouts initially assumed in the analysis. The copper packing factor for each winding version is fixed at 50%. The baseline configuration, winding version I, is representative of a standard mush winding comprising 7 parallel conductor strands wound onto the tooth 'in-hand'. Table 1 compares the FE calculated eddy-current losses for the different winding layouts. The losses are lowest when the conductors are located towards the rear of the slot (see Figs. 3c) and 3e)) and when the conductor height is minimal in the radial direction, Fig. 3f. The extent of the proximity effect can be deduced from the distribution of the magnetic flux local to the conductors, i.e. is greatest in the conductors that are placed close to the slot opening, Fig. 2.

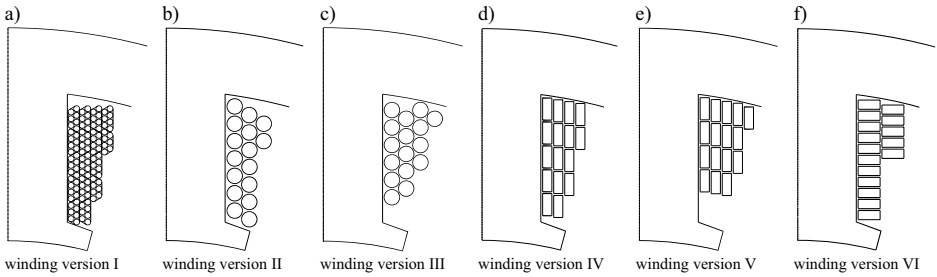

Fig. 3. Winding layouts considered: a) baseline 7-strands of parallel conductors wound uniformly around the tooth; b) single round conductor; c) single round conductor concentrated at rear of slot; d) bar conductor; e) bar conductor concentrated at rear of slot; f) bar conductor with a different orientation

Table 1 Relative power losses and R_{ac}/R_{dc} calculated for short-circuit condition (n = 6000rpm, f = 400Hz)

Winding version	I	II	III	IV	V	VI
$\Delta P_i/\Delta P$	1.00	0.54	0.34	0.81	0.62	0.30
R_{ac}/R_{dc}	7.62	4.10	2.94	6.97	5.90	2.66

R_{dc} is the DC resistance, R_{ac} is the AC resistance, which can be calculated form Joule's losses (1), ΔP_i is power losses for i-th winding version, ΔP is power losses for baseline winding version

Based on the initial findings, four new winding configurations were proposed, Fig. 4. In each case the conductors are located towards the rear of the slot and the effective conductor height is limited in the radial direction by use of parallel rectangular conductors. Two copper fill factors are compared, 32% and 48%, based respectively upon 2- and 3-parallel stranded rectangular conductors. Additionally the benefit of transposing the conductors between coil layers was investigated (winding versions IX and X).

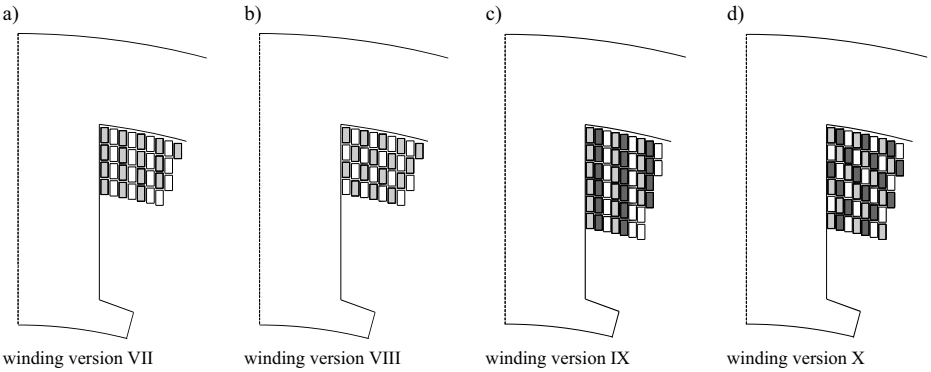

Fig. 4. Winding layouts: a) 2 parallel conductors; b) 2 parallel conductors transposed between layers; c) 3 parallel conductors; d) 3 parallel conductors transposed between layers

Table 2 Relative power losses and R_{ac}/R_{dc} calculated for short-circuit condition (n = 6000rpm, f = 400Hz)

Winding version	VII	VIII	IX	X
$\Delta P_i/\Delta P$	0.26	0.25	0.33	0.27
R_{ac}/R_{dc}	1.48	1.42	2.55	2.06

R_{dc} is the DC resistance, R_{ac} is the AC resistance, which can be calculated form Joule's losses (1), ΔP_i is power losses for i-th winding version, , ΔP is power losses for baseline winding version

Table 2 compares the FE calculated losses for the new winding layouts. It is shown that the proposed winding techniques give significant reductions in high frequency losses compared to the initial windings considered. The improvement gained through transposition of the conductors is relatively small and does not warrant the additional winding complexity. The lowest proximity losses occur in winding version VIII, Fig. 4a. However if it is desirable to maintain the same fill factor as the original baseline winding to achieve a low DC resistance, winding version X, Fig. 4b, may be preferred. To validate the computed results an experimental bench was constructed, Fig. 5. As rewinding a complete prototype machine would be expensive and time consuming, the measurements were confined to a single wound tooth. Two further stator segments were placed on either side to replicate the true slot profile, fig 5a, and the influence of the rotor was assumed to be negligible.

a) b) c)

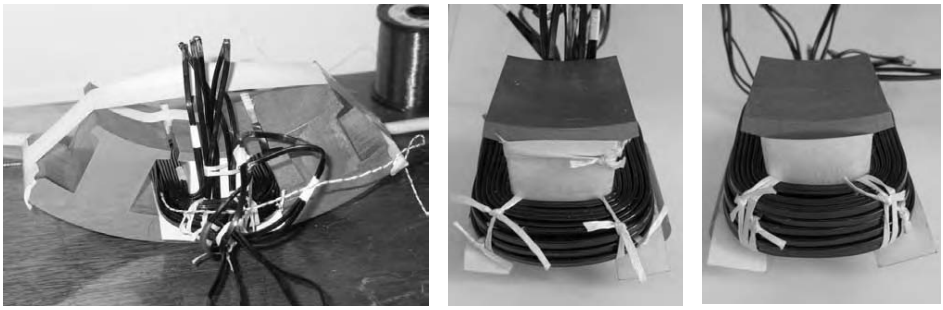

Fig. 5. The experimental bench: a) 3-tooth sector of the stator with wound coil; b) single tooth with 2-strands of parallel conductors; c) single tooth with 3-strands of parallel conductors

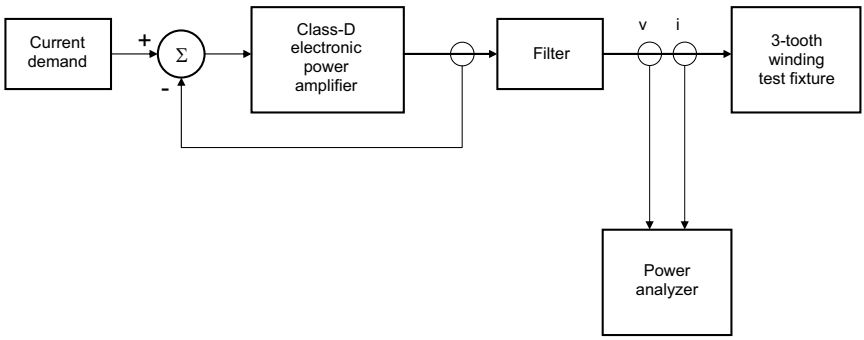

Fig. 6. Schematic of electrical system of the winding test rig

The circuit shown in Fig. 6 was used to measure the resistances of the different winding configurations. A class-D power amplifier under closed-loop current control and switching at a carrier frequency of 12kHz was used to energise the winding under test with a sinusoidal current waveform of variable frequency and magnitude. The current, voltage and power were measured using a high bandwidth power analyser, therefore allowing the change in resistance with frequency to be determined.

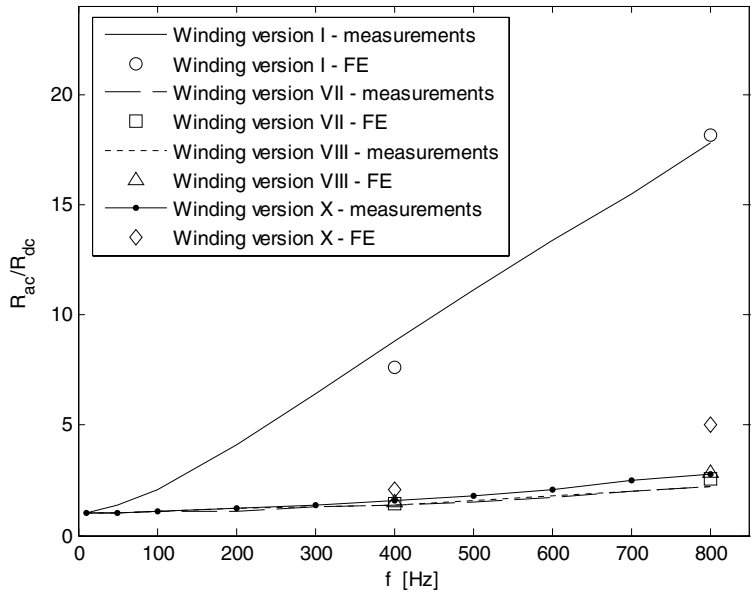

Fig. 7. R_{ac}/R_{dc} ratio vs. current frequency

The measured proximity effect is presented in Fig. 7 and is compared against the FE analyses. Whilst the use of a 2D FE analysis does not address end winding effects, which would be expected to be prominent considering the short lamination stack length here, the measured and the modelled results indicate very simlar trends. The benefit of the improved winding layouts can be clearly seen.

Conclusions

An investigation into the proximity losses in brushless AC permanent magnet motors used in hybrid/electric vehicle applications has been presented in this paper. The proximity effect in winding conductors is as a result of eddy-currents caused by magnetic fields generated by nearby conductors and is significant in these machines. For example, a 15 - fold increase in resistance over the motor operating speed range was observed in a winding comprising 7 parallel strands wound 'in-hand' onto the tooth using standard manufacturing methods. Several alternative winding layouts are compared using discrete time step 2D FEM with respect to fill factor and AC resistance. It is shown that the proximity effect can be significantly reduced with an appropriate arrangement of conductors and is minimised by locating the conductors towards the rear of the slot and minimizing height in the radial direction of the parallel conductor bundle forming each turn. The FEM analysis has been validated through measurements taken from a custom test bench.

References

[1] C. E. Carstensen, S. E. Bauer, R.B. Inderka, R. W. De Doncker, Efficiency Comparison of Different Winding Configurations for Switched Reluctance Vehicle Propulsion Drives, 20th International Electric Vehicle Symposium (EVS-20), Long Beach, USA, 2003

[2] C. R. Sullivan, Optimal Choice for Number of Strands in a Litz-Wire Transformer Winding, IEEE Trans. in Power Electronics, Vol. 14, No. 2, pp. 283 – 291, March 1999

[3] P. N. Murgatroyd, Calculation of proximity losses in multistranded conductor bunches, IEE Proceedings, Vol. 136, No. 3, pp. 115 – 120, May 1989.

[4] A. W. Lotfi, F. C. Lee, Proximity Losses in Short Coils of Circular Cylindrical Windings, 23rd Annual IEEE Power Electronics Specialists Conference, Vol. 2, pp. 1253 – 1260, June 1992.

Electromagnetic Fields in Mechatronics, Electrical and Electronic Engineering
A. Krawczyk et al. (Eds.)
IOS Press, 2006

Author Index

This page intentionally left blank

This page intentionally left blank

This page intentionally left blank